Bond, crack width and deflection in non-metallic textile reinforced concrete structures

Von der Fakultät für Bauingenieurwesen der
Rheinisch-Westfälischen Technischen Hochschule Aachen
zur Erlangung des akademischen Grades eines Doktors der Ingenieurwissenschaften
genehmigte Dissertation

vorgelegt von

Christopher Marvin Schmidt

Berichter:	Univ.-Prof. Dr.-Ing. Dr.-Ing. E.h. Josef Hegger
	Univ.-Prof. Dr.-Ing. Martin Claßen
	Univ.-Prof. Dr.-Ing. Dr.-Ing. E.h. Manfred Curbach

Tag der mündlichen Prüfung: 26.01.2026

Diese Dissertation ist auf den Internetseiten der Universitätsbibliothek online verfügbar.

Kurzfassung

Die Verwendung von nichtmetallischer textiler Bewehrung ermöglicht die Realisierung schlanker Betonbauteile, die sich durch hohe Tragfähigkeit, niedrigen Materialverbrauch und Korrosionsbeständigkeit auszeichnen. Aufgrund der damit verbundenen geringen Betondeckung sind bei Ausnutzung der hohen Zugfestigkeit der nichtmetallischen Bewehrung häufig die Nachweise zur Begrenzung der Rissbreite und Durchbiegung im Gebrauchszustand maßgebend. Dabei stellt insbesondere das unterschiedliche Verbundverhalten der textilen Gitterbewehrungen aufgrund der Materialvielfalt und individuellen Formgebung eine große Herausforderung bei der Herleitung von Modellen und Ansätzen zur Rissbreitenprognose dar. Für Biegebauteile werden außerdem zuverlässige Modelle zur Ermittlung der Durchbiegung benötigt, die auch die Mitwirkung des Betons im Zugbereich (Tension Stiffening) zutreffend erfassen müssen, wenn das Potential der hochfesten nichtmetallischen Bewehrung ausgeschöpft werden soll. Physikalisch basierte Modelle zur Ermittlung von Rissbreite und Durchbiegung bei Bauteilen mit nichtmetallischer textiler Bewehrung bieten hier die Möglichkeit einer hohen Zuverlässigkeit und sind gleichzeitig für die unterschiedlichen Materialien und Formen der textilen Gitterbewehrung anwendbar.

Die Grundlage zur Herleitung eines physikalisch basierten Modelles zur Rissbreitenprognose bilden experimentelle Untersuchungen, die eine umfassende Charakterisierung des Verbundverhaltens in Abhängigkeit von Querschnittsform, Oberflächenstruktur und Steifigkeit der textilen Gitterbewehrung erlauben. Anhand von Rissöffnungsversuchen (crack opening tensile tests) und deren Analyse unter Verwendung von faseroptischer Messtechnik wird eine analytische Beziehung zur Beschreibung der Rissöffnung in Abhängigkeit der maßgeblichen Einflüsse von Bewehrungsspannung, Bewehrungsgrad und Verbundverhalten abgeleitet. Unter Berücksichtigung von Tension Stiffening unterscheidet der Ansatz zwischen Einzelrissbildung und abgeschlossener Rissbildung und erfasst so die maßgebenden Charakteristika der unterschiedlichen textilen Bewehrungen. Die Erweiterung des Modells zur Rissbreitenprognose anhand von statischen und zyklischen Dehnkörperversuchen, ermöglicht die Berücksichtigung des Einflusses mehrlagiger Bewehrung durch den Ansatz einer effektiven Verbundfläche, da nicht die gesamte Oberfläche der einzelnen Bewehrungsstränge bei der Übertragung der Verbundkräfte mitwirken. Außerdem wird der Einfluss der Querschnittsform der Bewehrungsstränge auf den Rissabstand durch einen Geometriefaktor erfasst. Somit werden die ungleichmäßigen Spannungskonzentrationen der elliptischen Querschnitte berücksichtigt, die auch zu Spaltrissen führen können. Mit dem Modell lässt sich auch die Zunahme der Rissbreite infolge zyklischer Beanspruchung zutreffend prognostizieren.
Die Validierung des Modelles anhand der Dehnkörperversuche und die nachgewiesene Übertragbarkeit auf Biegebauteile anhand von 4-Punkt-Biegeversuchen ermöglicht zudem Vergleiche mit den verschiedenen Bemessungskonzepten zur Rissbreitenprognose der DAfStb-Richtlinie und des zukünftigen Eurocodes 2. Die Auswertungen verdeutlichen die höhere Leistungsfähigkeit des neuen Modellansatzes. Die Methodik zur analytischen Beschreibung der Verbundspannung unter Verwendung von Rissöffnungsversuchen ermöglicht es, das physikalisch basierte Modell zur Rissbreitenprognose in Betonbauteilen für beliebige nichtmetallische textile Bewehrungen anzupassen.

Zur genaueren Bestimmung der Biegeverformung von nichtmetallisch bewehrten Bauteilen wird abschließend ein Verfahren aufgezeigt, das neben einer iterativen Ermittlung der Querschnittskrümmungen die Einflüsse aus Tension Stiffening erfasst. Die Leistungsfähigkeit des Modells wird anhand der Biegeversuche bestätigt, das auch den Verformungszuwachs infolge zyklischer Belastung zutreffend abbildet, der neben dem Betonkriechen in der Druckzone vor allem auf den Verlust der verstiefenden Wirkung aus Tension Stiffening zurückzuführen ist. Das entwickelte Modell ermöglicht folglich die praxisnahe Bestimmung der Biegeverformungen unter statischen und zyklischen Beanspruchungen.

Abstract

Non-metallic textile reinforcement enables the construction of slender concrete structures, characterised by increased structural capacity, reduced material consumption and inherent corrosion resistance. The slender design featuring a thinner concrete cover, combined with the utilisation of the high tensile strength of non-metallic reinforcement, has directed greater focus towards limiting crack width and deflection at the serviceability state, as both often govern the design. In particular, the considerable diversity in bond behaviour exhibited by textile grids, arising from differences in both materials and geometries, poses a significant challenge when developing models and approaches. For flexural members, reliable models are required to predict the deflection, which must adequately capture the effects of tension stiffening to fully exploit the potential of high-strength non-metallic reinforcement. Therefore, physically based models for determining crack width and deflection in members with non-metallic textile reinforcement are required, which are reliable and also applicable across a wide range of textile reinforcement materials and geometries.

To derive a physically based model for predicting crack widths, a comprehensive characterisation of the bond behaviour is initially performed, addressing cross-sectional geometry, surface and stiffness of the textile girds. Based on crack opening tensile tests and their analysis using fibre optic measurements, a model is derived that describes the evolution of crack opening in relation to reinforcement stress, reinforcement ratio and bond behaviour, while accounting for tension stiffening. This approach, which distinguishes between single cracks and stabilised cracking, enables the identification of the relevant characteristics for various non-metallic textile reinforcements. The model for crack width prediction is expanded and validated using uniaxial tensile tests. In the case of multiple reinforcement layers, the capacity of bond stress is reduced by introducing an equivalent circumference, as the whole bond area does not fully contribute to the force transfer. Furthermore, the influence of the elliptical cross-sectional geometry of the fibre strands on the crack spacing is captured by a geometrically based stress-intensifying factor. This addresses the influence of the uneven multi-axial tensile stress state in the concrete, which also provokes splitting cracks. The model is also capable of accurately predicting the increase in crack width resulting from cyclic loading.
Comparisons between the proposed model and the design concepts for crack width prediction in the German DAfStb Guideline and the Final Draft of the Preliminary Eurocode 2, considering uniaxial tension and flexural loading, demonstrate the improved performance of the new model approach. The methodology of using crack opening tensile tests in conjunction with the analytical approach of the bond stress-crack opening relation enables the physically based model to be adapted for predicting crack widths in concrete members with any type of non-metallic textile reinforcement.

Finally, to more accurately determine the deflection of members with non-metallic reinforcement, a method is presented that adequately captures the effects of tension stiffening by iteratively calculating the cross-sectional curvatures. Validation of the model using four-point bending tests also confirms that the increase in deflection due to cyclic loading is primarily attributable to the loss of tension stiffening, in addition to concrete creep in the compression zone. The derived method thus enables the practical determination of deflections under static and cyclic loads.

Preface and acknowledgements

This thesis would not have been possible without the support I received during my time as a research assistant at the Institute of Structural Concrete at RWTH Aachen University, for which I would like to express my sincere thanks to all those involved. The financial support for the experimental program was provided by the German Federal Ministry for Economic Affairs and Climate Action within the framework of the technology transfer program “Lightweight Structures”, which is gratefully acknowledged.

Foremost, I would like to express my sincere gratitude to my supervisor, Univ.-Prof. Dr.-Ing. Dr.-Ing. E.h. Josef Hegger, former head of the Institute of Structural Concrete, for encouraging me to pursue this doctorate. Besides teaching me the “traditional” skillset of practical research, he gave me the opportunity to develop personally and professionally. These included coordinating research projects, managing the editorial office of the peer-reviewed journal “Der Bauingenieur”, lecturing courses and working in code provisional committees. I am particularly grateful for the trust he placed in me to conduct my research and manage projects and responsibilities independently. I would also like to thank Univ.-Prof. Dr.-Ing. Martin Classen, current head of the Institute of Structural Concrete, for enabling me to complete my research and this thesis, as well as for acting as reviewer of this work. Furthermore, I am grateful to Univ.-Prof. Dr.-Ing. Dr.-Ing. E.h. Manfred Curbach, former head of the Institute of Structural Concrete at TU Dresden, for reviewing my thesis and serving as co-examiner. Finally, I would like to thank Univ.-Prof. Dr.-Ing. Sven Klinkel, Dean of the Faculty of Civil Engineering, for presiding over the examination committee.

I am deeply grateful to my friends and colleagues for creating a supportive personal and professional environment during my time as researcher and throughout all stages of this thesis. My time at the institute would undoubtedly have been less diverse and less enjoyable without them, and the friendships formed are of the utmost value to me. With this in mind, special thanks go to Jan Ungermann, Georgios Christou, Jan Philip Schulze-Ardey, Sven Engel and Henrik Becks. Beyond their professional input, it was the personal conversations and shared experiences that made my time during the last six years considerably more enjoyable. I would also like to thank Annkathrin Sinning, Eduarda Dilkin, Christian Dommes and Till Janiak for the professional discussions and the personal exchanges we shared during our time working together. I am highly grateful to the student assistants, as well as the bachelor’s and master’s students, who assisted me during my experimental program and contributed substantially to this research. My sincere thanks also go to the laboratory staff for their support in carrying out the various experimental campaigns.

This work, and all the steps and developments that preceded it, would not have been possible without the support and encouragement of my family. They have my deepest gratitude. In particular, I would like to thank my parents for their unconditional and unwavering support. Their guidance, confidence, trust, and love throughout my life – and the knowledge that I can always rely on them – have formed the foundation of my personal development and, ultimately, the completion of this work.

Aachen, April 2026 Christopher Schmidt

Table of contents

1 Introduction 1
2 State of the art 5
2.1 General remarks 5
2.2 Non-metallic reinforcement in concrete members 6
2.3 Matrices 9
2.4 Bond behaviour of reinforced concrete 10
2.4.1 Force transfer mechanisms 10
2.4.2 Cyclic and sustained loading 12
2.4.3 Methodologies to describe the bond behaviour 15
2.4.4 Differentiation between rebars and textile grids 17
2.4.5 Experimental setups to describe the bond behaviour 18
2.5 Cracking in reinforced concrete members 21
2.5.1 Origins of tension to provoke cracking 21
2.5.2 Strain evolution regarding the cracking stage 24
2.5.3 Analytical consideration of local behaviour 25
2.5.4 Effective reinforcement area 29
2.6 Concepts to predict the crack width 30
2.6.1 Approach of KOENIG and TUE 32
2.6.2 Deformation compatibility for restrained members 32
2.6.3 Code provisions for crack width limitation 33
2.7 Deflection 37
2.8 Summary 39
3 Investigations to characterise the bond behaviour 41
3.1 Overview of the experimental campaigns 41
3.2 Investigated textile reinforcement 41
3.3 Characterisation using single-sided pull-out tests 43
3.3.1 Concept of the experimental campaign 43
3.3.2 Failure types and utilisation of pull-out force 44
3.3.3 Pull-out force related to occurring slip 48
3.4 Capacity of textile grids to regulate crack opening 51
3.4.1 Experimental representation of crack opening 51
3.4.2 Force transfer in relation to the crack opening 53
3.4.3 Influence of concrete tensile strength on the crack opening 56
3.4.4 Increase in crack opening due to load cycles 58
3.5 Determination of reinforcement strain evolution and bond stress distribution 60
3.5.1 Principles of measurements with distributed fibre optic sensors 61
3.5.2 Data post-processing of fibre optic measurement 62
3.5.3 Physically based derivation of strain and deformation evolution 64
3.5.4 Calibration and validation of FOS evaluation method 67
3.5.5 Evaluation of derived strain and deformation considering COT tests 69
3.5.6 Consideration of tension stiffening 75
3.6 Summary 79
4 Progressive cracking in the case of uniaxial tension 81
4.1 Overview and concept of the experimental series 81

4.2 Principal campaign to investigate progressive cracking 81
4.2.1 Experimental setup. 81
4.2.2 General behaviour 83
4.2.3 Evolution of crack widths on concrete surface 86
4.2.4 Reinforcement strain evolution and bond stress development. 92
4.3 Extension on multiple layers of textile grids 104
4.3.1 Considered variants 104
4.3.2 Performance regarding the crack width development 105
4.3.3 Force transfer at adjacent cracks - contribution of tension stiffening 110
4.4 Influences of variations of the concrete matrix 114
4.4.1 High-strength concrete. 114
4.4.2 Maximum aggregate size of 16 mm. 118
4.5 Summary 120
5 Prediction of crack width in the case of uniaxial tension 123
5.1 Revising key aspects of the bond behaviour of non-metallic textile reinforcement . 123
5.2 Experimentally based description of the bond behaviour 125
5.2.1 Approaches considering characterisation tests 125
5.2.2 Analytical description of the force-displacement behaviour 128
5.3 Method 1 – Simplified bond stress evolution. 130
5.4 Method 2 – Physically based formulation of bond force transfer for single cracks . 131
5.4.1 Overview of physically based representation of characterisation tests 131
5.4.2 Representation of the SPOc test. 132
5.4.3 Representation of the COT test 134
5.4.4 Description of single crack opening 136
5.5 Implementation of a physically based model for crack width prediction 138
5.5.1 Single cracking stage 138
5.5.2 Prediction of maximum crack spacing. 141
5.5.3 Maximum crack width at stabilised cracking 146
5.5.4 Prediction of an average crack width. 155
5.6 Extension to account for a cyclic loading regime 157
5.7 Summary 160
6 Crack width and deflection in flexural members 163
6.1 Outline and aims of the campaign 163
6.2 Experimental campaign on slabs 163
6.2.1 Concept and setup of four-point bending tests 163
6.2.2 Load-deflection behaviour 166
6.2.3 Failure characteristics 169
6.2.4 Crack width and crack spacing 170
6.2.5 Contribution of tension stiffening 174
6.3 Iterative determination of the cross-sectional curvature 175
6.4 Prediction of crack width and crack spacing 177
6.4.1 Short-term initial loading. 177
6.4.2 Increase in crack width due to cyclic loading 180
6.5 Approaches to predict the deflection 181
6.5.1 Principle considerations regarding cross-sectional curvature and deflection . 181
6.5.2 Describing the contribution of tension stiffening 183
6.5.3 Evaluation of approaches. 185
6.5.4 Deflection increase due to cyclic loading 187

6.6 Summary 191
7 Accuracy of the proposed physically based model in predicting the maximum crack width 193
7.1 Overview 193
7.2 Comparison of crack width prediction models 193
7.3 Simplified consideration of cyclic loading 196
8 Conclusion and Outlook 199
8.1 Summary 199
8.2 Practical implications 200
8.3 Further research 201
References 203
Appendix A A-1
Appendix B B-1
Appendix C C-1
Appendix D D-1

Notation

The following lists contain relevant units and symbols used within this thesis. Symbols that are not in this list are explained in the corresponding chapter or the Appendix.

Units

length:	mm, cm, m
cross-sectional area:	mm^2, m^2
mass:	kg
time:	s, h, d
frequency	Hz
force:	N, kN
bending moment:	kNm
stress:	MPa
strain:	mm/m
angle:	°

Abbreviations and other symbols

1D, 2D, 3D	one-dimensional, two-dimensional, three-dimensional
ACI	American Concrete Institute
AR	alkali-resistant
ASTM	American Society for Testing and Materials
BE	beam-end
CEB	Comité Euro-International du Béton
CFRP	carbon fibre-reinforced polymer
COT	crack opening tensile
COV	coefficient of variation
CSA	Canadian Standards Association
DAfStb	Deutscher Ausschuss für Stahlbeton (German Committee for Reinforced Concrete)
DIC	digital image correlation
DIN	Deutsches Institut für Normung (German Institute for Standardisation)
EC	Eurocode
EP	epoxy resin
FE	finite element
fib	International Federation for Structural Concrete
FOS	fibre optic sensor
FprEC2	Final Draft of the new Eurocode 2
FRP	fibre-reinforced polymer
GFRP	glass fibre-reinforced polymer
HSC	high-strength concrete
inf	inferior
JSCE	Japan Society of Civil Engineers

LVDT	linear variable differential transformers
MC	Model Code
NAD	German National Annex
NSC	normal-strength concrete
PE	polyethylene
PO	pull-out
PVC	polyvinyl chloride
SLS	serviceability limit state
SPO	single-sided pull-out
sup	superior
TRC	textile-reinforced concrete
ULS	ultimate limit state
℄	centre line/symmetry line

Latin lower-case letters

$a_{f,nm}$	textile cross-sectional area of fibre strand per metre
a_{nm}	nominal cross-sectional area of reinforcement per metre
b	width
c	concrete cover
d	effective depth
d_{eq}	equivalent diameter of reinforcement (nominal cross-section)
d_1	distance of most tensioned reinforcement centroid to surface
d_i	distance of reinforcement centroid to surface
$d_{g,max}$	maximum aggregate size, maximum diameter of aggregate
f_c	cylindrical concrete compressive strength
$f_{c,cube}$	cubic concrete compressive strength
f_{cm}	mean concrete compressive strength
f_{ck}	characteristic concrete compressive strength
f_{ct}	uniaxial concrete tensile strength
$f_{ct,ef}$	effective uniaxial concrete tensile strength
f_{ctm}	mean uniaxial concrete tensile strength
$f_{ct,sp}$	splitting concrete tensile strength
$f_{f,nm}$	tensile strength of non-metallic reinforcement related to the fibre strand
f_{nm}	nominal tensile strength of non-metallic reinforcement
h	height
h_{ef}	effective height
$k_{1/r}$	factor accounting for curvature
k_{fl}	factor accounting for linear strain distribution
l	length
l_b	bond length
l_e	embedded length
l_g	gauge length
l_f	free length
l_t	transfer length
n	number
n_{cr}	number of cracks

n_{layer}	number of reinforcement layers
s	slip between concrete and reinforcement
s_{l}, s_{ul}	slip at loaded, unloaded side
s_{r}	crack spacing
s_{rm}	average crack spacing
$s_{\text{r,max}}$	maximum crack spacing
t	time, thickness
t_0	concrete age at testing/loading
u	displacement, deflection
u_{max}	maximum deflection
w	crack width, crack opening
w_0	initial crack width
w_{k}	characteristic value of crack width
w_{m}	average crack width
w_{max}	maximum crack width
w_{surf}	crack width at surface
x	depth of neutral axis
$\bar{x}$	average value of sample
x_{c}	height of concrete compression zone
y_{nm}	yarn spacing
z	inner lever

Latin upper-case letters

A	empirical factor
A_{c}	gross cross-sectional area of concrete
$A_{\text{c,net}}$	net cross-sectional area of concrete
A_{ct}	tensile cross-sectional area of concrete
$A_{\text{ct,ef}}$	effective tensile cross-sectional area of concrete
$A_{\text{f,nm}}$	cross-sectional area of fibre strand
A_{nm}	nominal cross-sectional area of reinforcement
C, C_0	constant, empirical factor (bond stress)
D	damage parameter
E	Young's modulus
E_{c}	Young's modulus of concrete
$E_{\text{f,nm}}$	Young's modulus of fibre strand
E_{nm}	Young's modulus of reinforcement (nominal cross-section)
F	force, axial force
F_{b}	bond force
F_{bm}	mean bond force
F_{cr}	force at crack occurrence
M	bending moment
M_{cr}	bending moment at initial crack occurrence
M_{SLS}	bending moment at SLS criterion
M_{max}	maximum bending moment
U_{nm}	circumference of reinforcement
$U_{\text{nm,ef}}$	effective circumference of reinforcement

V_δ	coefficient of variation (log-normal distribution) acc. to Annex D.8 of Eurocode 0 [EC0]
V_x	coefficient of variation (normal distribution)

Greek letters

α, α_0	empirical factor (bond stress)
α_e	Young's modulus ratio of reinforcement and concrete
β, β_{ts}	factor describing tension stiffening
β_{adj}	factor describing tension stiffening at adjacent cracking
β_{single}	factor describing tension stiffening at single cracking
β_w	empirical factor (crack width)
γ, Γ	empirical factors (cyclic loading)
Δ	difference, additional
δ	slip
ε	strain
ε_c	concrete strain
ε_{cm}	average value of concrete strain
ε_{c1}	strain at maximum concrete strength
$\varepsilon_{c1,u}$	strain at uniaxial concrete compressive strength
ε_{cyc}	strain at cyclic loading
ε_m	average elongation, average strain
ε_{nm}	reinforcement strain
$\varepsilon_{nm,m}$	average value of reinforcement strain
$\varepsilon_{nm,max}$	maximum value of reinforcement strain
ζ	distribution factor
η	utilisation, relation
κ	curvature
λ	shear slenderness
ξ_{FOS}	transformation factor
ξ_F	factor accounting for cross-sectional geometry of fibre strand
ρ	reinforcement ratio
ρ_{ef}	effective reinforcement ratio
σ	stress
σ_c	concrete stress
σ_{nm}	reinforcement stress
σ_{nmr}	reinforcement stress present after initial crack occurrence
τ_b	bond stress
τ_{bm}	average bond stress
$\tau_{bm,k}$	characteristic value of average bond stress
ϕ	quantification factor
φ	creep coefficient

1 Introduction

Motivation

Concrete is responsible for more than 40% of the world's anthropogenic mass and shapes our environment more than any other building material. Its applicability for free-form constructions, ease of use, global access to raw materials, and low cost are the main reasons for the widespread application of concrete in daily engineering practice. The low tensile strength of concrete is mitigated by incorporating reinforcement, resulting in the widely employed composite material for more than a century. Despite its widespread use, concrete is associated with some key disadvantages, including significant greenhouse gas emissions, excessive structural self-weight and material usage, and the requirement of sufficient concrete cover to ensure long-term corrosion protection for the most commonly used reinforcement material, steel. However, the reduction or even abandonment of reinforced concrete structures is not a feasible alternative. The global population is continuously increasing, and the standard of living is rising. This leads to an increasing demand for buildings and infrastructure, which require the continued use of reinforced concrete as building material.

Consequently, there is an imperative to rethink how we build to meet the requirements of significantly reducing greenhouse gas emissions and satisfying the demand for a built environment that is liveable. It is acknowledged that there are promising approaches in the field of reinforced concrete: reducing the greenhouse emissions of concrete by almost entirely substituting the clinker; recycling materials such as aggregates to be reused in concrete rather than downcycling; advancing design approaches to fully account for the materials' structural capacities; reusing members, structures, and buildings for different applications; extending the service life of structures beyond 100 years; redefining the state-of-the-art of construction with new design strategies. However, most are only found as individual contributions, part of research, or have yet to be broadly implemented as a viable alternative to constructing new structures.
A promising way to accomplish the main objectives of the mentioned approaches is to substitute the steel reinforcement with non-metallic materials. This facilitates a reduction in concrete cover due to the absence of corrosion, thereby significantly reducing weight and material usage. The flexibility in the free formation of textile reinforcement supports the development of innovative designs for structures. The high tensile strengths of non-metallic reinforcements enable the fabrication of slender constructions. Furthermore, the lifespan is significantly extended and the requirement for high alkalinity in concrete is eliminated due to the reinforcement corrosion resistance, thus encouraging the use of alternative concrete binders or recycled concrete. The application of non-metallic reinforcement over a period exceeding five decades, accompanied by extensive research in material improvements and design approaches, has resulted in a state of the art where the construction of buildings using non-metallic reinforced concrete is nowadays a manageable task, although still the exception in application. A lack of demand and of diversity in supply still remains, whilst the broad spectrum of non-metallic reinforcements in terms of materials, types and shapes results in difficulties in their application in everyday design and construction.

This is of particular interest when addressing the serviceability of non-metallic textile reinforced concrete constructions, as this field of research is mostly not investigated. Especially, the limitations of crack width and deflection are often the decisive criteria in design, requiring additional reinforcement or increased cross-sectional dimensions. Moreover, most recent approaches in code provisions often adopt a conservative standpoint in meeting the serviceability criteria to ensure universal applicability for all potential reinforcements. Thus, the advantages offered by non-metallic

textile reinforcements are not fully exploited, which is contrary to the goals of material efficiency and sustainability. Consequently, models and approaches are required that allow for a progressive design in terms of limiting crack width and deflection while still guaranteeing serviceability.

Objectives

In order to ensure the feasibility of these approaches for all materials and shapes of non-metallic textile reinforcement, physically based models are derived. With regard to crack width prediction, an analytical description of the bond behaviour is required, for instance, by employing a robust experimental setup, such as the introduced crack opening tensile test. This is of particular interest in the case of textile grids, which exhibit significant variations in their bond behaviour due to their distinct shapes and manufacturing processes. Consequently, the developed comprehensive evaluation strategy addresses this challenge. Further aspects which are considered in this thesis are the consideration of the influence of multiple reinforcement layers, stress concentrations resulting from the elliptical cross-section of the fibre strands, and an adequate consideration of the close crack spacing generally attributed to textile-reinforced structures. This is also of importance for the derived model to determine the deflection, in which the influence of tension stiffening, contributing towards a reduced deformation, and concrete creep in the compression zone due to cyclic loading, requires consideration.

Methodology and structure

The analysis of the state of the art in Chapter 2 outlines that no efficient and robust crack width prediction approach for non-metallic textile reinforced concrete members has been developed yet. Consequently, a physically based model is derived that addresses the distinct behaviour of non-metallic reinforcement. The derivation is based on extensive experimental campaigns that provide a solid basis for an analytical description of the bond behaviour for various non-metallic reinforcements. In the first instance, the bond behaviour is characterised in Chapter 3 using experimental investigations at qualitative and quantitative levels that focus on various parameters which affect the bond. The introduction of crack opening tensile tests provides the basis for the derivation of a crack width-dependent bond stress value (i.e. bond stress-slip relation), which significantly improves the accuracy of the introduced physically based crack width prediction model. To gain a more profound understanding of the bond behaviour, fibre optic sensors are utilised to measure the reinforcement strain. This allows for the quantification of force transfer and bond capacity along the reinforcement for different cracking stages and reinforcement utilisation. In addition, the contribution of tension stiffening is quantified.

The different bond behaviour at multiple cracking is considered using uniaxial tensile tests (Chapter 4). This experimental campaign also enables the consideration of the influences of high-strength concrete, maximum aggregate size, and multiple reinforcement layers. Moreover, the investigation extends to additional crack opening resulting from cyclic loading. The results are utilised to validate the proposed crack width prediction model, as outlined in Chapter 5. The derivation of an analytical description of the bond behaviour as a bond stress-slip relation provides the basis for the prediction model. Thus, the individual elliptical-shaped cross-sectional geometry of the textile reinforcement is addressed. Furthermore, the contribution of tension stiffening and its consideration in the approach are discussed.

The model for crack width prediction is verified for flexural members through an experimental campaign conducted on slabs in Chapter 6. This campaign also constitutes the basis for the evaluation of concepts to determine the deflection, including the increase in deformation resulting from cyclic loading. Hereby, the reduced contribution of tension stiffening, and concrete creep in the

compression zone are quantified. In Chapter 7, the physically based model for crack width prediction is compared with concepts proposed by code provisions. This comparison confirms the necessity of the performed derivations and adaptations to account for the distinct bond behaviour of non-metallic textile reinforcement and shows significant improvements in adequately predicting the crack width when using the proposed model. Additionally, simplifications are provided to determine for the increase in crack opening due to cyclic loading. The observations, findings and procedures derived in this thesis are summarised in Chapter 8, where practical implications, further research questions and open topics are also highlighted.

2 State of the art

2.1 General remarks

Non-metallic reinforcement provides new opportunities in structural design. The high tensile strength relative to the cross-sectional area and material density, in combination with a concrete coverage solely defined by sufficient bond due to corrosion resistance, allows for slender, material-efficient and high-performance constructions. This shifts focus to revise the criteria for determining the required reinforcement ratio, as deflection control and crack width limitation often become the decisive factors.
The limitation of crack widths and the control of deflection are essential factors in ensuring the serviceability of reinforced concrete structures. In the context of steel reinforcement, the corrosion behaviour of the material is a key element in determining the crack width, as it prevents the premature failure of the structural elements. In the context of practical implementation, it is important to acknowledge the state-of-the-art approach that differentiates the required crack width limit according to the exposure of the member. The resistance of non-metallic reinforcement to corrosion enables a less stringent interpretation of crack width limits. It is widely accepted that the visual criterion is the defining factor for the allowable crack width. This is defined by either design codes or regulations. Visual appearance is of particular interest for exposed members with high visual expectations. For example, in a recently published scenario-based vignette study [Böf24], the importance of small crack widths in reinforced concrete was highlighted, as the participants named no visual cracks together with additional costs, carbon dioxide emissions and service life as main factors for acceptance and perceived sustainability. Further restrictions may be applied to water permeability or when ensuring the protection against corrosion of constructions underneath, such as strengthening or repairing of existing structures with a layer of non-metallic reinforced concrete.
The limitation of deformation must ensure the usability and functionality of the structure, as well as requires the (subjective) acceptance of the user. In the context of reinforced concrete structures, the deflection is typically constrained to a maximum of $l/250$ of the span-width, as proposed in Eurocode 2 [EC2] and adopted by the DAfStb Guideline "Concrete members with non-metallic reinforcement" [DAfStb24]. This limitation originates from the ISO 4356, which was published in 1977 [ISO4356]. As suggested by ACI 440-15.R1 [ACI15], a similar value of deflection at $l/240$ of the span is proposed. In contrast to reinforced concrete, the corresponding Eurocodes propose distinct criteria for steel structures and different criteria for wooden members. However, a universal limitation independent from the considered material is not identified, suggesting that a degree of interpretation is allowed when addressing the previously mentioned aims of deformation limitation.

The individuality of non-metallic reinforcements in terms of material types and shapes, on the one hand, facilitates a targeted application in corresponding constructions, but on the other hand necessitates design formats that take into account the reinforcement-specific behaviour. A brief overview is thus provided on non-metallic reinforcement used for concrete structures. The bond behaviour, which is decisive for crack width limitation and, in combination with the member stiffness, for deflection control, depends on the reinforcement used. Thus, this chapter focuses on the principle background to these three topics. However, the majority of research has focused on steel-reinforced members, and most code provisions either lack consideration of non-metallic reinforcement or rely on design codes originated from steel reinforced concrete. Therefore, the state of the art also refers

to research findings and approaches from this field.
In recent decades, research and practical application in the field of non-metallic reinforced concrete structures have been primarily focused on the analysis, description and transfer into design approaches of structural capacity and durability. As these research topics overlap with the perspective of this thesis, only a brief consideration is provided. Given the fact that the production of non-metallic reinforcement is dependent on the producer and undergoes continuous development, a detailed description regarding the types and materials is excluded.

2.2 Non-metallic reinforcement in concrete members

Non-metallic reinforcement is defined as a material class that substitutes the functions commonly attributed to metals in concrete structures, particularly with regard to the tensile capacity. Unlike metallic reinforcement, non-metallic reinforcement is a composite material that consists of fibre-reinforced polymers (FRPs), which are comprised of continuous or infinite fibres that can be impregnated with a polymer matrix. Bundling thousands of individual fibres to create a roving, and optionally combining multiple rovings, provides a fibre strand, which is capable of resisting sufficient tensile force. In order to activate the fibres in the core of a roving, an impregnation is required to transfer forces applied to the outer fibres to those in the core, thus enabling all fibres to equally contribute to the tensile resistance of the reinforcement. The flexibility in the placement of the rovings prior to impregnation provides enormous possibilities for the use of non-metallic reinforcement. In concrete construction, a typical use is either as short-length fibres with and without impregnation, which are added to the concrete mixture and comparable to steel fibres, resulting in a concrete class referred to as ultra-high performance fibre reinforced concrete. Or as reinforcements such as textile grids, rebars, tendons and sheets. A selection of different reinforcement types and materials is provided in Figure 2.1. In the following, carbon fibre-reinforced polymers are referred to as CFRP and glass fibre-reinforced polymers as GFRP.
Typical fibre materials include carbon, glass and basalt [Li22, Alk23], as well as various natural materials such as plant-based cellulose fibres (e.g. hemp [Lan14, Cha18] or flax [Fer19, Ric24]) and animal-based proteins [Ali21]. Aramid fibres were of focus in research but are nowadays not commonly used in construction due to their higher costs, a similar Young's modulus compared to glass fibres and their stress sensitivity under long-term loading [Nor93, Zhe95, Cur23].
The polymer matrix is often a thermosetting polymer, such as an epoxy resin or a vinyl ester resin. This prevents significant deformation of the reinforcement because the impregnation provides for stiff fibre strands. To allow for more flexible reinforcement, however, thermoplastic polymers are used instead, such as acrylate- or styrene-based dispersions [Api22]. The use of mineral-based impregnations proved to show higher resistance against elevated temperatures [Sch19a] and improvement in the bond capacity [Nad17]. However, due to the disadvantages presented by the processing of the impregnation, the use of mineral-based impregnations remains in the field of research and has not yet become commercially established.
Following the production of the first synthetic polymer, Bakelite [Bae09], at the beginning of the 20th century, fibre-reinforced polymers were first used commercially in the aerospace industry due to their high strength-to-weight ratio [Har02]. The automobile and shipbuilding sectors followed. In civil engineering, the use of rod-shaped and rebar-shaped FRPs to increase the structural capacity of constructions was first investigated as internal reinforcement in the USA in the early 1970s, having diameters of approximately 3 mm [Naw71]. To allow for a better utilisation of the concrete and improve the performance of the composite material, improvements were made regarding the bond behaviour by adding ribs or a sand coating on the surface of the rebars.

Besides FRP rebars, two-dimensional/planar and three-dimensional textiles are used for internal reinforcement. Initially, textiles without impregnation were used, referred to as *dry textiles*. Later, impregnation was added to improve the utilisation of the FRPs and enhance the durability of the reinforcement. In Germany, this was mainly investigated in Aachen [Heg12] and Dresden [Cur12]. While planar FRP textile reinforcement is commercially available, new research also focuses on three-dimensional textile reinforcement.
In addition, prestressing enables the full utilisation of the high tensile strength of FRPs by simultaneously reducing the width of cracks and the deflection of concrete members. Tendons, particularly made from CFRP, are used for internal and external prestressing [Sta19, Kue19, Sch20a]. Additional FRP sheets, also referred to as FRP laminates, are used for external reinforcement, especially for strengthening constructions (e.g. investigated in [Mot11, Att12]).
For strengthening applications, textile reinforcement is favourable over steel rebars, as it allows the application of a thinner additional layer of reinforced concrete or reinforced mortar (e.g. reported in [Riz03, Ber21a]). Another strengthening technique involves the use of near-surface-mounted reinforcement, where FRP rebars or sheets are placed in cut-in grooves and bonded with a groove filler, typically an epoxy resin or cement [Lor07, Zil14, Als19]. As both applications, prestressing and strengthening, are not considered in this thesis, no further consideration is provided.

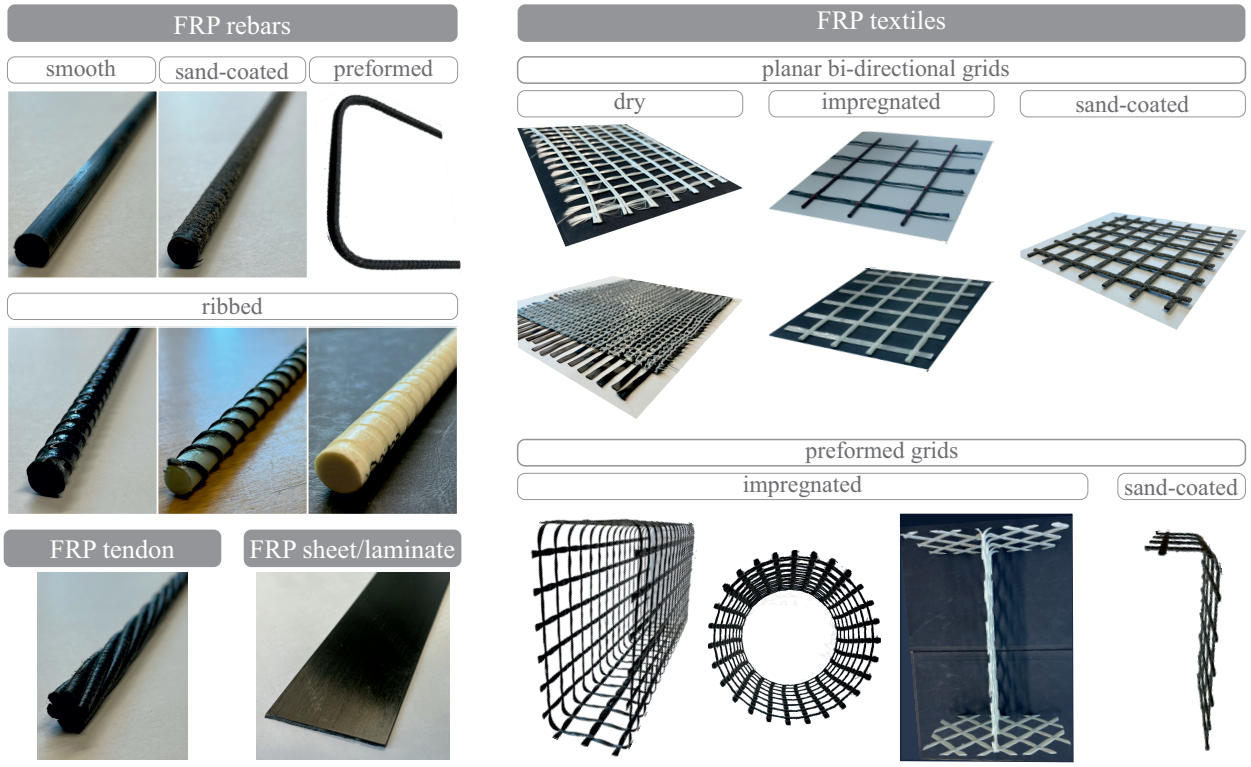


Figure 2.1: Selection of different types and materials of non-metallic reinforcements

Rebars
FRP rebars differ not only in terms of the fibre material and impregnation used, but also in terms of their cross-sectional geometry and surface finish. The commonly used production technique of pultrusion offers high flexibility in geometry while delivering a smooth surface [Cor13]. During pultrusion, axial rotation creates a wound rebar shape. To significantly increase the bond with concrete, the surface must be modified further (see, e.g., investigations in [Cos97]). By applying a coarse layer to the top of the smooth bar, for example coated sand particles [Ari12], it is possible to increase the bond capacity. Other approaches subtract or add material to achieve a ribbed geometry.

Subtraction can be achieved by milling [Moo08] or pressing/moulding [Cla25] the required profile into the smooth rebar (e.g. right-hand-sided picture of a ribbed GFRP rebar in Figure 2.1). Rib-shaped additions are created by winding or pressing an impregnated FRP strand around the smooth rebar [Rol18, Sol20] (the other two ribbed rebars in Figure 2.1). Another possibility to achieve a structured surface is braidtruding the individual rovings around a core strand, as shown for example in [Ive18]. Using thermosetting polymers for impregnation prevents plastic deformation of the rebars after setting. Therefore, the formation of bent or preformed FRP rebars must be completed before the resin sets. A typical application is the use as stirrups. This production technique reduces the material strength and Young's modulus in the bent area [Els07]. Using thermoplastic polymers enables forming after the rebar has hardened, while the bended region is still critical with respect to rupture, resulting in less tensile resistance compared to straight rebars [Elt13, Imj17].

Textiles

The production technique for textile reinforcement is based on processes established within the textile industry. The most common process involves placing FRP yarns transversely to the production direction. This allows for a multiaxial alignment of the fibre strands (see works in [Jes10, Sch15]). Nowadays, most planar FRP textiles show a bi-directional alignment with the orientation of the transversely placed yarns in 90° direction, known as the weft direction. This is followed by placing the yarns in the production/longitudinal direction, the warp direction (0° direction). The yarns are fixed to each other using knitting threads, then impregnation can be applied to the dry textile, either within the knitting process (inline technique) or in a separate processing step (offline). The spacing between the yarns in the grid is variable. The flexible application of dry textiles is of particular interest in the construction of shell-shaped structures. As impregnation significantly improves textile performance, pre-impregnated textiles allow flexible reinforcement layouts with resin hardening triggered post-placement.

Similar to rebars, using thermoplastic polymers allows some flexibility in the shaping of textile grids [Gel18, Hei23]. This is particularly interesting when preforming textile elements from a planar textile, allowing for a free definition of the geometry depending on the case of application. When considering thermosetting polymers, however, preforming must be realised before the resin sets.

The initially produced impregnated textile grids exhibited significant changes to the cross-sectional geometry of the yarns, known as waviness, which inevitably result from the continuous amount of fibres in the strand. Additionally, the areas where the warp and weft yarns intersect or where preformed textiles are redirected, known as *local undulations*, cause further changes to the cross-sectional geometry. Improvements in production techniques have reduced the waviness.

When a fixed geometric grid layout has to be provided, it is possible to place impregnated yarns directly before the resin sets, using frames or redirection units [Hau16, Gri16]. This method ensures a homogeneous structure of the yarns. A more homogeneous layout of the fibre strands in a textile grid increases material efficiency, as the cross-section of each fibre strand is utilised uniformly. Applying a small amount of prestressing also significantly reduces the stretching of the individual fibres at initial loading, as the fibres are not initially aligned straight in the longitudinal direction. Consequently, when tensile force is applied to the fibre strand, the full utilisation of the reinforcement with its characteristic linear-elastic behaviour is almost immediately achieved. Further motivation for reducing undulations is related to the bond behaviour. Undulations contribute to the transfer of forces acting in bond mechanisms, influenced by the cross-sectional geometry and shape of the undulations, as this affects the direction of the forces induced into the concrete (e.g. investigated in [Pre19a, Lee21, Sch25b]), which is discussed in detail in Section 2.4. This allows for an increased force transfer. However, this also results in higher concrete utilisation by inducing

lateral tensile stress, which causes concrete to crack and split before reaching the tensile strength of the reinforcements.

Using the flexible forming of textile reinforcements, it is possible to define a three-dimensional (3D) geometry of the reinforcement layout [Roy07, Gri22, Fri22]. The 3D reinforcement can improve the utilisation of the reinforcement due to an anchorage effect in the areas where a fibre strand is redirected [Hai17]. A study comparing 2D and 3D textile reinforcements revealed 3D textiles to be beneficial for the flexural behaviour of the concrete member [Kad19]. It was also reported that 3D textiles reduced the crack opening [Gie24].

2.3 Matrices

The term *concrete* is typically associated with a mineral-based matrix binding a filler material. The most elementary and widely used composition of the matrix is the result of hydrating cement clinker and water. The filler consists of fine (typically sand) and coarse aggregates (gravel or crushed stones). In order to extend the range of applications for concrete, additional materials are added to the concrete mixture. For example, these materials are used to reduce the hydration heat or to increase strength. The most recent focus has been on improving the sustainability of concrete structures, which is achieved by substituting either the cement clinker or the aggregates. The utilisation of non-metallic reinforcements has been demonstrated to accelerate this trend, thereby expanding the range of applications for concrete, as the necessity for concrete with high alkalinity to provide for corrosion resistance is no longer a requirement. In addition, it appears to be appropriate to utilise a high-performance reinforcement in terms of tensile strength, in combination with a high-performance matrix with regard to compressive resistance as well as high tensile strength and increased stiffness.
This resulted in the utilisation of high-strength and ultra-high strength concretes when employed in conjunction with non-metallic reinforcements (see, e.g., [Heg12, Bec21]). Furthermore, the utilisation of textile grids characterised by a narrow yarn spacing, in conjunction with the design of small concrete covers, has enabled the production of mixtures having a reduced aggregate size, typically ranging from 2 to 4 millimetres. In accordance with the European code provision's definition for concrete, which specifies a maximum aggregate size of at least 5 mm, these mixtures, characterised by their fine grain sizes, can be designated as *mortar*. However, in the course of research, several different terminologies were introduced to define these matrices (an overview is given, for example, in [Bie21a]), as the matrices with fine grain sizes provide for very high strengths, and the term 'mortar' would suggest otherwise. The use of high-strength and ultra-high strength concretes is predominantly associated with increases in cement content, a practice that is not consistent with the principles of sustainability.
Consequently, numerous solution strategies have been developed, including the use of supplementary cementitious materials as a substitute for cement clinker. Examples of such materials include (latent-)hydraulic binders such as blast furnace slag, other pozzolanic materials (e.g. fly ash or micro silica), limestone (an alternative to blast furnace slag), and, more recently, calcined clays [Ove24] and naturally existing alkali-activated pozzolans [Bon11, Rob18]. The utilisation of geopolymer binders [Neu16] and bacterial-based binders [Nod24] for reinforced concrete structures remains a subject of ongoing research, as it requires the determination of a feasible composition for use with (non-metallic) reinforcement.
Of significant importance for each of the matrices in the usual application range for steel reinforced concrete structures is the assurance of sufficient alkalinity of the binder during the life span (e.g. reported in [Ang11, Tan15, Vol16, Koe20, Vol24]). It is essential to ensure that the carbona-

tion of the concrete cover is progressing slowly enough to avoid loss of alkalinity in the vicinity of the reinforcement, thus preventing corrosion. In addition, carbonation along the crack surfaces occurs in the case of cracks with larger widths [All21]. However, if this is not the case, it is necessary to increase the concrete cover. This also provides restrictions when using concrete with recycled aggregates, as the progression of carbonation in the original concrete results in a faster carbonation rate of the concrete with recycled aggregates. Either larger concrete covers or higher cement content are therefore required. The result is a solution that is less economical and ecological [Mar23, Sin25]. However, the use of non-metallic reinforcement does not force these limits. Moreover, in the case of certain fibre materials, such as glass [Ben85, Sch09] and basalt [Wan21, Li22], a lower alkalinity of the concrete has been shown to enhance its usability as an alkaline environment damages the fibres. Consequently, future combinations of non-metallic reinforcements and matrices with low cement clinker content are a suitable alternative, as demonstrated in circular life cycle studies, for example, reported in [Lai19, Kro23, Lut23, Hav25].

Furthermore, it is evident that matrices utilised for the application in non-metallic reinforced concrete members should fulfil a range of requirements. Extending the aforementioned criteria of high strength, sustainability, and feasibility for the employed reinforcement type and material, the matrices need to fulfil the exposition requirements and also be practical and applicable on-site or in prefabrication plants. Recent technical approvals in Germany enable the use of non-metallic reinforcements such as the *Schoeck Combar* glass rebars [Sch19b] and the *solidian* carbon textile grids [sol.24] for normal-strength concrete, thereby ensuring a broad application range. This addresses concrete mixtures currently available in the construction industry in Germany, where supplementary cementitious materials can substitute approximately one third of the cement clinker and are easy to use, while the maximum aggregate size is, in general, at least 8 mm.
As a result, it seems suitable to consider not only the application of non-metallic reinforcement with high-performance or highly sustainable matrices, but also the feasibility for currently widely available and commonly used concrete mixtures to cover the period until new matrices are commonly employed in the construction industry. Consequently, the concrete mixtures utilised in the experimental campaigns presented in this thesis follow this approach and were selected to provide for normal to high strength concretes (strength classes ranging from C30/37 to C80/95 according to [EC2]), with supplementary cementitious materials and aggregate sizes of up to 16 mm, which are broadly available as ready-mixed concrete or in prefabrication plants.

2.4 Bond behaviour of reinforced concrete

2.4.1 Force transfer mechanisms

Bond between two materials allows for the transfer of force, with the region where bond occurs referred to as the *bond area*. In the context of reinforced concrete structures, the bond area is defined as the contact area between the reinforcement and the concrete, which is equivalent to the surface of the reinforcement. The length of the bond area required to transfer the force from the reinforcement to the concrete to achieve a state of equivalent strain between both materials is defined as *bond length*, while the length itself is referred to as *transfer length*. In the absence of an equivalent strain state being achieved, resulting in a partial transfer of force, the transfer length is shorter than the bond length. The transfer of forces along the bond length in relation to the slip occurring at the crack is referred to as *bond capacity*. Consequently, a high bond capacity is described as the ability to transfer large forces at a small slip.

Prior to cracking or outside the bond area, no significant force transfer between concrete and reinforcement occurs, and the strain of both materials is approximately equal due to adhesion, which allows for a transfer of low forces. With the force exceeding the provided capacity by adhesion, either a debonding between both materials occurs or other bond mechanisms have to substitute for adhesion. In reinforced concrete, an exceeding of the adhesive capacity usually occurs with crack initiation, as the reinforcement has to account for the forces released upon crack occurrence, which are transferred in the uncracked concrete. At this point, indicated as ① in Figure 2.2, a displacement between reinforcement and concrete occurs, defined as (local) *slip*, as shown in Figure 2.2 for a rebar and a textile yarn. The force transferred by friction at an infinitesimal area does not change with increasing slip. If a reinforcement with an even surface is considered, e.g. a smooth rebar, a pull-out of the reinforcement with a constant force being applied will eventually occur when the capacity of the friction is exceeded or the bond length is limited. For reinforcement with an uneven surface, being the ribs for rebars or the waviness and undulations for textile grids, mechanical interlocking contributes to (significant) force transfer. In the case of interlocking, the force is transferred by contact pressure applied by the reinforcement console, e.g. the rib, on the concrete. The capacity of interlocking to transfer force is dependent on the geometry, in particular on the acting surface and the force exerting angle, the distance of the reinforcement consoles and the concrete strength to account for the contact pressure due to tensile stress induced in the lateral direction.
The tensile strain results in a crack occurring at the reinforcement console. This cracking is described as internal cracking and is indicated by ②. GOTO [Got71] assumed that internal cracking eventually occurs at every rib of a steel rebar. Nevertheless, these internal cracks do not all propagate towards the concrete surface, which is of particular interest in the case of large concrete covers. As the force transfer increases, the existing internal cracks continue to open and propagate, and longitudinal cracks emerge in the bond area ③. In the event of inadequate concrete coverage, reduced concrete tensile strength, or the absence of transverse reinforcement, longitudinal cracking can result in the splitting of the concrete. This is of particular relevance to textile grids, as a low concrete coverage is frequently employed. The high acting forces result in the crushing of the concrete keys, reducing the magnitude of force transferred by interlocking ④, ultimately leading to either shearing off or splitting of the concrete keys. In the context of non-metallic reinforcement, the phenomenon of shearing off of the ribs for rebars or the transverse fibre strands at the local undulations in the case of textile grids has been observed [Sch20b]. This is a consequence of the subsequently added fibre strands, which serve as ribs or provide for the local undulation. The

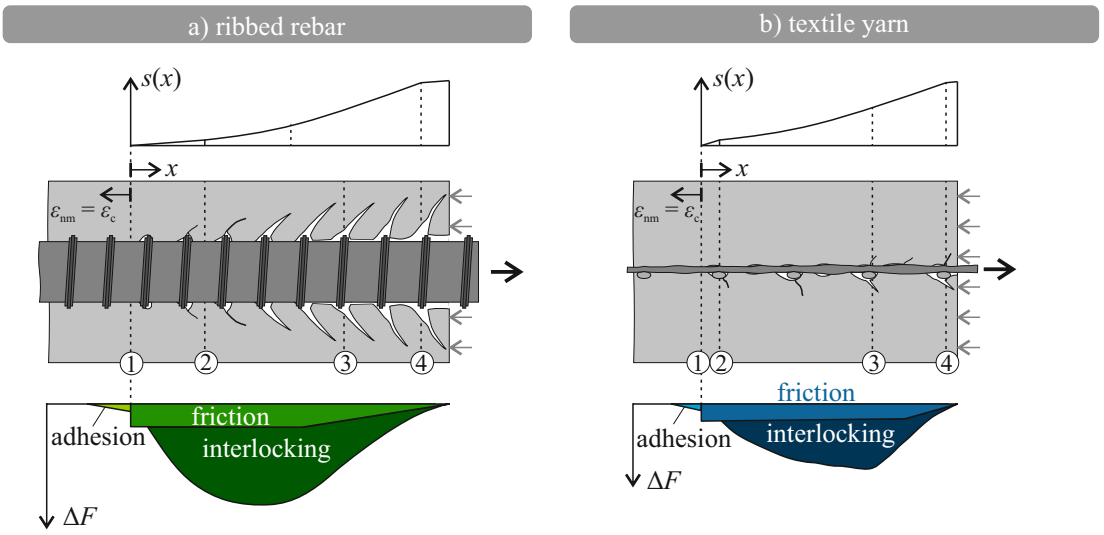


Figure 2.2: Illustration of main bond mechanisms for an embedded rebar and a textile yarn

experimental program conducted by COSENZA ET AL. [Cos97] revealed that the bond behaviour of FRP rebars is not adequately ensured by either a smooth surface or a subsequently added rib geometry that collapses at low load levels due to shearing off. The application of a sand coating to reinforcing bars (rebars) resulted in an adequate bond strength, yet the material exhibited a brittle failure mode.
The activation and contribution to the bond capacity of these three mechanisms are dependent on the applied force and the occurring slip. Therefore, at a global level, the area along the bond length is utilised differently. Consequently, when aiming for an analytical description of the bond behaviour without an incremental representation of infinitesimal areas, an approximation is necessary.

2.4.2 Cyclic and sustained loading

While the previous description focuses on the behaviour of a continuously pulling out of the reinforcement, in practical application, cyclic and sustained loading in the serviceability regime are the main situations. As the majority of research regarding these two situations focused on steel rebars, therefore this is addressed at first.

Steel rebars
The experimental campaign conducted by ELIGEHAUSEN ET AL. [Eli83] investigated the influence of cyclic loads applied at various levels of slip for steel rebars using pull-out tests. For peak values of bond stress being below 80% of the maximum stress reached in purely monotonic loaded tests, the performed ten load cycles led only to small increases in slip due to some propagation of the internal cracks and concrete creep. Significant damage to the bond interface occurred at higher bond stress values or when the maximum bond stress was exceeded and bond softening occurred. The experimentally observed slip increase or reduction in bond stress during cyclic loading is represented in material models by introducing a damage variable, which, for example, is assumed to correspond only to the total dissipated energy [Cia81]. Another energy-based approach was proposed by FEHLING [Feh90] by approximating the force transfer at each rib of a rebar using friction-spring elements to determine the energy dissipation in the case of cyclic load application. Regarding the study by ELIGEHAUSEN ET AL., the small number of load cycles provided for an uncertainty when transferring the observations to a high number of load cycles in combination to small values of slip, as the relation of dissipated energy to the absorbed energy in the case of a purely monotonic loaded specimen is high, while the damage occurring to the bond is small.
Research on bond fatigue affected by a high number of applied cycles of up to a million at a constant load level or sustained loading of 1000 hours was conducted by REHM and ELIGEHAUSEN [Reh79], which showed a significant increase in slip of the rebars with an embedded length of three times the diameter. The results were approximated by a linear relation in a double logarithmic scale for upper load levels between 0.4 and 0.85 of the monotonic maximum bond stress, with this relation still being used in the *fib* Model Code 2010 [MC10] to determine the slip increase for cyclic loading at a constant amplitude. BALÁZS [Bal98] investigated the influence of different loading schemes and load levels, showing that slip increase occurred at a subsequent increase of the upper stress level. In contrast, a subsequent decrease in the stress level did not lead to an additional increase in slip. Furthermore, high amplitudes in combination with a high upper load level significantly increased the resulting slip.
BAKTHEER ET AL. [Bak22] investigated the energy dissipation under fatigue loading and concluded that the main dissipation occurs due to the development of irreversible plastic slip. Using the area under the hysteretic loops does not account for all of the energy dissipation of the cyclic loading at the maximum bond stress, which is less in comparison to the peak value.

An empirical approximation of the slip increase considering different concrete strengths and the number of load cycles was recently published by KOSCHEMANN ET AL. [Kos25]. In an extensive experimental program using pull-out tests and beam-end tests considering a steel rebar with diameter of 16 mm, revealed the sensitivity to the upper load level and the resistance of high-strength concrete against failure due to bond fatigue. The use of fibre optic sensors to determine a continuous reinforcement strain evolution along the bond length in steel reinforced concrete was performed by LEMCHERREQ ET AL. [Lem23]. It was revealed that the peak of the bond stress evolution moves away from the loaded end during progressive cyclic loading while increasing in value. The authors assumed a reduced force transfer resulting from a combination of stiffness reductions and plastification of the concrete keys. The latter is occurring from a prevented closure of the internal secondary cracks by crushed concrete particles. Furthermore, a negative value of bond stress was determined at these areas at the unloaded stage. This is assumed to result from the counteracting friction at unloading, with no mechanical interlocking possible, which neglects this friction as the bond area close to the loaded end is highly damaged. Investigations in [Sch25b] showed similar results regarding the bond stress evolution in concrete members reinforced with textile grids.

In the case of cyclic load application, there is continuous damage to the materials. However, sustained loading results in concrete creep, which also increases the occurrence of slip over time. This long-term constant force transfer by interlocking leads to creep behaviour of the concrete keys, referred to as *bond creep*. In the investigation by FRANKE [Fra76], pull-out tests were conducted on steel rebars embedded at a length of four times the bar diameter in normal-strength concrete. The bond creep was described by a linear increase in time on a double logarithmic scale. This proposal continues to be used within the *fib* Model Code 2010 to determine the increase in slip for sustained loads. An adaptation to this proposal was suggested by KOSCHEMANN and CURBACH [Kos24] through the extension of the basis of the empirical model of FRANKE to account for a significantly increased loading duration of up to 3000 hours. It was revealed that the bond creep coefficient was up to twice as high as the one determined by the proposal of FRANKE.

FRP rebars

As previously indicated, the research summarised in the preceding paragraphs concentrated on steel rebars. In addressing the concrete behaviour in the context of cyclic or sustained loading, it is assumed that the observations are transferable on a qualitative level or are at least worthy of consideration for FRP reinforcements. However, it is essential to address additional influences that contribute to the bond behaviour. CASPARI [Cas22] performed a transfer of the linear approximation proposed by FRANKE to be used for GFRP rebars subject to sustained loading. Furthermore, he also investigated the influence of elevated temperatures of up to 60°C using pull-out tests. It was revealed that a time-dependent dissolution of the ribbed surface can occur, which led to a shift in the failure criterion from a shearing off of concrete keys at short-term loading to a shearing off of the rebar ribs in the case of sustained loading. Furthermore, CASPARI used the experimental results to perform a prognosis of the bond stress for long-term loading of up to 100 years. Investigations on the bond behaviour of GFRP rebars exposed to elevated temperatures for four and eight months showed that a significant reduction in the peak bond stress occurred for temperatures of 80°C, as reported in [Mas11]. However, lower temperatures, such as 60°C, did not affect the bond behaviour.

Experimental investigations comparing the bond behaviour of GFRP rebars and steel rebars subject to sustained loading revealed that the time-dependent increase in slip is in magnitude comparable between both types of rebars, while the lower Young's modulus of GFRP rebars compared to steel rebars resulted in a significantly larger initial value of slip [Vil15].

FRP grids

While the broad application of GFRP rebars in the construction sector has resulted in a wide field of research conducted, the bond behaviour of CFRP rebars and textile reinforcements in the case of sustained or cyclic loading has been focused on more rarely in research. SPELTER [Spe23] conducted uniaxial tensile tests using carbon textile grids placed in an alkali-watered environment under elevated temperatures of 40 and 60°C, which revealed the occurrence of considerable concrete creep during sustained loading at 85% of the tensile strength. Furthermore, some increase in the tensile strength of the reinforcement was observed compared to a short-term load application, referred to as the *training effect*. It was assumed that some initially unaligned fibres in the roving were straightened and therefore were capable of contributing to the tensile force resistance of the textile grid. This also led to an increase in crack opening in addition to concrete creep. Similar findings addressing the fatigue of textile reinforcement under cyclic loading were reported by WAGNER and CURBACH, who conducted tests on CFRP textile grids placed in high-strength concrete. They revealed that no rupture of the fibre strand occurred for up to 2 million load cycles independently of the loading regime [Wag19].

EL-GHADIOUI ET AL. [Gha20] conducted investigations on sustained loading over 5000 hours on beams subject to bending and reinforced with CFRP grids. The results revealed that the deflection increased by approximately 17% at the two investigated utilisation levels of 59% and 98% of the tensile strength of the grid. In the case of using CFRP rebars, similar increases in deflection of approximately 20% were reported by the authors while the reinforcement utilisation was lower at 50%. Almost identical tests on steel-reinforced beams at a utilisation of 64% showed deflection increases of about one third. However, at initial loading, the deflection of the steel-reinforced beams was 2.5 to 3 times lower compared to the carbon-reinforced specimens.

Interim conclusion

In conclusion, it may be assumed that the increases in slip, crack opening and deflection due to cyclic or sustained loading in non-metallic reinforced concrete members are comparable to those of steel-reinforced members in terms of the relative values. This hypothesis remains valid provided that the dominant factor is attributed to the concrete behaviour resulting from damage and concrete creep.

However, research findings indicated that the absolute increase in slip and crack opening is more pronounced in FRP-reinforced members. Despite the FPR reinforcements demonstrating resilience against fatigue failure, the transfer of substantial forces, in conjunction with elevated strain utilisation at the serviceability level and small concrete covers, induces a stress state within the concrete, thereby causing damage to the concrete through crushing and transverse cracking, thus facilitating further slip. Consequently, excessive bond creep and fatigue of the concrete in the bond area result in the reported findings. Furthermore, the pronounced reduced transversal stiffness of the FRP reinforcement, in conjunction with the potential for shearing off of the ribs or local undulations, demands a specific consideration in comparison to steel rebars.

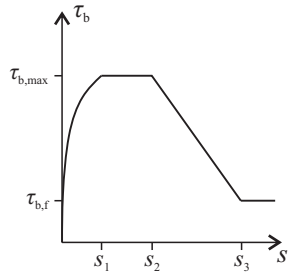
2.4.3 Methodologies to describe the bond behaviour

The most common method to describe the bond behaviour is to use an analytical approach, which describes the relation between the transferred bond force and the occurring slip. Assuming an infinitesimal element at which a constant transfer of bond force occurs, the differential equation of bond is obtained, stated as

$$\frac{\mathrm{d}^2 s(x)}{\mathrm{d}x^2} - \tau_\mathrm{b}(s) \cdot U_\mathrm{nm} \cdot \left(\frac{1}{E_\mathrm{nm} \cdot A_\mathrm{nm}} + \frac{1}{E_\mathrm{c} \cdot A_\mathrm{c}} \right) = 0. \tag{2-1}$$

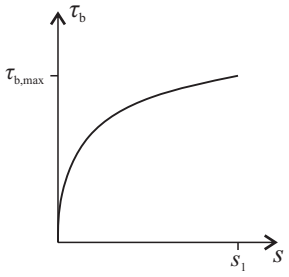
To utilise Equation 2-1 for a consideration of the transfer length and the slip occurring in a crack, an assumption on the description of the bond stress must be introduced. This is referred to as bond stress-slip relation, denoted as $\tau_\mathrm{b}(s)$, with various approximations being suggested in the literature. The most simplified approach of a constant value of bond stress assumes a force transfer solely by friction, which is used, for example, by AVESTON, COOPER and KELLY [Ave71] in their *ACK theory*. To account for adhesion and mechanical interlocking, the non-linear relation of the increasing bond stress until a maximum value is reached is often approximated by a power-law function. The approach presented by CIAMPI, BERTERO, ELIGENHAUSEN and POPOV [Cia81, Eli83], referred to as *BEP model*, advances the ascending bond stress by defining a plateau at the maximum bond stress and introducing bond softening until solely friction remains as bond mechanism, which is assumed to provide for a constant value of bond stress at large slip. The obtained description is depicted in diagram (a) of Figure 2.3 and was introduced to the CEB-FIP Model Code 1990 [MC90]. The formulation, stated in Equation 2-2, is still provided in the most recent *fib* Model Code 2020 [MC20] to approximate the local bond behaviour.
KOENIG and TUE [Kön96] slightly reformulated the ascending description of the BEP expression by introducing the parameter C, which was derived together with the parameter α based on experimental investigations and depending on the used reinforcement and concrete. The expression given in Equation 2-3 does not consider any softening behaviour, which is feasible considering smaller values of slip, as in the case during the serviceability state. Considering this and due to

(a) BEP model [Cia81, Eli83]



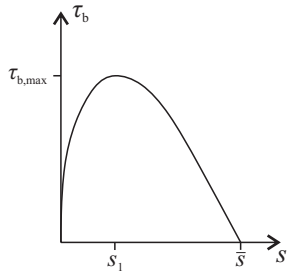
$$\tau_\mathrm{b}(s) = \begin{cases} \tau_{\mathrm{b,max}} (s/s_1)^\alpha & 0 \le s \le s_1 \\ \tau_{\mathrm{b,max}} & s_1 < s \le s_2 \\ \tau_{\mathrm{b,max}} - (\tau_{\mathrm{b,max}} - \tau_{\mathrm{b,f}}) \cdot \dfrac{s - s_2}{s_3 - s_2} & s_2 < s \le s_3 \\ \tau_{\mathrm{b,f}} & s_3 < s \end{cases} \tag{2-2}$$

(b) KOENIG and TUE [Kön96]



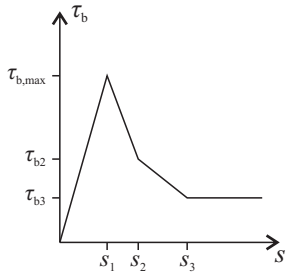
$$\tau_\mathrm{b}(s) = C s^\alpha \tag{2-3}$$

(c) FOCACCI ET AL. [Foc00]



$$\tau_\mathrm{b}(s) = C s^\alpha (1 - s/\bar{s}) \tag{2-4}$$

(d) RICHTER [Ric05]



$$\tau_\mathrm{b}(s) = s \left(\frac{\tau_\mathrm{i} - \tau_\mathrm{i-1}}{s_\mathrm{i} - s_\mathrm{i-1}} \right) \quad \text{for i} = 1...4 \tag{2-5}$$

Figure 2.3: Overview of analytical models to describe the bond stress-slip relation

the simplicity of the formulation, this power-law approach is utilised in the following chapters to describe the bond stress-slip relation of non-metallic reinforcement.
A continuous description of the bond behaviour, including hardening and softening, was introduced in a modified BEP expression by FOCACCI ET AL. [Foc00]. A similar expression as KOENIG and TUE is used and stated in Equation 2-4. The softening behaviour is approximated by introducing a factor $\bar{s}$ describing the value of end slip at which no force is transferred. Consequently, a loss of friction is assumed during the softening of bond.
In the case of textile reinforcement, it was found that a simple linear description provided satisfactory results. Experimental and numerical investigations using pull-out tests on textile grids having an embedded length equivalent to the yarn spacing, conducted by PREINSTORFER and KOLLEGGER [Pre20a], revealed that the bond hardening is adequately described by a linear stress-slip behaviour. A tri-linear approach introduced by ZASTRAU ET AL. [Zas03] allows for the consideration of a bond softening behaviour, which therefore attributes the occurrence of mechanical interlocking. This approach was modified by RICHTER [Ric05] to improve the description of the softening behaviour, resulting in four linear branches as shown in diagram (d) of Figure 2.3.

While all the previously mentioned descriptions require a calibration of their parameters, physically based models aim to address the bond mechanism directly. This is of particular interest in the case of mechanical interlocking, as its capacity in force transfer depends on the internal crack occurrence and propagation. The *thick-walled-cylinder model* proposed by UIJI and BIGAJ [Uij96] for ribbed bars in a concrete confinement attributes the surrounding concrete area to a cracked cylinder and an uncracked cylinder. The crack propagation is defined using the radial tensile stress exerted by the rebars and considering the concrete tensile behaviour, including tensile softening.
In general, the transfer forces are exerted by multiple ribs. The utilisation of the concrete in the bond area is subject to an interaction, approximated by a stress field, which can be referred to as global behaviour. As the utilisation of the concrete in this stress field is not homogeneous, consisting of areas of triaxial compression, uniaxial tension or compression, and compression-tension, the stress field is separated into different areas, as proposed by the *rigid-plastic discontinuous stress field model* of GALKOVSKI ET AL. [Gal23b]. Material models are used to describe the concrete behaviour subject to different stress states and geometrical properties arising from rib geometry and concrete cover.

Another methodology involves using energy-based approaches. FEHLING ET AL. [Feh22] propose to solve the differential equation of bond (Equation 2-1) to obtain a relation between the energy attributed to an incremental change in slip and the energy attributed to the incremental change in reinforcement strain. This assumption is transferred onto a crack width prediction approach, based on the work of LORENZ [Lor22].
BAKTHEER and CHUDOBA [Bak18] formulated a bond model using the thermodynamic potential to address fatigue behaviour. Considering the lateral pressure exerted on the bond area, they introduced a damage function. This approach is solved numerically to obtain the bond stress and slip.

It is evident that describing the bond behaviour using either of the previously mentioned methods and approaches, which are only a selection of the numerous proposals provided in the literature, is not a simple task. While most approaches focus on local force transfer over an infinitesimal length of the bond area, it is clear that this is a significant simplification. For example, in the case of a ribbed rebar, mechanical interlocking is only attributed to the area in front of the rib. However, friction applies to the entire rebar area and may be more pronounced in the case of rougher surfaces present on the rebar or due to the different distribution of concrete aggregates.

However, the continuous and homogeneous repetition of ribs and bond surfaces on rebars is the main reason why this simplification is well-suited. The bond stress-slip relation is approximately identical at every rib. Consequently, the question arises as to what extent this applies to textile grids, where repetition, e.g. local undulations, occurs at much longer distances than the rib distance in rebars and may exceed the transfer length.

2.4.4 Differentiation between rebars and textile grids

The previous two sections provided a general overview of bond behaviour and established that simply transferring the bond behaviour described for steel rebars to textile grids is not suitable. The continuous, repeating bond surface of rebars, which is defined by the spacing and geometry of the ribs and illustrated on the left-hand side of Figure 2.4, cannot be identically applied to textile grids.

The transfer of force from the textile grid involves a number of factors that contribute to the bond mechanism of adhesion, friction and mechanical interlocking. The contribution of adhesion and friction F_{fric} is dependent on the impregnation used (investigated, e.g., in [Val20]), as well as the presence of an additional coating, such as sand (reported, e.g., in [Bie18a, Bie21b, Pre23]). The latter significantly increases the force transferred by friction compared to a plain impregnated strand. The waviness of the fibre strand [Lor12], in conjunction with periodic changes in cross-sectional geometry [Bie18b] and cross-sectional shape [Kul13, Pre20b], referred to as *global undulation* or *waviness* , exerts a further influence on friction. These factors also significantly contribute to the contact pressure of the fibre strand on the concrete F_{p}, which is activated by a pull-out force [Pre20a]. Furthermore, alterations to the cross-section found at the intersections of fibre strands, defined as *local undulations* and denoted as F_{un}, exert pressure and interlocking forces. The resulting transversal tensile stress state in the concrete can lead to a delamination between reinforcement layer and concrete or spalling of the concrete cover at higher utilisations of the reinforcement, as reported, for example, in [Lor11]. That the local waviness of the fibre strands at these undulations also significantly contributes towards force transfer at lower reinforcement utilisation and small values of slip, was reported in [Sch25b].

This makes determining the actual bond behaviour at an infinitesimal section difficult, as there is

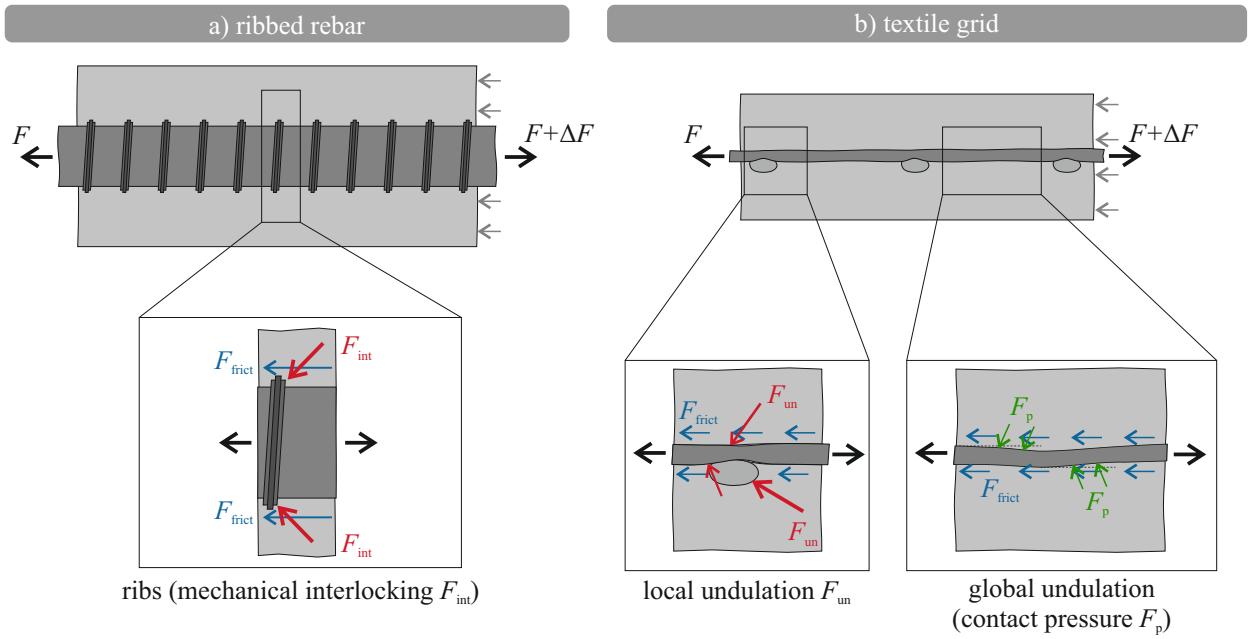


Figure 2.4: Local description of the acting bond mechanisms for a ribbed rebar and a textile grid

no uniform contribution of all the aforementioned factors to the transferred bond force. This is of particular interest when conducting experimental tests to characterise the bond behaviour of textile grids, since the predefined embedded length of the reinforcement results in different activation of the aforementioned factors, and the obtained results may provide for a different global description of the bond behaviour.

In the case of a combined use of rebars and textile grids, a separate analysis is required, due to the differing Young's moduli and characteristic bond behaviour. Moreover, the application of diverse reinforcements is influenced by time-dependent effects, including creep and relaxation. RUDLOF [Rud97] investigated the stress evolution of steel rebars, tendons and bars for prestressed concrete members, showing that bond behaviour and the cracking stage have a significant influence. The better bond of the rebars resulted in higher utilisation than of the tendons. Concrete creep or cyclic loading increased the difference in stress levels between the two reinforcement materials. Once cracking occurs, the stress levels converge as the transfer lengths of both reinforcements become equal. A reduced bond capacity at stabilised cracking, sustained loading, or cyclic loading was revealed to be less significant in terms of stress evolution than at a single crack. Nevertheless, as both factors influence the bond behaviour, the utilisation of the reinforcements may be affected. Research on strengthening steel-reinforced beams with FRP reinforcement has been conducted, for example, in [Wei09]. YOON ET AL. [Yoo11] investigated the influence of a combination of steel, CFRP and GFRP rebars in concrete beams, addressing the prediction of deflection, and extending the proposal in [Bis07] to hybrid reinforcement usage. A numerical solution to the differential equation describing the slip occurring in concrete members with multi-layer placement of two FRP reinforcements is presented in a research report by HEGGER ET AL. [Heg23], which determines the redistribution of bond forces between the reinforcements. Considering the application of additional textile reinforcement layers to strengthen prestressed concrete members, STEINBOCK [Ste21] proposed an analytically-based relation to determine the stress distribution in the different reinforcement layers, which is dependent on the Young's modulus and the bond behaviour. The DAfStb Guideline "Concrete members with non-metallic reinforcement" [DAfStb24] considers a combination of reinforcement materials with different bond stress values, as proposed by Eurocode 2 [EC2] and *fib* Model Code 2020 [MC20] for combining steel rebars and prestressing tendons.

2.4.5 Experimental setups to describe the bond behaviour

In general, experimental test setups used to depict the bond behaviour either focus on a derivation of an anchorage length or a description of the bond force in relation to the displacement between reinforcement and concrete. For determining the anchorage length, the slip is of secondary importance, as the aim of the corresponding test setups is to relate the anchorage length to the maximum transferred force with focus on the ultimate limit state. This leads to a differentiation when choosing the embedded length of the reinforcement in the setup. In the case of investigating the anchorage length, larger embedded lengths are considered to transfer large forces. On the contrary, to determine the bond force-slip relation, smaller lengths are considered to focus on the local behaviour.
In both cases, an evaluation step often applied in practice consists of converting the applied force into a mean value of bond stress, based on the assumption that the force transfer propagates along the whole transfer length. As the actual transfer length is often unknown, it is usually approximated by the length of reinforcement embedded in the concrete. This simplification results in a value of bond stress representing a smeared evolution along the transfer length rather than attributing the actual non-linear development.

If deformation at the loaded end is measured directly, a slip value representing the actual pull-out displacement of the reinforcement is obtained. However, as interference from tilting or other experimental disturbances may occur, most tests recommend measuring the slip at the unloaded end of the reinforcement, which requires a short embedded length so that almost immediately at force application a displacement occurs.
One example is the well-known RILEM RC6 pull-out test for rebars, with its simple test setup and large resistance against concrete spalling, with compressive stress developing transversely to the reinforcement that influences the bond behaviour. Conversely, beam-end tests, such as proposed in [ASTM15], provide a more accurate representation of the bond behaviour of an embedded rebar. The setup prevents transversal compressive stress from influencing the bond area. In addition, the concrete cover is adoptable as an investigation parameter. To avoid concrete spalling in the beam-end test, additional stirrups or similar reinforcement may be required, which, on the other hand, enables the investigation of the influence of confinement on the bond capacity.
As textile grids in particular allow for a reduction in concrete cover, concrete splitting becomes a dominant failure mechanism and must be accounted for in order to enable a realistic representation of bond capacity. Explicitly considering concrete splitting as failure is of importance, as in practise, members with small concrete covers generally have no additional reinforcement that allows concrete confinement. To determine the maximum force transfer value, single-sided pull-out tests (SPOs) are performed with a pre-defined embedded length l_e. The first type of SPO involves using a modified specimen in a uniaxial tensile test with a textile grid placed centrally within a concrete member. The end of the embedded length is reached when the central longitudinal fibre strand separates, either by cutting the strand prior to concreting (SPO type A in Figure 2.5) or by drilling the hardened concrete specimen and severing the fibre strand (type B). Type B tests, developed by LORENZ and ORTLEPP [Lor12], can be used on large reinforced members by cutting out the required section afterwards, making this method feasible for existing structures. An adaptation introduced by BIELAK ET AL. [Bie18b], referred to as SPO type A, addresses the possibility of concrete splitting being a failure mechanism. Therefore, the concrete area that actually contributes to the bond transfer mechanism is represented. This is done by tapering the cross-section along the embedded length. Crack initiation is realised using a thin separation sheet placed prior to concreting. Both test setups share the fact that the crack opening is measured, and therefore, for evaluating the slip, an assumption of the bond stress evolution is required.
The German DAfStb Guideline on non-metallic reinforced concrete members [DAfStb24] introduces a more simplified test setup, denoted as type C or SPOc. The setup follows the concept of a pull-out test, neglects the bond-free length and reduces the cross-sectional area of the concrete specimen to represent a single fibre strand in a concrete member. The embedded length is then defined in a way that allows a fully anchored reinforcement to be represented. With the specimen's width representing the transverse grid spacing and its depth representing the concrete cover to each side of the strand, splitting failure is adequately represented. As slip essentially does not occur at the unloaded side in the case of a large embedded length, slip must be measured at the loaded end. As is typical for pull-out tests, the transversal compressive stress influences the bond behaviour, increasing the bond capacity in the area close to load introduction due to the specimens' thin geometry. To reduce this effect, a non-adhesive layer is placed between the specimen and the load introduction. This influence is therefore only significant when investigating small embedded lengths. The test setup is employed in an extensive experimental campaign to characterise the bond behaviour of different textile grids in Section 3.3.

Textile grids with no impregnation or low transverse stiffness often exhibit pull-out failure as the predominant bond failure mechanism. To investigate pull-out failure for these reinforcements, the

double-sided textile pull-out test proposed in [Bie17] is a feasible alternative. A concrete specimen reinforced with a textile grid is provided with a notch to induce a crack. Clamping close to the notch allows transverse pressure to be applied to the concrete, which prevents splitting and does not improve the bond capacity of textile grids with no impregnation or low transverse stiffness.
Using pull-out tests comparable to the RILEM RC6 enables the investigation of the bond capacity when aiming to prevent concrete splitting. A concrete cube with a large cover significantly reduces splitting failure. With a short embedded length, slip at the unloaded end occurs at relatively low forces. The developed yarn pull-out test developed by SCHNEIDER ET AL. [Sch18] and illustrated in Figure 2.5 was designed to examine the impact of high temperatures on the bond performance of CFRP yarns. In this test, a single yarn is placed centrally between two concrete cubes, which are then moved apart. In the pull-out specimen, the embedded length must be shorter than that of the other concrete cube. Measuring the slip on the loaded side enables the full bond capacity of the reinforcement to be derived, excluding preliminary failure due to concrete splitting. A further adaptation of the yarn pull-out test setup allows for the investigation of preformed textile grids as proposed in [Bie21a].
Substituting the second concrete cube with a direct fixation of the fibre strand to apply the force as shown by the bottom-centred setup in Figure 2.5, PREINSTORFER ET AL. [Pre19b, Pre20c] suggested an adaptation of the RILEM pull-out test for textile grids with an embedded length of

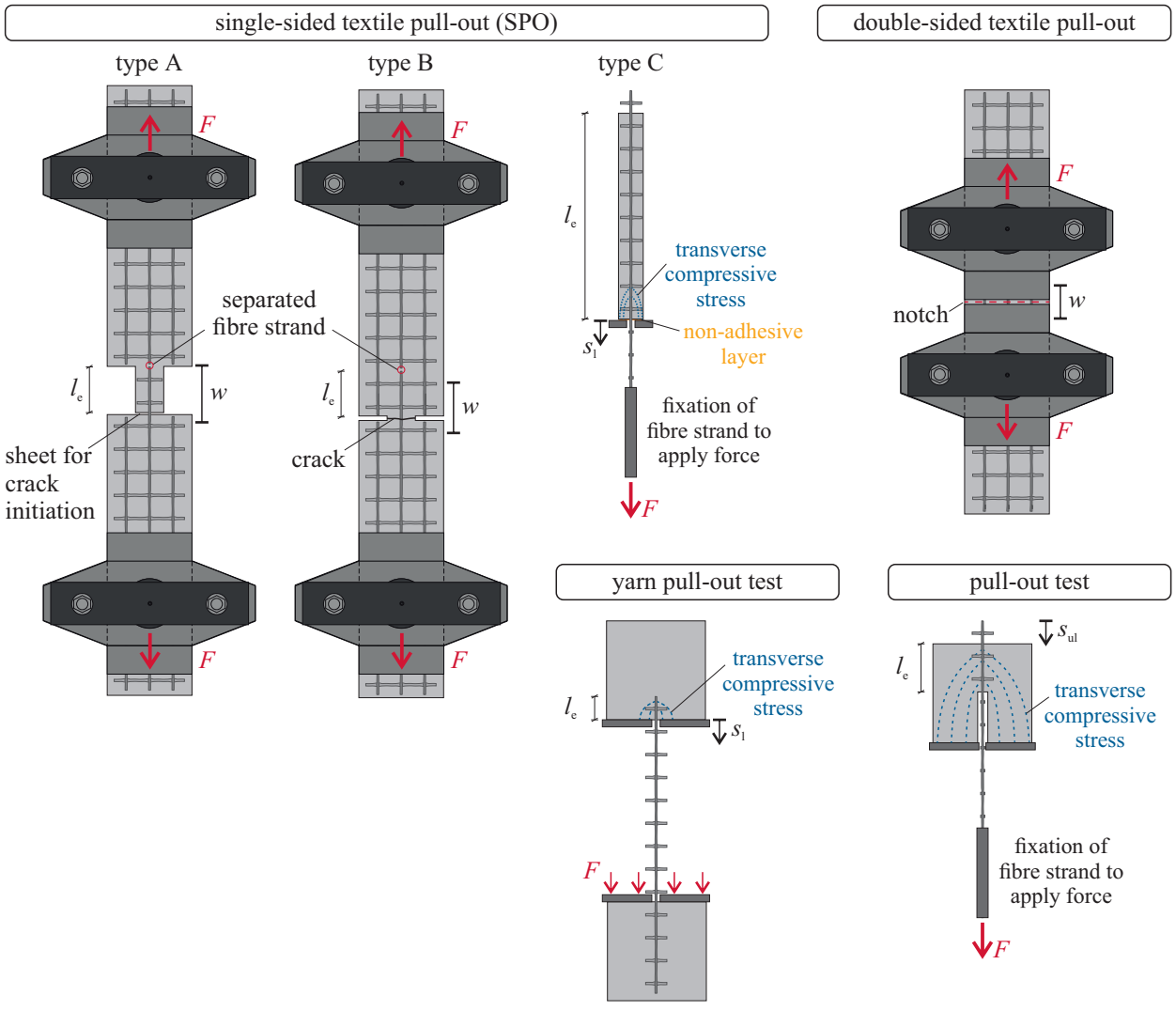


Figure 2.5: Test setups to describe and characterise the bond behaviour of textile grids (adapted from [DAfStb24, Bie17, Sch18, Pre19b])

one or two times the grid spacing and an edge length of 100 or 150 mm, respectively, to prevent concrete splitting.

The prescribed test setups prove to be partly insufficient when aiming for a derivation of a force-crack opening relation feasible to describe the bond behaviour at the serviceability state with small slip present. Either the boundary conditions of the tests do not resemble the actual situation of a crack in a reinforced member, or the embedded lengths limit the transfer length to propagate in full. In the case of no crack initiation provided from the beginning of loading, such as for the SPO type b setup, the obtained data lacks information regarding small slip values. In other cases, the significantly increased concrete cover reflects a state of force transfer in a large concrete volume, which is not reflected by the practical application.

2.5 Cracking in reinforced concrete members

The following descriptions of crack opening in reinforced concrete members introduce some definitions relating to the application of crack-inducing forces and the cracking stages. These distinctions are essential for deriving approaches to predict crack widths. Depending on the magnitude of tensile strain induced, an initial micro-level crack, defined as the level at which the aggregates and the matrix are considered separately, propagates through the cement matrix in the case of normal-strength concrete, or even through the aggregates in the case of ultra-high strength concrete. The crack then becomes visible at the macro level, which is observed as an instantaneous opening, and is often referred to as the case when the induced tensile stress exceeds the concrete's tensile strength. Upon crack occurrence, the released stress is either transferred by the reinforcement to the uncracked concrete sections or an indefinite crack opening occurs, which, in the case of externally applied loads, leads to an immediate failure. In other words, the reinforcement must account for the released stress. Otherwise, the reinforcement ruptures or, in the case of steel reinforcement, a large crack opening occurs due to yielding.
While the opening of the crack and the contribution of the reinforcement to limit the crack width is a localised phenomenon, the focus on a single crack is too restrictive. As is apparent, cracks occurring in close proximity to each other, referred to as *adjacent cracks*, necessitate a consideration of their transfer lengths and the potential interference between them.
In situations where tensile strain is induced by deformation, such as in restrained members subjected to temperature variations, the initiation of a single crack leads to a reduction in the magnitude of the deformation and consequently, also to a decrease in the opening of other cracks. This interaction also requires consideration.
Moreover, cracks in concrete members do not show identical widths. Main reasons are the variations in material parameters of both reinforcement and particularly concrete, aggregate distribution of the concrete, differences in the local contribution of the bond mechanisms, the stress states in the case of a non-perfect uniform state, as well as loading situations and histories. Therefore, a differentiation is required when assessing parameters such as the maximum width or the average value of all cracks.

2.5.1 Origins of tension to provoke cracking

At first, considering the global behaviour of a reinforced concrete member subject to tension, a differentiation is introduced to distinguish between two possible origins of tension which provoke cracking. One origin is that the stress is introduced by an external force. The reinforcement must account for the force released upon crack occurrence with a corresponding crack opening, while a

force equilibrium must be maintained. This is usually the case for externally loaded members. For the other case, the stress is the result of an internally induced strain. Due to restrained boundary conditions, the overall elongation of the member is restricted. The induced deformation is equal to the global deformation in order to meet the criterion of deformation compatibility. Consequently, the cracks open to fulfil deformation equilibrium. This behaviour is referred to as restraint-induced crack formation.

Externally loaded members

In practical applications, external loading frequently results in a bending moment, inducing a linear strain distribution over the cross-section of the member. In this case, when no axial compression is applied, cracks occur exclusively within the tensioned area where the stress exceeds the concrete tensile strength, leaving some sections to remain uncracked (Figure 2.6a).

In slender beams and slabs, having a large span and small height, the curvature of the cross-section and the deflection significantly higher when compared to deep beams with a small span and large height. This is particularly relevant for FRP textile-reinforced members, where a slender design at the ultimate limit state is possible due to the high tensile capacity of the reinforcement in comparison to steel-reinforced beams and slabs. Conversely, large deflections accompanied by significant crack opening occur for FRP-reinforced members, as in addition, the FRP reinforcement is capable of reaching multiple values in strain compared to the yielding point of steel. This is critical regarding the serviceability of the member as it may limit the full utilisation of the FRP reinforcement's tensile strength. For compact members, the curvature of the cross-section is less pronounced. This facilitates a simplification when focusing on the tensioned zone around the reinforcement, assuming a uniaxial stress state, as shown in Figure 2.6a.

Restraint-induced crack formation

As previously indicated, the case of deformation equilibrium is typically observed for restraint-induced loading. The most common reasons for internally applied loads leading to a strain field and deformation of the member are autogenous and drying shrinkage as well as temperature changes due to concrete hydration and ambient variations. The resulting restraint-induced stress has the potential to induce cracks. In the majority of structural systems, voluminous concrete members such as walls, slabs, plates and foundations are exposed to restrained displacement boundary conditions. The magnitude of the restraint-induced stress is affected by the time-dependent viscoelastic material behaviour of the concrete, particularly creep and relaxation, which reduce stress, and the concrete stiffness. In addition, the degree of restraint affects the magnitude of restraint-induced stress. Consequently, this is of particular interest for thick members, high degrees of restraint, and design situations with special requirements for crack width control [Tow65, Fin16a, Sch21a, Sch23a]. As demonstrated by these references, the majority of research has focused on plain or steel reinforced concrete members. The general mechanism and structural behaviour are not altered when steel rebars are substituted with non-metallic reinforcement, as the behaviour of the concrete is independent of the type of reinforcement used. It is worth considering the reductions in tensile strength and bond capacity of FRP reinforcement at elevated temperatures (e.g. at 80°C as reported in [Kat99, Hol23]) and the different thermal expansion of FRP compared to concrete [Bel14, Ayd18]. When determining the main factors leading to cracking, a common differentiation is introduced regarding the concrete age. In the early concrete age, the hydration-induced temperature development in a restrained structure leads to strains. The resulting restraint-induced stress is influenced by the concrete Young's modulus development and early creep behaviour [Emb89, Sch96, Sch02]. Following the temperature rise in the initial phase of concrete hydration, the subsequent cooling phase of the member increases the tensile stress. This increase can reach the concrete tensile strength, leading to early crack occurrence [Bre90, Spr94]. Additional tension is contributed from

early shrinkage [Alt01, Hol04]. Beyond the early age, sustained long-term stress development can lead to tension as high as the tensile strength, causing late cracking [Wei98, Gil01].

The temperature field in a structural member is conditioned by the concrete mixture, the cross-sectional geometry and the thermal boundary conditions [Jon94, Sch02, Zhu20]. Any change in temperature leads to an increase in strain, which results in stress development under restrained deformation. Concrete at an early age undergoes a large creep and relaxation process, reducing the stress increase over time [Tro67, Baž75, Baž00]. This viscoelastic material behaviour leads to a considerable and non-negligible reduction of the theoretical pure elastic stress evolution [Zhu20, Sch13, Jin20, Sch23a].
Restrained members exhibit a non-linear stress profile over height, consisting of a constant stress component induced, for example, by the global temperature change, a linear component due to different temperatures at the opposite surfaces and shrinkage, and a non-linear component particularly caused by self-equilibrium stresses, as visualised in Figure 2.6b.

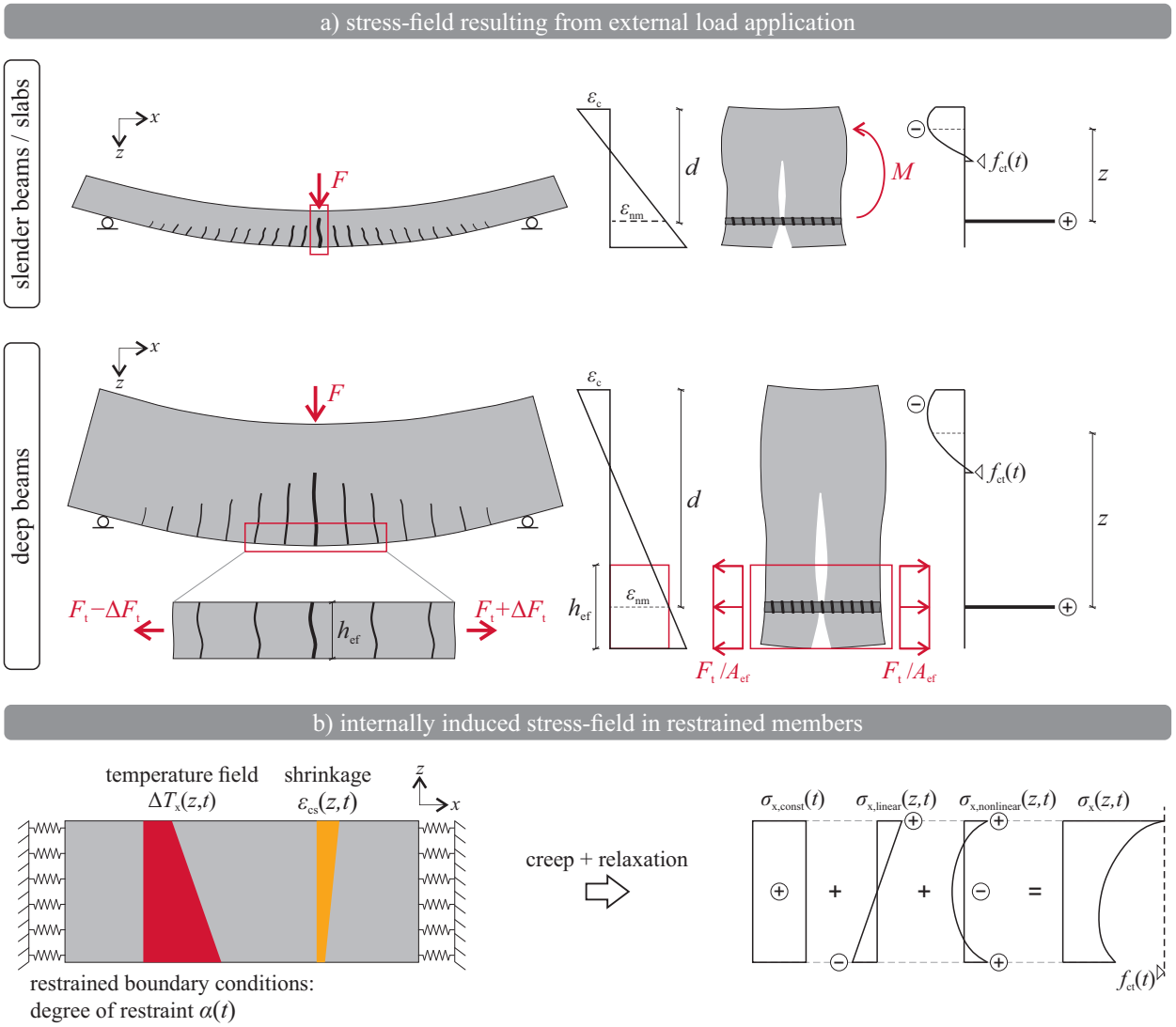


Figure 2.6: Stress-field and cracking induced by external and internal loading scenarios

2.5.2 Strain evolution regarding the cracking stage

Besides the difference in the origin of global deformation leading to cracking, a similar strain evolution of reinforcement and concrete is found for both cases, as a released force is always transferred by bond into the concrete. In the following description, the strain evolutions are addressed focusing on the local behaviour, while neglecting the influence of shrinkage and temperature changes. With crack occurrence, the continuous strain distribution in the concrete member changes, the reinforcement is activated to account for the force released upon cracking and transfers the force into the uncracked concrete region. Consequently, the concrete is subject to increasing tension with the ongoing force transferred, given that there is zero strain at the crack surface. While single cracks do not influence each other's strain evolution, adjacent cracks are characterised by the prevention of full propagation of force due to an intersection of the transfer lengths. Therefore, a distinction between the occurrence of single cracks and adjacent cracks is necessary when considering the strain evolution of reinforcement and concrete, as illustrated in Figure 2.7.
This also allows for a definition of distinct stages when describing the cracking behaviour of concrete members, which is generally referred to in literature. The onset of single cracks, followed by adjacent crack formation, marks the crack formation stage. Once no further cracks emerge on the member (stabilised cracking stage), the existing cracks undergo further opening. In the case of steel-reinforced members, the yielding defines another stage. However, this is not the case for reinforcement materials characterised by a linear-elastic behaviour, such as FRPs. A further differentiation introduced here is between static loading and cyclic loading.

Single cracks
In particular, single cracks are characterised by a complete transfer of the force released upon crack occurrence. The length of the force transfer, which is denoted by the transfer length l_t, is measured from the crack surface to the point at which the reinforcement strain is of equal value to the concrete strain, as illustrated in Figure 2.7a. As the magnitude of force increases, the transfer length also increases, remaining at a state of equal strains at its end. The slip at the crack increases, and the crack opens further. In the actual case of an inhomogeneous bond behaviour, due to scatter of local bond and concrete properties [Li17, Chu21], the transfer lengths on either side of the crack are not identical, despite the force transferred being equal on both sides. To account for this, a distinction is introduced between the transfer length developing on each side of a crack, denoted by l_t^a and l_t^b. The crack continues to open under the influence of cyclic loading. Both cyclic loading and bond creep do not reduce the value of reinforcement strain in the crack, as the same value of force is still transferred. Conversely, the force is transferred over a greater distance as the bond capacity is reduced. This phenomenon is accompanied by an increase in slip, which consequently leads to an increase in crack widths (Figure 2.7b).

Adjacent cracks
As crack formation progresses, the transfer lengths of the single cracks begin to interfere, resulting in the reinforcement strain no longer being equivalent in value to the concrete strain, as illustrated in Figure 2.7c. The continuous formation of cracks results in a combination of interfering strain evolution and full force transfer. The strain evolution and transfer length on one side of the crack are constrained by the adjacent crack, whereas on the other side, full propagation of the transfer length is possible. This also highlights the necessity to differentiate between single cracks and adjacent cracks with regard to bond behaviour. In the case of adjacent cracks, slip at the end of the transfer length is fixed, and no deformation between reinforcement and concrete occurs despite no equivalence of strains being reached. In the event of a reduction in bond capacity, there is a possibility that the transfer length of two formerly single cracks will interfere.

Stabilised cracking

The formation of new cracks is prevented between adjacent cracks when the concrete strain remains below its rupture strain. Once this state is achieved over the entire member, a stabilised cracking stage is present (Figure 2.7e+f). The application of increased load results in higher reinforcement strain, while the strain evolution of the concrete remains about identical to its prior state. In the case of bond hardening occurring for increased slip, some additional force transfer is possible. On the contrary, for excessive bond softening occurring close to the crack, the opposite effect occurs. In the case of a reduction in bond capacity due to cyclic loading or creep, a corresponding decrease in force transfer to the concrete is observed, resulting in a less pronounced decline in reinforcement strain along the transfer length (Figure 2.7d).

Therefore, to accurately predict the crack width, the strain evolution and the transfer length must be identified for each loading scenario and cracking stage.

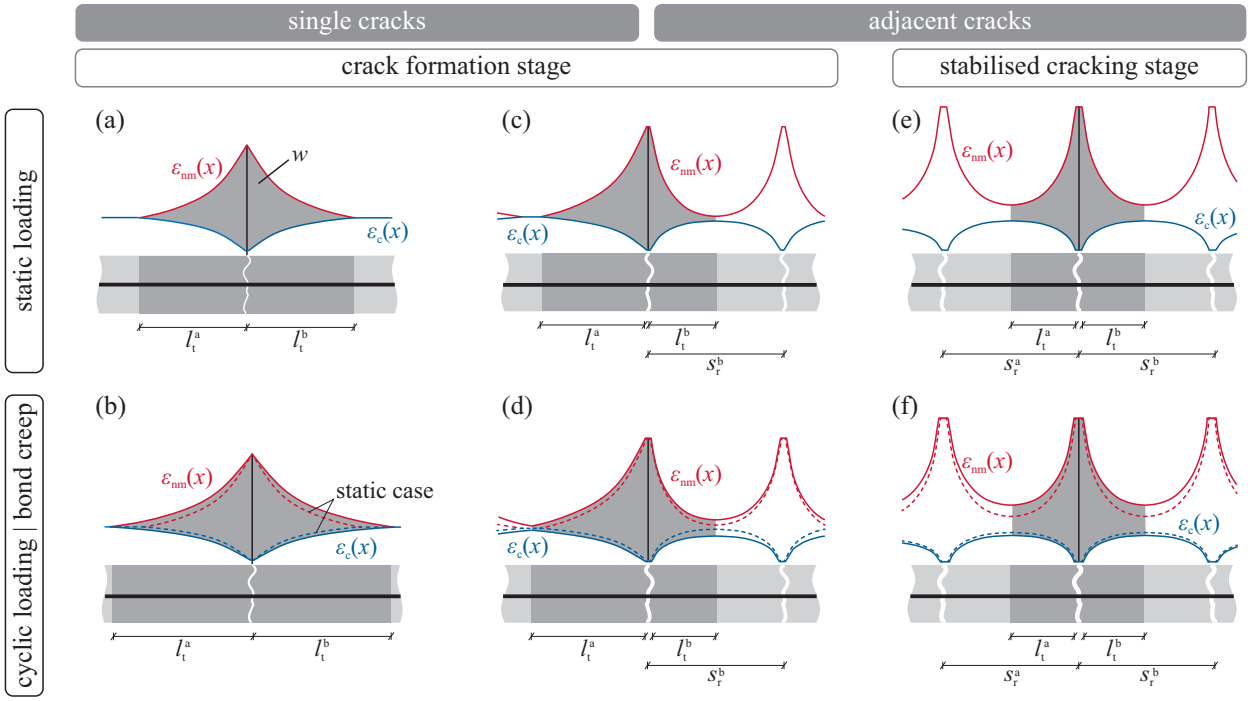


Figure 2.7: Description of reinforcement strain $\varepsilon_{nm}(x)$ and concrete strain evolution $\varepsilon_c(x)$ depending on the cracking stage and loading scenario

2.5.3 Analytical consideration of local behaviour

Using the previously described behaviour, an analytical approach to determine the crack width of an individual crack was formulated following the concept described, for example, by KOENIG and TUE [Kön96], which was also used as the basis in the *fib* Model Code 90 [MC90] and the German National Annex [EC2NAD]. Therefore, an idealisation of a single reinforcement in a concrete member subject to uniaxial tensile loading is introduced. The crack width is expressed as the slip occurring on each side of the crack

$$w = \delta^a + \delta^b = 2 \cdot \delta\,, \tag{2-6}$$

which is the displacement between reinforcement and concrete at the crack.

The displacement is expressed as the elongation, being the integral of the strain evolution, along the transfer length

$$\delta = u_{\mathrm{nm}} - u_{\mathrm{c}} = \int_0^{l_{\mathrm{t}}} \varepsilon_{\mathrm{nm}}(x)\,\mathrm{d}x - \int_0^{l_{\mathrm{t}}} \varepsilon_{\mathrm{c}}(x)\,\mathrm{d}x\,. \tag{2-7}$$

Assuming a transfer of force from the reinforcement towards the concrete and a force equilibrium between the two materials of the composite, the concrete strain is

$$\varepsilon_{\mathrm{c}}(x) = \rho \cdot \alpha_{\mathrm{e}} \cdot [\varepsilon_{\mathrm{nm,max}} - \varepsilon_{\mathrm{nm}}(x)] \tag{2-8}$$

with the reinforcement ratio $\rho = A_{\mathrm{nm}}/A_{\mathrm{c}}$, the stiffness ratio $\alpha_{\mathrm{e}} = E_{\mathrm{nm}}/E_{\mathrm{c}}$ between the Young's modulus of reinforcement and concrete, and the reinforcement strain in the crack $\varepsilon_{\mathrm{nm,max}}$. With the reinforcement strain evolution known, the crack width is determinable.

The combination of FRP fibres and impregnation leads to two definitions of the cross-sectional area. Either the cross-sectional area only addresses the FRP fibres, which is still of common use for textile reinforcement, or the impregnation is also considered as a nominal cross-sectional area defining the whole cross-section of the reinforcement. Consequently, as this thesis focuses on the bond behaviour, in the following, the nominal cross-sectional area is always used, denoted as A_{nm}, which follows the concept in [JSCE97, CSA12, DAfStb24].

Introducing bond as a behaviour accounting for the force transfer, the bond stress is expressed as the derivative of the reinforcement stress

$$\tau_{\mathrm{b}}(x) = \frac{A_{\mathrm{nm}}}{U_{\mathrm{nm}}} \cdot E_{\mathrm{nm}} \cdot \frac{\mathrm{d}\varepsilon_{\mathrm{nm}}(x)}{\mathrm{d}x} \tag{2-9}$$

related to the ratio of cross-sectional area and circumference of the reinforcement element U_{nm}.

Simplification to mean values

In the case of an analytical approach, a simplification is the consideration of a mean value of the strain along the transfer length for the reinforcement $\varepsilon_{\mathrm{nm,m}}$ and concrete $\varepsilon_{\mathrm{c,m}}$ to simplify the non-linear evolution. The approximation is

$$\int_0^{l_{\mathrm{t}}} \varepsilon_{\mathrm{nm}}(x)\,\mathrm{d}x = \varepsilon_{\mathrm{nm,m}} \cdot l_{\mathrm{t}}\,, \tag{2-10}$$

with an equivalent formulation for addressing the concrete strain. The crack width is then derived as

$$w = 2 \cdot \underbrace{l_{\mathrm{t}} \cdot (\varepsilon_{\mathrm{nm,m}} - \varepsilon_{\mathrm{cm}})}_{=\,\delta}\,. \tag{2-11}$$

In order to determine the value of the mean reinforcement and mean concrete strain, considering only the maximum reinforcement strain in a crack, a factor β is introduced (cf. [Ros76, Sch89]). This factor expresses the mean value as a reduction of the maximum strain in the crack $\varepsilon_{\mathrm{nm,max}}$ by a fraction of the strain difference $\Delta\varepsilon_{\mathrm{nm}}$. This is the difference between $\varepsilon_{\mathrm{nm,max}}$ and the minimum reinforcement strain $\varepsilon_{\mathrm{nm,min}}$ at the end of the transfer length. The average reinforcement strain is:

$$\varepsilon_{\mathrm{nm,m}} = \varepsilon_{\mathrm{nm,max}} - \beta \cdot (\varepsilon_{\mathrm{nm,max}} - \varepsilon_{\mathrm{nm,min}}) = \varepsilon_{\mathrm{nm,max}} - \beta \cdot \Delta\varepsilon_{\mathrm{nm}} \tag{2-12}$$

The factor β therefore expresses the effect of tension stiffening. The mean concrete strain is then expressed as

$$\varepsilon_{\mathrm{cm}} = \rho \cdot \alpha_{\mathrm{e}} \cdot \beta \cdot \Delta\varepsilon_{\mathrm{nm}}\,. \tag{2-13}$$

In a similar way, a mean bond stress is derived, which is introduced considering a dependence on the slip occurring

$$\tau_{\mathrm{bm}}(s) = \frac{A_{\mathrm{nm}}}{U_{\mathrm{nm}} \cdot l_{\mathrm{t}}} \cdot E_{\mathrm{nm}} \cdot \Delta\varepsilon_{\mathrm{nm}}\,, \tag{2-14}$$

which also allows for an expression of the transfer length as a function of reinforcement strain and bond stress. Considering the slip of the reinforcement, Equation 2-7 is rewritten to fit the assumption of mean strains and a mean bond strength:

$$\delta = \underbrace{\frac{A_{\mathrm{nm}} \cdot E_{\mathrm{nm}} \cdot \Delta\varepsilon_{\mathrm{nm}}}{U_{\mathrm{nm}} \cdot \tau_{\mathrm{bm}}(s)}}_{= l_{\mathrm{t}}} \cdot \underbrace{[\varepsilon_{\mathrm{nm,max}} - \beta \cdot \Delta\varepsilon_{\mathrm{nm}} \cdot (1 + \rho \cdot \alpha_{\mathrm{e}})]}_{= (\varepsilon_{\mathrm{nm,m}} - \varepsilon_{\mathrm{cm}})} \tag{2-15}$$

To determine the slip and the crack width, a proposal of the reinforcement strain difference is required.

Single crack width

In the case of a single crack, the strain of the reinforcement and the concrete are of equal value at the end of the transfer length, which allows for a definition of a boundary condition expressing the concrete strain using the reinforcement strain difference

$$\varepsilon_{\mathrm{nm,max}} - \Delta\varepsilon_{\mathrm{nm}} = \Delta\varepsilon_{\mathrm{c}} = \rho \cdot \alpha_{\mathrm{e}} \cdot \Delta\varepsilon_{\mathrm{nm}}\,. \tag{2-16}$$

The formulation in Equation 2-11 is restated using the expressions of Equation 2-15 with the consideration of the reinforcement strain difference $\Delta\varepsilon_{\mathrm{nm}}$ obtained in Equation 2-16 to determine the crack width in dependence on the maximum reinforcement strain

$$w = 2 \cdot (1 - \beta) \cdot \frac{\varepsilon_{\mathrm{nm,max}}^2 \cdot A_{\mathrm{nm}} \cdot E_{\mathrm{nm}}}{U_{\mathrm{nm}} \cdot \tau_{\mathrm{bm}}(s) \cdot (1 + \rho\,\alpha_{\mathrm{e}})} \tag{2-17}$$

and in dependence on the reinforcement stress σ_{nm} in the crack

$$w = 2 \cdot (1 - \beta) \cdot \frac{\sigma_{\mathrm{nm}}^2 \cdot A_{\mathrm{nm}}}{E_{\mathrm{nm}} \cdot U_{\mathrm{nm}} \cdot \tau_{\mathrm{bm}}(s) \cdot (1 + \rho\,\alpha_{\mathrm{e}})}\,. \tag{2-18}$$

Maximum width of adjacent cracks

Considering adjacent cracks where the concrete strain at the end of the transfer length is assumed to be below the concrete tensile strength and therefore no new crack forms, the reinforcement strain difference is

$$\Delta\varepsilon_{\mathrm{nm}} \leq \frac{f_{\mathrm{ct}}}{\rho_{\mathrm{ef}} \cdot E_{\mathrm{nm}}}\,. \tag{2-19}$$

This boundary marks the stabilised cracking stage.

In the case of adjacent cracks, the effective reinforcement area is considered using an effective reinforcement ratio $\rho_{\mathrm{ef}} = A_{\mathrm{nm}}/A_{\mathrm{c,ef}}$. The effective concrete area under tension $A_{\mathrm{c,ef}}$ is determined using the height of the effective reinforcement area h_{ef}, which may be determined using one of the approaches provided by Equations 2-22 to 2-25. The consideration of an effective reinforcement ratio accounts for the fact that the reinforcement force in the single crack is transferred to a concrete area which may be below the cross-sectional area of the member. With increasing distance to the crack, the height of the effective reinforcement area increases (cf. investigations in [Hel90]).
The uniaxial concrete tensile strength at the time of cracking, denoted as f_{ct}, is difficult to de-

termine in practical applications. During the occurrence of the first crack, lower percentiles of the assumed normally distributed concrete tensile strength in the member may be assumed. At the end of the crack formation stage, taking the upper percentiles is meaningful. Furthermore, the time-dependent development of the concrete strength, in particular during the first weeks, is highly dependent on concrete mixture, fresh concrete temperature, environmental conditions and post-treatment (e.g. investigations in [Tur16, Sch23a]). This opens room for interpretation. For example, the assumption of a too low tensile strength led to an underestimation of the later occurring crack widths and resulted in excessive damage to parking decks in Germany [Mei12, Fin16a]. Consequently, the German National Annex was adapted in 2015 to prevent a misinterpretation of the value of concrete tensile strength [EC2NADA1, Mei15, Fin16a], which resulted in more conservative predictions [Jin20].

The transfer length is at most able to propagate until the concrete strain reaches the tensile failure strain. This consideration allows for expressing Equation 2-15 utilising the expression of the reinforcement strain difference $\Delta\varepsilon_{\mathrm{nm}}$ in Equation 2-19 within the formulation in Equation 2-11. Considering this as a maximum value for a predicted crack width in dependence on the maximum reinforcement strain and substituting $A_{\mathrm{nm}}/\rho_{\mathrm{ef}}$ to be the effective concrete area under tension

$$w_{\max} = 2 \cdot \left[\varepsilon_{\mathrm{nm,max}} - \beta \cdot \frac{f_{\mathrm{ct}}}{\rho_{\mathrm{ef}} \cdot E_{\mathrm{nm}}} \cdot (1 + \rho_{\mathrm{ef}} \alpha_{\mathrm{e}}) \right] \cdot \frac{f_{\mathrm{ct}} \cdot A_{\mathrm{c,ef}}}{U_{\mathrm{nm}} \cdot \tau_{\mathrm{bm}}(s)} \tag{2-20}$$

and when considering the reinforcement stress

$$w_{\max} = 2 \cdot \left[\sigma_{\mathrm{nm}} - \beta \cdot \frac{f_{\mathrm{ct}}}{\rho_{\mathrm{ef}}} \cdot (1 + \rho_{\mathrm{ef}} \alpha_{\mathrm{e}}) \right] \cdot \frac{f_{\mathrm{ct}} \cdot A_{\mathrm{c,ef}}}{E_{\mathrm{nm}} \cdot U_{\mathrm{nm}} \cdot \tau_{\mathrm{bm}}(s)} \tag{2-21}$$

Considering Equations 2-18 and 2-21 as analytical approaches for a prediction of crack width, a reasonable assumption of β and a well-defined estimation of the mean bond stress considering the slip at the crack is required.

Opening of a crack

The obtained crack opening or slip is expressed as the occurring deformation of reinforcement and concrete along the transfer length due to the continuous force transfer provided by bond. Consequently, the approach does not consider the significantly smaller crack width at the reinforcement layer compared to the concrete surface nor the width at the surface, as has been reported in experimental campaigns [Got71, Sch21b, Bor10]. This phenomenon is attributable to two effects, visualised in Figure 2.8. Firstly, there is the occurrence of additional internal cracks at the locations of mechanical interlocking that do not propagate to the concrete surface, as reported by GOTO (Figure 2.8-I). Secondly, the *shear lag effect* described by BEEBY [Bee04, Bee05], defined as the influence of an eccentric force transfer by bond, results in an increase of the crack opening when distancing from the reinforcement layer and therefore a larger crack width (Figure 2.8-II). The extent to which these two effects contribute to the actual crack width at the concrete surface remains to be resolved [Sch21a]. A finite element numerical modelling study was conducted in [Sch22], incorporating a discrete representation of a steel rebar, including its rib geometry within a concrete volume. The study revealed that there was no significant divergence in predicted width between the analytical solution that neglected internal cracking and a shear lag effect.
Figure 2.11 also highlights the importance of differentiating between crack width at the surface and the crack width at the reinforcement layer, which are addressed differently in concepts for crack width prediction as highlighted in the upcoming section.

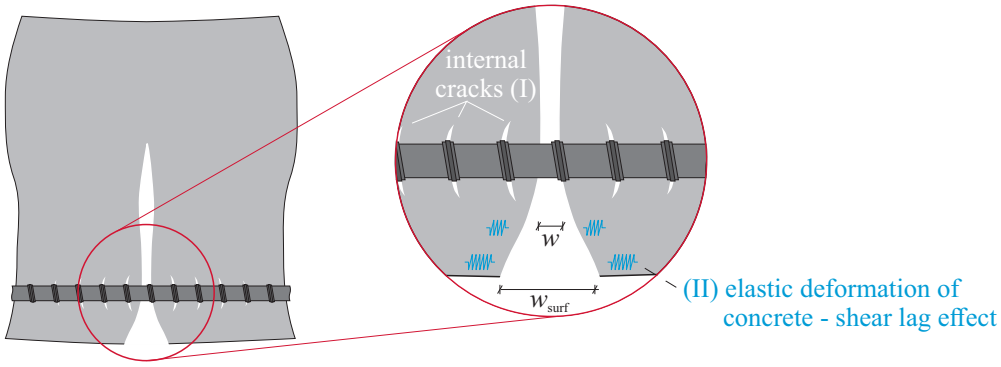


Figure 2.8: Effects contributing to the opening of a crack from reinforcement layer to member surface

2.5.4 Effective reinforcement area

The reinforcement has the capacity to restrict the crack width in its vicinity, which is defined as the effective reinforcement area. Outside this effective area, the crack is known to propagate "uncontrollably". In order to prevent the formation of interconnecting cracks, additional reinforcement is required, for example, in the web of members exhibiting a substantial depth.
While thin members typically exhibit only cracks that run through the entire cross-section, referred to as primary cracks, secondary cracks occur in the boundary zone around the reinforcement in thick members but do not propagate through the whole cross-section. The crack tips of branched secondary cracks are typically directed towards the nearest primary crack. In [Hel90, Böd10, Tur17, Sch25a], it is shown that the size of the boundary zone with secondary cracks is found to increase with the thickness of the member. The determination of the effective reinforcement area, including a differentiation for the member thickness, is addressed differently by the design approaches. While some code provisions, such as the North American Standards on FRP rebars [CSA12, ACI15, ACI22] do not consider an effective reinforcement area, the different Model Code and Eurocode 2 versions have applied this concept since the 1970s. The *fib* Model Code 2010 [MC10] and Eurocode 2 [EC2] assume the height of the effective reinforcement area

$$h_{ef} = \min\{2.5 \cdot d_1;\ (h-x)/3;\ h/2\} \tag{2-22}$$

with the latter two expressions addressing the boundaries of the height of the compression zone x in the case of bending, and of half the member height. This approach is also followed by the National Annex of Germany [EC2NAD], where a refinement is provided in the case of thicker members. For uniaxial tension

$$h_{ef} = \begin{cases} 2.5 \cdot d_1 & \text{for } h/d_1 \leq 5 \\ 2 \cdot d_1 + h/10 & \text{for } 5 < h/d_1 \leq 30 \\ 5 \cdot d_1 & \text{for } h/d_1 > 30 \end{cases} \tag{2-23}$$

and in the case of bending (see also [Kön96])

$$h_{ef} = \begin{cases} 2.5 \cdot d_1 & \text{for } h/d_1 \leq 10 \\ 2 \cdot d_1 + h/10 & \text{for } 10 < h/d_1 \leq 60 \\ 5 \cdot d_1 & \text{for } h/d_1 > 60 \end{cases} \tag{2-24}$$

while also the boundaries of $(h-x)/3$ and $h/2$ apply. The recently published *fib* Model Code 2020 [MC20] and the Final Draft to the Preliminary Eurocode 2 [FprEC2] restate the determination of the height, which is explained in detail in [Pér20]. Considering the distance between multiple reinforcement layers, denoted as s_y and the number of reinforcement layers n, the height of the effective reinforcement area is

$$h_{ef} = \min \begin{cases} \min\{d_1 + 5 \cdot d_{nm};\ 10 \cdot d_{nm};\ 3.5 \cdot d_1\} + (n-1) \cdot s_y \\ h - x \\ h/2 \end{cases} \tag{2-25}$$

A brief evaluation of applying these three different approaches in the case of small reinforcement diameters is provided in Figure 2.9. To address textile grids, a concrete cover of 15 mm was chosen. In this representation, the limitation of the compression zone height is neglected. The visualisation in Figure 2.9 reveals that for member heights h below a range of 80 mm (for $d_{nm} = 2$ mm) and 100 mm (for $d_{nm} = 10$ mm), the limitation of half the member height is decisive. For larger h/d_1 ratios, the approach proposed in *fib* Model Code 2020 determines h_{ef} below $2.5 \cdot d_1$ for diameters not exceeding 5.3 mm, which refers to textile grids. In contrast, the approach of the German National Annex addressing thicker members reinforced with rebars suggests a h_{ef} above $2.5 \cdot d_1$. Evidently, applying this approach is not feasible for textile grids and thin members, and a new consideration of the limitation of $h/d_1 \leq 5$ and $h/d_1 \leq 10$, is appropriate. Consequently, the question arises as to which definition provides the most feasible fit for textile grids.

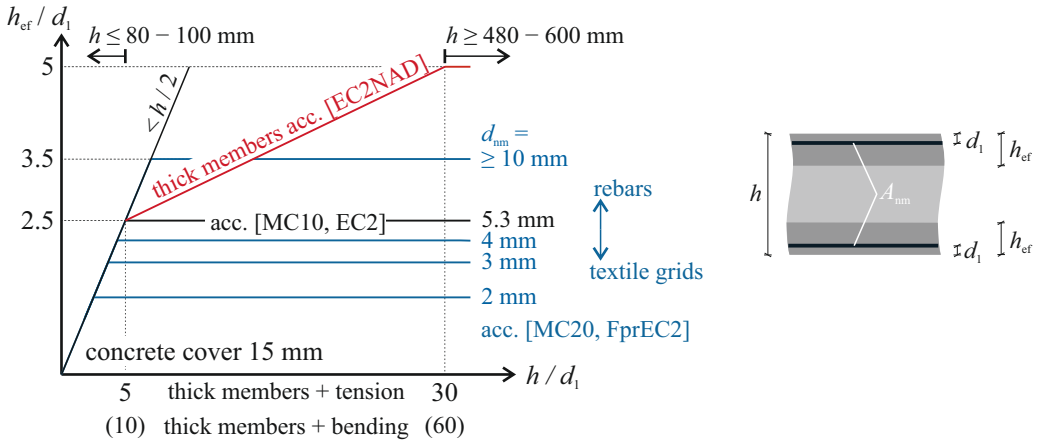


Figure 2.9: Determination of the height of the effective reinforcement area h_{ef} as defined by different code provisions

2.6 Concepts to predict the crack width

In the following section, an overview of different approaches to predicting crack widths is provided. These approaches are generally applicable to FRP-reinforced members, despite being primarily developed for use with smooth and ribbed steel rebars. When considering the introduction of calibration factors, it is necessary to differentiate between the FRP reinforcements and whether rebars or textile grids are employed. The considered concepts are listed in Table 2.1. Apart from the approach of deformation compatibility, which examines internal loading resulting from restraint-induced stress, all other concepts are oriented towards an external load situation. The *fib* Model Code 2020 and the Final Draft to the Preliminary Eurocode 2 also address the case of restraint-induced deformation using the degree of restraint.

In general, individual cracks exceeding the defined limitation are acceptable, provided that no deficit in the structural capacity of the members is observed and the function of the member is not compromised. Consequently, when assessing the efficiency of a code provision with regard to its accuracy in predicting the crack width, a logical assumption should be made. For instance, it may be permissible to allow a certain percentage of all cracks to exceed the prescribed width limit as proposed in [DBV16]. This addresses the wide range of scattering factors resulting from the concrete properties and possible crack patterns.

Table 2.1: Overview of concepts to predict the crack width

approach	rein-force-ment	consideration of bond stress	concept	prediction
KOENIG and TUE [Kön96]	steel rebars	explicit by calibration, slip-dependent	physically based model	maximum crack width
deformation compatibility [Böd10, Sch14]	steel rebars	mean value, but not directly defined	physically based model, equilibrium of global deformation	required number of cracks, widths below characteristic value
CEB-FIP Model Code 1990 [MC90], NA Germany [EC2NAD] and Austria [EC2NAA]	steel rebars	dependent on concrete strength, slip independent	analytical model	maximum crack width
fib Model Code 2020 [MC20], Final Draft to the Preliminary Eurocode 2 [FprEC2]	rebars + textiles	dependent on concrete strength, slip independent	empirical-based model	characteristic value, calibrated using mean value of crack width
DAfStb Guideline [DAfStb24]	FRP rebars + textiles	individually determined for reinforcement	analytical model	maximum crack width
ACI 440.1R-15 [ACI15]	FRP rebars	individually determined for reinforcement, slip independent	empirical-based model, indirect using rebar spacing	maximum rebar spacing and maximum rebar diameter

2.6.1 Approach of KOENIG and TUE

KOENIG and TUE provided in [Kön96] a crack width dependent bond stress relation that addresses the cracking stages and also considers the time-dependent effects of creep and cyclic loading, following a refinement of the analytical consideration of mean strains in Equation 2-15. The value of the mean bond stress is obtained using the description of the bond stress-slip relation in Equation 2-3

$$\tau_{\mathrm{bm}}(w) = \frac{C}{1+\lambda\cdot\alpha}\cdot\left(\frac{w}{2}\right)^{\alpha} \tag{2-26}$$

with additionally introducing a factor λ, which considers the influence of the cracking stage on the bond stress evolution

$$\lambda = \begin{cases} \frac{2}{1-\alpha} & \text{for } F \le F_{\mathrm{cr}} \text{ (single crack)} \\ \frac{1+\alpha}{1-\alpha}\cdot\left(\frac{F_{\mathrm{cr}}}{F}\right)^{1.5}+1.0 & \text{for } F \ge F_{\mathrm{cr}} \text{ (adjacent crack)} \end{cases} \tag{2-27}$$

considering the force F_{cr} required to induce a crack. Tension stiffening is addressed by determining

$$\beta = \frac{1+\lambda\cdot\alpha}{2+\lambda\cdot\alpha}. \tag{2-28}$$

The proposal requires a derivation of empirical factors C and α, which were provided in [Kön96] for steel rebars and in dependence on the concrete strength.

An additional crack opening in the case of a single crack is predicted as

$$\Delta w = [(1+\varphi_{\mathrm{b}})^{\alpha}-1]\cdot w, \tag{2-29}$$

which differentiates between the case of cyclic loading using the proposal in [Reh79]

$$\varphi_{\mathrm{b}} = (1+N_{\mathrm{cycl}})^{0.107}-1 \tag{2-30}$$

and the case of sustained loading as derived in [Fra76]

$$\varphi_{\mathrm{b}} = (1+10\cdot t)^{0.08}-1 \tag{2-31}$$

with the time considered in hours. For adjacent cracks at stabilised cracking, a simplification is introduced that accounts for the reduced value of mean concrete strain as less force is transferred, modifying Equation 2-21 to

$$w = 2\cdot\left[\sigma_{\mathrm{nm}}-\beta\cdot\frac{1}{(1+\varphi_{\mathrm{b}})^{\alpha}}\cdot\frac{f_{\mathrm{ct}}}{\rho_{\mathrm{ef}}}\cdot(1+\rho_{\mathrm{ef}}\cdot\alpha_{\mathrm{e}})\right]\cdot\frac{f_{\mathrm{ct}}\cdot A_{\mathrm{c,ef}}}{E_{\mathrm{nm}}\cdot U_{\mathrm{nm}}\cdot\tau_{\mathrm{bm}}(w)}. \tag{2-32}$$

2.6.2 Deformation compatibility for restrained members

Following the consideration of deformation equivalence in restraint members, TUE, SCHLICKE and BOEDEFELD proposed a model to determine the required reinforcement to achieve a state of compatible deformation between the restraint-induced deformation and the global deformation of the concrete member. The reinforcement ratio is determined to provoke a sufficient number of cracks with a specified width, so that deformation equivalence is fulfilled. Therefore, the restraint-induced force after crack occurrence and the restraint-induced strain must be determined, for example, by using the approaches provided in [Tue20].
Numerical investigations conducted by BOEDEFELD [Böd10] on thick concrete walls, representing

centric restraint due to the consideration of the foundation with a reinforcement layer located close to the surface and the consideration of secondary cracking, led to the proposal that about 30% of the force released upon the occurrence of the primary crack is transferred into the uncracked concrete section and is therefore not to be considered in the formation of the first secondary crack. This continuous transfer of force into the uncracked concrete regions is progressing for all secondary cracks occurring until no new secondary crack forms, as the remaining force is smaller than the concrete tensile strength.

As no secondary cracking is observed in thin concrete members and the cracks fully propagate through the cross-section, TUE and SCHLICKE [Tue20] proposed an iterative determination to obtain the required reinforcement stress to induce a sufficient number of primary cracks, so that the restraint-induced stress is reduced to a value below the concrete tensile strength considering the degree of restraint. Approaches to determine the required crack spacing are found, for example, in [Sch14].

As evident, also for the proposals using deformation compatibility to predict the crack width in both cases of thin and thick members, a functional relation between bond stress and slip is necessary.

2.6.3 Code provisions for crack width limitation

CEB-FIP Model Code 1990 and National Annex of Germany and Austria to Eurocode 2

The code provisions of the CEB-FIP Model Code 1990 and the National Annexes of Germany and Austria to Eurocode 2 [EC2NAD, EC2NAA] follow the analytically derived formulations presented in Section 2.5.3, assuming a mean value of reinforcement and concrete strain along the transfer length. The design crack width is set to be the maximum crack width resulting from a maximum crack spacing. A separation between single cracks and adjacent cracks at stabilised cracking is introduced using Equations 2-18 and 2-21, respectively. For design purposes, adaptations are introduced for a consideration of the non-linear strain evolution and tension stiffening, expressed by the factor β, and for a mean value of bond stress independent from the slip and approximated using the concrete tensile strength. The mean value of bond stress is determined under the assumption of a constant distributed force transfer along the transfer length. This consideration takes into account that the force transfer in the vicinity of the crack surface is significantly reduced due to damage to the concrete matrix, often referred to as a "bond-free" length. The mean value of bond stress is expressed in the very simplified approximation

$$\tau_{\mathrm{bm,m}} = 1.8 \cdot f_{\mathrm{ct}}\,, \tag{2-33}$$

with the CEB-FIP Model Code 1990 accounting for a reduced bond stress for single cracks in the case of sustained or repeated loading with $1.35 \cdot f_{\mathrm{ct}}$.

Tension stiffening is considered by approximated values of β. In the case of instantaneous load application, $\beta = 0.6$. For sustained or repeated loading, the CEB-FIP Model Code 1990 introduces a differentiation to account for the actual strain evolution. Considering a single crack, the non-linear evolution is also expressed with $\beta = 0.6$, while the reduction of the mean bond stress accounts for the increase in transfer length. On the other hand, the reduced capacity to transfer force between adjacent cracks is considered by an adapted value of $\beta = 0.38$.

The Eurocode 2 and the corresponding National Annexes of Germany and Austria introduce a simplification of the different cases presented in the CEB-FIP Model Code 1990, proposing $\beta = 0.4$ considering that sustained or repeated loading are the relevant scenarios for crack width limitation in structural design.

To account for the influence of large rebar spacing on the maximum crack spacing, the Eurocode 2 and the corresponding National Annexes of Germany and Austria propose an upper limitation for the maximum crack spacing. This upper limitation is defined as being 1.3 times the depth of the tensile zone of the member.

***fib* Model Code 2020 and Final Draft to the Preliminary Eurocode 2**

The formulations provided in the *fib* Model Code 2020 [MC20] are equivalent to the proposal in the Final Draft to the Preliminary Eurocode 2 [FprEC2], both follow the concept proposed with the limit state of crack width in the CEB/FIP Model Code 1978 [MC78]. Both recent code provisions consider FRP reinforcement and apply the identical formulations given for steel rebars. The concept is to determine a mean crack width and transfer this value to a characteristic crack width w_k, using an empirical calibration factor. The mean crack width is obtained by predicting a mean crack spacing and the mean strain difference of reinforcement and concrete, which is identical to the approach provided in the previous code provisions *fib* Model Code 2010 [MC10] and Eurocode 2 [EC2]. However, refinements are introduced to account for the reduced crack spacing observed in flexural members compared to members subject to uniaxial tension, denoted as k_{fl}, an additional crack opening due to the curvature of flexural members $k_{1/r}$, and the "bond condition" k_b depending on the casting position of the reinforcement layers. The characteristic value of crack width according to [MC20, FprEC2] is determined as follows:

$$w_k = \beta_w \cdot k_{1/r} \cdot s_{rm} \cdot (\varepsilon_{nm,m} - \varepsilon_{cm}) \tag{2-34}$$

The calibration factor $\beta_w = 1.7$ is equal to the proposal in the CEB/FIP Model Code 1978. REHM and MARTIN [Reh68] derived a similar calibration factor of 1.66 for the 95% quantile of all crack widths occurring in a member. The mean crack spacing is predicted as

$$s_{rm} = k_c \cdot c + k_{fl} \cdot k_b \cdot \frac{f_{ct} \cdot A_{nm}}{\tau_{bm,m} \cdot U_{nm} \cdot \rho_{ef}}, \tag{2-35}$$

which considers the influence of the concrete cover c to address internal cracks as initially reported in [Got71]. The impact of the concrete cover remains a subject of ongoing research discussion. Recent research on steel-reinforced members with very large covers [Pér13] demonstrated an influence on the crack spacing, although the conducted experiments fall outside the scope of typical applications, as concrete covers of 70 mm were investigated. A reasonable definition of the effective reinforcement area, in combination with an explicit consideration of the cracking stage, may account for this effect [Sch21a]. Furthermore, while the crack spacing increases in members with larger concrete covers compared to members with smaller covers, and the crack width on the concrete surface may be larger, the width at the reinforcement layer may be comparable in value due to the presence of internal cracks, as stated by the authors in [Pér13]. The consideration of the concrete cover with the empirical factor $k_c = 1.5$ can be traced back, among other investigations, to REHM and MARTIN [Reh68], while for plates a higher factor of 4.0 was proposed in [Reh68]. It is worth noting that low concrete covers were present during the time this calibration was derived.

The "bond condition" resulting from the casting position of the tensile reinforcement layer is differentiated in a good casting position, with $k_b = 0.9$, and a poor position, with $k_b = 1.2$.
The consideration of the linear strain distribution in the cross-section of flexural members compared to a constant distribution in the case of uniaxial tension, highlights the lower concrete stress present in the centre of the effective height, denoted as $\varepsilon_{c,mean}$, compared to the most tensioned fibre in the uncracked concrete region (see Figure 2.10 in accordance with [Pér20]). According to [Pér20], it is therefore necessary to consider $\varepsilon_{c,mean}$ to determine the crack spacing. Hereby, the

linear strain distribution in the uncracked concrete cross-section in combination with the retransfer is taken into account. The occurrence of additional cracks in uncracked regions of concrete members with only unbonded tendons as reinforcement was already reported, for example, in [Web82, Bus83], revealing that adjacent crack occurrence is not solely attributed to bond in flexural members. Consequently, the prediction of the crack spacing using the concrete tensile strength as an approximation for the concrete stress at adjacent cracking requires an adaptation by

$$k_{\mathrm{fl}} = \frac{1}{2} \cdot \left(1 + \frac{h - x - h_{\mathrm{c,ef}}}{h - x}\right). \tag{2-36}$$

In dependence on the effective height, the location of $\varepsilon_{\mathrm{c,mean}}$ does not necessarily correspond to the location of the reinforcement in the cross-section, as shown in Figure 2.10 for the uncracked concrete region (stage I) between the two cracks. However, applying this terminus accounts for the smaller crack spacing observed in flexural members compared to members subject to uniaxial tension, as evaluated in [Pér20].

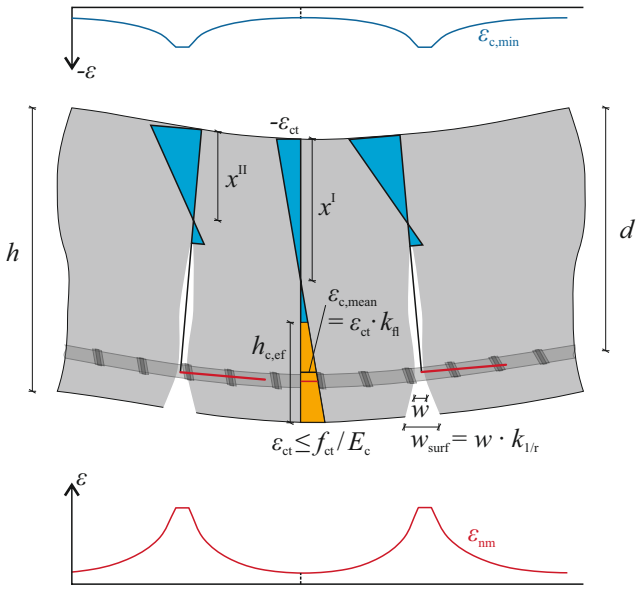


Figure 2.10: Illustration of the two factors accounting for the influence of the cross-sectional curvature in flexural members in *fib* Model Code 2020 according to [Pér20]

To account for the difference between the crack width at the reinforcement layer and the concrete surface resulting from the curvature of the cross-section, as visualised in Figure 2.10 for the crack on the right hand side, the geometrical-dependent factor

$$k_{1/\mathrm{r}} = \frac{h - x}{d - x} \tag{2-37}$$

is introduced in the formulation of *fib* Model Code 2020. According to the database evaluation performed in [Pér20], the introduction of $k_{1/\mathrm{r}}$ addresses the increased crack opening at the concrete surface due to the curvature and increases the accuracy of the prediction.

A limitation of the crack spacing to account for large rebar spacing is also introduced following the identical definition proposed by Eurocode 2 [EC2], which is defined as 1.3 times the depth of the tensile zone of the member.

As a final remark on the approach of *fib* Model Code 2020, the use of the term $(f_{ct} \cdot A_{nm}) / (\tau_{bm,m} \cdot U_{nm} \cdot \rho_{ef})$ is addressed. This term denotes the maximum attainable transfer length in the case of adjacent cracks. Consequently, it is considered in predicting the maximum crack width at stabilised cracking, assuming that the maximum crack spacing is equal to twice the maximum transfer length (approach in CEB-FIP Model Code 1990). In contrast to this analytically based assumption, the approach in the *fib* Model Code 2020 utilises this term solely to obtain some value of a mean crack spacing by calibration.

German DAfStb Guideline "Concrete members with non-metallic reinforcement"
According to the concept of crack width limitation proposed in the German National Annex to Eurocode 2, the DAfStb Guideline "Concrete members with non-metallic reinforcement" [DAfStb24] provides the first code provision in Germany to predict the crack width in FRP members, without introducing any differentiation with respect to the use of rebars or textile grids. The analytical model in the German National Annex remains almost identical in the DAfStb Guideline, with adaptations only regarding an explicit consideration of the characteristic value of the mean bond stress, designated as $\tau_{bm,k}$, and the factor to account for the non-linear strain evolution, i.e. tension stiffening. Both parameters are set individually for the used FRP reinforcement and must be provided in advance, for example, by the manufacturer of the reinforcement. A derivation method to obtain the value of bond stress is recommended based on an experimental campaign using uniaxial tensile tests. This method yields conservative results and is not universally applicable due to its reliance on the crack spacing and widths that emerge during the formation stage, as reported in [Sch23b, Sch24a]. Furthermore, no method to account for tension stiffening is provided, which is therefore recommended to be neglected. This assumption is based on the theoretical premise that no force transfer occurs and that the reinforcement strain along the transfer length remains constant at the value present in the crack. Nevertheless, this also signifies that the impact of both sustained and cyclic loading cannot be addressed by a reduction of the tension stiffening factor, as outlined in [EC2NAD].
The guideline allows for maximum crack widths of up to 0.7 mm when there are no special requirements, such as those related to visual appearance or sections with lapped joints. In all other cases, the maximum width is limited to 0.4 mm.

ACI Guide for the design and construction of structural concrete reinforced with FRP bars
The American Concrete Institute approved the design guideline ACI 440.1R-15 [ACI15], which provides a simple proposal to assure sufficient crack width limitation for FRP rebars by defining a maximum bar spacing in the transversal direction. The approach is consistent with the formulation provided in the ACI 318-14 [ACI14] code provision for steel reinforcement. The proposal in ACI 440.1R-15 considers a geometrical dependent factor (similar to formulation in Equation 2-37), the concrete cover and a parameter addressing the bond behaviour. The focus is on cracking resulting from flexural loading. The bond behaviour is accounted for by a reference value to the bond behaviour of steel rebars and is thus provided in advance. A selection of values for different FRP rebars is proposed in [Bak06], and a test procedure is provided in [CSA12]. The effect of sustained loading is not yet considered in [ACI15]. The more recently introduced code provision ACI 440.11-22 [ACI22], focusing on GFRP rebars, follows this concept.
ACI 440.1R-15 limits the maximum crack width to a range between 0.4 and 0.7 mm, while the ACI 440.1R-22 suggests a more progressive limit of 0.7 mm for GFRP rebars in cases where no special requirements are present.

Further proposals focusing on non-metallic reinforcements
The Japanese design code [JSCE97] was the first to focus on FRP reinforcement in concrete struc-

tures, adopting an empirical-based approach that considers the concrete cover and an experimentally derived parameter. The model explicitly accounts for two categories of reinforcement: FRP rebars and FRP textile grids. The maximum width is limited to 0.5 mm for the visual appearance. The Italian code provision [CNR-DT203] is founded on the empirical-based concept of the CEB/FIP Model Code 1978 [MC78], with the required parameters being determined in advance by means of an experimental test series. The focus remains on FRP rebars. The limitation is also 0.5 mm. The Canadian standard CSA S806-12 [CSA12] does not provide for an explicit prediction concept and only provides for a minimum reinforcement ratio of 0.3% of the gross cross-sectional concrete area in the case of CFRP rebars and 0.4% for GFRP rebars. However, it does propose a test method to determine the crack width and a bond coefficient (cf. ACI 440.1R-15) for FRP rebars. The maximum crack width should be limited to a range between 0.5 and 0.7 mm.

2.7 Deflection

The deflection of flexural members with non-metallic reinforcement is, in principle, analogous to that of conventional steel-reinforced members. However, with regard to the high strain utilisation and the slender design possible for FRP members, the control of deflection frequently becomes decisive. In order to assess the deflection, two differentiations are feasible. In the case of the entire member being uncracked, the deflection is estimated by determining the cross-sectional curvature using the full concrete cross-section, particularly the Young's modulus of the concrete. The assumption of linear elastic behaviour facilitates the straightforward calculation of the deflection. The issue of the load-dependent creep behaviour and the time-dependent evolution of the Young's modulus is strongly simplified by an adaptation of the Young's modulus. Hereby, concrete creep is approximated using a creep coefficient, with the Young's modulus being reduced accordingly. Consequently, a strategy to minimise deflection involves the prevention of concrete cracking in the serviceability state. Either prestressing, an adaptation of the cross-sectional height, or an increase in the concrete tensile strength may be required.
In the case of crack formation the assumption of a linear elastic behaviour of the cracked concrete is no longer appropriate. The strain in the most-tensioned fibre of the cross-section is a considerable multiple of the strain in the compression zone. The stiffness of the cracked cross-section is significantly reduced relative to the uncracked case, due to the reduction in the contributing area of the concrete. This is commonly implemented in design approaches by determining a composite stiffness, which resembles an adapted stiffness for an equivalent cross-section demonstrating linear elastic behaviour. For instance, LITZNER's approach [Lit95] involves the calculation of "flexural stiffness" through the moment of inertia of the uncracked and cracked cross-sections. While this approach was derived for steel reinforced concrete members, it is also applicable for non-metallic reinforcement, as LITZNER assumes a linear elastic behaviour of the reinforcement. Following the determination of a suitable approximation of the stiffness of the uncracked and cracked cross-sections, a feasible consideration of the contribution of tension stiffening is required. In the scenario where two cracks are located adjacent to each other, a certain amount of force is transferred to the uncracked region, which exhibits a greater degree of stiffness. Consequently, the deflection of the member is reduced in comparison to a scenario where no force transfer occurs, under the assumption that tensile forces are solely attributed to the reinforcement. Consequently, the contribution of tension stiffening is dependent on the magnitude of the force transfer.
Accordingly, a flexural member may be divided into three regions: firstly, the uncracked concrete region where the applied bending moment is below the tensile resistance of the concrete. Secondly, the crack itself, where all tensile force is accounted for by the reinforcement, as visualised

in Figure 2.11Ⓘ when neglecting the small contribution of concrete subject to tension. Thirdly, the region between adjacent cracks Ⓘ with a reduced reinforcement strain.

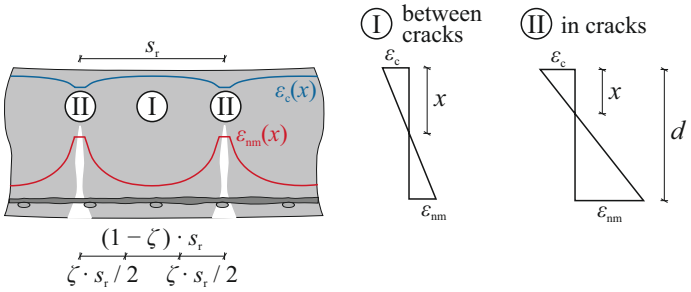


Figure 2.11: The uncracked and cracked concrete regions of a flexural member between adjacent cracks (adapted from [Lit95])

It is evident that determining the exact magnitude of tension stiffening and the cross-sectional curvature in the region between adjacent cracks is only possible in theory. When dealing with material parameters that are subject to variation, particularly those related to bond capacity along the reinforcement, a solid approximation is required. Utilising an experimental campaign, RAO [Rao66] discovered that, as the reinforcement strain increases, the contribution of tension stiffening decreases non-linearly. Utilising the test data, he derived an empirically determined relation to consider the contribution of tension stiffening. According to RAO, the strain difference

$$\Delta\varepsilon_{nm} = k \cdot \frac{\sigma_{nmr}}{\sigma_{nm}} \cdot \frac{f_{ct}}{\rho_{ef} \cdot E_{nm}} \tag{2-38}$$

with the reinforcement stress present after initial crack occurrence σ_{nmr} and the reinforcement stress σ_{nm} present in the crack.
Notably, the factor $k = 0.18$ provided in [Rao66] was derived using kp/cm^2. In [Reh68, Ros76] the stress after initial crack occurrence in the case of flexural members without axial load was approximated to be $\sigma_{nmr} \approx 0.18 \cdot f_{ct} \,/\, \rho_{ef}$. Considering this approximation and Equation 2-38, an average value of reinforcement stress is obtained

$$\sigma_{nm,m} = \sigma_{nm} \cdot \left(1 - \frac{\sigma_{nmr}^2}{\sigma_{nm}^2}\right). \tag{2-39}$$

This allows for an expression of the average reinforcement stress under the consideration of tension stiffening. The findings by RAO and the verifications provided in [Ros76] were adopted in the CEB-FIP Model Code 1990 [MC90] by introducing a distribution factor

$$\zeta = 1 - \beta_{TS} \cdot \left(\frac{\sigma_{nmr}}{\sigma_{nm}}\right)^2 \geq 0\,. \tag{2-40}$$

Hereby, the influence of sustained and cyclic loading is accounted for by reducing the tension stiffening factor β_{TS} to 0.5. In the case of an instantaneous load, $\beta_{TS} = 1.0$.
The *fib* Model Codes [MC10, MC20] and the Eurocodes 2 [EC2, FprEC2] do not explicitly provide for a further determination of the deflection. Solely a determination of an average parameter α_m, which provides for a simplified consideration of the cracked concrete section α_{II} and uncracked concrete section α_I is given

$$\alpha_m = \zeta \cdot \alpha_{II} + (1 - \zeta) \cdot \alpha_I\,, \tag{2-41}$$

considering the distribution factor ζ.
Approaches for utilising the distribution factor and the parameter α_m are, for example, presented in [Lit95, Fin16b].

Conversely, the ACI Guideline 440.1R-15 [ACI15] introduces an effective moment of inertia to determine the stiffness of the member for FRP rebars. Following the proposal for steel-reinforced members (for which background information is provided in, for example, [Bis05, Bis07]), a modification is introduced to account for the changing stiffness in the member resulting from the cracked and uncracked sections. This is denoted as γ in [ACI15]. As demonstrated in [Bis09, Bis11], a range of approximations for γ is provided, depending on the loading type and boundary conditions. Examples and references to obtain the moment of inertia of the uncracked cross-section and of the cracked cross-section are provided in [ACI15].

2.8 Summary

The application of non-metallic reinforcement in concrete structures is nowadays an established practice. Following several decades of research and practical applications, recent progress has been made in providing code provisions for a faster and standardised application of non-metallic reinforcement in the construction sector. The determination of the structural capacity using progressive while safe proposals is the result of this process. Despite these significant advancements, fundamental questions emerge when addressing the serviceability state. It is evident that conservative approaches for crack width prediction, which are often based on established methodologies derived for steel-reinforced members, are associated with a degree of uncertainty. In addition, while textile reinforcements do reveal a periodic and homogeneous surface, the sequence of changes in cross-sectional geometry occurs at larger distances in dependency of the yarn spacing when compared to the close rib spacing of rebars of comparable tensile capacity. Thus, in textile reinforced concrete, the bond mechanisms exhibit variation depending on the region utilised, leading to the local transfer of significant forces into the concrete. The resulting stress concentration of the concrete in the bond area has been shown to provoke crack formation and eventually results in a lower overall utilisation of the member when referring to the structural capacity, in comparison to the known behaviour of steel reinforced concrete. This challenges the derivation of a feasible approach and is not solved by test methods, which show some disadvantages in adequately characterising the bond behaviour at small slip representative for the serviceability limit state.

Consequently, the distinguished behaviour of non-metallic reinforcement, in particular textile grids, requires a re-evaluation of the bond behaviour. One strategy is to characterise and to quantify the bond capacity using experimental investigations, which are conducted in the following Chapter 3. Moreover, despite the analytical background of some code provisions, a reassessment is necessary for the crack width prediction. This addresses the bond behaviour and also long-term effects, such as cyclic loading. In the case of the latter, the research conducted on textile grids is limited.
With regard to deflection, the quantification of the contribution of tension stiffening in terms of higher reinforcement strains present in comparison to steel reinforcement is to be investigated in depth. This is of particular significance in the context of textile reinforcements, which allow the ultimate limit state design of slender members having a large span and small height due to high reinforcement utilisation and the reduced concrete cover. In this case, the crack spacing may provide for a transfer length where no significant force transfer is possible, which results in a lower contribution of tension stiffening as anticipated by the design approaches.

3 Investigations to characterise the bond behaviour

3.1 Overview of the experimental campaigns

The basis for an appropriate representation of the bond behaviour in an analytical, numerical, or physically based model to predict the crack opening and deflection is a well-defined approximation of the force transferred by the bond in relation to the displacement occurring between the reinforcement and concrete. One established solution strategy to derive this representation is the use of experimental investigations, which enable the derivation of a relation between force and displacement. As highlighted in the introduction of test setups in Section 2.4.5, each setup has its advantages and disadvantages regarding the boundary conditions and the assumptions made when evaluating the test data. For the analytical descriptions and the derivation of bond-slip relations, two different test types were considered for the FRP textile grids investigated in this thesis. The single-sided pull-out test type C, referred to as SPOc and presented in Section 3.3, provides for a force-slip relation, which is set in dependency to the embedded length. In addition, the crack opening tensile (COT) test is introduced in Section 3.4. This setup represents a single cracking stage and is used to determine a force-crack opening relation. As a consequence of the well-defined boundary conditions and the low scattering achieved in the COT tests in comparison to the SPOc tests, it is possible to undertake more in-depth research regarding the reinforcement strain evolution and bond behaviour of textile grids. This is done by using distributed fibre optical sensors (FOS), applied on the surface of the fibre strand. These measurements allow for the continuous determination of the reinforcement strain and thereby enabling the derivation of the bond stress evolution along the transfer length (see Section 3.5).

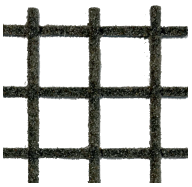
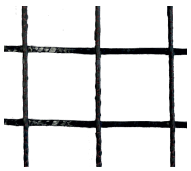
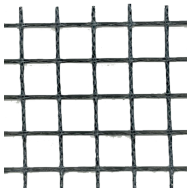
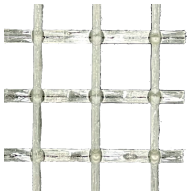
Both experimental campaigns of SPOc and COT followed two main objectives: Firstly, providing force-displacement relations that are feasible to describe the bond behaviour, thus enabling the derivation of analytical models to predict the crack width (performed in Chapter 5). Secondly, to obtain a deeper insight in the bond behaviour of FRP textile grids for several varied parameters. Of significance was the inclusion of extreme cases, such as the use of very small embedded lengths equivalent to the yarn spacing or the removal of the transverse fibre strand, as well as the behaviour under cyclic loading applied in a regime representing the serviceability state. Further parameters varied were the concrete strength, the embedded length, the orientation of the fibre strand and the use of coarser aggregates. Following this strategy, the SPOc tests focused on providing a comprehensive characterisation of the textile grids. In contrast, the bond capacity and the quantification of the bond force transferred in dependency to the crack opening were the primary focus of the COT tests.

3.2 Investigated textile reinforcement

Before presenting the evaluations of the experimental campaigns, starting with the SPOc test series in Section 3.3, an overview of the investigated planar, biaxial, warp-knitted FRP textile reinforcements is given in the following. In all experimental campaigns carried out in this thesis, different reinforcements were used aiming to provide for a broad spectrum of types and materials and to generalise the performed methodologies and derived approaches when applied to non-metallic reinforcement. In total, five different textile grids were considered, which are listed in Table 3.1 with their abbreviation used in this thesis, their fibre material and impregnation, the yarn spacing for the grids and the cross-sectional area. The textile grids were chosen to differentiate between the

material of the roving (carbon or glass) with their different Young's modulus, the impregnation consisting of either an epoxy resin (thermosetting polymer) or a polystyrene resin (thermoplastic polymer) which influences the surface of the fibre strands, and the yarn spacing to address possible influences of local undulations. Additional test series in the SPOc campaign investigated a sand-coated grid (CG1sc), which is identical to the reinforcement CG1 but the surface was post-treated with sand (fixated with the same epoxy resin) to improve the force transfer. As a result, the cross-sectional area, which considers the roving and the impregnation, is larger compared to the reference grid CG1. Additional information on the characteristics of the reinforcements is provided in Appendix B.2.
In all following investigations, the cross-sectional area of the fibre strands is approximated to have a circular cross-sectional geometry and refers to the area of roving and impregnation. Consequently, the reinforcement stress, Young's modulus, tensile strength, equivalent diameter, and bond area are set in relation to this cross-sectional area, denoted A_{nm}.

Table 3.1: Overview of the investigated FRP textile grids

index	product name	plan view of reinforcement	impregnation[1)]	yarn spacing y_{nm}	cross-sectional area A_{nm}[2)]
CG1 carbon grid	solidian GRID Q95-CCE-38-E8		epoxy resin (TS)	38 mm	warp: 7.5 mm² weft: 8.7 mm²
CG1sc carbon grid sand coated	solidian ANTICRACK Q95-CCE-38		epoxy resin (TS)	38 mm	warp: 15.4 mm² weft: 16.3 mm²
CG2 carbon grid	Wilhelm Kneitz SIT grid 50/50		polystyrene resin (TP)	50 mm	warp: 6.3 mm² weft: 5.4 mm²
CG3 carbon grid	hitexbau HTC 25/25-80-UWX		polystyrene resin (TP)	25 mm	warp: 3.3 mm² weft: 3.2 mm²
GG alkali resistant glass grid	solidian GRID Q121-RRE-38		epoxy resin (TS)	38 mm	warp: 10.3 mm² weft: 10.0 mm²

[1)] TS: thermosetting poylmer; TP: thermoplastic polymer
[2)] warp: 0°-direction; weft: 90°-direction

3.3 Characterisation using single-sided pull-out tests

3.3.1 Concept of the experimental campaign

The general characterisation of the bond behaviour was done using single-sided pull-out tests of type C, which also allowed for the derivation of bond force-slip relations. The test parameters varied in embedded length, concrete strength, maximum aggregate size, and the influence of the transverse fibre strands. The warp direction was the main investigated alignment, while also test series in the weft direction were conducted. In total, two hundred individual tests were performed on the five different FRP grids, with each series consisting of five tests. An overview of the varying test parameters for the investigated grids is provided in Table D.1. The used concretes are differentiated between a normal-strength concrete, denoted as NSC, which represents a concrete of strength class C30/37 according to the definition provided in Eurocode 2 [EC2], and a high-strength concrete (HSC) referring to a strength class of C80/95. The concrete mixtures and all obtained strength values are provided in Appendix B.1.

An overview of the test setup is given in Figure 3.1. The setup consisted of a supporting steel frame on which the specimen is placed with a PVC layer between the specimen and support to reduce lateral friction which may increase the bond capacity of the specimen. A steel plate is used as support, which is slit-in to allow a passing through of the fibre strand. The fibre strand is placed centrally in the specimen with one end protruding the concrete cuboid at the unloaded end to measure the slip s_{ul}. The load is applied through clamping. Therefore, the fibre strand is placed in a steel tube and moulded with an epoxy resin. This provided for a more uniform load introduction in the fibre strand without applying high lateral stress on the textile, preventing yarn rupture in or close to the clamping area. The slip on the loaded side s_l was determined using a laser displacement sensor clamped to the fibre strand. In addition, facet points were placed on the specimen and the fibre strand to allow for an evaluation of their displacement using digital image correlation (DIC).

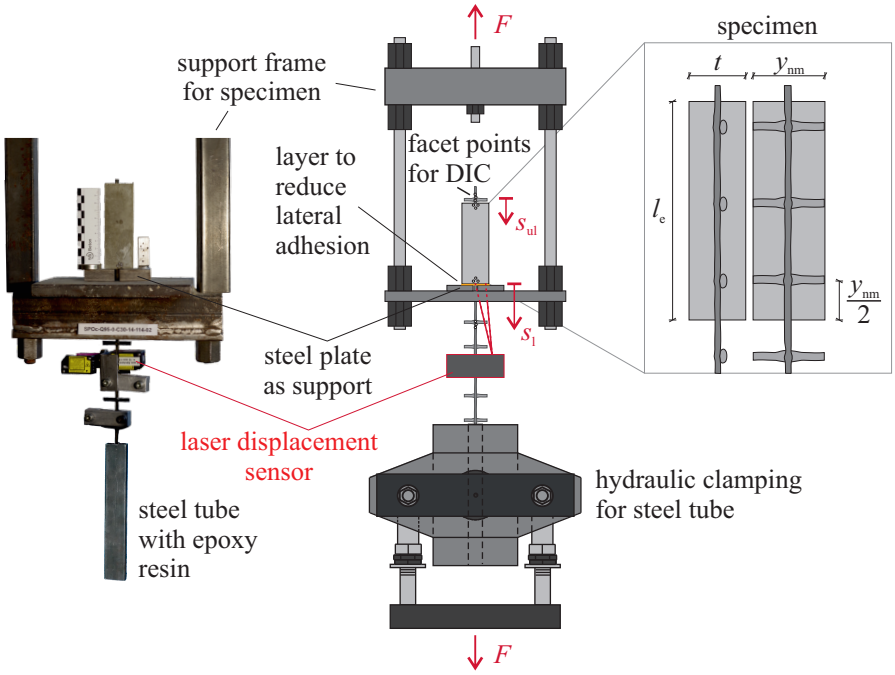


Figure 3.1: Test setup of single-sided pull-out tests type C (SPOc)

The specimens had a height defined by the embedded length l_e and a width equivalent to the transverse yarn spacing y_{nm}. The depth t was set to be 30 mm when using a concrete with a maximum aggregate size of 5.6 mm, which allowed for a concrete cover between 13 and 14 mm depending on the fibre strand height. For the three series conducted with a concrete having a maximum aggregate size of 16 mm, the depth was increased to 50 mm with the concrete cover enhancing accordingly. The fibre strand was positioned in the specimen, so that the initial intersection with the transverse strand was located at a distance from the loaded side equivalent to half of the yarn spacing. The load was applied continuously at a rate of 1 mm/min until failure occurred. While five tests were conducted for each series, not all results were ruled as valid and, consequently, were not considered for further analysis. Invalid test results were determined by either predominately damage to the fibre strand, which was not detected prior to the test but clearly revealed at the beginning of loading, or excessive tilting of the specimen during the test, resulting in a local stress introduction. In both cases, a failure at very low loading compared to the average gained from the valid tests was observed. The results of the invalid tests are provided in Appendix D.1. In total, of the two hundred tests conducted, 86% were ruled as valid. This "success rate", seemingly low, was primarily attributed to the sensitivity of the small specimens and the fibre strands, particularly reinforcement CG3, during specimen preparation and test conduction.

3.3.2 Failure types and utilisation of pull-out force

The observed failure types were characterised as follows, with a visual representation given in Figure 3.2. Splitting of the concrete is a typical failure observed in textile reinforced concrete members, because due to the waviness and undulation of the fibre strand in combination with small concrete covers, the concrete is subject to high forces transferred at local areas as reported for example in [Pre19a, Bie21a]. The concrete strength is exceeded and a longitudinal splitting crack forms, as visualised in Figure 3.2a. In the case of a full contribution of the embedded length, the longitudinal splitting crack immediately propagates through the specimen, resulting in instant failure. At larger embedded lengths, a continuous propagation of the splitting crack is often observed prior to failure. The force transfer is relocated towards the uncracked and not completely damaged concrete area, which may be visually simplified as the opening of a zip fastener and is therefore referred to as *zipping*. For example, this was reported in [Bie20, Bie21a] for textile grids and also for carbon rebars in [Sch23c]. As a result, an increase in embedded length does not necessarily provide a linear correlated improvement in bond capacity. PREINSTORFER [Pre19a] investigated in detail the effect of the fibre strand's cross-section in combination with its waviness on the occurrence of splitting. He showed that elliptical-shaped cross-sections tend to provoke splitting due to a non-uniform distribution of the tensile stress transferred in the surrounding concrete. This was generally confirmed by the conducted test series for CG1 and GG, as especially for specimens reinforced with CG1 splitting was the dominant failure type (75% of all valid tests).
When improving the bond capacity by adding an adhesive coating, e.g. sand as for CG1sc, the additional force induced by the improved adhesion and friction provoked splitting even more. Often, transverse cracks were observed in addition to the splitting crack, propagating from the surface to the reinforcement layer. These transverse cracks were localised at or behind a transverse fibre strand when viewed from the loaded side of the fibre strand, as exemplarily shown for the divided specimen with a longer embedded length in the bottom pictures of Figure 3.2a. In the test series where the transverse fibre strands were removed prior to concreting and for the specimens reinforced with the sand-coated grid, it was found that the occurrence of transverse cracks was not related to the transverse fibres strands. The fibre strands with a more circular-shaped geometry provoked longitudinal cracking in the lateral direction to the reinforcement layer, which was also

reported in [Pre19a]. In all specimens which failed due to concrete splitting, a shearing of the transverse fibre strands was observed.
Pull-out of the fibre strand typically occurred at low embedded lengths at which the provided bond length is not sufficient enough to allow for a force transfer which either is equivalent to the tensile strength of the fibre strand or induces concrete splitting. For the investigated grids, pull-out failure occurred at embedded lengths at or below three times the yarn spacing. During pull-out, the transverse strands were sheared off and a visible abrasion of the fibre strand impregnation with particles of crushed concrete remaining on the strand was observed (Figure 3.2b). For the reinforcements CG2 and CG3, both of which had a polystyrene resin impregnation and a more circular-shaped cross-section, pull-out failure occurred at about 40% of all valid tests. In comparison, pull-out failure was observed at less than 5% of all valid tests for CG1 and GG with an epoxy resin impregnation and a more elliptical-shaped geometry.
In instances where pull-out did not occur and the concrete strength was not exceeded by the induced splitting force, yarn rupture was finally observed as the tensile strength of the fibre strand was reached. This defines the third identified failure mechanism. The rupture was located either in the free length, as demonstrated in Figure 3.2c, or in close proximity to the steel tube or concrete specimen, indicating an influence of the clamping or transversal pressure, respectively. In 36% of all tests, yarn rupture was detected.

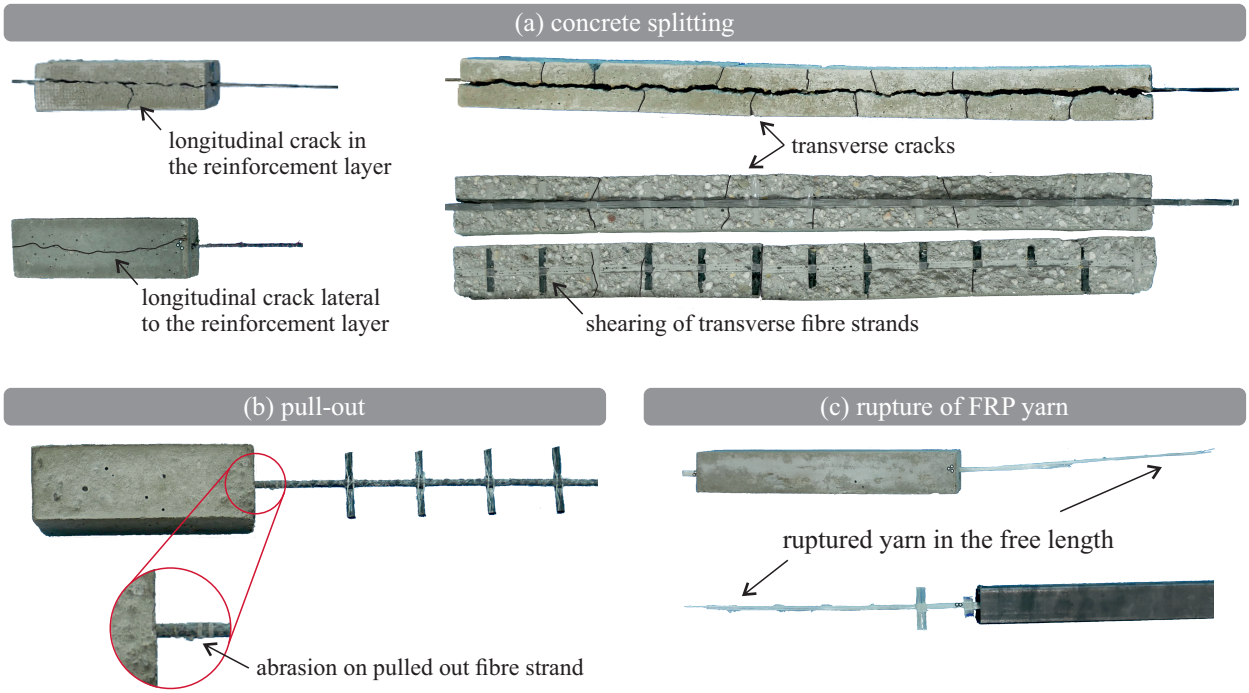


Figure 3.2: Observed failure types of SPOc tests

These three failure types are attributable to the maximum pull-out force measured in the SPOc tests. In the majority of cases, failure due to pull-out resulted in the lowest recorded force. Conversely, yarn rupture led to the highest force, as the tensile strength of the reinforcement was reached. An overview of the maximum pull-out force, as determined in each test related to the embedded length, is provided in Figure 3.3, with the observed failure type given. Furthermore, the average value of force determined for each test series is provided, as indicated by the rectangular boxes in Figure 3.3. The subsequent summary of the tests results focuses on the five investigated parameters.

Embedded length: In general, a pull-out force close to the mean tensile strength of the fibre strand in warp direction $F_{\mathrm{nm,m,0°}}$ is reached for embedded lengths exceeding 250 mm for the plain carbon grids and 114 mm for the sand-coated carbon grid and the glass grid. Furthermore, the investigation of the largest embedded length of 500 mm showed that concrete splitting cannot be ruled out as a failure type. Consequently, increasing the embedded length did not significantly increase the applied maximum pull-out force.
Conversely, at an embedded length equivalent to the yarn spacing, pull-out was determined for the plain carbon grids while the sand-coated carbon grid and the glass grid always failed due to splitting. This highlights the influence of the reinforcement characteristics regarding the fibre strand surface and undulations.
Test series investigating the weft direction, designated with the yellow colour for a normal-strength concrete (NSC), show that the maximum force is reduced in the case of reinforcements CG2, CG3 and GG in comparison to the corresponding test series in the warp direction. This is attributed to the reduced cross-sectional area of the weft-orientated fibre strand. For CG1, no significant difference between the maximum pull-out force was determined for specimens with NSC regarding the fibre strand orientation, as concrete splitting was the only failure type.
Concrete strength: The high-strength concrete (HSC) only increased the maximum pull-out force for the series reinforced with CG1 where half of the tests failed due to rupture of the yarn, while almost all specimens with NSC failed due to splitting. For the other investigated grids, dominantly yarn rupture occurred at an embedded length of three times the yarn spacing independently from the concrete strength. Similar observations are concluded for the weft direction. For reinforcements CG2 and GG, the use of HSC even resulted in a reduced pull-out force determined. This is assumed to result from counteracting effect: the increased bond capacity achieved by the high-strength concrete simultaneously led to a higher utilisation of the concrete due to the reduced transfer length, which in the end was dominant and resulted in concrete splitting.
Contribution of transverse fibre strands: By investigating the performance of the textile grids with removed transverse fibre strands (pictures of the fibre strands are provided in Figure D.1), a reduction in the maximum force applied was found, except in the case of CG1. Nevertheless, in all test series, the failure types remained identical to the specimens where the transverse fibre was not removed. The contribution of the transverse fibre strand to the force transfer is dependent on the reinforcement considered, which is particularly the result of the local undulation formed during the manufacturing process. In the cases of no significant contribution of this local undulation at loading close to the maximum pull-out force, shearing off of the transverse strands occurred prior to splitting failure (exemplary shown by series CG1-0°-114-NSC-w/o). In contrast, the contribution to the force transfer is present while not dominant and not relevant for the failure mechanism, as in the case of series with CG1sc, CG2, CG3, and GG. It is noteworthy, that this description only addresses the state at failure. At small forces applied, there is a considerable influence of the local undulation, as analysed in more detailed in the following Section 3.3.3.
Maximum aggregate size: The use of a concrete with a maximum aggregate size of 16 mm showed no influence regarding the value of the maximum pull-out force applied. While the specimens with CG1 and GG showed no change in the failure type, for reinforcement CG2 no splitting was observed, with four out of five specimens failing due to pull-out. As a result, the average maximum force was approximately 5% higher in the specimens with the coarser aggregates, which may be considered to be in the margin of scattering test results.

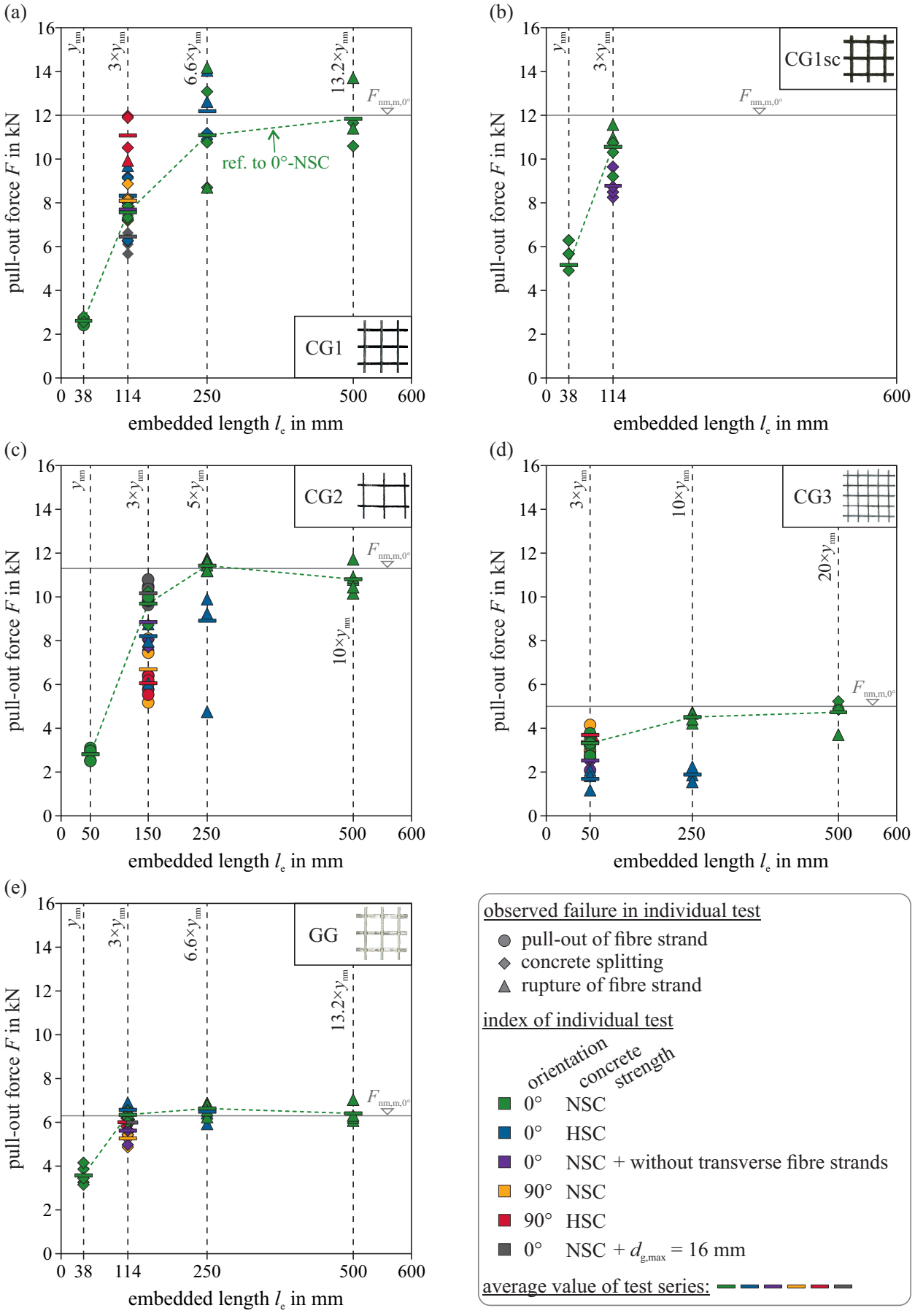


Figure 3.3: Results of SPOc tests: pull-out force in relation to the embedded length

3.3.3 Pull-out force related to occurring slip

To enable an analytical description of the bond behaviour in the following sections, mean curves are derived which represent the average value of the pull-out forces determined in each test series in relation to the occurring slip at the loaded end. The mean curves therefore represent all valid tests in each series and are limited to the least value of slip detected inside a test series prior to failure. As a result, the magnitude of the pull-out force of the mean curves is below the value of the maximum pull-out force shown in Figure 3.3.
The individual force-slip relations in each series revealed a large variation. This is a major drawback when using the SPOc test configuration to evaluate the bond behaviour at slip values of up to 0.5 mm, representing the serviceability state. The individual curves are provided in Appendix D.1 for reference. The obtained mean curves for the cumulated 41 test series are plotted for each investigated textile grid in Figure 3.4, with a differentiation between the concrete strength and maximum aggregate size introduced in the columns.
In general, two relations between the mean pull-out force and the slip are observed, either a non-linear relation, which could be described analytically by a power-law approach, or an approximately linear relation. The non-linear evolution is observed for all mean curves representing specimens with an embedded length of at least 3 times the yarn spacing. A linear relation is linked to the mean curves representing specimens in which the transverse fibre strand was removed. The removal resulted in a significant reduction of the pull-out force utilised at identical values of slip in comparison to specimens with an embedded length of at least three times the yarn spacing. The linear evolution of the curves allows the assumption that interlocking contributed to almost no force transfer, which is therefore traced back to the missing local undulation of the removed transverse fibre strand. The other case of an almost linear force-slip curve is represented for embedded lengths equivalent to the yarn spacing.
For specimens CG2-NSC-0°-38 (Figure 3.4c1) and CG3-NSC-0°-75 with and without transverse fibre strands (Figure 3.4d1), pull-out failure is revealed. After a non-linear increase, the curves show a plateau, and after large slip exceeding 2 mm the force decreases.
In theory, the pull-out force is required to be of identical value at each slip regardless of the embedded length until slip at the unloaded end of the SPOc specimen occurs. This theoretical assumption is represented satisfactorily by the obtained curves of all textile grids for fibre strands aligned in the warp direction. For reinforcements CG1 (Figure 3.4a) and GG (Figure 3.4e) this was also the case when considering the weft orientation.
In the case of steel rebars, it is generally assumed that a higher concrete strength leads to an increased utilisation of the bond capacity by allowing a transfer of larger forces compared to normal-strength concrete. This is due to the higher strength concrete providing more resistance against the occurrence of cracks in the bond interface area, which result from mechanical interlocking. As previously mentioned, an influence of the concrete strength is not generally represented by the pull-out tests, particularly at small slip where no influence of crack occurrence due to splitting is assumed. The sole exception to this observation is found in series CG1-HSC-0°-250 (Figure 3.4a2), where the use of a high-strength concrete resulted in a significant increase in the pull-out force in relation to the occurring slip.
The use of coarser aggregates with a maximum size of 16 mm did not lead to a change in the pull-out force behaviour in relation to the slip for the investigated reinforcements CG1 and CG2 (Figure 3.4a3+c3). Addressing the specimens with GG, the pull-out force of the concrete with the coarser aggregates is lower compared to the concrete with a maximum aggregate size of 5.6 mm when set in relation to the determined slip (Figure 3.4e3).

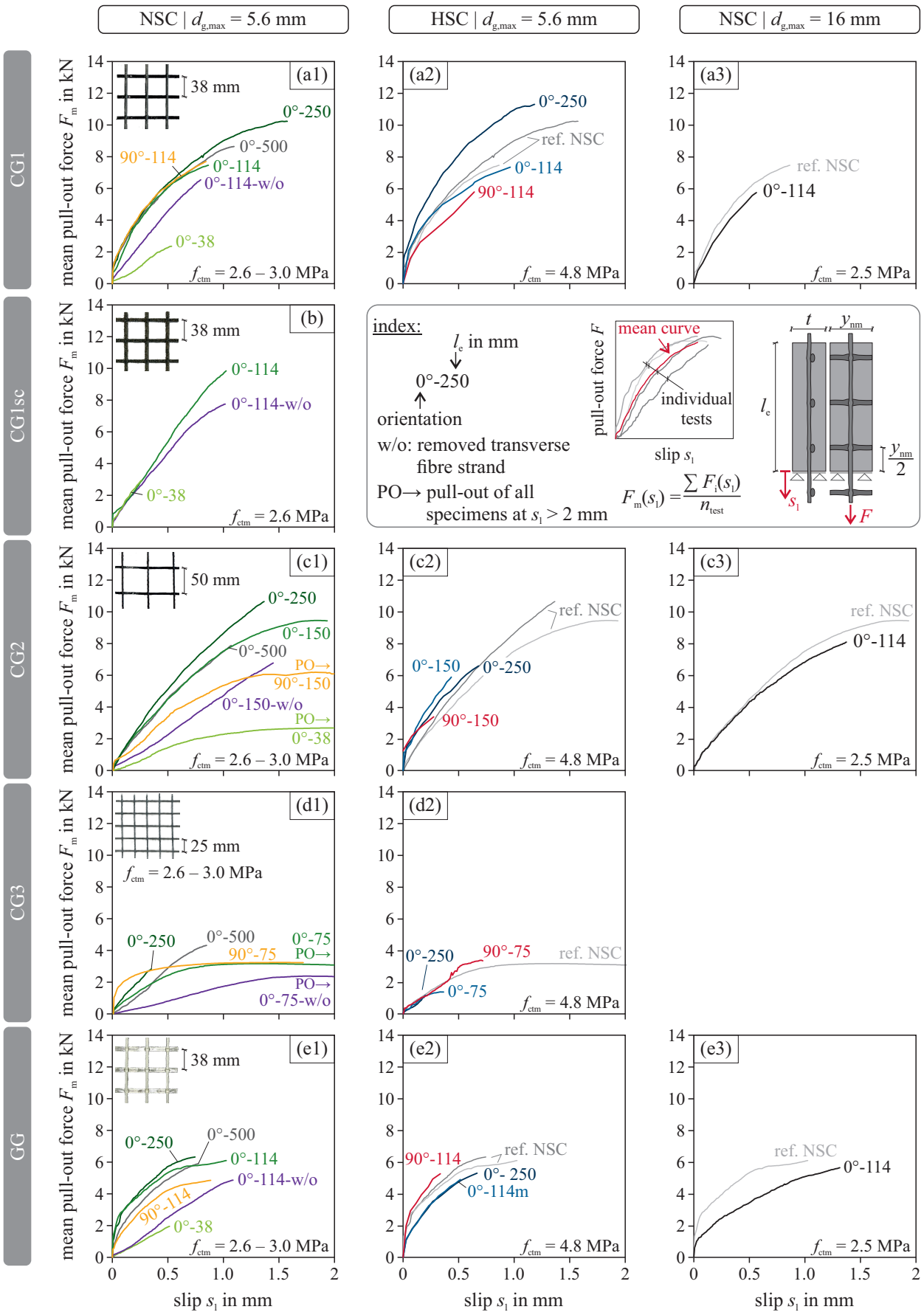


Figure 3.4: Results of SPOc tests: mean curves of pull-out force in relation to the slip

A final evaluation of the test data provided by the single-sided pull-out tests addresses the occurrence of slip at the unloaded side of the specimens. Figure 3.5 shows a consideration of average values derived for each test series at the time where slip at the unloaded side was detected. The average values are the slip s_l related to the load capacity F/F_{max}, which refers to the applied load at this time in relation to the maximum load. In most series of the five investigated grids, slip at the unloaded side s_{unl} occurred at least when two-thirds of the maximum load were reached and the slip at the loaded side was at least 0.35 mm. Exceptions were series CG3-NSC-90°-75 and CG3-HSC-0°-75 (Figure 3.5d), where the slip was 0.18 mm and 0.22 mm, respectively.
The evaluation in Figure 3.5 provides for an interpretation assuming a lower limit for a load capacity at which slip at the unloaded side occurred. This limit is visualised in each diagram as a dotted black line with the given percentage of load capacity and was defined by considering most data points. Exceptions of this limit were attributed to the following: the embedded length was set equivalent to the yarn spacing, as for specimens with CG2 and GG; the transverse fibre strands were detached, as for specimens with CG1 and CG3; or in the case of series CG2-NSC-0°-150-16mm with maximum aggregate size of 16 mm. For the latter, slip at the unloaded side occurred at a load capacity of 55% at $s_l = 0.76$ mm, which is beyond the scope of the serviceability state with regard to crack opening.

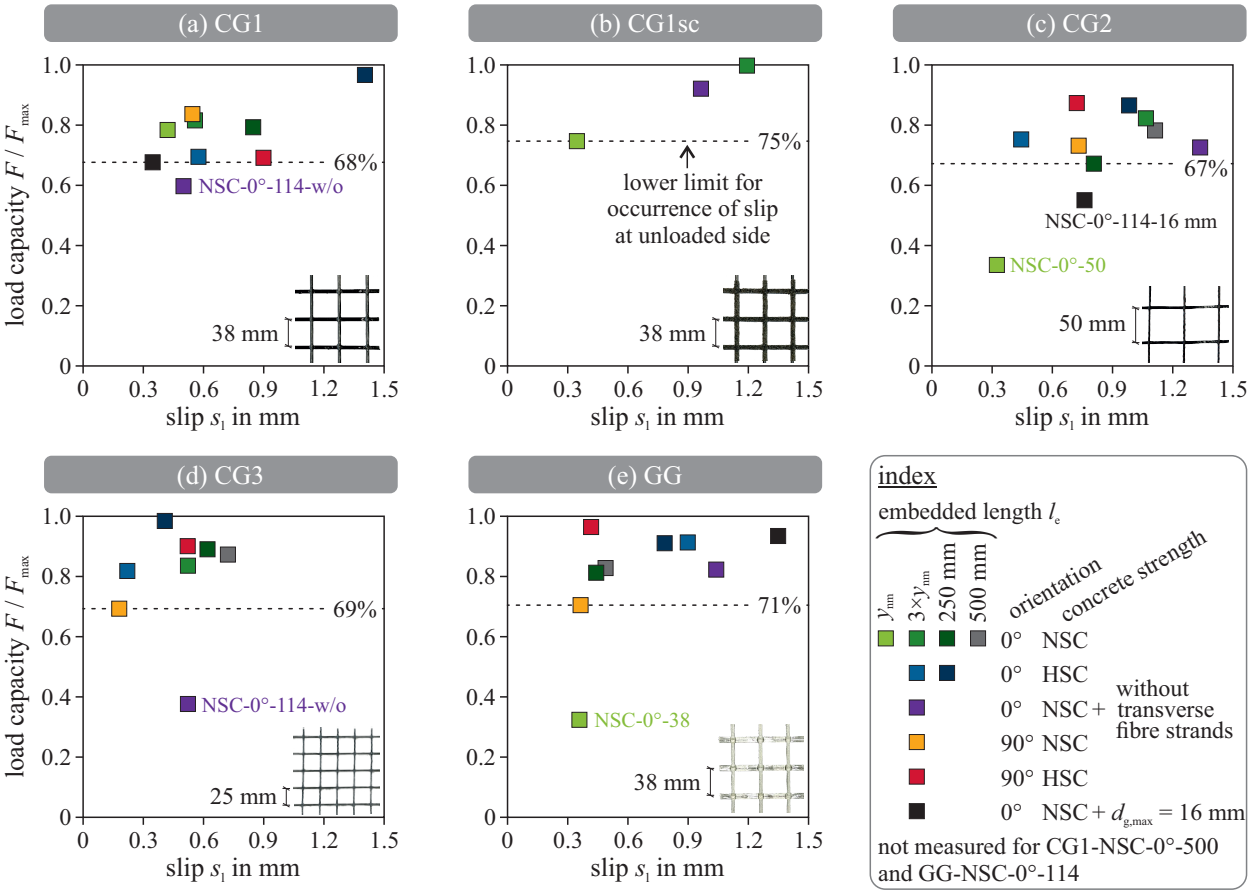


Figure 3.5: Results of the SPOc tests: average load capacity at which slip at the unloaded side occurred in relation to the slip at the loaded side

The investigations on the bond behaviour of grids using SPOc tests revealed, partially as confirmation of previous research (e.g. [Bie18a, Pre19a]) that

- increasing the embedded length did not necessarily increase the maximum pull-out force to reach fibre rupture as the splitting of the concrete member was often dominant;

- the usage of a high-strength concrete did not necessarily lead to the apparent increase in maximum pull-out force, less slip, or a change in the failure mode from splitting to fibre rupture when compared to the specimens with a normal-strength concrete;
- the occurrence of concrete splitting is attributed to the cross-sectional geometry of the fibre strands with elliptical shaped geometries tend to increase the potential for splitting,
- while for the possibility of splitting, local undulations, e.g. resulting from the intersection with the transverse fibre strand, have a considerable influence for some grids. The local undulations also influence the bond capacity.
- Slip at the unloaded side occurred at loading larger than two-thirds of the pull-out force when a sufficient embedded length of three times the yarn spacing was provided. The corresponding slip was at or above the values addressing the serviceability limit state.

3.4 Capacity of textile grids to regulate crack opening

At the crack surface of a concrete member subject to uniaxial tension, the concrete is unconstrained allowing for a deformation of the concrete matrix in the direction of the tensile force with no transversal compressive stress developing. This is in contrast to the boundary conditions present in the SPOc test setup and led to the consideration of a setup, which was explicitly developed to represent the situation of a reinforced concrete member at a single crack. The crack opening tensile (COT) tests are designed to represent the opening of a crack in relation to the reinforcement stress. The initiation of the crack is facilitated by a predefined weakening of the concrete cross-section, thereby enabling a controlled conduction of the test and allowing a more direct representation of the reinforcement's capacity to regulate the crack opening. As current code provisions mandate a value of bond stress to predict the crack width, a derivation of the bond stress in relation to the crack width is necessary, which is performed in Chapter 5 utilising the direct interpretation of the crack opening under defined load application.

3.4.1 Experimental representation of crack opening

The main approach in the COT test configuration is the resemblance of a uniaxial tensile state with a controlled crack opening considering only one fibre strand. The initiation of the crack is localised by dividing the concrete specimen, as illustrated in Figure 3.6b. With load application, the specimen's ends are continuously pulled apart, with the most deformation occurring at the initiated crack. The displacement between the crack surfaces is interpreted as opening w and is obtained with begin of loading, as no concrete tensile resistance is present.
The primary distinctions between the SPOc setup and the COT setup are the boundary conditions, fixed or unconstrained, and the measured displacements, either slip or crack opening. The controlled crack initiation and the consideration of a single fibre strand differentiate the COT setup from the well-known uniaxial tensile test setup (Figure 3.6c). In the latter, the formation of a crack occurs at the location of the lowest concrete tensile strength. Consequently, the measured crack opening in the uniaxial tensile test is fixed to the initial crack width. The width of the crack, as well as the associated reinforcement stress, are dependent on the equilibrium reached after crack initiation.

The validity of the proposed COT test setup is limited to a single cracking stage where no other crack occurs besides the initiated one. In general, the layout of the cross-sectional area of the specimen is chosen to represent the cross-section of a single fibre strand in a concrete member. In considering a symmetrical layout, the depth t is twice the concrete cover plus the strand thickness

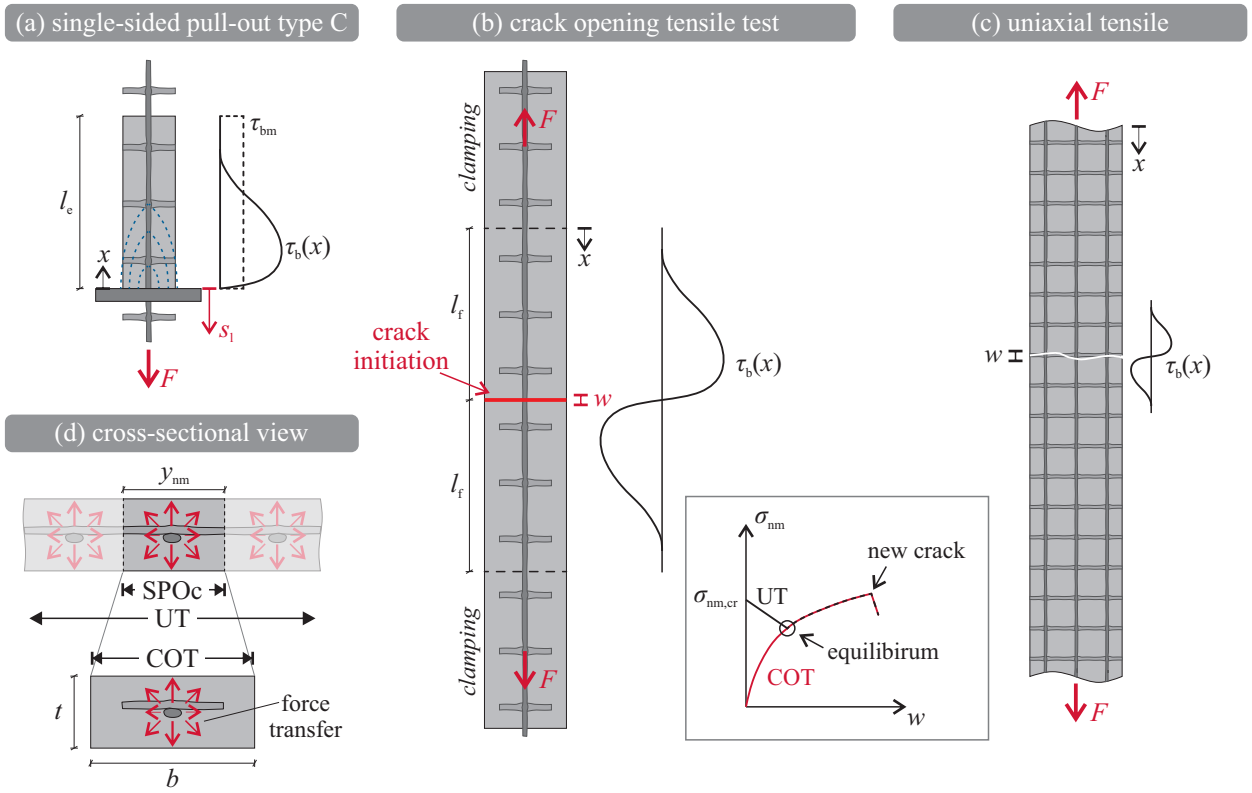


Figure 3.6: Differentiation between the COT test, SPOc test and uniaxial tensile test

and the width b is equal in value to the yarn spacing. However, this configuration frequently results in a cross-sectional area that is not efficient in preventing subsequent cracking before reaching the required value of crack opening. The required value of crack opening is defined by the test user, favourable are the limitations introduced by code provisions. Consequently, the cross-section of the COT specimen requires an increase in size.

The cross-section of the specimens in the conducted experimental campaign was modified by increasing the width, while the thickness remained unchanged. This configuration is justified by the assumption that for the investigated elliptical-shaped fibre strands the force transferred in the concrete is mostly directed laterally to the grid layer and limited by the concrete cover, as idealised in Figure 3.6d. Consequently, an increase in concrete cover could increase the bond capacity. In addition, the concrete cover is a fixed investigation parameter throughout most of the experimental campaigns of this thesis. With regard to the width, it is assumed that this effect is less pronounced, particularly at forces present at the serviceability stage. This also applies to the situation of interfering tensile stresses from neighbouring fibre strands, which is not represented in the COT layout, in particular when the width is increased. Therefore, the increased width provides for more concrete area which is utilised by the force transfer, presumably increasing the bond capacity. Once more, it is assumed that this effect is marginal due to the low reinforcement utilisation present at the serviceability stage. As demonstrated in Chapter 5, the validity of this assumption is evident.

The transfer length of the initiated crack is required to propagate without any influence of the load introduction area. Therefore, the length of the specimen is set to a distance without any influence of the clamping, defined as free length l_f, plus the length of the clamping of 200 mm, as shown in the setup visualised in Figure 3.7. The crack initiation is realised by passing the longitudinal fibre strand through two layers of a polyethylene-based (PE) sheet with an overall thickness of 150 μm. For easy test preparation, two identical frameworks were prepared and screwed together prior to concreting, closing the gap shown on the bottom left-hand side of Figure 3.7.

The test was conducted with a deformation-controlled loading of 1 mm/min. On both surfaces being parallel to the grid layer, a speckle field was applied on the concrete and pictures were manually taken using Pentax cameras at a rate of 0.2 kN to determine the crack opening. It should be noted that, despite the fact that only the state of single cracking was relevant to the study, the tests were continued with more cracks forming until anchorage failure in the clamping area or yarn rupture occurred.

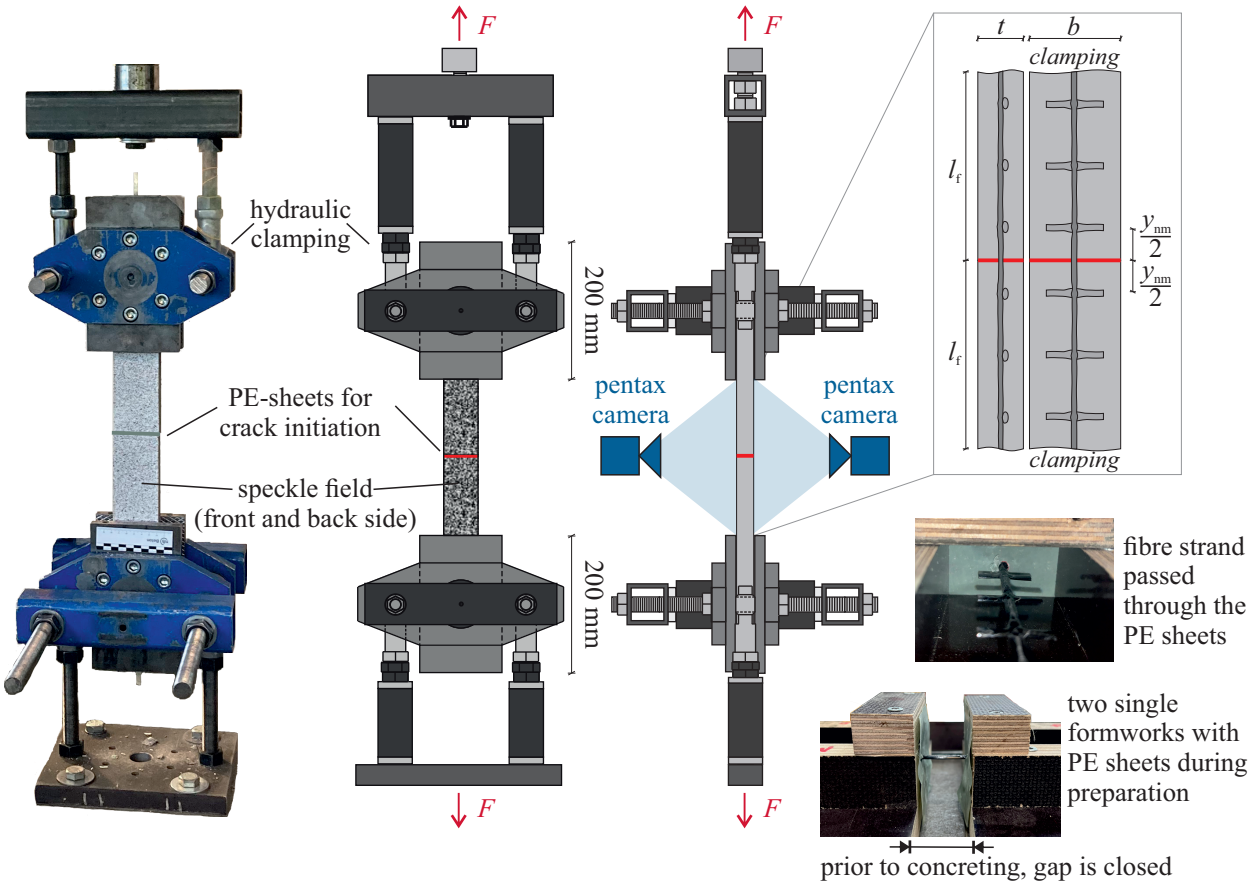


Figure 3.7: Setup of the COT test

3.4.2 Force transfer in relation to the crack opening

During the stage when only the initiated single crack is present, the transfer length increases along the free length l_f, as indicated in Figure 3.8a. This stage provides a controlled environment for deriving values of bond stress as a material parameter, which is done in Section 5.2. With the stress in the uncracked concrete reaching the tensile strength in the area of the lowest resistance, an additional crack occurs. The following reduction in force and crack width is typically in a deformation controlled test. In the presented test configuration, the discontinuity area close to the clamping presented a location, where this additional crack was often observed, as shown in the DIC visualisation on the bottom clamping in Figure 3.8b. Cracking in the free length was often restricted to higher applied forces as the shielded length provided an area in which the transferred force did not reach the tensile strength. At large forces, additional cracks occurred also in the free length (Figure 3.8c). Especially for a crack occurring in close vicinity to the initiated crack, the transfer length is significantly reduced to about half the crack spacing. As a result, the continuing crack opening of the initiated crack has a slower rate when related to the tensile force increase compared to the previous stages. Considering the bond stress evolution, exemplarily shown for the three stages in Figure 3.8, it becomes obvious that for a derivation of a value of bond stress, solely

the single cracking stage is feasible, as the occurrence of the other cracks is outside the controlled environment of the test setup.
The crack opening was determined by evaluating the two speckle fields using digital image correlation. This provided for an average value of displacement, one for the front side and one for the back side of the specimen. The average of these two values represented the crack opening located at the fibre strand, which is visualised by the red surface in Figure 3.8. This procedure allowed for a robust determination of the opening despite a non-uniform opening of the crack or the specimen being tilted.

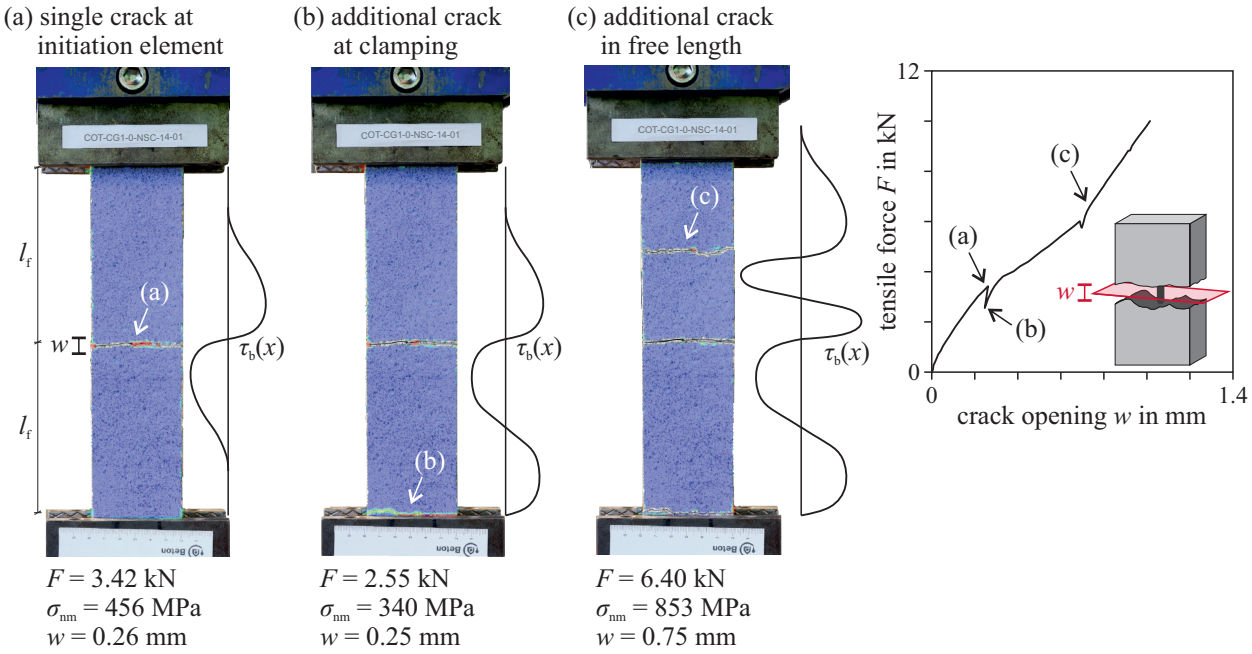
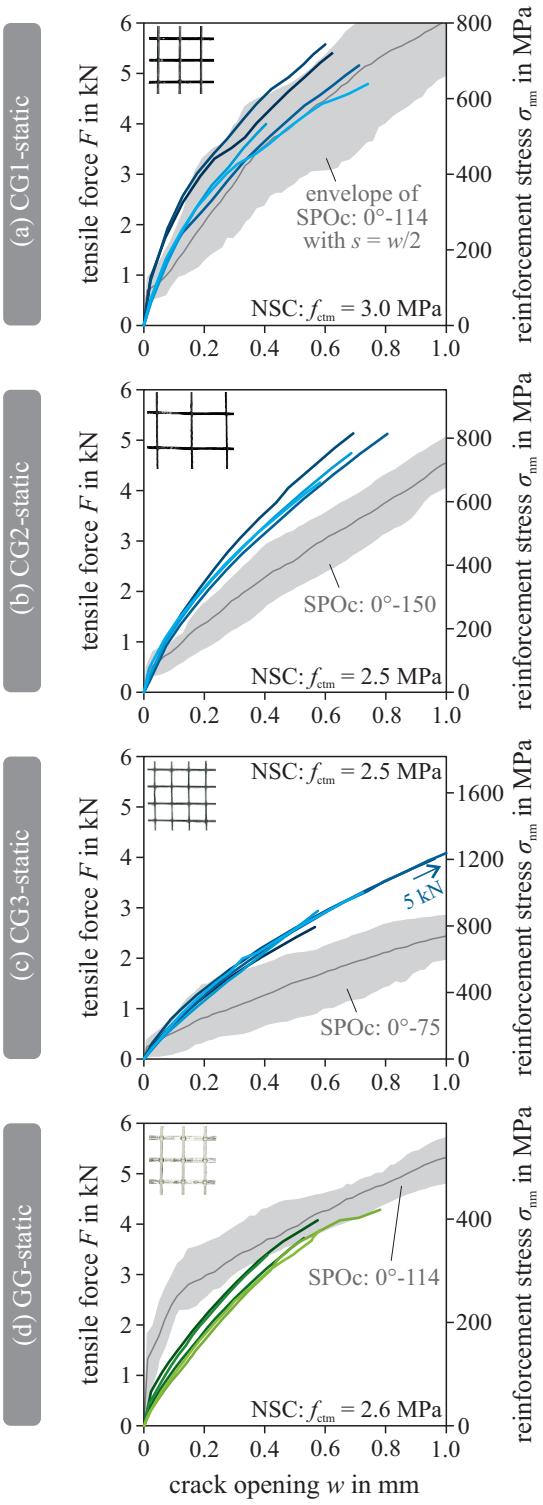


Figure 3.8: Three stages occurring in the COT tests with deformation field provided by DIC, qualitative representation of the bond stress, and obtained force-crack opening relation

The obtained non-linear force-crack opening relations of the conducted and valid COT tests on each of the four investigated grids CG1, CG2, CG3 and GG, orientated in the warp direction, are plotted in Figure 3.9. In addition, the results of the SPOc tests with an embedded length of three times the yarn spacing and assuming that the slip is equivalent to half the crack opening, are shown in Figure 3.9 as grey-coloured envelopes, set by the minimum and maximum values, with the mean curve resembled by the grey line. The results of the COT tests clearly show the significantly lower scattering between the individual tests compared to the SPOc tests. In the case of the three investigated carbon grids, the measured force-crack opening relation provides for an assumption of a higher bond capacity compared to the force-slip relation derived from the pull-out tests. This higher bond capacity is expressed by a lower crack opening compared to the assumed slip in the SPOc tests at identical tensile forces. Considering the glass grid, this observation is exactly the opposite (Figure 3.9d). The results of the SPOc tests lead to the assumption of a higher bond capacity present when compared to the COT specimens, in particular at low values of slip or crack opening. An influence of the concrete strength and Young's modulus between the COT tests and SPOc tests is negligible, as the values determined in the corresponding material tests were comparable values. For the COT specimens with reinforcement CG2, CG3 and GG, the tensile strength was even lower with $f_{ctm} = 2.5$ MPa and $f_{ctm} = 2.6$ MPa compared to 3.0 MPa determined for the SPOc specimens.



index		at additional crack occurrence		
		F [kN]	σ_{nm} [MPa]	w [mm]
CG1-static	-1	5.41	721	0.63
	-2	5.61	748	0.60
	-3	5.19	692	0.71
	-4	4.02	536	0.40
	-5	4.82	643	0.74
average:		5.01	668	0.62
CG2-static	-2	5.34	847	0.77
	-3	5.53	877	0.90
	-4	4.95	786	0.72
	-5	4.35	690	0.62
average:		5.04	800	0.75
test -1 was invalid and is therefore not considered				
CG3-static	-1	2.83	856	0.64
	-2	4.18	1266	1.05
	-3	4.95	1491	1.37
	-4	3.13	948	0.62
	-5	3.51	1062	0.80
average:		3.81	1156	0.90
GG-static	-1	4.08	398	0.57
	-2	3.72	363	0.53
	-3	3.39	331	0.41
	-4	4.29	418	0.79
	-5	3.87	378	0.58
average:		3.87	378	0.57

Figure 3.9: Force-crack opening relation of the static COT tests

With the occurrence of an additional crack, the assumption of a purely single cracking stage for the focused crack is not unconditionally provable in this test layout, further derivations of a stress-crack opening relation are not directly viable. Therefore, the continuing evolutions are not shown in the graphs of Figure 3.9. The chosen cross-sectional area of the concrete of 30×60 mm^2 provided for sufficient resistance to additional cracking until at least an opening of 0.4 mm was reached. The average crack opening prior to the occurrence of an additional crack was at least 0.58 mm in the case of specimens with GG at a utilisation of 61% of the reinforcement tensile strength (Figure 3.9d). For reinforcements CG1 (Figure 3.9a) and CG2 (Figure 3.9b), approximately 42% utilisation was

achieved, which still provided for a state in which adjacent crack occurrence is expected to occur when referring to practically designed members. As shown in Figure 3.9c, the occurrence of an additional crack at a reinforcement stress exceeding 1156 MPa, which is a utilisation of 77%, was explained by the very low reinforcement ratio of 0.18% of the specimens with CG3. Consequently, the obtained curves are feasible to be considered in an analytical approach for representing the single cracking stage.

In consideration of the observed test results after the formation of an additional crack, two principal characteristic developments of the crack opening in relation to the applied force are proposed. In either scenario, whether the occurrence of an additional crack is proximate to or coincident with the clamping, the plotted F-w curves exhibit a non-linear development that aligns with the trend of the prior relationship. This behaviour is attributed to the location of the additional crack, which, being at a sufficient spacing to the initiated crack, is capable of transferring most of the bond force. This phenomenon is depicted in Figure 3.8 in stage (b) and was observed for example in specimen CG1-static-3. The other observed characteristic displays the actual behaviour of adjacent crack occurrence which indicated a stiffening of the plotted curve as the additional force application resulted in a reduced crack opening compared to the previous force-opening relation. This was referred to as stage (c) in Figure 3.8 (observed for example in CG1-static-4).

3.4.3 Influence of concrete tensile strength on the crack opening

The results of the pull-out tests introduced in Section 3.3.3 already revealed that an increased concrete tensile strength is presumable not leading to an increase in the pull-out force at comparable values of slip. A similar observation was made in COT tests with high-strength concrete (HSC), as the force-crack opening curves in Figure 3.10 revealed when compared with the averaged curve of the test series with the normal-strength concrete (NSC). An increase is only visible in the case of specimens CG3 (Figure 3.10c). In this instance, all five tests with HSC exhibited higher tensile forces at equivalent crack openings compared to the average of the specimens with NSC. In contrast, specimens of series CG1-static-HSC (Figure 3.10a) and GG-static-HSC (Figure 3.10d) revealed a reduced force transfer. For specimens reinforced with CG2, shown in Figure 3.10b, the series indicated no difference regarding the concrete tensile strength.
The only significant effect of the high concrete strength was on the occurrence of the first additional crack. The higher resistance of the concrete led to a postponement of this crack formation, which then provided for valid F-w-curves at larger force and crack opening compared to the NSC specimens. In the case of specimens with CG3 and GG, the tensile strength of the reinforcement was reached resulting in a yarn rupture prior to the occurrence of another crack.

The question that arises is why does an increase in concrete strength not necessarily lead to an increase in the bond capacity of non-metallic reinforced specimens? It appears that the resistance of the fibre strands, including the impregnation, against pull-out in the case of friction and mechanical interlocking is lower than the resistance of the concrete. Three characteristics of the longitudinal fibre strands contributing to force transfer are considered in the following: friction f_{fric}, mechanical interlocking of the local undulation at the intersection with the transverse strands f_{un}, and waviness of the strand itself f_{wav}. In the case of mechanical interlocking, the transversal stiffness of the fibre strand (roving and impregnation) is significantly lower compared to the stiffness of the concrete. The application of contact pressure leads to the compaction of the strand into a smooth rope, resulting in the elimination of undulations, and thus the failure of interlocking. Consequently, the capacity of the textile grid to transfer force by mechanical interlocking is almost independent of the tensile strength and stiffness of the concrete. Conversely, an increase in concrete tensile strength

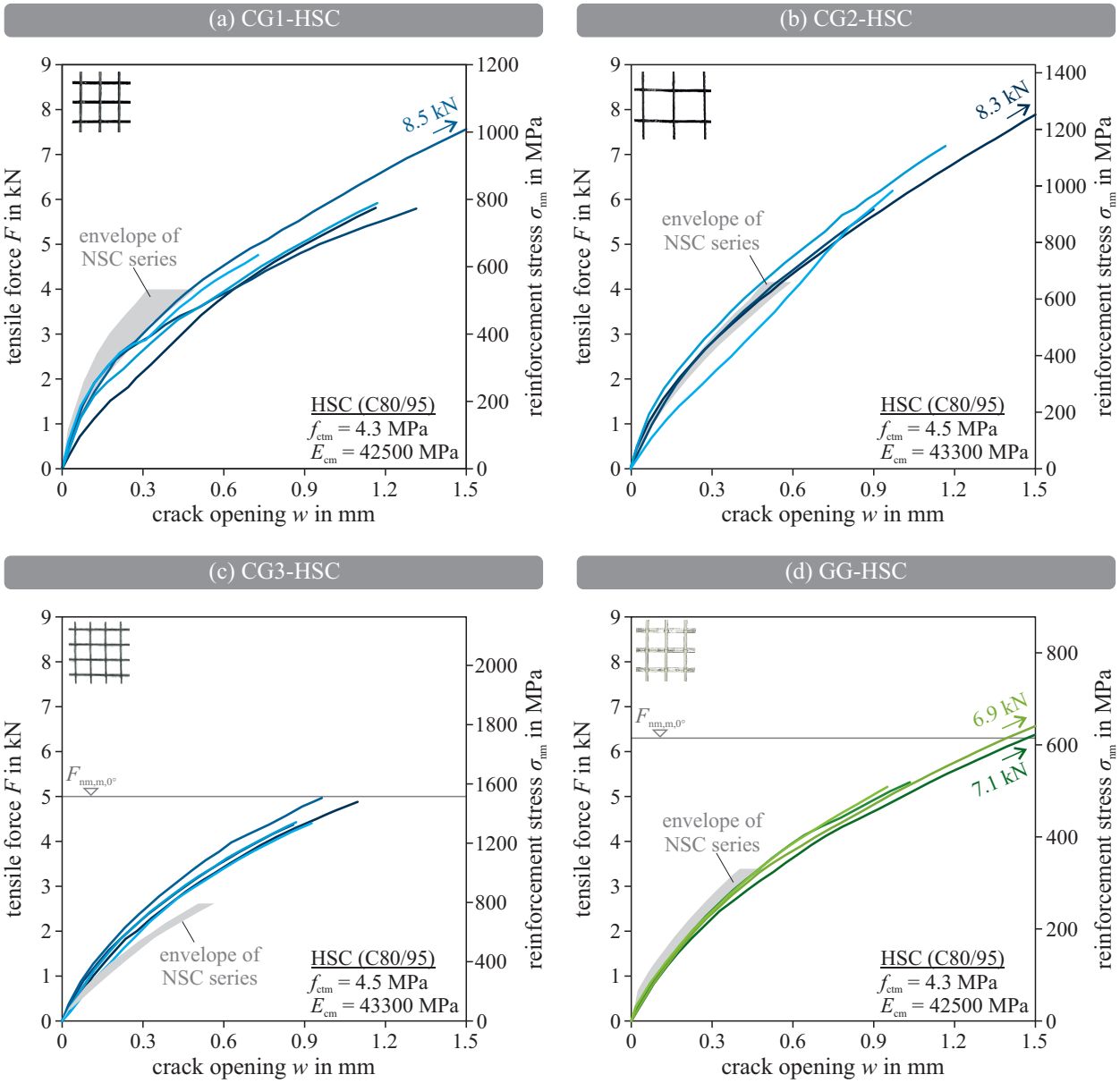


Figure 3.10: Force-crack opening relation of the static COT tests with a high-strength concrete

leads to an increase in friction reducing the smearing off of the cement paste and fine aggregates. Transferring these hypotheses to the four investigated grids, the following considerations are stated. In the case of CG1 and the GG, the dominant mechanism of force transfer at slip below 0.7 mm is attributed to the contact pressure and interlocking exerted by the local undulations and the waviness of the fibre strand, as illustrated in Figure 3.11a for reinforcement CG1. As the surface of both grids is very smooth, no significant influence of friction is assumed. Consequently, the influence of a higher concrete strength is negligible. The observation in Figure 3.10 indicates that the specimens with a normal-strength concrete even provide for less crack opening compared to the high-strength concrete specimens. When ruling out a possible scattering in the tests themselves, a reason for the increased bond capacity of the NSC specimens is assumed to be the result of the reduced stiffness of the concrete at mechanical interlocking. Presumably, the compacting of the undulations by contact pressure is less pronounced for concrete with less stiffness. As the pressure does not only lead to a straightening of the fibre strand but also to a compacting of the concrete, both the transverse stiffness of the fibres strand and the compressive stiffness of the concrete need consideration. In the case of a higher strength concrete ($E_{cm} \sim 43000$ MPa), the concrete compact-

ing is not as pronounced and therefore the fibre strand is straightened at lower forces compared to an NSC ($E_{cm} \sim 30000$ MPa). This also explains why the difference between the two concrete strengths in the force-crack opening relation of the specimens reinforced with the glass grid is less significant. As the stiffness of the glass fibre strand is less than of a carbon strand, with the Young's modulus of the glass strand being in between the Young's modulus of the normal and high strength concretes, the influence of the concrete strength on the straightening of the glass strand is not as pronounced.
Considering CG3, which showed almost no undulations and a rougher surface compared to reinforcements CG1 and GG, force transfer is dominated by friction (Figure 3.11b). This is also attributed to the impregnation as the polystyrene resin showed a rougher surface compared to the epoxy resin used for CG1 and GG. Consequently, the specimens with HSC showed a higher force transfer at equivalent crack opening compared to specimens with NSC, as friction is increased with increased strength and stiffness.
At last, specimens with CG2 (polystyrene resin) showed no influence of the concrete strength on the F-w-relation. It is assumed to be the result of a counteracting of the two mechanisms of friction. On the one hand increase of bond capacity and on the other hand mechanical interlocking inducing a compacting of the fibre strand, which decreases the capacity at higher concrete strength.

Comparing these hypotheses to the observations for the pull-out tests in Section 3.3.3, it is assumed that the SPOc results for the three grids CG2, CG3 and GG do not indicate any tendency regarding a possible influence of the concrete tensile strength on the force-slip behaviour. However, a clarification is necessary in the case of CG1. For the series SPOc-CG1-0°-HSC-250, having an embedded length of 250 mm and a high-strength concrete, a significant increase in the bond capacity was observed compared to the normal-strength specimens (see Figure 3.4). Conversely, for the SPOc series with an embedded length of 114 mm, no tendency was identified for the high concrete strength in comparison to the normal-strength concrete. This behaviour of the SPOc series is attributed to the fact that the combination of the transverse compressive stress and the higher concrete strength enables a greater contribution of friction, which is only utilised when a sufficient transfer length is present, as observed in the specimens with an embedded length of 250 mm.

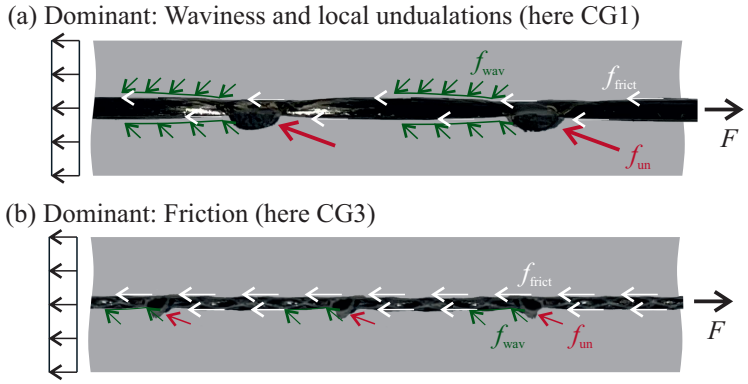


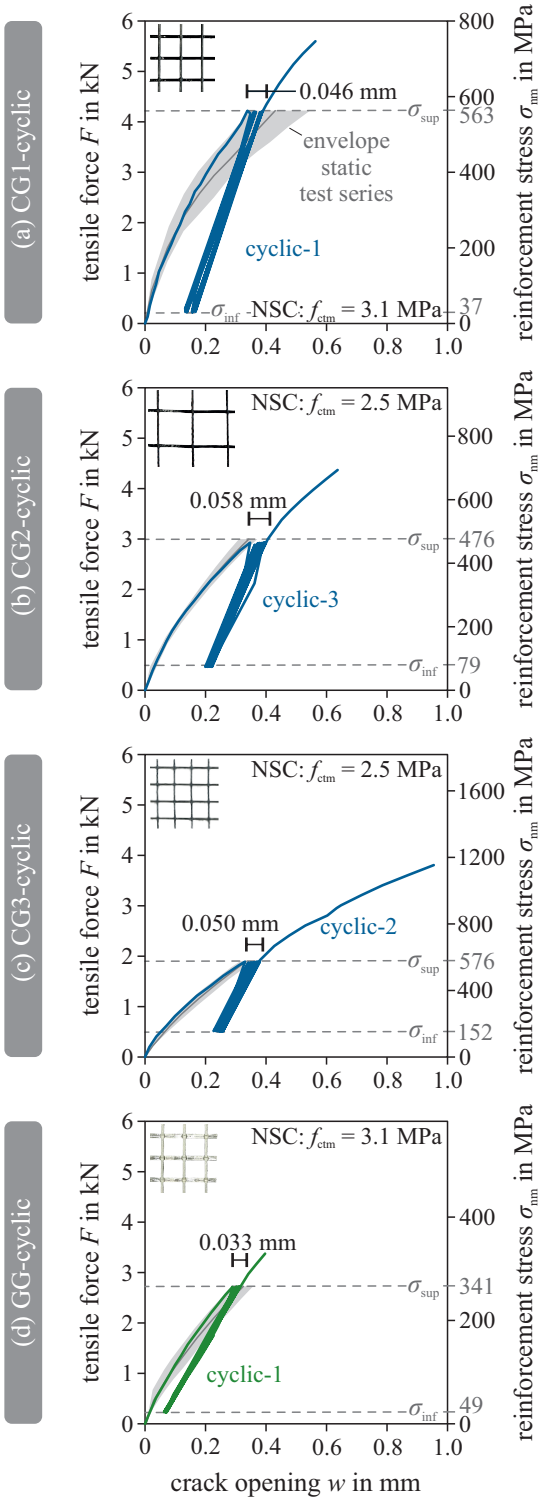
Figure 3.11: Visualisation of the acting force transfer mechanisms in different textile grids

3.4.4 Increase in crack opening due to load cycles

The reduced capacity in local force transfer by the individual bond mechanism in the case of cyclic loading results in an increase of slip and therefore opening of the crack. In general, the behaviour of a material subject to cyclic loading is characterised by an increase in deformation during the initial load cycles, followed by a period of relatively stable deformation, and, finally, in the case

of fatigue failure, a significant increase in deformation. The increase in deformation at a constant maximum load, representing the upper limit of the load amplitude, is attributed to the progressive damage sustained by the material under the cyclic regime (cf. [Pfa02, Bak21, Chr22]).
To briefly investigate the effect of cyclic loading on the crack opening, a limited number of ten load cycles were applied to COT test specimens. As evident, with these few cycles only a qualitative conclusion is possible, focusing on the potential cyclic loading has with regard to additional crack opening. The setup and conduction were consistent with the previously documented COT test series, having a free length of 152 mm, with the incorporation of a cyclic loading phase in the test procedure. The superior load level, indicated by σ_{sup}, was set to represent a crack opening of approximately 0.30 to 0.35 mm. The inferior load level σ_{inf} was set to an almost complete unloading of the specimen, at 0.5 kN, in order to facilitate the proper execution of the test. The loading and unloading rate was identical at 0.2 kN/s. Each series of the four investigated textile grids consisted of five specimens. The F-w-curve for one test from each series is plotted on the left-hand side in Figure 3.12. For each test, the crack opening initially obtained at the superior load level w_0 and the increase in the crack opening after ten load cycles denoted as $\Delta w_{cycl,10}$, are listed on the right-hand side in Figure 3.12.

In general, the initiated crack exhibited an average additional opening between 0.03 mm for GG and 0.06 mm for CG2 after ten cycles. The evaluation revealed significant relative increases in the crack opening, ranging from 8% for GG to 17% for CG2. This is particularly noteworthy for CG2, where the superior load level is only at a utilisation of 27% of the tensile strength, making the observed increase in crack opening remarkably large.
This finding underscores the necessity for a comprehensive consideration of load cycles at serviceability levels when assessing the bond capacity of textile grids. This study thus motivated a more detailed and representative evaluation of the influence of cyclic loading for the upcoming experimental campaigns in cases of uniaxial tension in Chapter 4 and bending in Chapter 6, considering 200,000 cycles.



index		crack opening at σ_{sup} w_0 [mm]	$\Delta w_{cycl,10}$ [mm]
CG1-cyclic	-1	0.338	0.046
	-2	0.356	0.049
	-3	0.334	0.035
	-4	0.361	0.027
	-5[1)]	(0.212)	(0.041)
average:		0.347	0.039

[1)] not considered in statistical evaluation as $\sigma_{sup} = 467$ MPa

CG2-cyclic	-1	0.314	0.056
	-2	0.410	0.055
	-3	0.347	0.058
	-4	0.335	0.064
	-5	0.381	0.067
average:		0.358	0.060

CG3-cyclic	-1	0.355	0.061
	-2	0.331	0.050
	-3	0.302	0.050
	-4	0.284	0.047
	-5	0.308	0.042
average:		0.316	0.050

GG-cyclic	-1	0.290	0.033
	-2	0.318	0.026
	-3	0.309	0.023
	-4	0.308	0.026
	-5[2)]	(0.318)	(0.022)
average:		0.306	0.027

[2)] not considered due to error in measurement

Figure 3.12: Influence of cyclic load application on the crack opening determined in the COT tests

3.5 Determination of reinforcement strain evolution and bond stress distribution

For a continuous determination of the strain evolution in the reinforcement, fibre optic sensors are a feasible solution, providing strain values of the relative deformation of the optical fibre at an incremental distance below 1 mm. The obtained strain of the optical fibre is then used to represent the reinforcement strain. Considering deformation and force equilibrium conditions, the reinforcement strain is then utilised to determine the concrete strain, bond stress, slip, and crack opening.

3.5.1 Principles of measurements with distributed fibre optic sensors

Distributed fibre optic sensors, often denoted as DFOS or, in this thesis, FOS, represent a class of measuring techniques that utilise the entire length of an optical fibre as a sensor. This allows for continuous and real-time measurements over extensive distances, which distinguishes FOS from conventionally used point sensors, providing data at discrete locations. The principle behind FOS is based on light scattering phenomena in the fibre, as light passes through the fibre undergoing scattering due to interactions with the fibre's internal structure. The analysis of this backscattered light then yields information regarding the physical conditions along the fibre. The most commonly exploited scattering mechanisms in FOS are Rayleigh [Pal22], Brillouin [Gol13, Mua19], and Raman [Mua19] scattering. Rayleigh scattering is an elastic process caused by microscopic fluctuations in the refractive index of the fibre, and it is typically used in optical time domain reflectometry to measure strain and temperature. It is most feasible for distances of a few metres while allowing a high spatial resolution below 1 mm. Brillouin and Raman scattering, on the other hand, are an inelastic process applied to obtain either strain or temperature, while their advantages are long-range measurements of several kilometres with a reduced resolution in metre-scale. In a FOS configuration, a laser pulse or continuous wave is initiated at one end of the optical fibre. By measuring the return time, the location of the backscattered signal along the fibre is determined. By analysing changes in frequency and intensity of the backscattered light, variations in strain or temperature are derived and quantified. This process enables the creation of a spatially resolved profile of physical parameters along the entire fibre.

FOS is utilised for the purpose of monitoring concrete or reinforced concrete members. The measurements are typically employed in the context of structural health monitoring of large members or structures, reported for example in [Vil13, Bar18, Bec24]. In research, typical applications include steel reinforcement [Hab97, Fis19, Gal21, Jan23, Lem23], textile grids [Bec22, Sch24b, Sch25b], and concrete surfaces in compression [Bec23a] and tension, including the crack formation and opening [Bec25b]. These applications facilitate a continuous measurement of one-dimensional deformation. Recent research has focused on the transition to a fibre optic sensor grid, which facilitates two-dimensional deformation measurement and consequently provides a deformation or strain field [Bec25a].
In the context of measurement accuracy and robustness, the thickness of the optical fibre and the type of fibre coating used are of importance [Her23, Sch25b, Bec25b]. Common fibre coatings used are either a polyimide coating or an acrylate coating, while a broad range of coatings and fibre thicknesses exists. For instance, as demonstrated in the investigations reported in [Bec23a, Sch25b, Bec25b], polyimide-coated fibres have been shown to provide a higher strain resolution in comparison to the smoothed strain evolution that is obtained when using an acrylate-coated optical fibre. Conversely, the polyimide-coated fibres have been observed to yield a greater number of dropouts where the fibre optic sensors do not obtain any value. The occurrence of these dropouts is attributable to local strain peaks that exceed the system's operational range, with the strain values being above the limit value or the strain gradient between two gauge points being too large. In addition, the polyimide fibre shows a high standard deviation when comparing the gauge points to the mean strain, which is not attributable to the noise as reported in [Bec23b]. In contrast, BECKS ET AL. [Bec23b] observed that the acrylate-coated fibre showed a constant very low standard deviation which is primarily the result of noise. Using different adhesives to fixate the fibre to the investigated material or applying a primer in advance, proved to increase the reliability of polyimide-coated fibres significantly [Bec25b]. Acrylate-coated fibres demonstrated an enhanced resistance to sudden increases in deformation, which typically results from the occurrence of a new crack, also without the usage of a primer [Sch25b].

In this thesis, two different fibre coatings, polyimide and acrylate, and two different adhesives, cyanoacrylate and epoxy resin were utilised, depending on the focused material, which was either the reinforcement or the concrete surface. An overview is provided in Table 3.2. To measure a continuous strain evolution in the longitudinal direction of the reinforcement, the optical fibres were placed on the grid and fixed to the strand using a cyanoacrylate adhesive as a chemical bond, taking into account the side of the strand that has a continuous profile and is not affected by the undulation. The utilisation of an acrylate coating was the predominant approach employed in the tests, as this coating, in combination with the cyanoacrylate adhesive, was found to provide the best measurements. As demonstrated in Appendix A.1, an explicit evaluation of the performance of the two different fibre coatings is provided and, in addition, the influence of different gauge lengths is analysed.
In certain uniaxial tensile tests, acrylate-coated optical fibres were employed to measure the crack opening on the concrete surface. The superior robustness of this fibre coating was a key factor in its selection, as it was anticipated that the sudden crack formation and subsequent opening would exert significant stress on the optical fibre. The adhesive in question was an epoxy resin, which possesses a lower degree of stiffness than cyanoacrylate. This is also advantageous in terms of the sudden crack occurrence and opening on the concrete surface. The good determination of the crack opening using this method is documented in Appendix A.2. Nevertheless, as the measurement of crack opening on the concrete surface using DIC proved to be robust and the optic sensors did not provide an enhanced accuracy, DIC was used as main measuring technique throughout this thesis.

The principal gage pitch and gauge length were set to 0.65 mm, with a measuring rate ranging from 3.125 Hz to 25 Hz. This range is dependent on the number of channels used and, consequently, the number of optical fibres utilised simultaneously in the FOS system. The system employed was the ODiSI 6108 system from Luna Innovations Incorporated, which detects strain variations using the Rayleigh backscattering method.

Table 3.2: Overview of the used fibre coatings and adhesives for FOS

fibre coating	adhesive (chemical bond)	applied on	considered experimental campaign
polyimide	cyanoacrylate	textile grid (only CG1, CG2)	cyclically loaded uniaxial tensile tests - Section 4.2
acrylate	cyanoacrylate	textile grid	crack opening tensile tests - Section 3.5 uniaxial tensile tests - Chapter 4 four-point bending tests - Chapter 6
acrylate	epoxy resin	concrete surface	uniaxial tensile tests - Appendix A.2

3.5.2 Data post-processing of fibre optic measurement

Prior to utilising the FOS measurement, a post-processing is to be conducted to obtain the required reinforcement strain evolution. This is attributed to the sensitivity of the measurement technique, where anomalies resulting from local peaks in the measured strain provide values that are not plausible in relation to the main data set obtained. Typically, these local peaks exceed the strain measurements in the immediate vicinity, as shown in Figure 3.13a. Filtering and smoothing options are used to eliminate the anomalies when only single data points are affected. For the obtained experimental data, the procedure and post-processing software presented in [Jan23] was used. At first, dropouts represented as NaN-values in the strain reading, were linearly interpolated using the

previous and following data values. In the case of single peak values and single values outlining the other values in the vicinity, the smoothing of the data set using a Bessel filter provided a well-defined elimination of these presumed anomalies. The Bessel filter was used in general for smoothing the strain curve, reducing the influence of high frequencies on the strain curve by filtering out high or low values, including the mentioned peaks, and considering these values with reduced intensity. A fifth-degree Bessel polynomial ($n = 5$) and a frequency variation of $f = 0.1$ rad/s were considered. This allowed for peak values to be eliminated without smoothing the strain curve to an extent where an evaluation of the actual material strain evolution was not possible. This is of particular concern at locations where a sudden change in the cross-section occurs, such as at a local unevenness of the grid or local undulations.

While the applied filtering and smoothing of local anomalies resulted in an accurate representation of the "true" strain evolution, the elimination of anomalies for a set of adjacent data points required an additional post-processing step. In some sections, irrational strain values were determined which are not eliminated by the used Bessel filter method in a satisfying manner as the quantity exceeded the effectiveness of the applied Bessel filter. The respective values may be characterised as a section of irrational high strain values with a linear increase to the local maximum, resembling a rooftop shape at the localised crack, as highlighted in Figure 3.13b. The reason behind this anomaly is expected to result from a debonding of the chemical bond by exceeding the elastic capacity of the used cyanoacrylate adhesive. This allows for a free linear-elastic elongation of the optic fibre debonded section with a peak in the crack at which the fibre strain reaches its maximum value. The strain values at which the debonding occurred depended on the condition of the chemical bond. Differences in application lead to a debonding already at small crack widths, while in general the anomaly was related to large crack opening, mostly in combination with a multiple crack occurrence or during cyclic loading. To filter the data, the respective values were eliminated from the data set and linearly interpolated prior to smoothing with the Bessel filter.

After filtering and smoothing the data provided by the fibre optic measurement, the elasticity of the chemical bond and the fibre coating is considered. The maximum strain value of the optical measurement at the crack $\varepsilon_{\mathrm{FOS,max}}$ exceeds the actual reinforcement strain $\varepsilon_{\mathrm{nm,max}}$ in the crack determined by the applied load F as shown in Figure 3.13c. This behaviour is also attributable to the non-uniform cross-sectional area and Young's modulus of the fibre strand, which are assumed by constant averaged values A_{nm} and E_{nm} provided as material parameters. The difference between the two strain values is accounted for by an introduced reduction factor $\xi_{\mathrm{FOS}} = \varepsilon_{\mathrm{nm,max}} / \varepsilon_{\mathrm{FOS,max}}$. Prior

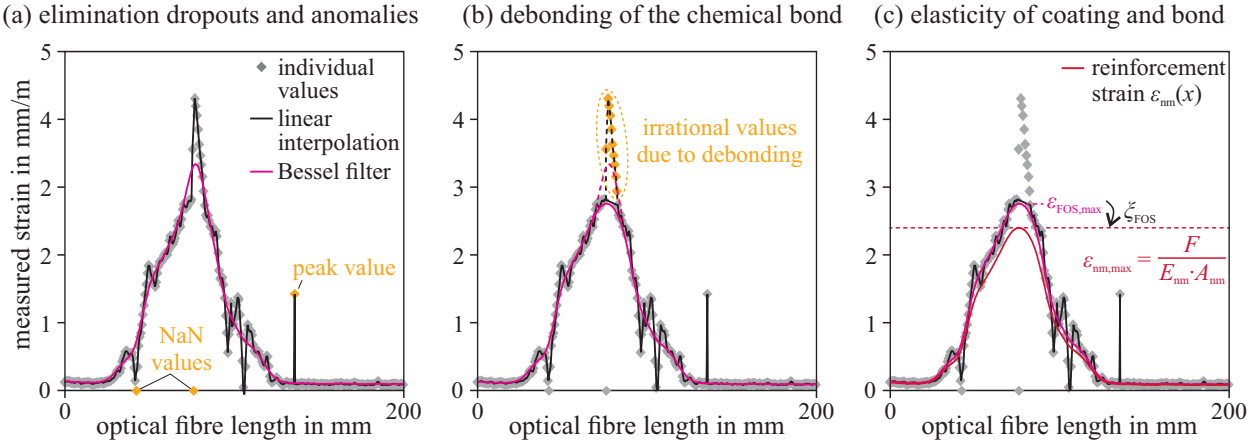


Figure 3.13: Visualisation of performed post-processing of the obtained data from FOS with an acrylate-coated fibre (adapted from [Sch25b])

to this step, possible eccentricities of the test specimen resulting in an inhomogeneous elongation of the longitudinal fibre strands were taken into account. Due to the elasticity of the chemical bond and the scattering of material characteristics, in particular the Young's modulus of the reinforcement, the reduction factor ξ_{FOS} had to be determined individually for each specimen and time step. Once the post-processing steps were applied to the raw data from the fibre optic strain measurements, the strain values provided feasible values of the reinforcement strain evolution.

3.5.3 Physically based derivation of strain and deformation evolution

When provided with post-processed strain values of the fibre optic measurement, these increments $\varepsilon_{\mathrm{nm,i}}(t)$ are assumed to resemble the strain evolution in the reinforcement with the time serving as the indicator for the loading history. The index i refers to the gauge point at which the strain increment of the fibre optic measurement is determined. In the following consideration, the presented approximations and approaches always focus on a fixed time.
The utilisation of individual strain values to obtain the displacement of reinforcement or concrete and, consequently, the slip as well as to determine the crack opening, constitutes a principle methodology. This is reported in cases of discrete strain measurements such as strain gauges for example reported in [Rob01, Kam13] and when using FOS for example in [Fis19, Ber21b, Vor21, Bec22, Gal23a, Jan23, Sch25b, Bec25b].
Considering force equilibrium, a discrete value of bond stress at each gauge point is derived

$$\tau_{\mathrm{b,i}} = \frac{E_{\mathrm{nm}} \cdot A_{\mathrm{nm}} \cdot (\varepsilon_{\mathrm{nm,i+1}} - \varepsilon_{\mathrm{nm,i}})}{U_{\mathrm{nm}} \cdot \Delta x} \tag{3-1}$$

using the adjacent reinforcement strain values $\varepsilon_{\mathrm{nm,i}}$ and $\varepsilon_{\mathrm{nm,i+1}}$ for each increment of length $\Delta x = (x_{\mathrm{i+1}} - x_{\mathrm{i}})$, which is of equal value to the gauge length. The location of the crack is represented by the zero transition of the bond stress values. The end of the transfer length is obtained when the bond stress reaches zero values again, as no strain differences between reinforcement and concrete occur.
The value of concrete strain per increment is obtained as follows

$$\varepsilon_{\mathrm{c,i}} = \frac{E_{\mathrm{nm}} \cdot A_{\mathrm{nm}}}{E_{\mathrm{c}} \cdot A_{\mathrm{c}}} \cdot (\varepsilon_{\mathrm{nm,max,av}} - \varepsilon_{\mathrm{nm,i}}). \tag{3-2}$$

As the determined maximum reinforcement strain for each crack is not of equal value, the average of all maximum strain values, denoted as $\varepsilon_{\mathrm{nm,max,av}}$, is introduced. In the case of multiple crack occurrences, this approach leads to some inaccuracy when determining the concrete strain values close to the crack. Another approach, presented for example in [Gal23a], is a segmented focus on the individual crack and the corresponding transfer length with consideration of $\varepsilon_{\mathrm{nm,max,av}}$ as the maximum reinforcement strain in each crack. The result is a discontinuity of concrete strain at the transition between two cracks. The reason for the differences in the maximum strain values is attributed to differences in the stiffness of the reinforcement, the Young's modulus of concrete, the non-uniform opening of the cracks and the ability of the crack surfaces to transfer some tensile force at small crack opening.

The mean values of reinforcement strain, concrete strain and bond stress in the transfer length are obtained by summing all the values provided by the fibre optic measurement. This is expressed as an integral approach considering a separate evaluation on each side of an individual crack:

$$\begin{aligned} \varepsilon_{\mathrm{nm,m}}^{\mathrm{a}} \cdot l_{\mathrm{t}}^{\mathrm{a}} &= \int_{x_{\mathrm{a}}}^{x_{\mathrm{cr}}} \varepsilon_{\mathrm{nm}}(x)\,\mathrm{d}x = \sum_{i=x_{\mathrm{a}}/\Delta x}^{x_{\mathrm{cr}}/\Delta x} \varepsilon_{\mathrm{nm,i}} \cdot \Delta x \\ \varepsilon_{\mathrm{nm,m}}^{\mathrm{b}} \cdot l_{\mathrm{t}}^{\mathrm{b}} &= \int_{x_{\mathrm{cr}}}^{x_{\mathrm{b}}} \varepsilon_{\mathrm{nm}}(x)\,\mathrm{d}x = \sum_{i=x_{\mathrm{cr}}/\Delta x}^{x_{\mathrm{b}}/\Delta x} \varepsilon_{\mathrm{nm,i}} \cdot \Delta x \end{aligned} \tag{3-3}$$

The location of the crack is x_{cr}, the determination of the coordinate at the end of the transfer length is obtained as $x_{\mathrm{a}} = x_{\mathrm{cr}} - l_{\mathrm{t}}^{\mathrm{a}}$ and $x_{\mathrm{b}} = x_{\mathrm{cr}} + l_{\mathrm{t}}^{\mathrm{b}}$. The end of the transfer length was determined by differentiating between the cases of a single crack and adjacent cracks. For a single crack, the end of the transfer length is defined as the location of equivalent strain values of reinforcement and concrete. This is the point at which the reinforcement strain evolution reaches the value of the concrete tensile strength, approximated as $f_{\mathrm{ct}}/E_{\mathrm{cm}}$, which is the threshold. Due to the noise of the FOS measurement, which is not fully compensated by the applied Bessel filter, the strain values fluctuate around the concrete tensile strength with some values being slightly above and some values being below the threshold. Therefore, in order to apply robustness to the determination strategy for the end of the transfer length, the threshold is to be determined using the average of five consecutive strain values. In the case of adjacent cracks, the end of the transfer length is at the local minimum of the strain evolution between these two cracks, which is used in the evaluation strategy to determine x_{a} and x_{b}.
The mean concrete strain is then expressed as

$$\begin{aligned} \varepsilon_{\mathrm{cm}}^{\mathrm{a}} \cdot l_{\mathrm{t}}^{\mathrm{a}} &= \int_{x_{\mathrm{a}}}^{x_{\mathrm{cr}}} \varepsilon_{\mathrm{c}}(x)\,\mathrm{d}x = \sum_{i=x_{\mathrm{a}}/\Delta x}^{x_{\mathrm{cr}}/\Delta x} \varepsilon_{\mathrm{c,i}} \cdot \Delta x \\ \varepsilon_{\mathrm{cm}}^{\mathrm{b}} \cdot l_{\mathrm{t}}^{\mathrm{a}} &= \int_{x_{\mathrm{cr}}}^{x_{\mathrm{b}}} \varepsilon_{\mathrm{c}}(x)\,\mathrm{d}x = \sum_{i=x_{\mathrm{cr}}/\Delta x}^{x_{\mathrm{b}}/\Delta x} \varepsilon_{\mathrm{c,i}} \cdot \Delta x \end{aligned} \tag{3-4}$$

and the mean bond stress as

$$\begin{aligned} \tau_{\mathrm{bm}}^{\mathrm{a}} \cdot l_{\mathrm{t}}^{\mathrm{a}} &= \int_{x_{\mathrm{a}}}^{x_{\mathrm{cr}}} \tau_{\mathrm{b}}(x)\,\mathrm{d}x = \sum_{i=x_{\mathrm{a}}/\Delta x}^{x_{\mathrm{cr}}/\Delta x} \tau_{\mathrm{b,i}} \cdot \Delta x \\ \tau_{\mathrm{bm}}^{\mathrm{b}} \cdot l_{\mathrm{t}}^{\mathrm{b}} &= \int_{x_{\mathrm{cr}}}^{x_{\mathrm{b}}} \tau_{\mathrm{b}}(x)\,\mathrm{d}x = \sum_{i=x_{\mathrm{cr}}/\Delta x}^{x_{\mathrm{b}}/\Delta x} \tau_{\mathrm{b,i}} \cdot \Delta x\,. \end{aligned} \tag{3-5}$$

The exemplary evaluation of the methodology is visualised in Figure 3.14. The evolution of the bond stress depicted in Figure 3.14b shows decisive changes in the gradient resulting from changes in the cross-sectional area of the longitudinal fibre strand at local undulations, as the localisation of the transverse strands indicates. Increasing thickness of the fibre strand resulted in increased bond stress due to the discontinuity providing an area of interlocking and reduced local slip. The increased bond stress at the intersection of the fibre strands is also attributed to the significant force transfer at these local undulations.
As shown in Figure 3.14c, the concrete strain in the crack is zero. For small crack openings, the

ability of the crack surfaces to transfer a softening tensile force resulted in some value of strain being determined in the crack.

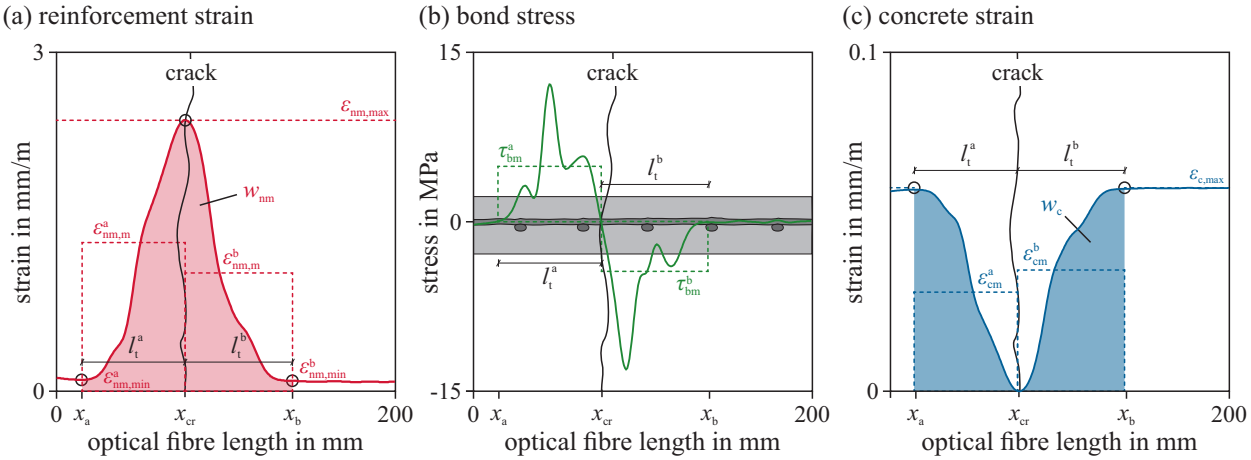


Figure 3.14: Evolutions of the reinforcement strain, bond stress and concrete strain obtained by a physically based consideration of the post-processed FOS measurements (adapted from [Sch25b])

The slip is obtained as the difference between the deformation of the reinforcement and the concrete

$$\begin{aligned} \delta_\mathrm{a} &= u_\mathrm{nm}^\mathrm{a} - u_\mathrm{c}^\mathrm{a} = \int_{x_\mathrm{a}}^{x_\mathrm{cr}} \left(\varepsilon_\mathrm{nm}(x) - \varepsilon_\mathrm{c}(x)\right) \mathrm{d}x = \sum_{i=x_\mathrm{a}/\Delta x}^{x_\mathrm{cr}/\Delta x} \left(\varepsilon_\mathrm{nm,i} - \varepsilon_\mathrm{c,i}\right) \cdot \Delta x \\ \delta_\mathrm{b} &= u_\mathrm{nm}^\mathrm{b} - u_\mathrm{c}^\mathrm{b} = \int_{x_\mathrm{cr}}^{x_\mathrm{b}} \left(\varepsilon_\mathrm{nm}(x) - \varepsilon_\mathrm{c}(x)\right) \mathrm{d}x = \sum_{i=x_\mathrm{cr}/\Delta x}^{x_\mathrm{b}/\Delta x} \left(\varepsilon_\mathrm{nm,i} - \varepsilon_\mathrm{c,i}\right) \cdot \Delta x \end{aligned} \tag{3-6}$$

on each side of the crack. The crack width is

$$w = w_\mathrm{nm} - w_\mathrm{c} = \delta_\mathrm{a} + \delta_\mathrm{b}. \tag{3-7}$$

The elongation of the reinforcement with no transfer of force in the crack is considered by the continuous fibre optic measurement and, consequently, not explicitly considered in Equation 3-7. The factor β, introduced in the analytical description of the local behaviour in Section 2.5.3 to simplify the non-linear strain evolution, and referred to as the tension stiffening factor, is determined as follows:

$$\begin{aligned} \beta_\mathrm{a} &= \frac{1}{\varepsilon_\mathrm{nm,max} - \varepsilon_\mathrm{nm,min}} \cdot \left(\varepsilon_\mathrm{nm,max} - \frac{1}{l_\mathrm{t}^\mathrm{a}} \int_{x_\mathrm{a}}^{x_\mathrm{cr}} \varepsilon_\mathrm{nm}(x)\, \mathrm{d}x \right) \\ \beta_\mathrm{b} &= \frac{1}{\varepsilon_\mathrm{nm,max} - \varepsilon_\mathrm{nm,min}} \cdot \left(\varepsilon_\mathrm{nm,max} - \frac{1}{l_\mathrm{t}^\mathrm{b}} \int_{x_\mathrm{cr}}^{x_\mathrm{b}} \varepsilon_\mathrm{nm}(x)\, \mathrm{d}x \right) \end{aligned} \tag{3-8}$$

3.5.4 Calibration and validation of FOS evaluation method

The COT tests allowed for a well-defined evaluation basis to determine the accuracy of the fibre optic measurement due to the set boundary conditions and defined test configuration. The applied force is fully transferred in the fibre strand at the crack initiation element without additional force attributed to the concrete surfaces. Moreover, the low variation determined in the previous COT tests introduced in Section 3.4 promotes the evaluation with regard to the validity of the obtained data. Therefore, COT tests were conducted reinforced with CG1 and GG and an optical fibre applied on the longitudinal textile fibre strand, which were identical in configuration to the COT tests in Section 3.4. The specimens were prepared simultaneously with the COT tests having no optical fibre and concreted with the same batch. Different concrete strengths resulting from hardening were not determined by the simultaneously conducted material tests. This allowed for a direct comparison of the COT test series to investigate a possible influence of the optical fibre application on the bond behaviour and therefore the force-crack opening relation, which is depicted in Figure 3.15.

In the case of the specimens reinforced with CG1, the COT tests prepared with the optical fibre showed no different behaviour compared to the COT specimens without an optical fibre for crack openings below 0.2 mm (Figure 3.15a). At larger crack openings the specimens with the optical fibre showed a slightly higher force at identical openings. This difference between the forces applied between both series is insignificant as the value is approximately 0.2 kN, which is a reinforcement stress of 27 MPa, at the end of the single cracking stage. Regarding reinforcement GG, the COT test specimens prepared with an optical fibre showed also a slightly higher force at an identical crack opening compared to the test series without the fibre (Figure 3.15b). The difference between the two averages is again at about 0.2 kN (reinforcement stress of 20 MPa). The slight rise in tensile forces is attributed to the enhanced bond capacity of the specimens with fibre optic sensors. As the application of the adhesive increased the bond surface, so did the contribution of friction. As a conclusion, the application of the optical fibres on the textile grids has a measurable but insignificant influence on the bond behaviour, which is therefore neglected.

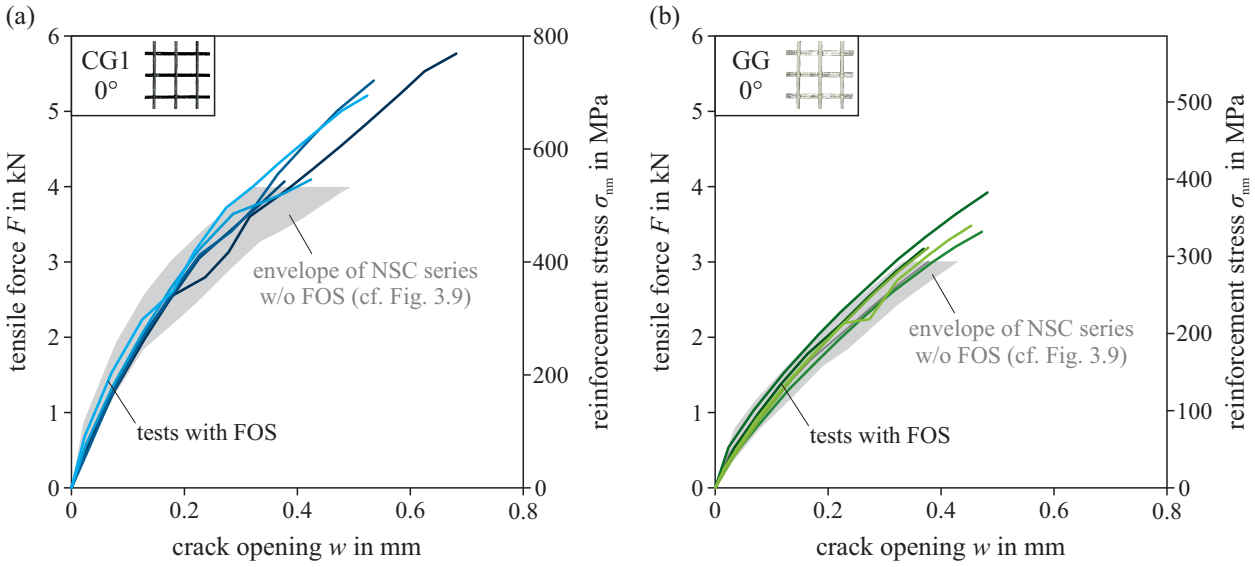


Figure 3.15: Comparison of the COT test results of specimens with and without (w/o) an optical fibre employed on the fibre strand

Considering the fibre optic measurement derived from the COT tests, a determination of the crack opening in relation to the applied tensile force is done for each measured time step, using the

physically based consideration provided in Equations 3-6 and 3-7. The graphical evaluation for the first specimen of each series is presented on the left-hand side in Figure 3.16. The obtained individual data values are compared to the crack opening determined using DIC. As the results in Figure 3.16 demonstrate, both measurement techniques of FOS and DIC agreed almost perfectly with each other at the single cracking stage and even after the occurrence of an additional crack. Discrepancies were only revealed at an adjacent cracking stage at which a crack formed near the initiated crack resulting in a significant change in the reinforcement strain evolution, which is focused in detail in the following Section 3.5.5.

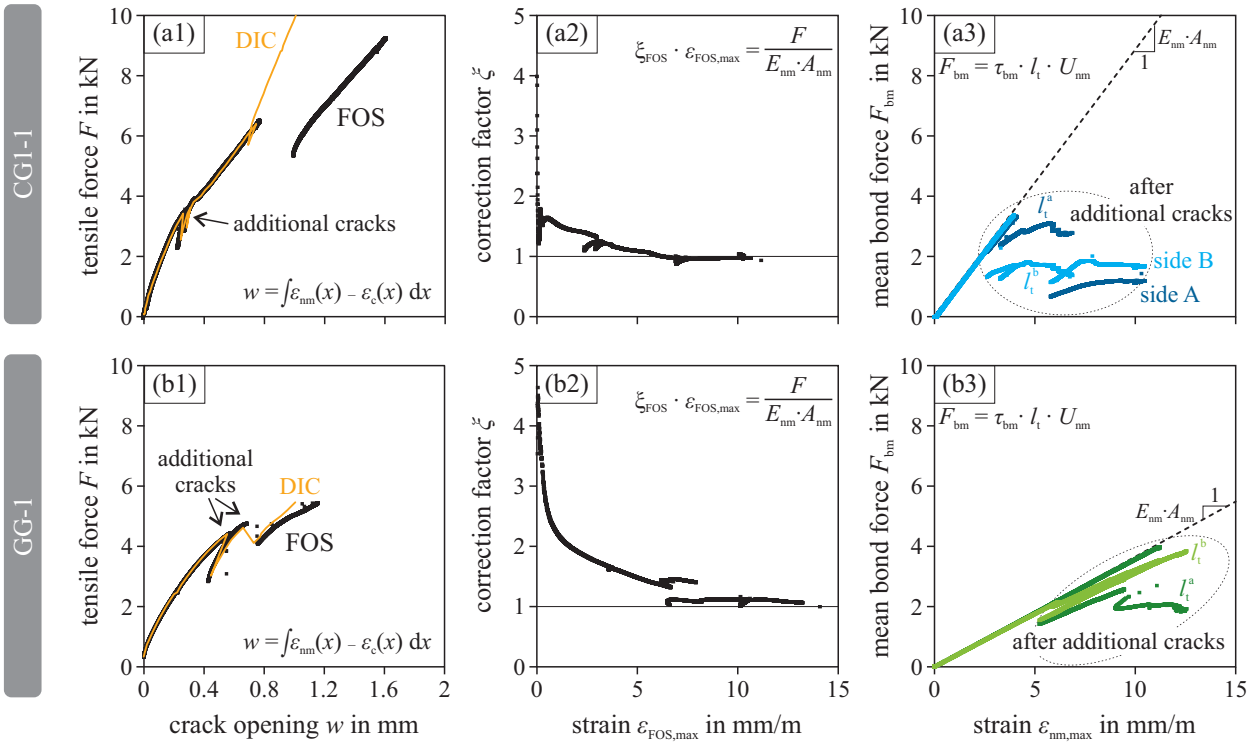


Figure 3.16: Accuracy of FOS to determine the crack opening and obtaining the force transfer by using the calibration factor ξ_{FOS}

Contrary to the crack opening, which is well approximated by the strain evolution of the fibre optic sensors, the mean strain evolution and bond force evolution require the determination of the reinforcement strain values using the reduction factor ξ_{FOS}. As shown in the centre column of Figure 3.16, the correction at low strain values of the fibre optic measurement ε_{FOS} using ξ_{FOS} is significant to fulfil an equivalence of values between the fibre optic strain and the reinforcement strain. At higher strain values, the factor ξ_{FOS} trends towards one. This behaviour was observed in all COT tests utilised with an optical fibre. As previously mentioned, the assumed reinforcement strain is determined using the material parameters for the cross-section and Young's modulus of the textile grid. When the reinforcement utilisation is low, the textile fibres straighten, resulting in a Young's modulus for the strand lower than the material parameter. The Young's modulus was obtained using tensile tests following the procedure outlined in [DAfStb24], focusing on the reinforcement strain values measured at 10% and 60% of the tensile strength. This influence of a low Young's modulus was particularly pronounced for reinforcement GG, presumably because of significant straightening of the glass fibres.

The verification of the applied procedure using the factor ξ_{FOS} is illustrated in the right-hand column of Figure 3.16. The reinforcement strain in the crack $\varepsilon_{nm,max}$ is related to the determined mean bond force F_{bm} considering the formulation of the mean value of bond flow, given in Equation 3-5

multiplied by the circumference of the fibre strand. In the case of a single crack, the applied force, expressed by the dashed line in Figure 3.16 as a force-strain relation, is required to be equivalent to the determined mean bond force assuming a transfer of the complete force from the reinforcement to the concrete. This is met by the evaluation using FOS. With additional cracking and the transition into a crack formation stage, this assumption is not true as some value of force is not transferred to the concrete. It is apparent, that at higher strain values $\varepsilon_{nm,max}$ and therefore crack opening the mean bond force is reduced, particularly for CG1. This is analysed in detail in the following section. To conclude, the proposed method with calibrating the measured strains using a factor ξ_{FOS} to obtain the reinforcement strain and determine the force transfer is valid.

3.5.5 Evaluation of derived strain and deformation considering COT tests

Evolution of reinforcement strain, bond and concrete stress

The following section focuses on the first specimen of both series (CG1 and GG) at chosen load levels, with the results plotted in Figure 3.17. In addition, the DIC picture taken at the last loading stage is provided in Figure 3.17 for reference.

During a stage of a single crack at the initiation element, indicated by the blue lines in Figure 3.17, the assumed non-linear evolution of the reinforcement strain showed a full transfer of the force in the set length of 114 mm between the crack and the clamping. At the end of the transfer length, the reinforcement strain was equal in value to the concrete tensile strength at approximately 0.1 mm/m. In the case of specimen CG1-1, the bond stress evolution showed a peak value at the local undulation with the transverse fibre strand and a continuous decline in bond stress to the end of the transfer length, which was about the provided length of 114 mm (= three times the yarn spacing). For specimen GG-1, a shorter transfer length of about 76 mm, being twice the yarn spacing, at similar peak values of bond stress was required.

Due to the test configuration, the occurrence of an additional crack in the vicinity of the initiated crack influenced the strain evolution. At this stage, indicated by the yellow lines in Figure 3.17, the end of the transfer length was defined by the local minimum of the reinforcement strain evolution. The bond stress was zero and, in a mathematical expression, changed the algebraic sign. The transferred force is not equal in value to the applied force as well shown in the case of specimen GG-1.

For both specimens, crack ② occurring on side B of the initiated crack resulted in a reduced force transfer compared to side A, as previously shown in the different values of mean bond force plotted in Figure 3.16. For specimen CG1-1, the reduction in transferred force was larger compared to GG-1. This is attributed to the differences in crack spacing.

Considering the last evaluated load level (red curves), the difference between the peak reinforcement strain value and the minimum value between two cracks in CG1-1 were relatively lower compared to specimen GG-1. Consequently, the different bond capacities of the two textile grids provided for a significant different behaviour at the adjacent crack occurrence.

The concrete stress evolution also reveals that the maximum concrete tensile stress prior to the occurrence of a crack is below the value determined in the material tests, denoted as f_{ct}. This was also observed in the subsequent test campaigns and is addressed in detail later in Section 5.5.3.

For both specimens, the obtained crack opening of fibre optic measurement and DIC (cf. Figure 3.16) showed a discrepancy at a certain load level, which resulted from a crack occurring in close vicinity to the initiated crack. In Figure 3.17, this crack is indicated by the number of appearance as ④. At this stage, the reinforcement strain was not declining between these two cracks in a significant matter, a determination of a local minimal value was almost impossible and therefore also a definition of the transfer length of both cracks. This provided a problem in the proposed

evaluation method, which is addressed by assuming both cracks as one crack. This assumption results in an inaccurate representation of the actual member behaviour, overestimating the crack opening, which was shown previously in Figure 3.16. The transferred force between these two adjacent cracks was very low close to zero as the bond stress evolution reveals. As apparent, no force was transferred and no tension stiffening was occurring at cracks in close proximity to each other.

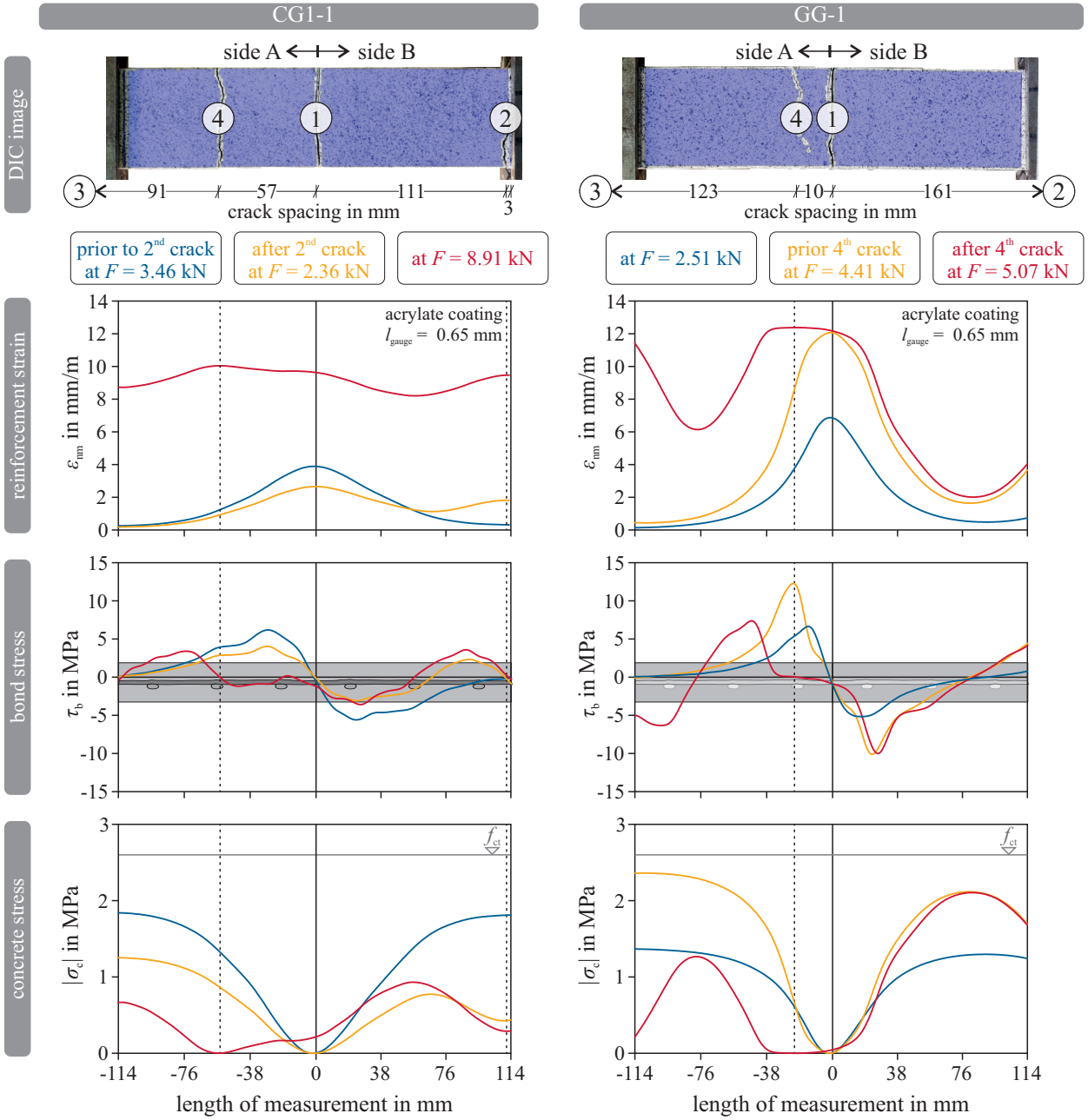


Figure 3.17: Strain and stress evolution of two COT tests determined using FOS

Bond behaviour at static loading

In order to evaluate the bond capacity, each side of the initiated crack was analysed separately, until the formation of an adjacent crack affected the single-crack behaviour. For example, the evaluation procedure is shown in Figure 3.18 for specimen CG1-2. The reinforcement strain evolution at three different load steps is shown on the right-hand side. By differentiation, the bond stress evolution was obtained, which is plotted in the middle diagram of Figure 3.18. As already pointed out, the local peaks observed in the evolution corresponded very well with the localisation of the local undulations where the fibre strands intersect. The additional occurrence of another crack, represented by the purple curves, resulted in a significant reduction in bond stress and therefore transferred force. With the additional crack occurring at an undulation in the clamping at a distance of 136 mm from the initiated crack, the transfer length of the initial crack is reduced to 57 mm. As shown by the bond stress evolution, still one intersection was inside the transfer length, which allowed for some force transfer with a magnitude of 2.2 MPa in bond stress, which is about half in value compared to the maximum of 5 MPa determined at an early loading state (red curve).

When deriving the mean value of bond stress τ_{bm} from the bond stress evolution and plotting it in relation to the determined slip for each measured loading step, as shown on the right-hand side in Figure 3.18, the influence of the cracking stage becomes visible. At single cracking, a non-linear mean bond stress to slip relation is represented with an onset of bond softening becoming visible at increasing slip prior to occurrence of a new crack. This loading step is highlighted with a yellow circle and resembled by the yellow curves shown in the two left-handed graphs. The new crack occurred in the other half of the specimen, which did not influence the force transfer of this observed side. In the contrary to the assumed onset of bond softening, the mean bond stress curve increased, as the fibre strand is capable of transferring large forces by the continued utilisation of friction and interlocking along the transfer length. As the bond stress evolution reveals prior to the next crack occurrence, represented by the red curves and red circle, peak values of 5 MPa at the first intersection and 7 MPa at the second undulation were determined. The mean bond stress was $\tau_{bm} = 3.45$ MPa at a slip of 0.27 mm. With the occurring adjacent crack, the value of the mean bond stress was significantly reduced to 0.85 MPa. Initially, the value of slip is reduced to 0.16 mm, as the additional crack occurrence reduced the opening of the initiated crack due to the deformation-controlled loading of the specimen. At first, no increase in the mean bond stress is

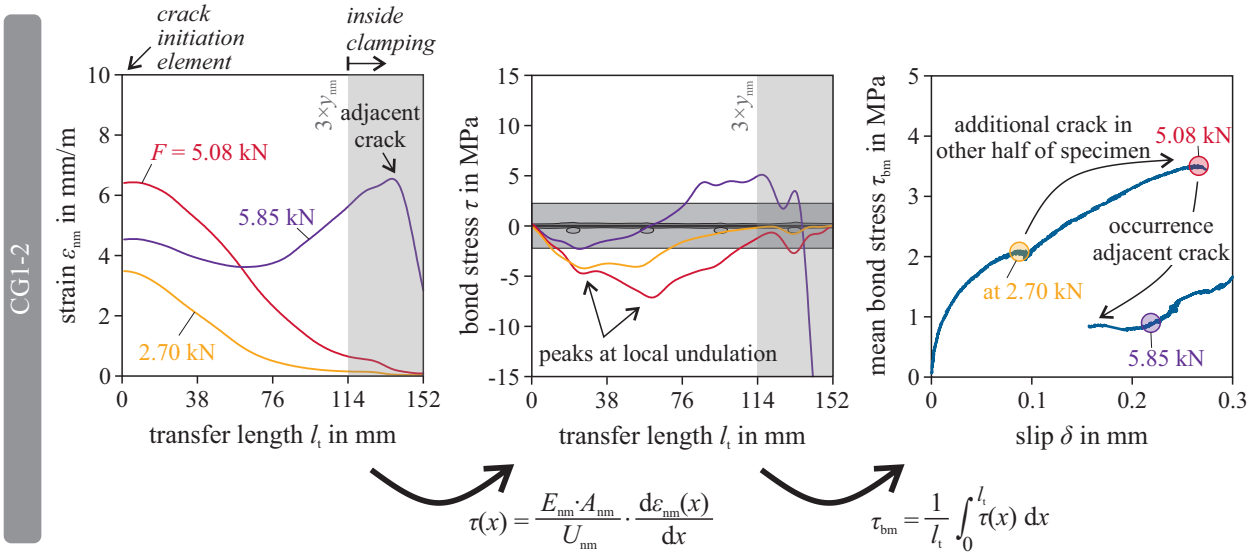


Figure 3.18: Correspondence between measured reinforcement strain, derived bond stress and determined mean value of bond stress, exemplarily shown for specimen CG1-2

recognisable with the continuing loading and slip increase. Then, at a slip of about 0.22 mm, more force is transferred again. At the end of the test, the value of bond stress at an adjacent cracking stage was 1.72 MPa at a slip of 0.3 mm.
This detailed evaluation of one specimen leads to three main observations: Firstly, textile grids are capable of high force transfer if a sufficient number of intersections, referred to as local undulations, are contributing to interlocking. This is provided at a single cracking stage, as well shown for reinforcement CG1, and also allows for a "stiffening" of the mean bond stress-slip relation after already some bond softening was indicated, because with the increasing transfer length an additional intersection is fully activated. Secondly, with the occurrence of an adjacent crack, the transfer length is reduced in such a way that only one or two intersections in the transfer length contribute towards the force transfer. This is attributed to the transfer length of a single crack expanding prior to adjacent crack occurrence until about three or four local undulations are included. With the next crack generally forming at a local undulation due to a reduced concrete area being present, an adjacent crack forms in the close vicinity to the end of the present transfer length. Thus, dividing the transfer length of the existing single crack in half. Finally, also when adjacent cracks are present, there is still some increase in bond capacity provided with increasing slip, which becomes of importance when considering the stabilised cracking stage in detail in Chapter 4.

These observations regarding the single cracking stage are revised considering all specimens monitored with FOS, which were in total five specimens of the two test series. In Figure 3.19 the mean bond force and the value of mean bond stress are plotted in relation to the determined slip or transfer length. As both sides of the initiated crack were considered, overall 20 curves were obtained for each evaluation. Besides the previously introduced mean bond stress-slip relation, an evaluation of the mean bond force F_{bm} related to the slip and the transfer length is introduced in the four graphs in Figure 3.19a+b. As the mean bond force is equivalent to the force transferred, a comparison to the derived force-slip relation in SPOc tests, introduced in Section 3.3, is made with plotting the corresponding mean curves for an embedded length of 114 mm in the graphs. This reveals similar observations made regarding the different results provided by the two test concepts of SPOc and COT in Section 3.4.2. The force-slip relations determined in the COT tests for CG1 provided a stiffer bond behaviour and higher forces at identical slip (Figure 3.19a1). The opposite is observed with regard to specimens with GG (Figure 3.19b1).

Addressing the relation of force to transfer length, both grids showed the transfer of recognisable force when the transfer length reached at least the first intersection (Figure 3.19a2+b2). When two intersections were within the transfer length, the force increased considerably, supporting the assumption that the local undulations present at the intersection contributed significantly to the bond capacity of the two reinforcements CG1 and GG, as they were impregnated with similar resin and produced in a similar way by the same manufacturer.
The mean bond stress-slip curves support the previous observations made in the case of CG1-2 as shown in Figure 3.19a3+b3. In some specimens, an onset of bond stiffening was observed as a result of adjacent crack occurrence with no slip present at the end of the transfer length. This becomes also visible when considering the evolution of the mean bond force in relation to the transfer length, as at some point, the value of the transfer length remained fixed while the bond force continued to increase. For some specimens with CG1, the onset of bond softening occurred at a low value of slip of 0.06 mm and a mean bond stress of approximately 1.8 MPa on average (Figure 3.19a3). In the case of specimens with GG, bond softening was not as pronounced and an onset was revealed for a slip exceeding 0.15 mm (Figure 3.19b3).
In general, the evaluation of all ten with FOS-equipped specimens showed a very low scattering of the individual tests, with differences occurring only at high loading when adjacent cracks occurred.

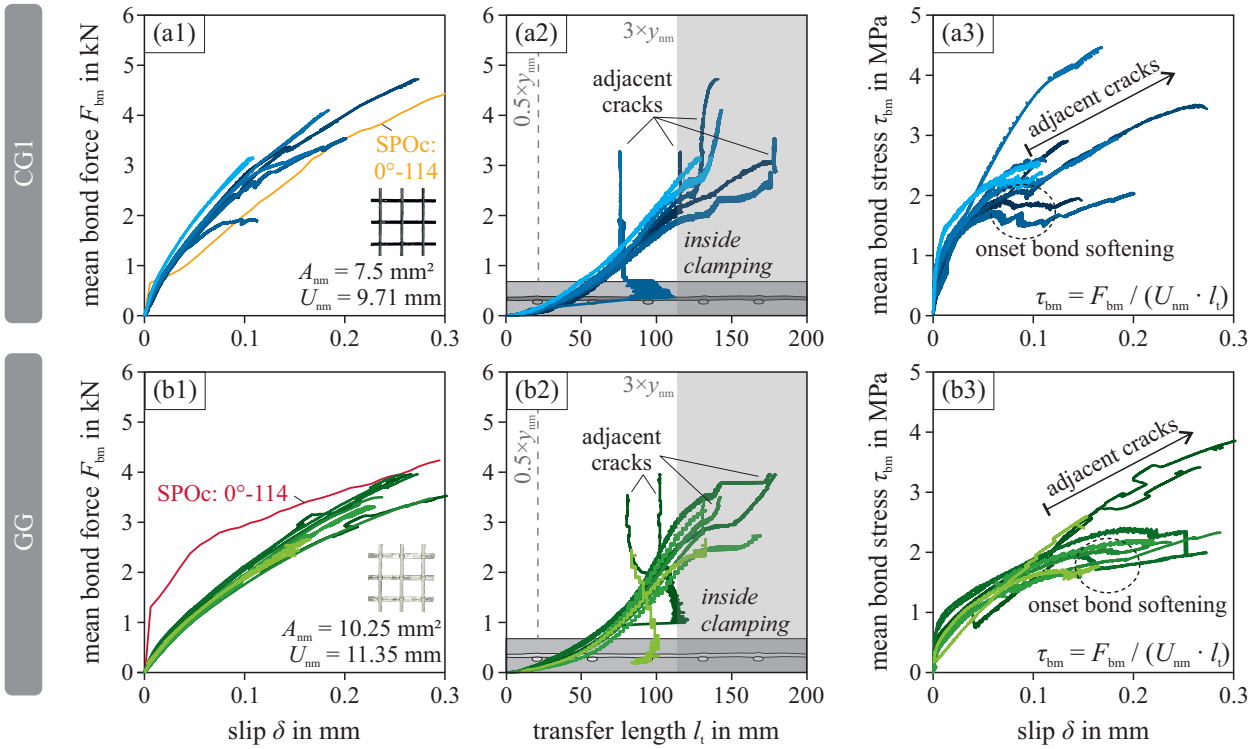


Figure 3.19: Evaluation of the bond capacity in the COT specimens equipped with FOS

Bond behaviour at cyclic loading

In the following, results provided by fibre optic measurements on cyclically loaded specimens are discussed. The tests conducted are identical in setup and execution to the cyclic COT tests presented in Section 3.4.4. These tests revealed that the cyclic load application led to an increase of the crack opening, resulting from a shift in the bond mechanisms and a decrease in their contributing to the force transfer. At first, the evolutions of the reinforcement strain and bond stress for two specimens, reinforced with CG1 and GG, are provided in Figure 3.20. The corresponding strain at the superior and inferior load levels for the first cycle, last cycle and thereafter at increased loading are plotted.

For specimen CG1-3-cyclic, the application of ten load cycles resulted in an increase in transfer length accompanied by a change in the strain and stress evolution (Figure 3.20a). This behaviour was not visible for specimen GG-5-cyclic (Figure 3.20b), which apparently was only marginal affected by the cyclic loading despite the strain levels being higher compared to CG1-3-cyclic, as the superior load level had the identical force applied. Notable is the bond stress of specimen CG1-3-cyclic, as at the superior load level of the first cycle a local peak was observed at a distance of approximately 5 mm from the initiated crack with a stress of 9 MPa. This peak decreased over subsequent load cycles. During the cyclic load application, greater force is transferred at locations distant from the crack. This resulted in a bond stress evolution that shifted towards the less utilised areas of the fibre strand. It is important to note that the absolute peak values of bond stress are significantly higher in this specimen compared to specimen CG1-2-static, which was evaluated previously (cf. Figure 3.18). Focusing the inferior load level, the reinforcement strain evolution revealed an almost constant value along the transfer length before the strain declined. In the case of specimen CG1-3-cyclic, the strain value is constant along a length of 1.5 times the yarn spacing and a decline in strain was detected at the second intersection with a transverse fibre strand. For specimen GG-5-cyclic, the distance of a constant strain value was approximately half the yarn spacing, which corresponded to the location of the first intersection. Specimen GG-5-cyclic revealed a simi-

lar behaviour, while no adjacent crack was present at the evaluated steps. Also changes in the strain and stress evolutions resulting from local undulations were less pronounced.

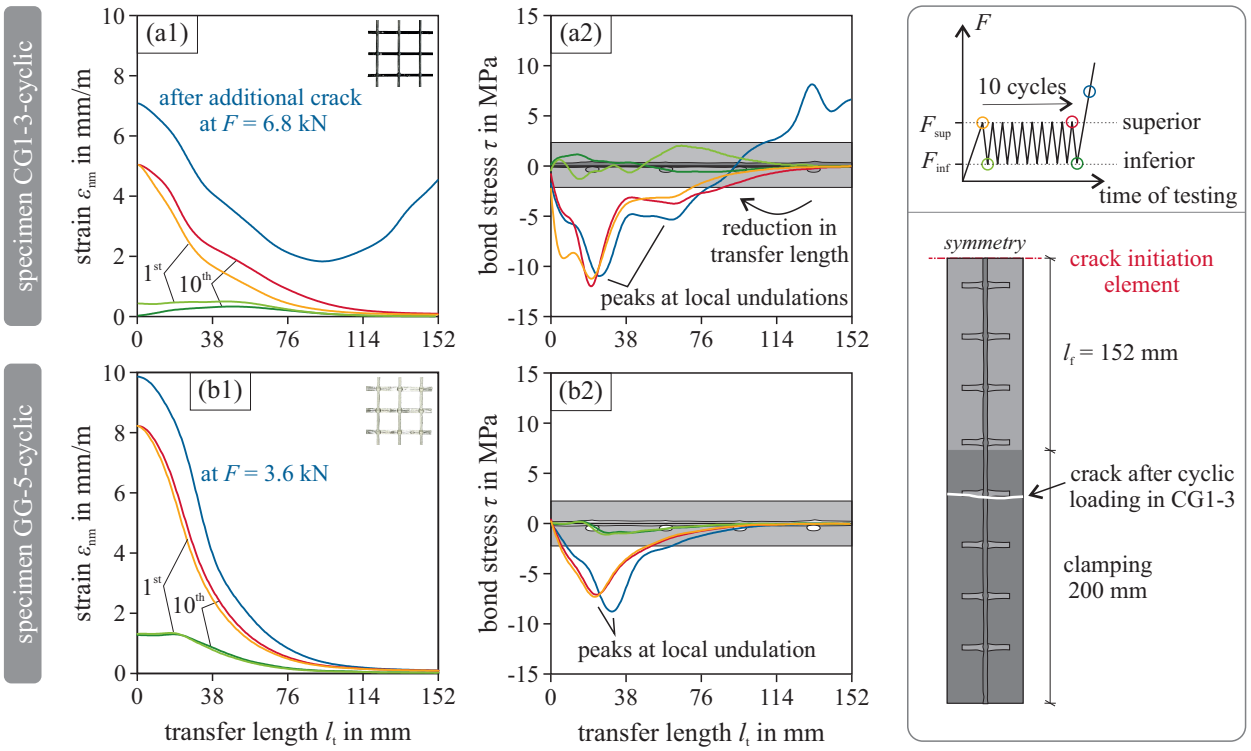


Figure 3.20: Evaluation of the reinforcement strain and bond stress of two specimens subject to ten load cycles

The force related to the crack opening and to the transfer length as well as the mean bond stress-slip relation are visualised in Figure 3.21. Again, only one side of the initiated crack at the single cracking stage of two specimens, designated as CG1-3-cyclic and GG-5-cyclic, is focused. The comparison of the crack opening determined by FOS and DIC showed almost complete compliance. The cyclic loading did not damage the fibre optic sensors or lead to an incoherence of the obtained data. The evaluations revealed that the additional crack opening during the cyclic loading phase was the result of an increase in the transfer length, which is expressed by a reduction of the determined mean value of bond stress and an increase in slip. The absolute increase in transfer length from the first to last cycle was 12 mm, being about 10% of the initial value, for specimen CG1-3-cyclic (Figure 3.21a2) and 5 mm (about 5%) considering GG-5-cyclic (Figure 3.21b2).
In the case of CG1-3-cyclic, fluctuations in the values of the transfer length and the slip were determined between the inferior and superior load levels. These anomalies were attributed to the post-processing method employed for the FOS data. Specifically, alterations in the localisation of the end of the transfer length, which was defined as the point of equivalent strain values between reinforcement and concrete, led to these deviations. This resulted in small differences when determining the transfer length and therefore the slip values between the inferior and superior load levels. While observed for a limited number of specimens, no influence on the values determined at the superior load level and beyond was found.

In summary, the application of ten load cycles resulted in an increased transfer length. This is attributed to the reduction in the bond capacity of the textile grids and was pronounced for the specimens reinforced with CG1 and less visible for specimens with GG. A significant increase in slip was not observed as a result of a redistribution of the transferred force to less utilised areas of

the fibre strand at the failure of the local bond mechanism, expressed, for example, by a shearing of at local undulations accompanied by a reduced interlocking effect by the intersection. The lack of a significant slip increase is presumably attributable to the limited number of load cycles that have been conducted.

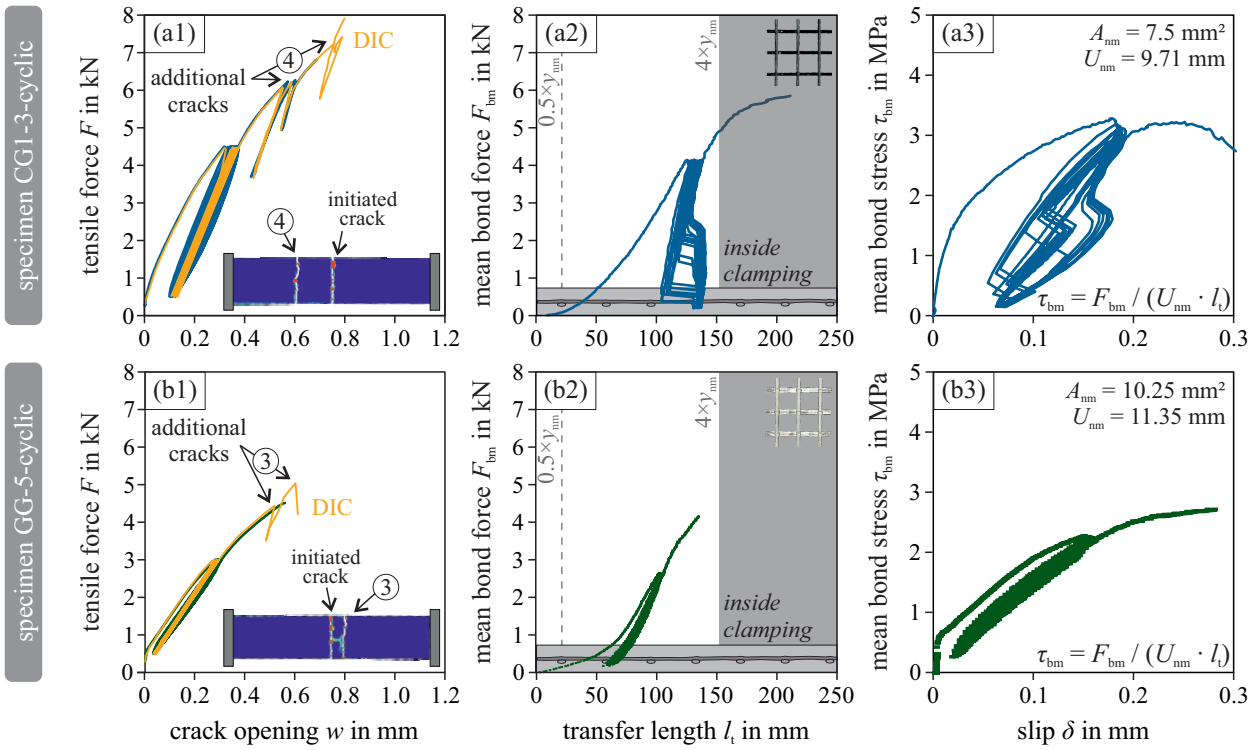


Figure 3.21: Evaluation of the crack opening, the force-transfer length relation and the mean bond stress-slip relation in the case of cyclic loading

3.5.6 Consideration of tension stiffening

The previous observations using FOS revealed that the contribution of tension stiffening is considerably high in the case of single cracks, as the force is re-transferred at small lengths in the uncracked concrete. When observing a stage with adjacent cracks, the strain evolution of reinforcement CG1 showed a significant reduction in force transfer when less than two local undulations at the intersecting fibre strands were within the transfer length. This situation occurred frequently at the considered COT specimens, as the spacing between the initiated and the adjacent crack was below four times the yarn spacing. When considering a stabilised cracking stage, the limitation of the bond mechanisms to transfer force, resulted in reduced tension stiffening capability of the reinforced concrete member. These observations are, in general, also found in conventional steel reinforced concrete members. Thus, the *fib* Model Codes 2010 and 2020 consider this behaviour by introducing a differentiation for the contribution of tension stiffening depending on the cracking stage present (cf. Section 2.6.3). Consequently, a similar differentiation seems also legible for non-metallic reinforcements.

With these considerations in mind, the following evaluations focus on the quantification of tension stiffening. An approach to express tension stiffening effects is, for simplicity, the introduction of a factor, denoted in this thesis as β. The analytical description in Section 2.5.3 was employed to derive a calculation terminus in Equation 3-8 for the determination of β using a given reinforcement strain evolution.

Observations

In order to undertake an investigation into the quantification of the tension stiffening contribution to the crack opening, four specimens from the COT test series, which were equipped with fibre optical sensors, are considered. In each case, two specimens were reinforced with CG1 and GG and were subjected to either a purely static load or to additional ten load cycles. The tension stiffening factor β is determined for each measured step by the FOS and is provided in Figure 3.22. A value of β close to 1.0 suggests a larger contribution of tension stiffening, resulting in a lower value of the average reinforcement strain in comparison to a value of β close to zero. The assumption of $\beta = 0$ implies no contribution from tension stiffening and describes a constant value of reinforcement strain along the transfer length, i.e. the strain in the crack.

The evaluation in Figure 3.22 shows for both textile grids and at a single cracking stage an increase of β with increasing reinforcement strain. The β-value started at approximately 0.3 at small forces and approached 0.8 prior to the occurrence of an adjacent crack. At the occurrence of an adjacent crack, the contribution of tension stiffening is reduced. Considering both specimens with CG1, the values of β immediately dropped to 0.45 and 0.6, regardless of the loading scenario (Figure 3.22a2). In the case of the specimens with GG, the reduction of β was initially less pronounced as revealed in Figure 3.22b2. At large crack opening and close spacing between adjacent cracks, the value of β decreased. For specimen GG-3-static, the lowest value was found to be 0.35.

Focusing on the influence of cyclic load application on β, which is illustrated on the right-hand side of Figure 3.22, two observations are revealed. At first, regarding the value of the factor β at the superior load level, a decrease of β was observed for specimen CG1-3-cyclic, from 0.74 to 0.69, following ten load cycles (Figure 3.22a3). For the specimen GG-5-cyclic in Figure 3.22b3, the value of β remained constant. This finding aligns with the previous observation, which noted a change in the reinforcement strain and bond stress evolutions particularly for the specimens reinforced with CG1 (cf. Figure 3.20). At second, focusing the inferior load level, no changes in the

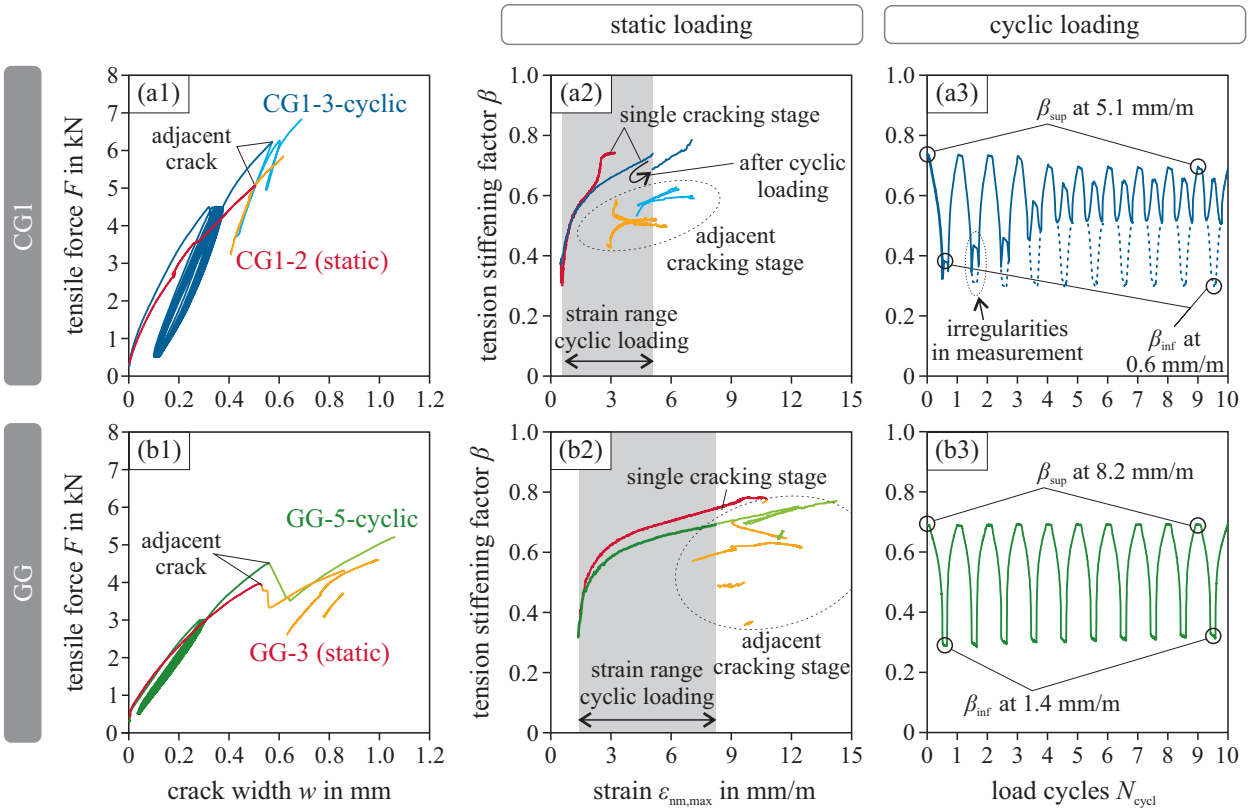


Figure 3.22: Influences of cracking stage and loading scenario on the tension stiffening factor β

value of β are observed for specimen GG-5 cyclic, while the plotted curve for specimen CG1-3-cyclic shows an irregularity in the fibre optical measurement. At inferior loading, the value of β did not decrease further, which would be expected with the assumed evolution visualised as a dashed curve in the diagram, but increases significantly. Therefore, the lowest value of β does not correspond to the inferior load level. With more load cycles applied, this discrepancy increased. The reason for this irregularity is revealed when going back to the reinforcement strain evolution provided in Figure 3.20. It becomes evident that changes in the evolution between the initial and tenth load cycle at the inferior load level occurred, identified as a shift from the local maximum of reinforcement strain from the crack initiation element away. This had a significant impact on the feasibility of determining the factor β at unloading through the utilisation of the proposed methodology, which is fixed to a sufficiently determined position of the local maximum of the strain evolution.

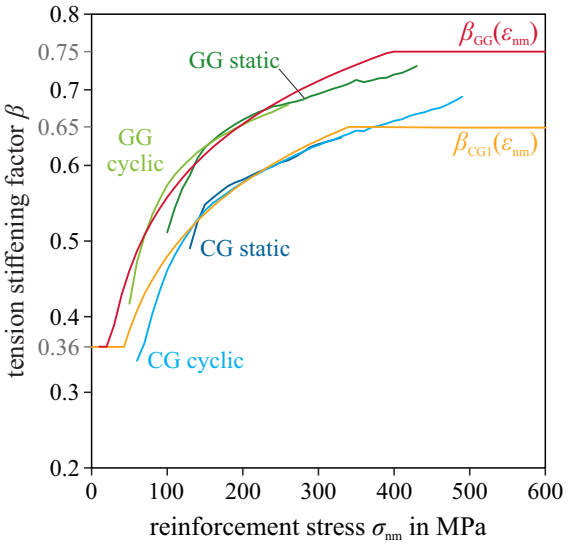
Generalisation and quantification

Aiming to provide a quantification of β based on average values derived from the COT test series equipped with fibre optic sensors, three cases are introduced. In the first case, a single cracking stage and a static loading scenario are considered and the value of β is determined based on the utilisation of the reinforcement strain in the crack. For a cyclic load application, a reduction of β is applicable. It is important to note that the considered data is only able to provide an evaluation based on a limited number of load cycles at specific superior and inferior load levels. Consequently, only a preliminary consideration is feasible at this stage, therefore no quantification is proposed. Further discussion is provided in Chapter 4, with a more detailed investigation into the influence of cyclic loading at serviceability levels. Thirdly, a constant value of β is provided for adjacent cracks. This constant value also refers to the stabilised cracking stage and considers the influence of the crack spacing. This is done by introducing a differentiation addressing the yarn spacing to account for the influence of the local undulations on the bond capacity of the textile grids.

The evaluations of all determined values of β in relation to the reinforcement stress in the crack during a single cracking stage were considered to determine averaged curves for both grids and the two loading scenarios. As illustrated in Figure 3.23, the curves demonstrate a logarithmic progression of β in response to increasing reinforcement stress, exhibiting small variations regarding the loading scenario. In addition, a shift in the curves is observed between the two different grids. This is attributed to the observation that GG showed a greater contribution of tension stiffening at equivalent reinforcement stress compared to CG1.

An analytical description was derived from these observations using the least-squares curve fitting approach to determine a value of β with regard to the reinforcement strain present in the single crack. A lower and an upper β-value were introduced for each grid. The upper value is constrained to 0.65 and 0.75, respectively, as the test data for the purely statically loaded specimens did not provide a sufficient data basis to justify significantly higher values. The lower value is 0.36 for both grids. Between these two limits, the increase of β is approximated using the reinforcement strain and a natural logarithm with the formulation provided in the table of Figure 3.23.

In the case of adjacent cracks, a differentiation is introduced. Crack spacing s_r that exceeds four times the yarn spacing enables at least two intersecting fibre strands to be within the transfer length. Consequently, the value of β is larger than compared to close adjacent cracks where β is reduced to 0.36 for both grids due to the significantly reduced bond capacity at short transfer lengths. However, as a differentiation of β according to the presumed crack spacing is practically not feasible and at least with transition to the stabilised cracking the distances between adjacent cracks is assumed to be below four times the yarn spacing. Therefore, the conservative assumption of $\beta = 0.36$ is followed in the case of an adjacent/stabilised cracking stage.



textile grid	β
	single crack
CG1-0° GG-0°	$0.36 \leq 0.14 \cdot (\ln(\varepsilon_{nm}) + 10.5) \leq 0.65$ $0.36 \leq 0.14 \cdot (\ln(\varepsilon_{nm}) + 9.9) \leq 0.75$
	adjacent cracks with $s_r \geq 4 \cdot y_{nm}$
CG1-0° GG-0°	0.54 0.49
	adjacent cracks with $s_r < 4 \cdot y_{nm}$
CG1-0° GG-0°	0.36

Figure 3.23: Representation of averaged value curve of β (diagram) and derived values of β for different cracking stages (table)

The reinforcement strain dependent formulation of the tension stiffening factor β for a single crack given in Figure 3.23 is briefly evaluated regarding its actual improvement in terms of crack width prediction. This is done by comparing the strain-dependent formulation with the assumption of a constant value of β, which is set to the upper limit given in Figure 3.23 for a single cracking stage: for CG1 $\beta = 0.65$ and for GG $\beta = 0.75$. The evaluation is provided in Figure 3.24. In addition, the envelope obtained from all test series with an NSC, including specimens with and without FOS, is plotted.

As apparent from Figure 3.24, the difference between the two considerations of β in the given limitations is marginal. The strain-dependent formulation provides for a reinforcement stress value being at most 32 MPa lower in the case of CG1 and 25 MPa lower for GG when compared to the assumption of a constant value. More progressive values are obtained for the strain-dependent formulation solely when the upper limit is exceeded. When considering the envelope of the series

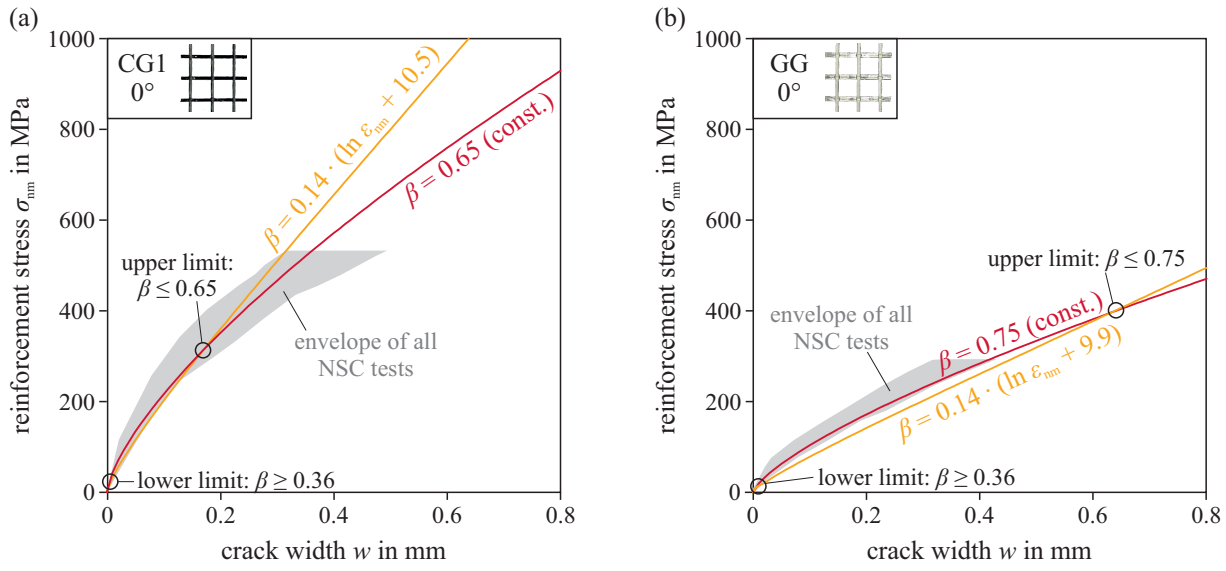


Figure 3.24: Comparison on crack width prediction when using either a reinforcement strain-dependent formulation or a constant assumption for the factor β

with NSC, it becomes evident that the assumption of a constant value of β yields more satisfactory results compared to the proposed strain-dependent formulation. In the case of series with CG1 (Figure 3.24a), the stress-crack width curve determined using a constant value for $\beta = 0.65$ is at the lower boundary of the envelope for crack widths below 0.17 mm. At larger crack widths, the curve represents approximately the average value of the envelope. For the specimens with GG evaluated in Figure 3.24b, the constant value of $\beta = 0.75$ is consistently at the lower boundary of the envelope. Consequently, the implementation of a strain-dependent determination of β does not contribute to the improvement of a crack width prediction approach. Thus, in the case of single cracking, the assumption of a constant value for the tension stiffening factor β referring to the upper limit of 0.65 for CG1 and 0.75 for GG is sufficiently accurate.

3.6 Summary

A variety of experimental test setups are available for the purpose of characterising the bond behaviour of reinforcements. In the case of non-metallic textile grids, two setups were employed, namely the single-sided pull-out test type C (SPOc) and the introduced crack opening tensile (COT) test. The experimental campaign, which consisted of SPOc and COT tests, focused on various parameters to characterise the bond behaviour of five different textile grids.
The SPOc test configuration is a valuable experimental method for addressing the characterisation of the anchorage behaviour of textile grids, which is its primary focus. However, in the case of evaluating bond characteristics to be used in design approaches at the serviceability stage where the full utilisation of the reinforcement is not to be expected, only a rudimentary determination of robust values is possible, in particular, due to the large scattering of the individual test data. Therefore, the presented experimental campaign focused on the qualitatively based characterisation obtained by the SPOc test series.
Embedded lengths equivalent to the yarn spacing showed a significant reduction in the transferred force at identical slip when compared to specimens with an embedded length of at least three times the yarn spacing. This is of particular interest in cases where the distance between adjacent cracks is approximately twice the yarn spacing. In such cases, it is not expected that a significant force transfer will occur.
Furthermore, for the investigated grids, in particular CG1, a significant force transfer at low reinforcement utilisation was attributed to the local undulations, where two fibre strands intersect. This was identified by conducting tests where the transverse fibre strands and the corresponding undulations were removed prior to testing, showing that less force transfer was possible at identical values of slip compared to specimens with a fully intact fibre strand.
The use of high-strength concrete did not result in an increased load transfer at identical slip. Using a concrete mixture with a maximum aggregate size of 16 mm revealed no positive or negative impact on the bond capacity. However, the limited scope of the series does not allow for a general conclusion.

For an explicit consideration of the crack opening attributed to the serviceability stage, the newly introduced COT tests proved to be highly feasible. This test setup enables a robust and quantitatively based evaluation of the bond capacity. The implementation of FOS on the fibre strands facilitated a more profound investigation into the bond behaviour.
Hereby, the observation that the use of a higher strength concrete did not implicitly improve the bond capacity was underlined. This phenomenon was primarily attributed to the reduced transverse stiffness of the textile grids, when mechanical interlocking significantly contributed to the force transfer.

The application of ten cycles at a loading representing the crack opening at the serviceability stage revealed a significant increase in the opening. Consequently, it is essential to consider the impact of a cyclic loading phase, analogous to a practical scenario, on the increase of crack widths and to integrate this consideration into the development of design approaches.
Transfer lengths being below twice the yarn spacing combined with higher reinforcement utilisation resulted in a significant reduction in force transfer, particularly for grids showing a substantial contribution of local undulations to the bond capacity of the reinforcement.
This behaviour also had consequences for the contribution of tension stiffening. A low force transfer results in almost no tension stiffening, which then does not provide for a reduced opening of the cracks. Utilising FOS, it was possible to quantify the contribution of tension stiffening and derive values for the tension stiffening factor, which require validation (see Chapter 5).

The characterisation of the bond behaviour of textile grids provides the basis for the ongoing experimental evaluation of the crack width development in Chapter 4, followed by the derivation of physically based approaches to determine an analytical formulation of the bond stress-slip relation and to obtain a crack width prediction model in Chapter 5.

4 Progressive cracking in the case of uniaxial tension

4.1 Overview and concept of the experimental series

Having characterised the bond behaviour of a single non-metallic reinforcement fibre strand in a concrete matrix, this chapter addresses the crack opening in dependency on the progressive occurrence of cracks in a uniaxial tensile strain state. Furthermore, the consideration of the influence of multiple reinforcement layers and the crack width increase due to cyclic loading is addressed. The present chapter provides an experimental basis for the validation of the methodology proposed in Chapter 5, where an approach to predict the crack width in the case of single cracking and adjacent cracking is derived.

The objective of the experimental campaign was to determine the strain evolution of the composite materials, the bond behaviour, and the crack development under static and cyclic loading. A total of 34 uniaxial tensile (UT) tests were conducted on concrete members reinforced with textile grids CG1, CG2, CG3 and GG. The principal test series focused on a single layer of reinforcement and a normal-strength concrete (see Section 4.2). Multiple reinforcement layers with different spacing between the grids were considered for reinforcement CG1 in Section 4.3. In addition, the experimental campaign is extended to cover influences from using a high-strength concrete (Section 4.4.1) and having a normal-strength concrete with a maximum aggregate size of 16 mm (Section 4.4.2). Besides the latter series with the maximum aggregate size of 16 mm, cyclic loading was addressed in all other cases. The cyclic regime is intended to represent the long-term behaviour of the serviceability limit state. The number of applied load cycles was set at 200,000, equivalent to about five load scenarios per day over 100 years of service life. This procedure allows for a representation of an increase in crack width due to the continuous loading and unloading of variable forces. The main measurement techniques employed were the utilisation of distributed fibre optic sensors (FOS), which were applied on the fibre strands to obtain the reinforcement strain evolution and to derive the bond stress and contribution of tension stiffening, and digital image correlation (DIC) to determine the crack width on the concrete surface.

4.2 Principal campaign to investigate progressive cracking

4.2.1 Experimental setup

The principal campaign focused on the influence of cracking stages and cyclic loading in the case of a single reinforcement layer. The test setup and specimen geometry were unified, a normal-strength concrete (NSC) with a maximum aggregate size of 5.6 mm was used, and the chosen carbon grids CG1, CG2 and CG3 and the glass grid GG were investigated in warp direction. The test setup is shown on the left-hand side in Figure 4.1 and the test specifications are provided in Table 4.1. The width of the specimens of 190 mm allowed the placement of five fibre strands of CG1 with a reinforcement ratio $\rho = 0.66\%$ and of GG with $\rho = 0.90\%$, four strands of CG2 with $\rho = 0.44\%$, or seven and eight strands of CG3 and $\rho = 0.41\%$ and $\rho = 0.46\%$, respectively. The thickness of 30 mm resulted in a concrete cover of 13.5 mm on each side for specimens reinforced with CG1, CG2, and GG, or a cover of 14 mm when using reinforcement CG3. A saw-cut for each reinforcement is shown on the right-hand side of Figure 4.1. The total length of the specimens was 1200 mm with a clamping length of 250 mm on each side, providing for an investigation length of 700 mm. Clamping was achieved mechanically by applying a torque of 800 Nm to the steel

bolts, resulting in a transverse compression on the specimen of approximately 14 MPa, so that no slippage of the anchorage occurred during the test.
The test procedure consisted of three phases. The first phase, denoted "s", consisted of applying static deformation until a single crack occurred within the investigation length where the fibre optic sensors were located. A possible crack occurrence in the clamping area was neglected. In the case of cyclic loading, referred to as phase "c", no further deformation was applied. The superior load level F_{sup} was set equally to either 12 kN for specimens with CG1 and CG2 or 10.3 kN for specimens reinforced with CG3 and GG, representing a load level at which single cracks were present. The chosen superior level resulted in the occurrence of concrete tensile fatigue with additional crack formation during the cyclic loading phase as the uncracked concrete was subjected to a tensile stress utilisation of approximately 0.6 to 0.7 times the average tensile strength determined in material tests, which is close or at the 5% fractile of the concrete tensile strength according to [EC2]. The inferior load level should allow for a reinforcement strain close to zero, for testing purposes it was set to $F_{inf} = 2$ kN. The 200,000 load cycles were applied at an amplitude of 5 kN (CG1 and CG2) or 4.15 kN (CG3 and GG) at a frequency of 2.0 Hz. The oscillation is approximately 40 to 60% of the mean concrete tensile strength. After the cyclic loading regime, deformation was applied again in phase "f". The principal campaign included 16 tests in four series. The series on CG1 and CG2 contained two purely statically loaded and three cyclic tests, while the series with CG3 and GG included one purely static and two cyclic tests.

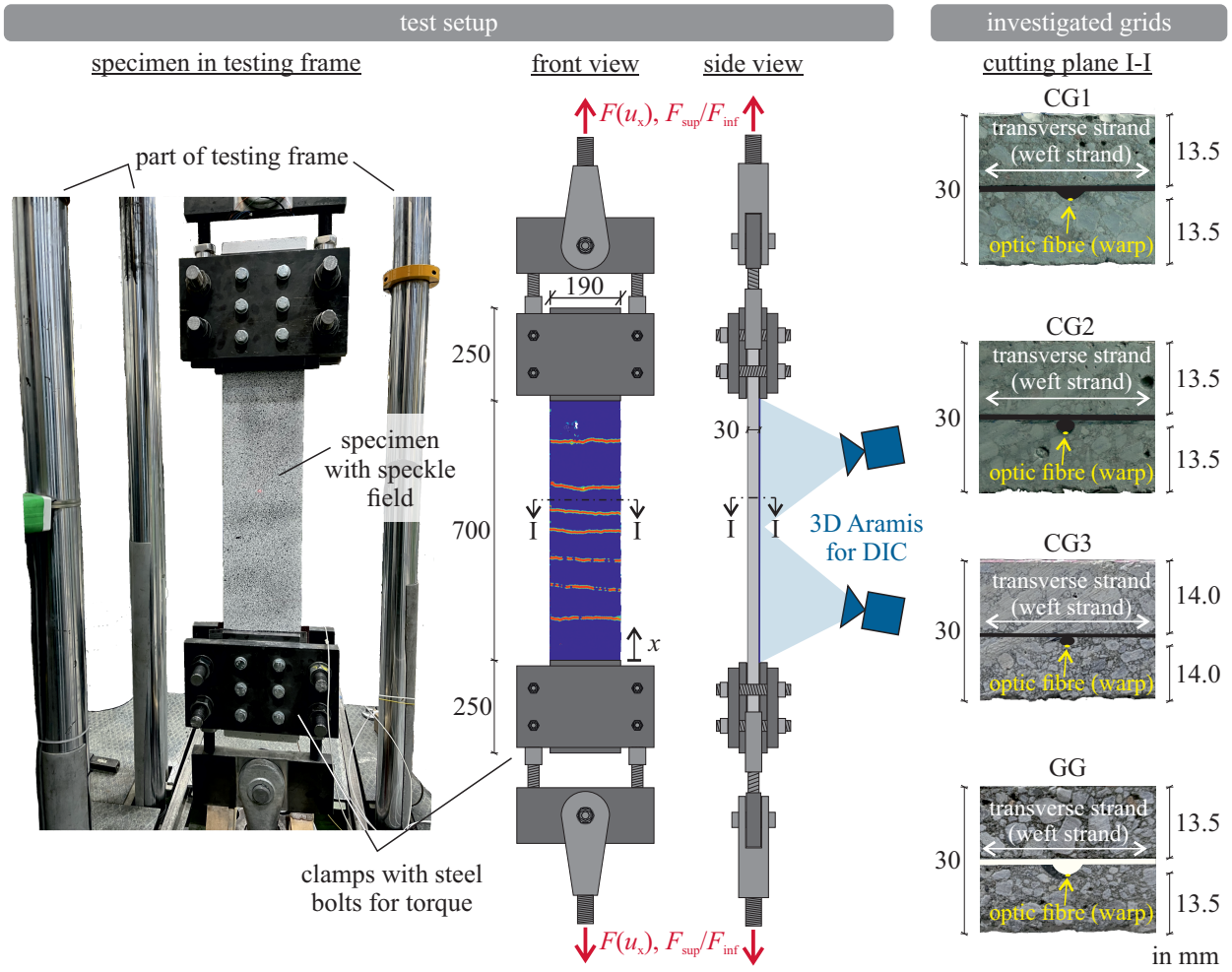


Figure 4.1: Setup of uniaxial tensile tests on textile grids for the principal campaign (adapted from [Sch25b])

Table 4.1: Specifications of the uniaxial tensile tests of the principal campaign with NSC

identifier	number of tests	ρ [%]	f_{ctm} [MPa][1)]	$\sigma_{nm,sup}$ [MPa]	$\sigma_{c,sup}$ [MPa]	$\sigma_{nm,inf}$ [MPa]
CG1-static	2	0.66	3.1 – 3.2	320	-	53
CG1-cyclic	3		3.1 – 3.3		$2.1 \approx 0.66\ f_{ctm}$	
CG2-static	2	0.44	3.3	476	-	79
CG2-cyclic	3		3.4		$2.1 = 0.62\ f_{ctm}$	
CG3-static	1	0.41 – 0.46	3.0	390 – 445	-	76 – 87
CG3-cyclic	2				$1.8 = 0.61\ f_{ctm}$	
GG-static	1	0.9	3.0	201	-	39
GG-cyclic	2				$1.8 = 0.61\ f_{ctm}$	

[1)] obtained from splitting test: $f_{ctm} = 0.9 \cdot f_{ct,sp}$ acc. to [EC2]

4.2.2 General behaviour

Starting with investigating the elongation in longitudinal direction ε_m, defined as relative displacement in the free length, large differences in the bond behaviour of the considered grids are revealed. The elongation was determined using DIC, with the speckle field applied on the surface of the specimens. As shown in Figure 4.2, which presents the outcomes for specimens reinforced with carbon grids, the crack formation stage governed at varying levels of reinforcement utilisation, magnitude of force reduction due to crack occurrence, number of cracks, and specimen elongation. During this stage, in general, a better bond capacity and increased force transfer resulted in more cracks accompanied with smaller crack opening. This provided for less force reduction upon the occurrence of a new crack. A similar behaviour is attributed to increased reinforcement ratios, which was not the case here. In addition, distinct Young's moduli of the grids resulted in insignificant differences regarding the crack opening due to elongation of the fibre strand in the cracks. Therefore, it is obvious that the reinforcement CG1 provided for the highest bond capacity of all three investigated carbon textile grids. On the contrary, this resulted in a pronounced stabilised crack stage until fibre rupture was reached, in which only continuously increasing crack opening was detected. An influence of the transverse fibre strands on provoking cracking localised at a transverse strand due to the reduction of the concrete area is, in general, possible. However, in the tests conducted in the principal campaign, no such influence was detected by comparing the crack spacing in specimens with CG1 (yarn spacing of 38 mm) and CG3 (yarn spacing of 25 mm). A more detailed analysis is provided in the following sections.

Regarding the influence of the cyclic load application at a serviceability state, the reduction of the bond capacity is visible by the increasing elongation during the cycles, as shown in the diagrams on the right-hand side of Figure 4.2. In the case of single cracks, the load cycles led to increasing transfer lengths as less force was transferred in an infinitesimal bond length, which resulted in increased crack opening. For adjacent cracks, the transfer length was fixed in length and a reduction in the bond capacity led to a reduced transfer of force in the concrete. The effect of tension stiffening is reduced and an extended opening of the cracks occurred.
For all specimens, the cyclic loading was applied at a stage with at least one crack present that was not influenced by an existing crack and was localised inside the investigation area of the fibre optic sensors. While in some specimens these two requirements were met with the initial crack occurring inside the investigation length, for example in CG3-cyclic-1 and -2 (Figure 4.2c2), in

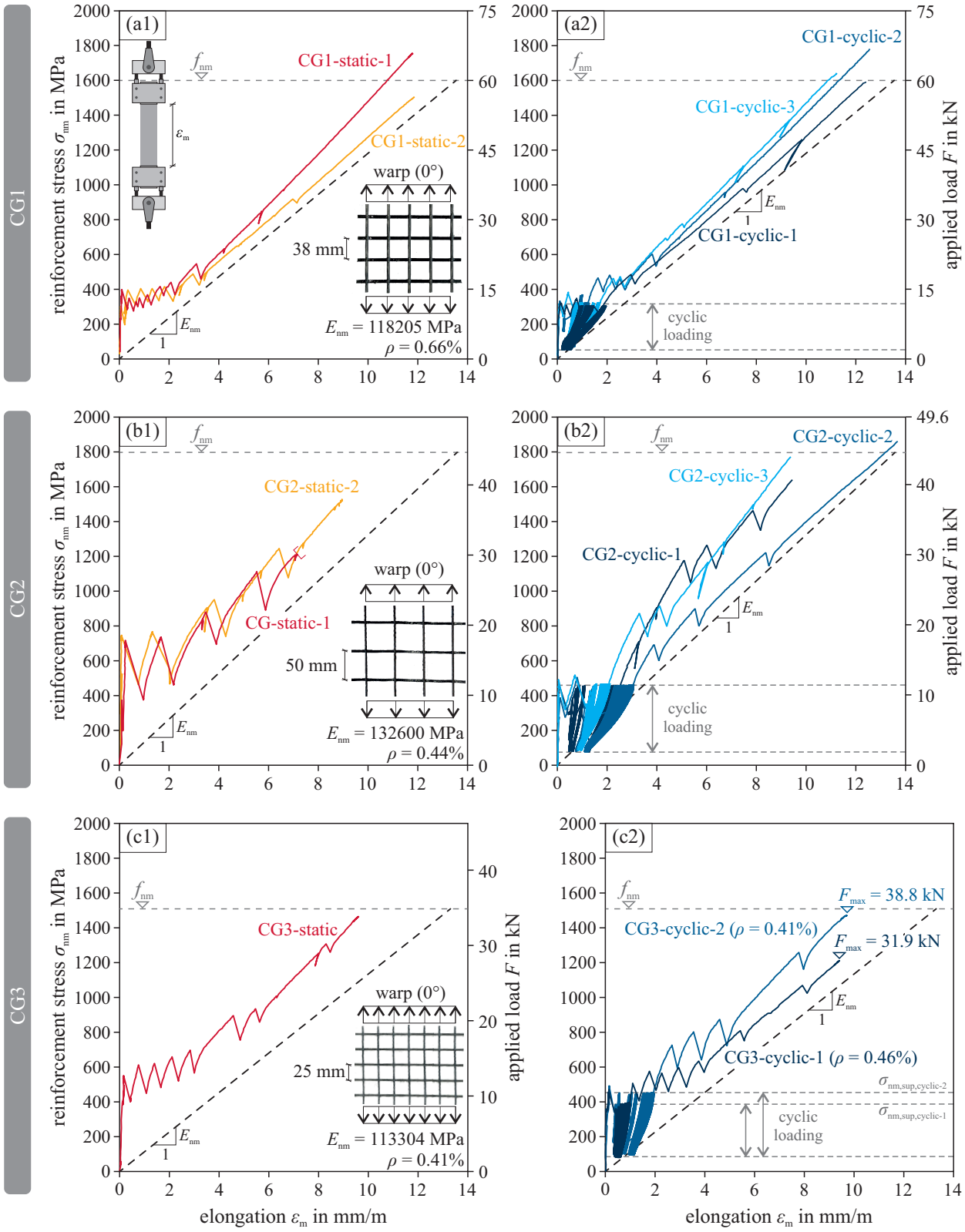


Figure 4.2: Elongation related to reinforcement stress and tensile force in the UT tests of specimens with carbon grids and normal-strength concrete

other specimens, at most three cracks were allowed to occur in the specimens at the beginning of the load cycles (e.g. CG1-cyclic-1, Figure 4.2a2). The high utilisation of the concrete under tension resulted in concrete tensile fatigue, which provoked additional crack formation during the cyclic loading phase. For example, investigations reported in [Cor84] showed concrete cracking after 1000 cycles under similar loading conditions.

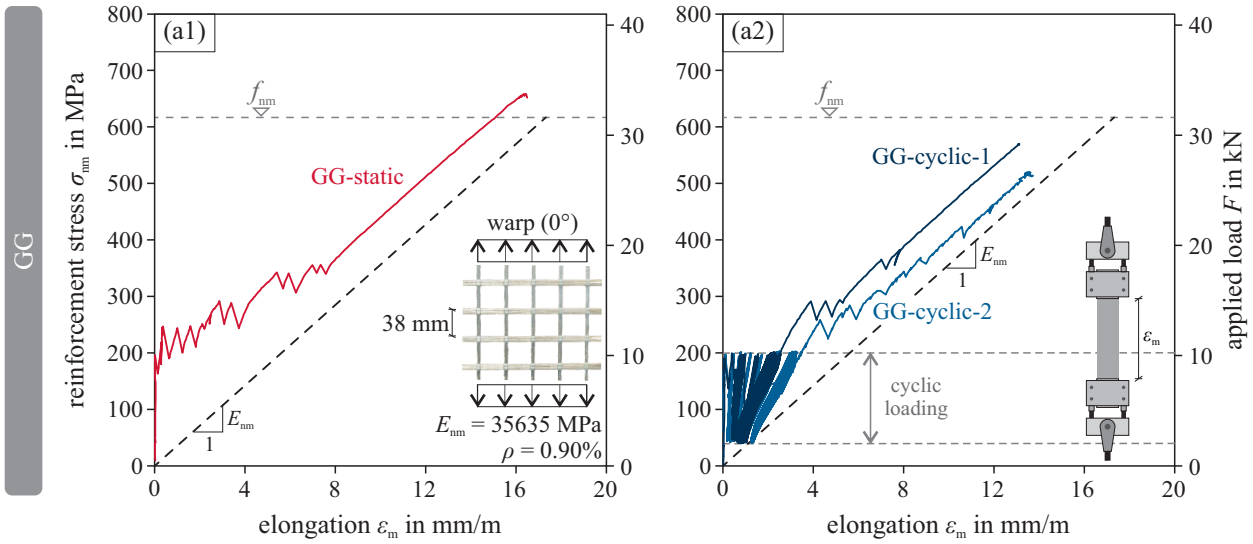


Figure 4.3: Elongation related to reinforcement stress and tensile force in the UT tests of specimens with GG and normal-strength concrete

While the reduction of the force transfer capacity of the new cracks was also subject to a reduced bond interface, a larger increase in elongation compared to specimens with no new crack formation was not revealed in general, as shown in Figure 4.2a2, for example, for specimens CG1-cyclic-2 (no new cracks during cyclic loading) and CG1-cyclic-3 (two additional cracks). The detailed analysis of the crack opening during cyclic loading is addressed in Section 4.2.3.

While a crack opening expressed by the increase of elongation of the cyclically loaded specimens was clearly revealed, the final loading phase showed a similar behaviour compared to the purely statically loaded specimens. Crack formation occurred at identical load levels and the elongation was comparable without an increase attributed to the previously performed cyclic loading. In conclusion, the application of a cyclic load at a serviceability state resulted in a substantial increase in crack opening and the formation of additional cracks in the case of concrete tensile fatigue. The increased loading that occurred subsequent to the cyclic phase did not result in a different crack formation, as defined by the number of cracks and the load level at which they occurred. A difference between the purely statically loaded specimens and the specimens under cyclic loading is, however, notable with regard to the reinforcement stress at failure. For reinforcements CG1 (Figure 4.2a) and CG3 (Figure 4.2c), no difference in the failure loads was observed. In the case of reinforcement CG2, the cyclic load application led to an increased reinforcement stress prior to yarn rupture compared to the static loaded specimens (Figure 4.2b). As the test of the specimen CG2-static-1 had to be terminated at approximately 30 kN due to a malfunction in the hydraulic loading, the actual load capacity of this specimen was not determined. This leaves the maximum reinforcement stress of 1526 MPa of specimen CG2-static-1 as sole reference, marking a decline of approximately 230 MPa below the average failure stress observed in the three cyclically loaded specimens, which is about 13% of the uniaxial tensile strength of the fibre strand. Consequently, the possibility of a positive effect of cyclic loading on the tensile strength of reinforcement CG2, which is referred to as *training effect* and was reported for example in [Spe19, Gha22], is revealed.

The observations described in the previous paragraphs are identically stated for the three specimens reinforced with the glass grid (GG), with the evaluation of the reinforcement stress in relation to the elongation plotted in Figure 4.3. The glass grid has the largest bond surface of all four investigated grids, while the Young's modulus is about 3.5 times and the tensile strength 2.5 times lower compared to the carbon grids. This resulted in a crack formation stage which extended

until approximately 360 MPa (= 50% of reinforcement utilisation) and half of the elongation until failure. Under a purely qualitative comparison, the stress-elongation behaviour of the specimens with GG is similar to that of the specimens with CG3, despite the occurrence of two more cracks on average. On the other hand, the maximum load reached at the static loaded specimen GG-static was more than 90 MPa higher compared to the two cyclically loaded specimens, which failed approximately 15% below the tensile strength of the fibre strand. A training effect was not observed for reinforcement GG.

4.2.3 Evolution of crack widths on concrete surface

The evaluation of the DIC measurements also allows for the determination of the individual crack opening, which is used to obtain the average crack width w_{m} and the maximum crack width w_{max} in relation to the reinforcement stress. The resulting curves are plotted for each specimen in Figures 4.4 and 4.5. In addition, the crack patterns obtained by the DIC image prior to failure, including the order of crack appearance, is provided in the figures.

Series CG1

Focusing first on the evaluation of the five specimens reinforced with CG1, which are shown on the upper half of Figure 4.4, the initial crack in the investigation length occurred at a tensile force between 11.30 kN and 13.24 kN, which is equal to a tensile concrete stress of 2.0 MPa and 2.3 MPa, respectively. This was approximately two-thirds of the mean concrete tensile strength. The initial crack occurrence resulted in a reduction of the applied force due to the deformation-controlled testing, with an initial crack width of 0.13 mm on average at a reinforcement stress of 240 MPa. With regard to the purely statically loaded specimens, most cracks occurred below an average crack width $w_{\mathrm{m}} = 0.4$ mm and reinforcement stress of 575 MPa, which is about 36% of the tensile strength of a single fibre strand. In specimen CG1-static-2 the last crack, denoted ⑦, occurred at a significantly higher loading with $\sigma_{\mathrm{nm}} = 896$ MPa. As already indicated by the stress-elongation relation in the previous section, the influence of the cyclic loading is significant on crack opening. With the occurrence of cracks after cyclic loading, the average crack width reduced, resulting in no observable difference between purely statically and cyclically loaded specimens. In all three tests subject to cyclic loading, the stabilised cracking stage was reached after the load cycles. At stabilised cracking, between six and nine cracks were present with an average crack spacing $s_{\mathrm{rm}} = 80$ mm, which is about 2.1 times the yarn spacing. The relation between average and maximum crack spacing was 0.72 mm on average. At failure, the maximum crack width of the cyclically loaded specimens was slightly larger compared to the static loaded ones. Also, the relation between the average crack width and maximum width was 0.79 at failure, which is slightly higher compared to 0.73 at the beginning of the stabilised cracking stage.

The previous investigations of the reinforcement CG1 led to the assumption that at stabilised cracking, almost no force is transferred to the uncracked concrete. Therefore, tension stiffening is negligible. This seems also applicable at crack formation when a small spacing between adjacent cracks was present, providing for a transfer length of approximately the yarn spacing, which was identified already by the single-sided pull-out tests in Section 3.3. There, small embedded lengths resulted in a significantly reduced bond capacity. Consequently, a simplified approach to determine the average crack width at stabilised crack is introduced

$$w_{\mathrm{m,calc}} = s_{\mathrm{rm}} \cdot \frac{\sigma_{\mathrm{nm}}}{E_{\mathrm{nm}}}, \tag{4-1}$$

indicating that along the provided transfer length, which is assumed to be the determined average value of crack spacing, the reinforcement strain is constant. Compared to the test data for CG1

in Figure 4.4 with the value for s_{rm} set individually for each test, the black coloured dashed line visualises the application of Equation 4-1 on the test data. The simplified approach shows a very good representation of the actual test results. This is also the case when addressing the crack width at initial crack occurrence.
The assumption that this approach is also applicable when addressing the maximum crack width by utilising the maximum crack spacing at the stabilised cracking stage was not verified by the tests. The widths predicted were significantly larger, as the increased contribution of tension stiffening provided by the larger crack spacing and therefore transfer lengths was not considered.

Series CG2
The lower bond capacity of grid CG2 compared to the other textile reinforcements was already pointed out in the previous consideration of the reinforcement stress-elongation curves. The five specimens with CG2 showed the largest average and maximum crack widths of all four test series, accompanied by the lowest number of cracks occurring and, consequently, also the largest crack spacings. This is confirmed by the graphical evaluations given in the upper half of Figure 4.5. As the concrete strength in the two statically loaded specimens was higher in comparison to all other specimens in the series, the initial crack occurred at a concrete tensile stress of 3.2 MPa on average, with a width of 0.48 mm. In the three cyclically loaded specimens, the initial crack occurred at a concrete stress between 1.7 and 2.2 MPa with a width of 0.17 to 0.25 mm. However, the low bond capacity of this reinforcement resulted in an average crack width of 0.4 mm reached either after only approximately 80 load cycles (CG2-cyclic-1) or prior to the onset of the cyclic loading phase, when the load was increased to reach the superior load level of 12 kN (CG2-cyclic-3).
During cyclic loading, at most one more crack occurred as observed for specimens CG2-cyclic-1 and CG2-cyclic-2. Addressing all five specimens in the following, stabilised cracking was reached between 794 MPa and 1346 MPa, with four to six cracks being present when neglecting the cracks occurring in the vicinity of the clamping. The average crack width was 0.92 mm with an average crack spacing between 110 mm (2.2 times yarn spacing) and 150 mm (3 times yarn spacing). The ratio between average and maximum crack spacing was 0.84 on average.
The simplified approach in Equation 4-1 provided for a very well fit of the average crack width solely at the time when the last crack occurred, which marks the transition to stabilised cracking. This was in particular the case for the cyclically loaded specimens as the significant influence of the cyclic phase on crack opening was not adequately represented.

Series CG3
With regard to the tests with reinforcement CG3, where two different reinforcement ratios were chosen for the two cyclically loaded specimens, the plotted reinforcement stress-crack width curves on the bottom side of Figure 4.4 allow for the following observations: in the case of the statically loaded specimen, the initial crack occurred at a concrete stress of 2.2 MPa and opened up to 0.19 mm at a reinforcement utilisation of 401 MPa, corresponding to 27% of the reinforcement tensile strength. For both cyclically loaded specimens, the initial crack occurred at slightly lower concrete stress values of 2.1 MPa for specimen CG3-cyclic-1 and 2.0 MPa for CG3-cyclic-2, respectively. Despite specimen CG3-cyclic-1 having an increased reinforcement ratio of 0.46%, as eight fibre strands were placed, the reinforcement stress at initial cracking was approximately equivalent to that of CG3-cyclic-2, which had a reinforcement ratio of 0.41% as seven fibre strands were placed. The slightly larger initial crack width of specimen CG3-cyclic-1 with 0.18 mm compared to a width of 0.15 mm of specimen CG3-cyclic-2 is attributed to the approximately 0.7 kN higher force released upon cracking.
The larger cracking force in specimen CG3-cyclic-1 indicates that the concrete tensile strength was higher than in specimen CG3-cyclic-2, which also explains the lack of additional crack occurrence

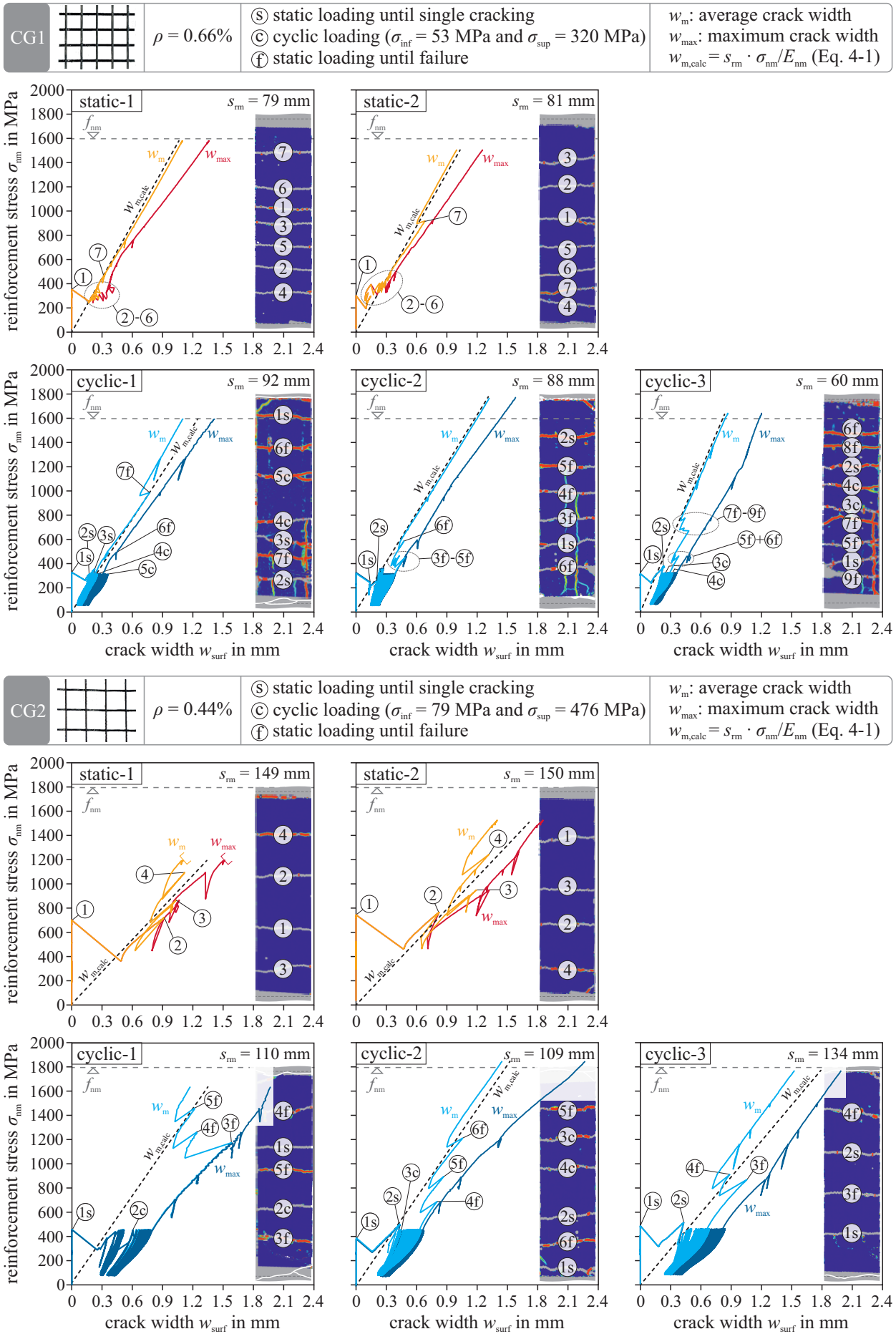


Figure 4.4: Average and maximum crack width evolution related to the reinforcement stress in the UT tests of specimens with CG1 and CG2 and normal-strength concrete

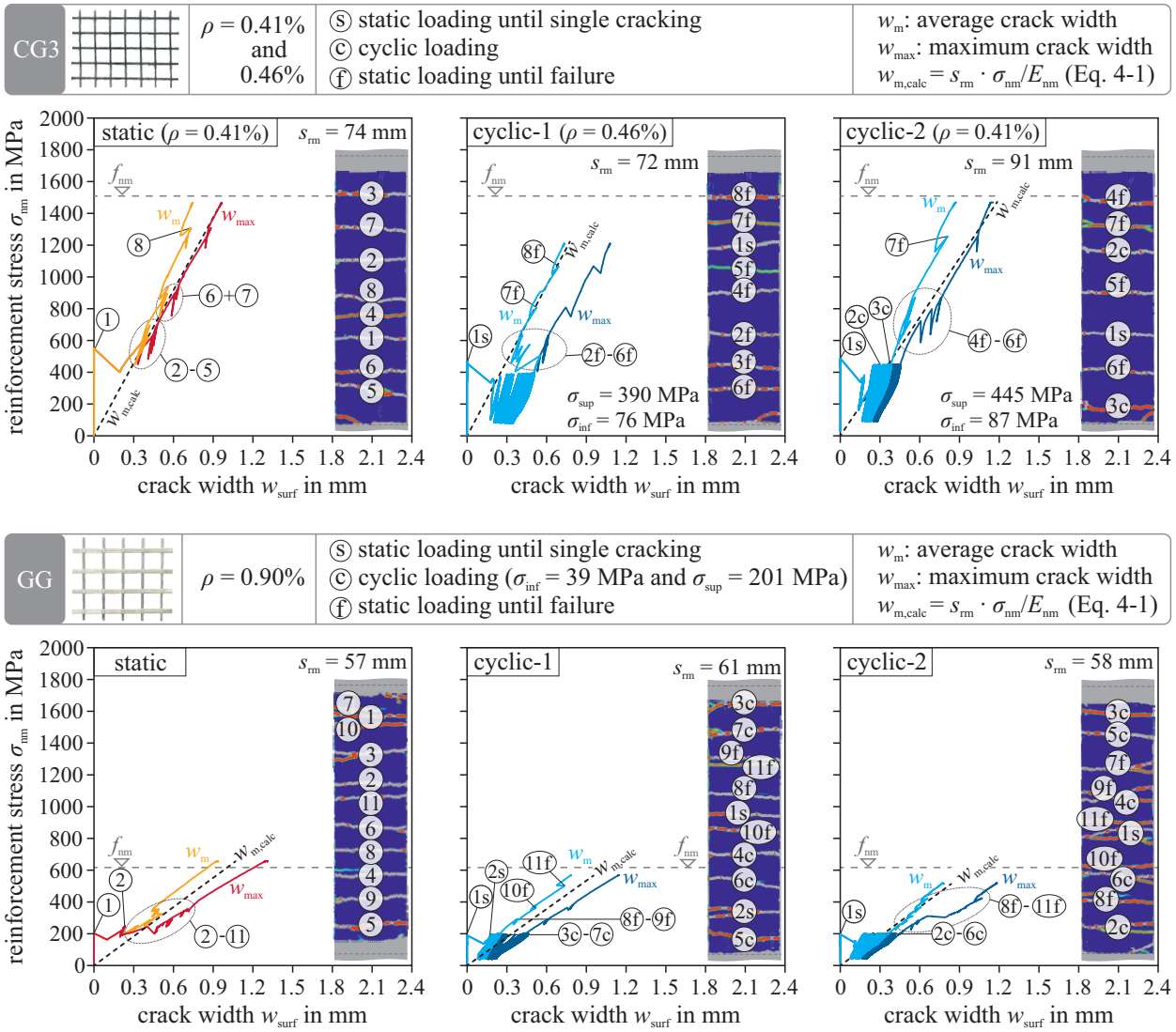


Figure 4.5: Average and maximum crack width evolution related to the reinforcement stress in the UT tests of specimens with CG3 and GG and normal-strength concrete

during cyclic loading due to concrete tensile fatigue as observed in the series with reinforcement CG1. The lack of additional cracking in specimen CG3-cyclic-1 resulted in a significant increase in the crack opening of the initial crack (1s). For example, a crack width of 0.4 mm was already reached after 8000 load cycles. In the contrary, in specimen CG3-cyclic-2 two new cracks formed during cyclic loading and the average crack width did not exceed 0.4 mm during this phase.

Stabilised cracking was observed at 1210 MPa on average for specimens CG3-static and CG3-cyclic-2 with $\rho = 0.41\%$ and an average value of crack width of 0.66 mm for the statically loaded specimen and 0.05 mm larger for the cyclically loaded one. The increased reinforcement ratio of specimen CG3-cyclic-1 led to a lower average crack width at the beginning of stabilised cracking of 0.47 mm at a reinforcement stress of 749 MPa. At a comparable stress of 1210 MPa, which was the failure stress of this specimen, the average width was determined to be 0.73 mm, which is slightly larger compared to the two other specimens and attributed to the larger increase in width during the cyclic phase.

When considering all three specimens of series CG3, the relation between average crack width and maximum crack width at the stabilised cracking stage was 0.7 and at failure 0.73. The absolute values of the average and maximum crack width are lower compared to the tests with CG1. In the case of specimens CG3-static and CG3-cyclic-1, eight cracks were observed with an average crack spacing of 73 mm, which is 2.9 times the yarn spacing. In test CG3-cyclic-2 only seven cracks

occurred, the average spacing was 91 mm, which is equal to 3.6 times the yarn spacing.
Using the simplified approach expressed by Equation 4-1, the average crack width of specimen CG3-cyclic-1 is predicted very accurately. For the other cyclically loaded specimen CG3-cyclic-2, the approach does not fit the average width but the maximum crack width. This contrary observation is assumed to result from the different contribution of tension stiffening in the tests, while the simplified approach neglects tension stiffening. In the case of specimen CG3-cyclic-2, the lower reinforcement ratio and the larger crack spacing allowed for more pronounced force transfer and therefore contribution of tension stiffening, which cannot be represented accurately by the simplified approach. For the purely statically loaded specimen, the approach provides a good fit for the average and maximum crack width until crack ⑦ occurred, as the two curves are close.

Series GG
At last, the specimens reinforced with GG are considered. The reinforcement ratio of 0.90% accompanied by a good bond capacity, led to the largest number of cracks of all series, with eleven per specimen. Initial cracking occurred at a concrete tensile stress between 1.7 and 1.8 MPa, leading to a crack width of 0.10 to 0.13 mm. During cyclic loading, six new cracks formed in each of the two specimens. Stabilised cracking was reached at different reinforcement utilisations, reaching from 340 MPa, which is 55% of the reinforcement tensile strength in the case of specimen GG-static, to 505 MPa for specimen GG-cyclic-1, corresponding to 82% of the tensile strength. The average crack spacing of 59 mm equals 1.6 times the yarn spacing. The ratio between average and maximum spacing was 0.71 on average, which is comparable to reinforcements CG1 and CG3. The fine crack pattern allowed for an assumption similar to the specimens with CG1 that almost no tension stiffening was present and the simplified approach in Equation 4-1 would provide for a good fit. Nevertheless, this is not the case for reinforcement GG, as shown on the bottom half of Figure 4.5. The simplified approach overestimates the actual average crack width. Apparently, tension stiffening provided a considerable contribution to crack width reduction. This required a good bond capacity for close adjacent cracks with a distance of less than twice the yarn spacing.

Detailed focus on cyclic loading
The previous discussion revealed that the increase in crack width during the cyclic loading phase highly depends on the occurrence of cracks during this phase. To provide for some additional insight, the average crack width at inferior and superior loading and the maximum crack width during the 200,000 load cycles were evaluated and plotted in Figure 4.6 for all four test series.
In general, when one or two cracks were present or occurred during the cyclic loading phase, significant crack opening of at least 0.1 mm was detected at the superior load level, as in CG1-cyclic-2, all specimens reinforced with CG2, and CG3-cyclic-1. The crack opening at superior loading continuously increased until about 100,000 cycles, after which only small increases were revealed. Conversely, the crack width increase was most pronounced during the first 10,000 cycles when at least three cracks were present. After the initial 10,000 load cycles, the cracks opened slightly further. The maximum crack width increase was at most 0.05 mm at the superior load level. When more than four cracks occurred, the crack width at the superior load level remained almost constant, as for CG1-cyclic-1, CG1-cyclic-3, and the specimens with GG.
Considering the average crack width at the inferior load level $w_{m,inf}$ at a load of 2 kN, the opening remained almost constant after the application of 500 cycles. Small changes in value only occurred due to additional crack formation. The only exceptions were specimen CG2-cyclic-1, where the width increased about 0.1 mm until the second crack appeared at about 10,000 cycles, and specimen CG3-cyclic-1, with a continuous increase in average crack width at inferior loading by about 0.15 mm in total. Both exceptions were attributed to the fact that only one crack was present.

Overall, the occurrence of new cracks during cyclic loading resulted in an instant decrease in average crack width. With the following cycles, the average crack width returned to the value prior to the crack occurrence. As a result, the overall opening of cracks during cyclic loading at a serviceability level remained only small in the cases where a sufficient number of cracks was present or additional cracks occurred during the cyclic loading. When this was not the case, cyclic loading increased the crack width by a considerable value even when the utilisation of the

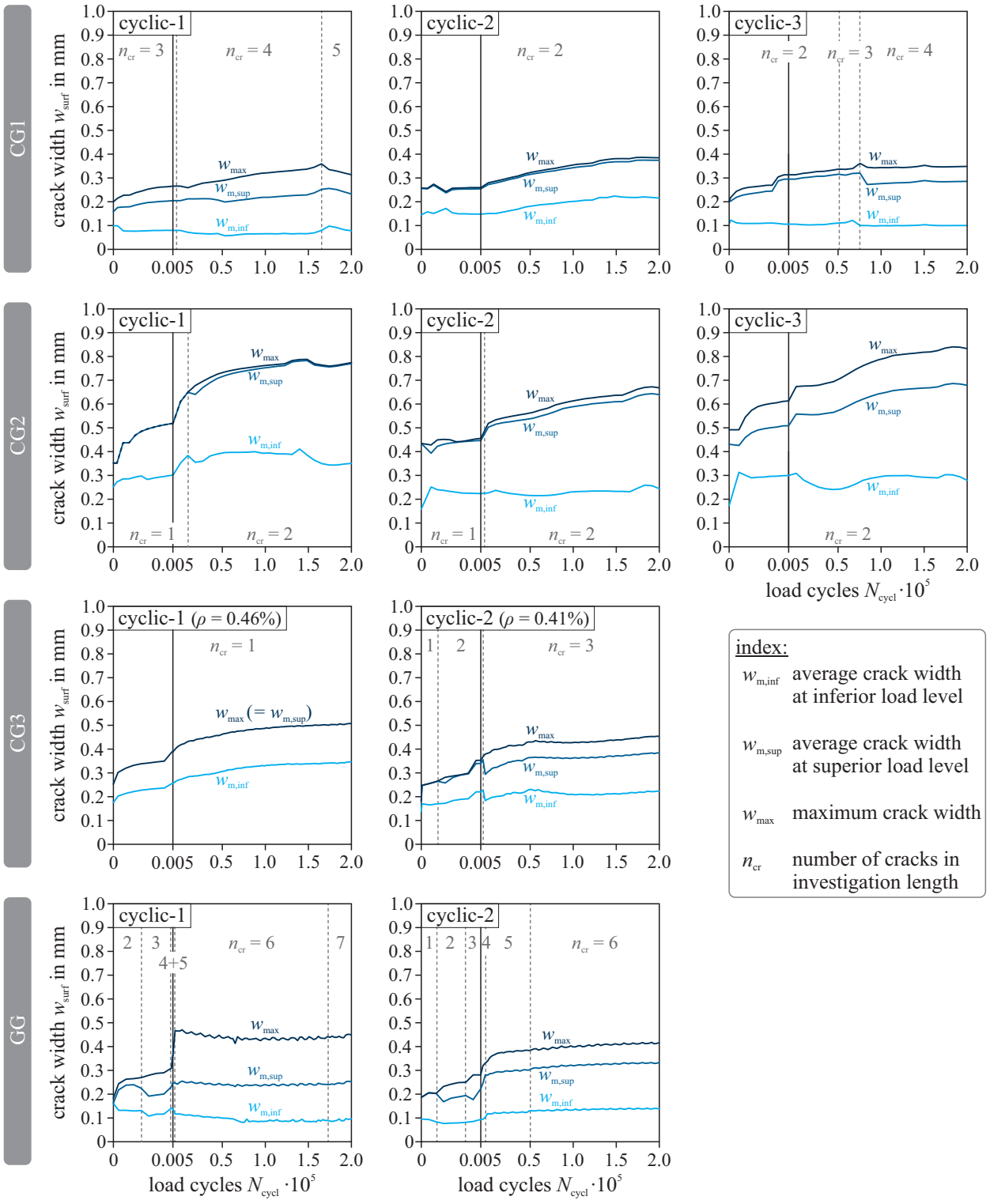


Figure 4.6: Evolution of average and maximum crack width during the cyclic loading phase in the UT tests of specimens with a normal-strength concrete

reinforcement was below 33% of the tensile strength, as was observed for specimens CG2-cyclic-3 and CG3-cyclic-1.

The four series are addressed separately in the following paragraph, confirming the previously stated observations. In the case of series CG1-cyclic, depicted in the first row of Figure 4.6, the average crack width at superior loading $w_{m,sup}$ increased by 0.1 mm considering all three specimens. In the case of specimen CG1-cyclic-2 no additional cracks formed during the cyclic loading phase. The existing two cracks showed no significant opening during the first 10,000 cycles, followed by an almost constant opening up to $w_{m,sup} = 0.37$ mm after which no further increase was detected. Regarding the two other specimens, the crack opening increased until two additional cracks formed during the cyclic loading phase. Considering CG1-cyclic-1, this was the case after 165,000 cycles with the occurrence of the fifth crack and for specimen CG1-cyclic-3 after the fourth crack. In both cases, these cracks resulted in a small decrease in the average width. As the most cracks appeared in specimen CG1-cyclic-1, the final crack widths after the cyclic loading phase were the smallest among the considered specimens with $w_{m,sup} = 0.23$ mm.
The low reinforcement ratio and the low bond capacity of CG2 resulted in large crack widths prior to the cyclic loading phase, which then significantly increased by 1.5 times of $w_{m,sup}$ in the case of specimens CG2-cyclic-2 and -3 and twice the value of $w_{m,sup} = 0.35$ mm for specimen CG2-cyclic-1. The occurrence of a second crack during cyclic loading or even when two cracks were already present, did not influence the crack opening in a notable manner.
The different reinforcement ratios of the two cyclically loaded specimens reinforced with CG3 had no visible effect on the occurrence of another crack or a reduced crack opening during the cyclic loading phase, as shown in the third row of Figure 4.6. Prior to cyclic loading, the average crack width at the superior load level was 0.2 mm for both specimens. After applying 200,000 cycles, the value of $w_{m,sup}$ increased to 0.51 mm in the case of specimen CG3-cyclic-1 with no additional cracking observed. Notable is also the increase in the average crack width at the inferior load level, which increased up to 0.35 mm and was twice the value in comparison to the initial width. This increase is considerably larger when compared to all other specimens, where the increase at the inferior load level was at most 0.1 mm. Regarding specimen CG3-cyclic-2, the average crack width at superior loading increased by 0.18 mm to $w_{m,sup} = 0.38$ mm, and at inferior loading from 0.15 mm to 0.22 mm.
At last, the specimens with reinforcement GG are evaluated referring to the bottom row of Figure 4.6. During cyclic loading, five additional cracks formed. Prior to the formation of the last two cracks at approximately 5,000 load cycles, the average crack width at superior loading increased by about 0.1 mm, considering both specimens. The large values of the maximum crack width determined in specimen GG-cyclic-1 were attributed to one crack, denoted as (4c), which showed an approximately 0.15 mm larger width compared to the second largest crack. With the occurrence of the two last cracks, only minor changes in the crack width were observed.

4.2.4 Reinforcement strain evolution and bond stress development

To gain further insight into the behaviour of the specimens during crack formation, the reinforcement strain and bond stress evolutions obtained using FOS were evaluated. Furthermore, the bond stress-slip relation and a consideration of tension stiffening were derived, similar to the COT test series in Section 3.5. At first, the purely statically loaded specimens are considered with a detailed analysis provided for one specimen reinforced with each of the four investigated grids in Figure 4.7. The derived evolutions are plotted at different loading stages resembling single cracks, adjacent cracks and stabilised cracking. In addition, the crack pattern obtained by DIC is provided,

which corresponds to the loading of the last presented strain evolution. This is then followed by a similar evaluation considering the cyclically loaded specimens.

Purely static tensile loading

The observation of the reinforcement stress-crack width behaviour of the specimens reinforced with CG1 is clarified with the visualised reinforcement strain on the left-hand side of Figure 4.7, focusing on specimen CG1-static-1. For the single cracking stage (green curves) and when the first adjacent crack ② (yellow curves) occurred at a reinforcement stress of 293 MPa, the force transfer by bond provided for a significant decline in the strain evolution.

This significant decline changes with the subsequent occurrence of more cracks. Considering, for example, the evolution at crack ①, the peak value of the bond stress was between 3.1 and 3.6 MPa. With the transition to a stabilised crack stage after the occurrence of crack ⑦, the close spacing of cracks ① to ⑥, being between 52 mm and 83 mm, resulted in a reduction of the transferred force as the reinforcement strain is almost constant. The peak values of bond stress were then less than 1.7 MPa. As apparent, the low bond stress in combination with the short transfer lengths led to almost no force transfer. In the cases where more length for the force transfer is provided, the bond stress increased in value to more than 4 MPa, e.g. between cracks ⑥ and ⑦ with a spacing of 125 mm corresponding to 3.3 times the yarn spacing of CG1. Considering the simplified approach of neglecting the effect of tension stiffening at stabilised cracking, as expressed by Equation 4-1 in the previous section, is apparently reasonable for the specimens reinforced with CG1. The close crack spacing at stabilised cracking led to a state in which the carbon grid is not capable of transferring significant forces to the concrete. The localisation of the transverse fibre strands, which are depicted in the graph of the bond stress evolution, revealed that disruptions in the bond stress are close to the position of a local undulation. As assumed in Chapter 3, these local undulations of CG1 significantly contribute to a force transfer. At close crack spacing where only one or two transverse strands were located between two adjacent cracks and therefore at most one undulation was within the transfer length, no significant force transfer is provided, and the contribution of tension stiffening in reducing the crack opening is negligible when referring to the average crack width.

In comparison, the evaluation of a specimen reinforced with CG2 revealed that tension stiffening is considerably larger even at stabilised cracking for this textile grid. As the reinforcement strain evolution plotted on the right-hand side of Figure 4.7 reveals, the large crack spacing of more than 2.6 times the yarn spacing allowed for a sufficient force transfer to the uncracked concrete. For example, at a maximum reinforcement stress of 1186 MPa, which is represented by the blue curve in Figure 4.7, the reinforcement strain is reduced from the peak value in the crack to the local minimum between two adjacent cracks by at least 1.5 mm/m, which is equivalent to a stress of 200 MPa. The corresponding bond stress evolution showed peak values of above 5 MPa at this load level. In the case of a single crack, the determined bond stress had peak values of about 2.0 MPa at a maximum strain of 2.7 mm/m. This is significantly less compared to the peak value of 3.6 MPa in the case of a single crack in specimen CG1-static-1 at a similar reinforcement strain. Although tension stiffening could contribute to a reduction in crack width for specimens CG2-static, these specimens still exhibited the largest crack widths among all test specimens. In addition, disruptions were also visible with their position being identical to the localisation of the transverse fibre strands, similar to the bond stress evolution in specimen CG1-static-1. Apparently, these undulations of reinforcement CG2 also provided for some additional bond, while the contribution to the overall bond capacity is lower, and friction plays the major role. At stabilised cracking, the contribution of friction and the provided long transfer lengths resulting from the large crack

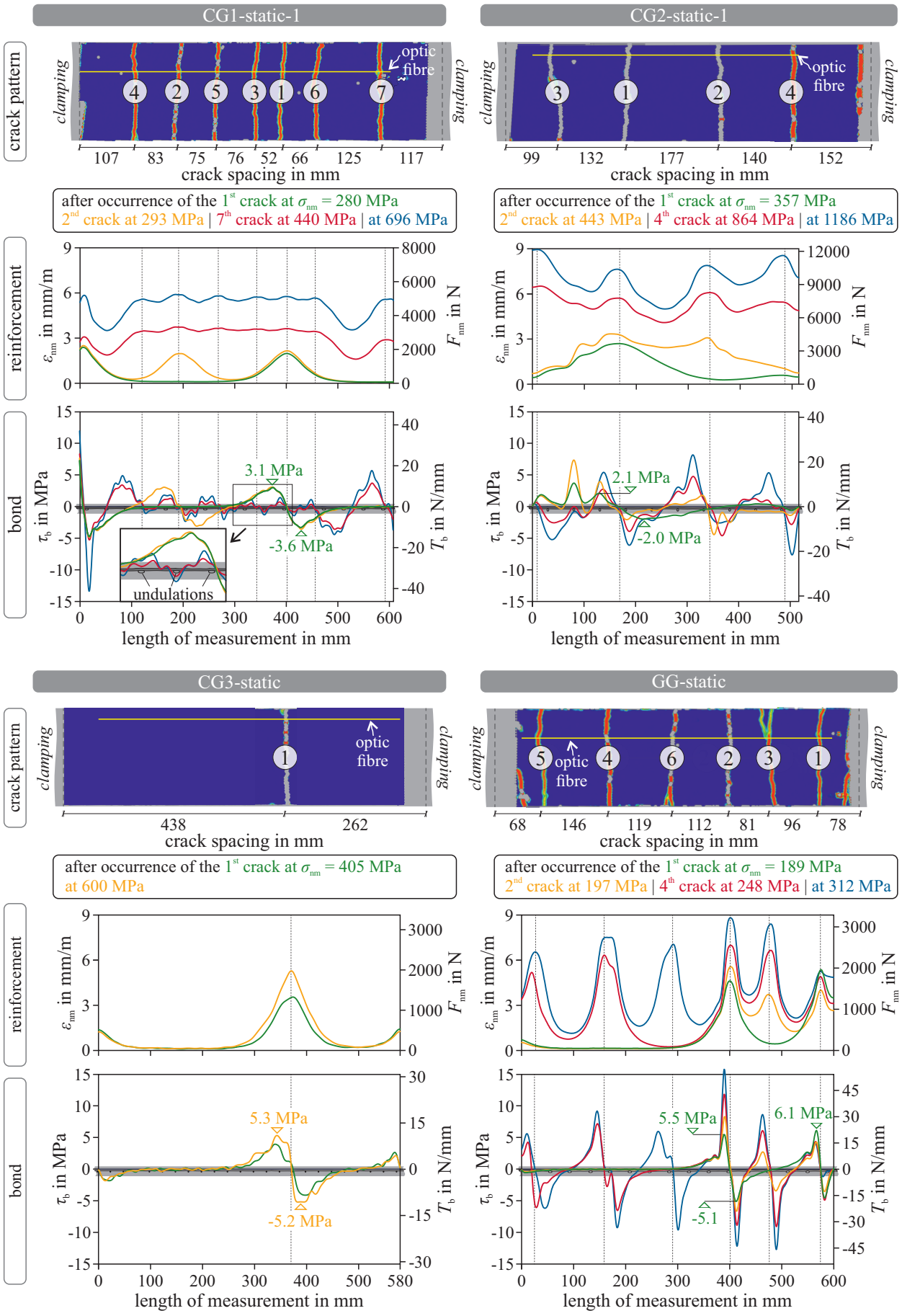


Figure 4.7: Evolution of reinforcement strain and bond stress at different loading stages with corresponding crack pattern for purely statically loaded specimens (adapted from [Sch25b])

spacing led to values of bond stress being significant above the values observed in the specimens with CG1.

Unfortunately, the fibre optic sensor in specimen CG3-static prematurely failed at a reinforcement stress of 600 MPa while only the single crack ① had occurred. Therefore, the evaluation of the reinforcement strain and bond stress evolution plotted on the left-hand side of Figure 4.7 only represents a single cracking stage. The peak values of the derived bond stress evolution were approximately 5.3 MPa. An influence of the local undulations at the intersection of the fibre strands is also likely for CG3, as revealed by the bond stress evolution.

The last evaluation addresses the specimen reinforced with GG, with the plotted evolutions shown on the right-hand side of Figure 4.7. While the crack pattern and the strain evolution suggest a stabilised cracking stage for the last monitored load level, five more cracks occurred prior to failure after the loss of the FOS measurement. A significant decrease in reinforcement strain from a crack to the local minimum between two adjacent cracks was revealed for all four visualised load levels. The peak values of the bond stress often exceeded 10 MPa, with a maximum of 16 MPa for the peak value on the left side of crack ② at a reinforcement strain of 312 MPa. At single cracking, the peak value was determined to 5.5 MPa at the same crack and side. Between most adjacent cracks, at least three transverse fibre strands were present; between cracks ② and ③, only two strands were available for force transfer. Nevertheless, this closer crack spacing did not lead to a significant reduction of the bond stress and the contribution of tension stiffening in comparison to the observations made for the specimens reinforced with CG1. Apparently, the glass grid provides for a high bond capacity even at close crack spacing.

The different capacity of force transfer regarding the cracking stages and the chosen reinforcement is also clearly shown in Figure 4.8, where the mean bond force transferred per fibre strand F_{bm} is related to the reinforcement strain in the crack $\varepsilon_{\mathrm{nm,max}}$. Exemplarily, a crack in the statically loaded specimens CG1-static-1, CG2-static-1 and GG-static is considered. The plots in the upper diagrams of Figure 4.8 reveal that at single cracking, the force transfer developed is identical to the theoretical force present in each fibre strand in the crack, which is visualised by the dotted black line. With the occurrence of adjacent cracks during the crack formation stage, the reduction in transfer length did not allow for a full force transfer, reducing the contribution of tension stiffening.
As pointed out in the previous paragraphs, the specimens with CG1 show no significant bond capacity at stabilised cracking due to the small crack spacing. Figure 4.8a1 shows that the determined mean bond force at stabilised cracking was only approximately 0.2 kN on average. These values did not significantly change with increasing reinforcement strain. In contrast, at the single cracking stage, a mean bond force of about 2.7 kN at a strain value of 3.2 mm/m was determined, which was ten times the value of the mean bond force at stabilised cracking.
For the specimen with CG2 considered in Figure 4.8b1, the influence of a stabilised cracking stage on a reduced force transfer is less pronounced. While at single cracking, a mean bond force of at most 5 kN was determined, at stabilised cracking and identical reinforcement strain of 7.6 mm/m, the value of mean bond force is still approximately 1.6 kN, which is a reduction of about two-thirds in value. It is also revealed that the specimen with CG2 showed an increase in force transfer at stabilised cracking for increasing strain values, which is different compared to the observations made for specimen CG1-static-1.
While the specimen with GG in Figure 4.8c1 showed a softer force-strain behaviour and the value of mean bond force is lower compared to the two specimens with the carbon grids, for example, at reinforcement strain of 7.6 mm/m the mean bond force was 2.7 kN, the behaviour is similar. At

crack formation, the force transferred was reduced, while there was always an increase in value present when the reinforcement strain increased with further load application. As the optical fibres failed before the stabilised cracking stage was reached, no evaluation for this case was possible.

The fibre optical measurements used in the three uniaxial tensile tests considered in the previous paragraph are further utilised to plot the value of mean bond force related to the transfer length present for each crack side and each measured step. This provided 6,000 to 38,000 individual data points, which were plotted in bottom half of Figure 4.8. To provide for a simplified visualisation, an envelope including all data points for each specimen is added, coloured in blue.
As assumed for the specimen with CG1, transfer lengths below the yarn spacing y_{nm} resulted in almost no force transfer. This is confirmed by the evaluation provided in Figure 4.8a2. With increasing available transfer lengths, more force is transferred. The maximum value of bond force of approximately 3 kN was reached at a transfer length of 158 mm, which was 4.2 times the yarn spacing.
Addressing specimen CG2-static-1, evaluated in Figure 4.8b2, almost no transfer length below the yarn spacing of 50 mm was determined. This was due to the large crack spacing observed in this specimen at stabilised cracking. The maximum value of mean bond force of about 5 kN was determined for crack ② at a transfer length of 174 mm, which corresponded to 3.5 times the yarn spacing.
As all cracks were considered in this evaluation, also values of mean bond force at transfer lengths below one times the yarn spacing of specimen GG-static were determined, as shown in Figure 4.8c2. In comparison to specimen CG1, larger values of bond force were transferred at lengths

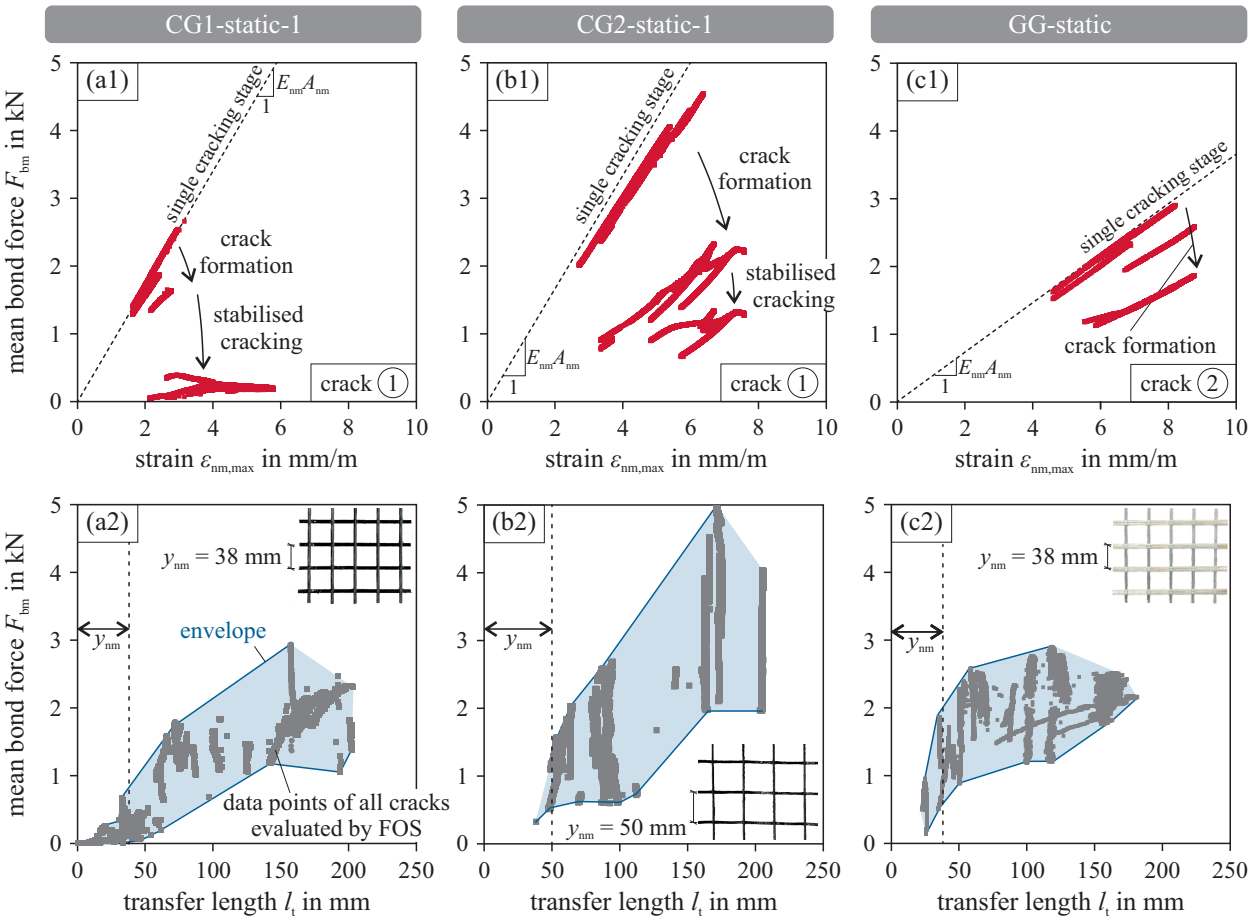


Figure 4.8: Mean bond force in relation to the reinforcement strain (focusing on one crack) and to the tranfer length (for all cracks) in the statically loaded specimens

below $y_{nm} = 38$ mm. At a transfer length of 38 mm, a mean force of 0.5 to 1.9 kN was determined for the specimen with GG, while in specimen CG1-static-1 the maximum force value at this transfer length was 0.7 kN.

At last, the contribution of tension stiffening is quantified by utilising the approach in Equation 3-8 to determine the factor β. The evolution of this factor is derived in relation to the time of testing for both sides of a selected crack and is plotted in Figure 4.9. In addition, the average value β_m is provided, considering all cracks in the specimen. For single cracks, the β_m-value is determined in a range between 0.56 for specimen CG2-static-1 (Figure 4.9b) and 0.83 for specimen GG-static (Figure 4.9d).
At stabilised cracking, the lowest value of β_m was found in specimen CG1-static-1 with 0.50 (Figure 4.9a). The development of the individual β-values revealed the sensitivity to the occurrence of an adjacent crack. A significant change in value on the particular side of the existing crack is found when a new crack occurred. In some cases, in particular present in specimen GG-static, the β-values remained almost constant until an adjacent crack occurred (Figure 4.9d).
Comparing these observations to the β-values determined in the COT test series for reinforcements CG1 and GG (cf. Figure 3.23a+d), it was found that both experimental campaigns provided similar values in the case of single cracks. For specimens with CG1, this was also true at adjacent cracking.

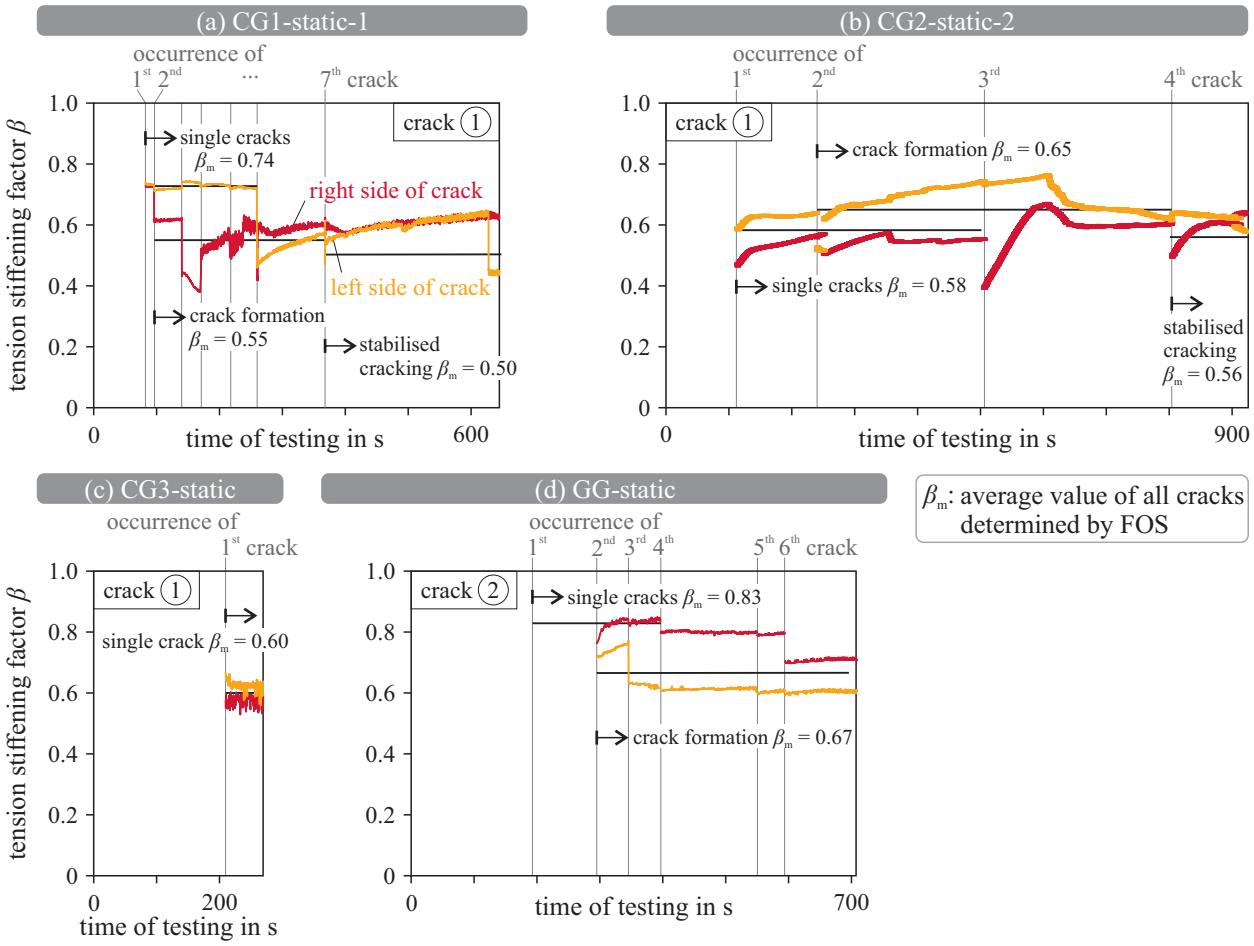


Figure 4.9: Evaluation of the tension stiffening factor β focusing on one crack in the statically loaded specimens

Cyclic loading phase

In the following paragraphs, the influence of cyclic loading on the bond stress evolution, the slip and the influence of tension stiffening are exemplarily evaluated for two specimens, CG1-cyclic-1 and CG3-cyclic-2. For specimens of series CG1-cyclic, a polyimide-coated optical fibre was used, which allowed for a very high resolution of the fibre strains, while for series CG3 an acrylate-coated optical fibre was applied. A detailed discussion on the influence of the type of optical fibre considered is provided in Appendix A.1.

At first, the reinforcement strain and bond stress evolution evaluated at different loading times for the two specimens are discussed using the evaluation provided in Figure 4.10. As pointed out in the previous Section 4.2.2, new cracks occurred during cyclic loading due to concrete tensile fatigue. The reinforcement strain evolution in both specimens also revealed the assumed increase in either transfer length or in magnitude of the local minimum between two adjacent cracks, as the cyclic loading reduced the bond capacity.

The usage of a polyimide-coated fibre in specimen CG1-cyclic-1 resulted in more abrupt changes in the derived reinforcement strain. When determining the bond stress as derivation of the strain evolution, these changes consequently resulted in significant spikes of stress values. For example, considering the evolution plotted at the occurrence of crack (3s), the maximum absolute values of bond stress were either 6.7 MPa for the left side of crack (1s) or | −7.4 | MPa for the right side of crack (3s) where the clamping influenced the force transfer. These values of bond stress are about twice the value determined in the statically loaded specimen CG1-static-1 (cf. Figure 4.7), where an acrylate-coated optical fibre was applied. In general, higher values of bond stress are to

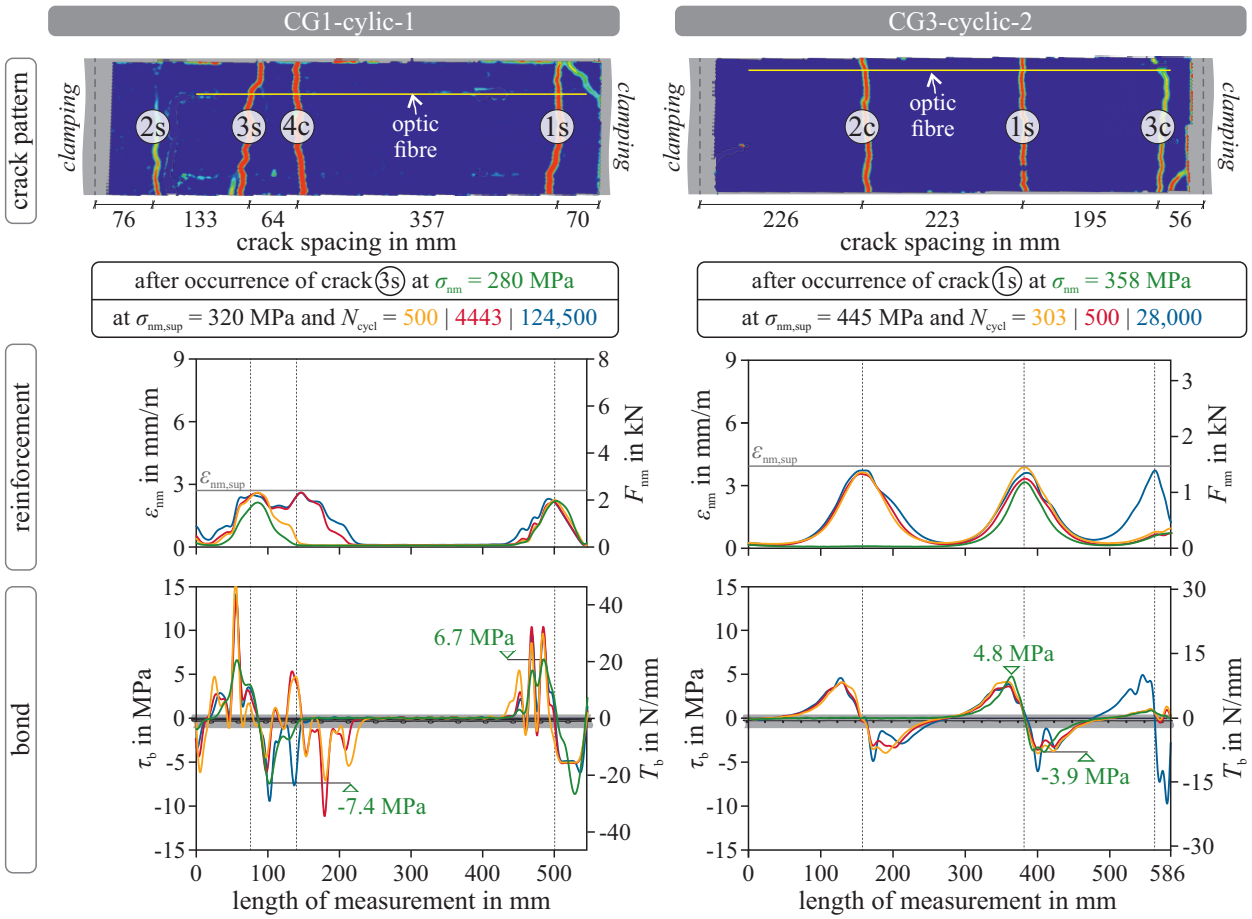


Figure 4.10: Evolution of the reinforcement strain and bond stress with the corresponding crack pattern in the case of cyclic loading for specimens CG1-cyclic-1 and CG3-cyclic-2

be expected in the case of significant changes in the transferred force caused by changes in the cross-sectional geometry. Studies focusing on the influence of geometrical parameters on the occurrence of concrete splitting showed that a transfer of large forces in a local area induced concrete cracking, as, for example, reported in [Pre20a, Pre20b]. Therefore, the high values of bond stress and the abrupt changes in the bond stress evolution detected using a polyimide-coated optical fibre may be a reasonable result. Despite the high individual values of bond stress, the mean bond force determined is equivalent to the force applied on each fibre strand in the crack.
The smoother reinforcement strain and bond stress evolution obtained by the acrylate-coated optical fibre applied in specimen CG3-cyclic-2 showed that, due to cyclic loading, the bond capacity was reduced as the increase in bond stress starting from the crack is less steep. In the case of the left side of crack (1s), the peak value in bond stress of 4.8 MPa at the occurrence of this crack, was not reached during the cyclic loading phase, despite the actual reinforcement strain being larger. Conversely, a plateau is visible for the cyclic loading stages, which suggests that the force transferred was approximately equivalent during the cyclic load application. A similar observation was made with regard to the COT tests subjected to ten load cycles (cf. Section 3.5.5).

For a second step in the analysis, the diagrams in Figure 4.11 provide an evaluation of the slip and the tension stiffening factor β for the two specimens at the static and cyclic loading phases. At static loading, the derived slip and β values are set in relation to the reinforcement strain in the crack $\varepsilon_{\mathrm{nm,max}}$. For the cyclic loading phase, the values at the superior load level were considered and related to the load cycles to investigate changes that particularly resulted from cyclic loading.
Considering specimen CG1-cyclic-1 at static loading, the slip determined on both sides of crack (1s) increased with increased reinforcement strain (Figure 4.11a1). With the occurrence of cracks (2s) and (3s), the reinforcement strain dropped back due to the deformation-controlled load application in the test setup, while no full elastic behaviour was observed and a plastic deformation remained of about 0.01 mm. One side of both cracks was influenced by an adjacent crack, which had occurred previously either at the clamping in the case of crack (1s) or crack (2s), expressed by a marginal difference in the determined values of slip for each side of the crack.
For the initial 500 load cycles, plotted in Figure 4.11a2, a significant increase in slip was only observed for the left side of crack (3s), denoted as "b", which increased by about 0.05 mm during the first 400 cycles but then decreased again to its initial value of approximately 0.07 mm. This corresponded to the observations made for the crack width detected on the concrete surface, as discussed in A.2. During the first 500 cycles only a marginal increase in the maximum crack width was measured utilising DIC.
A significant opening of the crack width was observed during ongoing cyclic loading, which was also revealed by the FOS measurements and is visualised in Figure 4.11a3. The largest opening was determined for the right side of crack (4c), which was about 0.06 mm at the end of the cyclic loading phase. As already discussed, the reduction in bond capacity is more significantly influencing single cracks due to the increase in transfer length and correspondingly the slippage of the reinforcement. In the case of the tension stiffening factor β, considerable changes were also shown after about 4,000 cycles, as the differentiation between single cracks and adjacent cracks revealed. After the application of almost 125,000 cycles, the value of $\beta = 0.8$ remained approximately constant in the case of a single cracking, whereas for adjacent cracks, the value of β was about 0.42 on average (see Figure 4.11b3).

Addressing the results of specimen CG3-cyclic-2, the slip increase during the static loading phase was only marginal by 0.01 mm for a stress increase of about 110 MPa (Figure 4.11c1). The tension stiffening factor β remained constant at 0.75 on average for both sides of crack (1s). In contrast to the other specimen with CG1, the value of slip doubled during the first 300 cycles, which was

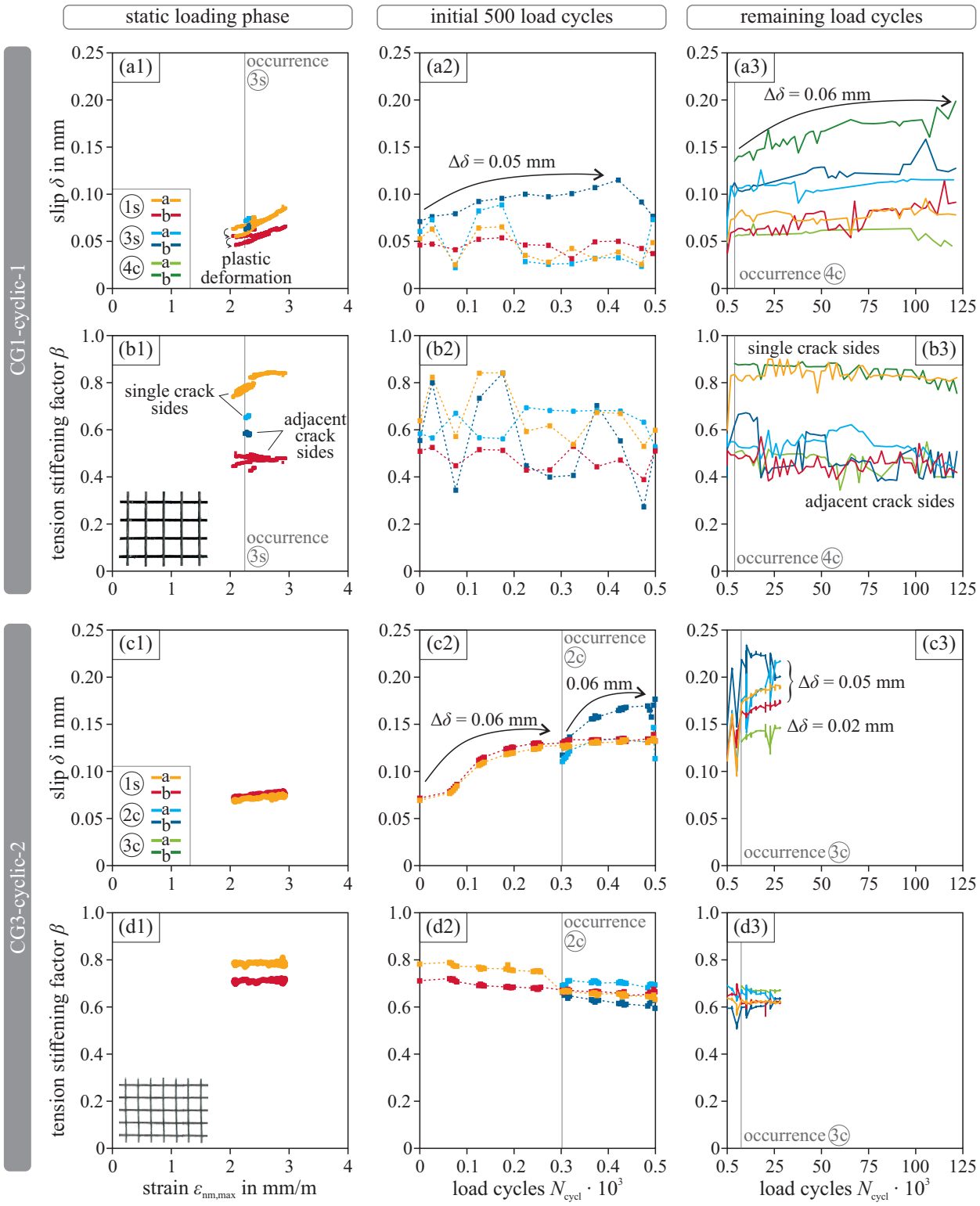


Figure 4.11: Evolution of slip and the β-factor during the static phase and at the superior load level during the cyclic phase for specimens CG1-cyclic-1 and CG3-cyclic-2

an increase by 0.06 mm (Figure 4.11c2). Shortly after 300 cycles, the second crack (2c), occurred with a value of slip similar to the slip determined at both sides of the initial crack. While the initial crack (1s) only opened slightly, both slip values of crack (2c) increased by 0.06 mm when reaching 500 load cycles. With the slip increase, the β-values declined to about 0.67 at the occurrence of the second crack and to 0.65 after 500 cycles when considering all four crack sides (Figure 4.11d2). With regard to the β-values obtained for more than 500 cycles, it was revealed that at a higher

number of load cycles applied, initially, no significant change of β was observed for all four crack sides (Figure 4.11d3). With ongoing load cycles, crack (3c) occurred, which resulted in some difference in the value of β. This was already indicated by the strain and bond stress evolution of specimen CG3-cyclic-2 shown in Figure 4.10. For the two cracks (1s) and (2c), the value of β was on average about 0.05 lower compared to the value of crack (3c). After 28,000 cycles, the optical fibre failed. During 500 and 28,000 cycles, the slip for all five evaluated crack sides increased by 0.02 to 0.05 mm.

Concluding, in the case of single cracks, significant crack opening was revealed due to cyclic loading. The contribution of tension stiffening remains constant after about 1000 cycles, however lower compared to the purely static specimens.

General observations

Based on the fibre optic measurements, the following general observations were made with regard to all four investigated grids:

- Local undulations of the fibre strand contributed significantly to the force transfer. In the case of stabilised cracking, the close crack spacing may result in a state where no significant force is transferred due to missing local undulations in the transfer length. This was most pronounced for specimens reinforced with CG1.
- A significant force transfer is possible when the transfer length is larger than at least the yarn spacing. As a result, tension stiffening only contributed to a reduction in the reinforcement strain and, consequently, to a reduction in crack opening, when the crack spacing was more than twice the yarn spacing.
- Utilising the reinforcement strain evolution, the tension stiffening factor β was quantified in dependence on the cracking stage. As shown by the COT tests in the previous chapter, the factor β was found between 0.6 and 0.8 at the single cracking stage. The β-values were reduced, as expected, for cyclic loading or in the case of adjacent cracks. The value of $\beta = 0.36$ determined in the COT test was confirmed as lower limit.

These observations reveal an apparent contradiction: How is it possible that, despite a close crack spacing and an insufficient force transfer the magnitude of factor β suggested some contribution of tension stiffening? Otherwise, the value of β would be close to zero. Therefore, a reconsideration of the calculative basis on deriving the factor β with regard to the contribution of tension stiffening is provided in the following.

By definition, the factor β describes the relation between the maximum, average and minimum reinforcement strain values corresponding to a crack, as shown by the equations provided in the upper half of Figure 4.12, referred to as "strain relation". The average concrete strain ε_{cm} is then determined considering force equilibrium and utilising β, as proposed in Equation 2-13. Considering the experimentally derived reinforcement strain evolution, as exemplarily shown in Figure 4.12 for the single crack (1) of CG1-static-1, the value derived for β is 0.72. The average concrete strain is then determined to $\varepsilon_{cm} = 1.35 \cdot 10^{-3} \cdot \rho \alpha_e$. In this particular case, with the reinforcement ratio $\rho = 0.66\%$ and the Young's modulus ratio $\alpha_e = 3.8$, the average concrete strain of 0.034 mm/m and an average concrete stress of 1.05 MPa are obtained.

Evaluating now the stage of adjacent cracks at a higher reinforcement utilisation of 5.76 mm/m in crack (1), the obtained value of β is 0.48. This is expectedly lower than in the case of a single crack, but does not directly indicate the significant decrease in the contribution of the concrete strain. As apparent from the calculation provided in the upper half of Figure 4.12, the reinforcement strain difference $\Delta\varepsilon_{nm}$ is only 0.21 mm/m. As a result, the value of the average concrete strain ε_{cm} is reduced by about 93% to $0.10 \cdot 10^{-3} \cdot \rho \alpha_e$. The average concrete stress is then 0.08 MPa, which is negligible. In particular, when considering the small transfer lengths present at stabilised cracking,

a consideration of tension stiffening does not provide for a significant reduction in the determined crack width. This is the reason why the simplified approach in Equation 4-1 provided a very good fit to the test data of series CG1, as shown in Section 4.2.3. In conclusion, the value of the tension stiffening β does not compulsorily indicate the actual proportion of the deformation of the concrete in the transfer length that contributes towards crack width reduction.

Next, the contribution of tension stiffening towards a reduced crack opening at the stabilised stage is investigated in the case of applying the analytical consideration provided in Section 2.5.3. This is visualised in the lower half of Figure 4.12. At first, a brief sensitivity analysis of the analytical consideration is done for different concrete tensile strengths f_{ct}, resembling a lower strength concrete of class C20/25, a normal-strength concrete (C30/37), and a high-strength concrete (C80/95). Further parameters varied are the reinforcement ratio with a low value of 0.5% and a high reinforcement ratio of 2.0% and the factor β. The plotted curves resemble the relative contribution of tension stiffening when analytically determining the average reinforcement strain and the concrete deformation. This is expressed in the analytical formulation by the reduction term on the average strain difference $(\varepsilon_{nm,m} - \varepsilon_{cm})$ (cf. Equations 2-12 and 2-13), including the factor β. With increasing maximum reinforcement stress, which refers to the stress in the crack, the contribution of the force transfer becomes less significant. At lower stress values, the analytical model implies an almost full reduction of the stress value, which actually indicates the transition to the single cracking stage. The evaluation also shows the expected influence of a higher concrete tensile strength, providing for an increased force transfer, as the adjacent cracking is postponed to higher reinforcement utilisations. Furthermore, large reinforcement ratios reduce the relative contribution of the force transfer due to a reduction in transfer length, resulting in the practically known fine crack pattern. This converges to the theoretical consideration of a reinforcement ratio being 100%, meaning no concrete present, and the pure elastic behaviour of the reinforcement material would be considered. At last, a lower value of β indicates that less force is transferred. Therefore, the relative contribution to a reduction in crack opening is less pronounced.
While the plotted curves were determined considering the Young's modulus of CG1, the curves only differ insignificantly when investigating different materials such as steel or glass reinforcement. This is because the only factor considering the Young's modulus ratio is related to the reinforcement ratio, expressed as $\rho\alpha_e$, which is almost zero when considering all reasonable values and configurations. Therefore, the influence of the concrete Young's modulus is also not of importance.
The reinforcement strain and stress as well as the concrete stress evolution are plotted in the right-hand bottom corner of Figure 4.12, utilising the FOS measurements of specimen CG1-static-1. The influence of the occurrence of a new crack, which is crack ⑤, is highlighted. Prior to the formation of crack ⑤, the force transfer from the reinforcement to the concrete resulted in a maximum concrete tensile stress of 1.48 MPa between cracks ② and ③. At this peak value, crack ⑤ formed and a significant reduction in concrete stress to about 0.24 MPa between the three cracks occurred. In contrast, the reinforcement stress is reduced only slightly by this crack occurrence.
Going back to the quantification of tension stiffening, an exploitation of the experimentally determined concrete stress at crack occurrence σ_{ct} is done for the analytical consideration. This individual data point ($\sigma_{ct} = 0.24$ MPa and $\rho = 0.66\%$) is plotted in the diagram on the left-hand bottom corner of Figure 4.12 and represented as a red rhombus. In this particular case, the contribution of tension stiffening is approximately 4% for a maximum reinforcement stress of 363 MPa and an stress difference $\Delta\sigma_{nm}$ of 38 MPa. This evaluation exemplifies that the low value of the concrete tensile stress significantly reduced the relative contribution of force transfer into the uncracked concrete. In addition, when determining the average concrete strain ε_{cm} using the provided exper-

imental data, again value of about $0.1 \cdot 10^{-3} \cdot \rho\alpha_e$ is obtained.
In additional, this evaluation highlights another point: the occurrence of new cracks at relatively low concrete stresses compared to the concrete tensile strength and the resulting reduced contribution of tension stiffening towards a reduction in crack opening must be addressed. This is done in Section 5.5.3.

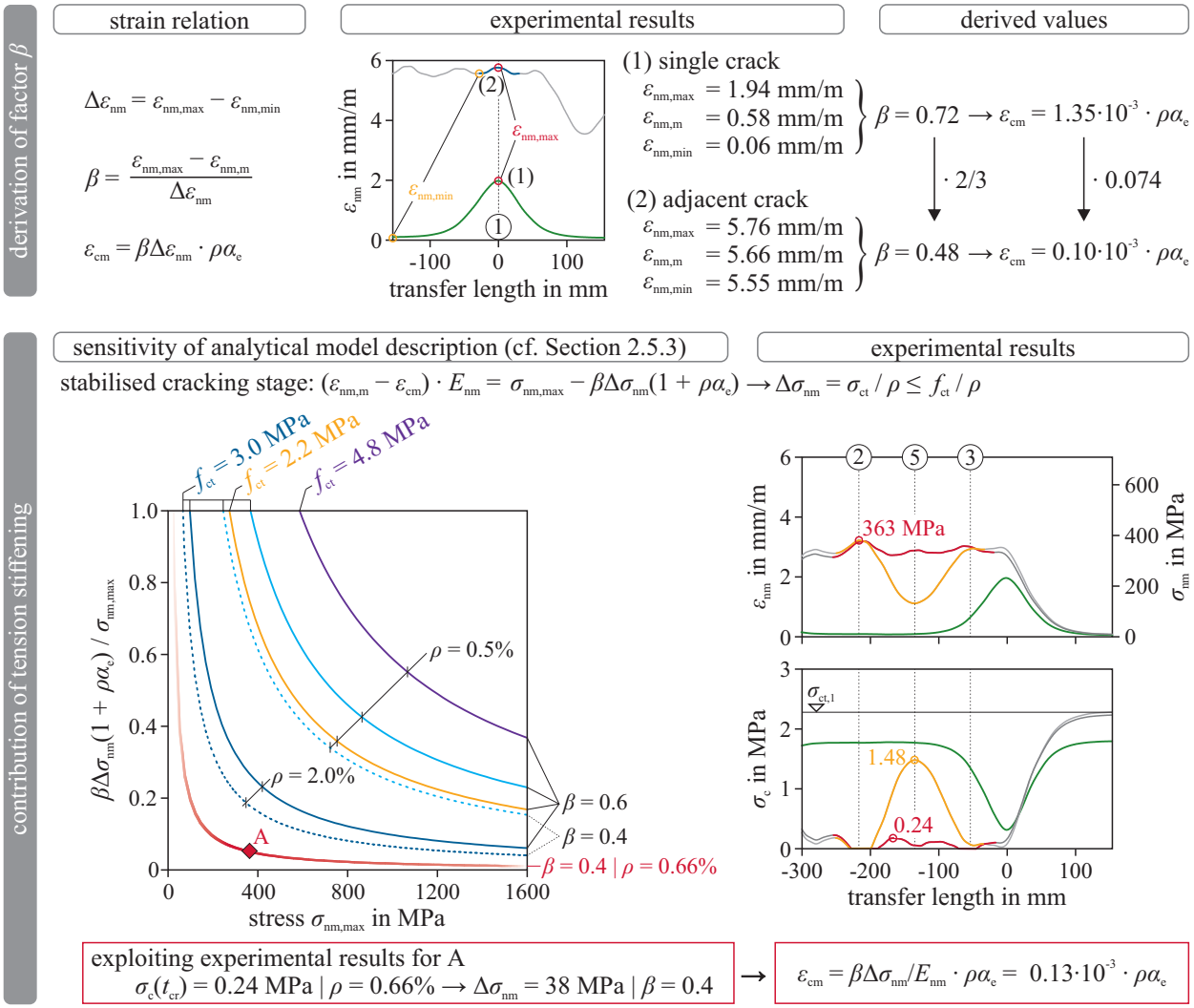


Figure 4.12: Reconsideration of the contribution of tension stiffening with regard to the quantitative description provided by the β-factor

4.3 Extension on multiple layers of textile grids

4.3.1 Considered variants

The experimental program of uniaxial tensile tests was extended to investigate the influence of placing multiple layers of a textile grid in a member on the overall bond capacity and the capacity to limit the crack width. Three configurations of reinforcement placement were considered, which are shown as cross-sectional representations in Figure 4.13. The objective of the reinforcement layout was to investigate, whether a direct placement of two textile grids on each other with almost no concrete coverage in between the longitudinal fibre strands provides for a similar bond performance when compared to either a single textile layer or multiple layers with a sufficient spacing in between.

The concrete cover was set consistently to approximately 13.5 mm. The considered reinforcement was solely CG1. The first series, denoted as CG1-2L, had an almost direct placement of the grids on each other with only 2 mm of spacing between the layers at the locations of the longitudinal fibre strands. Considering the centroids of the longitudinal strands, the distance between the two centres of both layers was 5 mm. The series CG1-2L+ had a larger distance of 16 mm between the centroids of the longitudinal strands, which was 13 mm of spacing between the layers at the locations of the longitudinal fibre strands. The spacing was intended to be equivalent to the concrete cover, and this series should represent the case of a spacing that allows for sufficient force transfer. The objective of these two configurations was to investigate the possibility of a reduced force transfer due to an insufficient concrete area available at close layer spacing.

The last series, CG1-4L, had specimens reinforced with four textile layers to investigate the possible significant reduction in force transfer of two layers being "packed in" or surrounded by the outer grids. The distance between the centroids of the longitudinal strands was 5.5 mm on average, with a spacing between the layers at the locations of the longitudinal fibre strands of 2.5 mm.

The different reinforcement layouts resulted in different reinforcement ratios as the number of longitudinal fibre strands was identical, with five per layer. Addressing also the previously introduced series CG1 with only one reinforcement layer and a reinforcement ratio $\rho = 0.66\%$, this program additionally allowed for a consideration of the influence of increased reinforcement ratios. On the other hand, the different ratios are to be considered when comparing these series with each other.

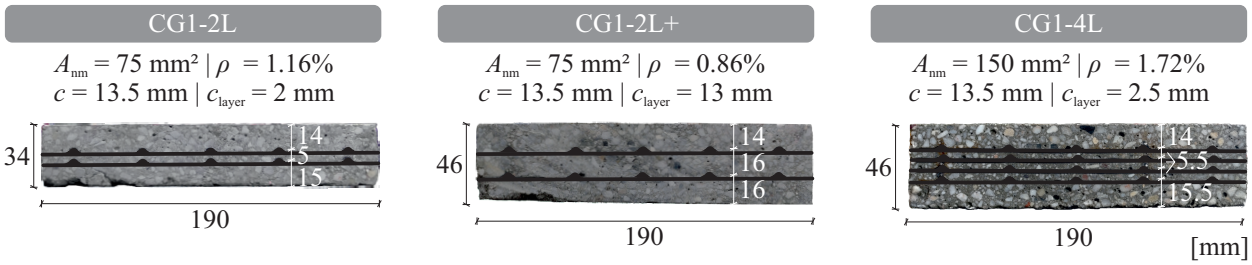


Figure 4.13: Cross-sectional layout of the three series investigating the influence of multiple reinforcement layers

The extended test program was identical to the setup of the principal campaign as described in Section 4.2.1. Each series consisted of one purely static test and two tests with an additional cyclic loading phase. Due to the doubled and quadrupled tensile resistance of the specimens, the contact pressure in the clamping area was increased to 800 Nm applied on each steel bolt for the two-layer series and up to 1200 Nm for the specimens with four layers of textile grid. The concrete was the normal-strength mixture (NSC) with a maximum aggregate size of 5.6 mm and a targeted strength class of C30/37. The superior load level for the specimens with two layers was equivalent to that

of specimens with a single reinforcement layer and set to $F_{sup} = 12$ kN. For the specimens with four layers of carbon grid, the superior load level was increased to 19 kN. The inferior load level was set to 2 kN for all three series, identical to the previous series of uniaxial tensile tests. An overview of the specifications of the cyclic loading phase is given in Table 4.2. Due to the different cross-sectional areas of the specimens, the utilisation of the concrete and therefore the possibility of concrete tensile fatigue leading to additional crack occurrence during the cyclic loading phase was different for each series.
The instrumentation using digital image correlation (DIC), to determine the crack formation and opening on the concrete surface, and using fibre optic sensors (FOS), placed on the fibre strands, was identical to the principal campaign. In the three series, only acrylate-coated optical fibres were considered due to their robustness and the very good results provided in the previous series. The gauge length was set to 0.65 mm. The measurement rates of the DIC and FOS were not changed compared to the settings of the previous series.

Table 4.2: Specifications of the cyclic loading phase in uniaxial tensile tests with multiple reinforcement layers

index	reinforcement layout	f_{ctm} [MPa]	F_{sup} [kN]	$\sigma_{nm,sup}$ [MPa]	$\sigma_{c,sup}$ [MPa]	F_{inf} [kN]	$\sigma_{nm,inf}$ [MPa]
CG1-2L	2 layers $c_{layer} = 2$ mm	2.3	12.0	160	$1.86 = 0.81 \cdot f_{ctm}$	2.0	27
CG1-2L+	2 layers $c_{layer} = 13$ mm	2.4	12.0	160	$1.37 = 0.57 \cdot f_{ctm}$	2.0	27
CG1-4L	4 layers $c_{layer} = 2.5$ mm	2.3	19.0	127	$2.17 = 0.95 \cdot f_{ctm}$	2.0	13

4.3.2 Performance regarding the crack width development

General behaviour

The reinforcement stress related to the elongation of the investigation length ε_m is plotted in Figure 4.14. At first, the purely statically loaded specimens, including the specimens with a single layer (CG1-static-1 and CG1-static-2), are considered in Figure 4.14a. As the most visible effect was the result of the higher reinforcement ratios, this led to a transition to the stabilised cracking stage at lower elongation. Furthermore, the stress-elongation evolution at stabilised cracking was almost identical to the linear elastic behaviour of the sole fibre strand. The larger elongation was the result of more cracks present and less overall stiffness of the member due to almost no contribution of tension stiffening, as reported in the previous Section 4.2 for members reinforced with CG1.
Despite the fact that the force released upon initial crack occurrence was larger due to the increased concrete cross-section, the higher reinforcement amount of the specimens with multiple reinforcement layers compensated for this. This resulted in a lower value of reinforcement stress at initial cracking for all specimens of the three series CG1-2L, CG1-2L+ and CG1-4L when compared to the single-layer specimens. The magnitude of reinforcement stress reduction occurring after a new crack formed was less at higher reinforcement ratios. The higher reinforcement ratios led to more cracks occurring during the crack formation stage, while the increase in elongation until a new crack formed is lower due to the increased overall stiffness of the member.
The cyclic loading phase also did not result in such large displacements as observed for the single

layer specimens (cf. Figure 4.2) due to the increased stiffness, smaller crack openings and a lower reinforcement strain at the superior load level, accompanied by a lower amplitude. In addition, Figure 4.14b-d revealed that the stress-elongation curves of all specimens within a series evolved almost identical.

All specimens in the three series failed due to rupture of the fibre strand, except the two cyclically loaded specimens of series CG1-4L, where an anchorage failure in the clamping area occurred at a reinforcement utilisation of approximately 88% of the tensile strength, which was expressed by a splitting of the concrete accompanied by longitudinal cracking.

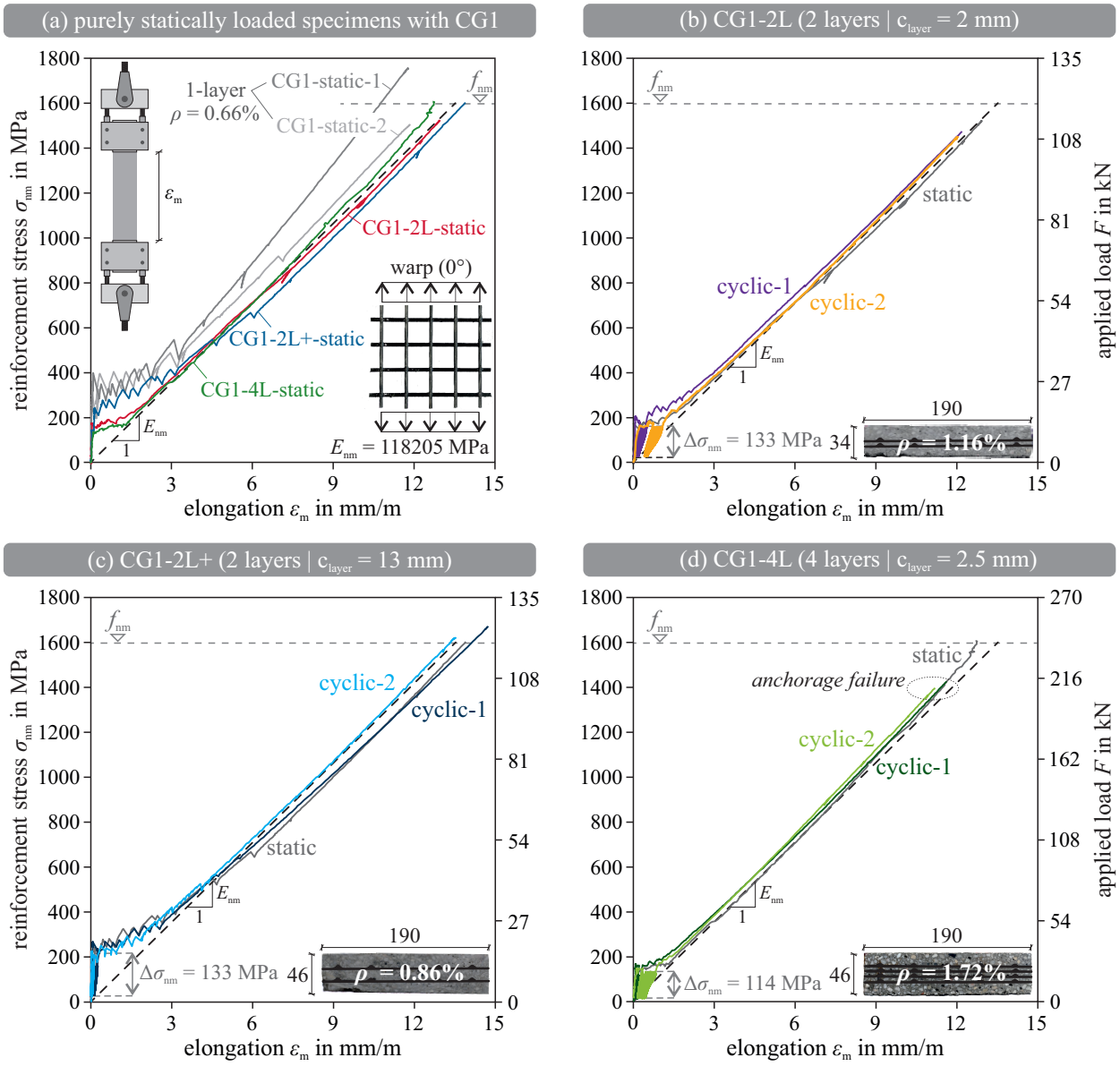


Figure 4.14: Elongation related to reinforcement stress and tensile force in the uniaxial tensile tests of specimens reinforced with multiple layers of CG1

Crack widths

The second evaluation of the test results considered the crack width development, highlighted by the evolution of the average crack width and the maximum crack width. The corresponding curves of the three test series are provided in Figure 4.15. As expected, the reinforcement ratio affected the crack width and the number of cracks determined in each specimen. With a higher reinforcement ratio, the crack width was reduced. In the case of the specimens with four layers

($\rho = 1.72\%$), the average crack width did not even exceed the limit of 0.4 mm. At this high reinforcement ratio, 19 to 20 cracks inside the investigation length were observed, which was twice the number of cracks formed in the specimens with two layers of reinforcement and the larger spacing between the layers (series 2L+), which had half the reinforcement ratio. With more cracks occurring, the discrepancy between average and maximum values of the width increased, also indicating that more cracks had small crack widths.

Furthermore, the higher reinforced specimens ($\rho \geq 1.16\%$) revealed another difference when compared to the specimens with a larger spacing of the reinforcement layers ($\rho = 0.86\%$) and a single layer ($\rho = 0.66\%$). After the formation of most cracks, the maximum crack widths of the higher

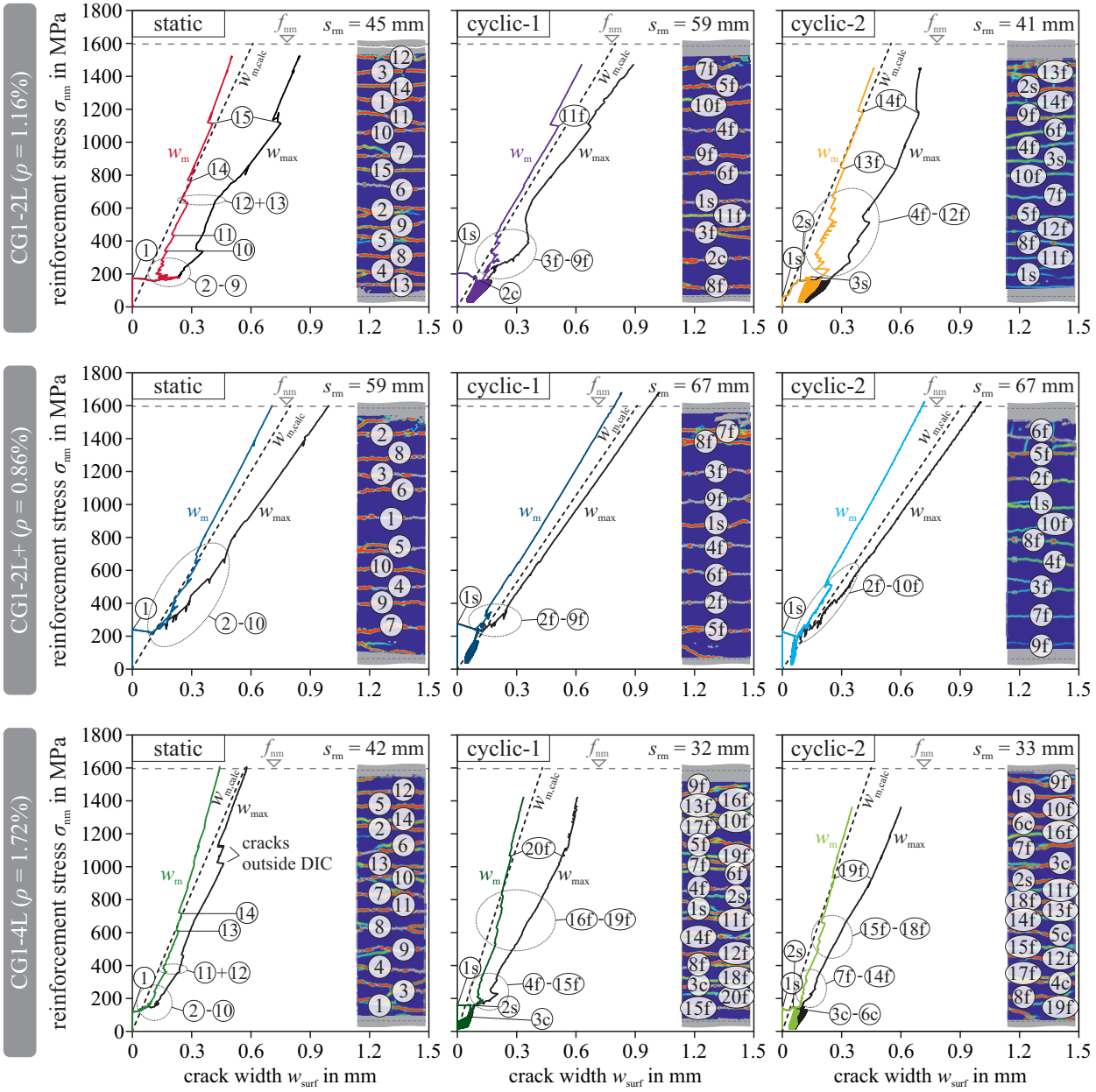


Figure 4.15: Average and maximum crack width evolution related to the reinforcement stress in the uniaxial tensile tests of specimens reinforced with multiple layers of CG1

reinforced specimens showed pronounced reductions and no continuous linear increase. This is found, for example in specimens CG1-2L-cyclic-1 after crack (9f) or specimen CG1-4L-static after crack (12). Apparently, at these higher reinforcement ratios, a redistribution in reinforcement strain in the crack occurred and, therefore, also a change in the contribution of each crack opening to the total elongation. The cracks with the largest opening and the highest utilisation of reinforcement stress started to close or not open further with a reduction of the reinforcement stress in these cracks. Due to compatibility with the member deformation, the closing of some cracks required an opening of other cracks, which apparently were the ones with a lower crack opening. This behaviour is also observed for members under restrained conditions, where the maximum crack width decreased over time or the opening was not as pronounced in comparison to all cracks, e.g. as reported for steel-reinforced members in [Sch23a].
In addition, the higher reinforced specimens ($\rho \geq 1.16\%$) also showed a different behaviour in the occurrence of new cracks. A significant number of cracks occurred at various load levels with new cracks forming in between existing cracks where already a close crack spacing was present. Apparently, the concrete was subject to a local multiaxial tensile stress state provoking cracking close to existing cracks. This behaviour is focused on in the following Section 4.3.3, where the fibre optic measurements are evaluated.
Regarding the average crack spacing s_{rm} for the higher reinforced specimens, it was at most 59 mm, which was below 1.6 times the yarn spacing. In certain instances, for example, in the case of the two specimens designated CG1-4L-cyclic-1 and -2, the average crack spacing was observed to be less than the yarn spacing of CG1. The specimens CG1-2L+ showed a larger average value of crack spacing, ranging from 59 mm to 67 mm, which was still below 1.8 times the yarn spacing.

As concluded from the previous observations, the contribution of tension stiffening is assumed to be insignificant in the case of small crack spacing in members reinforced with CG1, because the force transferred to the uncracked concrete is very small. This also applies in particular to the specimens of series CG1-2L and CG1-4L, and is highlighted by plotting the simplified approach to determine an average value of crack width $w_{m,calc}$ according to Equation 4-1 as a dashed black line in Figure 4.15. For the two series CG1-2L and CG1-4L, the average crack width of the tests is well predicted by the simplified approach at stabilised cracking. An overestimation of the approach only occurred when at high reinforcement stress another crack occurred, for example, in the case of specimen CG1-2L-cyclic-1 and crack (11f) or for the occurrence of crack (14) in specimen CG1-4L-static. Therefore, the simplification of neglecting any contribution of tension stiffening allows for a reasonable prediction of the average crack width at stabilised cracking for reinforcement utilisations which represent the serviceability limit state. A slightly different development of crack width was observed for to the three tests of series CG1-2L+, where the average crack widths are overestimated by the simplified prediction.
The improved bond capacity in the case of placing multiple layers of reinforcement with some spacing is also visible when evaluating the crack opening during the cyclic loading phase. The two specimens of series CG1-2L+ showed only a marginal additional opening despite having only one single crack in this phase. When comparing the average crack width for reinforcement stress below approximately 600 MPa of the specimens with directly placed reinforcement layers (series CG1-2L) to the values of series CG1-2L+, the average crack width in series 2L was larger than the one obtained for series 2L+. With the transition to the stabilised cracking stage, the higher reinforced specimens of series CG1-2L showed lower average crack widths. In the case of comparing the maximum values of crack width, this was not observed. The maximum width in series CG1-2L+ was lower despite having a lower reinforcement ratio compared to series CG1-2L. Therefore, an adequate spacing between multiple layers of reinforcement seems to improve the performance of

reinforcement CG1 with regard to crack width limitation under serviceability loading conditions, despite a lower reinforcement ratio present. In addition, the contribution of tension stiffening during crack formation and at stabilised cracking was assumed to be slightly larger as a sufficient amount of force was transferred between two adjacent cracks. This addresses an increased bond capacity, which was not observed in the other series.

Crack opening during cyclic loading

In general, the performance to limit the crack width below 0.4 mm was very good, considering all nine specimens with more than one reinforcement layer. This is also highlighted when investigating the crack opening during the cyclic loading phase in detail, as the evaluation in Figure 4.16 shows. For all specimens, the crack width prior to the cyclic loading phase was small. The largest values were determined for specimen CG1-2L-cyclic-2 with a maximum crack width of 0.17 mm. During cyclic loading, in three specimens no additional cracks occurred (CG1-2L-cyclic-2, both CG1-2L+-cyclic), in two specimens one new crack formed (CG1-2L-cyclic-1, CG1-4L-cyclic-1), and only in specimen CG1-4L-cyclic-2 four more cracks were detected in the investigation length. As for the other series presented in Section 4.2, new cracks most likely occurred due to concrete tensile fatigue.

During cyclic loading, a significant opening of cracks was only observed in both specimens CG1-2L-cyclic ($\rho = 1.16\%$). In the case of CG1-2L-cyclic-1, the maximum crack width increased by 0.07 mm, which was an increase of 70% from the initial value prior to the cyclic loading phase. For specimen CG1-2L-cyclic-2 the increase was of similar magnitude despite no additional crack occurring during the cyclic loading phase. Both the average and maximum crack width values

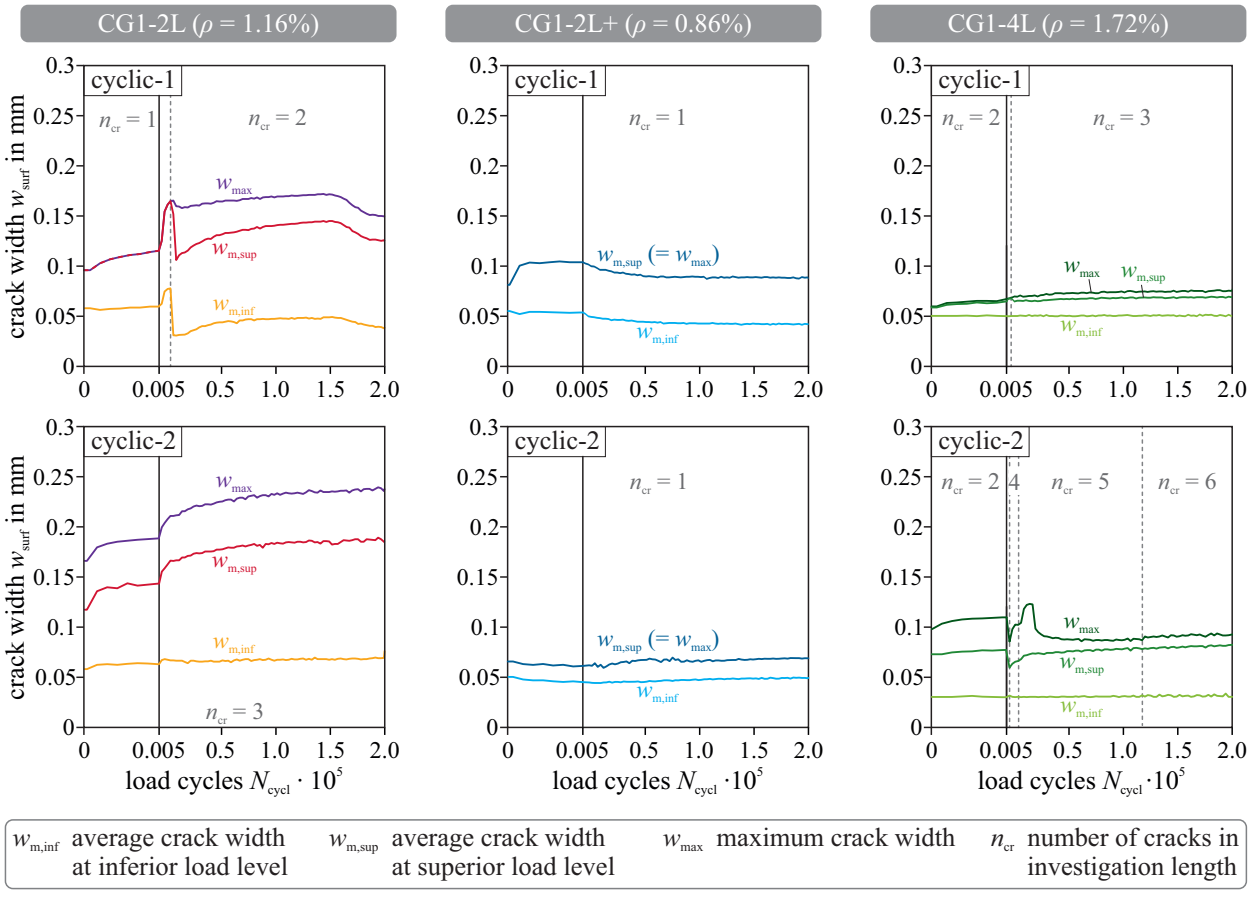


Figure 4.16: Evolution of average and maximum crack width during the cyclic loading phase in the uniaxial tensile tests of specimens with multiple layers of CG1

increased by 0.07 mm, while no reduction due to additional crack occurrence during the cyclic loading phase was observed. The major increase in width occurred during the first 50,000 cycles. The minimum crack width did not change during the cyclic loading phase.
The specimens of series CG1-2L+ and CG1-4L showed no significant crack opening due to cyclic loading. The reasons are either the positive influence of a sufficient spacing between reinforcement layers, as discussed in the previous paragraph for specimens CG1-2L+, or the very high reinforcement ratio of 1.72% for specimens CG1-4L.

4.3.3 Force transfer at adjacent cracks - contribution of tension stiffening

Reinforcement strain evolution

In the following evaluation, the force transfer and the possible contribution of tension stiffening at adjacent cracks is addressed utilising the fibre optic measurements. The reinforcement strain is plotted in Figure 4.17 for the three purely statically loaded specimens with multiple reinforcement layers. The strain evolution is shown for chosen load levels providing for identical maximum reinforcement stress and strain values when comparing the test results. In addition, two reinforcement layers were selected, which represent the top and bottom layer of the specimens CG1-2L-static and CG1-2L+-static and the bottom and third layer of specimen CG1-4L-static. The top layer was the closest to the surface at which the concrete was poured in. In the case of series CG1-4L, the 3rd layer was next below the top layer.
The lowest shown load levels represented a single cracking stage. For the higher reinforced specimens CG1-2L-static and CG1-4L-static, the initial cracks resulted in a reinforcement stress of 150 MPa. In the case of specimen CG1-2L+-static, the lower reinforcement ratio in combination with a higher force released upon initial crack occurrence resulted in a higher reinforcement stress of 250 MPa.
Considering all three specimens at this single cracking stage, no difference in the reinforcement evolution between the two grid layers was observed. The magnitude of the maximum strain in the crack and the transfer length were almost identical. The only variation in value or the influence of an already existing adjacent crack was due to the fact of small eccentricity in the reinforcement layers, leading to some slight bending of the specimen, which was almost fully compensated with ongoing crack formation. Therefore, it is concluded that in the case of single cracks, the effect of multiple layers and different spacing between these layers did not result in an unequal contribution of the layers towards force transfer, utilisation and crack width reduction. The significant influencing parameters remained the reinforcement ratio, as it governs the force necessary to induce cracks, the transfer length and therefore the crack spacing, and the transition from a single cracking stage towards a stabilised stage.
Close to the onset of stabilised cracking, another parameter gains importance, as the discussion in the previous section revealed. The spacing between the reinforcement layers and, therefore the capacity to transfer force, either led to almost no force transfer between two adjacent cracks in the case of small spacing or allowed for some transfer when sufficient spacing is provided. This was clearly the case for specimen CG1-2L+-static, as the local minimum strain values show visible differences in magnitude compared to the maximum strain values, despite the crack spacing being in a similar range compared with specimen CG1-2L-static (higher reinforcement ratio and almost no spacing between the reinforcement layers). Nevertheless, the strain evolution for specimen CG1-2L-static showed some force transfer between the adjacent cracks as long as the crack spacing was at least equivalent to the yarn spacing of 38 mm. This is assumed to be the result of only a partial influence of the close grid spacing on the provided bond area. In a geometrical perspective of the cross-section of the fibre strand, only approximately one third of the strand's surface and therefore

bond area was influenced by the fibre strand of the other layer. Contrary to this partial interference of the fibre strands' bond area was the situation of specimen CG1-4L-static, where the bond area of the two inner layers was almost fully influenced by the outer two fibre strands. This resulted in almost no force transfer, as revealed by the strain evolution of the 3rd reinforcement layer of specimen CG1-4L-static in Figure 4.17, while the bottom reinforcement layer of this specimen still indicated some force transfer.

Summarising these observations, the spacing between reinforcement layers influences the bond capacity, as a "packing" of grid layers reduces the bond areas of the individual fibre strands. As a result, adjacent cracks lead to a reduced force transfer and contribution of tension stiffening. This influence was already addressed in a recommendation in the DAfStb Guideline [DAfStb24] to place textile grids with sufficient spacing, while the practical realisation has proven difficult, and a direct placing of reinforcement layers on each other is more efficient during construction. In this case, a reasonable consideration of the influenced bond capacity is required. In addition, the evaluations revealed that the inner layers performed in less force transfer compared to the outer reinforcement layers, while the maximum strain values were approximately equal indicating an

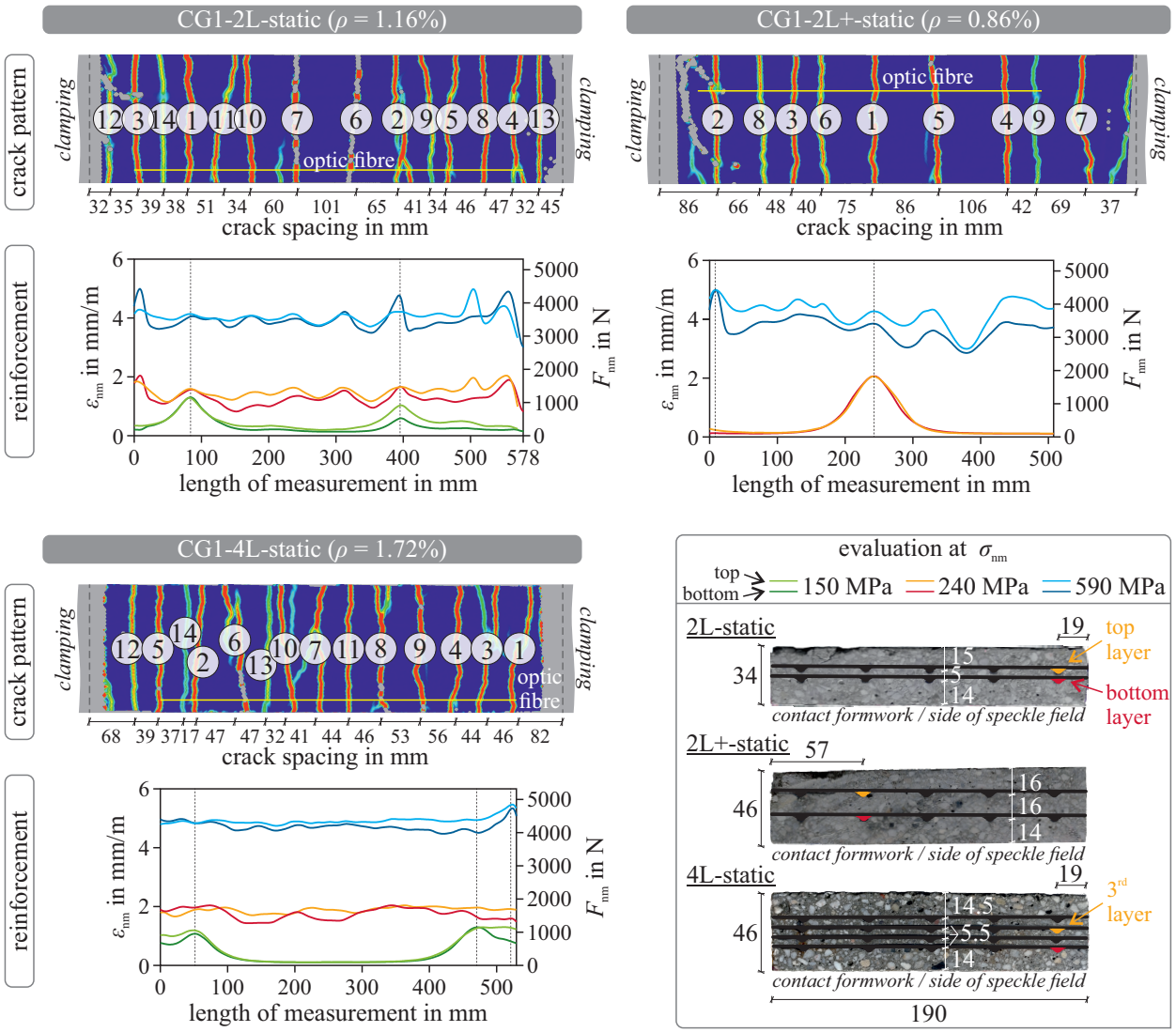


Figure 4.17: Evolution of the reinforcement strain at two selected grid layers with the corresponding crack pattern and at chosen load levels for purely statically loaded specimens

equivalent activation in the cracks. This is particularly addressed when deriving an approach to predict the crack width in Section 5.5.1.

Bond and tension stiffening

While in the previous paragraph a qualitative evaluation of the force transferred and the bond capacity was introduced, a quantitative consideration is provided in the following. In Figure 4.18, the mean bond force and the tension stiffening factor β are related to the maximum reinforcement strain, focusing on one side of a selected crack per specimen and distinguishing between the two reinforcement layers, which are identical to the previous evaluation. In the case of the higher reinforced specimens CG1-2L-static and CG1-4L-static the transition of single cracks to an adjacent cracking stage occurred at low reinforcement stress and therefore at lower mean bond force F_{bm}, which was at most 1 kN (Figure 4.18a1+c1). For specimen CG1-2L+-static, the transition occurred at twice this value ($F_{\mathrm{bm}} = 2$ kN,Figure 4.18b1).

The enhanced bond capacity by adequate spacing between reinforcement layers in CG1-2L+-static, visualised in Figure 4.18b1, is further demonstrated by the continuous decline in the mean bond force for the transition from single cracks to the stabilised cracking stage with sufficient crack spacing. This behaviour is analogous to the observations made for specimens reinforced with a single layer, as shown, for example, in the case of specimen CG1-static-1 evaluated in Figure 4.8a1. In specimen CG1-2L-static, the bond force at the stabilised cracking stage is approximately half in value to that of specimen CG1-2L+-static, which is on the level of the specimens with a single layer. The overall low transfer of bond force in specimen CG1-4L-static of below 0.25 kN for the bottom reinforcement layer and the very low bond force (below 0.05 kN) of the third layer confirmed the previous observations of no significant bond capacity of inner reinforcement layers and

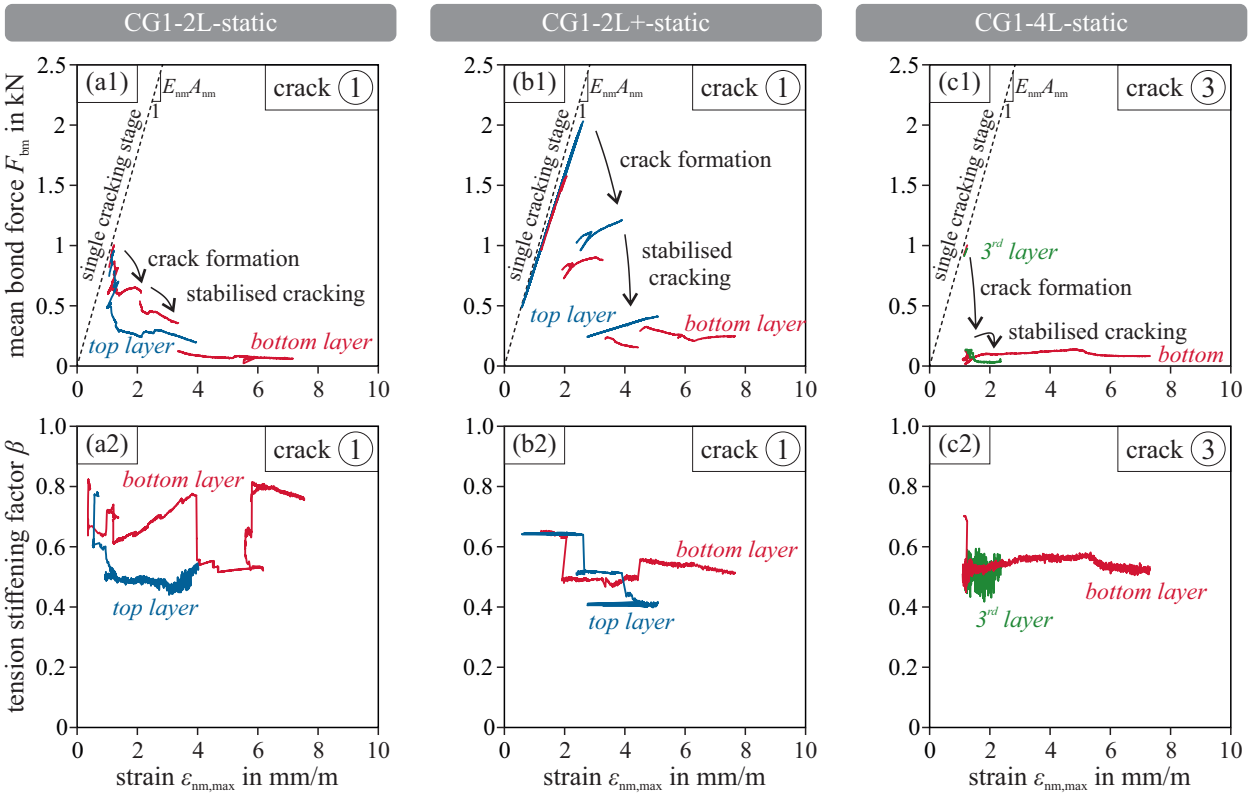


Figure 4.18: Evolution of the mean bond force and the tension stiffening factor in relation to the reinforcement strain in a crack at two reinforcement layers for purely statically loaded specimens

the lack of sufficient tension stiffening in highly reinforced specimens due to the very low crack spacing.

The evaluation of the tension stiffening factor is presented in the second row of Figure 4.18, which indicated a reduced or negligible force transfer and is in contrast to the aforementioned observations. The determined tension stiffening factor β suggested that tension stiffening remains a viable consideration. This is evidenced by the magnitude of β, which was a minimum of 0.4 (top layer if CG1-2L+-static in Figure 4.18b2), and, for instance, in the stabilised cracking stage of specimen CG1-4L-static, between 0.45 and 0.55 considering the bottom layer (Figure 4.18b3). As was highlighted in the preceding discussions at the end of Section 4.2.4, the hypothesis that the determination of β without taking into account the actual force transferred to the uncracked concrete between two cracks is misleading. The contribution of tension stiffening appears negligible due to the observed low bond forces and the low concrete tensile strength present at the formation of new cracks in the case of close layer spacing.

At last, addressing the question whether cyclic loading had a visible effect on the force transfer of multiple reinforcement layers, a short evaluation of the mean bond force evolution in relation to the maximum reinforcement stress is presented in Figure 4.19. One cyclically loaded specimen of each series is considered, focusing on an exemplarily selected crack at the stress level of formation of adjacent cracks prior to cyclic loading.
The preceding discussion on the impact of cyclic loading on a reduced force transfer indicated by the specimens with a single layer of reinforcement, is not reflected in this magnitude when considering the additional crack opening. The difference from the theoretical single cracking stage is only the result of the adjacent crack formation of the focused cracks present before the beginning of the cyclic loading.
The loading until failure following the cyclic loading phase showed no difference from the purely statically loaded phase. The overall transferred force had a comparably low magnitude. The resulting fine crack pattern did not provide for a sufficient transfer length, the magnitude of the mean bond force at the stabilised cracking stage was below 250 N for all three considered cracks and therefore specimen layouts.

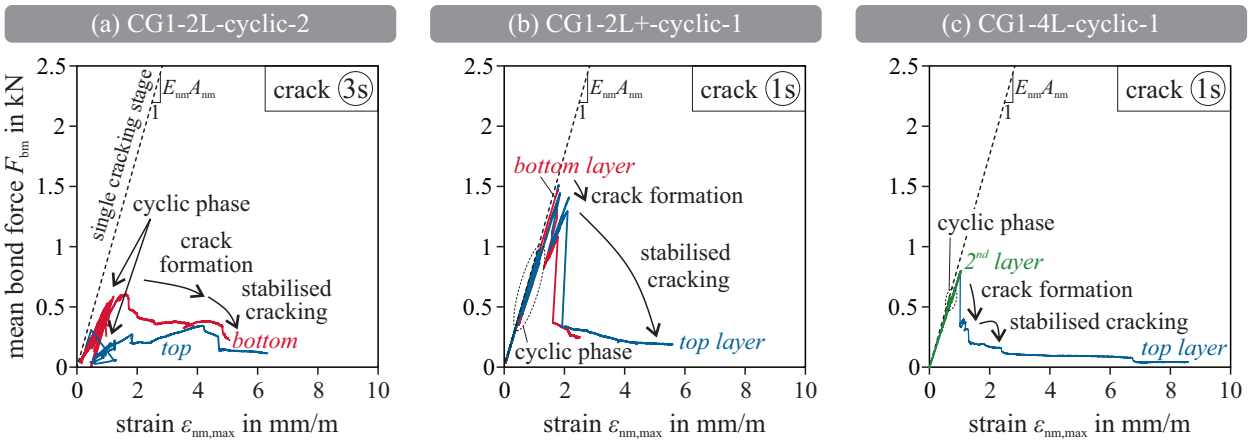


Figure 4.19: Evolution of the mean bond force in relation to the reinforcement strain in a crack at two reinforcement layers for cyclically loaded specimens

4.4 Influences of variations of the concrete matrix

As to this point, the focus of Chapter 4 was on providing a sound basis for the derivation of a crack width prediction approach, including a consideration of the influence of a multiple-layer reinforcement layout. In the following, two other factors, namely a higher concrete strength and the use of coarser aggregates, are discussed.

4.4.1 High-strength concrete

In general, the use of a concrete with a higher strength includes an increased tensile strength, which results in a larger force released upon crack occurrence. With regard to bond, the higher tensile strength implies also a higher bond capacity, hence, allowing for a transfer of higher forces between concrete and reinforcement in the uncracked concrete regions. These two effects counteract each other when focusing on the crack development. Contrary, the SPOc and COT tests evaluated in Chapter 3 revealed that a larger tensile strength did not subsequently lead to an increased bond capacity and a better performance of the reinforcement with regard to crack width limitation. Consequently, to address this topix in the scope of uniaxial tension and multiple cracking, two different carbon textile grids, namely CG1 and CG2, with a high-strength concrete (HSC) are considered. The identical test setup and procedure for cyclically loaded specimens described in Section 4.2.1 is used. The specifications of this series are provided in Table 4.3.

Table 4.3: Specifications of the UT tests for specimens with a high-strength concrete

index	reinforcement layout	f_{ctm} [MPa]	F_{sup} [kN]	$\sigma_{nm,sup}$ [MPa]	$\sigma_{c,sup}$ [MPa]	F_{inf} [kN]	$\sigma_{nm,inf}$ [MPa]
CG1-HSC	single layer $\rho = 0.66\%$	5.0	12.0	320	$2.1 = 0.42 \cdot f_{ctm}$	2.0	53
CG2-HSC	single layer $\rho = 0.44\%$	5.0	12.0	476	$2.1 = 0.42 \cdot f_{ctm}$	2.0	79

Elongation

The reinforcement stress-elongation curves plotted in Figure 4.20 reveal that for both investigated carbon grids, compared to the specimens with a normal-strength concrete (NSC), cracks occurred at higher loading and the number of cracks is lower (for NSC, cf. Figure 4.2). Both effects resulted in a higher load reduction after crack formation. The elongation increase due to cyclic loading was smaller despite the presence of a single cracking stage when compared to the specimens with NSC. In all six tests, rupture of the fibre strands was determined as failure. In the case of specimens CG2-HSC, this was at a significantly lower reinforcement stress compared to the mean tensile strength f_{nm}. This phenomenon is attributed to the uneven distribution of the applied force among the four fibre strands in the area close to the clamping at a load close to failure, as the crack pattern showed only a partial lateral crack propagation following an inclination.

The lower number of cracks and therefore the larger crack spacing led to a considerable distance of the stress-elongation curve from the pure elastic behaviour of the reinforcement, which indicated that tension stiffening is still existing at stabilised cracking. This is particular interest for reinforcement CG1, as the investigations with NSC revealed a different behaviour.

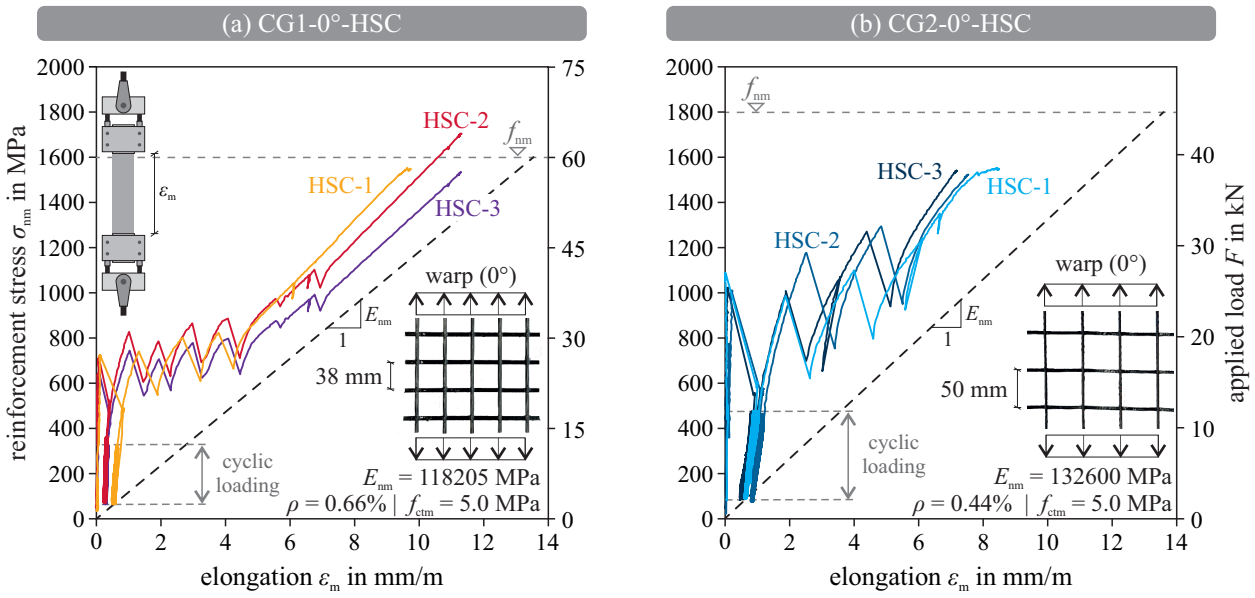


Figure 4.20: Elongation related to reinforcement stress and tensile force in UT tests of specimens reinforced with high-strength concrete

Crack width

Before discussing the low crack opening during the cyclic loading stage in detail, the following must be addressed. The higher tensile strength resulted in higher force released upon initial crack occurrence resulted in larger initial crack widths. In addition, as the superior load of 12 kN during cyclic loading was only utilising 42% of the mean concrete tensile strength, no additional cracks occurred due to concrete tensile fatigue.

The large initial crack width prior to cyclic loading exceeded 0.40 mm in five specimens, excluding specimen CG1-HSC-3. For the latter, the initial crack width was 0.19 mm, as the force prior to the crack formation was only 24 kN and 3.2 kN lower than in the case of the other specimens with CG1 (Figure 4.21). As previously mentioned, during cyclic loading no increase in crack opening for the three specimens of series HSC-CG1 was observed. This behaviour requires almost no damage of the concrete area close to the bond surface at superior loading, while during unloading, the slip is not fully elastically compensated. Some additional slip remained, continuously increasing the crack opening at inferior loading. The fact that almost no reduction of the bond capacity at superior loading due to damage of the bond area was observed is attributed to the higher concrete tensile strength improving the bond capacity of the concrete matrix, accompanied by the lower utilisation of the high-strength concrete compared to a normal-strength concrete. Of even more significance was the effect of the larger crack width and higher reinforcement stress prior to cyclic loading. This resulted in specimens HSC-CG1-1 and -2 in a crack opening that was not reached during the load cycles. The increase of bond damage and slip during the cyclic loading phase was of such low magnitude that almost no additional slip was measured at the end of the cyclic phase.

In the case of the three specimens HSC-CG2, the width of the single crack increased between 0.05 and 0.07 mm when referring to the mean load level of 7 kN. Contrary to CG1-HSC, the specimens HSC-CG2 showed a larger increase at the superior load level compared to the inferior load level during the cyclic phase, resulting in the "V"-shape of the stress-crack width evolution in Figure 4.21, complying with observations in the previous test series.

Generally, stabilised cracking was reached with fewer cracks compared to the corresponding NSC-series, while the number of cracks differed in specimens HSC-CG1 between four and seven. In contrast, specimens HSC-CG2 all showed only three cracks at the stabilised cracking stage. While

in this evaluation only the cracks in the investigation length were considered and cracks occurring in the clamping area were neglected, the actual number of cracks increases by two, as at each clamping a transverse crack was observed. The crack spacing for specimens HSC-CG1 was between 88 mm (2.3 times the yarn spacing y_{nm}) and 123 mm ($3.2 \times y_{nm}$). For the specimens HSC-CG2, the crack spacing was between 146 mm ($2.9 \times y_{nm}$) and 190 mm ($3.8 \times y_{nm}$). At this crack spacing, the provided transfer length is assumed to allow almost the full force transfer when considering the observations in the previous sections.

As performed for the previous test series in Sections 4.2 and 4.3, an average crack width is predicted using the simplified approach provided by Equation 4-1. Similar to most test series with CG1, except the specimens with a close reinforcement layer spacing, this simple approach fits well to the average crack width determined in the three tests HSC-CG1 at the crack formation stage and slightly overestimates the actual width at stabilised cracking. This is also the case for two specimens with CG2, namely HSC-CG2-1 and -3. For the other specimen, HSC-CG2-2, with the largest crack spacing, the simplified prediction approach significantly overestimates the average crack width measured in the test.

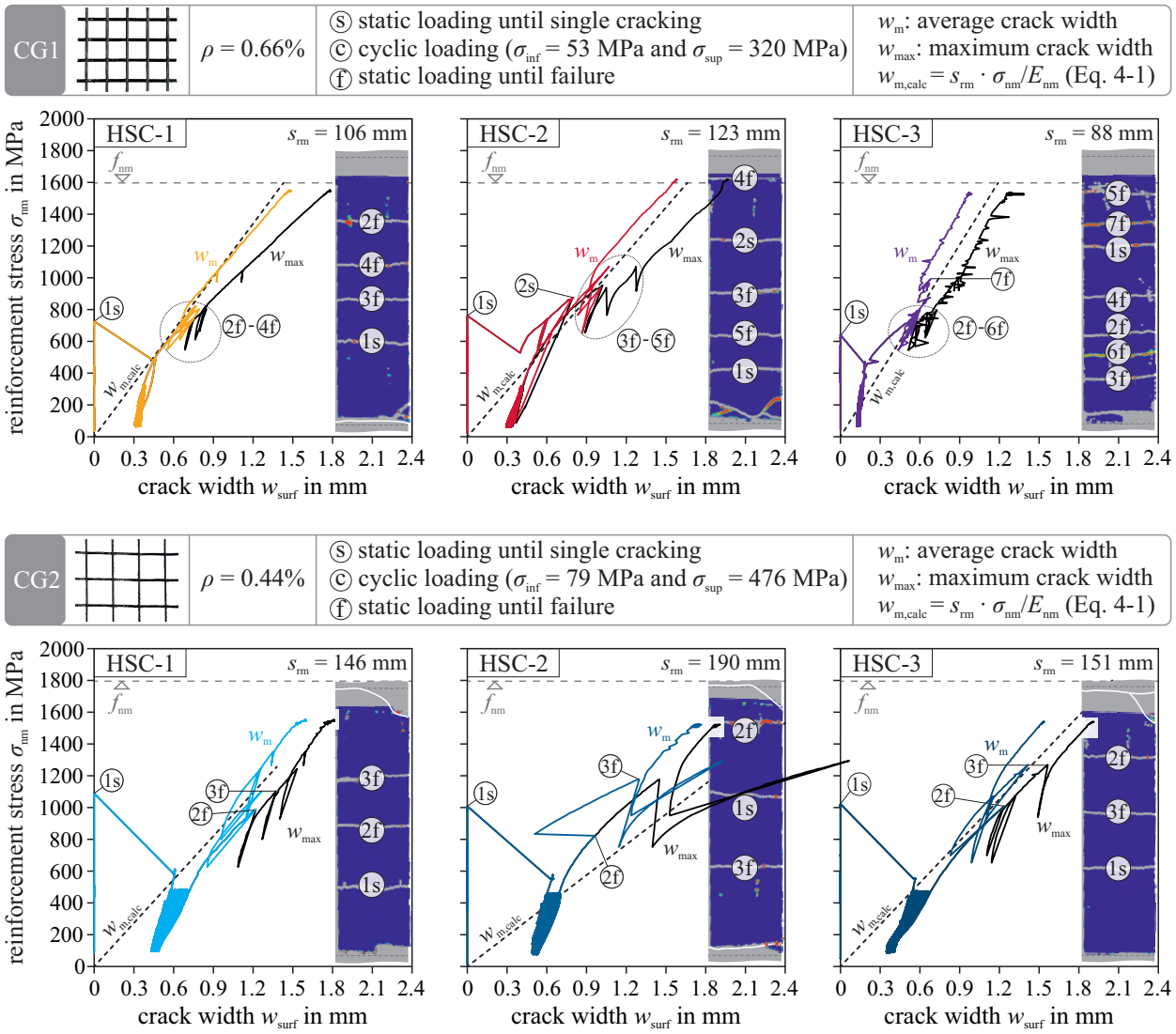


Figure 4.21: Average and maximum crack width evolution related to the reinforcement stress in the UT tests of specimens with high-strength concrete

Bond capacity

Finally, an evaluation of the bond capacity using the reinforcement strain measured by the fibre optic sensors is presented in Figure 4.22. Exemplarily, specimen CG1-0°-HSC-1 is considered, as the previous investigations showed some significant difference in crack opening and bond force transfer in comparison to the test series conducted using an NSC. In Figure 4.22, the mean bond force is plotted in relation to the maximum reinforcement strain and the transfer length. In addition, the mean bond stress-slip evolution is given. The initial crack, denoted as ①, is coloured in red for the evaluation of the left or "a"-side of the crack and in orange for the right or "b"-side. The other three cracks ② to ④ are coloured in grey and are only plotted for the mean bond force evaluation as a reference.

The bond force to strain evolutions of all cracks revealed the previously observed perfect representation of the single cracking stage (see Figure 4.22a). With crack formation, less force is transferred compared to the single cracking stage, but in contrast to the observations in the test series with an NSC, the transition to the stabilised cracking stage did not result in a significant reduction below 0.5 kN and remained above 1.8 kN. Considering the side b of crack ①, the occurrence of an adjacent crack led to only a slight reduction in bond stress when compared to the single cracking stage. The major reason for this behaviour is the larger crack spacing resulting from the high concrete tensile strength, which provided for a sufficient transfer length. This is visualised in Figure 4.22b, where almost no transfer lengths below the yarn spacing y_{nm} of 38 mm were determined. For the highlighted crack ①, the evolutions show that larger mean bond forces above 3 kN were transferred at lengths of approximately 100 mm ($\sim 2.6 \times y_{nm}$). During cyclic loading, the transfer lengths remained almost constant, as confirmed by the observed low crack openings (see Figure 4.21). The evaluation also shows that at the inferior load level, no reduction in the transfer length occurred. Consequently, the slip also did not decrease at this loading regime, as shown in Figure 4.22c. The stress values dropped at the occurrence of cracks, as, due to the displacement-controlled test setup, the applied force was reduced. At these stress drops, the slip decreased only slightly, indicating a large proportion of remaining plastic slip. Due to the sufficient transfer lengths, no drop to almost zero bond stress occurred.

The observations showed that the main influences of a high concrete strength in comparison to a normal-strength concrete are the following: the force released upon cracking is larger due to the higher tensile resistance, which led to larger forces released and a larger width of the newly occurred crack. In addition, the crack spacing is larger. Therefore, larger forces are transferred and

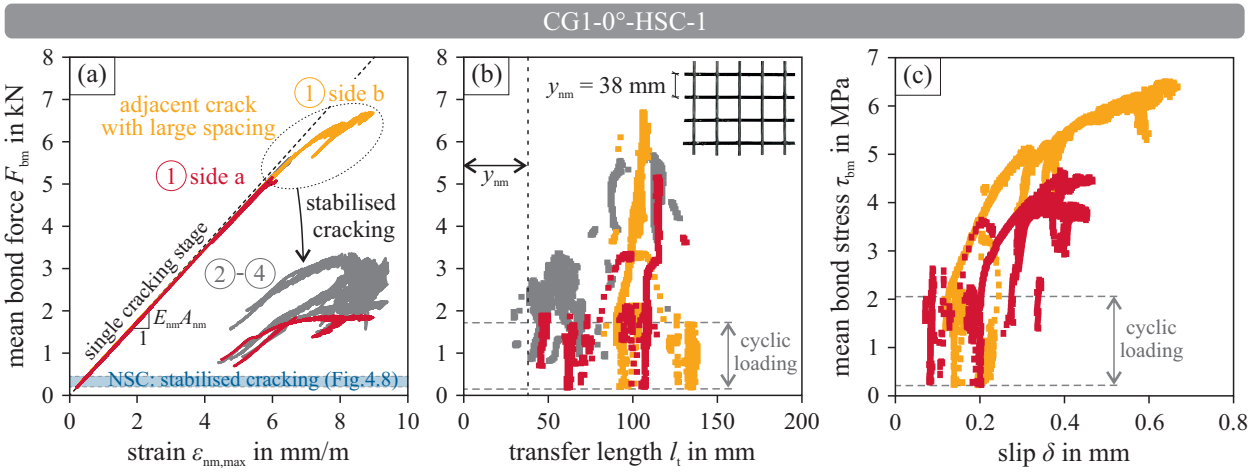


Figure 4.22: Evolution of the mean bond force and the mean bond stress in relation to the maximum reinforcement strain, the transfer length and the slip in specimen CG1-0°-HSC-1

the contribution of tension stiffening is more pronounced. In contrast, the bond capacity is assumed not to be influenced by the concrete strength, as already revealed by the COT tests in Section 3.4.3.

Consequently, when addressing a crack width prediction approach for HSC solely the determination of the spacing for adjacent cracks requires consideration. The bond capacity is adopted from NSC and therefore must not be modified.

4.4.2 Maximum aggregate size of 16 mm

The second parameter considered in this section is the use of coarser aggregates in the concrete mixture, referring to a larger maximum aggregate size. Most structures using non-metallic textile reinforcements do not use aggregates exceeding 8 mm in size, due to either the close mesh spacing or a low concrete cover, which do not prove to be feasible with larger aggregate sizes. Contrary, using larger aggregate sizes reduces the amount of cement required, and the greenhouse emissions of the concrete. Furthermore, this allows the use of established concrete mixtures in the construction industry, pushing the application of non-metallic textile reinforced concrete. Coarser aggregates are also accompanied by improvements in the structural capacity, when for example addressing the shear capacity, which depends on aggregate interlocking and therefore the coarseness of the shear crack surfaces (e.g. reported in [Bie21a]).
The test setup used for investigating the influence of coarser aggregates was identical to the one described in Section 4.2.1, only the concrete cover was increased to adapt for the use of a maximum aggregate size $d_{g,max}$ of 16 mm. The concrete cover was changed to 23.5 mm on both sides, with the thickness of the specimens increasing to 50 mm. Keeping the amount of reinforcement constant with respect to the previous test series, the larger concrete cover leads to a lower reinforcement ratio between 0.27 and 0.54 %. For the reinforcement CG1, CG2 and GG, a single uniaxial tensile test with a purely static loading was conducted. The saw-cuts obtained after testing visualise the cross-sectional layout, as shown in Figure 4.23.

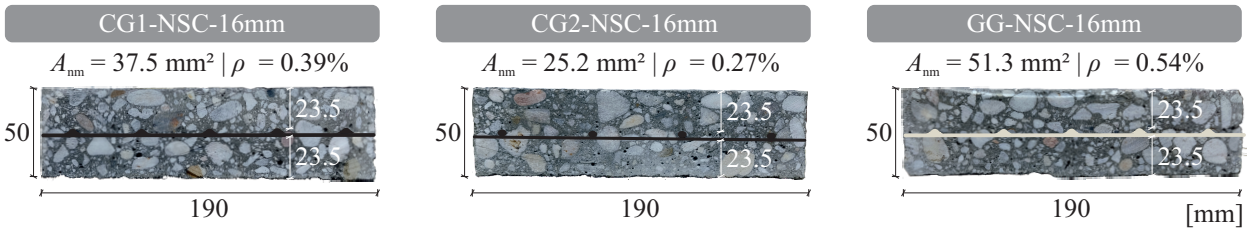


Figure 4.23: Cross-sectional layout of the tests with a maximum aggregate size of 16 mm.

Elongation
A reduced reinforcement ratio inevitably resulted in a smaller number of cracks, larger crack spacing and crack widths as well as higher forces required to induce cracks, which also increased the force reduction occurring upon crack formation. This is shown in the reinforcement stress-elongation evolutions plotted in Figure 4.24, in comparison with the previously shown test series having a concrete cover of about 13.5 mm and are additionally provided as grey lines in both figures. The increased concrete cross-section is particularly significant in the case of GG-16mm, in which the force at initial crack occurrence was approximately twice in value at 22.5 kN compared to the series tests with $d_{g,max} = 5.6$ mm. As a result, the widths of the two initial cracks were extremely large.

In general, the comparison of the two different aggregate sizes shows no influence on the failure type and failure load. The textile grids in the specimens with $d_{g,max} = 16$ mm performed similarly,

all three tests showed a rupture of the fibre strand at loads also determined in the tests with $d_{g,max} = 5.6$ mm. For all three specimens with a maximum aggregate size of 16 mm, the elongation during crack formation was similar or lower in magnitude compared to the specimens with 5.6 mm. Due to the lower number of cracks, the crack width was larger in the specimens with $d_{g,max} = 16$ mm. In specimen CG1-16mm, five cracks in the investigation length were detected, and for specimen CG2-16mm three cracks occurred. This number is similar to the number of cracks determined in the specimens with the high-strength concrete. In the specimen with the GG, in total, eight cracks occurred due to the higher reinforcement ratio compared to the specimens with CG.

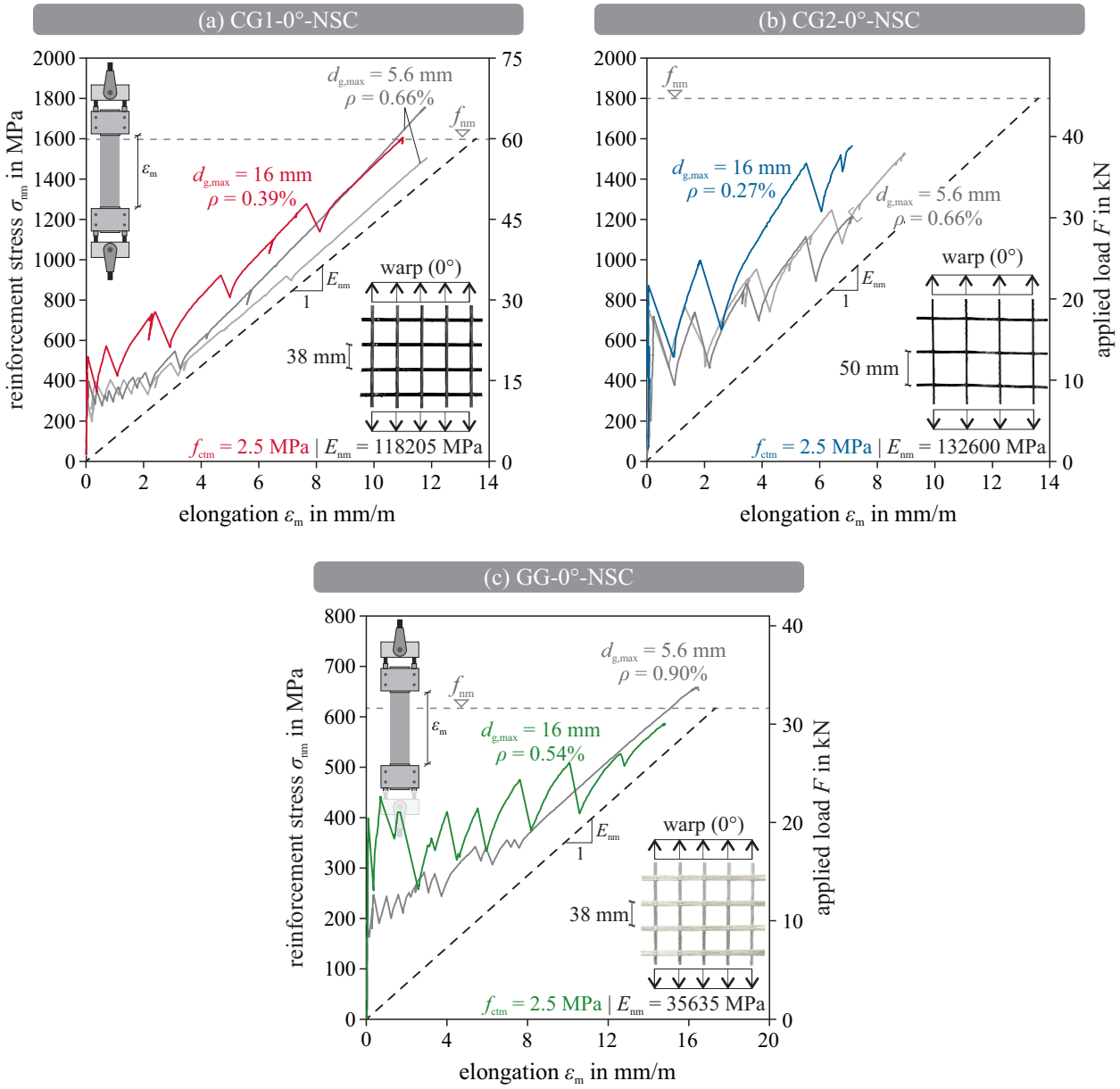


Figure 4.24: Elongation related to reinforcement stress and tensile force in uniaxial tensile tests of specimens with a concrete having a maximum aggregate size of 16 mm

Crack width

As done for all other test series, the average and maximum crack widths are evaluated in relation to the reinforcement stress. For the three tests with $d_{g,max} = 16$ mm the curves are plotted in Figure 4.25. For all three specimens, the crack width of the initial crack exceeded a width of 0.4 mm before the second crack occurred. In the case of specimen GG-16mm, the occurrence of

the second crack resulted in a significant immediate opening of crack ② to above 1.2 mm, while the initial crack closed by approximately half its width to 0.25 mm. Apparently, the close location of crack ① to the clamping resulted in a better bond capacity and therefore a reduced crack opening, which was then compensated for by the excessive opening of crack ②.
Even at large reinforcement utilisation close to the mean tensile strength f_{nm}, at least one additional crack formed in each specimen, resulting from the low reinforcement ratio, which required larger forces to induce another crack. The low number of cracks observed in the specimens with a carbon grid led to an average crack spacing of 117 mm in specimen CG1-16mm ($3.1 \times y_{nm}$) and of 147 mm in specimen CG2-16mm ($2.9 \times y_{nm}$). In the specimen GG-16mm, an average crack spacing of 65 mm was determined, being 1.7 times the yarn spacing.
Considering the simplified approach in Equation 4-1 to predict the average crack width $w_{m,calc}$, the evaluation in Figure 4.25 shows a good fit to the test data in the case of carbon grids as previously shown for the specimens with $d_{g,max} = 5.6$ mm in Figures 4.4 and 4.5.
Overall, the behaviour in the uniaxial tensile tests for the specimens with a maximum aggregate size of 16 mm, with regard to elongation and crack width evolution, was similar to that found in the specimens with a 5.6 mm maximum aggregate size.

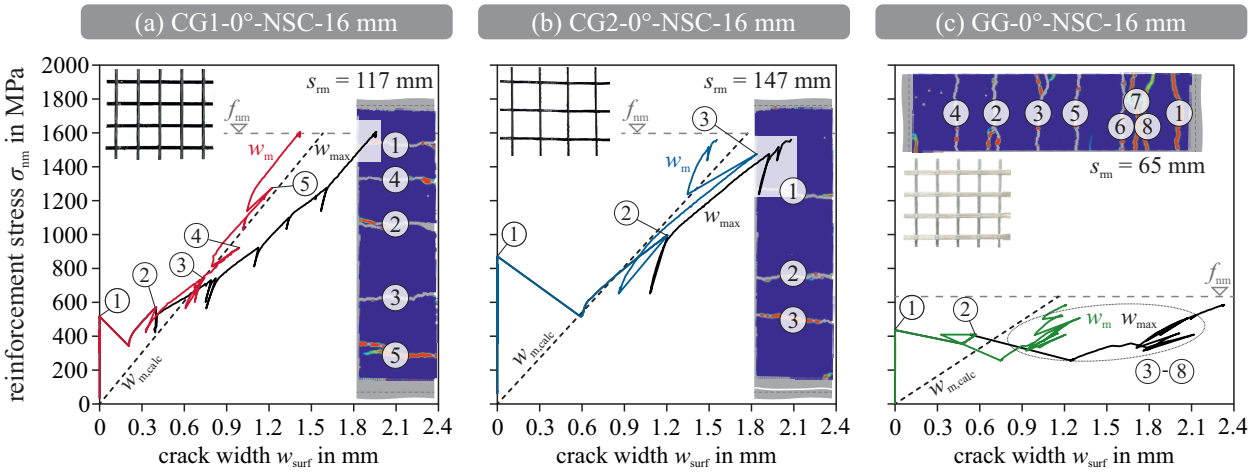


Figure 4.25: Average and maximum crack width evolution related to the reinforcement stress in the uniaxial tensile tests of specimens with a maximum aggregate size of 16 mm

4.5 Summary

The experimental campaign conducted was designed to facilitate a more profound understanding of the behaviour of non-metallic textile-reinforced members subject to uniaxial tension in a well-conditioned state. The investigations on the bond behaviour using fibre optic sensors, established a substantial basis for the identification of the primary factors influencing crack development. The following summary outlines the general observations and conclusions that were derived from the investigations, differentiating between the five major factors that were considered.
The **type of reinforcement** revealed, as expected, the most pronounced influence on the bond behaviour. The surface of the textile grid facilitates substantial force transfer via the bond mechanisms of friction and mechanical interlocking with the occurrence of slip. In the case of interlocking, this is provided by local undulations at intersecting fibre strands and from the waviness (global undulations) of the fibre strands. While some force transfer resulting from adhesion was identified, the influence of adhesion was marginal. Consequently, the bond capacity of each reinforcement type differs and is dependent on the transfer length provided, which is of particular interest in the

case of close crack spacing, and the reinforcement utilisation. It was determined that, for instance, in the case of CG1, a close spacing of adjacent cracks or a high utilisation of the reinforcement resulted in straightening and the shearing off of the local undulations. As a consequence, these undulations were no longer able to contribute to the force transfer. Consequently, the contribution of the uncracked concrete sections to a reduced elongation, referred to as tension stiffening, is also dependent on the crack spacing and reinforcement utilisation.

Cyclic loading, conducted with 200,000 cycles at a serviceability loading regime, resulted in a substantial increase in the crack opening in the case of a single layer of reinforcement and a normal-strength concrete. In particular, when no new cracks formed, the additional opening was significant. In certain test series, new cracks formed during the cyclic loading regime due to concrete tensile fatigue. This phenomenon resulted in a reduction of the overall crack width increase, as the increased number of cracks allowed for a distribution of the additional elongation resulting from cyclic loading. Concrete tensile fatigue and the occurrence of new cracks during cyclic loading proved to be of no negative concern with regard to additional crack opening. In the case of high-strength concrete or multiple reinforcement layers, which consequently result in higher reinforcement ratios, the influence of the cyclic phase on additional crack opening was found to be less pronounced. Furthermore, in the case of a single cracking stage, the reduced bond capacity resulting from cyclic loading had a substantial impact on the crack opening due to the increase in transfer length. In comparison, for adjacent cracks the reduced force transfer did not lead to these large crack openings. Furthermore, the presence of additional cracks with a homogeneous crack pattern ensured a more uniform distribution of overall elongation across these cracks. Consequently, single cracks necessitate explicit consideration of cyclic loading, even in circumstances where there is low utilisation of the reinforcement, as is the case at the serviceability state.

Multiple layers of textile grids significantly influenced the crack development in the investigated specimens. In general, higher reinforcement ratios resulted in reduced crack widths, with a greater number of cracks occurring and greater resistance to additional crack opening during cyclic loading. Nonetheless, it is imperative to consider the arrangement of the reinforcement layers, specifically whether they are positioned directly on top of each other or with adequate spacing between them, which was in the investigated case equivalent to the concrete cover of approximately 13 mm. The latter configuration was found to offer improved bond capacity, with an enlarged surface area leading to an increased transfer length and, consequently, a larger contribution of tension stiffening. It is therefore necessary to consider the spacing between multiple reinforcement layers in order to adequately represent the actual force transfer and the occurring slip.

High-strength concrete showed no superior bond capacity in comparison to specimens with a normal concrete strength at short-term loading. In accordance with the observations made in the SPOc and COT tests Chapter 3, the higher concrete tensile strength did not improve the force transfer. In addition, the elevated forces that were released upon the occurrence of a crack resulted in a large initial opening and a decrease in the number of cracks. The latter was the result of an increase in transfer length in the case of adjacent cracks, as the crack spacing was larger compared to specimens with a normal-strength concrete. During the cyclic loading phase, the crack width exhibited marginal increases, attributable to reduced utilisation of the concrete, resulting from the higher concrete tensile strength with no concrete tensile fatigue failure. Consequently, a high-strength concrete led to larger crack spacing and reduced additional crack opening during cyclic loading, with no differences in the bond capacity revealed when compared to a normal-strength concrete.

Using a **maximum aggregate size of 16 mm** did not result in any alteration in the crack width development under conditions of a purely static loading regime. It is therefore concluded that the utilisation of larger aggregate sizes does not necessitate an adaptation in terms of a crack width prediction.

5 Prediction of crack width in the case of uniaxial tension

In order to predict the crack width following a physically based consideration of the strain evolution of both reinforcement and concrete along the transfer length, it is necessary to account for a feasible representation of the slip-dependent bond stress evolution. The experimental characterisation campaigns of single-sided pull-out tests (SPOc) and crack opening tensile tests (COT) outlined in Chapter 3 are utilised to derive an analytical description of the force-displacement relation (Section 5.2.2). This description accounts for the force transferred from the reinforcement to the concrete along the transfer length and allows for the derivation of either simplified formulations (Section 5.3) or explicit formulations (Section 5.4) to obtain the required bond stress-slip relation or bond stress-crack opening relation. In the case of the explicit formulations, the physical interaction between both composite materials is considered in a representation of the two test setups. The subsequent derivation then enables the establishment of the analytical formulation of the mean value of bond stress, dependent on the considered reinforcement and its unique bond behaviour. This is achieved by incorporating the contribution of tension stiffening.
In Section 5.5.1, the methodology with explicit formulations are introduced in a physically based model to predict the crack width and are validated by utilising the results obtained from the uniaxial tensile (UT) tests in the context of a single crack. As the characterisation tests represent a single crack allowing continuous propagation of the transfer length, the model is extended to address the different behaviour occurring for adjacent cracks and therefore represents the stabilised cracking stage (Sections 5.5.2 to 5.5.4). This requires the prediction of crack spacing and a consideration of the different bond behaviour. As observed in the UT tests, this is of particular interest in the case of close crack spacing where a significantly reduced bond capacity was found. Furthermore, the impact of specific textile grid characteristics, namely the elliptical cross-sectional geometry and the arrangement of multiple layers of reinforcement with minimal spacing, is addressed. The final consideration concerns with the impact of cyclic loading on the opening of existing cracks, as outlined in Section 5.6. The aim is to quantify the increase in crack width in response to the applied load cycles, taking into account the reduction in bond capacity.
To summarise, the objective of this chapter is to present a methodology for predicting the crack width in concrete members reinforced with textile grids. The methodology takes into account the individual bond capacity of the reinforcement, the cracking stage, and the influence of cyclic loading at the serviceability limit.

5.1 Revising key aspects of the bond behaviour of non-metallic textile reinforcement

In advance to the derivation of a description of the bond behaviour, the bond mechanism of textile grids contributing to the force transfer are revised. Therefore, four principal phases are introduced based on the observations made, in particular during the COT tests in Section 3.4. These four phases are visualised in Figure 5.1. The area at which the bond mechanisms are acting is referred to as l_b and is the bond length or transfer length. In the first phase, force is transferred by adhesion only, similar to all reinforcement types and materials. In the case of an additional treatment of the textile surface, for example, using a sand coating, the adhesive force is increased. Independently from the occurrence of cracks, adhesion is always present in the areas where no slip is occurring. In Figure 5.1, the adhesion is represented by the magenta coloured rhombuses. With the occur-

rence and visible opening of a crack, in general, the force is too large to be transferred solely by adhesion. Therefore, adhesion fails in the corresponding area, marking the second phase.
The force transfer mechanisms resulting from undulations are differentiated in a global part, which addresses the continuous waviness of the fibre strand, and the local undulations, which occur at the intersection of longitudinal and transverse fibre strands. Undulations allow for a force transfer by applying contact pressure on the concrete. A sufficient force transfer by contact pressure requires a certain resistance of both the concrete and the reinforcement material. In Phase 2, the bond length may not reach the intersection of the first transverse fibre strand and force is solely transferred by friction F_{fric}, contact pressure resulting from global undulations F_{p} and adhesion.
With increasing force applied, the bond length propagates and includes local undulations, which is referred to as Phase 3. Mechanical interlocking occurs at the local undulations, denoted as F_{un}. In some textile grids, the contribution is significant, as revealed for CG1. With the resulting deformation of the longitudinal fibre strand, some areas of the strand are no longer in contact with the concrete due to the fibre strand waviness, leading to a partial failure of the other bond mechanisms, namely of friction and contact pressure. In Figure 5.1, this is highlighted in Phase 3 for the areas behind the local undulations. The deformation of the longitudinal strand leads to a passive contribution of the transverse fibre strand, as interlocking of the longitudinal strand with the fixed transverse strand occurs. The resulting force is transferred utilising the transverse strand. This effect is amplified by an increased contact pressure on the other side of the longitudinal strand, as the stiffness of the transverse strand redirects the uneven longitudinal strand with its larger cross-sectional area behind the intersection. The longitudinal strand itself is then pulled through the small channel surrounded by concrete and the transverse strand, which leads to a reduction in the cross-section and therefore to an additional pressure on the surrounding concrete. This mechanism is highly dependent on the transverse stiffness of the textile reinforcement and the waviness of the strands and eventually fails prior to concrete crushing, as shown by the COT and UT test series.
The lack of sufficient transverse stiffness and resistance at the intersection of the textile strand, plus the straightening of the fibre strand under increasing loading, eventually lead to a loss of most transfer mechanisms in the highly utilised sections (Phase 4). The transverse fibre strands are sheared off of the longitudinal strand. Neither a significant contribution of friction is provided nor contact pressure is activated, as either the undulations are diminished due to the straightening of the fibre strand or an abrasion of the concrete has occurred. In the case of single cracks, the local failure of the bond mechanism is compensated by the less utilised areas further away from the crack surface. In the case of adjacent cracks with close crack spacing, the local failure cannot be

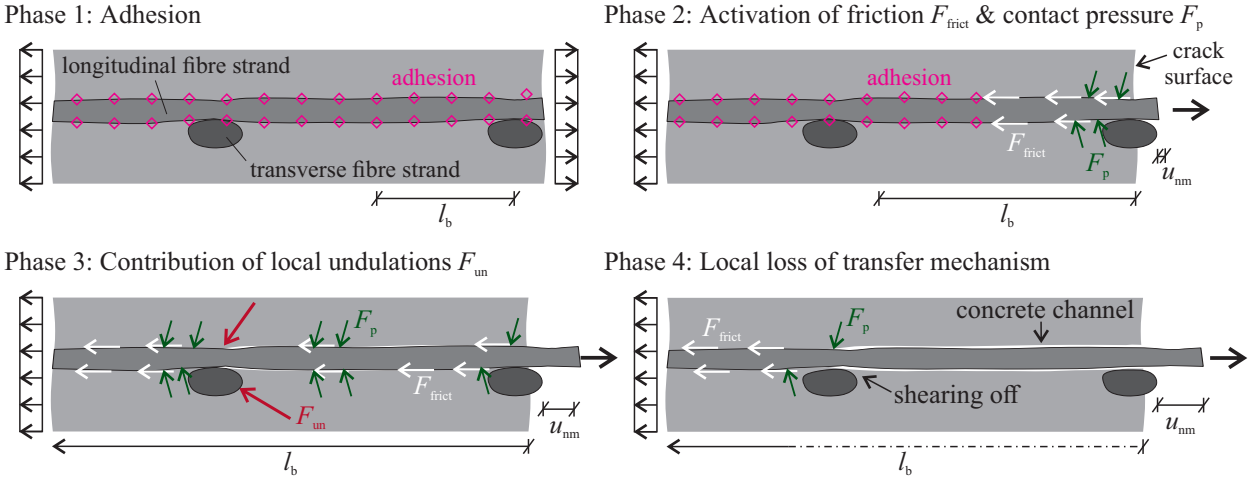


Figure 5.1: Phases of force transfer at a crack for textile grids

compensated. The local bond area is already damaged, so that with the occurrence of an adjacent crack in the vicinity to this area, no significant force transfer is possible any longer. As a result, most contribution of tension stiffening is lost and the reinforcement strain is not considerably reduced between two adjacent cracks. This phenomenon is more pronounced in textile grids where contact pressure is the dominant bond mechanism, which are textiles showing more waviness. The straightening and reduction of the cross-sectional area result in the described loss of contact to the surrounding concrete channel.

5.2 Experimentally based description of the bond behaviour

5.2.1 Approaches considering characterisation tests

Before proposing two methods in the following Sections 5.3 and 5.4 to obtain a characterisation of the bond behaviour in terms of an analytical formulation, the previously described experimental campaigns, namely single-sided pull-out tests of type C (SPOc) and crack opening tensile tests (COT), are summarised in the following with an overview provided in Table 5.1.

Single-sided pull-out tests type C provide as one main characteristic the maximum load anchored in a concrete specimen in relation to the embedded length. In addition, the failure modes of concrete splitting, pull-out of the fibre strand, and rupture of the fibre strand outside of the concrete member in relation to the concrete tensile strength, the concrete cover and the embedded length are considered. This information aims at identifying a certain failure mode, in particular for the ultimate limit state design.
The test setup also allows for the determination of the slip at the loaded and unloaded sides of the specimen, both of which are of importance when deriving a formulation of transferred force in relation to the deformation of the reinforcement. In order to derive force-slip relations an assumption of approximating the actual bond stress evolution along the reinforcement is necessary. Therefore, the changing cracking stage in an actual concrete member consisting of single cracks with the force-dependent transfer length and adjacent cracks with a point of no slip occurrence between two cracks and scattering transfer lengths on each side of the crack is not represented. Furthermore, when transferring the slip to a crack opening in a concrete member, a relation has to be set. In this thesis, the relation is in general assumed to be $s = w/2$. Other works (e.g. [Got71, Tas13] and code provisions (e.g. [MC20, DAfStb660]) consider an area of full bond plastification, where no notable force transfer occurs. This area is also referred to as *bond-free length*. Consequently, a different relation between slip and crack opening is assumed. This phenomenon remained undetected in the SPOc test setup, as the deformation of the concrete at the loaded side is prevented. Furthermore, plastification and significant damage to the bond area occur at larger crack openings, which are outside the scope of the serviceability state (see, e.g., [Fin16a, Sch21a]).
In addition, the influence of lateral pressure applied by the boundary condition of the SPOc specimen is worth mentioning. In general, lateral pressure improves the bond performance, while, in contrast, the soft lateral stiffness of textile fibre strands may lead to a state at which this influence of pressure is insignificant. With larger embedded lengths in the tests, the influence of the pressure cone is reduced as it affects only the bond area close to the support of the thin concrete specimens.
The experimental campaign in Section 3.3 clearly highlighted another important fact. The test results in a series tend to scatter largely when determining force-slip relations, because of the small specimen dimensions and the sensitivity regarding a perfect test conduction. This results in a major disadvantage when the test results are used to determine an experimentally based characteristic material value.

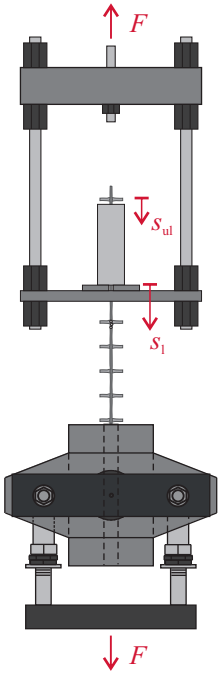
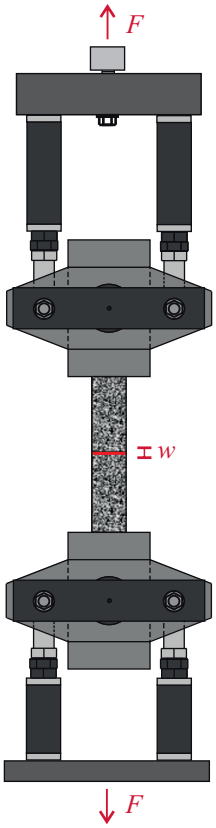
Crack opening tensile tests, on the other hand, directly provide a force-crack opening relationship for the single cracking stage. Neither a consideration of the relation between measured slip and crack opening nor the development of the bond length or the bond stress evolution is required to derive an approach for predicting the crack width using proposals, such as [MC20, EC2NAD, DAfStb24]). Nevertheless, some limitations are introduced with the test setup in Section 3.4. Firstly, only a single cracking stage is represented. Following the assumption that adjacent cracking is characterised by a crack pattern with crack widths below the single cracking stage at equivalent reinforcement stress values, this approach is feasible but slightly conservative. On the other hand, as the description of the force transfer mechanisms in Section 5.1 highlighted, this assumption has to be validated regarding a close crack spacing. Secondly, when the contribution of tension stiffening is undetermined, any derived value of bond stress is only a mere calculative value without a mechanical sound basis and therefore does not represent a material characteristic. Thirdly, the cross-sectional design of the test specimens may provide for no full representation of the layout when compared to practical members. For example, the concrete cover remains unchanged in the COT setup and the width exceeds the transversal yarn spacing, leading to a lower reinforcement ratio compared to the practical member design. It is worth discussing whether the additional concrete cross-sectional area provided improves the actual bond capacity and if a derived calculative value is transferable to members with a significantly higher reinforcement ratio. Finally, the own COT tests only considered specimens with one single fibre strand and not a multiple reinforcement layer layout. All four limitations are checked in this chapter using the uniaxial tensile tests to validate the proposed methodology.

Despite the advantages and disadvantages inherent in the two described test setups, a relation of force to either slip or crack opening is obtained. This relation is, for example, approximated by a power-law approach of the experimentally obtained data as done in the following Section 5.2.2. Having established this approximation, two methods are introduced to characterise the bond behaviour as analytical expression, which are feasible to be implemented in a model predicting the width of a single cracking.

Method 1 refers to a simplified approach, assuming a constant value of bond stress along the bond length. In the case of pull-out tests the bond length is assumed to be equivalent to the embedded length, due to the lack of data allowing for a determination of the actual bond length. This consequently leads to unsatisfactory results when addressing the slip and force applied at the serviceability limit state, as the embedded length is a parameter set in advance by the test layout. The influence of the embedded length on the force-slip relation was highlighted in the experimental program using SPOc tests (Section 3.3). In an optimal case, no significant difference in the force-slip relation for different embedded lengths is determined. Nevertheless, the question arises as to which embedded length it seems to be appropriate to determine the mean value of bond stress $\tau_{\mathrm{bm}}(s)$. For example, one could evaluate only the embedded length in a SPOc test at which slip at the unloaded side occurred and the corresponding force. In contrast, the evaluation procedure using COT tests does not explicitly consider the bond length, the sole undetermined factor remains the tension stiffening factor β. As previously pointed out, this is the advantage of the COT test setup in comparison to pull-out tests.

Method 2 aims for a realistic representation of the actual composite behaviour. The test setups are represented in a physically based formulation describing the materials' displacements and the force transfer. By introducing a bond stress-slip relation, the test data is utilised to obtain an analytically derived formulation for the bond stress evolution. This allows for the determination of the bond length and the slip.

Table 5.1: Overview of methods to derive an expression of the bond stress as a material parameter for crack width prediction using the SPOc and COT test setups

	single sided pull-out test type C (SPOc)	**crack opening tensile test (COT)**
	cf. Section 3.3 and [DAfStb24]	cf. Section 3.4
test setup		
output values	- force F - slip at loaded side s_l and unloaded side s_{unl}	- force F - crack opening w
analytical formulation (e.g. power-law approach)	$F(s_l) = A_{SPO} \cdot s_l^{\alpha_{SPO}}$ (loaded side, cf. Eq. 5-1) $F(s_{unl}) = A_{SPO,unl} \cdot s_{unl}^{\alpha_{SPO}}$ (unloaded side)	$F(w) = A_{COT} \cdot w^{\alpha_{COT}}$ (cf. Eq. 5-2)
assumptions	- single cracking stage is decisve - focus on a single fibre strand - some influence of lateral pressure - tension stiffening undetermined - slip and crack width are related to each other (e.g. $s = w/2$) - in general: $l_b = l_e$	- single cracking stage is decisve - focus on a single fibre strand - tension stiffening undetermined, simplification: $\beta = 0$ - cross-section of specimen not representative when compared to actual members → low reinforcement ratio
Method 1: simplified bond stress evolution (cf. Section 5.3)	constant value of bond stress along the bond length	
Method 2: analytical formulation bond stress evolution (cf. Section 5.4)	$\tau_b(s) = C \cdot s^{\alpha} \rightarrow \tau_{bm}(w) = \frac{C \cdot w^{\alpha}}{2^{\alpha} \cdot (\alpha + 1)}$ (cf. Eq 5-13)	

5.2.2 Analytical description of the force-displacement behaviour

To utilise both methods, it is feasible to approximate the test data, for example by force-slip or force-crack opening relations. Considering the mean test curves of a series determined in Chapter 3, the introduction of an analytical description using the power-law approximation provided by KOENIG ET AL. [Kön96] allows for the representation of the observed non-linear behaviour. This is applied on the results of both characterisation test campaigns.

SPOc tests provide for a pull-out force-slip relation, which is described using two parameters:

$$F_{\mathrm{b}}(s_{\mathrm{l}}) = A_{\mathrm{SPO}} \cdot s_{\mathrm{l}}^{\alpha_{\mathrm{SPO}}} \text{ [N]} \tag{5-1}$$

In general, the parameter A_{SPO} considers the maximum pull-out force, as higher values of A_{SPO} are attributed to larger pull-out forces determined in the tests. The parameter α_{SPO} represents the rate of force increase in relation to the slip at the loaded side s_{l}, in a mathematical expression, with lower values of α_{SPO} indicating a steeper increase in pull-out force. This approach is limited to increasing force at increasing slip and is incapable of representing a pull-out behaviour. In the few cases where pull-out occurred following a non-linear increase in force, this was at a slip greater than that covered by the serviceability limit state.
Often a direct derivation of a bond stress description is performed with the assumption that the transfer length is equal to the embedded length, which is in fact only permissible for one single value of force, namely the exact moment when slip is measured at the unloaded end. However, for rebars the bond stress evolution along the embedded length is well approximated by a constant approach when using of small embedded lengths, where slip occurs at the unloaded side at a very low value of applied force. As textile grids do not show this kind of homogeneous bond surface when focusing of small embedded lengths, a sufficient length is required to justify a similar approximation. This length was determined to be at least three times the yarn spacing in the SPOc test series. On the other hand, using pull-out tests with long embedded lengths would provide for conservative and unrepresentative derived values of bond stress due to an overestimation of the actual transfer length.

To derive the parameters A_{SPO} and α_{SPO} for each test series, a curve fitting approach using a non-linear least squares method to fit the power-law approach in Equation 5-1 was utilised on the mean pull-out force-slip curves. No explicit consideration of adhesion was implemented, which would require an additive term considering the force transferred by adhesion at zero slip. However, adhesion was considered implicitly by the used curve fitting approach as no neglecting of the force attributed to adhesion was done. For further investigations provided in the following, the calibration parameters A_{SPO} and α_{SPO} are averaged for series in which the calibration parameters had similar values. An overview of selected SPOc configurations is provided in Table 5.2, with the given limitation until which slip at the loaded side the approximation using Equation 5-1 is valid. The individual listing of the determined parameters A_{SPO} and α_{SPO} is provided in Table D.2.
The listing in Table 5.2 shows that no consistent values of the calibration parameters corresponding to the textile grid were derived. Solely for CG1, consistent values for $A_{\mathrm{SPO}} = 8200$ and $\alpha_{\mathrm{SPO}} = 0.5$ were found for the seven series with concretes having a maximum aggregate size of 5.6 mm and an embedded length of at least 114 mm. Still, the derived average values show some scattering for both calibration parameters as expressed by the coefficients of variation V_{x} of 7.6% and 11%, respectively. The coefficient of variation V_{x} is determined as average of the individual coefficient of variations V_{δ} within a test series following the concept in Annex D.8 of Eurocode 0 [EC0].

Table 5.2: Derived calibration parameters A_{SPO} and α_{SPO} and maximum value of slip for the validity of the analytical description in Equation 5-1 for selected SPOc configurations

textile grid	orientation	concrete strength	$d_{g,max}$ [mm]	l_e [mm]	A_{SPO} [-] (V_x [%])	α_{SPO} [-] (V_x [%])	$s_l \leq$ [mm]
CG1	0° + 90°	NSC + HSC	5.6	≥ 114	8200 (7.6)	0.5 (11.0)	0.8
CG1sc	0°	NSC	5.6	114	10000	0.88	1.0
CG2	0°	NSC	5.6 + 16	≥ 150	8000 (13.1)	0.72 (6.5)	1.0
CG3	0°	NSC	5.6	250	6100	0.73	0.4
GG	0°	NSC	5.6	114	6600	0.31	1.0

This clarifies two main problems when using the SPOc tests to derive a description of the bond force-slip relation and to utilise this description at the serviceability limit stage, e.g. for a crack width prediction approach. Firstly, a derivation is dependent on the embedded lengths considered and therefore underlays some uncertainty in terms of which embedded lengths were chosen in the test layout. In theory, as pointed out previously, the influence should not be of concern for comparison of different embedded lengths with regard to the pull-out force-slip relation, when the embedded lengths ensure the occurrence of slip at the unloaded side at some loading prior to failure. But, due to the acting of different force transfer mechanisms with different magnitudes along the fibre strand, which is not necessarily repeated after every transverse yarn, there is still some uncertainty provided by the mere material characteristic of the textile grid. This justifies the difficulty to determine average values of the calibration parameters for each grid. Secondly, the small and slender test specimens tend to provoke scattering resulting from the test preparation and conduction, which is partially compensated by a sufficient amount of specimens per series when focusing on an average value. For deriving a characteristic value or description, for example for a design approach, this significant scattering inevitably leads to very conservative values which do not represent the actual bond capacity, as reported e.g. in [Sch23b, Sch24a].

COT tests are evaluated using the identical approach. The well-defined test results, showing a considerably lower variation compared to the SPOc tests, are approximated as follows:

$$F_b(w) = A_{COT} \cdot w^{\alpha_{COT}} \text{ [N]} \tag{5-2}$$

The two calibration parameters A_{COT} and α_{COT} are derived again by curve fitting using a non-linear least squares method with the accuracy of the fitted curve expressed using the coefficient of variation V_δ, which are listed in Table 5.3 for each of the eight test series.
Addressing the parameter A_{COT}, the discrepancy in values between the normal-strength and high-strength concrete follows the previously discussed observations Section 3.4.3. For example considering CG1, the HSC showed a reduced bond capacity compared to the NSC series, which is followed by the lower value of $A_{COT} = 5500$.
The exponential parameter α_{COT} is identical for NSC and HSC with the reinforcements CG1 and CG2. In the case of CG3 and GG, the value of α_{COT} for the series with a high concrete strength is lower compared to the normal-strength concrete. Motivated to provide for identical values of α_{COT} independent from the strength, an adaptation of the best-fitted value for parameter α_{COT} is done, choosing α_{COT} to be identical to the value of the NSC series. This requires a re-derivation of the other parameter A_{COT}. The obtained coefficient of variation is at most 5% for all cases.

Table 5.3: Derived calibration parameters for an analytical description of the force-crack opening relation

index		A_{COT} [-]	α_{COT} [-]	V_δ [%]
CG1-0°	NSC	7000	0.59	1.2
	HSC	5500	0.59	0.9
CG2-0°	NSC	6200	0.71	0.5
	HSC	6300	0.71	0.7
CG3-0°	NSC	4300	0.77	1.3
	HSC	5000	0.67	4.2
		5200[1)]	0.77[1)]	5.0
GG-0°	NSC	6100	0.72	0.5
	HSC	5300	0.67	4.2
		5400[1)]	0.72[1)]	3.2

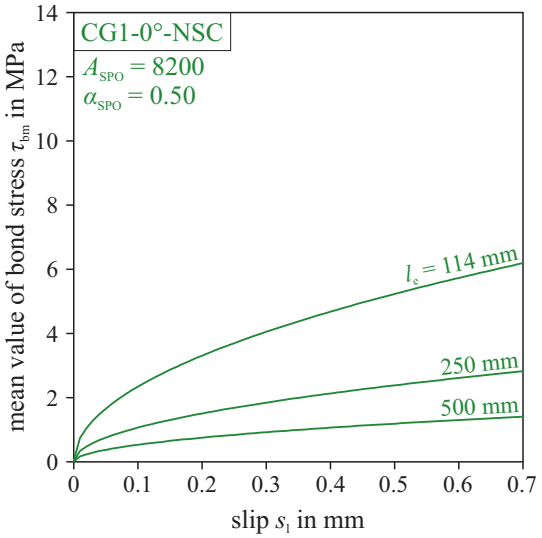
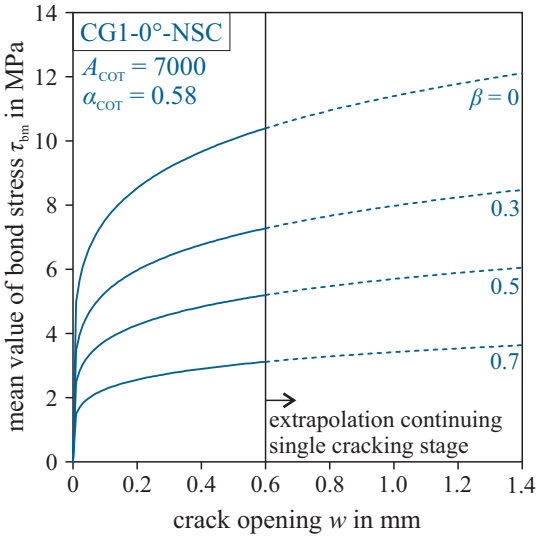
[1)] adapted curve fitting with presetting of α_{COT}

5.3 Method 1 – Simplified bond stress evolution

Having established the description of the test data with a power-law approximation, the bond stress is determined in Method 1 by assuming a constant distribution along the transfer length. In the case of the SPOc tests, force equilibrium with the required assumption of the transfer length being equivalent to the embedded length provides for an expression of the mean bond stress following Equation 5-3. Considering the calibration parameters A_{SPO} and α_{SPO} (cf. Table 5.2), the mean bond stress is exemplarily plotted for CG1-0°-NSC on the left-hand side of Table 5.4. As expected, the value of mean bond stress is lower when a larger embedded length l_e is considered, visualising the previously described dependency on the chosen embedded length.

For the COT tests, the approach of mean strain values for the single cracking stage given in Equation 2-18 is considered. For compliance between the slip-dependent bond stress and the crack opening-related force resembled by the power-law, it is assumed that twice the slip is equivalent to the occurring crack opening, because the measurement technique employed in the COT tests already attributed for a possible influence of a "bond-free" length. The obtained Equation 5-4 is utilised by considering the approximation of the force according to Equation 5-2 with the parameters A_{COT} and α_{COT} provided in Table 5.3. A graphical evaluation of Equation 5-4 for different assumptions of β is exemplarily done for the reinforcement CG1 and plotted on the right-hand side in Table 5.4. The validity of the COT tests is limited to a single cracking stage, which is not met by the conducted tests for larger crack widths above about 0.6 mm on average. Therefore, an extrapolation is performed as shown in Table 5.3. As evident, the mean value of bond stress is significantly dependent on the influence of tension stiffening represented by the factor β, which remains undetermined at this time. This highlights the importance of a profound assumption on the effect of tension stiffening, as the determined mean value of bond stress is significantly reduced in the case of a larger contribution of the uncracked concrete expressed by a higher value of β. Therefore, the determined mean value of bond stress must be paired with the corresponding value of β for further considerations (e.g. in code provisions) and is then solely a calculative value that does not represent an actual material parameter. For the determination of a resilient value of β, an approach such as followed in Method 2 is required.

Table 5.4: Mean value of bond stress utilising Method 1 and evaluation for reinforcement CG1

SPOc	COT
$\tau_{bm}(s_l) = \frac{F_b(s_l)}{U_{nm} \cdot l_e}$ (5-3)	$\tau_{bm}(w) = \frac{2 \cdot (1-\beta) \cdot F_b^2(w)}{E_{nm} \cdot U_{nm} \cdot A_{nm}^2 \cdot (1+\rho\alpha_e)}$ (5-4)
with $F_b(s_l) = A_{SPO} \cdot s_l^{\alpha_{SPO}}$	with $F_b(w) = A_{COT} \cdot w^{\alpha_{COT}}$
	

5.4 Method 2 – Physically based formulation of bond force transfer for single cracks

5.4.1 Overview of physically based representation of characterisation tests

Method 2 establishes a physically based representation of the SPOc and COT tests to explicitly describe the force-slip and force-crack opening relation. Consequently, this necessitates the implementation of an analytical framework in which the boundary conditions and the constitutive laws governing the materials' behaviour are taken into account. The principal consideration in this approach is the approximation of the bond stress evolution. An overview of different approximations is found in Figure 2.3. In the following, the power-law formulation of KOENIG and TUE, as stated in Equation 2-3, is considered.

The analytical framework of the setups of SPOc test and COT test is the representation of an elastic fibre, which corresponds to the textile reinforcement, in an elastic concrete matrix until macrocracking occurs, as visualised in Figure 5.2. The elastic material behaviours of reinforcement and concrete are linked by assuming a force transfer through bond. The bond stress is described in dependence on the slip $\tau_b(s(x))$. The slip is defined as the difference in displacement of reinforcement and concrete. Utilising deformation equilibrium and the boundary conditions, descriptions of the reinforcement displacement $u_{nm}(x)$ and the concrete displacement $u_c(x)$ are obtained. The boundary conditions in the two test setups differ. As a result, the displacement of the concrete matrix is zero at the loaded end for the SPOc test and at the unloaded end for the COT test. The variable x represents the location of evaluation, with $x = 0$ referring to the loaded side. The equa-

tions stated in the following are the final expressions of the explicit formulations evaluated for the occurring slip. The full terminology regarding the displacement of the reinforcement and concrete matrix and the derivation of the corresponding equations is provided in Appendix C.1.
Having established this framework, the formulations of displacements and force transfer are obtained for the SPOc test (Section 5.4.2) and the COT test (Section 5.4.3).

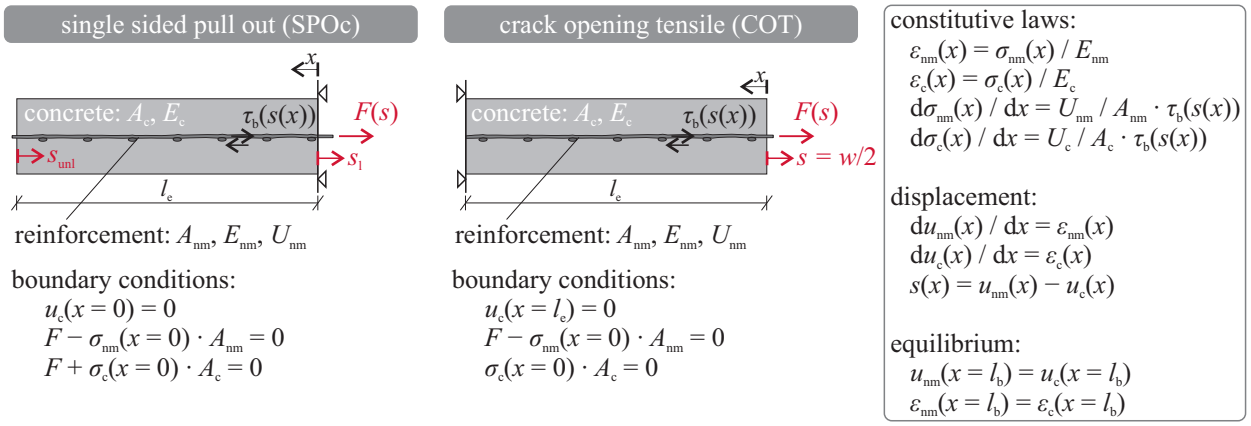


Figure 5.2: Analytical framework of SPOc and COT tests as basis for an explicit formulation of material displacements and force transfer

5.4.2 Representation of the SPOc test

Considering the SPOc test setup with a fixed displacement of the concrete matrix at the loaded side, the slip $s(x)$ is obtained by the difference between reinforcement displacement $u_{nm}(x)$ and concrete displacement $u_c(x)$. Utilising the differential equation of bond (cf. Equation 2-1) and introducing the case of the embedded length exceeding the bond length where no slip occurs, the slip is described as follows:

$$s(x) = \begin{cases} 0 & \text{for } x \geq l_b \\ \frac{1+\rho\alpha_e}{2 \cdot A_{nm} \cdot E_{nm}} \cdot \left[\tau_b(s(x)) \cdot U_{nm} \cdot x^2 + 2 \cdot F \cdot x + \frac{F^2}{\tau_b(s(x)) \cdot U_{nm}} \right] & \text{for } 0 \leq x \leq l_b \end{cases} \tag{5-5}$$

The bond length is determined to $l_b = F / (\tau_{bm}(s_l) \cdot U_{nm})$, resembling the distance required to transfer the force in the concrete. The mean bond stress $\tau_{bm}(s_l)$ is obtained as the integral of the bond stress evolution $\tau_b(s(x))$ over the occurring slip at the loaded side $s_l = s(x = 0)$. As apparent, the formulation in Equation 5-5 requires an assumption of the bond stress evolution, which addresses the real situation where the force transferred at each local point is dependent on the occurring slip. Therefore, a numerical approximation is required. In addition, a function of the bond stress $\tau_b(s(x))$ must be introduced to solve Equation 5-5.
The SPOc test provides for a force-slip relation, with the slip measured at the loaded side of the specimen. This relation was approximated in a power-law approach in Equation 5-1 with the parameters A_{SPO} and α_{SPO} determined for each test series, which are considered to introduce an explicit formulation of the bond stress evolution. Utilising Equation 5-5 and solely considering the slip at the loaded side $s_l(x = 0)$, the force F is substituted by the performed approximation of the test data according to Equation 5-1. The bond stress evolution $\tau_b(s(x))$ is then derived as a function of the slip at the loaded side of the concrete matrix

$$\tau_b(s_l) = \tau_b(s(x = 0)) = \frac{A_{SPO}^2 \cdot (1 + \rho\alpha_e)}{2 \cdot U_{nm} \cdot A_{nm} \cdot E_{nm}} \cdot s_l^{(2 \cdot \alpha_{SPO} - 1)}. \tag{5-6}$$

It becomes obvious that the derived Equation 5-6 is again a power-law expression. For simplicity in the upcoming evaluations, a step back in expressing the bond stress evolution is performed in the following, which uses the original indexation of KOENIG and TUE $\tau_b(s) = C \cdot s^{\alpha}$. The parameters C and α are therefore derived as

$$C = \frac{A_{SPO}^2 \cdot (1 + \rho \alpha_e)}{2 \cdot U_{nm} \cdot A_{nm} \cdot E_{nm}} \tag{5-7}$$

and

$$\alpha = 2 \cdot \alpha_{SPO} - 1\,. \tag{5-8}$$

The feasibility of this expression is demonstrated in the following by using the description in Equation 5-5 to determine the slip in a member representing the SPOc test, which is compared to the slip measured in the corresponding tests. Therefore, the bond stress evolution is expressed by the power-law approach in Equation 5-6 with the parameters A_{SPO} and α_{SPO} given in Table 5.2. The bond stress evolution, expressed as $\tau_b(s(x)) = C \cdot (s(x))^{\alpha}$, requires a numerical solution to solve the explicit formulation in Equation 5-5.

As the following small study aims only to show the feasibility of the described approach, a simplification was introduced to avoid a numerical solution. Hereby, the bond stress $\tau_b(s(x))$ at the corresponding evaluation point x was determined using the slip at the previously determined evaluation point $x-1$. Solely for the slip at the loaded side, the determined slip at the previous load step was considered. Each load step represented an increase of $F_{max}/450$. For the graphical interpretation given in Figure 5.3, the slip at the loaded side s_l and at the unloaded side s_{unl}, which is

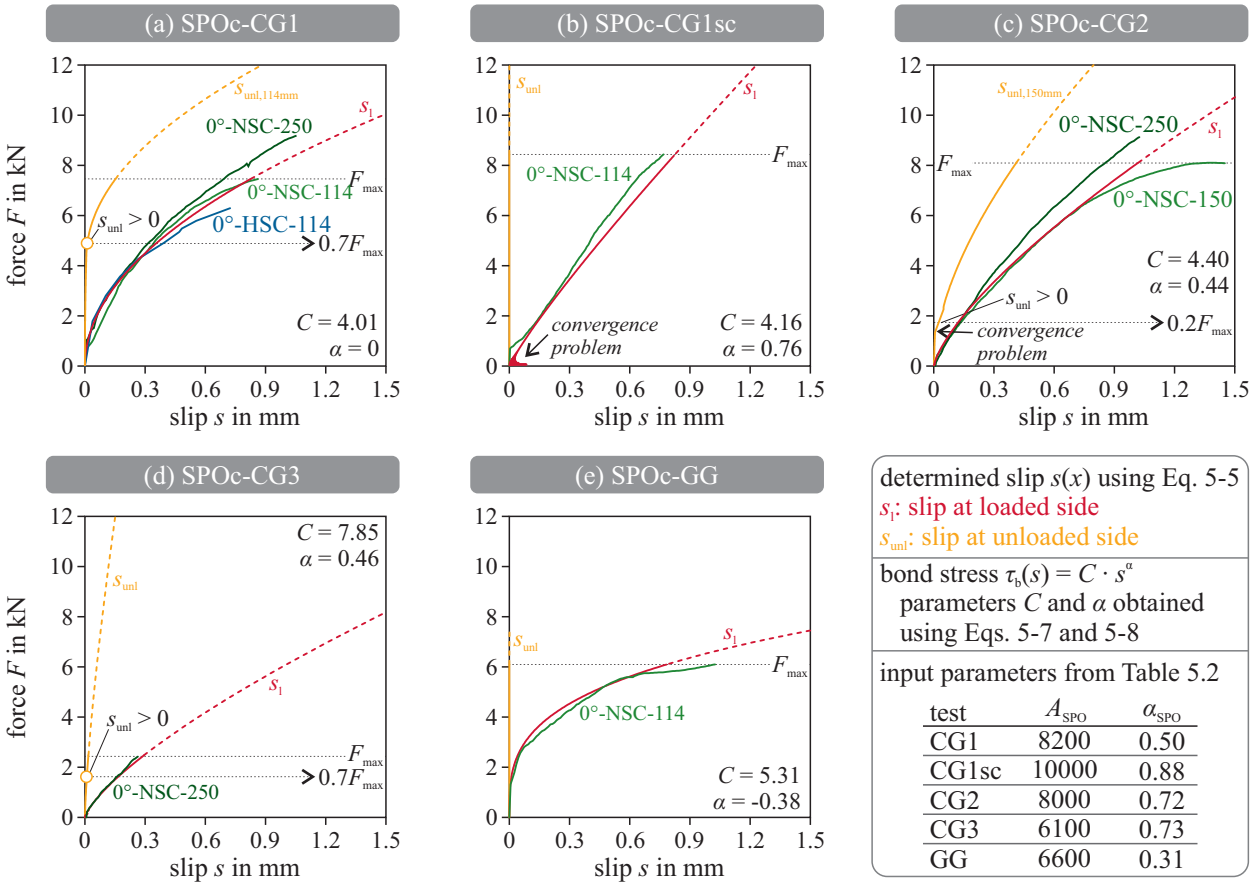


Figure 5.3: Modelling of the force-slip relation using an explicit analytical formulation to resemble the test data of selected SPOc test series

the slip at the end of the embedded length, are plotted. In Figure 5.3, the mean curves of selected test series of each investigated grid in the SPOc experimental campaign are shown as reference. Overall, Figure 5.3 demonstrates the accurate prediction of the force-slip relation when compared to the averaged curves of the selected test series. The discrepancies were observed as a result of variations in the parameters A_{SPO} and α_{SPO} within the series with the same textile grid. Considering the slip at the unloaded side, the start of slippage (for selected series with CG1 and CG3) or the cases of no slippage at all (series with CG1sc and GG) is projected well. Solely in the case of grid CG2, convergence problems at low values of slip ($s < 0.06$ mm) are observed (Figure 5.3c), which is due to the neglect of a numerical solution. In the case of series CG2-0°-NSC-150, this convergence problem resulted in a projected slip at the unloaded side already at approximately 20%, while the tests revealed that slip at the unloaded side occurred at approximately 54% on average of the tests in this series. However, a convergence problem did not generally result in infeasible outcomes, as evidenced by the predicted slip at the loaded side for CG1sc (Figure 5.3b).

One important exclusion from the physically derived explicit formulation must be mentioned regarding the application of this approach on the test data of series GG-0°-NSC-114. The negative value of the parameter α indicates that as slip increases, the bond stress diminishes – a phenomenon referred to as bond softening. At larger values of slip, bond softening is a usually observed behaviour and pull-out occurs. In this case, it refers to an immediate softening, which is not likely to have actually occurred in this test series.

Concluding this small feasibility study, the explicit formulation in Equation 5-5 allows for an accurate representation of the actual observed specimen behaviour. Consequently, a power-law approach representing the bond stress-slip relation in members similar to the conducted SPOc tests is sound. The link between the experimentally obtained data and the bond stress-slip relation is expressed by the parameters C in Equation 5-7 and α in Equation 5-8. One limitation is set to the implemented analytical bond stress evolution: The occurrence of bond softening at larger values of slip is not represented by the approach and therefore no pull-out behaviour is predictable. When this case is to be addressed, another analytical function of the bond stress must be chosen.

5.4.3 Representation of the COT test

A similar approach is followed when considering the COT tests by taking into account the different boundary conditions compared to the SPOc tests. It is assumed that the concrete matrix is held at the ends of the specimens due to the clamping, $u_{\mathrm{c}}(x = l_{\mathrm{e}}) = 0$, and a free displacement of the matrix in the direction of the crack is possible. The slip $s(x)$ is then expressed following the differential equation of bond (cf. Equation 2-1):

$$s(x) = \begin{cases} 0 & \text{for } x \geq l_{\mathrm{b}} \\ \frac{1+\rho\,\alpha_{\mathrm{e}}}{2 \cdot A_{\mathrm{nm}} \cdot E_{\mathrm{nm}}} \cdot \left[\tau_{\mathrm{b}}(s(x)) \cdot U_{\mathrm{nm}} \cdot x^2 + 2 \cdot F \cdot x + \frac{F^2}{\tau_{\mathrm{b}}(s(x)) \cdot U_{\mathrm{nm}} \cdot (1+\rho\,\alpha_{\mathrm{e}})^2} \right] & \text{for } 0 \leq x \leq l_{\mathrm{b}} \end{cases} \tag{5-9}$$

The proposed explicit formulation in Equation 5-9 is only valid when there is no slip occurring at the end of the embedded length, which requires that the bond length does not exceed the embedded length. Rather than determining the point of no slip on the fibre strand, the bond length is considered and again obtained by $l_{\mathrm{b}} = F / (\tau_{\mathrm{bm}}(s_{\mathrm{l}}) \cdot U_{\mathrm{nm}})$. Consequently, Equation 5-9 predicts the crack width in the case of a single cracking stage, where the transfer length is able to fully propagate and transfer the full force from the reinforcement to the concrete.
As the formulation in Equation 5-9 considers the elastic deformation of the concrete matrix, the bond stress evolution is determined utilising the force-crack opening relation from the COT

test. As done previously, the bond stress evolution is expressed using the power-law formulation $\tau_b(s) = C \cdot s^{\alpha}$. The parameters C and α are therefore derived as

$$C = \frac{A_{COT}^2 \cdot 2^{2 \cdot \alpha_{COT}}}{2 \cdot U_{nm} \cdot A_{nm} \cdot E_{nm} \cdot (1 + \rho \alpha_e)} \tag{5-10}$$

and

$$\alpha = (2 \cdot \alpha_{COT} - 1) \,. \tag{5-11}$$

To obtain a crack width, it is assumed that twice the slip is equivalent to the crack opening, which is accurate as the required parameters C and α are derived on the basis of a test setup already accounting for a bond free length and the elastic deformation of the concrete matrix. As the bond force evolution depends on the slip, the slip is expressed as half the crack opening in the following formulations. Utilising the formulation of Equation 5-9 in the case of the slip being determined at the loaded side ($x = 0$), the crack opening is obtained

$$w = 2 \cdot s(x = 0) = \frac{F^2}{\tau_b(s) \cdot U_{nm} \cdot A_{nm} \cdot E_{nm} \cdot (1 + \rho \alpha_e)} \,. \tag{5-12}$$

For the sake of completeness, a similar comparison as done for the pull-out representation in Figure 5.3 is provided for the COT tests. In Figure 5.4, the mean curve of the test results and the prediction of the explicit formulation are plotted. As revealed previously in Table 5.3, the application of a power-law approach with curve-fitted parameters to represent the COT results yielded a highly

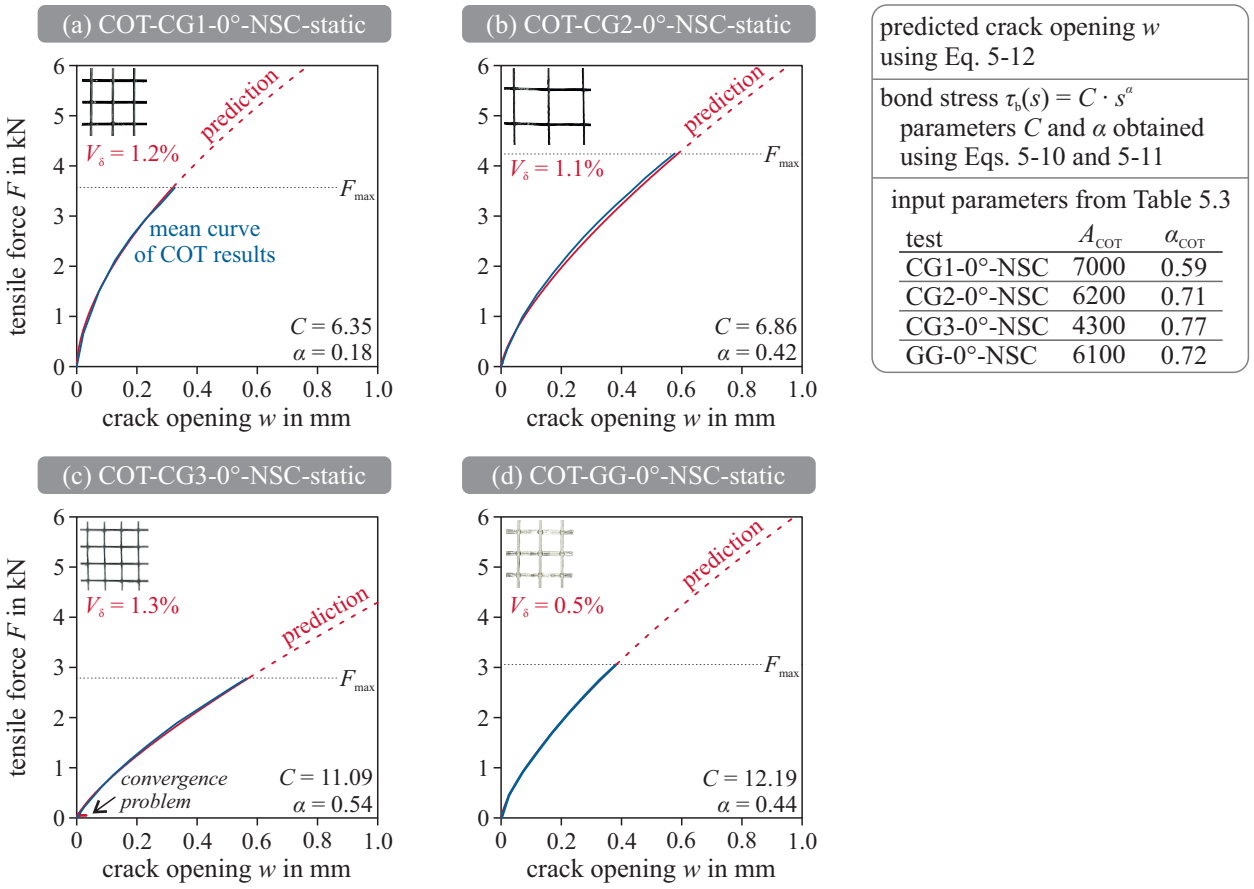


Figure 5.4: Modelling of the force-crack opening relation using an explicit analytical formulation to resemble the test data of the COT test series with NSC

accurate representation. Consequently, the explicit formulation also provides for a near-perfect fit to the mean test results for every textile grid, as demonstrated in Figure 5.4. This underscores the efficacy of physically based representations of characterisation tests, provided that an appropriate assumption regarding the bond stress is made.

5.4.4 Description of single crack opening

Both test configurations evidently enable the analytical characterisation of bond stress as a function of slip or crack opening. While the derived approaches accurately represent the test results, it is important to note that they are not directly comparable, as they yield different bond stress values. It is not possible to formulate a self-contained solution that would link both test setups to a unified solution with the chosen analytical description. This was already revealed with the comparison of the test results in Section 3.4, which showed that the force-slip relations of the SPOc tests and force-crack opening relations of COT tests do not provide for identical results. Moreover, employing a power-law approach for the description of bond stress evolution, without considering bond softening behaviour, imposes limitations on the derived analytical descriptions. As no self-contained solution is apparent, the question arises as to which methodology and analytical representation are more appropriate for modelling the crack opening in concrete members.
For the following evaluations and further investigations, the analytical description utilising the data obtained by the COT tests is considered. The reasons for this choice are as follows: the COT test represents the actual situation of a single crack with the present boundary conditions more accurately when compared to the SPOc test setup. Moreover, the obtained test results demonstrated a substantial reduction in the standard deviation of the values. In the context of employing the SPOc tests, a further decision that merits attention is the identification of feasible embedded lengths for consideration.

Having determined the parameters C and α for the explicit formulation of the analytical bond stress-slip relation, the last step for applying the obtained material parameters to a crack width prediction approach of a single crack is to transfer the bond stress-slip relation $\tau_\mathrm{b}(s) = Cs^\alpha$ to a crack width dependent mean value of bond stress. The mean value of bond stress τ_bm expresses the average bond stress transferred at a certain slip. It is obtained by integrating the bond stress evolution between zero slip and slip at the crack, which is then divided by the overall slip (equal to the slip at the crack) to determine the average. Again, the slip at the crack is expressed as half the crack opening.

$$\tau_\mathrm{bm}(w) = \frac{1}{s} \cdot \int_0^s \tau_\mathrm{b}(s)\,\mathrm{d}s = \frac{2}{w} \cdot \int_0^{w/2} \tau_\mathrm{b}\left(\frac{w}{2}\right)\,\mathrm{d}w = \frac{C \cdot w^\alpha}{2^\alpha \cdot (\alpha+1)} \tag{5-13}$$

With the analytical description of the bond stress, the remaining undetermined parameter is the tension stiffening factor. The attempt to determine a more precise value of the mean bond stress was already introduced in Section 5.3 by establishing Equation 5-4 using the parameters A_COT and α_COT. Given that neither the COT nor the SPOc test setups explicitly provide a method to derive a reasonable value for the tension stiffening factor β, this parameter remained undetermined in Section 5.3.
To consolidate the connection between the experimental data used to determine curve-fitted values and the analytically explicit formulation, with the tension stiffening factor β remaining as the sole undefined parameter, the following is considered: The plotted blue and red curves in Figure 5.5 represent the experimentally determined value of mean bond stress according to Equation 5-4 with chosen values of β. These curves are identical to the evaluation in Table 5.3. By adding the plots

of the analytical formulation according to Equation 5-13 for each of the four test series of different textile grids, identified as red curves, it is evident that the evolution between the simple approach given in Equation 5-4 and the analytical solution fits well and corresponds closely for β-values of approximately 0.6 to 0.7. This observation motivates assuming that Equations 5-4 and 5-13 provide an equivalent value:

$$\frac{2 \cdot (1-\beta) \cdot F_{\mathrm{b}}^2(w)}{E_{\mathrm{nm}} \cdot U_{\mathrm{nm}} \cdot A_{\mathrm{nm}}^2 \cdot (1+\rho\alpha_{\mathrm{e}})} = \frac{C \cdot w^{\alpha}}{2^{\alpha} \cdot (\alpha+1)} \tag{5-14}$$

Considering the description of the bond force derived from the COT test data as $F_{\mathrm{b}}(w) = A_{\mathrm{COT}} \cdot w^{\alpha_{\mathrm{COT}}}$ (cf. Equation 5-2) in Equation 5-14, the required value of β is then obtained as:

$$\beta = 1 - \frac{1}{4 \cdot \alpha_{\mathrm{COT}}} \tag{5-15}$$

Figure 5.5 provides the determined β-values for the four test series according to Equation 5-14. They range from 0.58 for reinforcement CG1 to 0.65 for reinforcements CG2 and GG. When these values are compared to the derived β-values from the COT tests equipped with FOS, as provided in Figure 3.23, the analytically obtained values are found to be approximately within the range of the upper limit values of the FOS evaluation, which showed to be a suitable approximation in the case of crack width prediction (cf. Section 3.5.6).

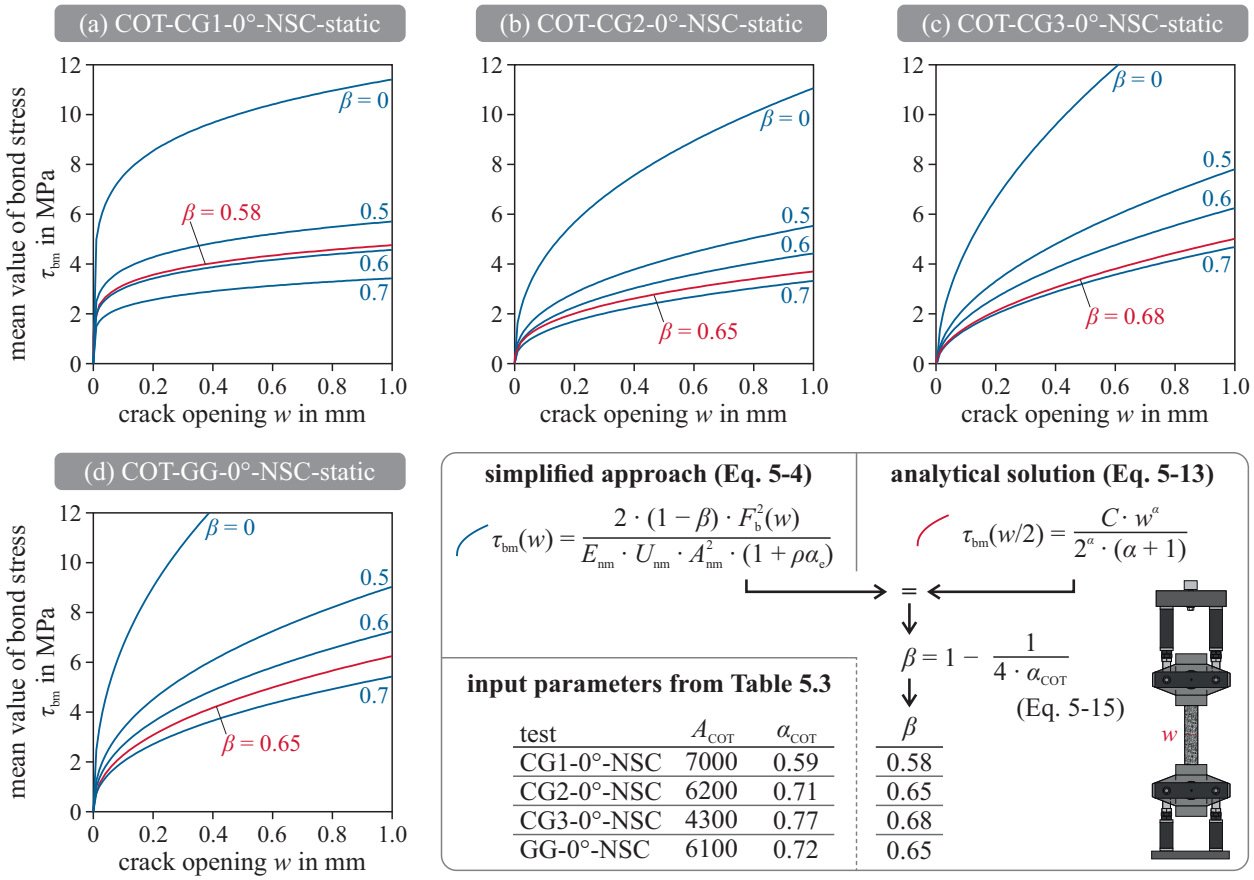


Figure 5.5: Comparison of the mean value of bond stress as a function of crack opening obtained with both an undetermined (blue curves) and an analytically derived (red curves) tension stiffening factor β, based on the COT test results

5.5 Implementation of a physically based model for crack width prediction

The analytical representation of the bond behaviour with a function of mean bond stress $\tau_{\mathrm{bm}}(w)$ and a tension stiffening factor β allows for a profound utilisation of a physically based model. Therefore, a differentiation between single cracks (Section 5.5.1) and the stabilised cracking stage (Section 5.5.3) is considered. In the model and the following descriptions, specific characteristics regarding bond behaviour of textile grids are introduced stepwise.

5.5.1 Single cracking stage

The physically based description of crack opening in the case of a single crack is rather simple, as only the transfer length and the average strain values of reinforcement and concrete along the transfer length have to be determined. This approach forms the basis of the formulation provided by the German Annex to Eurocode 2 [EC2NAD], which is expressed in Equation 2-18. Using an approximation of the bond stress evolution, such as, for example, the derived $\tau_{\mathrm{bm}}(w)$ using Equation 5-13, the transfer length is obtained:

$$l_{\mathrm{t}} = \frac{\sigma_{\mathrm{nm}} \cdot A_{\mathrm{nm}}}{\tau_{\mathrm{bm}}(w) \cdot U_{\mathrm{nm,eq}} \cdot (1 + \rho \alpha_{\mathrm{e}})} \tag{5-16}$$

The force is assumed to be fully accounted for by the reinforcement, with no contribution from tensile force transfer via interlocking crack surfaces at small crack openings. To consider the influence of multiple reinforcement layers with close spacing to each other, an equivalent circumference $U_{\mathrm{nm,eq}}$ is introduced at this point in advance, which is addressed later in this section.

Utilising COT tests

The crack width of a single crack is predicted using the physically derived formulation in Equation 2-18, which is equivalent to the expression of the explicit formulated analytical solution provided in Equation 5-12. It is noteworthy that the two expressions, Equations 2-18 and 5-12, initially differ in their representation of the bond capacity, referring either directly to the bond stress evolution as in Equation 5-12, or to a mean value of bond stress as in Equation 2-18, respectively. In addition, the introduced tension stiffening factor β according to Equation 5-15 is essential for the fulfilment of this equivalence between the two physically based concepts.

To validate the proposed methodology of expressing the bond stress-slip relation as a power-law function using COT tests for a crack width prediction approach of single cracks, the results of the uniaxial tensile (UT) tests with a single layer of reinforcement are used. In the following, only the single cracking stage is considered. In Figure 5.6, the experimentally obtained crack widths on the concrete surface are plotted for each individual DIC-measurement step in relation to the reinforcement stress. This results in a data set of individual values, which represent the crack width evolution of each UT specimen. The data plotted in Figure 5.6 summarises the test series for each textile grid to one colour and only differentiating between the concrete strength (normal-strength concrete and high-strength concrete) and the maximum aggregate size (5.6 mm and 16 mm). The predictions of the crack width are plotted as a continuous curve using the obtained parameters C and α to determine the mean value of bond stress as a function of crack width and the tension stiffening factor. In general, the proposed methodology is very well suited to predict the width of single cracks, as revealed in Figure 5.6. Even the results of the UT tests with specimens having the larger maximum aggregate size of 16 mm, for which no COT tests were conducted to obtain separate calibration parameters, are accurately represented. Solely two inconsistencies are found.

Firstly, the specimens with high-strength concrete (HSC) and reinforced with CG1 are not well predicted using the explicitly obtained parameters for this concrete strength, but are better represented by the normal-strength concrete prediction. Consequently, the parameters C and α obtained for the NSC are also used in the following for members with HSC. Secondly, the crack widths of the purely statically loaded specimens with CG2 are underestimated for crack widths exceeding 0.4 mm. This is partly attributable to the crack widths in the UT tests extending beyond the calibrated regime, which, in this instance, was only valid up to a crack opening of 0.62 mm (cf. COT test results in Figure 3.9).

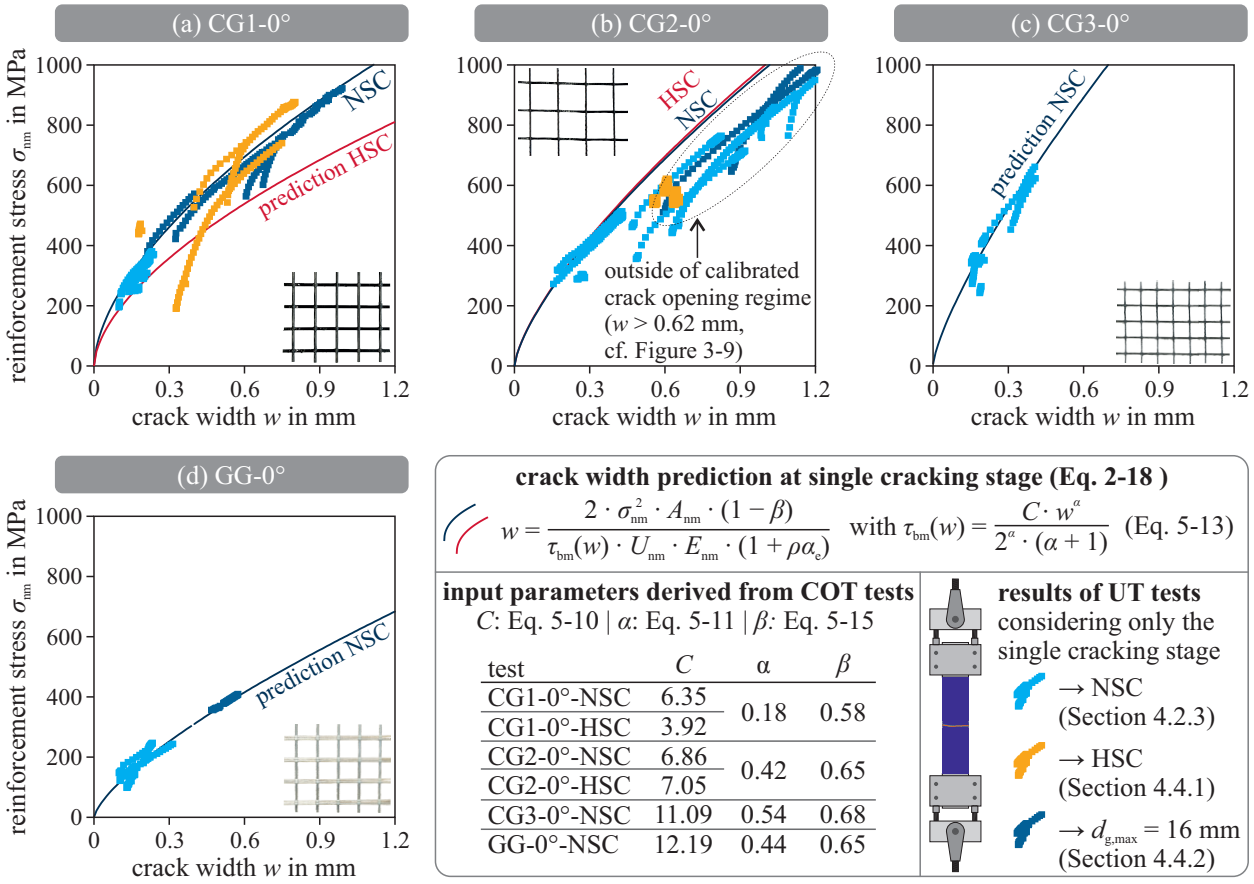


Figure 5.6: Validation of the analytical bond stress-slip relation derived from COT tests for predicting the crack width of UT specimens at the single cracking stage

Multiple layers of textile reinforcement

The next validation step addresses the feasibility of the proposed methodology for multiple layers of textile grids. For this, the test series with two and four layers of CG1 evaluated in Section 4.3 are considered. As revealed by the evaluation of these three test series, the specimens having two layers of reinforcement placed with a sufficient spacing to each other, denoted as CG1-2L+, showed a similar behaviour with regard to the crack width evolution as the specimens with a single reinforcement layer. In contrast, the two series in which the grids were placed directly on each other, series CG1-2L and CG1-4L, indicated a reduced bond capacity in comparison to the members with only a single reinforcement layer. Similar findings regarding the reduction in concrete compressive strength have been reported in relation to the influence of multiple reinforcement layers [Boc17] or the vertical displacement of fibre strands in multiple layers [Boc18].

Therefore, an adaptation is required, which addresses the situation of multiple layer spacing. This is done by introducing an equivalent circumference of a fibre strand by considering a simplified approach, visualised in Figure 5.7. The equivalent circumference, denoted as $U_{nm,eq}$, accounts for

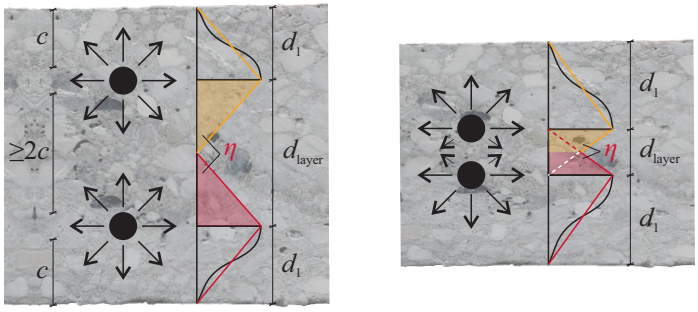
a reduced bond area in the case where the force transfer is influenced by another reinforcement layer. Consequently, the equivalent circumference expresses the observed reduced bond capacity. Considering the area between the fibre strand and the concrete surface, the force is transferred to the concrete through the whole provided area, limited only to the concrete cover c. The concrete cover is a fixed boundary condition in the COT test setup and the calibration parameters to describe the bond stress-slip relation are derived considering this state. As an additional geometrical parameter, the distance from the centre of the fibre strand to the concrete surface is considered, denoted as d_1. The distance between the centre of the fibre strands of different layers is introduced as d_{layer}.
For d_{layer} being at least twice the value of d_1, it is assumed that the circumference is equivalent to that of a single-layer case. In other words, when the spacing between the reinforcement layers is at least twice the concrete cover, no adjustment of the circumference is required. This is visualised for the first case in Figure 5.7 and referred to as *sufficient spacing*.
If the force transfer of two layers interfere with each other and the concrete area between the reinforcement layers becomes overstressed, a full utilisation of the bond capacity is no longer possible, leading to a reduced bond flow. This phenomenon is further intensified when the reinforcement layers are placed directly on top of each other, which results in a smaller effective bond zone and is illustrated in the second case of Figure 5.7 as *close spacing*. Because the actual contribution of the bond zone to the force transfer remains unknown, which is illustrated in Figure 5.7 as a non-linear development, a linear simplification based on the distance between multiple reinforcement layers is introduced.

Assuming that the bond zone in the area between two reinforcement layers is identical for each fibre strand, the interfering linearly approximated bond zones are addressed using Equation 5-17 (right-hand side of Figure 5.7). The approximation expressed by η uses a relation factor ξ considering the distance between layers d_{layer} and to the concrete surface d_1. Following this, the equivalent circumference of a fibre strand is determined according to Equation 5-19. This formulation of the equivalent circumference is restricted to cases where the fibre strands are placed vertically aligned to each other and not offset from one another.

The test results of the three uniaxial tensile test series with multiple layers of reinforcement (CG1-2L, 2L+, 4L) are used to validate the proposed methodology of expressing the bond stress-slip relation while considering an equivalent circumference. The circumference of a single fibre strand

Case 1: sufficient spacing ($d_{\text{layer}} \geq 2d_1$)

Case 2: close spacing ($d_{\text{layer}} < 2d_1$)



linearly approximated bond zone:

$$\eta = \xi \cdot (2 - \xi) \leq 1 \qquad (5\text{-}17)$$

$$\xi = d_{\text{layer}} / (2 \cdot d_1) \qquad (5\text{-}18)$$

equivalent circumference:

$$U_{\text{nm,eq}} = U_{\text{nm}} \cdot \frac{1 + \eta \cdot (n-1)}{n} \qquad (5\text{-}19)$$

U_{nm}: circumference of a single fibre strand
n: number of reinforcement layers

Figure 5.7: Effect of multiple textile layers on bond force transfer through reduced circumference

of the considered reinforcement CG1 is 9.71 mm. Figure 5.8 presents both the predicted and experimentally measured crack widths for the single cracks in the test series. The evaluation shows the good feasibility of the proposed methodology, which is capable of predicting small crack widths below 0.2 mm observed in the three test series during the single cracking stage. Solely for the crack widths of the purely statically loaded specimen CG1-2L-static (Figure 5.8a), the prediction underestimated the test data for widths between 0.1 and 0.2 mm. The evaluation also highlights the significance of the introduced equivalent circumference on the crack width prediction approach. Without this consideration, the predicted crack width at identical reinforcement stress would be assumed to be lower, leading to a significant underestimation of the widths obtained in the tests. For example, the equivalent circumference $U_{\mathrm{nm,eq}}$ for series CG1-4L with four reinforcement layers is 4.9 mm^2, which is about half of the circumference of an individual fibre strand. The predicted width would be only half the value obtained if the influence of close spacing was neglected.

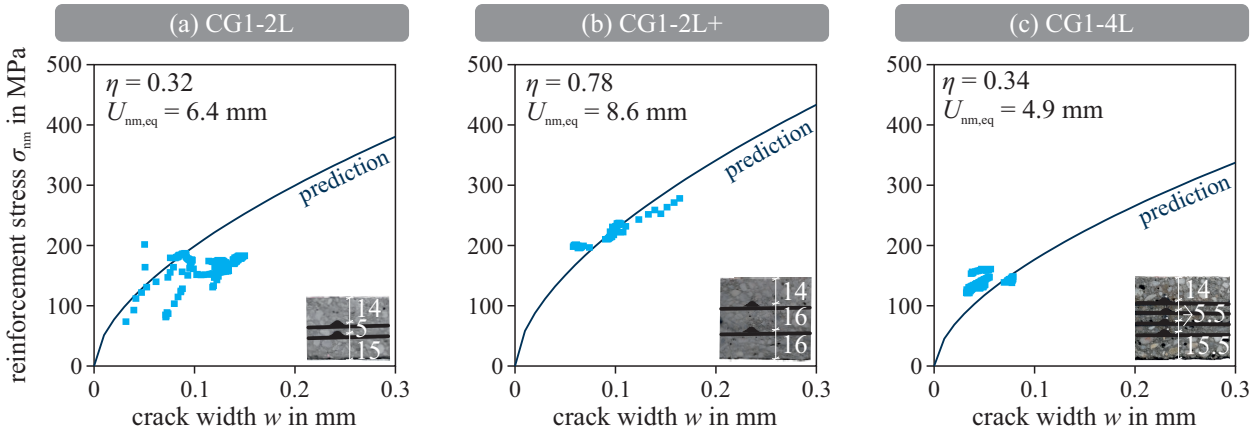


Figure 5.8: Validation for multiple reinforcement layers of CG1 using an equivalent circumference to account for the influence of the close spacing between grids

In conclusion, the physically based model enables an accurate prediction of the crack width under uniaxial tensile loading at the single cracking stage. Therefore, the determination of the mean value of bond stress as a function of crack width and the tension stiffening factor requires calibrated parameters obtained through COT tests. In the case of multiple layers of reinforcement grids, a reduction of the circumference describing the bond area is required. This accounts for the reduced bond area as the concrete between the layers is subject to interfering force transfers. To extend this model to predict the maximum crack width at the stabilised cracking stage, a prediction of the maximum crack spacing is required.

5.5.2 Prediction of maximum crack spacing

Following the physical concept of expressing the crack width as the reinforcement deformation relative to the concrete deformation along the transfer length, crack spacing becomes the essential factor when addressing adjacent cracks. In a homogeneous material, a new crack forms when the transferred force exceeds the material's tensile strength. Assuming a single crack with its transfer length l_{t}, the minimal distance at which the adjacent crack forms is defined by the tensile resistance and the transferred force.

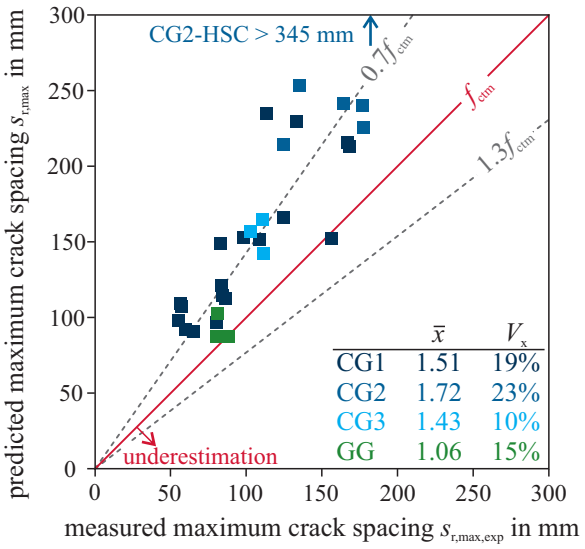
$$l_{\mathrm{t}} = \frac{f_{\mathrm{ct,ef}} \cdot A_{\mathrm{c,net}}}{\tau_{\mathrm{bm}}(w) \cdot U_{\mathrm{nm,eq}}} \tag{5-20}$$

The tensile resistance is given by the effective tensile strength of the concrete matrix $f_{\mathrm{ct,ef}}$ and the net cross-sectional area $A_{\mathrm{c,net}}$, both at the considered location where an adjacent crack forms.

As concrete is an anisotropic material with scattering material strength within the matrix, no fixed or exact value of tensile strength can be determined. The concrete tensile strength scatters by about 30% from the average value when assuming the 5% and 95% fractiles as the minimum and maximum values, respectively. In the case of slender members, determining the cross-sectional area contributing to the tensile resistance requires additional consideration. The net cross-sectional area, which accounts for the cross-section of the longitudinal reinforcement, appears to be preferable, although the difference compared to the total concrete cross-sectional area under tension is generally marginal and typically below 2%. However, transverse fibre strands are also associated with a reduction in the cross-sectional area. Still, most recent code provisions for steel-reinforced members, such as [MC20, FprEC2, DAfStb24], do not account for transverse reinforcement. The German Annex to Eurocode 2 [EC2NAD] introduced a limitation on the maximum crack spacing, specifying it as twice the mesh spacing for welded mesh fabrics made of ribbed wires, which in Germany typically have mesh sizes between 150 mm and 250 mm. Evidently, the quantification itself is not transferable to textile reinforcement.
The previously evaluated uniaxial tensile tests revealed that cracks frequently occurred at or in close proximity to the location of the transverse fibre strand. Two main factors have been identified as contributing to this behaviour. First, the presence of transverse fibre strands reduced the cross-sectional area of the concrete. The height of the transverse fibre strands was about 2 mm on average for all four considered textile grids. In the case of the uniaxial tensile tests, the concrete cross-section contributing to the tensile resistance would therefore be reduced by about 7% at the locations where transverse fibre strands were present. Second, in some grids, a significant amount of force is transferred at the intersections with the transverse fibre strands (local undulations), which provoked the occurrence of a crack in this area.

This opens an undetermined spectrum of where the cracks occur and at which spacing, despite the initially simple physical consideration. In the current European code provisions, two approaches are followed to obtain a value of crack spacing. The *fib* Model Code 2020 and the Final Draft to the Preliminary Eurocode 2 follow an empirical-based approach for determining an average crack width, which is then calibrated to a characteristic crack width used for design. The characteristic crack spacing is therefore only considered implicitly. Contrary to this approach, the German Annex to Eurocode 2 [EC2NAD] provides an explicit definition of the maximum crack spacing, which is considered in the following.
The formulation in Equation 5-20 is utilised to predict the maximum crack spacing, which is assumed to be twice the transfer length: $s_{\mathrm{r,max}} = 2l_{\mathrm{t}}$. The average concrete tensile strength is assumed to be identical to the strength determined in material tests ($f_{\mathrm{ct,ef}} = f_{\mathrm{ctm}}$). The net cross-sectional area is derived by excluding the area of longitudinal and transverse fibre strands. The mean value of bond stress is obtained using the validated approach given by Equation 5-13 with the calibration parameters of C and α for the corresponding reinforcement grid and concrete strength class. For the bond area, the equivalent circumference $U_{\mathrm{nm,eq}}$ is taken into account. The crack spacing to be validated is set to be the maximum crack spacing measured in the corresponding test at the stabilised cracking stage, denoted $s_{\mathrm{r,max,exp}}$. With these considerations, the predicted values $s_{\mathrm{r,max}}$ are compared to $s_{\mathrm{r,max,exp}}$ using the diagram in Figure 5.9. For reference, the diagonal describing the perfect prediction is added as well as the diagonals referring to different assumptions of the effective concrete tensile strength, namely the 5% fractile ($0.7f_{\mathrm{ctm}}$) and the 95% fractile ($1.3f_{\mathrm{ctm}}$). Data points located on the right side of the diagonals indicate an underestimated crack spacing, leading to predicted crack widths smaller than those observed.
The evaluation in Figure 5.9 reveals that assuming the average concrete strength as the effective tensile strength leads to almost no underestimation, with the exception of specimen GG-0°-NSC-

16mm which is slightly underestimated ($s_{r,max}/s_{r,max,exp}$ = 92 mm/104 mm = 0.89). However, the prediction yields low accuracy, which is evident from the broad scatter of the data points. The results of the three specimens of series CG2-0°-HSC show a significant overestimation of the prediction when referring to absolute values. The data values are off chart in the diagram in Figure 5.9, as a spacing of 356 mm was predicted while the experimentally determined crack spacing was 190 mm. A relation to the textile grid, the concrete strength, the cross-sectional area, or the number of reinforcement layers was not found. For all three carbon grids, the prediction exhibited a substantial overestimation of the maximum crack spacings. The $s_{r,max}/s_{r,max,exp}$-ratio, denoted as $\bar{x}$ in Figure 5.9, was greater than 1.4. The determined coefficient of variation V_x, indicates a significant variation in the prediction, particularly for the series with CG1 and CG2 with 19% and 23%, respectively. Solely the maximum crack spacing observed in the series reinforced with GG is accurately predicted ($\bar{x} = 1.06$).



test series		$f_{ct,ef} = f_{ctm}$ [MPa]	$A_{c,net}$ [mm^2]
CG1-0°	NSC	3.1 – 3.3	5150
	HSC	5.0	5150
	NSC-16mm	2.5	8950
	NSC-2L	2.4 – 2.5	5360
	NSC-2L+	2.5 – 2.6	7640
	NSC-4L	2.8 – 3.3	6540
CG2-0°	NSC	3.3 – 3.4	5220
	HSC	5.0	5220
	NSC-16mm	2.5	9020
CG3-0°	NSC	3.0	5370
GG-0°	NSC	3.0	5040
	NSC-16mm	2.5	8840

Figure 5.9: Evaluation of the performance for predicting the maximum crack spacing obtained at the stabilised cracking stage, considering the effective concrete tensile strength $f_{ct,ef}$ and a net cross-sectional area of the concrete $A_{c,net}$

This evaluation highlights the difficulty in predicting accurate values of the maximum crack spacing. It also emphasises that the consideration of a net cross-sectional area is a solid approach for the considered parameters in the experimental campaign using uniaxial tensile tests. However, the prediction is highly dependent on a feasible determination of the scattering material properties of the concrete. For example, considering the effective tensile strength to be the 5% fractile of the average concrete tensile strength ($0.7f_{ctm}$), leads to a value $\bar{x}$ closer to 1.0, representing the perfect fit. This consideration implies the phenomenon that the actual concrete tensile strength in the specimens is not reached at the transition to the stabilised cracking stage.

According to the observations made in the UT tests, new cracks formed in the area where a *shielded length* is assumed. The shielded length is defined as the area close to an existing crack, where the successive force transfer does not exceed the concrete's tensile resistance. In general, it is assumed that the shielded length is approximately equal to the transfer length. Apparently, this was not the case for the uniaxial tensile tests. This phenomenon is confirmed by the observed crack pattern and the late crack occurrence. For example, an examination of the specimens reinforced with GG

revealed many cracks with very close crack spacing, which is interpreted as a local transfer of substantial forces that surpass the concrete tensile strength, thereby inducing the formation of two distinct cracks. Late crack occurrence refers to the formation of one or two cracks at high levels of reinforcement utilisation and when the stress-elongation behaviour indicates that the stabilised cracking stage is already present. Consequently, from the observation, the transferred force exceeds the concrete's tensile resistance before reaching the full transfer length. Therefore, it is concluded that cracking occurred apparently at a lower concrete tensile strength or higher (locally occurring) tensile stresses.

The local transfer of substantial tensile stresses is well-known in textile reinforced concrete members. It is often attributed to be the reason for the occurrence of longitudinal cracks, which eventually leads to concrete splitting. Effects known to contribute to this local stress transfer and longitudinal crack formation are allocated to undulations and waviness, as well as to the cross-sectional geometry (e.g. reported in [Pre19a, Pre20b]).
Therefore, the influence of the cross-sectional geometry on the occurrence of adjacent cracks of a fibre strand is analysed in detail. Considering a circular cross-section, a homogeneous transfer of forces along the circumference and a uniform bond flow occurs, as illustrated in Figure 5.10. In contrast, an elliptical cross-sectional geometry leads to a non-uniform stress distribution in the surrounding concrete matrix. While the bond flow and force transfer remain constant along the elliptical circumference, the stress is localised along the minor axis (length a in Figure 5.10) where a larger ratio of circumference and cross-sectional area of the fibre strand is located. As a result, the force F^{a} acting along the minor axis is higher than the force F^{b} (major axis). The discussion at the end of Section 4.2.4 referring to Figure 4.12 showed that a new crack formed close to an existing crack where the concrete stress is significantly below the mean value of tensile strength. Furthermore, these lateral stresses induce a biaxial tensile stress state in the concrete. Experimental research revealed a reduced tensile resistance of concrete subjected to biaxial tension in comparison to that of uniaxial tension. The well-known proposal by KUPFER [Kup73] assumes that the biaxial strength is below the uniaxial tensile strength. Similar observations were reported in [Lee04, Kwa06].

To quantify the lateral stresses exerted by the elliptical cross-section of the fibre strand, an approach is to introduce a factor, such as done for example by PREINSTORFER ET AL., which assumed a rectangular stress distribution related to both axes and introduced a factor denoted as α_F. This factor is determined using the lengths of the semi-axes a and b. As the bond flow is dependent on the bond stress-slip behaviour, it is expressed in dependence on the crack width to provide for a more general formulation.

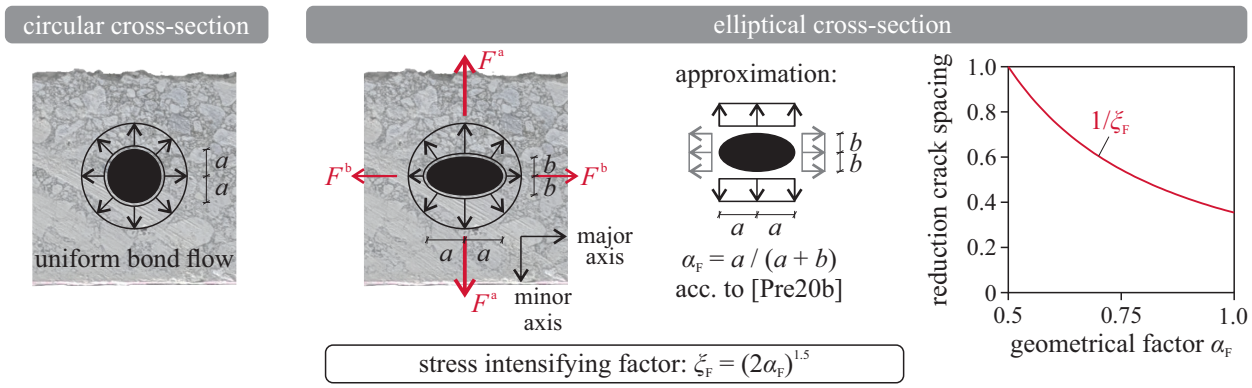


Figure 5.10: Influence of the cross-sectional geometry on force transfer and stress concentration

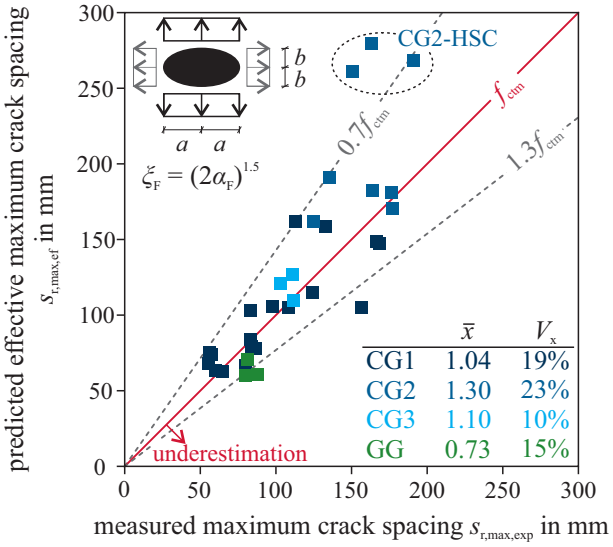
The utilisation of the concrete matrix in the direction of the major axis is neglected in the following, as the resulting force is smaller. In addition, an influence of stress concentration in the direction of the major axis is already accounted for by introducing the net cross-sectional area of the concrete with an explicit consideration of the transverse fibre strand. Therefore, the bond flow along the minor axis is considered further. The definition of the maximum crack spacing given in Equation 5-20 considers the bond flow through the expression $\tau_{bm}(w) \cdot U_{nm,eq}$, which must account for the stress concentration, by means of a stress intensifying factor

$$\xi_F = (2 \cdot \alpha_F)^{1.5} = \left(2 \cdot \frac{a}{a+b}\right)^{1.5}. \tag{5-21}$$

The exponent 1.5 introduces a feasible consideration to account for various effects, including a local plastification of the concrete in close proximity to the fibre strand (eg. reported in [Pre19a]), the simplified assumption of a rectangular stress distribution, and the inhomogeneity of the fibre strand in the longitudinal direction, which produces additional stress concentration.
The expression in Equation 5-20 is restated to include the stress intensifying factor for the bond flow, from which the effective maximum crack spacing is then derived:

$$s_{r,max,ef} = \frac{2 \cdot f_{ct,ef} \cdot A_{c,net}}{\tau_{bm}(w) \cdot U_{nm,eq} \cdot \xi_F} \tag{5-22}$$

The effective maximum crack spacing described in Equation 5-22 is used to predict the maximum crack spacing for the test data set, with the results illustrated in Figure 5.11. In general, the same approach as in Figure 5.9 was followed: the effective concrete tensile strength and net cross-sectional area remain identical to the values given in the table in Figure 5.9, the only difference being the introduction of the stress intensifying factor ξ_F. Figure 5.11 also includes the determined average of all values $\bar{x}$ and the coefficient of variation V_x in respect to the four considered grids.
Focusing on the two reinforcements CG1 and CG2, the consideration of the influence of the elliptical cross-sectional geometry leads to a significant improvement, with an average value $\bar{x} = 1.04$



test series	$2a$ [mm]	$2b$ [mm]	ξ_F
CG1-0°	4.8	2.7	1.45
CG2-0°	3.5	2.3	1.33
CG3-0°	2.5	1.7	1.30
GG-0°	5.7	3.2	1.45

Figure 5.11: Evaluation of the performance for predicting the maximum crack spacing obtained at the stabilised cracking stage, considering the elliptical cross-sectional geometry of the fibre strand through the stress intensifying factor ξ_F.

in the case of CG1. The variation is also reduced significantly when considering absolute values. This is particularly evident for the three specimens of series CG2-0°-HSC, where the overestimation was reduced to 1.6 times the measured crack spacing compared to 2.1 times in the previous evaluation in Figure 5.9. The prediction for reinforcement CG3 is also considerably improved, with an average value of 1.10. A significant underestimation and lower accuracy are observed for the specimens reinforced with GG, for which the previous approach provided a better fit. With the introduction of the stress intensifying factor ξ_F, which is more pronounced for the elliptical geometry of the glass fibre strand, the prediction of an effective maximum crack spacing is consequently less accurate. It is worth noticing that the values of the coefficient of variation do not differ from the previous evaluation in Figure 5.9 as it serves as a relative reference indicator.

In general, it is worth considering what degree of accuracy can realistically and reasonably be expected in matching the predictive approach to the test data, given the high influence of variations in the materials' parameters on the crack spacing prediction. It is well established that the crack spacing and crack widths in a concrete member exhibit significant variability, which introduces additional challenges for every prediction approach. This is confirmed once more by the own uniaxial tensile tests. It seems to be reasonable to consider the net cross-sectional area, including the transverse fibre strands, in cases where a significant reduction in the tensile concrete cross-section is expected (at least 3 to 4%). Moreover, it is appropriate to address the elliptical cross-sectional geometry of the fibre strand using a stress intensifying factor, as it accounts for stress concentrations in the concrete matrix close to the bond zone, which induces cracking at lower total transferred forces compared to a circular cross-section. In the context of predicting the effective concrete tensile strength, it is reasonable to assume that it is equivalent to the average concrete tensile strength. This approach aligns with the current code provision methodologies in [MC20, EC2, FprEC2, DAfStb24] for determining crack width limitations.

5.5.3 Maximum crack width at stabilised cracking

Approaches and methodology

A sound prediction of maximum crack width is now possible as a feasible prediction of the maximum crack spacing has been made. Hereby, it is essential to acknowledge that the determination of a maximum crack spacing value has already exposed the unresolvable problem of the inhomogeneous material parameters of concrete, which only allows for an empirical-based assumption of the tensile strength. Consequently, a different assumption with regard to the tensile strength significantly influences the outcome of the predictions.

The two most significant findings made during the experimental campaigns are the reduced influence of tension stiffening in conjunction with a lower bond capacity and the previously discussed stress concentrations due to the elliptical cross-sectional geometry. Regarding tension stiffening, one approach worth considering is to neglect any contribution of tension stiffening. This is attributable to the outcome of the uniaxial tensile tests, which demonstrated that a straightforward prediction method for the average crack width (cf. Equation 4-1) yields satisfying to good results when no tension stiffening is considered. It is reasonable to assume that this principle is also applicable to the prediction of the maximum crack width. On the other hand, the evaluation of the fibre optical measurements and the determination of the tension stiffening factor β revealed the potential to account for tension stiffening, yet with a reduced value compared to the single cracking stage.
To resolve this contradiction regarding the actual contribution of tension stiffening, it is necessary to investigate thoroughly the bond capacity along the transfer lengths below two times the yarn spacing and at higher reinforcement stresses compared to the single cracking stage. This is as

both, short transfer length and high stresses, revealed in the UT test series to be import influencing factors regarding the contribution of tension stiffening and therefore the observed crack width. Considering short transfer lengths, this was already done using the SPOc test layout by employing specimens with embedded lengths equivalent to the yarn spacing. The evaluation presented in Figure 3.4 revealed a substantial reduction of transferred force compared to specimens where a greater embedded length was provided.

Following these observations, three cases are stated in the following to study their feasibility in predicting the maximum crack width within the physically based model. An overview is provided in Table 5.5. The first case follows the considerations of bond capacity and tension stiffening as introduced for a single cracking stage in Section 5.5.1. The second case provides for an adaptation of the tension stiffening factor β by either neglecting tension stiffening or by reducing the value to 0.36. The latter refers to the observations made in the COT test series (cf. Section 3.5.6). In both cases, keeping the description of the bond stress-crack width relation derived for a single crack also for adjacent cracks, is motivated by the following: In general, higher values of mean bond stress are obtained due to zero displacement at the end of the transfer length between two adjacent cracks (cf. [Kön96, Sch21a]). Furthermore, as the prediction focusses the maximum crack width, the observed lower bond capacity due to short transfer lengths is more attributed to smaller crack spacings.
However, to address the influence of short transfer lengths, a third case is considered. Therefore, the results gained in the SPOc test series with embedded lengths equivalent to the yarn spacing are considered (cf. Section 3.3.3). The corresponding SPOc tests for the grids CG1, CG2 and GG showed a linear evolution of the bond force with regard to the slip. Expressing the bond force F_{b} in relation to the circumference of the reinforcement U_{nm} and the transfer length, the bond stress is obtained. The transfer length in the considered SPOc tests was equal to the yarn spacing y_{nm}. In the case of reinforcement CG3, no SPOc series with an embedded length of one yarn spacing was conducted. Therefore, the series with an embedded length of three times the yarn spacing, denoted as CG3-0°-NSC-75, is considered as substitution. The bond capacity for Case 3 is expressed by Equation 5-23 in Table 5.5 when assuming that twice the slip is equivalent to the crack width ($w = 2s$). The bond force $F_{\mathrm{b},0.5}$ is obtained by evaluating the bond force-slip relation at a value of slip of 0.5 mm, which is provided in Figure 3.4. In the case of a linearly increasing bond stress-crack width relation, the tension stiffening factor $\beta = 0.5$.

Table 5.5: Case study regarding the representation of bond capacity and tension stiffening within the physically based model for the stabilised cracking stage

	Case 1	Case 2	Case 3
bond capacity	$\tau_{\mathrm{bm}}(w) = \frac{C \cdot w^{\alpha}}{2^{\alpha} \cdot (\alpha + 1)}$ acc. to Equation 5-13		$\tau_{\mathrm{bm}}(w) = \frac{F_{\mathrm{b},0.5} \cdot w}{2 \cdot y_{\mathrm{nm}} \cdot U_{\mathrm{nm}}}$ (5-23) linearly increasing acc. to SPOc test results
tension stiffening	$\beta = 1 - \frac{1}{4 \cdot \alpha_{\mathrm{COT}}}$ as for single cracks acc. to Equation 5-15	$\beta = 0$ or 0.36 acc. to observations in Section 3.5.6	$\beta = 0.5$ due to linear increasing bond stress

All three cases approximate the bond behaviour by introducing assumptions to quantify the bond capacity and the tension stiffening effect, which were derived using experimental setups. An alternative strategy to describe the bond behaviour is to undertake an analysis using the finite element method and numerical approaches. Such an analysis would require a detailed modelling of the fibre strand, including surface and material behaviour of roving and impregnation.

General formulation

Prior to investigate the influence of these three cases regarding the prediction of the maximum crack width, the extension of the physically based model for stabilised cracking is introduced. The maximum crack width at the stabilised cracking stage is assumed to correspond to the adjacent cracks having the maximum spacing between each other. Considering the basic formulation of the crack width in Equation 2-11 in terms of mean strain values, the maximum crack width is

$$w_{\max} = s_{\mathrm{r,max,ef}} \cdot (\varepsilon_{\mathrm{nm,m}} - \varepsilon_{\mathrm{cm}}) \,. \tag{5-24}$$

Following the derivation for adjacent cracks presented in Equation 2-21, the consideration of the stress intensifying factor ξ_{F} allows for the formulation of the maximum crack width as

$$w_{\max} = s_{\mathrm{r,max,ef}} \cdot \left[\frac{\sigma_{\mathrm{nm}}}{E_{\mathrm{nm}}} - \beta_{\mathrm{adj}} \cdot \frac{f_{\mathrm{ct,ef}} \cdot (1 + \rho_{\mathrm{ef}} \alpha_{\mathrm{e}})}{\rho_{\mathrm{ef}} \cdot E_{\mathrm{nm}} \cdot \xi_{\mathrm{F}}} \right] . \tag{5-25}$$

The obtained expression in Equation 5-25 is almost identical to the known approaches in *fib* Model Code 90 [MC90] and the German Design Guideline [DAfStb24] for the crack width prediction at stabilised cracking.

Finally, the point of transition from the crack formation stage to the stabilised stage is addressed. This is necessary to introduce a lower limit of the maximum crack spacing so that the utilisation of Equation 5-22 does not result in unrealistic and to progressive predictions. The lower limit in crack spacing is obtained assuming that the last crack is occurring at the end of the prescribed transfer length l_{t} of the remaining single crack (obtained acc. to Equation 5-16):

$$\underbrace{\frac{\sigma_{\mathrm{nm}} \cdot A_{\mathrm{nm}}}{\tau_{\mathrm{bm}}(w) \cdot U_{\mathrm{nm,eq}} \cdot (1 + \rho\, \alpha_{\mathrm{e}})}}_{= l_{\mathrm{t}}} = \underbrace{\frac{2 \cdot f_{\mathrm{ct,ef}} \cdot A_{\mathrm{c,net}}}{\tau_{\mathrm{bm}}(w) \cdot U_{\mathrm{nm,eq}} \cdot \xi_{\mathrm{F}}}}_{= s_{\mathrm{r,max,ef}}} \tag{5-26}$$

Simplifying Equation 5-26 provides for the reinforcement stress, at which the transition to stabilised cracking occurs:

$$\sigma_{\mathrm{nm,trans}} = \frac{2 \cdot f_{\mathrm{ct,ef}} \cdot (1 + \rho\, \alpha_{\mathrm{e}})}{\rho_{\mathrm{ef}} \cdot \xi_{\mathrm{F}}} \tag{5-27}$$

In the consideration of the transition, it is important to note the introduction of two distinct definitions of the reinforcement ratio within a single equation. During the single cracking stage, the focus is exclusively on the concrete cross-sectional area, excluding the longitudinal fibre strands. In the case of stabilised cracking, as illustrated previously, the effective concrete area is considered in the calculation of crack spacing. Consequently, the net concrete cross-section is obtained by deducting the area of the longitudinal and transverse fibre strands.
Substituting the reinforcement stress in the expression to predict the crack width at the single cracking stage according to Equation 2-18

$$w = 2 \cdot (1 - \beta) \cdot \frac{\sigma_{\mathrm{nm,trans}}^2 \cdot A_{\mathrm{nm}}}{E_{\mathrm{nm}} \cdot U_{\mathrm{nm,eq}} \cdot \tau_{\mathrm{bm}}(w) \cdot (1 + \rho\, \alpha_{\mathrm{e}})} \,, \tag{5-28}$$

and considering the derived formulation of the mean bond stress $\tau_{bm}(w)$ according to Equation 5-13, the crack width at which the transition occurs is obtained:

$$w_{trans} = \left[\frac{8 \cdot f_{ct,ef}^2 \cdot A_{nm} \cdot (1-\beta) \cdot 2^{\alpha} \cdot (\alpha+1) \cdot (1+\rho\alpha_e)}{U_{nm,eq} \cdot E_{nm} \cdot \rho_{ef}^2 \cdot \xi_F^2 \cdot C} \right]^{\frac{1}{\alpha+1}} \tag{5-29}$$

Consequently, the determined crack width w_{trans} is the crack width at which the transfer length at the single cracking stage is equivalent to the effective maximum crack spacing in a concrete member. The formulation in Equation 5-29 already considers the expression of the mean value of bond stress $\tau_{bm}(w)$ as a function of the calibration parameters C and α.

Finally, in order to facilitate the consideration of both, the transition to the stabilised cracking stage and to allow for adjacent cracks with a spacing greater than the maximum spacing at stabilised cracking, the effective maximum crack spacing is then obtained as follows:

$$s_{r,max,ef} = \frac{2 \cdot f_{ct,ef} \cdot A_{c,net}}{\tau_{bm}(w) \cdot U_{nm,eq} \cdot \xi_F} \geq \frac{2 \cdot f_{ct,ef} \cdot A_{c,net}}{\tau_{bm}(w_{trans}) \cdot U_{nm,eq} \cdot \xi_F} \tag{5-30}$$

Note that for the lower limit the mean bond stress is obtained using the crack width at the time of transition w_{trans}.

Case study to the predicted force transfer between adjacent cracks

Having established an approach to predict the maximum crack width at stabilised cracking, which is expressed in Equation 5-25, the influence of the three introduced cases regarding the bond capacity and tension stiffening is addressed in the following. Therefore, a case study is preformed to highlight the sensitivity of Equation 5-25 in regard to the determined force transfer described by the three cases.

The contribution of force transfer is quantified by introducing the parameter χ. When no force is transferred, χ is zero, and in the case of perfect bond and the immediate full force transfer, $\chi = 1.0$. Therefore, subtraction term in the formulation of the mean strain difference in Equation 5-25 is considered to be equivalent to the parameter χ. For evaluation purposes, the parameter χ is normalised in regard to the reinforcement stress:

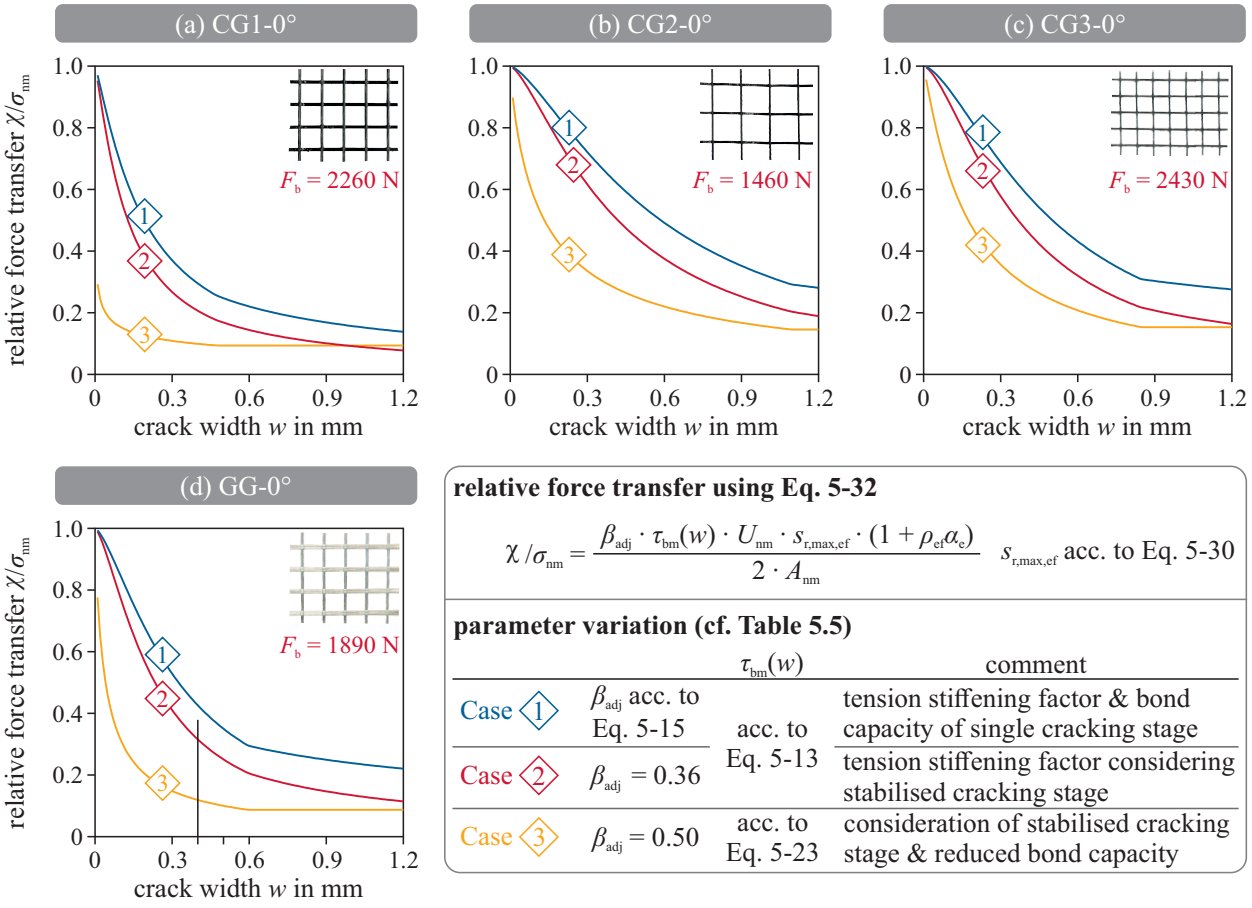
$$\frac{\chi}{\sigma_{nm}} = \frac{\beta_{adj} \cdot \tau_{bm}(w) \cdot U_{nm,eq} \cdot s_{r,max,ef} \cdot (1+\rho_{ef}\alpha_e)}{2 \cdot A_{nm}} \tag{5-31}$$

Considering in Equation 5-31 the proposals of each case regarding the bond capacity and tension stiffening given in Table 5.5, the curves plotted in Figure 5.12 for the four textile grids are obtained. Note, that for Case 2 the evaluation is done with $\beta = 0.36$ as no consideration of tension stiffening results in no force transfer. For Case 3, the bond force F_b required to apply Equation 5-23 is obtained from the SPOc test results and given in Figure 5.12.

In general, all three cases reveal that with larger crack widths, the relative value of the transferred force, which is expressed by χ/σ_{nm}, decreases. This is attributed to the non-linear bond stress evolution, which also indirectly influences the formulation given by Equation 5-25 with regard to the maximum crack spacing. The first two cases utilise the same definition of the bond capacity, but consider different values for β. Case 1 in Figure 5.12 has the identical contribution of tension stiffening as for a single crack. This is, of course, a mere theoretical consideration, as the previous investigations showed that the bond capacity for textile grids for adjacent cracks is lower. As expected, the assumed force transferred is lower in the second case compared to Case 1, which is the result of the smaller β-value.

The assumptions introduced in Case 3 reveal the largest reduction in the relative force transfer of all three cases. For example, when evaluating the crack width at 0.4 mm in the case of reinforcements CG1, the relative force transfer χ/σ_{nm} is about 10% of the full full transfer. For Case 2 approximately 20% and for Case 1 30% of the full force are assumed to be transferred. At large crack widths above 1.0 mm, the relative force transfer determined for Case 2 falls below the value obtained for Case 3.

In conclusion, this case study shows that assuming the bond stress evolution to be identical for single cracking and stabilised cracking requires an adaptation of the tension stiffening factor β as proposed in Case 2, to account for the experimental findings showing the reduced contribution of tension stiffening in the case of adjacent cracks. Furthermore, an adaptation of the bond stress can be considered reasonable, which was exemplified in Case 3 by introducing the linear function in Equation 5-23 using results from the SPOc tests.



relative force transfer using Eq. 5-32

$$\chi/\sigma_{nm} = \frac{\beta_{adj} \cdot \tau_{bm}(w) \cdot U_{nm} \cdot s_{r,max,ef} \cdot (1 + \rho_{ef}\alpha_e)}{2 \cdot A_{nm}}$$

$s_{r,max,ef}$ acc. to Eq. 5-30

parameter variation (cf. Table 5.5)

	β_{adj}	$\tau_{bm}(w)$	comment
Case 1	β_{adj} acc. to Eq. 5-15	acc. to Eq. 5-13	tension stiffening factor & bond capacity of single cracking stage
Case 2	$\beta_{adj} = 0.36$		tension stiffening factor considering stabilised cracking stage
Case 3	$\beta_{adj} = 0.50$	acc. to Eq. 5-23	consideration of stabilised cracking stage & reduced bond capacity

Figure 5.12: Case study to determine the assumed relative force transfer in relation to the maximum crack width

Validation of physically based model

In the following, the physically based model for predicting the maximum crack width is validated using the UT test series. At first, the focus is on the qualitative representation of the maximum crack width measured in the UT test series on normal-strength concrete with a maximum aggregate size of 5.6 mm and a single layer of reinforcement. To utilise the model following Equation 5-25, the mean bond stress and tension stiffening is considered as previously proposed by Case 2 and Case 3. For the second case, the tension stiffening factor β holds 0.36 or tension stiffening is neglected ($\beta = 0$). The obtained prediction curves are plotted in Figure 5.13, with the test data represented as an envelope of the maximum and minimum values of crack width. Hereby, all

cracks after the occurrence of the second crack or after the cyclic loading stage are considered. The effective maximum crack spacing $s_{r,max,ef}$ was determined following Equation 5-30. For reference, the minimum value, which is the crack spacing at the predicted transition to the stabilised cracking stage, is given for each series in Figure 5.13. To provide for a better visualisation, the evaluation focuses on crack widths below 1.6 mm.

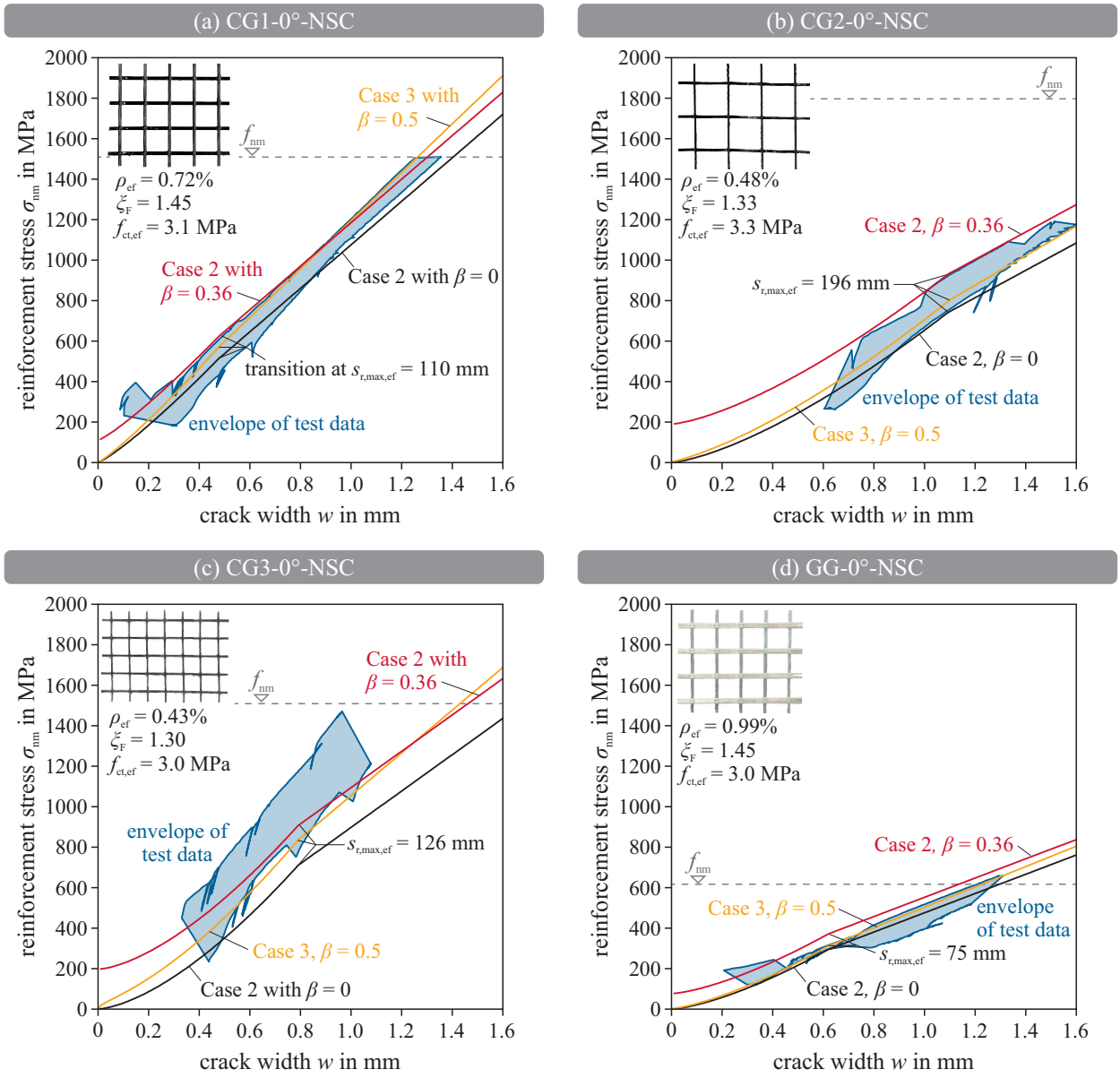


Figure 5.13: Validation of maximum crack width prediction considering the UT tests with normal-strength concrete and a single layer of reinforcement

As evident when focusing on Figure 5.13, the approach of Case 2 with $\beta = 0.36$ reflects the upper reinforcement stresses of the test data of series CG1 and CG2, which intends an underestimation of the maximum crack width. On the other hand, for Case 2 and $\beta = 0$ the prediction is at the lower reinforcement stresses of the two test series. For series CG3 in Figure 5.13c, assuming $\beta = 0.36$ shows to be more feasible, while in case of series GG (Figure 5.13d), $\beta = 0$ proves to be more accurate. Regarding the approach of Case 3, the obtained crack widths are in general between the two predictions of Case 2. Therefore, this approach is not considered in the further evaluations.
The evaluation in Figure 5.13 also highlights the importance of considering the transition to the stabilised cracking stage, which is addressed by the introduced limitation of the maximum crack

spacing in Equation 5-30. This limitation prevents the determination of low values of maximum crack spacing at the stabilised stage, which would result in an underestimation of the crack width.

Verification regarding different boundary conditions

At last, the model is verified using the approaches of Case 2, considering the remaining UT test series which show different boundary conditions. In Figure 5.14, the first row shows the series with multiple layers of reinforcement, the second row illustrates the influence of a maximum aggregate size of 16 mm, and the last row presents the series with high-strength concrete. Case 2 with $\beta = 0.36$ is plotted as red curve in the diagrams and $\beta = 0$ is shown in black.

In general, the validation revealed that both approaches provided good results. The consideration of tension stiffening, as done in the first approach, led to a more progressive prediction. In the case of CG1-0°-NSC-16mm, this resulted in a noticeable underestimation of the test result for crack widths above 0.8 mm (Figure 5.14b1), which are assumed to be outside the scope of the serviceability limit state. In addition, the prediction for single cracks becomes decisive for crack widths below 0.8 mm when considering the results of these tests. This classification of the prediction also applies to GG-0°-NSC-16mm, where both approaches did not meet the test result (Figure 5.14b3).

Three observations are worthy of remark. Firstly, the sensitivity of the prediction with regard to the assumed effective concrete tensile strength $f_{\mathrm{ct,ef}}$, which was set to be equivalent to the mean concrete tensile strength f_{ctm} obtained in the material tests. In order to quantify this sensitivity, the focus is directed towards test series CG1-0°-NSC-4L (Figure 5.14a3). The approaches resulted in a significant overestimation of the crack widths above 0.2 mm of the test data envelope. To calibrate the two approaches to achieve a better fit with the test data, it is possible to utilise an adapted value of the effective concrete tensile strength. Upon execution of the aforementioned step, the strength $f_{\mathrm{ct,ef}}$ is reduced to approximately 2.2 MPa, representing a decrease of 29% of the mean concrete tensile strength of 3.1 MPa. This result corresponds to the 5% fractile of the mean concrete tensile strength, and therefore, while not conclusive, the outcome is plausible.

The second observation is addressed to the contribution of tension stiffening in cases where effective reinforcement ratios exceed 1.0%. In such cases, it has been demonstrated that the calculated reduction in crack width, as outlined in Equation 5-25 with $\beta = 0.36$, is less than 0.04 mm when compared to the approach that neglects tension stiffening. Consequently, neglecting tension stiffening does not yield a significantly more conservative crack width prediction.

Finally, it is evident that the observed overestimation is attributable to the transition to stabilised cracking. Referring again to series CG1-0°-NSC-4L, the transition was assumed to occur at a crack width $w_{\mathrm{trans}} = 0.11$ mm and a lower limit of crack spacing of 83 mm. A comparison with the actual test data revealed that the stabilised cracking stage was reached at significantly larger crack widths and, consequently, a smaller maximum crack spacing of 56 mm.

In conclusion, a brief statistical evaluation is provided regarding the performance of the approach in Case 2 utilising the expression in Equation 5-25 with $\beta = 0.36$ and $\beta = 0$, respectively. As illustrated in Table 5.6, the average reinforcement stress considering all tests in each series is compared to the predicted value of reinforcement stress. This is done in relation to the corresponding maximum crack width. To enable a statistically based comparison of the prediction to the average of the test data, the procedure provided in Annex D.8.2 of Eurocode 0 [EC0] is applied. This allows for a comparison with regard to the average fit and the coefficient of variation of the ratio between prediction and test data. The procedure in Annex D.8.2 of Eurocode 0 assumes a log-normal distribution of the test values with the estimated value $\bar{\Delta} = \sigma_{\mathrm{nm,calc}}(w)/\sigma_{\mathrm{nm,test}}(w)$, expressing the relation between prediction and test data. To translate the estimated value into a parameter that better visualises the suitability of the prediction, a nominal estimated value is introduced, determined as $\bar{x} = \exp\left(\bar{\Delta}\right)$. The perfect prediction corresponds to an estimated value of $\bar{\Delta} = 0$, therefore

$\bar{x} = \exp(0) = 1$, which indicates the perfect fit under the assumption of a normal distribution and no variation. Using this approach, the nominal estimated value also indicates whether the prediction underestimates the maximum crack width ($\bar{x} > 1$) or overestimates it ($\bar{x} < 1$). An overestimation of the actual crack width refers to conservative predictions, as to meet the criterion of the serviceability limit state a higher reinforcement ratio is determined by the prediction. The obtained coefficient of variation V_δ requires no nomination, a low variation of the ratio between prediction and test data is assumed for values of V_δ below 10%.

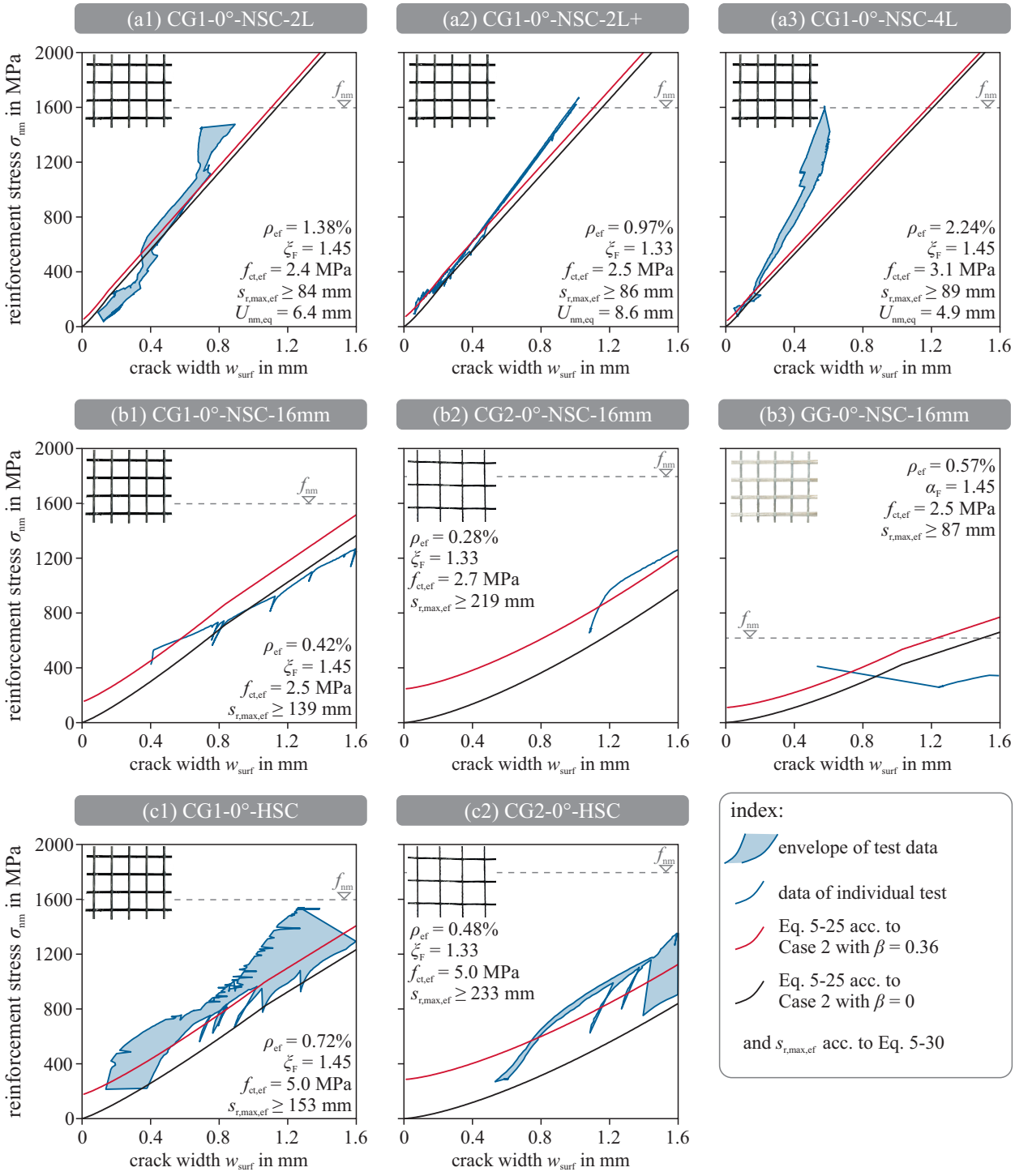


Figure 5.14: Verification of maximum crack width prediction using Case 2 by considering the UT tests with multiple reinforcement layers (a), maximum aggregate size of 16 mm (b), and high-strength concrete (c)

The previous considerations revealed that, during crack formation, the approaches naturally provide a less accurate prediction at the crack formation stage when single cracks and adjacent cracks are present. In addition, the tests in each series themselves vary. Therefore, the statistical evaluation considers only the reinforcement stress values for which the coefficient of variation in the test series was below or equal to 30% to address the variation in test data. In the case of the specimens with a maximum aggregate size of 16 mm, only a single test was conducted. Therefore, the first threshold limit was not applied and all test data was considered.
Summarising, Table 5.6 presents the two statistical parameters of nominal estimated value $\bar{x}$ and coefficient of variation V_δ for both considerations of tension stiffening. As apparent, in many cases both predictions provide for a good fit of the test data, as observed in the previous graphical evaluations. Only the test GG-0°-NSC-16mm is excluded from the following discussions as the predictions were unable to meet the test data, which was already apparent from the evaluation in Figure 5.14. The nominal estimated values $\bar{x}$ were on average 1.05 for $\beta = 0.36$ and $\bar{x} = 0.82$ for $\beta = 0$. The coefficient of variation was always below 30% on average. The consideration of tension stiffening tends to underestimate the crack widths. Neglecting the contribution of tension stiffening provides for more conservative values and a larger scattering. Insufficient predictions of the approaches, for example in the case of series CG2-0°-NSC, where large variations in the predictions were determined, are also found in the graphical evaluations. In this particular case, the approaches met the envelope of the test data at the minimum and maximum boundaries.

Table 5.6: Statistical performance of the maximum crack width prediction at stabilised cracking with two different values of the tension stiffening factor β ($\bar{x} > 1$ indicates underestimation of crack width)

test series	Equation 5-25 with $\beta = 0.36$		Equation 5-25 with $\beta = 0$	
	$\bar{x}$	V_δ [%]	$\bar{x}$	V_δ [%]
CG1-0°-NSC	1.07	12.3	0.89	19.9
CG2-0°-NSC	1.01	14.2	0.72	42.0
CG3-0°-NSC	0.90	6.1	0.65	28.0
GG-0°-NSC	1.15	15.3	0.86	39.9
CG1-0°-NSC-2L	1.07	26.0	0.97	26.3
CG1-0°-NSC-2L+	0.96	7.3	0.84	14.5
CG1-0°-NSC-4L	0.74	21.0	0.66	20.9
CG1-0°-NSC-16mm[1)]	1.09	14.4	0.89	28.9
CG2-0°-NSC-16mm[1)]	0.93	6.3	0.68	18.3
GG-0°-NSC-16mm[1)]	1.79	48.6	1.43	67.5
CG1-0°-HSC	0.95	7.6	0.75	14.5
CG2-0°-HSC	0.94	14.6	0.59	12.5
overall average[2)]	**1.05**	**16.1**	**0.82**	**27.1**

[1)] single test, therefore all test data was considered

[2)] weighted average, considering the number of tests of each series

To summarise the efficiency of two different interpretations of tension stiffening considered in the crack width prediction approach with regard to accuracy, it is found that, in the case of uniaxial tension, both interpretations provide reasonable and satisfying results. In cases where a more progressive consideration is intended, the prediction using Equation 5-25 and including an assumed contribution of tension stiffening with a value of $\beta = 0.36$, is feasible. However, the obtained

values signalise a slight underestimation of the actual crack width, as also the qualitative validation revealed by often predicting the minimum crack width values of the test data envelops (cf. Figure 5.13 and Figure 5.14). Neglecting a contribution of tension stiffening obviously leads to a more conservative prediction, which results in an overestimation of the crack widths when the variation in test data is addressed ($\bar{x} = 0.83$). This evaluation revealed that both interpretations of tension stiffening provide a sound and feasible fit to the test data. A further evaluation with final remarks is addressed in Section 7.2.

5.5.4 Prediction of an average crack width

The consideration of an average crack width or crack spacing is purely theoretical and serves to derive a representative average value that can be converted into a design value, which is feasible to fulfil the serviceability limit state criterion. For example, this is done in the *fib* Model Code 2020 [MC20], where an average crack width is used to determine a characteristic value for design by utilising an empirically calibrated factor, denoted as k_w and set to 1.7. In general, the determination of the average crack width requires an approximation of the average crack spacing. When pure physical considerations are applied, the average crack spacing is between one and two times the transfer length of the corresponding single crack, which are the minimum and maximum values of crack spacing. An exact determination of the average crack spacing is not possible in this consideration due to the anisotropy of the concrete with an inhomogeneous strength field, in particular the tensile strength and the bond strength, within the member. The cracks occur simply at a location by "coincidence", therefore the average spacing is only quantifiable with an empirical-based approach. Numerous research consider the ratio between maximum and average crack spacing in steel reinforced concrete members, which max be assumed to be 1.5, aiming for the geometric mean between the minimum and the maximum crack spacing. In the case of steel reinforced concrete members, KOENIG and TUE determined a ratio of 1.39 [Kön96]. Independent of the reinforcement and considering an inhomogeneous strength field of a material matrix, the ratio between maximum and average spacing was determined to be 1.337 [Wid66], which was verified to be used for reinforced concrete members in [Chu21].

A brief statistical evaluation of the experimentally determined data with regard to the crack spacing and crack width is done and listed in Table 5.7. The ratio between the maximum and the average crack spacing was found to range from 1.04 to 1.58. With regard to the maximum to the average crack width, the ratio was in the range of 1.30 to 2.00. The coefficient of variation determined for all ratios was below 20%, which is notably low considering the overall variation in material strength and the different parameters investigated in the twelve series.
In the context of this statistical evaluation, the maximum crack width is estimated to be approximately 1.5 times the average crack width. This value aligns with the proposals outlined in earlier code provisions, such as [MC10]. In contrast, the factorisation of 1.7, as introduced in [MC20] for steel reinforced concrete members, is not represented by the test data.
The empirically derived ratio in [Wid66] appears to be applicable in the context of establishing a correlation in the case of crack spacing. However, this ratio is not suitable for establishing a link between maximum crack width and a representative average value. KOENIG and TUE addressed that the two ratios of spacing and width do not coincide, as it might initially appear. The primary reasons for this discrepancy are threefold. Firstly, the maximum crack width does not necessarily correspond to the maximum crack spacing when considering a real concrete member. Furthermore, the distribution of material parameters, particularly those of concrete, introduces additional variations between the two parameters of crack spacing and crack width. Thirdly, the transfer length of two adjacent cracks is not of equal length and the local minimum in reinforcement strain evaluation

is not exactly at mid-distance. This finding was confirmed by the numerous FOS measurements that have been conducted and presented previously.

Table 5.7: Ratios between maximum and average crack spacing and maximum and average crack width at the stabilised cracking stage derived from uniaxial tensile tests

test series		number of tests	crack spacing $s_{r,max}/s_{r,m}$ [mm/mm]	crack spacing $\bar{x} = \frac{s_{r,max}}{s_{r,m}}$ (V_x)	crack width on surface w_{max}/w_m [mm/mm]	crack width on surface $\bar{x} = \frac{w_{max}}{w_m}$ (V_x)
CG1-0°	NSC	5	114 / 80	1.43 (16%)	0.66 / 0.48	1.38 (13%)
	HSC	3	138 / 106	1.30 (18%)	0.99 / 0.72	1.37 (10%)
	NSC-16mm	1	169 / 117	1.44 (-)	1.57 / 1.04	1.50 (-)
	NSC-2L	3	68 / 48	1.42 (3%)	0.70 / 0.41	1.70 (17%)
	NSC-2L+	3	85 / 65	1.31 (9%)	0.35 / 0.23	1.54 (6%)
	NSC-4L	3	56 / 36	1.58 (17%)	0.43 / 0.25	1.77 (19%)
	average for reinforcement CG1			1.39 (14%)		1.49 (15%)
CG2-0°	NSC	5	156 / 130	1.19 (14%)	1.48 / 0.92	1.61 (10%)
	HSC	3	169 / 162	1.04 (6%)	1.39 / 1.07	1.30 (5%)
	NSC-16mm	1	200 / 147	1.36 (-)	1.85 / 1.35	1.38 (-)
	average for reinforcement CG2			1.15 (13%)		1.47 (13%)
CG3-0°	NSC	3	109 / 79	1.38 (12%)	0.89 / 0.61	1.45 (12%)
GG-0°	NSC	3	83 / 59	1.41 (7%)	0.91 / 0.57	1.60 (6%)
	NSC-16mm	1	104 / 65	1.58 (-)	2.09 / 1.05	2.00 (-)
	average for reinforcement GG			1.46 (8%)		1.75 (12%)
	overall average			**1.30 (16%)**		**1.51 (14%)**

When utilising the findings in Table 5.7 in regard to a crack width prediction, Equation 5-25 is feasible when substituting the determination for the maximum crack width by a formulation for the average width. This is done by using the determined ratio of 1.5, which then provides for a prediction of the average crack width:

$$w_m = \frac{s_{r,max,ef}}{1.5} \cdot \left[\frac{\sigma_{nm}}{E_{nm}} - \beta_{adj} \cdot \frac{f_{ct,ef} \cdot (1 + \rho_{ef}\alpha_e)}{\rho_{ef} \cdot E_{nm} \cdot \xi_F} \right] \tag{5-32}$$

5.6 Extension to account for a cyclic loading regime

The cyclic loading regime applied in the uniaxial tensile tests with 200,000 load cycles revealed a significant increase in crack width due to the continuous damaging of the bond interface, which reduced the bond capacity. Depending on the utilisation of the concrete tensile strength, concrete tensile fatigue occurred and led to the occurrence of additional cracks. These influenced the further development of the crack opening. Furthermore, it is important to clearly identify the current cracking stage when evaluating the crack width increase. For a single crack the reduction in bond capacity leads to an increase in transfer length in contrast to the reduction in force transfer in the case of adjacent cracks. The uniaxial tensile tests also revealed no significant crack opening due to the cyclic loading regime in the cases of very high reinforcement ratios ($\rho \geq 1.72\%$), multiple layers of reinforcement with sufficient spacing (cf. series UT-CG1-2L+ in Figure 4.16), and high concrete strength.
This is addressed in the following consideration by deriving different calibration parameters for each case. To provide for an extension of the proposed crack width prediction approaches in the previous Section 5.5, at first, a general solution strategy is followed using the previously stated assumptions on the bond stress-crack width relation and differentiating between the stages of single cracking and stabilised cracking. The introduction of a simplified term including a determination of two empirical factors using the UT test data enables the prediction of the crack width increase as a function of the number of load cycles.

Focusing on the single cracking stage at first, the crack width after the application of load cycles is expressed using the initial crack width w_0 and the adaptation of the average bond stress $\tau_{\mathrm{bm,cycl}}(w)$ considering the reduction in bond capacity. Due to the increase in the transfer length occurring at single cracking, the reinforcement strain evolution changes and, consequently, the tension stiffening factor β must be redefined. This is realised by "updating" the initial crack width using the ratio between the average values of bond stress and the tension stiffening factors

$$\Delta w = \frac{w_{\mathrm{cycl}}}{w_0} = \frac{\tau_{\mathrm{bm},0}(w)}{\tau_{\mathrm{bm,cycl}}(w)} \cdot \frac{1-\beta_{\mathrm{cycl}}}{1-\beta_0}. \tag{5-33}$$

When considering the bond stress evolution using the power-law expression in Equation 2-3 and the average value of bond stress as described in Equation 5-13, the two calibration parameters C and α must be redefined to account for the different bond stress evolutions resulting from the cyclic loading.
Considering the mean bond stress (Equation 5-13) and the β-factor derived in Equation 5-15 for the initial state and the state after cyclic loading, the relative increase in crack width is then

$$\Delta w = \frac{C_0 \cdot w^{\alpha_0} \cdot 2^{\alpha_{\mathrm{cycl}}} \cdot (\alpha_{\mathrm{cycl}}+1) \cdot \left(2^{\alpha_{\mathrm{cycl}}-1} \cdot (\alpha_{\mathrm{cycl}}+1) + \frac{1}{1+\rho_{\mathrm{ef}}\alpha_{\mathrm{e}}}\right)}{C_{\mathrm{cycl}} \cdot w^{\alpha_{\mathrm{cycl}}} \cdot 2^{\alpha_0} \cdot (\alpha_0+1) \cdot \left(2^{\alpha_0-1} \cdot (\alpha_0+1) + \frac{1}{1+\rho_{\mathrm{ef}}\alpha_{\mathrm{e}}}\right)}. \tag{5-34}$$

To determine the calibration parameters C_{cycl} and α_{cycl}, setups such as the COT test are required. In Section 3.4.4, test series subjected to cyclic loading were evaluated, although the ten load cycles applied permit only a qualitative evaluation. Despite this fact, these COT tests revealed that the increase in crack opening is easily described by "updating" the parameter C_{cycl} by using a power-law approach according to Equation 2-3, while the parameter α_{cycl} remains identical to the initial value. This observation would significantly simplify the formulation in Equation 5-34. Nevertheless, the cyclically loaded UT tests, discussed in Section 4.2.2, revealed that significantly increase in crack

width occurred during the first 10,000 load cycles, while at a high number of cycles above 100,000 the opening remained almost constant. Therefore, a sole attribution of the additional crack opening to an adaptation of the parameter C only provides for a feasible prediction in the case of a large number of load cycles.
Consequently, both parameters C_{cycl} and α_{cycl} are expressed by their initial value with a reduction term considering the decrease in bond capacity, which is approximated by applying a natural logarithm to the number of load cycles N_{cycl}. This reads to

$$C_{\mathrm{cycl}} = C_0 - \Gamma \cdot \ln(N_{\mathrm{cycl}}) \tag{5-35}$$

and

$$\alpha_{\mathrm{cycl}} = \alpha_0 - \gamma \cdot \ln(N_{\mathrm{cycl}})\,. \tag{5-36}$$

with an introduction of the empirical factors Γ and γ, which have to be fitted by the test data, for example the UT series. The formulation in Equation 5-34 is then restated, introducing the two empirical factors and for simplification, the term $(1+\rho_{\mathrm{ef}}\alpha_{\mathrm{e}})$ is assumed to be approximately 1.0. Following a series of transformations, the predicted crack width increases is expressed as follows:

$$\Delta w = \left[w_0^{-\gamma \cdot \ln(N_{\mathrm{cycl}})} \cdot 2^{2 \cdot \gamma \cdot \ln(N_{\mathrm{cycl}})} \cdot \left(\frac{\alpha_0 + \gamma \cdot \ln(N_{\mathrm{cycl}}) + 1}{\alpha_0 + 1} \right)^2 \cdot \frac{C_0}{C_0 - \Gamma \cdot \ln(N_{\mathrm{cycl}})} - 1 \right] \cdot w_0 \geq 0 \tag{5-37}$$

It is noteworthy that, due to the curve fitting method used in the following to determine the empirical factors Γ and γ, a small number of load cycles may result in a negative crack width increase Δw, which clearly is not realistic. The crack width increase must be positive.

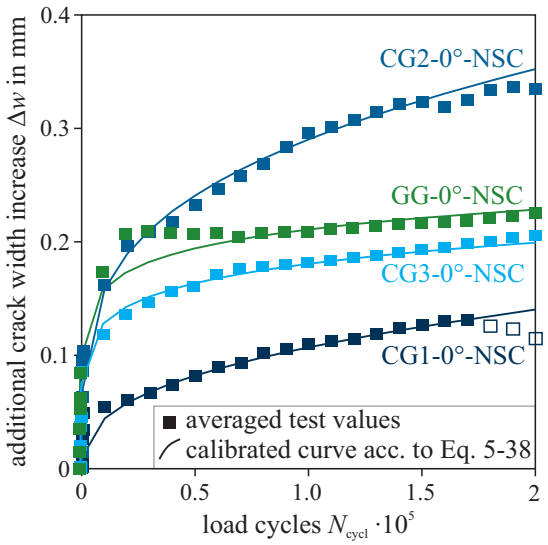
In the case of adjacent cracks, for example at the stabilised cracking stage, where the crack spacing is fixed and does not change during the load cycles, the approach is worthy of being considered critically beforehand when the contribution of tension stiffening is neglected. In the absence of any contribution from the concrete, no force transfer by bond occurs. A decrease in bond capacity is irrelevant to this case. In other words, the reinforcement strain evolution between the two adjacent cracks is constant at the maximum value and no change in the evolution is possible. Consequently, the presence of cyclic loading does not result in a calculated increase in crack width.
Furthermore, a consideration of cyclic loading expressed by adjusted parameters of bond stress and tension stiffening results in a formulation that is equally undetermined to that given in Equation 5-34. Therefore, for the sake of simplicity, the crack width increase Δw for adjacent cracks is assumed to be smaller or equal as to a single crack. In general, the stabilised cracking stage is more robust to an increase in crack width due to cyclic loading as the induced decrease in bond capacity is less pronounced for adjacent cracks, and the higher number of cracks allows for a better homogenisation of the individual crack widths, as the applied deformation is distributed more equally between the cracks.

Based on the derived parameters C_0, Γ, α_0, and γ the crack width increase Δw was determined according to Equation 5-37 and compared with the average crack width increase of the UT tests. In general, this approach is capable to describe the crack width increase under cyclic loading for both, the single cracking stage and stabilised cracking stage. To visualise the comparison between prediction and the UT test data, exemplary the four test series with one reinforcement layer and a normal-strength concrete are plotted in Figure 5.15. In test series CG1-0°-NSC, the determined average value of maximum crack width decreased after 170,000 load cycles, as in the first specimen (cyclic-1) an additional crack occurred. In the other two specimens, no additional crack width increase was observed at this stage. Therefore, these three data points were not considered in the

following calibration. Utilising the approach given in Equation 5-37 for the approximation of the test data, the calibration parameters Γ and γ are derived by curve fitting using the least squares method. The determined parameters are listed in the table of Figure 5.15. For reference, the initial calibration parameters for purely statically loading C_0 and α_0, taken from Figure 5.6, are also provided.

Focusing on the CG1 test series with either a high-strength concrete (HSC), two reinforcement layers with spacing (2L+) or four layers (4L), the test results presented in Chapter 4 showed that no significant crack width increase due to cyclic loading occurred. Consequently, for these cases, the calibration parameters Γ and γ were set to be zero. With the determination of the calibration parameter Γ, the value of 0.38 was found to be feasible for the three carbon grids (CG1, CG2, CG3) in the case of a single reinforcement layer. It is noteworthy that, for the series CG2-0°-HSC, the perfect curve fitting value for Γ is 0.35 (correspondingly $\gamma = -0.019$). For simplicity and accepting a marginal loss in accuracy, the parameter Γ was changed to 0.38. For some cases, one of the two calibration parameters was determined to be almost zero, which was then set to zero for the same reasons.

The diagram in Figure 5.15 reveals the good fit of the calibrated curves using the expression in Equation 5-37 for all four test series considered. With the derived parameters, the observation stated in Chapter 4 is also met: during the first ten thousand load cycles, the crack opening increases visibly, whereas at higher numbers of load cycles, the additional opening is less pronounced, and beyond 150,000 load cycles, no significant further increase in width occurs. In Section 7.3, this approach and the derived calibration parameters are revisited to introduce some possible simplifications and a comparison to test results obtained for flexural members.



test series		C_0	Γ	α_0	γ
CG1-0°	NSC	6.35	0.38	0.18	-0.015
	NSC-2L		0.19		
	NSC-2L+				0
	NSC-4L		0		
	HSC				
CG2-0°	NSC	6.83	0.38	0.42	-0.012
	HSC				0.022
CG3-0°	NSC	11.09	0.38	0.54	0
GG-0°	NSC	12.19	0	0.44	0.014

Figure 5.15: Crack width increase Δw as average from the UT test series and approximated by a logarithmic relation representing the test data using calibration parameters Γ and γ

The derived calibration parameters Γ and γ are, of course, only valid for the boundary conditions set in the test setup, the given material characteristics and the chosen load levels. The formulation in Equation 5-37 is sensitive to the values provided by the two calibration parameters. Minor variations have a substantial impact on the obtained value of the additional crack width. The presented approach is therefore not robust and should be used with caution, which is the result of the "natural" higher scatter of test data obtained during cyclic loading, compared to tests subject to a pure static loading regime, and the relatively small number of tests conducted. Furthermore, the occurrence of additional cracks during the cyclic loading phase due to concrete tensile fatigue, which

influenced the widths of all cracks present, introduced additional inaccuracy. For future research, or when more robust calibration parameters are to be derived, the COT test setup is a favourable alternative.

5.7 Summary

In this chapter a methodology for predicting the crack width of concrete members reinforced with non-metallic textile grids under uniaxial tension was developed. Starting point were characterisation tests for the bond capacity and an analytically consistent model based on a well-known and established maximum crack width approach (cf. [MC90, Kön96]). While the approaches introduced and pursued in this chapter are physically based, a series of assumptions and approximations were introduced to facilitate a consistent and forward-solving strategy.
Characterisation tests, such as the single-sided pull-out test type C (SPOc) or the newly introduced crack opening tensile (COT) test (cf. Chapter 3), provided for bond force-slip or bond force-crack opening relations, respectively. Both relations are feasible to derive a mathematical function for an approximation of a slip-dependent bond stress evolution at the state of a single crack. In this study, a power-law approach was chosen, which proved validity as a steady increase in force at increasing slip was experimentally verified at slip values representing the serviceability limit state. By using a curve fitting method, the two required parameters were determined, denoted A_{SPO} and α_{SPO} when using the SPOc tests or A_{COT} and α_{COT} for the COT tests. The bond stress-slip relation was established through the utilisation of an explicit formulated physically based model that represented the boundary conditions of the two test setups. This enables the establishment of a correlation between the calibration parameters obtained through experimental means and the analytical description of the bond stress-slip relation. The bond stress-slip relation describes the single cracking stage by means of a power-law approach utilising two parameters C and α. In addition, the proposed model allows the determination of a tension stiffening factor β to quantify the contribution of the uncracked concrete section to a reduced crack opening.
To account for the different bond behaviour exhibited by the textile grids under investigation, specific values for C and α were obtained for each reinforcement. Moreover, the validity of the proposed method is dependent on the presence of a sufficient transfer length, as confirmed by the COT tests and the uniaxial tensile tests. The bond behaviour considerably changes at transfer lengths below twice the yarn spacing. This phenomenon is attributed to higher reinforcement stresses in conjunction with the adjacent cracks, as well as the distinct bond mechanisms that act at the local scale of the fibre strand. As a consequence of variations in local undulations, waviness and friction, a bond behaviour is observed (cf. Section 5.1) that, in particular, requires a re-evaluation of the contribution of tension stiffening.

The validation of the proposed model was accomplished by focusing on the single cracking stage and a state of uniaxial tension at first. The prediction of the crack is performed according to the approach outlined in Equation 2-18. This approach assumes a crack width dependent mean value of bond stress, as determined by Equation 5-13. The calibration parameters C and α are taken into account, along with the tension stiffening factor β (Equation 5-15). In order to account for the influence of a compacted placement of multiple reinforcement layers with small spacing between each layer, which was found to significantly reduce the bond capacity, an equivalent circumference was introduced. The equivalent circumference is calculated by considering the spacing between the reinforcement layers, as well as the number of layers.

In the second validation step, the stabilised cracking stage was addressed. Therefore, a feasible determination of the maximum crack spacing is required. The experimental campaign, which employed the uniaxial tensile tests discussed in Chapter 4, and investigations reported literature, demonstrated that a close crack spacing is a characteristic of textile reinforced concrete members. Furthermore, an adjacent crack frequently occurrs in the transfer length of an existing crack rather than outside of this transfer length. These observations were attributed, at least in part, to the elliptical cross-section of the fibre strand, which has been identified as a factor that leads to localised stress concentrations along the strand's circumference. These concentrations subsequently result in premature cracking. In order to account for this phenomenon, a stress intensifying factor was introduced. This factor considers the geometrical characteristics of the fibre strand, as assumed in [Pre19a, Pre20b] in the context of concrete splitting. In addition, a lower limit was imposed on the maximum crack spacing, with the objective of ensuring a realistic behaviour and a physically solid transition between single cracks in the crack formation stage and the stabilised cracking stage. The stress intensifying factor and the lower limit allowed for the definition of the effective maximum crack spacing according to Equation 5-30. Having established this, a maximum crack width prediction at stabilised cracking using the formulation given in Equation 5-25 is possible.

The general formulation in Equation 5-25 considers an approximation of the mean value of bond stress and the contribution of tension stiffening. It was found that considering the bond stress relation determined for the single cracking stage provided feasible results when an adjustment to the tension stiffening factor is made in the case of stabilised cracking. On the other hand, taking the observed reduced bond capacity directly into account, which was done by utilising the results in the experimental campaign on single-sided pull-out tests, proved to provide similar results and no enhancement of the prediction. Consequently, an adjustment regarding the contribution of tension stiffening was considered by two different assumptions, the first one using the value of $\beta = 0.36$ (progressive assumption), obtained in the COT test series in the case of stabilised cracking, and the second assumption neglects the contribution of tension stiffening. Both resulted in good predictions and proved to be suitable for consideration in the following evaluations (see Section 6.4 and Chapter 7).

To conclude, a methodology was derived and presented in this chapter to determine the maximum crack width in textile-reinforced members subject to uniaxial tension. These approaches consider the different cracking stages, the bond stress-slip relation, the number and spacing of multiple reinforcement layers, the influence of the elliptical cross-section of the fibre strand on inducing new cracks, and the influence of cyclic loading. The validated model will be verified also for members subjected to bending in Chapter 6.

6 Crack width and deflection in flexural members

6.1 Outline and aims of the campaign

The previous investigations concentrated on characterising the bond behaviour at a single cracking stage, deriving a physically based model to predict the crack width, and extending this model to the stabilised cracking stage. In addition, the increase in crack width due to cyclic loading was addressed. All of the aforementioned steps were performed at a state of uniaxial tension. In this chapter, the transfer to members subject to bending is addressed, with the focus on two main objectives: to demonstrate the applicability of the proposed model for predicting the crack width of flexural members; to establish a methodology for predicting the deflection of these members under static and cyclic loading. The experimental campaign on slender textile reinforced concrete slabs constituted the basis for this.
The campaign was performed on a total of twelve four-point bending tests on slabs. The slabs were reinforced with multiple grid layers of reinforcements CG1, CG2, CG3 and GG, and followed the test strategy that had been introduced with the uniaxial tensile tests. Thus, one static test and two tests with a cyclic loading phase representing the serviceability state for the limitation of crack width were conducted in each series.
Starting with the general description and evaluation of the experimental campaign outlined in Section 6.2, the two main objectives of this chapter are addressed. The crack width prediction is focused in Section 6.4 and the deflection prediction in Section 6.5. Special attention is on the influence of the cross-section curvature on the crack opening and the contribution of tension stiffening regarding deflection, in particular at higher reinforcement utilisations and in case of cyclic loading.

6.2 Experimental campaign on slabs

6.2.1 Concept and setup of four-point bending tests

The purpose of the test configuration was to establish a methodology for situations where large deflections and crack openings are occurring prior to the distinct stabilised cracking stage. The specimens were prepared in a prefabrication plant. Consequently, the concrete mixture utilised in this study differed from those employed in the preceding experimental campaigns. In this instance, the maximum aggregate size was increased to 8 mm and the concrete was likewise classified as a normal-strength concrete. The primary motivation behind the selection of a prefabrication facility was to validate the feasibility of thin concrete members reinforced with textile grids in an environment that more closely resembles a practical application of textile reinforcement than the controlled conditions of a laboratory setting. The adaptation of the concrete mixture was conducted to substantiate the general applicability of the analytical model to diverse concrete mixtures. The three specimens of each series were simultaneously concreted with an identical batch. The concrete mixture is provided in Appendix B.1.

The four series, differentiated oneself according to the used reinforcement, consisted of one purely statically loaded specimen and two specimens with an additional cyclic loading phase. The setup of the four-point bending tests is visualised in Figure 6.1. The intended cross-section had a width of 300 mm and a height of 110 mm, while the actual dimensions were measured prior to testing due to deviations in the prefabrication plant and are provided in Table 6.1. The location of the

reinforcement and the concrete cover c were both measured after the tests using saw cuts. A shear slenderness a/d of approximately 10 was chosen to avoid the occurrence of shear failure.

The series denoted as S-CG1 consisted of two layers of reinforcement CG1 (Figure 6.1b), with the index "S" referring to slab. For series S-CG2 and S-CG3 also two layers of textile grids were chosen, while in both, an overlapping joint was placed in mid-span, as the provided textile reinforcement was limited in total length. The lap joint had a length of 900 mm in the case of series S-CG2 (reinforcement CG2, Figure 6.1c), being about 18 times the yarn spacing, and for series S-CG3 of 300 mm (12 times the yarn spacing of reinforcement CG3, Figure 6.1d). This allowed the investigation of the influence of different lap lengths. Series S-GG was reinforced with three layers of GG with an additional layer placed in mid-span to account for the larger tensile forces induced by the bending moment to allow for a higher ultimate loading of the member (Figure 6.1e).

The test load was applied displacement-controlled during static loading and force-controlled during the cyclic loading phase employing a single hydraulic cylinder. The distance of 700 mm between the two loading points was ensured by using a steel load traverse. The test procedure for the cyclically loaded specimens consisted of three distinct phases, which are in accordance with the procedure of the uniaxial tensile tests described in Chapter 4. At first, the static deformation was increased until the onset of the stabilised cracking stage was reached, representing the adjacent crack pattern typically occurring during the service life. At this stage, the superior load level F_{sup} was defined for the following cyclic loading phase. The inferior load level F_{inf} was intended to allow for a bending moment close to the cracking moment M_{cr}. The frequency was set to 2.0 Hz, and 200,000 cycles were conducted. Thereafter, a statically increasing deformation was applied until failure occurred. The tests were conducted at different concrete ages, resulting in varying concrete parameters and, consequently, differing load levels, with an overview provided in Table 6.2.

The linear strain distribution and the calculated reinforcement stress in the cross-section is iteratively determined following the procedure introduced in Section 6.3.

Table 6.1: Specifications of the four-point bending tests at mid-span (excluding additional reinforcement to realise the lap joint)

index		t_0 [d]	n_{layer} [-]	h [mm]	b [mm]	d [mm]	c [mm]	a/d [-]	ρ [%][1)]
CG1	static	13	2	106	300	87	15.5	10.3	0.46
	cyclic-1	14		107	300	87	15.5	10.3	0.46
	cyclic-2	114		110	300	91	15.0	9.9	0.44
CG2	static	29	2	106	300	90	13.0	10.0	0.28
	cyclic-1	30		107	300	90	14.0	10.0	0.28
	cyclic-2	117		103	300	90	12.0	10.2	0.29
CG3	static	28	2	110	300	93	14.0	9.7	0.28
	cyclic-1	46		110	300	93	14.0	9.7	0.28
	cyclic-2	116		110	300	93	14.0	9.7	0.28
GG	static	27	4	110	300	88	13.5	10.2	1.24
	cyclic-1	54[2)]		110	300	90	12.5	10.0	1.21
	cyclic-2	117		110	300	90	12.5	10.0	1.21

[1)] related to the concrete cross-section $b \cdot d$

[2)] test interrupted after 55,000 load cycles and restarted after 109 days.

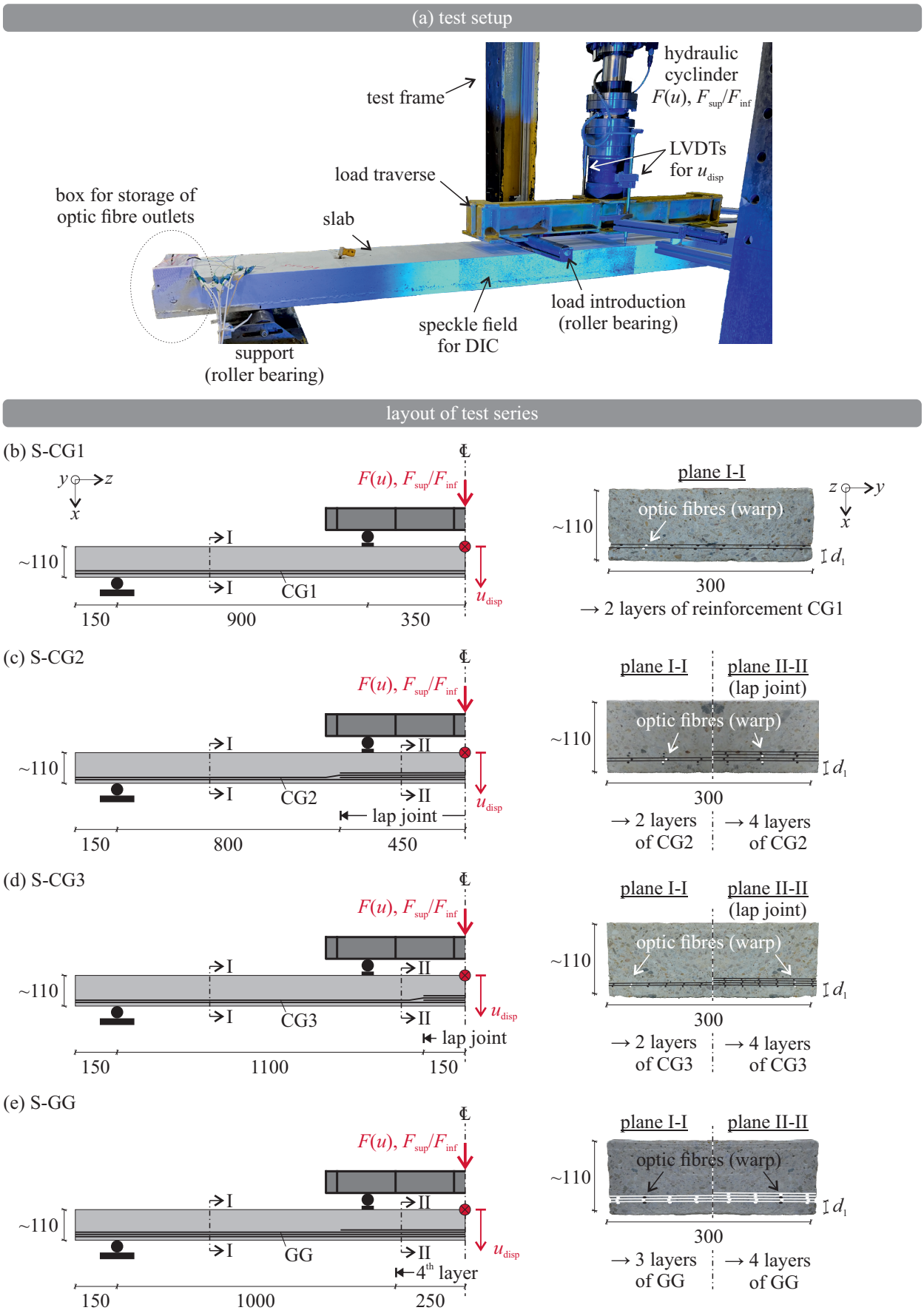


Figure 6.1: Test setup and reinforcement layout of the slabs

Fibre optical sensors were placed on several longitudinal fibre strands in all reinforcement layers, except the layers just resembling the lap joint or the 4th layer for series S-GG. The optical fibre was acrylate coated and fixated with a cyanoacrylate adhesive as a chemical bond on the side of the fibre strand that has a continuous profile and is not affected by local undulations. The gage pitch and gauge length were set at 0.65 mm with a measuring rate of 6.25 Hz to obtain a continuously distributed strain measurement. The post processing is done identically to the previous investigations, as described in Section 3.5. The speckle field for digital image correlation (DIC) was sprayed on one side of the specimen, covering a length of approximately 650 mm from mid-span, to investigate the crack behaviour in the area of constant and linear bending moments. The deflection was measured by two linear variable differential transformers (LVDTs), positioned on each side at mid-span on the top of the specimen, as depicted in Figure 6.1. At the end of the specimens, a polystyrene box was installed to safely store the optical fibres during concreting and test preparation.

6.2.2 Load-deflection behaviour

The load-deflection behaviour is evaluated in relation to the applied bending moment. The depicted deflections in Figure 6.2 resulted from the average of both vertical LVDT measurements. Hereby, the self-weight of the concrete slab (density of 2350 kg/m^3) and the load traverse of 0.37 kN led to an additional moment of 0.69 kNm at mid-span. For reference, the vertical axis on the right-hand side of each diagram provides for a calculated reinforcement stress, which is obtained using the design geometric parameters of a fixed height of the member of 110 mm and a concrete cover of 14 mm. For reference, the determined linear moment-deflection relation, assuming no contribution of tension stiffening and a fully cracked slab, is plotted as a black dashed line and denoted as $\kappa_{\mathrm{II,ideal}}$. Furthermore, the change in the reinforcement stress between the superior and inferior load levels is given.

The moment-deflection curves in Figure 6.2, with consideration of the data provided in Table 6.2, allow for the following observations. Initial cracking occurred in the area close to the load introduction in the direction of mid-span. The moment at initial cracking depended on the concrete tensile strength and ranged from 1.7 kNm (specimens S-CG1-static and -cyclic-1, Figure 6.2a) to 2.7 kNm (specimen S-GG-cyclic-2, Figure 6.2d). Considering the serviceability criterion for deflection with $l/250 = 10$ mm according to [MC20, EC2, FprEC2, DAfStb24] as point of interest, this criterion was met at very low bending moments compared to the failure load and before reaching a crack width limit of 0.4 mm (see in detail evaluation in Section 6.4) and prior to reaching a stabilised cracking stage. In the given test configuration with its high slenderness, the moment at the deflection limit, denoted as M_{SLS}, was reached at 1.14 to 1.56 times the cracking moment (cf. Table 6.2). This was below 28% of the ultimate load for series S-CG1, S-CG2 and S-GG, and below 41% in the case of series CG3. For the latter, the transition to stabilised cracking occurred at about 50 to 60% of the ultimate bending moment at mid-span (Figure 6.2c). In the case of the other three series (S-CG1, S-CG2 and S-GG), most cracks occurred at a bending moment below one-third of the failure load, resulting in a pronounced stabilised cracking stage. Some additional cracks occurred at higher loading in the area closer to the supports and in the vicinity of existing cracks (cf. Section 5.5.2).

The increase in deflection due to cyclic loading depends on the superior load level, the magnitude of the amplitude, the concrete strength and stiffness as well as the reinforcement type and reinforcement ratio. For higher load levels and amplitudes as well as lower concrete strength and stiffness, the deflection increase is more pronounced. All three criteria were met in specimen S-CG2-cyclic-1

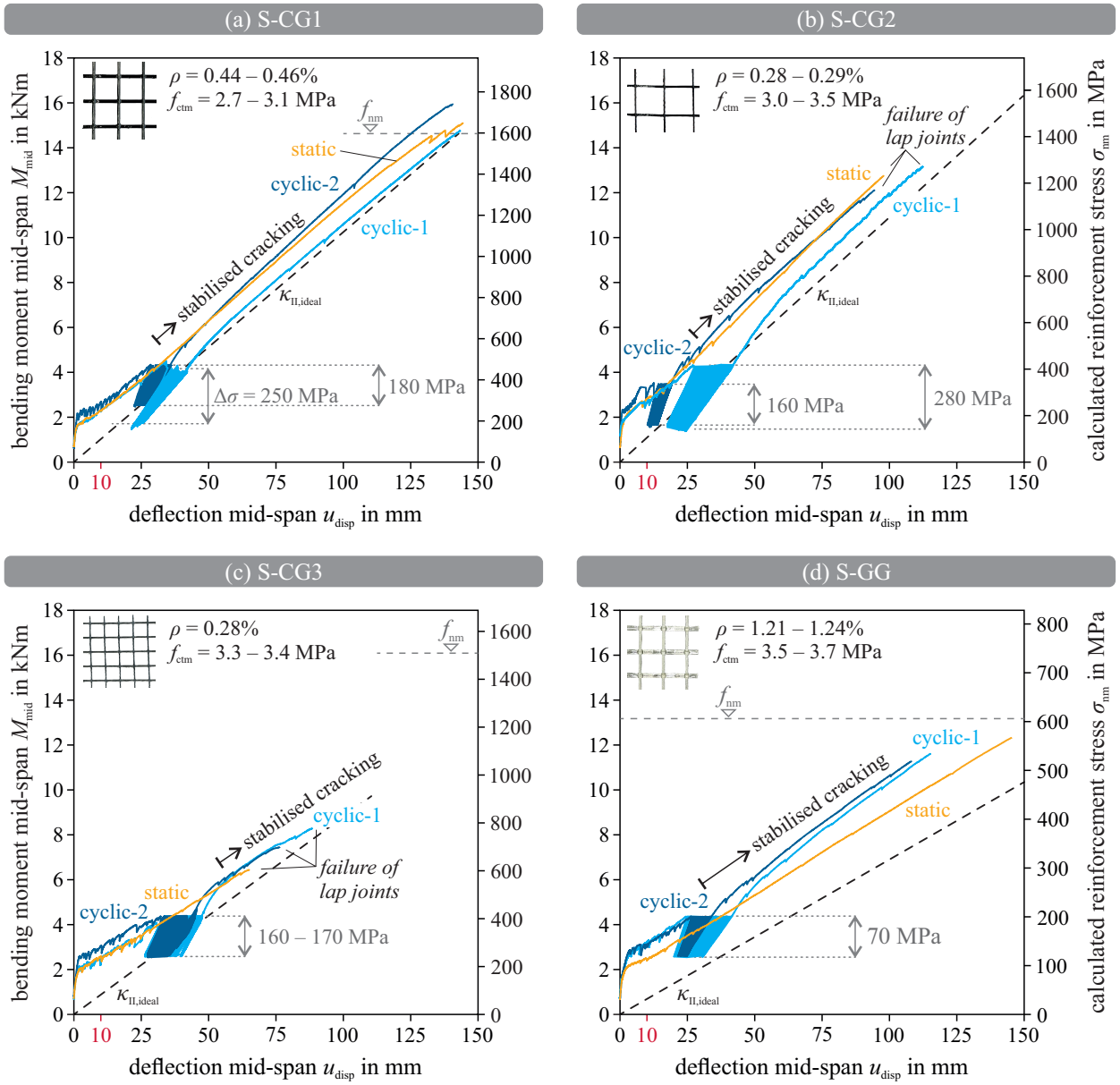


Figure 6.2: Evaluation of bending moment in relation to deflection at mid-span

and, as a result, the largest increase was detected with $\Delta u_{\text{sup}} = 14.4$ mm (Figure 6.2b). In contrast, the lowest increase of 4.7 mm was present in the same series in specimen S-CG2-cyclic-2, where the bending moment at the superior load level was the lowest and a higher concrete strength was present. Nevertheless, even in this case of the lowest increase in deflection, the magnitude of the increase was almost at least half the SLS deflection criterion of $l/250$, being 5 mm.

Despite different concrete strengths and Young's moduli present and the different magnitude of influence from cyclic loading, the deflection increase is characterised by an identical or a parallel evolution of the moment-deflection curves within a series. At stabilised cracking, the curves developed linearly. Only in the case of the specimens with S-GG, the moment-deflection curve of the purely statically loaded specimens showed a lower stiffness compared to the other two cyclically loaded slabs. This is justified by the significantly lower concrete tensile strength resulting in a lower bending moment present at initial cracking, an earlier transition to the stabilised cracking stage and a smaller number of cracks with larger openings and less stiffness of the uncracked concrete sections.

In the context of the idealistic moment-deflection curve, the distance to the actual test data serves as an indicator of the presence of tension stiffening, as this phenomenon reduces the deflection of the member. The findings of this evaluation demonstrated a correlation between the magnitude of the contribution of tension stiffening and the textile grid employed. This observation is analogous to the results obtained in the uniaxial loading tests discussed in Chapter 4. For instance, specimens with reinforcement S-CG1 exhibited a reduced contribution of tension stiffening at the stabilised cracking stage in comparison to specimens with GG, where the contribution of tension stiffening is pronounced. In order to quantify the contribution of tension stiffening it is necessary to determine the reinforcement strain evolution along the transfer length. This is provided by the fibre optic sensors and is presented in Section 6.2.5.

Table 6.2: Bending moment and member deflection at mid-span of the slabs

index		M_{cr} [kNm]	M_{SLS} [kNm][1)]	M_{sup} [kNm]	M_{inf} [kNm]	Δu_{sup} [mm][2)]	M_{max} [kNm]	$u_{M,max}$ [mm]
CG1	static	1.73	2.31	-	-	-	15.09	144
	cyclic-1	1.68	2.23	4.0	1.7	12.5	14.76	143
	cyclic-2	2.18	2.67	4.4	2.6	7.5	15.94	141
CG2	static	2.02	2.81	-	-	-	12.76	988
	cyclic-1	1.84	2.63	4.3	1.5	14.4	13.15	112
	cyclic-2	2.29	2.94	3.5	1.7	4.7	12.11	94
CG3	static	2.04	2.57	-	-	-	6.45	65
	cyclic-1	1.96	2.47	4.4	2.6	12.0	8.28	88
	cyclic-2	2.60	3.03	4.4	2.6	10.4	7.45	77
GG	static	2.00	2.39	-	-	-	12.33	146
	cyclic-1	2.52	3.21	4.4	2.6	17.1	11.60	115
	cyclic-2	2.74	3.11	4.4	2.6	8.0	11.28	108

[1)] at $l/250 = 10$ mm

[2)] due to cyclic loading at superior load level

To summarise the observations with a particular focus on the serviceability limit state, as evident, the deflection is depending on the design of textile-reinforced members. The benefits gained from the high utilisation of the reinforcement material in comparison to steel reinforced concrete members are partially reduced due to larger deflections. A similar conclusion was drawn, for example, in [Spa23]. However, these substantial deflections are attributable to the elevated strain utilisation of the linear elastic behaviour exhibited by the non-metallic reinforcement in comparison to steel rebars, with the latter undergoing yielding at approximately 2.5 mm/m. Greater tensile strain has been shown to increase the curvature of the cross-section, leading to an enhancement in deflection, particularly when the depth of the cross-section is minimal, as is the case in the present experimental campaign. Furthermore, the contribution of tension stiffening is less pronounced due to the high utilisation of reinforcement and closer crack spacing compared to steel reinforced members, as highlighted in the UT test campaign (cf. Chapter 4). Furthermore, it is imperative to acknowledge the substantial increase in deflection that was observed due to the application of cyclic loading, a factor which demands careful consideration.

6.2.3 Failure characteristics

With regard to the failure of the specimens, it is distinguished between slabs with and without lap joints. For the latter (series S-CG1 and S-GG, Figure 6.2a+d) tensile failure of the reinforcement occurred. The area in which the rupture of the fibre strands was detected was located either in close proximity to the load introduction area for specimens S-CG1 or at the end of the additional reinforcement layer in the case of S-GG. This is due to discontinuities at these locations, which led to stress concentrations and lateral pressure on the reinforcement, forcing the rupture of the strands.
In the case of the test series S-CG2 and S-CG3 (Figure 6.2b+c), failure occurred in the lap joint accompanied by longitudinal splitting cracks in the reinforcement layer. Prior to failure, splitting cracks were observed close to the beginning of the lap joint. In the case of specimens S-CG2, where the joint measured 900 mm in length, longitudinal cracks propagated stepwise to the next flexural crack in the direction of mid-span until the sudden failure of the lap joint occurred. In circumstances where the concrete strength between reinforcement layers is exceeded, macro-cracking of the concrete occurs. Consequently, the area affected is unable to participate in force transfer. The remaining areas of the lap must account for the redistributed force. For specimens S-CG2, part of the lap is less utilised and is capable of accounting for redistributed forces, resulting in stepwise longitudinal crack propagation.
When the lap joint is realised with a short length, as in the case of specimen S-CG3 with 300 mm, no stepwise longitudinal crack propagation was observed. The whole lap is almost fully utilised, resulting in the entire lap failing immediately.

Besides the different behaviour at failure of the lap joints, differences in the magnitude of the maximum bending moments between the statically and cyclically loaded slabs are revealed by Figure 6.2b+c. While in series S-CG2 all three slabs exhibited analogous failure moments, for series S-CG3 an elevated failure load was observed in the two cyclically loaded specimens in comparison to the purely statically loaded specimen. In the previously evaluated bond characterisation tests, reinforcement CG2 demonstrated a reduced contribution of local undulations to the force transfer, with friction proving to be the predominant force transfer mechanism (cf. Section 3.4). Friction was found to be less influenced by the cyclic loading, as the surfaces of the grid and concrete in the contact zone experienced less damage. Consequently, no change in the local stress concentration occurred when comparing the purely statically loaded slabs with the cyclically loaded slabs. As the failure of the lap joints in series S-CG2 occurred at comparable bending moments, the local stress concentration inducing the longitudinal cracks was of no difference between the slabs.
In contrast, with regard to series S-CG3, it is assumed that the local stress concentration is reduced by cyclic loading. Consequently, lap failure with longitudinal cracking occurred at higher bending moments for specimens S-CG3-cyclic (Figure 6.2c). Furthermore, the short length of the lap joint prevented force redistribution, which would have been advantageous in terms of maximum loading for the statically loaded specimens S-CG3-static.

In consideration of series S-GG, Figure 6.2d reveals that the cyclically loaded specimens exhibited reduced failure moments in comparison to the purely statically loaded specimen. This is explained by the presence of a localised stress concentration at the beginning of the additional reinforcement layer. The crack pattern (provided in Appendix D.4) revealed that at this location the largest crack opening was measured and the rupture of the fibre strands was found. This area was subjected to even greater utilisation when cyclic loading was applied, inducing additional damage to the reinforcement and provoking rupture of the fibre strand.

6.2.4 Crack width and crack spacing

Concrete surface at the layer of reinforcement

The evaluations of the average crack width and maximum crack width, located at the layer of the reinforcement, in relation to the calculated reinforcement stress are plotted in Figure 6.3. Consequently, the crack width is related to the actual, yet calculated, tensile bending force in the reinforcement. The envelopes of the average and maximum crack widths of the uniaxial tensile test campaign (UT) are plotted as a grey area in the diagrams. The crack pattern of each specimen visualised by DIC is provided as reference on the right-hand side of Figure 6.3. In addition, the average and maximum values of crack spacing were determined for the evaluated cracks and are also provided in the figure.

The evaluation indicates that the average and maximum crack widths of the three tests in each series exhibited a high degree of similarity in relation to the reinforcement stress. The most suitable example is provided for series S-CG1 (Figure 6.3a). In the few cases of discrepancy, e.g. for the maximum crack width evolution of specimen S-GG-static (Figure 6.3d2), this is justified with a low concrete tensile strength, which corresponds to the observations made in the moment-deflection curve in Figure 6.2. In the case of series S-CG3, the maximum crack width was identified in the area of the largest bending moment where the lap joint was located (see Figure 6.3c2). Consequently, the reinforcement stress was determined considering four layers of reinforcement. The obtained maximum stress of approximately 740 MPa was lower than the reinforcement stress outside the lap joint, where only two reinforcement layers were present.

The maximum crack width during the cyclic loading regime increased by at most 0.15 mm for specimen S-CG3-cyclic-1 (Figure 6.3c2). For all other eleven specimens, the increase of the maximum crack width was below 0.11 mm. A lower maximum crack width of a flexural member in comparison to the UT tests is only applicable to the series S-CG1 and S-CG3 (Figure 6.3a2+c2). The other series S-CG2 and S-GG showed maximum crack widths that were in the range or are even greater than the widths represented by the envelopes of UT series (Figure 6.3b2+d2).
The average crack widths of the slabs were lower than or at most the minimum values of the envelope of the UT series. The only exception is attributed to the average crack width evolution of specimen S-GG-static, which falls in the range of the average values obtained in the UT series (Figure 6.3d1). Consequently, the maximum crack width occurring in flexural members is generally not less than of members subject to uniaxial tension, while this was found to be the case with regard to the average crack width.

The average crack spacing was found to range between the yarn spacing (S-CG2-cyclic-1 with $y_{\mathrm{nm}} = 50$ mm) at 51 mm and twice the yarn spacing (S-CG3-cyclic-2, $y_{\mathrm{nm}} = 25$ mm) at 50 mm. The maximum crack spacing throughout the experimental campaign was determined to be 113 mm in specimen S-CG2-static. In comparison with the UT results, the crack spacing is significantly reduced. This explains the on average lower crack widths determined at bending, given that the cracks formed in closer proximity to each other.

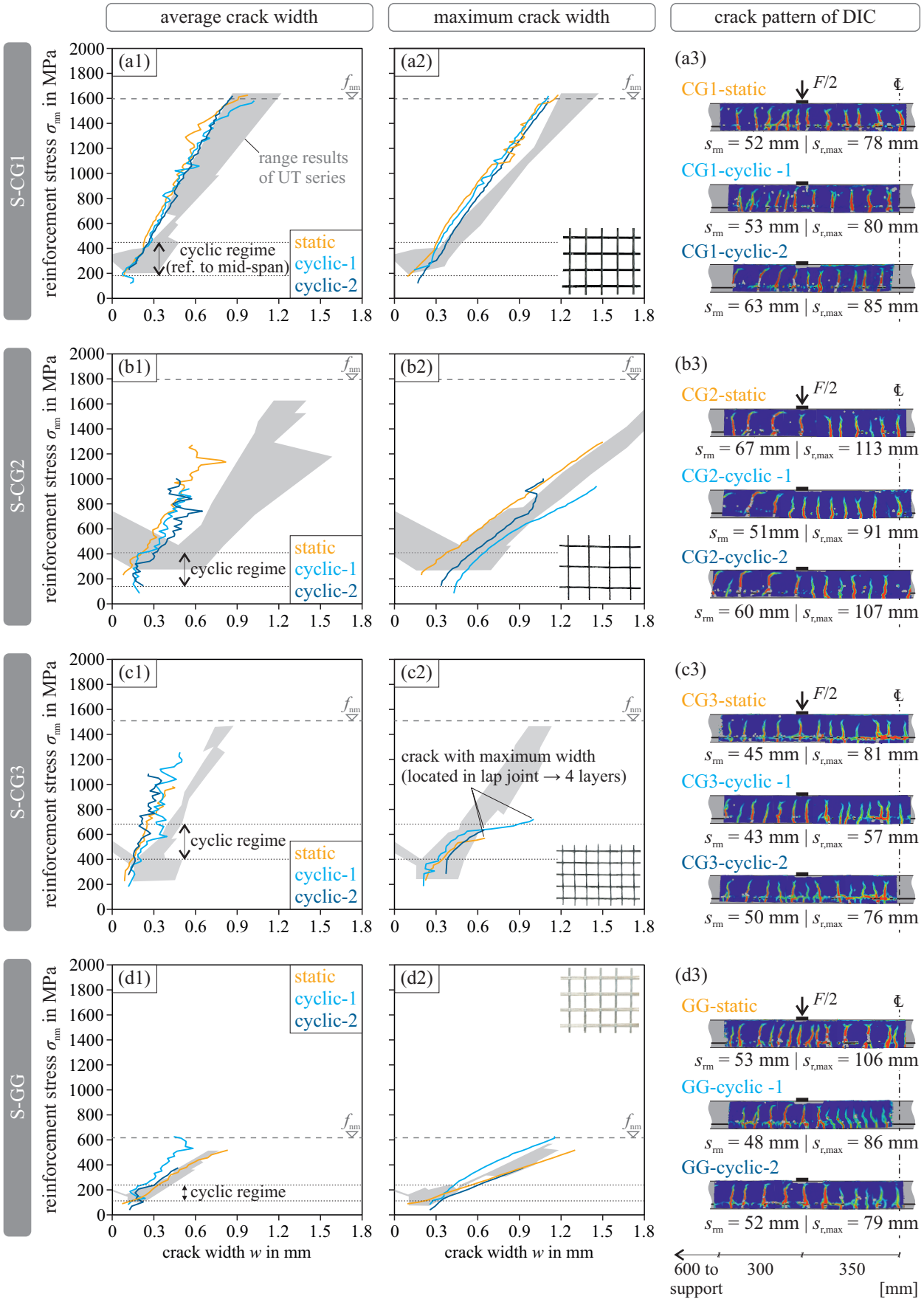


Figure 6.3: Evolution of average and maximum crack width at the height of the reinforcement layer and crack pattern determined using DIC of the four-point bending tests

Reinforcement strain evolution

Given the identical evaluation strategy as utilised for the COT and UT campaigns, fibre optical sensors are employed to obtain the reinforcement strain. In Figure 6.4, the strain evolution in the bottom (left-hand side in the diagram) and the upper (right-hand side) reinforcement layer at selected load levels is plotted for the purely statically loaded specimens. The first load level represented the time at which the deflection criterion of $l/250$ was reached, while the subsequent load level corresponded to the time at which the majority of cracks occurred and the stage of stabilised cracking was assumed. In addition, the iteratively obtained reinforcement strain is provided as grey dotted lines.

The iteratively obtained reinforcement strains comply well with the measured values at the cracks, with the strain values derived by FOS clearly revealing the contribution of tension stiffening. Discrepancies between the iteratively obtained and measured strains were attributable to the non-uniform Young's modulus and cross-sectional area of the fibre strands. The slightly varying crack widths of adjacent cracks in regions of the same bending moment were confirmed by the FOS measurements, and led to a reduced reinforcement strain compared to the iteratively obtained ones.

In the case of additionally arranged reinforcement layers in mid-span, the reinforcement strain declined at the beginning of these layers (Figure 6.4b-d). Nonetheless, the lap joint in S-CG2-static demonstrated the capacity to adequately transfer the applied force without any indications of failure at this time (Figure 6.4b).

Despite the spacing between adjacent cracks being equal or below the values determined in the UT series, with average transfer lengths being below the yarn spacing, there was still force transfer detected in both evaluated reinforcement layers. This is in contrast to the observations made in the UT tests, where no significant force transfer was observed at these small transfer lengths. Therefore, the bond capacity in the slabs was substantially pronounced compared to the UT series in the case of adjacent cracks and high reinforcement utilisations. This suggests that some contribution of tension stiffening has to be considered for this case.

Difference between layer of reinforcement and most-tensioned concrete fibre

As the crack widths addressed in the prediction approaches refer to the reinforcement layer, and as the serviceability criterion for non-metallic reinforcement generally is concerned with visual appearance, the increase in crack opening from the reinforcement to the member surface should be considered. It is evident that the substantial deformations undergone by the slabs have a significant impact on the curvature of the cross-section, thereby contributing to the considerable crack opening. The *fib* Model Code 2020 and the Final Draft to the Preliminary Eurocode 2 address this influence of the curvature by introducing a factor $k_{1/\mathrm{r}}$ (cf. Equation 2-37). As illustrated in Figure 6.5, this subject is addressed by measuring the surface crack width at the layer of reinforcement and at the bottom of the specimen. The obtained increase is then compared to the determined factor $k_{1/\mathrm{r}}$. Exemplarily, specimen S-CG1-static is considered with the evolution of the average crack width relation $w_{\mathrm{bot}}/w_{\mathrm{reinf,surf}}$ in dependence of the reinforcement stress being plotted in the diagram of Figure 6.5. Considering this detailed evaluation of the crack width relation, the value of $w_{\mathrm{bot}}/w_{\mathrm{reinf,surf}}$ increased to 1.5 at a reinforcement stress of 450 MPa, which corresponds to the time at which the transition to a stabilised cracking stage occurred. Then the value of the relation $w_{\mathrm{bot}}/w_{\mathrm{reinf,surf}}$ decreased to approximately 1.25 before the failure of the specimen was reached. When considering the crack width of 0.4 and 0.7 mm on the concrete surface at the level of the reinforcement layers, this was reached at $w_{\mathrm{bot}}/w_{\mathrm{reinf,surf}}$-values of approximately 1.3. This value corresponds to the average of $w_{\mathrm{bot}}/w_{\mathrm{reinf,surf}}$ for specimen S-CG1-static, which was 1.3. The factor $k_{1/\mathrm{r}}$ was determined through the strain distribution of the cross-section, yielding a value of 1.22. This value remained approximately constant with respect to the reinforcement stress.

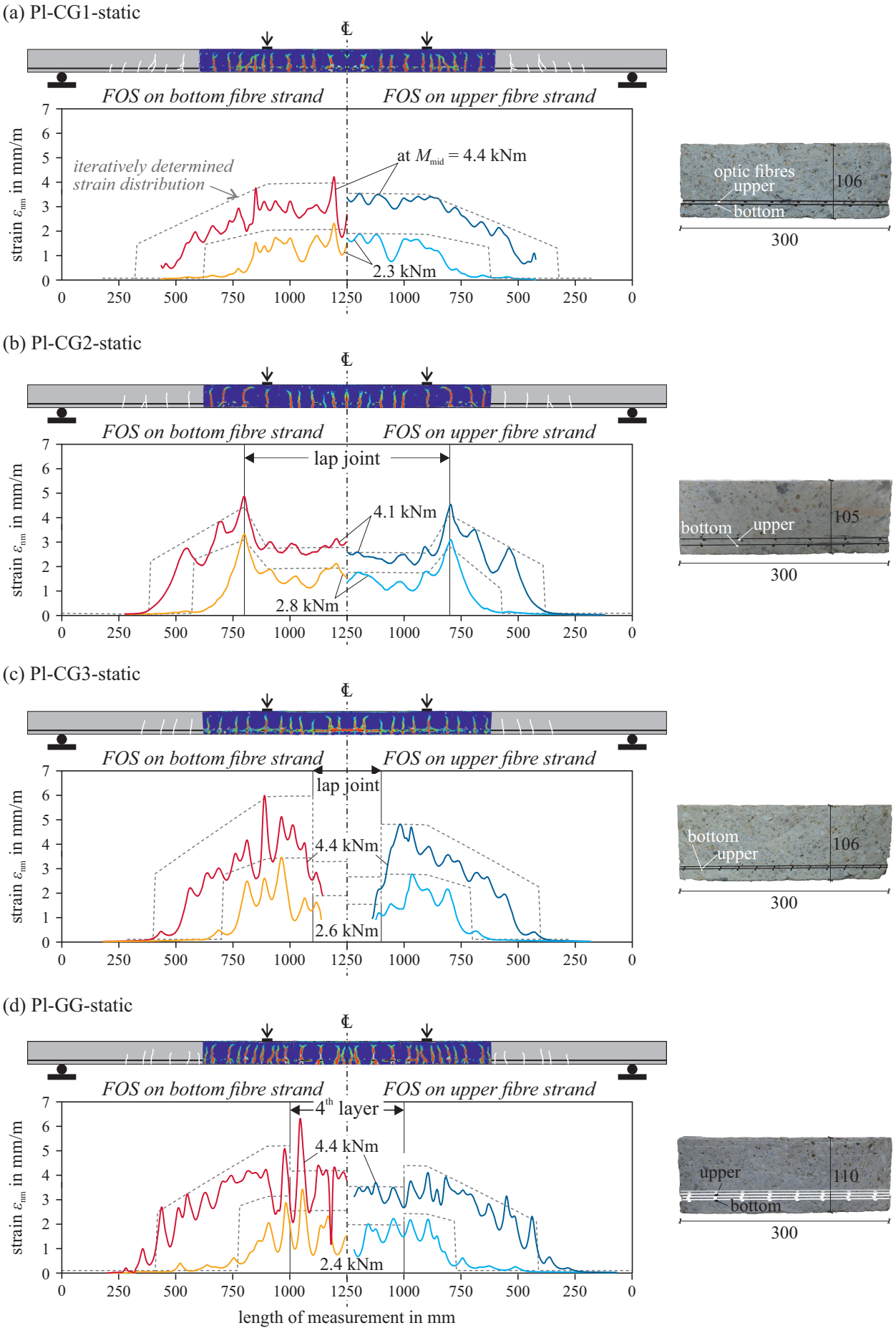
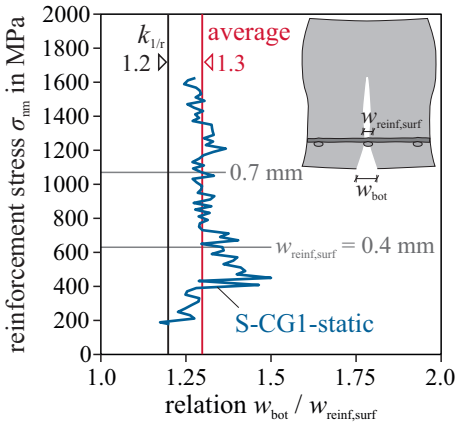


Figure 6.4: Reinforcement strain evolution for different reinforcement layers at selected load levels of the purely statically loaded four-point bending tests



series	average relation $w_{bot}/w_{reinf,surf}$ $\bar{x}$	COV [%]	Eq. 2-37 [MC20] $k_{1/r}$ [-]
S-CG1	1.3	3.2	1.2
S-CG2	1.3	2.9	1.2
S-CG3	1.5	18.8	1.2
S-GG	1.4	6.1	1.2

Figure 6.5: Relation between the width at the most-tensioned concrete fibre w_{bot} and at the reinforcement layer on the concrete surface $w_{surf,reinf}$, and the curvature factor $k_{1/r}$

This is also confirmed when considering all specimens, with the factor $k_{1/r}$ being almost constant in the applicable range due to the linear elastic behaviour of the reinforcement. The changes in the height of the compression zone between 12 and 17 mm or, expressed as the x/d-ratio, between 0.12 and 0.19 did not result in significant changes in the value of $k_{1/r}$. In all tests, the relation of $w_{bot}/w_{reinf,surf}$ was found to be slightly larger than the factor $k_{1/r}$. At maximum, the relation was 1.5 in series S-CG3, with a coefficient of variation of about 19%, which was considerably larger in comparison to the very low values in the other series. This may be explained by the shear lag effect (cf. Section 2.5.3), referring to the elastic behaviour of concrete outside the effective reinforcement area.
Concluding, the consideration of the curvature by a factor $k_{1/r}$, which may follow the description provided in Equation 2-37, seems reasonable, while the actual difference between the two focussed layers of crack width measurements was revealed to be slightly larger in this experimental campaign. No difference between static and cyclic loading was found.

6.2.5 Contribution of tension stiffening

The influence of tension stiffening is addressed by determining the tension stiffening factor β using the reinforcement strain evolution obtained by the FOS measurement according to Equation 3-8. The evolution of β in dependence on the reinforcement strain in the corresponding crack $\varepsilon_{nm,max}$ is plotted for the right side of the crack with the maximum width. It is differentiated between the top and bottom reinforcement layers. In addition, the derived β-values of Chapter 5 are used for illustration in Figure 6.6. For reference, the range where the maximum crack width observed in the bending tests was below 0.7 mm is indicated in Figure 6.6.
In general, the value of β significantly depended on the reinforcement type and reinforcement layer. For example, in the case of S-CG1-static in Figure 6.6a, the evolution of the β-value of the bottom layer was above or at the values determined for the single cracking stage by the COT campaign ($\beta_{single} = 0.58$). For the top layer and at a reinforcement strain ranging between 1.8 and 3.7 mm/m, the β-values were approximately 0.36, which corresponds to the derived COT-value for adjacent cracks β_{adj}. However, at the occurrence of another crack in the slab, the β-values increased again exceeding 0.6.
Considering the other three slabs, the obtained β-values mostly ranged within the determined values for single and adjacent cracks with large variations. At higher reinforcement utilisation, there is a tendency towards $\beta_{adj} = 0.36$ revealed. As apparent, the generalised assumption of the β_{single}-value using the COT test results, which were analytically determined, provides for a satisfying

result at low reinforcement utilisations which are linked to the stage of single cracks. The derived value in the case of adjacent cracks, set with $\beta_{adj} = 0.36$, provides for a conservative representation of the actual tension stiffening factor, particularly in the case of reinforcements.

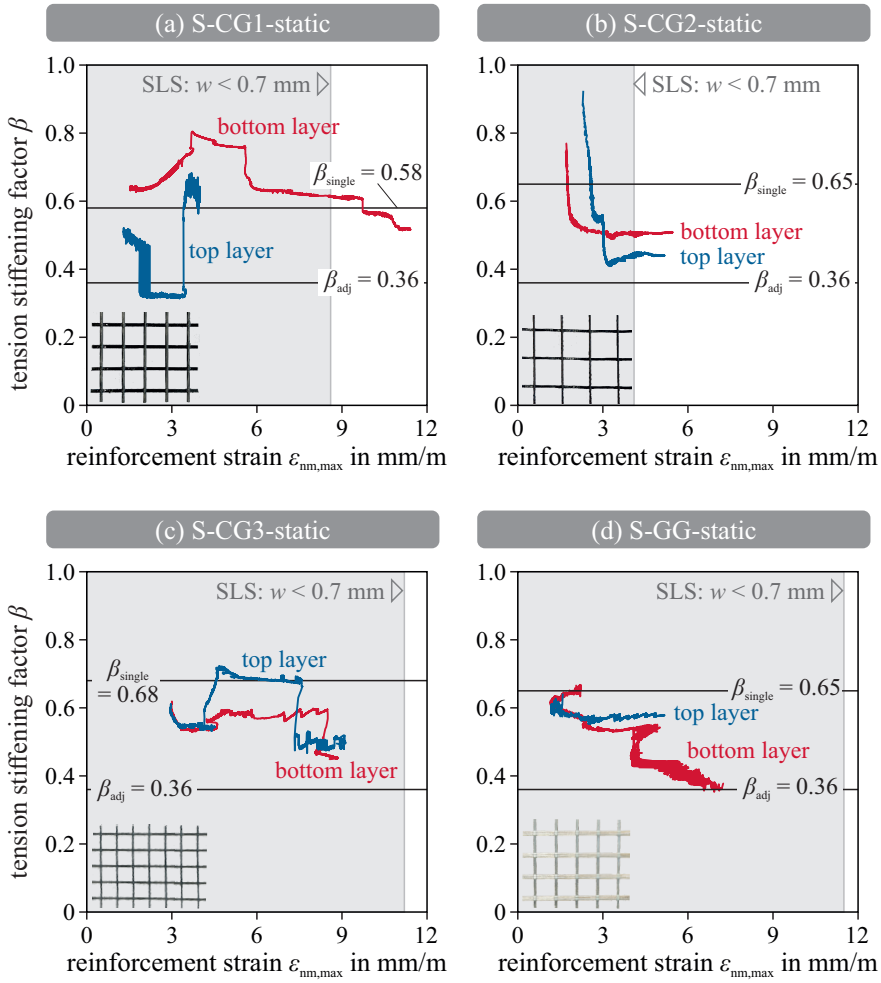


Figure 6.6: Evolution of the tension stiffening factor β in relation to the reinforcement strain evaluated for the crack with the maximum width in the purely statically loaded slabs

6.3 Iterative determination of the cross-sectional curvature

In order to quantify the contribution of tension stiffening and the influence on the deflection behaviour based on the crack width prediction, the curvature of the cross-section is required. The curvature is indicative of the relation between minimum concrete strain and reinforcement strain in relation to the depth

$$\kappa = \frac{\varepsilon_{nm,1} - \varepsilon_{c,min}}{h - d_1} \tag{6-1}$$

with focus on the most-tensioned reinforcement layer. The strain distribution is iteratively determined based on force equilibrium. For the purposes of this analysis, the tensile behaviour of the concrete, including tensile softening, is assumed to be negligible. The compressive behaviour, approximated by using the description of the uniaxial concrete compression provided in [EC2] and visualised in Figure 6.7, is obtained in dependence on the strain distribution in the compression zone. In order to consider the reinforcement stress, it is necessary to determine the strain of each layer. An iterative approach is required to establish the force equilibrium with initial strain values

of the uniaxial concrete compression strength, denoted as strain value ε_{c1u}, and the rupture strain of the most utilised reinforcement layer $\varepsilon_{nm,u}$. The maximum bending moment of the cross-section is achieved if one of the two initial values is met, which identifies either compressive failure of the concrete or rupture of the fibre strand. Finally, the bending moment M_{calc} is obtained using the inner levers of the reinforcement layers $x_{nm,i,lever}$ and of the concrete $x_{c,lever}$. This methodology is also used to determine the strain distribution in the cross-section for a corresponding moment.

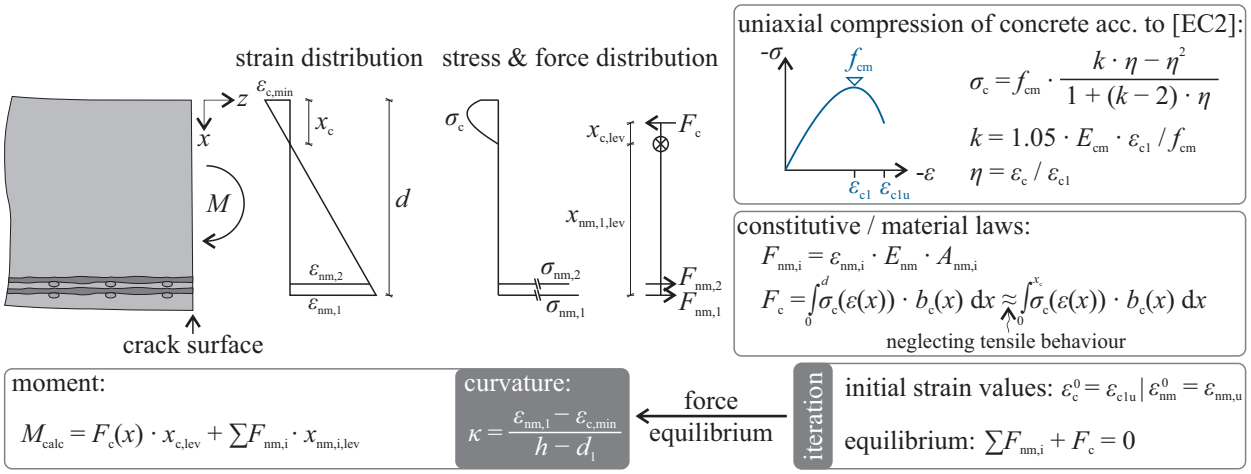


Figure 6.7: Schematic representation of the determination of the cross-section curvature

To provide for a reasonable determination of the concrete compressive force F_c, the integral description shown in Figure 6.7 is approximated by a summation of 50 individual sectors representing the compression zone following the trapezoidal rule:

$$F_c = \int_0^{x_c} \sigma_c(\varepsilon(x)) \cdot b_c(x)\,dx = \sum_{i=0}^{50} \frac{\sigma_c(\varepsilon(x_i)) + \sigma_c(\varepsilon(x_{i+1}))}{2} \cdot \frac{x_c}{50} \cdot b \tag{6-2}$$

The width of the compression zone of each sector $b_c(x)$ is the width of the specimen b for the rectangular cross-section. The height of each sector is the height of the compression zone divided by the number of sectors $x_c/50$. The value of force in each sector is approximated using the average of the minimum and maximum values of stress obtained by the minimum and maximum values of concrete strain of each sector, using the description of the uniaxial concrete compression in [EC2].

The determination of the curvature also allows for the approximation of the deflection of a member (see Section 6.5), which is obtained by the double integral of the curvature:

$$u(z) = \int_0^z \int_0^z \kappa(z)\,dz\,dz \tag{6-3}$$

The variable z refers to the evaluation position in the longitudinal direction of the member. The double integral is solved by summation of sector-wise determined deformations, applying again the trapezoidal rule. For a reasonable determination of the deflection, the member is divided into 2,000 increments. In the case of the four-point bending tests, the required boundary conditions are obtained by assuming zero deflection at the supports and zero rotation of the cross-section in mid-span. To account for the different behaviour of uncracked and cracked concrete sections, a differentiation is introduced if the bending moment in the section exceeds the cracking moment. In this first consideration, no influence of tension stiffening contributing to a reduction in the magnitude of the curvature is considered, but is implemented and discussed in detail in Section 6.5.

6.4 Prediction of crack width and crack spacing

6.4.1 Short-term initial loading

In the following, the experimentally obtained maximum crack widths are used to verify the proposed prediction model introduced in Section 5.5 for flexural slabs. Accordingly, the primary step in this investigation is to differentiate between the approach for a single cracking stage and the approach for the stabilised cracking stage. The prediction of widths for single cracks is performed using Equation 2-18 with the crack width-dependent mean value of bond stress obtained individually for the considered reinforcement and the equivalent circumference of the fibre strand

$$w_{\text{single}} = \frac{2 \cdot (1-\beta) \cdot \sigma_{\text{nm}}^2 \cdot A_{\text{nm}}}{E_{\text{nm}} \cdot U_{\text{nm,eq}} \cdot \tau_{\text{bm}}(w) \cdot (1+\rho\alpha_{\text{e}})}. \tag{6-4}$$

In the case of adjacent cracks, one final refinement is considered to address the closer crack spacing observed in the experimental campaign. The larger stress at the most-tensioned layer of the member compared to the reinforcement layer in the uncracked area is addressed in the *fib* Model Code 2020 by a factor k_{fl} [Pér20, MC20]. The general expression of the stress distribution factor k_{fl} is given in Equation 2-36, and the simplified expression for a rectangular cross-section in the uncracked section with $x = h/2$ is according to [Pér20]

$$k_{\text{fl}} = \frac{h - h_{\text{c,ef}}}{h}. \tag{6-5}$$

Having established this, the maximum crack spacing is predicted according to Equation 5-30 considering the stress distribution factor in flexural members

$$s_{\text{r,max,ef}} = \frac{2 \cdot f_{\text{ct,ef}} \cdot A_{\text{c,net}} \cdot k_{\text{fl}}}{\tau_{\text{bm}}(w) \cdot U_{\text{nm,eq}} \cdot \xi_{\text{F}}} \geq \frac{2 \cdot f_{\text{ct,ef}} \cdot A_{\text{c,net}} \cdot k_{\text{fl}}}{\tau_{\text{bm}}(w_{\text{trans}}/2) \cdot U_{\text{nm,eq}} \cdot \xi_{\text{F}}}. \tag{6-6}$$

Consequently, this leads to an assumption where the transfer length, limited by the crack spacing, is required to also be reduced.
The prediction of the maximum crack width at stabilised cracking for flexural members remains almost identical as formulated in Equation 5-25, solely again the stress distribution is considered:

$$w_{\text{max}} = s_{\text{r,max,ef}} \cdot \left[\frac{\sigma_{\text{nm}}}{E_{\text{nm}}} - \beta_{\text{adj}} \cdot \frac{f_{\text{ct,ef}} \cdot (1+\rho_{\text{ef}}\alpha_{\text{e}}) \cdot k_{\text{fl}}}{\rho_{\text{ef}} \cdot E_{\text{nm}} \cdot \xi_{\text{F}}} \right] \tag{6-7}$$

Note, that for differentiating between the β-values according to the cracking stage, in Equation 6-7 β_{adj} is introduced. In the prediction of the stabilised cracking stage, two different assumptions of the contribution of tension stiffening are followed: either tension stiffening is considered with β_{adj} chosen to be 0.36 or the contribution of tension stiffening is neglected.

Of significant importance becomes the definition of the effective area of reinforcement $h_{\text{c,ef}}$, which influences the effective tensile cross-sectional area of the concrete, the effective reinforcement ratio as well as the stress distribution factor k_{fl}. In the case of single cracks, a well-defined approximation of the effective area is not sensitive with regard to the determined crack width. Conversely, the prediction of the maximum crack width at stabilised cracking is highly sensitive regarding the definition of the effective area, as it is required to determine the crack spacing and transfer length. Common definitions of $h_{\text{c,ef}}$ were provided in Section 2.5.1, which are worth discussing. The following evaluation was performed using the established definition of $h_{\text{c,ef}} = 2.5d_1$ for thin reinforced concrete members according to Equation 2-22. This was done as the other definitions proved

to provide for less accurate predictions which tend towards an underestimation of the experimentally derived maximum crack width, in particular following the proposal in [MC20, FprEC2] (cf. Equation 2-25).

The verification focused on the evaluation of the proposed model with respect to the test data curves, representing the relation of reinforcement stress and maximum crack width, which is shown separately for each grid in Figure 6.8. As done for the statistical evaluation of the uniaxial tensile tests in Section 5.5.3, again only the reinforcement stress values for which the coefficient of variation in the test series was below or equal to 30% was considered to address the variation in test data. The evaluation for the proposed model is listed in Table 6.3 as a statistically based comparison of the prediction to the average of the test data, utilising the procedure provided in Annex D.8.2 of Eurocode 0 [EC0]. To determine a nominal estimated value $\bar{x}$, the log-normal distribution of the test values with the estimated value $\bar{\Delta} = w_{\max}/w_{\max,\exp}$, is transferred ($\bar{x} = \exp\left(\bar{\Delta}\right)$). The nominal estimated value indicates whether the prediction underestimates the maximum crack width ($\bar{x} > 1$), which refers to progressive predictions, as to meet the criterion of the serviceability limit state a

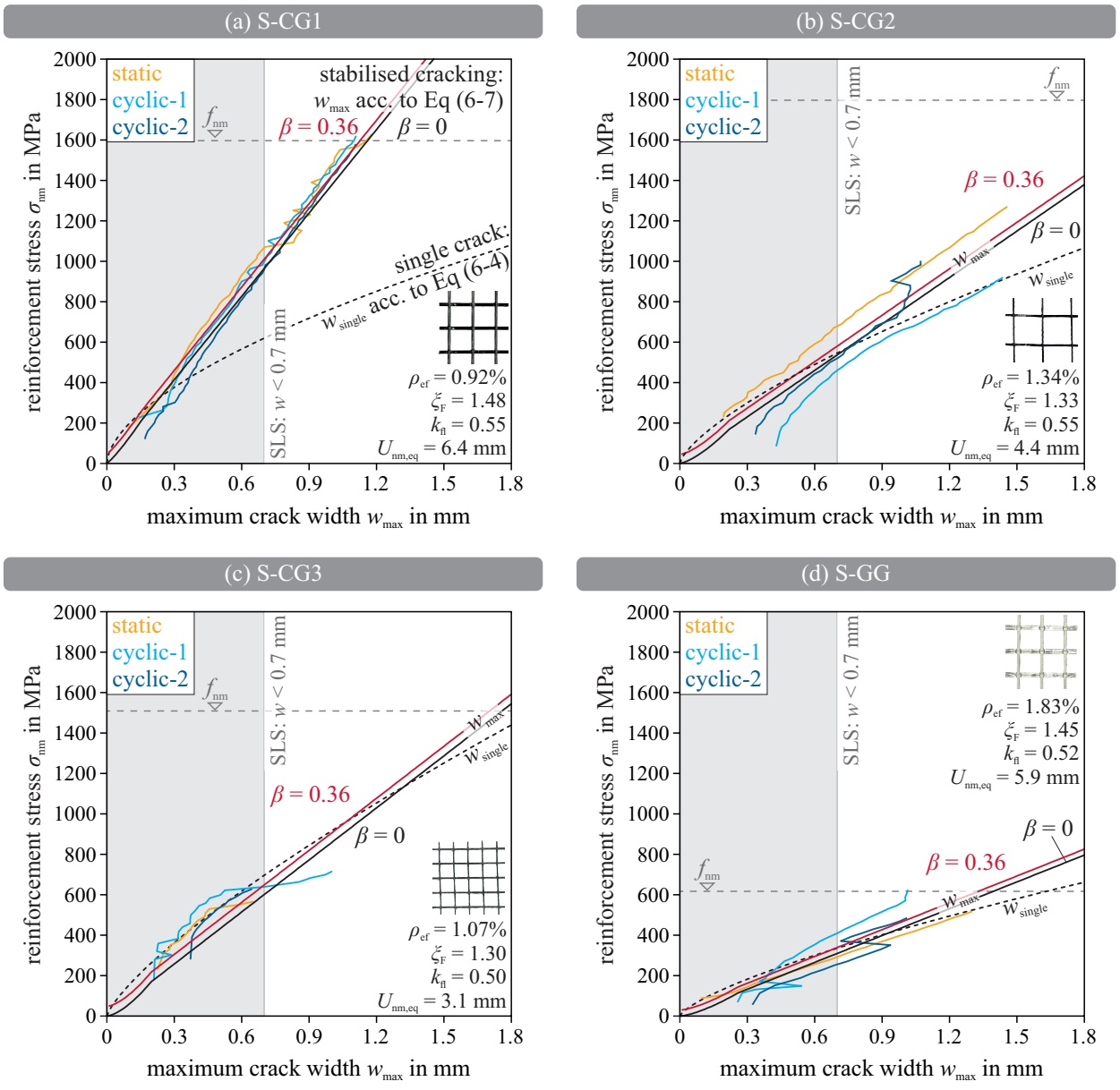


Figure 6.8: Comparison of crack width prediction with test data regarding the maximum crack width in flexural members

lower reinforcement ratio is determined. In addition, the obtained coefficient of variation V_δ is provided.
Since the observed increase in crack width due to the cyclic loading phase is marginal, all twelve slabs were considered in the following analysis.

The comparison of the test results with the model with the two assumptions for β visualised in Figure 6.8 shows a well-defined prediction for all specimens. The predicted crack widths are close to the average values as shown by the statistical evaluation in Table 6.3, with a tendency of overestimating when tension stiffening is considered ($\beta = 0.36$), except for series S-CG3 where an underestimation of the reinforcement stress was found. The average accuracy is approximately 1.00 at a coefficient of variation of 9%. When no tension stiffening is considered, all predictions tend to slightly underestimate the test data, with $\bar{x} \approx 0.91$ and a coefficient of variation of 8%.
The evaluation of all four reinforcements revealed that the single cracking stage is negligible for this member layout. This is because the state of single cracks occurring in the investigated flexural members is restricted to the initial loading phase with low reinforcement utilisation and crack opening. The graphical representation shows that this case is also well covered by the approach for the stabilised cracking stage. Furthermore, the transition to the formation of adjacent cracks occurred in these three series at low values of reinforcement stress; consequently, the corresponding approach seems to be more feasible.
The second general observation is that a consideration of tension stiffening with $\beta = 0.36$ resulted in calculated maximum crack widths being approximately 0.05 mm lower compared to the values determined when neglecting tension stiffening.
Discussing the underestimation obtained by the model in the case of reinforcement CG3 (Figure 6.8c), this is attributed to larger contribution of tension stiffening compared to the set value of $\beta = 0.36$, which was not explicitly derived for CG3 in Chapter 3. An increase of the value of β to account for a larger influence of tension stiffening would consequently improve the performance of the approach formulated in Equation 6-7.

Table 6.3: Statistical performance of the crack width prediction for adjacent cracks considering two different values of the tension stiffening factor β ($\bar{x} > 1$ indicates underestimation of crack width)

test series	Equation 6-7 with $\beta = 0.36$		Equation 6-7 with $\beta = 0$	
	$\bar{x}$	V_δ [%]	$\bar{x}$	V_δ [%]
S-CG1-0°-NSC	1.04	8.0	0.97	5.4
S-CG2-0°-NSC	1.04	9.4	0.97	8.8
S-CG3-0°-NSC	0.84	6.8	0.73	8.7
S-GG-0°-NSC	1.08	10.1	0.96	8.3
overall average	**1.00**	**8.6**	**0.91**	**7.8**

6.4.2 Increase in crack width due to cyclic loading

Considering the crack width increase during the cyclic loading phase, it is revealed that the magnitude in increase is less pronounced compared to the uniaxial tensile tests (cf. Chapter 4 and Figure 5.15). The influence of concrete tensile fatigue was not of significance in this experimental campaign.

The uniaxial tensile tests using reinforcement CG1 revealed that multiple reinforcement layers proved to significantly reduce the crack opening during cyclic loading. This is confirmed by the four-point bending test series, as revealed in Figure 6.9. In this figure, the additional maximum crack width increase of the eight individual tests with a cyclic loading phase is plotted in relation to the applied load cycles. In addition, the initial maximum crack $w_{0,\max}$ and the concrete tensile strength are provided. This also highlights another, expected effect: A higher concrete tensile strength resulted in less crack opening during cyclic loading. The reduction in bond capacity, including bond creep, is less pronounced in members with a higher concrete tensile strength. This was also shown in the uniaxial tensile tests with a high-strength concrete (HSC), where no considerable increase in crack opening during cyclic loading was detected. The evaluation in Figure 6.9 also shows that the increase in crack opening was the greatest during the first 10,000 cycles.

In Section 5.6, an approach to determine the crack opening in relation to the number of load cycles and the bond capacity was introduced. With two parameters, denoted as Γ and γ, the decrease in bond capacity is approximated. The consideration of the uniaxial tensile tests revealed that the parameter γ is assumed to be zero in the case of multiple reinforcement layers. This was taken into account in the following evaluation of the approach expressed by the formulation in Equation 5-33. The approach introduced in Section 5.6 focuses on the single cracking stage, as this stage is decisive in the case of single and adjacent cracks. Consequently, the derived parameters were expected to provide for an overestimation of the maximum crack opening when addressing the adjacent crack pattern in the flexural members. This was proven to be true, and the remaining parameter Γ was reduced in value compared to the uniaxial tensile tests. The predictions of the crack opening are plotted as black dashed lines for the corresponding test.
In the case of reinforcements CG1 and CG2, $\Gamma = 0.12$ proved to allow a suitable fit for three of the four test results (Figure 6.9a+b). Solely for specimen S-CG1-cyclic-2, this assumption of Γ led to an overestimation of the crack opening and a lower Γ-value of 0.07 described the test data more accurately. Focusing on the two specimens S-CG3-cyclic evaluated in Figure 6.9c, the derived Γ-values of 0.33 for cyclic-1 and 0.19 in the case of specimen cyclic-2 are lower compared to the value of 0.38 obtained in the uniaxial tensile tests (cf. Figure 5.15). Nevertheless, this reduction is significantly lower compared to the two other carbon grids. In the case of series S-GG in Figure 6.9d, the parameter Γ was determined to be zero for uniaxial loading and the crack opening was described using the second calibration parameter γ. To follow the introduced concept for flexural members, an adaptation of Γ was done with $\gamma = 0$. The derived Γ-values were 0.26 in the case of specimen S-GG-cyclic-1 and 0.12 for S-GG-cyclic-2.

The obtained inconsistency in the best-fitted Γ-values in three series (CG1, CG3, GG) and between all series does not allow for a generally applicable formulation of the approach introduced with Equation 5-33. For simplicity, one could propose that the increase in crack opening due to the cyclic loading regime was approximately 0.1 mm, which was an increase of about 25% of the initial maximum crack width. Furthermore, as previously pointed out, the influence of cyclic loading on the crack width evolution was not significant and is covered by the refined approaches in the previous Section 6.4.1. However, a final consideration addressing both uniaxial tension and flexure is provided in Section 7.2.

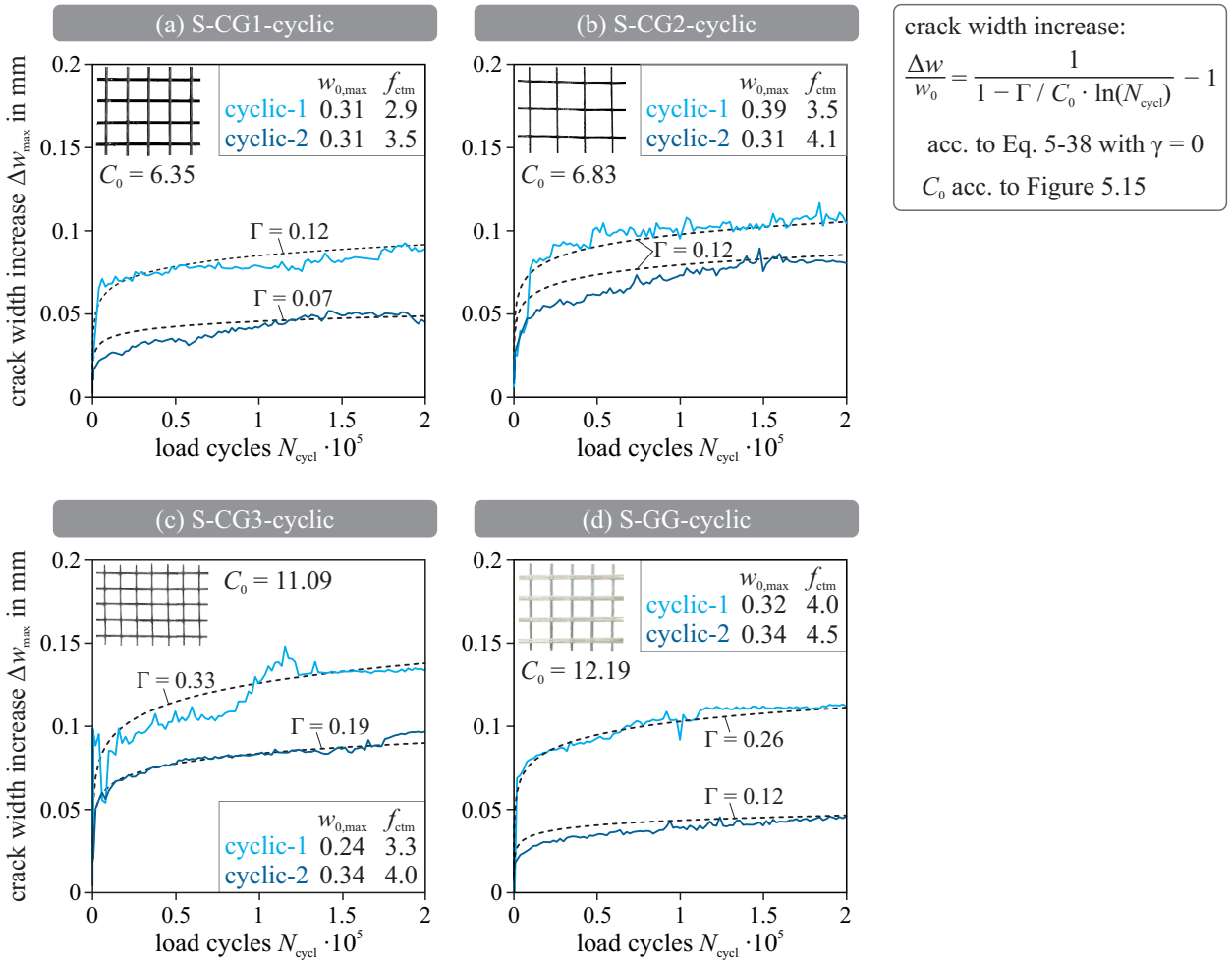


Figure 6.9: Maximum increase in crack width due to cyclic loading with redefined prediction approach according to the approach in Equation 5-37

6.5 Approaches to predict the deflection

6.5.1 Principle considerations regarding cross-sectional curvature and deflection

To accurately predict the deflection in a reinforced concrete member, it is necessary to consider the non-linear strain evolution of reinforcement and concrete. This allows for a determination of the curvature at each section of the member. Assuming that the concrete's behaviour under uniaxial compression and short-term static loading is represented sufficiently, for example by the non-linear approximation given in [EC2] (cf. Figure 6.7), a well-defined representation of the reinforcement strain evolution is required. It becomes apparent that this representation is difficult to derive when addressing an adequate consideration of tension stiffening, as the strain evolution determined using FOS revealed in the previous discussion (see e.g. Figure 6.4). Greater challenges emerge in instances of change to the cross-sectional strain distribution, such as long-term loading, which arises from the visco-elastic behaviour of concrete. A comprehensive evaluation of the absolute strain increase in concrete requires a detailed knowledge of the concrete's material behaviour, particularly with regard to its mixture and the environmental boundary conditions to which it is exposed. In the context of practical applications, the lack of these information tend to result in an inaccurate approximation of concrete creep, for example when utilising the proposed method by

code provisions [MC20, FprEC2, DAfStb24], where a creep coefficient is determined based on an empirical formulation and is then used to reduce the Young's modulus of the concrete.

Before proceeding to an examination of the influence of cyclic loading, at first, three approaches to predict the deflection for the short-term static case are focused. One strategy employed is a simplified and conservative approach, which involves the consideration of two states: the curvatures of the uncracked concrete section, designated as κ_I, and the cracked section, denoted by κ_{II}. The deflection is thus obtained by integrating the curvature evolution twice, as described by Equation 6-3. This approach disregards the contribution of tension stiffening, consequently leading to an overestimation of the actual deflection, as outlined in the upcoming Section 6.5.3.
The second approach explicitly accounts for tension stiffening. Consequently, it is necessary to consider the continuously decreasing absolute contribution at increasing utilisation of the reinforcement. As shown in Figure 6.6, the difference between the mean reinforcement strain and the maximum reinforcement strain in the crack declines with increasing reinforcement strain. Following the derivation of an adequate approximation of the contribution of tension stiffening, an average curvature is to be determined. In this instance, the average value of reinforcement strain must be used in place of the maximum value. The deflection is then described using the average curvature of the cracked concrete section.
This consideration is followed by some simplifications introduced by the more recent code provision approaches [EC2, MC10, MC20, FprEC2, DAfStb24] to approximate the average curvature, which resembles the third approach investigated in this study. In Figure 6.10a the moment distribution, curvature evolution and the corresponding deflection in the case of a four-point bending test is illustrated, neglecting the influence of the self-load. The actual curvature evolution is simplified to an evolution following the moment distribution, represented by the red curve in Figure 6.10a. The maximum value of curvature is expressed as average curvature κ_m, which considers tension stiffening and the contribution of the uncracked concrete section. As the representation of the cur-

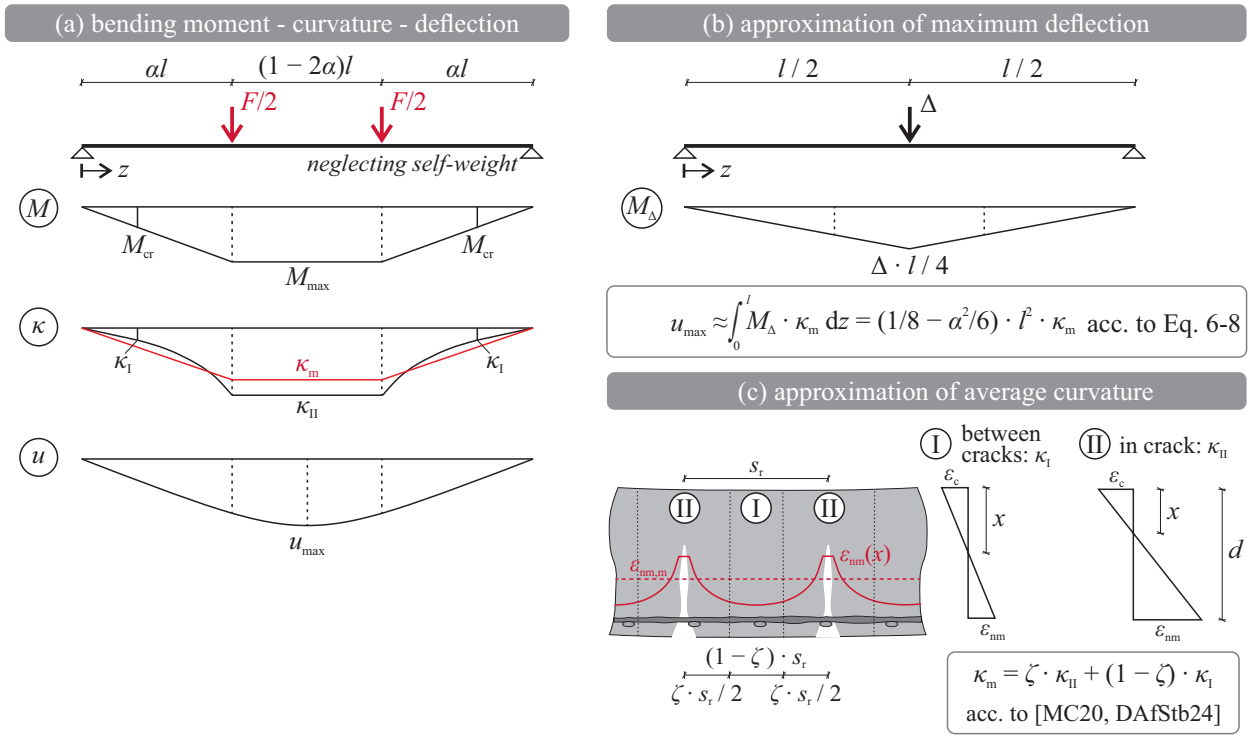


Figure 6.10: Approach using an average curvature κ_m to determine the maximum deflection in a flexural member representing the case of a four-point bending test

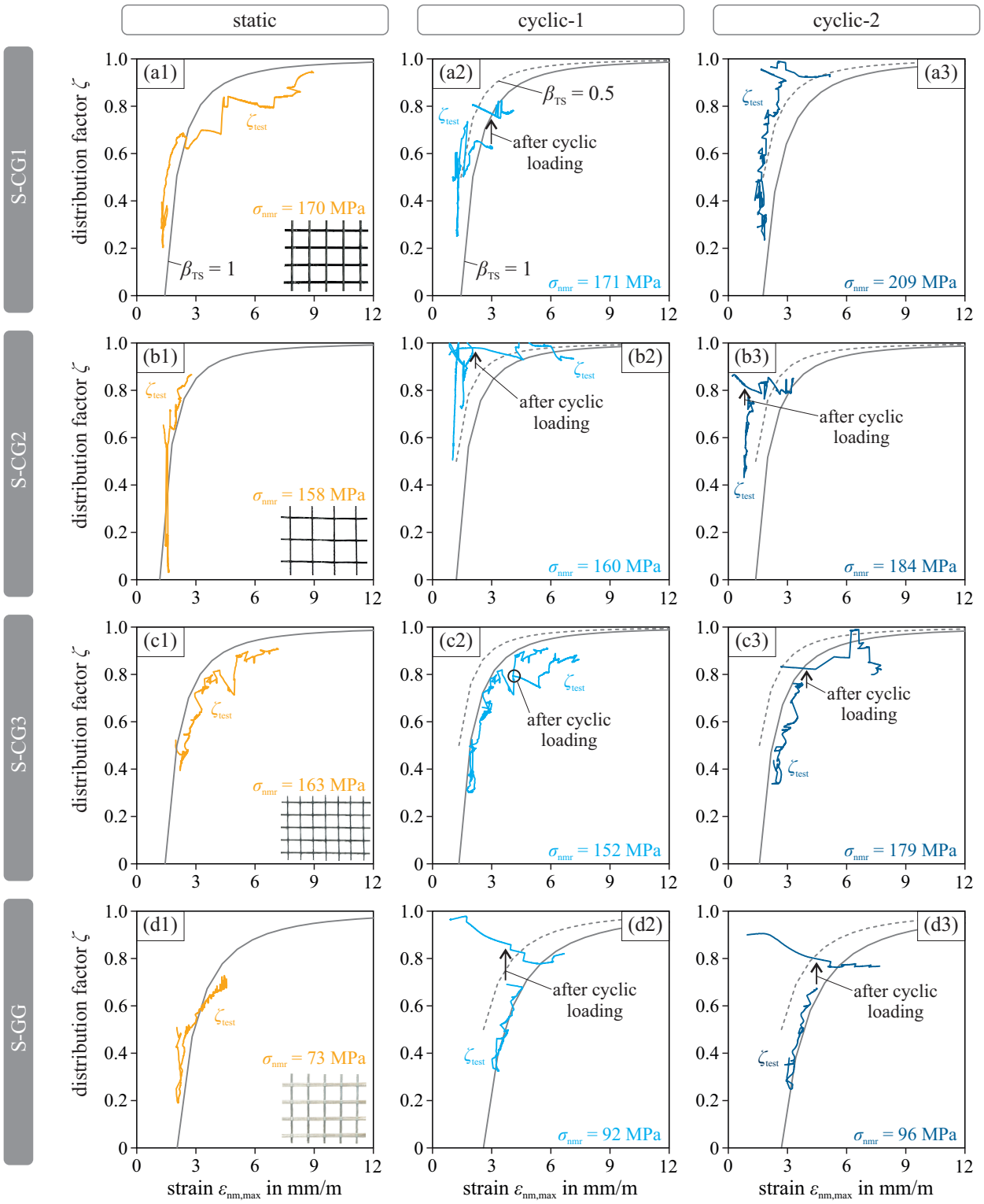
vature evolution is qualitatively identical to the moment distribution, the maximum deflection is approximated

$$u_{\max} \approx \int_{z=0}^{l} M_{\Delta} \cdot \kappa_{\mathrm{m}} \, \mathrm{d}z = \left(\frac{1}{8} - \frac{\alpha^2}{6} \right) \cdot l^2 \cdot \kappa_{\mathrm{m}} \,. \tag{6-8}$$

This formulation utilises the principle of superposition known from basic mechanics with M_{Δ} representing the moment distribution obtained by a single point load, denoted as $\Delta = 1$ and localised at the point of focus, as visualised in Figure 6.10b. As is apparent, the maximum deflection $u_{\max}$ is determined in mid-span. The average curvature is approximated by introducing a distribution factor ζ (cf. Equation 2-40), which sets a ratio between the curvature of the uncracked and cracked sections, with the latter addressing the strain distribution in the crack. With this strategy, the contribution of tension stiffening is accounted for, as visualised in Figure 6.10c.
Before evaluating these three approaches to predict the deflection using an analytical-based consideration of the curvature, the following Section 6.5.2 focuses on the description and consideration of tension stiffening.

6.5.2 Describing the contribution of tension stiffening

Due to a reduction in bond capacity at increasing reinforcement utilisation in combination with a transition to a stabilised cracking stage, the contribution of tension stiffening is not constant. Thus, an analytical description requires a consideration either of the reduction in bond capacity or, indirectly, of the reinforcement utilisation. As highlighted in the previous chapters, a reduction of the bond capacity is difficult to implement in a prediction approach. Therefore, and to follow the principal strategy of the code provision approaches [EC2, MC10, MC20, FprEC2, DAfStb24], the distribution factor ζ_{calc} is derived by the expression stated in Equation 2-40 using the reinforcement strain at initial cracking. The accuracy of this solution depends on a suitable approximation of the reinforcement strain after initial cracking. In this case, a simplified, while established, approximation was chosen, which determines the inner lever z with $0.9 \cdot d$. In this approximation, tension stiffening is also accounted for by the parameter β_{TS}, which is in the case of initial loading 1.0. The calculated distribution factor ζ_{calc} is plotted in relation to the maximum reinforcement strain as grey curve in Figure 6.11. In the case of sustained or cyclic loading, code provision approaches suggest a reduction of the tension stiffening factor by 50% ($\beta_{\mathrm{TS}} = 0.5$ in Equation 2-40), which results in a reduced distribution factor that is also visualised as a grey dashed line in Figure 6.11. The test data is obtained from the fibre optic measurements, the distribution factor is determined as $\zeta_{\mathrm{test}} = \varepsilon_{\mathrm{nm,m}} / \varepsilon_{\mathrm{nm,max}}$ utilising the full length of the fibre optic sensors, which is another form of interpreting the graphical analysis in Figure 6.11. The comparison of the test data and the analytically determined distribution factor focusing on the purely statically loaded specimens is given in the left column in Figure 6.11 and for the cyclically loaded specimens in the middle and right columns.
The graphical representation reveals that in all four cases, the analytically determined distribution factor with $\beta_{\mathrm{TS}} = 1$ fitted well to the factor obtained using the actual reinforcement evolution. At initial crack occurrence with very small widths, the crack formation process begins at a low level of reinforcement utilisation and the distribution factor initially exhibits a steep increase, as for example shown in Figure 6.11b1.
Thereafter, the evolution of the distribution factor is characterised by the formation of new cracks and the subsequent opening of existing ones. This evolution is accompanied by an increase in the utilisation of reinforcement and a reduction in the contribution of tension stiffening. In the case of reinforcement CG1 (Figure 6.11a), the analytical solution tended to slightly overestimate the contribution of tension stiffening for maximum reinforcement strain values below 2.4 mm/m. The



distribution factor ζ acc. to [MC20, DAfStb24]

$\zeta_{calc} = 1 - \beta_{TS} \cdot \left(\frac{\varepsilon_{nmr}}{\varepsilon_{nm}}\right)^2$ acc. to Eq. 2-40

$\beta_{TS} = 1$: short-term initial loading

$\beta_{TS} = 0.5$: accounting for cyclic loading

approximation for reinforcement strain at initial crack occurrence: $\varepsilon_{nmr} = \frac{M_{cr}}{z \cdot A_{nm} \cdot E_{nm}}$ $z \approx 0.9 \cdot d = 0.9 \cdot (h - d_1)$

distribution factor ζ obtained from tests

$\zeta_{test} = \frac{\varepsilon_{nm,m}}{\varepsilon_{nm,max}}$

with strain values derived considering full length of optic sensor

Figure 6.11: Comparison of the analytically determined distribution factor ζ_{calc} following the concept in [MC20, DAfStb24] and the derived ζ_{test} using the data provided by FOS

reduced determination of ζ_{calc} using $\beta_{TS} = 0.5$ would provide for an almost perfect fit for this reinforcement utilisation. This phenomenon was also observed in the cyclically loaded specimens of series S-CG2 (Figure 6.11b2+3). However, the usage of $\beta_{TS} = 0.5$ is attributed to the reduction of the contribution of tension stiffening during cyclic loading, rather than a priori. At larger reinforcement utilisations of CG1, some underestimation was found in the case of the purely statically loaded specimen.
The influence of the cyclic loading phase is also revealed by the increase in value of the distribution factor at equivalent strain values. Exceptions were only found in the case of series S-CG3, where no change of ζ_{test} was found (Figure 6.11c), and for specimen S-CG2-cyclic-1, where $\zeta_{test} \approx 1$ was reached at once (Figure 6.11b1).
To conclude, the analytical representation of the distribution factor using a quadratic ratio of reinforcement strain after initial cracking ε_{nmr} and the considered loading ε_{nm} without a reduction (β_{TS} remains to be 1.0), is satisfactory also in the case of non-metallic textile reinforcement and static loading. A reduction of the contribution by 50% for cyclic loading as proposed by code provisions was not found.

6.5.3 Evaluation of approaches

The adequate representation of the contribution of tension stiffening using the distribution factor ζ facilitates the application of the previously presented approaches to predict the deflection in mid-span of the test slabs. Following the description in 6.5.1, Approach 1 is represented by neglecting tension stiffening in the cracked concrete region and determining the deflection using the iterative determination of the cross-sectional curvature (cf. Section 6.3). The calculative procedure in this approach is also required for the other two approaches, as both depend on the obtained strain distribution in the cross-section and the curvature, respectively. The second approach is characterised by a direct consideration of the distribution factor to derive an average curvature of the cracked section

$$\kappa_{II,m}(x) = \frac{\zeta \cdot \varepsilon_{nm,1}(x) - \varepsilon_c(x)}{h - d_1}. \tag{6-9}$$

Approaches 1 and 2 determine the deflection of the whole member by utilising the curvature evolution along the slab, analytically determined by the double-integral. The third approach is based on the determination of an average curvature κ_m for the whole member to utilise the formulation given in Equation 6-8, following the proposal of the code provision.
The obtained moment-deflection curves at mid-span of the three approaches are plotted in Figure 6.12 and compared to the test results of the purely statically loaded slabs. As the focus is on the serviceability limit state, the diagrams in Figure 6.12 only provide for deflections of up to 50 mm. The full plots are provided in Appendix C.3. To summarise one observation in advance, the difference between Approach 2 and Approach 3, both considering tension stiffening, is marginal when a uniform reinforcement layout along the whole slab was present, as it was the case for specimen S-CG1-static (Figure 6.12a).
The evaluation in Figure 6.12 verifies the very good prediction of Approach 2. It also shows the evident overestimation of deflection when neglecting tension stiffening, as revealed by the moment-deflection curve of Approach 1, denoted as a dark grey line in Figure 6.12. The third approach appears to underestimate the deflection determined in the tests, which results from the incompatibility of considering different reinforcement layouts along the slabs. Approach 3 uses the curvature determined at mid-span where the maximum bending moment is located and the curvature is calculated using four textile layers in the case of the slabs reinforced with CG2, CG3 and GG. Consequently, the deflection of Approach 3 is lower compared to Approach 2 and the test data. This

is particularly significant in the case of S-CG3-static (Figure 6.12c), where the deflection is highly underestimated compared to the test evolution at values exceeding the serviceability criterion of 10 mm. in the case of the two other specimens, S-CG2-static (Figure 6.12b) and S-GG-static (Figure 6.12d), a similar discrepancy between Approach 3 and test observation was found at elevated deflections, which were out of the scope of the diagrams in Figure 6.12 but are depicted in Figure C.2. It is evident that in the case of S-CG3-static, the lap joint measuring 300 mm in length, which contains four reinforcement layers, is comparatively smaller in length when compared to the remaining cracked section, in which only two reinforcement layers were placed. However, neglecting the lap joint with its two additional reinforcement layers or the additional layer in series S-GG resulted in a significant overestimation of the deflection determined in the test and consequently does not provide a reasonable alternative.

It is noteworthy to highlight the sensitivity of the prediction approaches regarding the accurate determination of the bending moment at initial cracking, denoted as $M_{cr,calc}$ in Figure 6.12. This is due to the cracking moment, and consequently the concrete tensile strength, influencing the magnitude of the contribution of tension stiffening via the distribution factor ζ. Larger cracking moments provide less tension stiffening and larger deflections.

The provided evaluation revealed that the consideration of tension stiffening is crucial for a well-defined and progressive prediction of the deflection. In the general case of having a uniform reinforcement layout, Approach 3 proved to be feasible as well, which is the proposal in the code provision for κ_m defined identically in *fib* Model Code 2020, Eurocode 2 and DAfStb Guideline

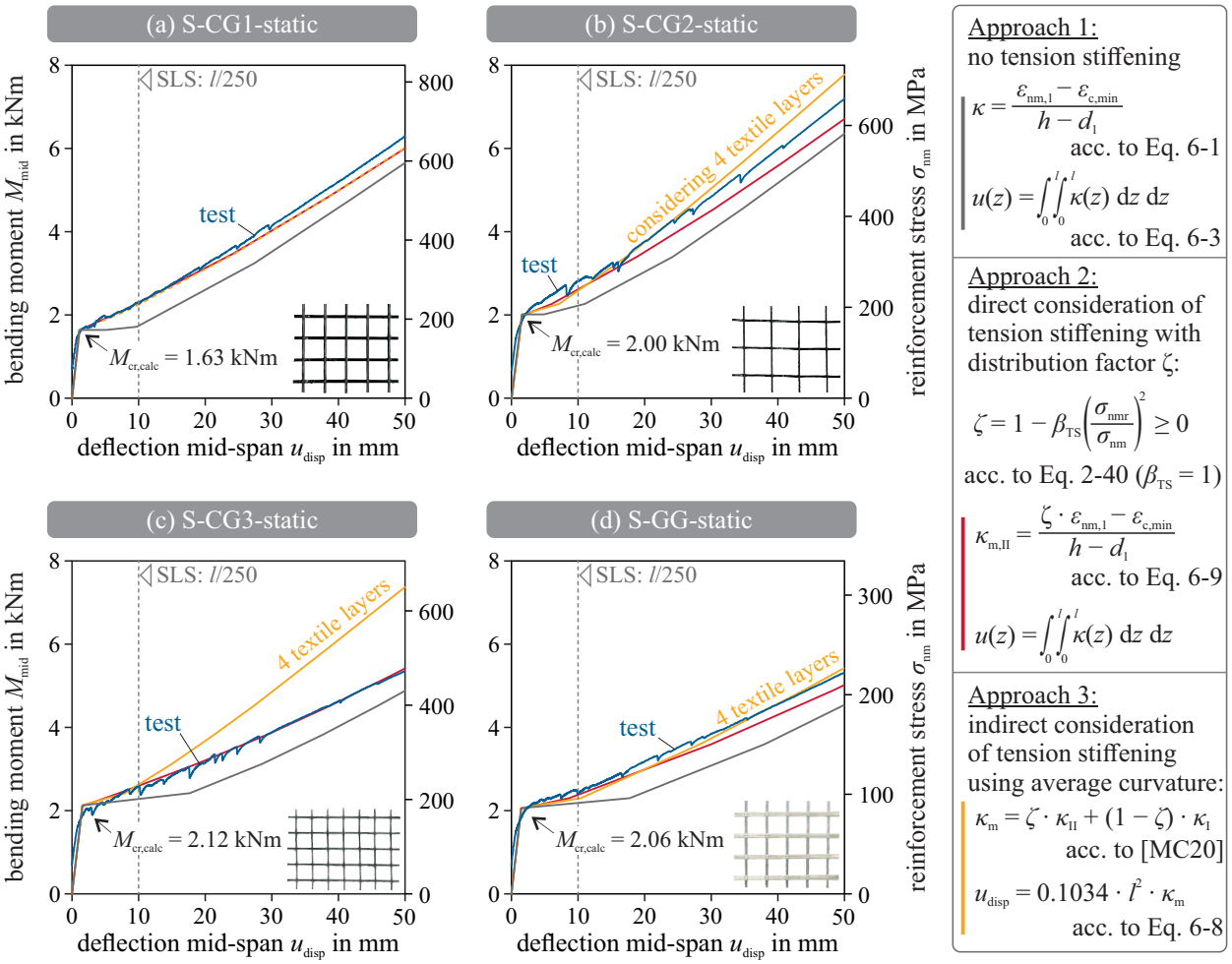


Figure 6.12: Moment-deflection prediction of analytical-based approaches compared to the test results of purely statically loaded four-point bending tests

[DAfStb24]. An almost perfect representation of the moment-deflection curve of the purely statically loaded slabs was possible by the iterative determination of the cross-sectional curvature using an average value of reinforcement strain in the cracked concrete section, which accounts for the contribution of tension stiffening, referred to as Approach 2.

6.5.4 Deflection increase due to cyclic loading

The increase in deflection is significantly influenced by the level and magnitude of the cyclic load and the material properties of the concrete. In the case of flexural members, the cyclic loading results in an increase in the concrete compressive strain, which in turn increases the cross-sectional curvature. In the member's compression zone, the calculated compressive strain was at most 0.80 mm/m at the superior load level prior to the cyclic phase, which refers to approximately 23% of the concrete compressive strength f_{cm}. Consequently, the strain increase at this state is attributed to the predominantly linear component of the stress-strain relation of concrete under compression.
In the case of creep or cyclic loading, an increase in the compressive strain occurs while the corresponding stress remains unchanged. This results in plastic deformations of the concrete, which one could refer to as damage. Moreover, the contribution of the uncracked concrete sections between adjacent cracks is lower, resulting from a reduced bond capacity. This behaviour has been previously observed in experiments employing fibre optic sensors, with some tests demonstrating negligible contribution of tension stiffening in the loading range of the cyclic regime. Assuming that the latter effect is considered in an approach by assuming a reduced or neglected consideration of tension stiffening, the change in the concrete's compressional behaviour under cyclic loading is more difficult to assess.
The problem is clarified by utilising the second approach introduced in the previous Section 6.5.3 to predict the deflection occurring during the initial static loading phase of the cyclically loaded slabs. In Figure 6.14, the predicted deflection using Approach 2 for the first cyclically loaded specimen of each series is represented by the dashed grey lines. Identical to the prediction in the case of the purely statically loaded slabs, it is observed that the prediction is highly accurate. However, the predictions derived from Approach 2 are evidently incompatible with the increase in deflection resulting from the cyclic loading. Furthermore, subsequent to the cyclic phase, during which additional force was applied, Approach 2 underestimates the deflection of the test slabs. This phenomenon is attributed to the damage sustained by the concrete in the compression zone, where cracks were present during cyclic loading.

Consideration of strain redistribution

Consequently, to determine the deflection resulting from damage to the compression zone in the area of existing cracks, the strain increase and reduction in the concrete compressive resistance have to be considered. The strain and stress redistribution over the cross-section occurring during the cyclic loading is visualised in the upper half of Figure 6.13 in the case of a low utilisation of the concrete compressive strength. Due to the cyclic loading, the absolute value of the concrete compressive strain increases. This additional increase is denoted as $\varepsilon_{c,cyc}$. In literature (e.g. [Gao98, Pfa02, Vis21]), it is generally acknowledged that in the case of a uniaxial and uniform compressive cyclic loading, no change in the corresponding stress value σ_{c0} occurs when the strain utilisation ε_{c0} does not exceed the strain ε_{c1} referring to the compressive strength f_{cm}. In the case of increased loading after the cyclic phase, the concrete compressive behaviour is approximated by a shifted stress-strain curve by an increase of $\varepsilon_{c,cyc}$, as depicted in Figure 6.13.
In the context of a flexural member, the compressive zone is not subject to a uniform loading. In instances where substantial strain increases occur prior to cyclic loading, which exceed the

value of ε_{c1}, a decrease of the corresponding stress value must be considered. In the presented test configuration, this was not the case. Consequently, no reduction in the compressive stress at the most-compressed fibres occurred. Nevertheless, the change in the strain distribution provides for a larger compression zone. Therefore, to achieve force equilibrium, the concrete stress decreases, whilst the reinforcement strain and stress increase. It is important to consider this in terms of the cross-sectional curvature, since the adaptation of both the strain values for concrete and reinforcement leads to an increase in curvature, and consequently, deflection.

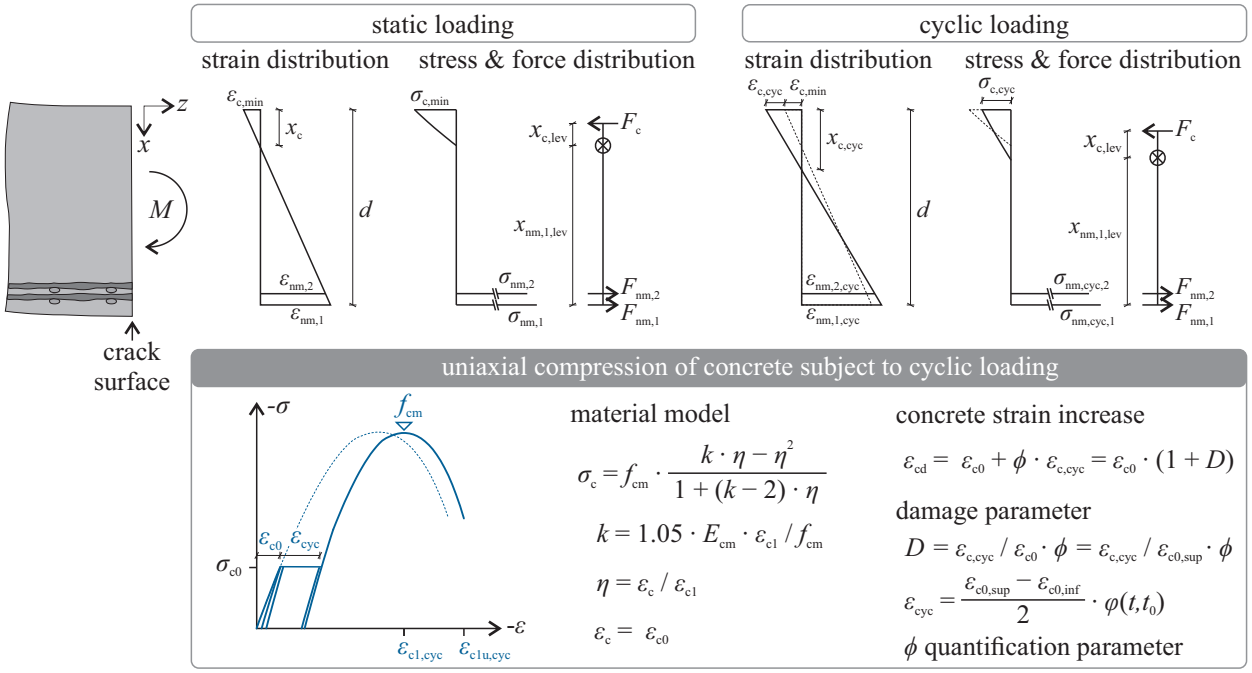


Figure 6.13: Influence of cyclic loading on the distribution of strain and stress in the cross-section with consideration of a damage-based material model for concrete subject to uniaxial compression

To account for the observed concrete behaviour, in particular the increase in compressive strain and the change in the stress-strain relation, a possible modelling strategy is the adaptation of Young's modulus E_{cm}. This method is considered a simple way to approximate the larger strain values required to obtain the same concrete stress utilisation at initial loading, σ_{c0}. For instance, in the context of sustained loading, the effect of concrete creep is evaluated by introducing an effective Young's modulus. In the case of the considered test series, an alternative approach is adopted, as it is not possible to determine a suitable reduction of the Young's modulus using the provided data. The approach is more implicit. Solely the concrete strain is adapted to account for the influence of the cyclic loading. The concrete strain after cyclic loading, denoted by ε_{cd}, is comprised of two components: the initial concrete strain ε_{c0}, and the cyclic strain increase $\varepsilon_{c,cyc}$:

$$\varepsilon_{cd} = \varepsilon_{c0} + \phi \cdot \varepsilon_{c,cyc} = \varepsilon_{c0} \cdot (1 + D) \tag{6-10}$$

The formulation to determine the concrete compressive stress remains unchanged and the strain is set to be the initial strain. With this modelling approach, the value of concrete stress is attributed to the strain values after cyclic loading. The difficulty arises in adequately determining the damage parameter D. In the experimental campaign, no material tests on concrete behaviour under cyclic loading were conducted. Therefore, the approach to determine the strain increase due to cyclic loading provided by the *fib* Model Code 2020 is taken into account. This approach utilised the

empirical-based formulation to determine a value of concrete creep in a set time interval $\varphi(t,t_0)$, with the time interval adapted to account for the number and the frequency of load cycles. This is, naturally, a very rudimentary approach, a comment in the *fib* Model Code 2020 informs about a possible underestimation of the determined strain increase. As a result, an additional calibration factor ϕ, which is obtained using the four-point bending tests, is introduced to quantify the value of the cyclic strain. The damage parameter

$$D = \frac{\varepsilon_{\text{cyc}}}{\varepsilon_{\text{c0}}} \cdot \phi \leq \frac{\varepsilon_{\text{cyc}}}{\varepsilon_{\text{c0,sup}}} \cdot \phi \tag{6-11}$$

is determined as a relative parameter using the initial strain value and the cyclic strain increase

$$\varepsilon_{\text{cyc}} = \frac{\varepsilon_{\text{c,sup}} - \varepsilon_{\text{c,inf}}}{2} \cdot \varphi(t,t_0)\,. \tag{6-12}$$

The concrete strain values are obtained by the iteratively determined strain distribution at initial loading. The approach in Equation 6-12 of the *fib* Model Code 2020 uses the amplitude of the concrete stress, which is expressed by the concrete strains, at the superior and inferior load levels prior to cyclic loading. The definition in Equation 6-11 allows for an interpretation of the damage parameter in dependency of the initial strain value, with less absolute strain increase attributed to the sections of the compression zone which are less utilised. To determine feasible strain values after cyclic loading, at maximum, the damage resulting from the strain increase under superior loading is considered.

Deflection prediction

Evidently, the proposed procedure is a simple and not profound method to determine the strain increase required to predict the deflection observed after cyclic loading. In Table 6.4, the required parameters for the application of this procedure and the determined deflection are provided. To fit the calculated deflection $u_{\text{calc,sup}}$ to the deflection measured in the test series $u_{\text{test,sup}}$, the quantification parameter ϕ is adapted to integer values between 1 and 8, which demonstrates a substantial variability of ϕ. In the majority of cases, a moderate quantification of the approximated cyclic strain increase was necessary to fit the test data. However, some predictions require unrealistically large quantification factors, for example $\phi = 8$ in the case of CG2 cyclic-1.

Table 6.4: Parameters to approximate the strain increase due to cyclic loading, contribution of tension stiffening (TS) and relative comparison to deflection of the tests

index		t_0 [d]	$\varphi(t,t_0)$ [-]	$\varepsilon_{\text{c0,sup}}$ [mm/m]	D/ϕ [-]	ϕ [-]	$\varepsilon_{\text{cyc}} \cdot \phi$ [mm/m]	u_{TS} [mm]	$\frac{u_{\text{calc,sup}}}{u_{\text{test,sup}}}$ [-]
CG1	cyclic-1	14	0.703	0.71	0.50	4	1.41	4.6	0.96
	cyclic-2	114	0.254	0.73	0.20	1	0.15	6.4	0.96
CG2	cyclic-1	30	0.650	0.75	0.44	8	2.62	3.7	1.01
	cyclic-2	117	0.324	0.56	0.24	1	0.13	4.8	1.03
CG3	cyclic-1	46	0.530	0.76	0.42	4	1.23	5.8	0.95
	cyclic-2	116	0.310	0.76	0.25	6	1.06	8.2	0.95
GG	cyclic-1	54	0.378	0.80	0.30	2	0.48	9.6	0.96
	cyclic-2	117	0.245	0.80	0.19	1	0.16	10.5	1.11

Furthermore, the prediction approach allows for the determination of the deflection increase resulting from cyclic loading for different assumptions on the contribution of tension stiffening. Assuming that either tension stiffening is fully contributing, with $\beta_{TS} = 1$ to obtained ζ in Equation 2-40, or neglected $\beta_{TS} = 0$, the difference in both predicted deflections provides the deflection increase u_{TS} (see Table 6.4). The magnitude of the determined deflection increase u_{TS} in comparison to the overall predicted deflection increase resulting from cyclic loading indicates that the primary cause of the observed increase in deflection is attributed to the loss of tension stiffening. This significant reduction in the contribution of tension stiffening for flexural members was already revealed by the FOS measurement and is confirmed by the prediction. As the used approach still accounts for a differentiation of uncracked and cracked sections, neglecting tension stiffening is only attributed to the cracked concrete section. Neglecting tension stiffening proved to be advantageous in comparison to the code provision formulation, which suggests reducing the contribution of tension stiffening only by 50%. As revealed in Table 6.4, the predictions are close to the deflections measured in the tests ($u_{calc,sup}/u_{test,sup} \sim 1.0$).

For the first cyclically loaded test of each series, Figure 6.14 presents a graphical representation of the deflection prediction following Approach 2, both with and without consideration of tension stiffening. The prediction with tension stiffening is illustrated by the red dotted curves. The predictions for the second tests are found in Figure C.3. Both Figures reveal a key observation: the predictions with tension stiffening provide suitable results for the deflection after the cyclic phase and only slightly overestimate the test results for most of the load range. Only for specimen S-CG2-cyclic-1 the deflection is significantly overestimated (Figure 6.14b).

A more detailed focus on the approximated cyclic strain increase reveals that the determined creep coefficient, denoted by $\varphi(t,t_0)$, is at most 0.7 for specimen S-CG1-cyclic-1 (cf. Table 6.4), which was tested earliest at a concrete age of 14 days. The values of the creep coefficients decreased with increased age at testing. Consequently, the determined damage parameter D shows the same trend. In addition, the strain values at the superior and inferior load levels do not significantly differ between the reinforcement types. The quantification factor ϕ shows the actual inaccuracy and lack of robustness of the proposed methodology using the *fib* Model Code 2020 approach in Equation 6-12 to approximate the cyclic strain increase.

In summary, the increase in deflection is considerable. The contribution of tension stiffening is significantly reduced during cyclic loading and is assumed to be negligible in this case. However, it is essential to address the absolute strain increase in the compression zone of the flexural member, which also results in an increase of the depth of the compression zone, a decrease of the inner level and consequently larger reinforcement strain values. A determination of the cross-section curvature, taking into account the change in strain distribution, has been shown to facilitate a satisfactory and accurate prediction of member deflection subsequent to cyclic loading. In addition, it is possible to predict the ongoing deflection of slabs under increased loading by calculating the strain obtained from cyclic loading. This is based on the almost negligible tension stiffening and the only slightly higher predicted deflection. Nevertheless, this approach is significantly dependent on a suitable determination of the strain increase in the compression zone. The investigation employed the approach of *fib* Model Code 2020 to approximate the strain increase in concrete resulting from cyclic loading using an equivalent creep coefficient. In the majority of cases, it was necessary to increase the strain value by a factor significantly greater than its original value.
In the absence of characterisation tests, which focus on the behaviour of concrete when subjected to cyclic loading, it is impossible to formulate a robust and solid strain increase estimation. The application of alternative methods derived from existing literature did not result in the identification

of more robust values. Furthermore, the majority of the methodologies documented in the existing literature concentrate on the examination of concrete fatigue, with an emphasis placed on higher utilisation of concrete compressive strength and larger amplitudes.

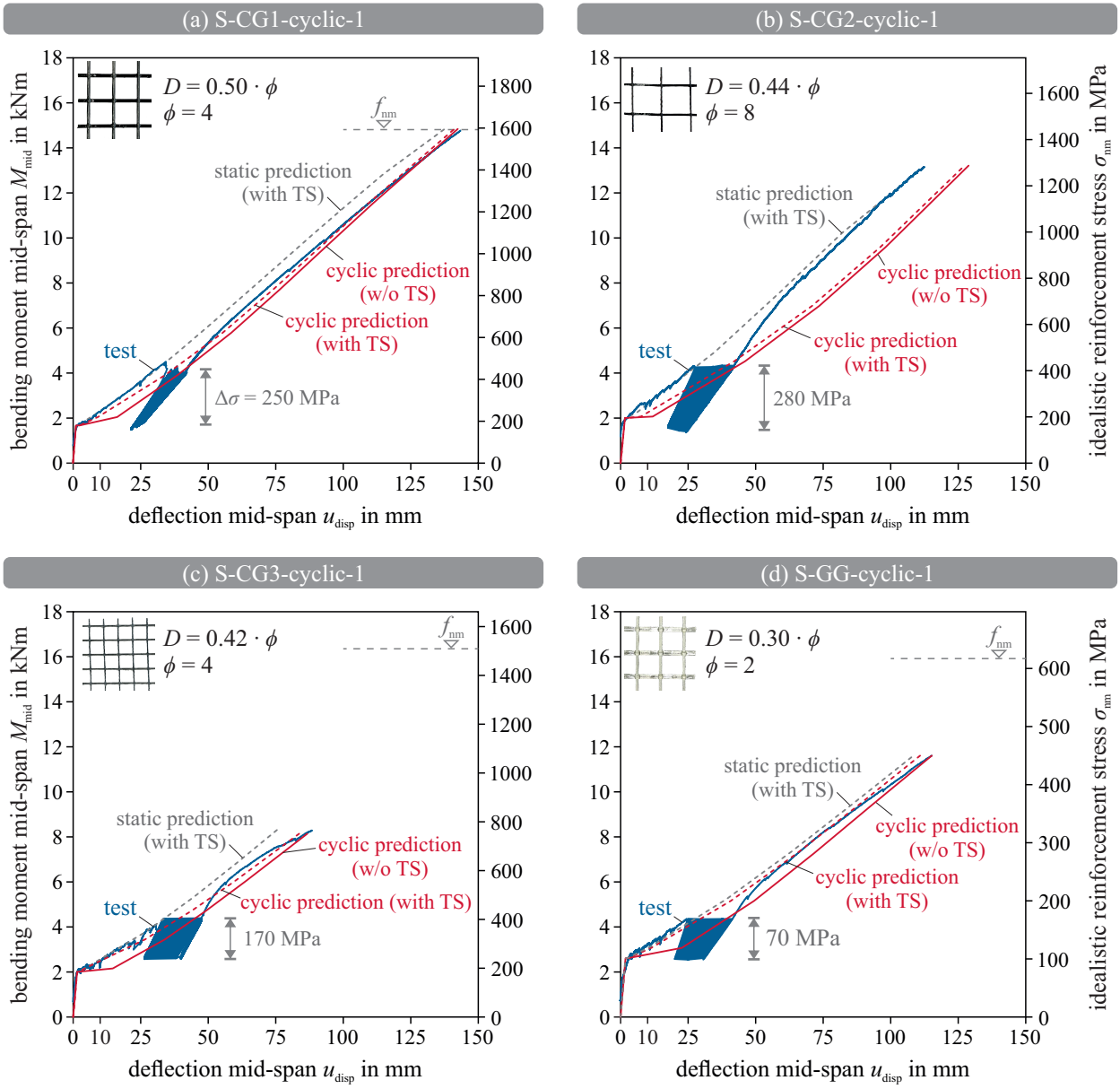


Figure 6.14: Moment-deflection prediction of the analytical-based Approach 2 accounting for cyclic loading for different considerations of tension stiffening (TS)

6.6 Summary

The investigations in this chapter focused on slender concrete slabs reinforced with multiple layers of textile grids. The objectives of these investigations were to demonstrate the applicability of the physically based model for predicting the crack width and to establish a methodology for predicting the deflection, considering static and cyclic loading conditions.

The flexural members exhibit a reduced crack width and crack spacing in comparison to members subjected to uniaxial tensile loading. This results from the linear strain distribution of the cross-section in the case of bending moments and has been addressed in the approach proposed by [MC20, FprEC2]. Evidently, a similar consideration for concrete members with non-metallic

reinforcement is reasonable (cf. Section 6.2.4).
In flexural members, an adjacent crack pattern is already present at low load levels. Consequently, the derived physically based model, with the consideration of Equation 6-7 for the stabilised cracking stage, is more feasible for flexural members. In this study, two strategies were evaluated, considering tension stiffening with $\beta = 0.36$ and neglecting tension stiffening (Section 6.4.1). Both strategies revealed a very good fit to the test data for all textile grids. The consideration of tension stiffening yielded in a more progressive prediction with slight underestimation of the crack width on the concrete surface, without tension stiffening more conservative values and an overestimation are obtained. With regard to the variation, both strategies proved to be robust (COV < 11%).
During cyclic loading, the maximum crack width increased by approximately 0.1 mm on average for all four considered textile grids. The approach introduced in Section 5.6 allows for a profound determination of the increase in crack opening (see Section 6.4.2). Nevertheless, it is essential that this approach is validated using different test series in future research.

In the second part of this chapter, approaches to predict the deflection in slabs with non-metallic textile reinforcement were considered and applied to the test data. In the context of instantaneous static loading, the contribution of tension stiffening is imperative in determining feasible predicted deflections (Section 6.5.3). Hereby, it is reasonable to utilise the distribution factor to account for tension stiffening (as given in Equation 2-40), as proposed in [MC20, FprEC2, DAfStb24]. A suitable determination of the deflection is obtained when integrating the distribution factor in the considered model approach, which iteratively determines the curvatures of the cross-section (referred to as Approach 2).
With regard to cyclic loading, tension stiffening should be disregarded, and the additional strain increase in the concrete compression zone resulting from creep to the material must be taken into account. When determining the deflection of a member subjected to an static load application after a cyclic phase, it is sufficient to consider the additional strain increase in concrete compression resulting from concrete creep and the full contribution of tension stiffening to obtain a feasible prediction (Section 6.5.4).

7 Accuracy of the proposed physically based model in predicting the maximum crack width

7.1 Overview

In the preceding chapters, the accuracy of the physically based model was evaluated through both qualitative and quantitative means. This model was employed in the context of predicting the crack width in textile reinforced concrete under uniaxial tension and was verified for flexural members. In the following Section 7.2, the model is compared to existing code provisions in terms of accuracy in predicting the maximum crack width using the conducted uniaxial tensile and flexural tests.

The final aspect focuses on a simplified approach to account for the influence of cyclic loading at the serviceability stage (Section 7.3). The approach introduced and evaluated in Sections 5.6 and 6.4.2 has been derived for the reinforcements investigated and is therefore to be employed exclusively under conditions analogous to those under consideration with regard to concrete behaviour and calibration parameters. As the latter are dependent on the individual reinforcement, a feasible practical implementation is worth discussing.

7.2 Comparison of crack width prediction models

In the following section, the performance of the proposed model for textile reinforcements, as stated by Equation 6-4 (single cracking stage) and Equation 6-7 (stabilised cracking stage), is evaluated and compared against two existing code provision formulations. One is the analytical-based consideration as outlined in [MC90, EC2NAD, DAfStb24], which is formulated in Equation 2-21. The second code provision formulation is the empirical-based model given in [MC20, FprEC2]. For the latter, the calibration factor β_w is adapted according to the findings derived from the conducted experimental campaigns. This increases the accuracy of the empirical-based model with regard to the considered test results, as the model uses an average value of crack width to determine the characteristic value, which is set in this study to be the maximum crack width. In the case of uniaxial tension, $\beta_w = 1.5$, and for flexural members, $\beta_w = 1.9$.
In the evaluation, the effective reinforcement area is determined by utilising a height of $2.5d_1$ (see Equation 2-22), as it has been shown to provide the best results in comparison to the other definitions provided in Section 2.5.1.
Two cases are considered for comparison, both addressing the prediction of the maximum crack width. The aim is to allow a comparison of the accuracy on average (general evaluation) and in the case of the largest possible crack width (characteristic value). For both comparisons, the predicted reinforcement stress σ_{calc} is compared to the determined stress in the tests σ_{test}, providing for an estimated value in each test. An estimated value exceeding 1.0 indicates a progressive performance of the model, as it predicts larger reinforcement stress present at the corresponding crack width compared to the determined test values. Consequently, when designing the member, a lower reinforcement amount would be determined, which is not covered by the test results. In the "general evaluation", the average estimated value of all tests is considered. The second case, "characteristic evaluation", accounts for the variation in the test procedure and material characteristics when determining the bond stress by considering a characteristic value of bond stress. In addition, the maximum of all estimated values is considered. This represents the case of the most underestimated predicted crack width.

A range of crack widths, ranging from 0.1 mm to 0.7 mm, has been evaluated. The evaluation is conducted stepwise in steps of 0.1 mm and considers all crack widths at or below the corresponding value. Each series of the UT-tests, except the specimen UT-GG-NSC-16mm, was taken into account. For each series, the estimated value was determined using the procedure in Annex D.8.2 of [EC0], which was identical to the previously conducted method in Sections 5.5.3 and 6.4.1.

General evaluation

The comparison of the average estimated values is shown in Figure 7.1 and differentiates between uniaxial tension and flexural loading. The estimated values obtained were averaged for each crack width within the prescribed range and are plotted as single data points in Figure 7.1. Two different considerations of the contribution of tension stiffening were evaluated. Either tension stiffening was taken into account with $\beta = 0.36$ (red data points and lines in Figure 7.1), or it was neglected (black data points and lines). In addition, the table in each diagram of Figure 7.1 shows the overall average of all estimated values $\bar{x}$ as well as the average of the coefficients of variation $\bar{x}(V_\delta)$. When considering the state of uniaxial tension, the evaluation in Figure 7.1a reveals that the proposed model provides for the best fit when considering the average estimated value and a contribution of tension stiffening expressed by $\beta = 0.36$ ($\bar{x} = 0.98$). The code provisions demonstrate a certain degree of underestimation of the actual reinforcement stress, with the analytical formulation being the most conservative (Figure 7.1a2). It is important to note that the application of the original calibration factor $\beta_w = 1.7$ according to [MC20, FprEC2] in the empirical-based formulation in Figure 7.1a3 (indicated by the dashed lines Figure 7.1a3) results in an estimated value that is approximately 13% lower compared to the case with the adapted β_w-factor. This yields results

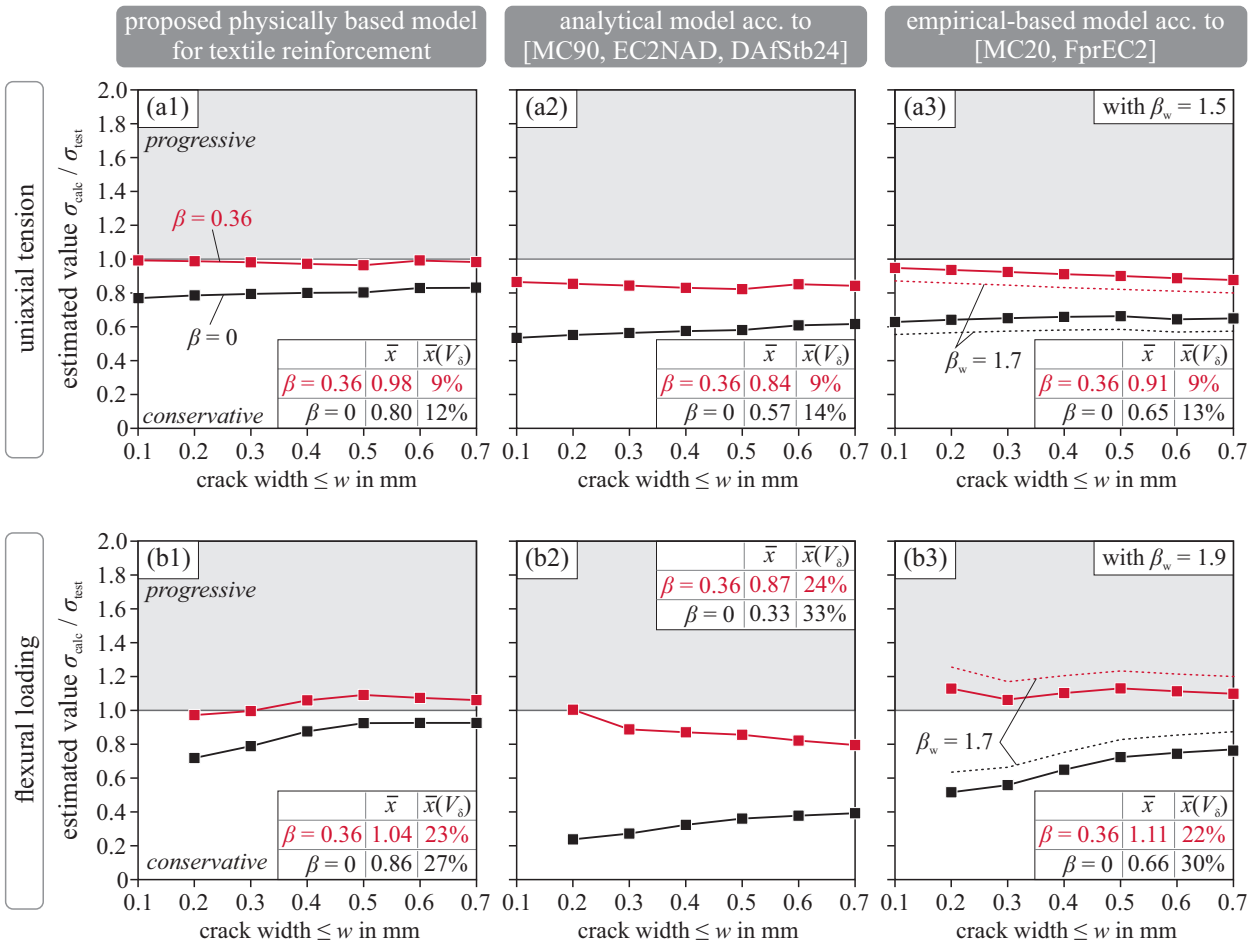


Figure 7.1: Evaluation of different models to predict the maximum crack width

that are analogous to those obtained from the analytical formulation. However, all three models indicating a low scattering of the predicted crack widths, as the coefficient of variation is 9% when tension stiffening is considered, and approximately 13% when it is neglected.

In the case of flexural loading, displayed in Figure 7.1b, again the physically based model revealed the most appropriate fit on average when considering tension stiffening ($\bar{x} = 1.04$, Figure 7.1b1). By neglecting tension stiffening, a more conservative prediction is obtained ($\bar{x} = 0.86$).
While the analytical formulation provides feasible results when tension stiffening is considered ($\bar{x} = 0.87$, Figure 7.1b2), neglecting tension stiffening results in very conservative outcomes, with $\bar{x} = 0.33$. Despite adapting the calibration factor in the empirical-based formulation to 1.9, the performance did not demonstrate sufficient improvement to compete with the other two models (Figure 7.1b3). The consideration of tension stiffening results in the most progressive prediction of all three models, with $\bar{x} = 1.11$. Utilising the original calibration factor would result in a substantial overestimation when tension stiffening is considered.
Addressing the averages of the coefficients of variation ($\bar{x}(V_\delta)$), all models demonstrate significant scattering of approximately 30% when neglecting tension stiffening, and below 25% in the cases of considering tension stiffening.

Characteristic evaluation
In the previous comparison, the mean value of bond stress obtained by the COT tests was utilised. This neglects the influences of varying material parameters and differences resulting from the test conduction, which is generally accounted for by introducing a characteristic value of the material parameter. To obtain a characteristic value, the approach proposed by Eurocode 0, Annex D.7 [EC0] is utilised. The approach describes the derivation under consideration of variations in individual material characteristics, which were determined in a test series. The characteristic value of bond stress is determined to

$$\tau_{\mathrm{bm,k}} = \tau_{\mathrm{bm}} \cdot (1 - k_{\mathrm{n}} \cdot V_{\mathrm{x}}) \tag{7-1}$$

using the coefficient of variation V_{x} and the characteristic fractile factor k_{n}. The latter is dependent on the number of tests conducted to obtain the average value. In the case of the five COT tests in a series and the 5% fractile of the test sample, $k_{\mathrm{n}} = 2.33$. Exemplarily, the coefficient of variation is assumed to be 0.1 (cf. Annex D.7 in [EC0]). Using Equation 7-1, the characteristic value of bond stress is approximately 77% of the average value.

Regarding the crack width prediction models, a comparison is made considering the maximum estimated value of $\sigma_{\mathrm{calc}}/\sigma_{\mathrm{test}}$ for the characteristic value of bond stress. The comparison is motivated to assure a solid prediction for the possibility of individual cracks showing large widths. This includes the consideration of the experimentally based variation by the characteristic value of bond stress. The evaluation is visualised in Figure 7.2 separately for each model. Only the cases with consideration of tension stiffening ($\beta = 0.36$) are shown, as the previous evaluation revealed that neglecting tension stiffening yields too conservative results.
Similar to the previous discussion, the evaluation demonstrates that the proposed model is reliable for predicting crack widths with enhanced precision (Figure 7.2a). For both cases of uniaxial tension and flexure, an almost perfect prediction ($\bar{x} \sim 1.0$) is achieved for all crack widths. In the case of the analytically based code provision model (Figure 7.2b), solid predictions are also found, however with less accuracy compared to the model in Equation 6-7. For flexural members, the model is slightly progressive for crack widths below 0.5 mm, while slightly underestimating the test results for large widths or in the case of uniaxial tension. For the empirical-based model shown in Figure 7.2c, again, the adapted calibration factors β_{w} are considered. Nevertheless, the accuracy

of the predictions is not improved in comparison to the other two models and provides unsuitable progressive results in the case of flexure.

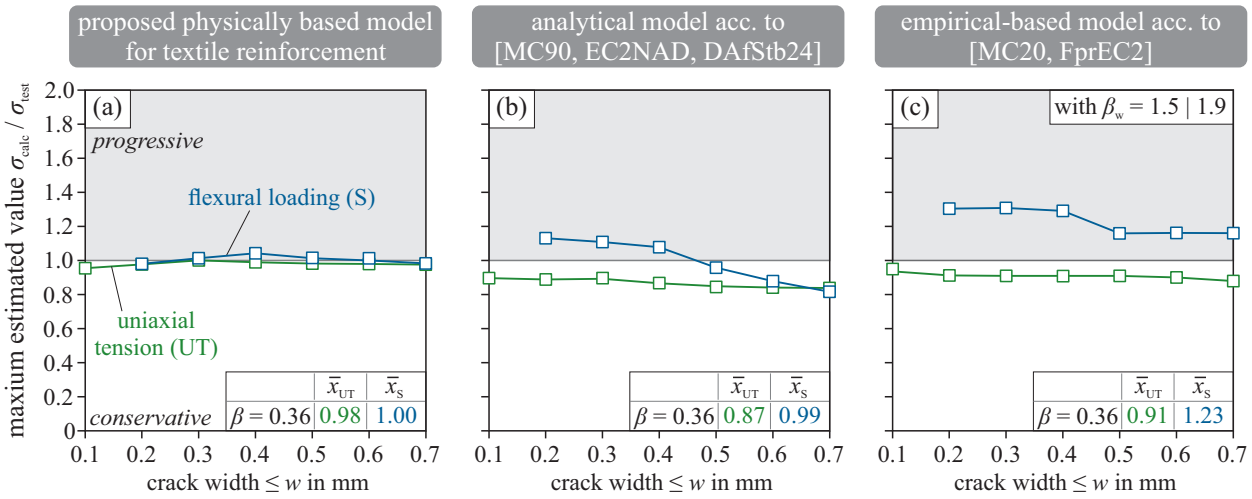


Figure 7.2: Evaluation of different models to predict the maximum crack width at a characteristic level regarding the bond capacity

7.3 Simplified consideration of cyclic loading

The increase in crack width due to cyclic loading is significantly dependent on the considered textile grid. Therefore, the derived simplified consideration introduces conservative assumptions to provide for a unified proposal feasible for all investigated textile grids. The assumptions are stated by employing the general formulation provided in Equation 5-37. Firstly, the calibration parameter γ is neglected. The motivation behind this choice is that the assumption of a value of γ equal to zero has been demonstrated to provide reasonable to good results in predicting the additional crack opening in various configurations in the UT tests and for all cases of the bending tests. Moreover, this considerably simplifies the formulation of Equation 5-37. Secondly, the experimental investigations revealed that the increase in crack opening is less pronounced for more than 10,000 load cycles. Therefore, the calibration parameter Γ is becoming dominant. Taking these two assumptions into consideration, the formulation in Equation 5-37 is restated, with the introduction of a factor Γ/C_0, which serves to transfer the reinforcement-specific material parameter C_0 to a more general description. This step is referred to as *simplification* and indicated by the green columns in Figure 7.3b. The crack width increase in dependency of the number of load cycles applied is

$$\frac{\Delta w}{w_0} = \frac{1}{1 - \Gamma/C_0 \cdot \ln(N_{cycl})} - 1\,. \tag{7-2}$$

To enable a *conservative simplification* with a unified value for all investigated textile reinforcements, the factor Γ/C_0 is adapted to be 0.042 for uniaxial tension. This values is attributed to series UT-GG-NSC, which had the largest Γ/C_0-factor. The experimental campaign on flexural members revealed that the crack width increase during cyclic loading is less pronounced, which is partially attributed to the presence of mostly adjacent cracks. Consequently, a lower value for Γ/C_0 is determined to be 0.030 (attributed to series S-CG3). It is evident that the proposed simplification method is highly dependent on the boundary conditions and materials investigated in this thesis.

To facilitate a brief evaluation of the influence of the two introduced simplifications, Figure 7.3 is provided. The magnitude of the predicted additional crack opening with regard to the used factor Γ/C_0 in relation to the cycles is shown in Figure 7.3a. The evaluation indicates that the implementation of a conservative simplification of $\Gamma/C_0 = 0.042$ results in a predicted increase in crack width by 100% following 200,000 load cycles. A reduction to $\Gamma/C_0 = 0.030$, as proposed for flexural members, results in an increase of 58% of the initial opening after 200,000 cycles.
The two simplification steps are used to determine an estimated value by comparing the prediction and the test results. As depicted in Figure 7.3b, the estimated values are presented for each relevant test series of the uniaxial tensile tests and four-point bending tests. The missing UT test series in Figure 7.3b did not demonstrate an increase in crack opening and, as a result, were disregarded. For reference, the estimated values using the best fit method applied on the test data in Section 5.6 for the UT tests and in Section 6.4.2 for the bending tests are also provided (blue columns). As demonstrated in Figure 7.3b, with each simplification, the estimated value decreases, referring to an overestimation of the crack opening and resulting in a conservative approach when the value is below 1.0. This is of particular significance when focusing on the conservative simplification. For example, in the case of series UT-CG2-HSC, the estimated value is a mere 0.13, implying that the actual crack opening is below 1/6 of the predicted value.
In summary, the utilisation of the conservative simplification of Equation 7-2 with a unified value of Γ/C_0 independent from the considered reinforcement results in a considerable overestimation of the actual crack opening for some textile grids and concrete strength classes. In addition, it is noteworthy that the employment of alternative approaches, such as the formulation presented by KOENIG and TUE (cf. Equation 2-29), does not yield more precise results. As outlined in the investigations described in Section 3.4, a dependency on the crack opening resulting from the derived bond behaviour at single cracking was not found.

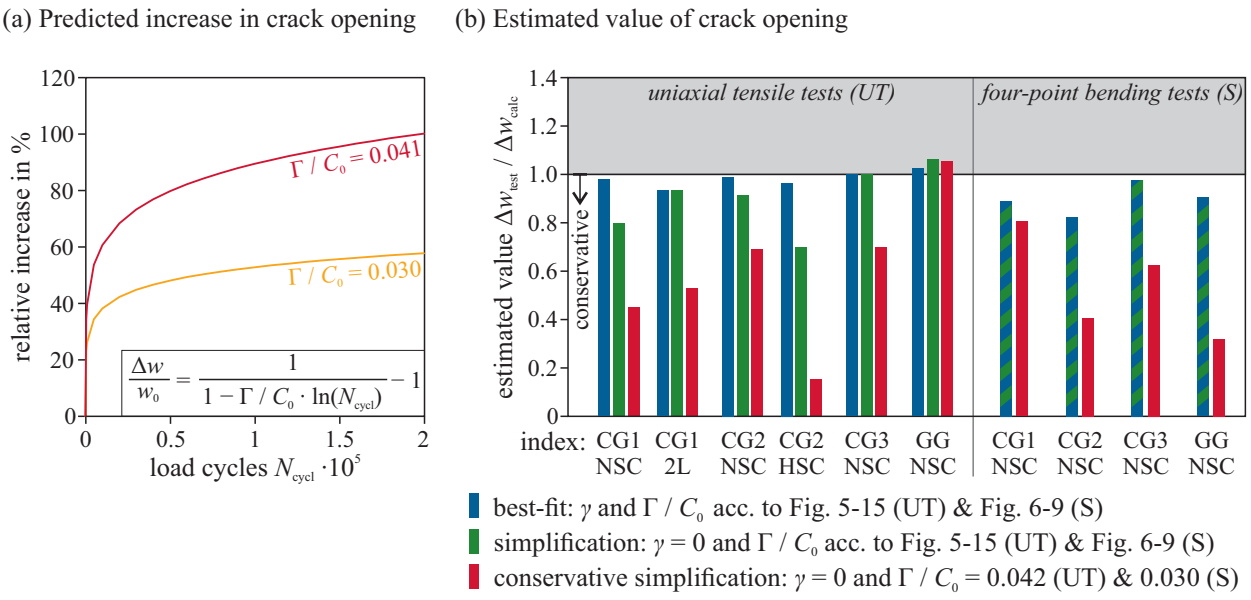


Figure 7.3: Influence of simplifications to predict the crack opening resulting from cyclic loading

8 Conclusion and Outlook

8.1 Summary

The design of non-metallic textile reinforced concrete members requires particular consideration of the serviceability limits of crack width and deflection, as these parameters decisively regulate the reinforcement ratio and cross-sectional geometry. With regard to the crack width, limitations are imposed by visual appearance and functionality of the member, as the corrosion resistance of the reinforcement does not require any limitations, in contrast to steel rebars. In the case of flexural members, deflection becomes the primary design criterion. Both limitations result in a low utilisation of the reinforcement's tensile capacity. Consequently, models and approaches allowing for a progressive and accurate prediction of crack widths and deflection are required. In addition, the influence of various materials and the differently shaped textile grids show distinguished bond behaviours that must be appropriately addressed within these models.

Therefore, the bond behaviour was characterised by experimental campaigns on single-sided pull-out (SPOc) tests and crack opening tensile (COT) tests. Both campaigns focused on a single fibre strand by varying different parameters. It was revealed that the bond capacity significantly depends on the provided friction, the presence of local undulations, the utilisation of reinforcement, and bond length (cf. Section 3.6). In the case of local undulations resulting from intersections with transverse fibre strands, it was found that force transfer is provided by mechanical interlocking only at low reinforcement utilisation, which are present at the serviceability state. On the other hand, when the bond length is too short to encompass at least two local undulations, the contribution of interlocking becomes negligible in the case of larger reinforcement utilisation accompanied by the occurrence of significant slip. The transverse fibre strands are sheared off as well as straightening and compressing of local undulations due to the low transverse stiffness of the reinforcement preventing an efficient interlocking. In the absence of force transfer by local undulations, friction becomes the predominant bond mechanism. In the case of short-term loading, the results revealed that variations in the concrete tensile strength exhibited minimal impact on the bond capacity, which was also primarily attributed to the transverse compression of the fibre strand. The observations highlighted that in order to adequately predict the crack width using analytically derived bond stress relations, a formulation that is dependent on the crack width is required. It was shown that a robust experimental setup, such as the COT test, provides the experimental basis for a feasible derivation of the bond behaviour in the case of uniaxial tension and a single crack.

The employment of COT tests enables a physically based representation of the composite's deformation behaviour, which then allowed for the derivation of an analytical bond stress-crack opening relation, with individual parameters addressing the different behaviour of the investigated textile grids (Section 5.4). The representation also enabled the derivation of a tension stiffening factor that quantifies the contribution of the uncracked concrete to a reduced crack opening. The validity of this factor was confirmed through the measurements with fibre optic sensors (FOS) in all experimental campaigns. The results of uniaxial tensile (UT) tests were used to validate the proposed method for deriving the bond stress-crack opening relation. Moreover, the UT test series provided the basis for further adaptations to the derived crack width prediction model (Section 5.5). In case of reinforcement layouts containing multiple layers of textile grids, it is necessary to reduce the bond stress, given that the full bond area does not contribute to the force transfer. This was addressed by introducing an equivalent circumference, which quantifies the reduced bond area resulting from close layer spacing. As the UT tests also provided insight into the force transfer for

adjacent cracks, it was revealed that the elliptical cross-sectional geometry of the fibre strands resulted in a multi-axial tensile stress state. This, in turn, provoked the occurrence of adjacent cracks at shorter spacing compared to a circular cross-section. Consequently, a stress-intensifying factor was introduced that accounts for the cross-sectional geometry. With regard to the contribution of tension stiffening, the requirement for differentiation between single cracks and adjacent cracks was confirmed. It was also revealed that neglecting tension stiffening yielded results that were conservative while still reasonably accurate at the stabilised cracking stage. The application of 200,000 cycles at a load level representing the serviceability state resulted in a substantial increase in crack widths in the case of single cracks. In the presence of adjacent cracks, the observed increase was less pronounced. Bond creep was identified as the primary cause of the additional crack opening. Consequently, long-term behaviour must be addressed through the implementation of an adequate approach. This was achieved by introducing an additive term to the initial crack width that accounts for the additional opening, with empirically derived parameters for the investigated textile grids (Section 5.6).

The crack width prediction approach was verified for flexural members by using experimental investigations on four-point bending tests of slabs. Among other findings, it was revealed that closer crack spacing occurred in comparison to the scenario of uniaxial tension. This is analogous to observations in steel-reinforced members, wherein the linear strain distribution of the cross-section forces the formation of cracks at closer crack spacing. This was accounted for in the approach to improve the prediction accuracy (Section 6.2.4). Additionally, the investigations conducted on tension stiffening revealed that the proposed factors for single and stabilised cracking stages are also valid in the case of bending.

A comparison with recent code provisions demonstrated an enhancement in the accuracy of predicting the maximum crack width (Section 7.2). Consequently, the introduced methodology of using a solid experimental setup, such as the COT test, in combination with the analytical description of the bond stress-crack width relation, enables an improved and accurate prediction of the crack width in non-metallic textile reinforced concrete structures using the physically based model.

The deflection of the investigated flexural members was determined through the utilisation of an iterative approach to determine the curvature under consideration of the contribution of tension stiffening and bond creep in the case of cyclic loading (Section 6.5.3). The investigations focusing on additional deflection due to cyclic loading showed that tension stiffening is to be neglected in order to obtain a feasible prediction (Section 6.5.4).

8.2 Practical implications

Recent crack width prediction models rely on input parameters representing bond stress and the contribution of tension stiffening. The parameters should be predetermined and, in most cases, are to be provided by the reinforcement manufacturer. Currently employed experimental methods, such as the ones recommended by the current version of the German DAfStb Guideline on non-metallic reinforced members, were found not to resemble the actual situation of crack opening, as they did not explicitly focus on the serviceability stage, resulting in a conservative characterisation of the bond capacity. Furthermore, substantial variations in the experimental data led to a significant reduction in the derived characteristic bond stress values. These deficits, primarily arising from the absence of an adequate experimental setup, were solved by the COT test setup and the evaluation method provided to obtain a sufficient bond stress-crack width relation and a quantifi-

cation of the tension stiffening effect for single cracks. The simplicity of the setup, in combination with a straightforward measuring concept that exclusively determines the crack opening, facilitates the broad application of this method. Moreover, the provided generalisation of the evaluation method enhances its usability. Consequently, the COT test configuration and the generalised evaluation method are considered to be included in the subsequent generation of the DAfStb Guideline, which is intended to supersede Annex R in the German National Annex to the next generation of Eurocode 2.

In the context of quantifying tension stiffening at stabilised cracking at short-term loading, using the factor $\beta = 0.36$ leads to accurate predictions for both uniaxial tension and bending. Furthermore, a simplified approach to determine the additional crack opening resulting from cyclic loading at the serviceability stage was provided. The physically based prediction model that has been adapted for application to non-metallic textile reinforcement yields an accurate and progressive determination of the required reinforcement amount to effectively limit the crack width. This approach is widely applicable to all types of textile reinforcement and aligns with the principle design framework outlined in the *fib* Model Codes and Eurocodes 2. Consequently, this method ensures direct practical applicability.

In order to determine the deflection at short-term loading, the utilisation of the cross-sectional curvature under consideration of tension stiffening enables an accurate prediction. The transfer of the procedures applied for steel reinforced concrete members is applicable to textile-reinforced structures. Adaptations are required when focusing on scenarios of cyclic loading, also when occurring at the serviceability state. The contribution of tension stiffening is to be disregarded, and the creep of the concrete compression zone is to be taken into account in the determination of the cross-sectional curvature. The deflection at short-term loading and the additional deformation resulting from cyclic loads are significant and remain a decisive design criterion. To avoid additional reinforcement or an increased cross-section, elevation during construction, prestressing or an optimised structural design is required.

8.3 Further research

The research yielded insights into the behaviour of textile reinforced concrete members with regard to bond behaviour, particularly the evolution of the reinforcement strain obtained by FOS. This revealed several open questions that are of interest for the further advancement of crack width prediction approaches. Further investigations addressing the long-term material behaviour have to be considered, for example, by using the COT test setup. In this thesis, only a limited number of load cycles were applied in the COT tests, and the subsequent experimental campaigns' expansion to 200,000 cycles was not considered in the COT tests. The robust setup of the COT tests is expected to significantly improve the assessment of changes in bond behaviour due to cyclic loading in the case of a single crack and the consideration of a single fibre strand. Furthermore, future investigations should address the influence of sustained loading and the resulting bond creep on crack opening. To date, there has been a scarcity of investigations on bond creep, with the majority of these focusing on steel rebars. This research gap has to be addressed. Again, the COT test setup and the evaluation method presented in this thesis provide a feasible strategy to investigate these scenarios. An approximation of the resulting crack width increase is then to be quantified and implemented in either a physically based, analytical, empirical-based or numerical model.

In addition, these investigations also provide the basis for quantifying the influence of sustained loading on the deflection of flexural members reinforced with textile grids. In this thesis, the inves-

tigations regarding cyclic loading revealed a significant increase in deflection, which, consequently, must also be quantified for permanent loads. In particular, the influence of bond creep on the contribution of tension stiffening has to be addressed, as well as whether neglecting this contribution, as proposed in the case of cyclic loading, yields feasible and representative results.

The presented methodology, consisting of an experimentally based method to characterise bond behaviour and its subsequently use in a physically based crack width prediction model that accounts for the specific behaviour of textile reinforced concrete, was applied using four different impregnated grids and three different concrete mixtures. Despite this sound basis, the strategy requires further validation considering various parameters, such as its transferability to different reinforcements, for example, grids without an impregnation, preformed textiles or sand-coated grids, because of different bond behaviour and the associated crack patterns. Additionally, the applicability to different concrete types must be assessed, including those with alternative matrices or recycled aggregates, as well as those used in additive manufacturing, in particular 3D-concrete printing, which is characterised by a non-monolithic nature and fine aggregate sizes. Future investigations should also consider the influence of coarser aggregates on the bond capacity, including long-term loading scenarios. The investigations conducted in this thesis demonstrated no recognisable differences in the bond behaviour when using aggregates with a maximum size of 16 mm. However, it should be noted that only a limited number of test series were conducted without consideration of long-term effects. Consequently, the obtained results need to be verified.

As outlined in this thesis, the varying contributions of bond mechanisms are dependent on both the textile grid in terms of material and shape, and the reinforcement utilisation. This hypothesis should be verified, for example, by using computed tomography scans to visualise the influences of local undulations, waviness of the fibre strand, and changes due to cyclic loading. This is of particular interest for mechanical interlocking, which is dependent on the transversal stiffness of the fibre strand. A realistic depiction of the textile grid, as obtained through the use of 3D scans, enables the discrete modelling in a finite element environment, thereby quantifying the contribution of bond mechanisms.

The provided approaches for predicting crack width and deflection, in conjunction with methods for characterising bond behaviour, establish a solid basis for further research. For instance, with regard to the combination of grids, rebars and prestressing tendons, the distinct bond behaviour and stiffness of the reinforcements result in heterogeneous, time-dependent activations and contributions to force transfer. This nearly unexplored topic requires ongoing investigations and further attention in future models and approaches.

References

[ACI14] American Concrete Institute: Building code requirements for structural concrete (ACI 318-14) and Commentary (ACI 318R-14): Reported by ACI Committee 318. Farmington Hills, Michigan, U.S.A., 2014.

[ACI15] American Concrete Institute: Design and Construction of Structural Concrete Reinforced with FRP Bars. Farmington Hills, Michigan, U.S.A., 2015.

[ACI22] American Concrete Institute: Building Code Requirements for Structural Concrete Reinforced with Glass Fiber-Reinforced Polymer (GFRP) Bars: Code and Commentary. Farmington Hills, Michigan, U.S.A., 2023.

[Ali21] Ali, M. F.; Hossain, M. S.; Ahmed, S., et al.: Fabrication and characterization of eco-friendly composite materials from natural animal fibers. *In*: Heliyon Vol. 7 (5), 2021, e06954. DOI: 10.1016/j.heliyon.2021.e06954.

[Alk23] Al-Kharabsheh, B. N.; Arbili, M. M.; Majdi, A., et al.: Basalt Fiber Reinforced Concrete: A Compressive Review on Durability Aspects. *In*: Materials (Basel, Switzerland) Vol. 16 (1), 2023. DOI: 10.3390/ma16010429.

[All21] AL-Ameeri, A. S.; Rafiq, M. I.; Tsioulou, O.: Combined impact of carbonation and crack width on the Chloride Penetration and Corrosion Resistance of Concrete Structures. *In*: Cement and Concrete Composites Vol. 115, 2021, p. 103819. DOI: 10.1016/j.cemconcomp.2020.103819.

[Als19] Al-Saadi, N. T. K.; Mohammed, A.; Al-Mahaidi, R., et al.: A state-of-the-art review: Near-surface mounted FRP composites for reinforced concrete structures. *In*: Construction and Building Materials Vol. 209, 2019, pp. 748–769. DOI: 10.1016/j.conbuildmat.2019.03.121.

[Alt01] Altoubat, S. A.; Lange; David A.: Creep, Shrinkage, and Cracking of Restrained Concrete at Early Age. *In*: ACI Materials Journal Vol. 98 (4), 2001, pp. 323–331. DOI: 10.14359/10401.

[Ang11] Angst, U. M.; Elsener, B.; Larsen, C. K., et al.: Chloride induced reinforcement corrosion: Electrochemical monitoring of initiation stage and chloride threshold values. *In*: Corrosion Science Vol. 53 (4), 2011, pp. 1451–1464. DOI: 10.1016/j.corsci.2011.01.025.

[Api22] Apitz, A.; Schmitz, J.; Hückler, A., et al.: New thermoplastic carbon fiber reinforced polymer rebars and stirrups. *In*: Structural Concrete Vol. 23 (2), 2022, pp. 923–938. DOI: 10.1002/suco.202100434.

[Ari12] Arias, J. P. M.; Vazquez, A.; Escobar, M. M.: Use of sand coating to improve bonding between GFRP bars and concrete. *In*: Journal of Composite Materials Vol. 46 (18), 2012, pp. 2271–2278. DOI: 10.1177/0021998311431994.

[ASTM15] American Society for Testing and Materials: Test Method for Comparing Bond Strength of Steel Reinforcing Bars to Concrete Using Beam-End Specimens. West Conshohocken, PA, 2015. DOI: 10.1520/A0944-10R15.

[Att12] Attari, N.; Amziane, S.; Chemrouk, M.: Flexural strengthening of concrete beams using CFRP, GFRP and hybrid FRP sheets. *In*: Construction and Building Materials Vol. 37, 2012, pp. 746–757. DOI: 10.1016/j.conbuildmat.2012.07.052.

[Ave71] Aveston, J.; Cooper, G. A.; Kelly A.: The Properties of Fibre Composites. *In*: *Conference Proceedings of NPL Conference*. Ed. by National Physical Laboratory. IPC Science and Technology Press, Ltd., 1971, pp. 15–24.

[Ayd18] Aydin, F.: Experimental investigation of thermal expansion and concrete strength effects on FRP bars behavior embedded in concrete. *In*: Construction and Building Materials Vol. 163, 2018, pp. 1–8. DOI: 10.1016/j.conbuildmat.2017.12.101.

[Bae09] Baekeland, L. H.: The synthesis, constitution, and uses of Bakelite. *In*: Industrial & Engineering Chemistry Vol. 1 (3), 1909, pp. 149–161.

[Bak06] Bakis, C. E.; Ospina, C. E.; Bradberry, T. E., et al.: Evaluation of crack widths in concrete flexural members reinforced with FRP bars. *In*: Composites in civil engineering. Proceedings of CICE 2006, Third International Conference on FRP Composites in Civil Engineering. Ed. by Mirmiran, A.; Nanni, A. Miami, Fla.: Dep. of Civil and Environmental Engineering Florida Internat. Univ, 2006, pp. 307–310. ISBN: 0-615-13586-2.

[Bak18] Baktheer, A.; Chudoba, R.: Pressure-sensitive bond fatigue model with damage evolution driven by cumulative slip: Thermodynamic formulation and applications to steel- and FRP-concrete bond. *In*: International Journal of Fatigue Vol. 113, 2018, pp. 277–289. DOI: 10.1016/j.ijfatigue.2018.04.020.

[Bak21] Baktheer, A.; Chudoba, R.: Experimental and theoretical evidence for the load sequence effect in the compressive fatigue behavior of concrete. *In*: Materials and Structures Vol. 54 (2), 2021. DOI: 10.1617/s11527-021-01667-0.

[Bak22] Baktheer, A.; Spartali, H.; Chudoba, R., et al.: Concrete splitting and tip-bearing effect in the bond of anchored bars tested under fatigue loading in the push-in mode: An experimental investigation. *In*: Materials and Structures Vol. 55 (3), 2022. DOI: 10.1617/s11527-022-01935-7.

[Bal98] Balázs, G. L.: Bond under Repeated Loading. *In*: ACI Symposium Publication Vol. 180, 1998, pp. 125–143. DOI: 10.14359/5875.

[Bar18] Barrias, A.; Rodriguez, G.; Casas, J. R., et al.: Application of distributed optical fiber sensors for the health monitoring of two real structures in Barcelona. *In*: Structure and Infrastructure Engineering Vol. 14 (7), 2018, pp. 967–985. DOI: 10.1080/15732479.2018.1438479.

[Baž00] Bažant, Z. P.; Baweja, S.: Creep and Shrinkage Prediction Model for Analysis and Design of Concrete Structures: Model B3. *In*: ACI Special Publications Vol. 194, 2000, pp. 1–84.

[Baž75] Bažant, Z. P.: Theory of creep and shrinkage in concrete structures: A precis of recent developments. *In*: Mechanics today Vol. 2 (1), 1975, pp. 1–93.

[Bec21] Beckmann, B.; Bielak, J.; Bosbach, S., et al.: Collaborative research on carbon reinforced concrete structures in the CRC/TRR 280 project. *In*: Civil Engineering Design Vol. 3 (3), 2021, pp. 99–109. DOI: 10.1002/cend.202100017.

[Bec22] Becks, H.; Bielak, J.; Camps, B., et al.: Application of fiber optic measurement in textile-reinforced concrete testing. *In*: Structural Concrete Vol. 23 (4), 2022, pp. 2600–2614. DOI: 10.1002/suco.202100252.

[Bec23a] Becks, H.; Baktheer, A.; Marx, S., et al.: Monitoring concept for the propagation of compressive fatigue in externally prestressed concrete beams using digital image correlation and fiber optic sensors. *In*: Fatigue & Fracture of Engineering Materials & Structures Vol. 46 (2), 2023, pp. 514–526. DOI: 10.1111/ffe.13881.

[Bec23b] Becks, H.; Brockmann, D.; Hegger, J., et al.: Monitoring the Fatigue–Induced Strain Evolution of Concrete Bridges using Fiber Optic Sensors. *In*: ce/papers (EuroStruct 2023) Vol. 6 (5), 2023, pp. 1119–1126. DOI: 10.1002/cepa.2033.

[Bec24] Becks, H.; Lippold, L.; Winkler, P., et al.: Neuartige Konzepte für die Zustandsüberwachung und -analyse von Brückenbauwerken – Einblicke in das Forschungsvorhaben SPP100+. *In*: Bauingenieur Vol. 99 (10), 2024, pp. 327–338. DOI: 10.37544/0005-6650-2024-10-63.

[Bec25a] Becks, H.; Hegger, J.; Classen, M.: Two-dimensional strain measurement and crack detection of reinforced concrete using fiber optic sensors. *In*: The Essence of Structural Engineering for Society - IABSE Congress Ghent. Ed. by International Association for Bridge and Structural Engineering. 2025, accepted.

[Bec25b] Becks, H.; Högemann, M.; Hegger, J., et al.: Assessing crack formation and strain distribution in concrete structures using externally installed fiber optic sensors. *In*: Case Studies in Construction Materials Vol. 22, 2025, e04744. DOI: 10.1016/j.cscm.2025.e04744.

[Bee04] Beeby, A. W.: The influence of the parameter ϕ/ρ_{eff} on crack widths. *In*: Structural Concrete Vol. 5 (2), 2004, pp. 71–83. DOI: 10.1680/stco.2004.5.2.71.

[Bee05] Beeby, A. W.: The influence of the parameter ϕ/ρ_{eff} on crack widths. *In*: Structural Concrete Vol. 6 (4), 2005, pp. 155–165. DOI: 10.1680/stco.2005.6.4.155.

[Bel14] Bellakehal, H.; Zaidi, A.; Masmoudi, R., et al.: Behavior of FRP Bars-Reinforced Concrete Slabs under Temperature and Sustained Load Effects. *In*: Polymers Vol. 6 (3), 2014, pp. 873–889. DOI: 10.3390/polym6030873.

[Ben85] Bentur, A.; Ben-Bassat, M.; Schneider, D.: Durability of Glass–Fiber–Reinforced Cements with Different Alkali–Resistant Glass Fibers. *In*: Journal of the American Ceramic Society Vol. 68 (4), 1985, pp. 203–208. DOI: 10.1111/j.1151-2916.1985.tb15298.x.

[Ber21a] Bergmann, S.; May, S.; Hegger, J., et al.: Shear Strengthening of Reinforced Concrete T Beams Using Carbon Reinforced Concrete. *In*: ACI Special Publication Vol. 345 (1), 2021, pp. 169–184.

[Ber21b] Berrocal, C. G.; Fernandez, I.; Rempling, R.: Crack monitoring in reinforced concrete beams by distributed optical fiber sensors. *In*: Structure and Infrastructure Engineering Vol. 17 (1), 2021, pp. 124–139. DOI: 10.1080/15732479.2020.1731558.

[Bie17] Bielak, J.; Li, Y.; Hegger, J., et al.: Numerical and Experimental Characterization of Anchorage Length for Textile Reinforced Concrete. *In*: Strain-Hardening Cement-Based Composites. Ed. by Mechtcherine, V.; Slowik, V.; Kabele, P. Springer Verlag, 2017, pp. 409–417. ISBN: 978-94-024-1193-5. DOI: 10.1007/978-94-024-1194-2{\textunderscore }48.

[Bie18a] Bielak, J.; Li, Y.; Hegger, J., et al.: Characterization procedure for bond, anchorage and strain-hardening behavior of textile-reinforced cementitious composites. *In*: Proceedings of The Eighteenth International Conference of Experimental Mechanics. Ed. by Van Hemelrijck, D.; Aggelis, D.; De Belie, N., et al. Vol. 2. Basel, Switzerland: MDPI, 2018. DOI: 10.3390/ICEM18-05224.

[Bie18b] Bielak, J.; Spelter, A.; Will, N., et al.: Verankerungsverhalten textiler Bewehrungen in dünnen Betonbauteilen. *In*: Beton- und Stahlbetonbau Vol. 113 (7), 2018, pp. 515–524. DOI: 10.1002/best.201800013.

[Bie20] Bielak, J.; Schmidt, M.; Hegger, J., et al.: Structural Behavior of Large-Scale I-Beams with Combined Textile and CFRP Reinforcement. *In*: Applied Sciences Vol. 10 (13), 2020. DOI: 10.3390/app10134625.

[Bie21a] Bielak, J.: Shear in slabs with non-metallic reinforcement. Dissertation. Aachen: RWTH Aachen University, 2021. DOI: 10.18154/RWTH-2021-09163.

[Bie21b] Bielak, J.; Rempel, S.; Felber, M., et al.: Sanierung des Rheinstegs bei Albbruck mit Carbonbeton. *In*: Beton- und Stahlbetonbau Vol. 116 (7), 2021, pp. 488–497. DOI: 10.1002/best.202100024.

[Bis05] Bischoff, P. H.: Reevaluation of Deflection Prediction for Concrete Beams Reinforced with Steel and Fiber Reinforced Polymer Bars. *In*: Journal of Structural Engineering Vol. 131 (5), 2005, pp. 752–767. DOI: 10.1061/(ASCE)0733-9445(2005)131:5(752).

[Bis07] Bischoff, P. H.: Deflection Calculation of FRP Reinforced Concrete Beams Based on Modifications to the Existing Branson Equation. *In*: Journal of Composites for Construction Vol. 11 (1), 2007, pp. 4–14. DOI: 10.1061/(ASCE)1090-0268(2007)11:1(4).

[Bis09] Bischoff, P. H.; Gross, S. P.; Ospina, C. E.: The Story Behind Proposed Changes to ACI 440 Deflection Requirements for FRP-Reinforced Concrete. *In*: SP-264: Serviceability of Concrete Members Reinforced with Internal/External FRP Reinforcement. Ed. by Alkhardji, T.; Bischoff, P. H.; Ospina, C. E. Farmington Hills, Michigan, U.S.A.: American Concrete Institute, 2009, pp. 53–76. ISBN: 9780870313431. DOI: 10.14359/51663260.

[Bis11] Bischoff, P. H.; Gross, S. P.: Equivalent Moment of Inertia Based on Integration of Curvature. *In*: Journal of Composites for Construction Vol. 15 (3), 2011, pp. 263–273. DOI: 10.1061/(ASCE)CC.1943-5614.0000164.

[Boc17] Bochmann, J.; Curbach, M.; Jesse, F.: Carbonbeton unter einaxialer Druckbeanspruchung. *In*: Beton- und Stahlbetonbau Vol. 112 (5), 2017, pp. 293–302. DOI: 10.1002/best.201700006.

[Boc18] Bochmann, J.; Curbach, M.; Jesse, F.: Carbonbeton unter Druck. *In*: Beton- und Stahlbetonbau Vol. 113 (1), 2018, pp. 22–32. DOI: 10.1002/best.201700053.

[Böd10] Bödefeld, J.: Rissmechanik in dicken Stahlbetonwänden bei abfließender Hydratationswärme. Ed. by Bundesanstalt für Wasserbau. Karlsruhe, 2010.

[Böf24] Böffel, C.; Bielak, J.; Kaluza, L., et al.: Perceived sustainability and acceptance of carbon-reinforced concrete – Results of scenario-based vignette experiments. *In*: Proceedings of the Human Factors and Ergonomics Society Europe Chapter Annual Meeting in Lübeck. Ed. by Waard, D. de; Manzey, D.; Brookhuis, K., et al. 2024.

[Bon11] Bondar, D.; Lynsdale, C. J.; Milestone, N. B., et al.: Effect of type, form, and dosage of activators on strength of alkali-activated natural pozzolans. *In*: Cement and Concrete Composites Vol. 33 (2), 2011, pp. 251–260. DOI: 10.1016/j.cemconcomp.2010.10.021.

[Bor10] Borosnyói, A.; Snóbli, I.: Crack width variation within the concrete cover of reinforced concrete members. *In*: Epitoanyag - Journal of Silicate Based and Composite Materials Vol. 62 (3), 2010, pp. 70–74. DOI: 10.14382/epitoanyag-jsbcm.2010.14.

[Bre90] Breitenbücher, R.: Investigation of thermal cracking with the cracking-frame. *In*: Materials and Structures Vol. 23, 1990, pp. 172–177.

[Bus83] Buschmeyer, W.: Vorspannung ohne Verbund: Bemessung und Konstruktion. Dissertation. Essen: Universität-Gesamthochschule-Essen, 1983.

[Cas22] Caspari, C.: Zur Verbundverankerung von Glasfaserkunststoffbewehrungsstäben in Betonbauteilen unter Kurzzeit- und Langzeitbeanspruchung. Dissertation. Technischen Universität Kaiserslautern and Technische Universität Kaiserslautern, 2022. DOI: 10.26204/KLUEDO/6881.

[Cha18] Chaudhary, V.; Bajpai, P. K.; Maheshwari, S.: Studies on Mechanical and Morphological Characterization of Developed Jute/Hemp/Flax Reinforced Hybrid Composites for Structural Applications. *In*: Journal of Natural Fibers Vol. 15 (1), 2018, pp. 80–97. DOI: 10.1080/15440478.2017.1320260.

[Chr22] Christou, G.; Schmidt, C.; Hegger, J., et al.: The effect of concrete fatigue on the cyclic behaviour of composite dowels - derivation of a design approach based on experimental findings. *In*: Engineering Structures Vol. 253, 2022, p. 113743. DOI: 10.1016/j.engstruct.2021.113743.

[Chu21] Chudoba, R.; Li, Y.; Rypl, R., et al.: Probabilistic multiple cracking model of brittle-matrix composite based on a one-by-one crack tracing algorithm. *In*: Applied Mathematical Modelling Vol. 92, 2021, pp. 315–332. DOI: 10.1016/j.apm.2020.10.041.

[Cia81] Ciampi, V.; Eligehausen, R.; Bertero, V. V., et al.: Analytical Model tor Deformed Bar Bond under Generalized Excitations (Report No. UCB/EERC-82123). Ed. by University of California. Berkeley, California, USA, 1981.

[Cla25] Clark, J. C.; Davids, W. G.; Lopez-Anido, R. A., et al.: Continuously Formed Fiber-Reinforced Thermoplastic Composite Rebar for Concrete Reinforcement. *In*: Journal of Composites Science Vol. 9 (7), 2025, p. 378. DOI: 10.3390/jcs9070378.

[CNR-DT203] CNR Advisory Committee on Technical Recommendations for Construction: Guide for the Design and Construction of Concrete Structures Reinforced with Fiber-Reinforced Polymer Bars. 2007.

[Cor13] Correia, R. J.: Pultrusion of advanced fibre-reinforced polymer (FRP) composites. *In*: *Advanced Fibre-Reinforced Polymer (FRP) Composites for Structural Applications*. Ed. by Jiping Bai. Vol. 42. Cambridge, UK: Woodhead Publishing Limited, 2013, pp. 207–251. ISBN: 978-0-85709-864-1. DOI: 10.1533/9780857098641.2.207.

[Cor84] Cornelissen, H. A. W.; Reinhardt, H. W.: Uniaxial tensile fatigue failure of concrete under constant-amplitude and programme loading. *In*: Magazine of Concrete Research Vol. 36 (129), 1984, pp. 216–226.

[Cos97] Cosenza, E.; Manfredi, G.; Realfonzo, R.: Behavior and Modeling of Bond of FRP Rebars to Concrete. *In*: Journal of Composites for Construction Vol. 1 (2), 1997, pp. 40–51. DOI: 10.1061/(ASCE)1090-0268(1997)1:2(40).

[CSA12] Canadian Standards Association: CSA S806 - Design and construction of building structures with fibre-reinforced polymers. Mississauga, Ontario, Canada, 2012.

[Cur12] Curbach, M.; Ortlepp, R.: Sonderforschungsbereich 528: Textile Bewehrungen zur bautechnischen Verstärkung und Instandsetzung: Abschlusssbericht – gekürzte Fassung. Ed. by Curbach, M.; Ortlepp, R. 2012. http://nbn-resolving.de/urn:nbn:de:bsz:14-qucosa-86425.

[Cur23] Curbach, M.; Hegger, J.; Schladitz, F., et al., eds.: Handbuch Carbonbeton: Einsatz nichtmetallischer Bewehrung. Berlin: Ernst & Sohn a Wiley brand, 2023. ISBN: 978-3-433-03206-0. DOI: 10.1002/9783433608661.

[DAfStb24] Deutscher Ausschuss für Stahlbeton: DAfStb-Richtlinie Betonbauteile mit nichtmetallischer Bewehrung. Berlin, 2024.

[DAfStb660] Deutscher Ausschuss für Stahlbeton: Erläuterungen und Beispiele zur DAfStb-Richtlinie "Betonbauteile mit nichtmetallischer Bewehrung": DAfStb-Heft 660. DIN Media, 2024. ISBN: 978-3-410-65941-9.

[DBV16] DBV: Merkblatt Begrenzung der Rissbildung im Stahlbeton- und Spannbetonbau. Ed. by Deutscher Beton- und Bautechnik-Verein E.V. Berlin, 2016.

[DIN10a] Deutsches Institut für Normung e.V.: Beton – Zusammenstellung von DIN EN 206-1 Beton – Teil 1: Festlegung, Eigenschaften, Herstellung und Konformität und DIN 1045-2 Tragwerke aus Beton, Stahlbeton und Spannbeton – Teil 2: Beton; Festlegung, Eigenschaften, Herstellung und Konformität; Anwendungsregeln zu DIN EN 206-1. Berlin, 2010.

[DIN10b] Deutsches Institut für Normung e.V.: Prüfung von Festbeton - Teil 6: Spaltzugfestigkeit von Probekörpern: Deutsche Fassung EN 12390-6:2009. Berlin, 2010.

[DIN19a] Deutsches Institut für Normung e.V.: Prüfung von Festbeton - Teil 2: Herstellung und Lagerung von Probeköpern für Festigkeitsprüfungen: Deutsche Fassung EN 12390-2:2019. Berlin, 2019.

[DIN19b] Deutsches Institut für Normung e.V.: Prüfung von Festbeton - Teil 3: Druckfestigkeit von Probekörpern: Deutsche Fassung EN 12390-3:2019. Berlin, 2019.

[DIN21] Deutsches Institut für Normung e.V.: Prüfung von Festbeton – Teil 13: Bestimmung des Elastizitätsmoduls unter Druckbelastung (Sekantenmodul): Deutsche Fassung EN 12390-13:2021. Berlin, 2021.

[EC0] Deutsches Institut für Normung e.V.: Eurocode 0: Grundlagen der Tragwerksplanung: Deutsche Fassung EN 1990:2002 + A1:2005 + A1:2005/AC:2010. Berlin, 2010.

[EC2] Eurocode 2: Design of concrete structures - General rules and rules for buildings. Brussels, 2011.

[EC2NAA] Eurocode 2 NA: National Annex for Austria – Nationally determined parameters – Eurocode 2: Design of concrete structures – Part 1-1: General rules and rules for buildings. Vienna, 2015.

[EC2NAD] Eurocode 2 NA: National Annex for Germany – Nationally determined parameters – Eurocode 2: Design of concrete structures – Part 1-1: General rules and rules for buildings. Berlin, 2013.

[EC2NADA1] DIN EN 1992-1-1/NA/A1: Nationaler Anhang – National festgelegte Parameter – Eurocode 2: Bemessung und Konstruktion von Stahlbeton- und Spannbetontragwerken: Teil 1-1: Allgemeine Bemessungsregeln und Regeln für den Hochbau; Änderung A1. Berlin, 2015.

[Eli83] Eligehausen, R.; Popov, E. P.; Bertero, V. V.: Local bond stress-slip relationships of deformed bars under generalized excitations. 1983. DOI: 10.18419/opus-415.

[Els07] El-Sayed, A. K.; El-Salakawy, E.; Benmokrane, B.: Mechanical and Structural Characterization of New Carbon FRP Stirrups for Concrete Members. *In*: Journal of Composites for Construction Vol. 11 (4), 2007, pp. 352–362. DOI: 10.1061/(ASCE)1090-0268(2007)11:4(352).

[Elt13] El-Tahan, M.; Galal, K.; van Hoa, S.: New thermoplastic CFRP bendable rebars for reinforcing structural concrete elements. *In*: Composites Part B: Engineering Vol. 45 (1), 2013, pp. 1207–1215. DOI: 10.1016/j.compositesb.2012.09.025.

[Emb89] Emborg, M.: Thermal stresses in concrete structures at early ages. Dissertation. Lulea, 1989.

[Feh22] Fehling, E.; Lorenz, P.; Schlicke, D.: Energiebasierte direkte Berechnung der Bewehrung zur Rissbreitenbegrenzung. *In*: Beton- und Stahlbetonbau Vol. 117 (9), 2022, pp. 680–688. DOI: 10.1002/best.202200069.

[Feh90] Fehling, E.: Zur Energiedissipation und Steifigkeit von Stahlbetonbauteilen unter besonderer Berücksichtigung von Rissbildung und verschieblichem Verbund. Dissertation. Darmstadt: Technische Universität Darmstadt, 1990.

[Fer19] Ferrara, G.; Coppola, B.; Di Maio, L., et al.: Tensile strength of flax fabrics to be used as reinforcement in cement-based composites: experimental tests under different environmental exposures. *In*: Composites Part B: Engineering Vol. 168, 2019, pp. 511–523. DOI: 10.1016/j.compositesb.2019.03.062.

[Fin16a] Fingerloos, F.; Hegger, J.: Erläuterungen zur Änderung des deutschen Nationalen Anhangs zu Eurocode 2 (DIN EN 1992-1-1/NA/A1 2015-12). *In*: Beton- und Stahlbetonbau Vol. 111 (1), 2016, pp. 2–8. DOI: 10.1002/best.201500064.

[Fin16b] Fingerloos, F.; Hegger, J.; Zilch, K.: EUROCODE 2 für Deutschland: DIN EN 1992-1-1 Bemessung und Konstruktion von Stahlbeton- und Spannbetontragwerken Teil 1-1: Allgemeine Bemessungsregeln und Regeln für den Hochbau mit Nationalem Anhang: Kommentierte und konsolidierte Fassung. 2nd ed. Berlin: Beuth Verlag GmbH and Wilhelm Ernst & Sohn, 2016.

[Fis01] Fischer, L.: Das neue Sicherheitskonzept im Bauwesen: Ein Leitfaden für Bauingenieure, Architekten und Studenten. Bautechnik Spezialheft. Berlin: Ernst & Sohn, 2001.

[Fis19] Fischer, O.; Thoma, S.; Crepaz, S.: Distributed fiber optic sensing for crack detection in concrete structures. *In*: Civil Engineering Design Vol. 1 (3-4), 2019, pp. 97–105. DOI: 10.1002/cend.201900008.

[Foc00] Focacci, F.; Nanni, A.; Bakis, C. E.: Local Bond-Slip Relationship for FRP Reinforcement in Concrete. *In*: Journal of Composites for Construction Vol. 4 (1), 2000, pp. 24–31. DOI: 10.1061/(ASCE)1090-0268(2000)4:1(24).

[FprEC2] European Committee for Standardization: Final Draft to the Preliminary Eurocode 2: Design of concrete structures - Part 1-1: General rules - Rules for buildings, bridges and civil engineering structures (FprEN 1992-1-1). Brussels, 2023.

[Fra76] Franke, L.: Einfluss der Belastungsdauer auf das Verbundverhalten von Stahl in Beton (Verbundkriechen): DAfStb-Heft 268. Ernst & Sohn, 1976.

[Fri22] Friese, D.; Scheurer, M.; Hahn, L., et al.: Textile reinforcement structures for concrete construction applications—-a review. *In*: Journal of Composite Materials Vol. 56 (26), 2022, pp. 4041–4064. DOI: 10.1177/00219983221127181.

[Gal21] Galkovski, T.; Lemcherreq, Y.; Mata-Falcón, J., et al.: Fundamental Studies on the Use of Distributed Fibre Optical Sensing on Concrete and Reinforcing Bars. *In*: Sensors (Basel, Switzerland) Vol. 21 (22), 2021. DOI: 10.3390/s21227643.

[Gal23a] Galkovski, T.; Mata-Falcón, J.; Kaufmann, W.: Experimental investigation of bond and crack behaviour of reinforced concrete ties using distributed fibre optical sensing and digital image correlation. *In*: Engineering Structures Vol. 292, 2023, p. 116467. DOI: 10.1016/j.engstruct.2023.116467.

[Gal23b] Galkovski, T.; Mata-Falcón, J.; Kaufmann, W.: Stress field model for bond in reinforced concrete ties. *In*: Engineering Structures Vol. 294, 2023, p. 116759. DOI: 10.1016/j.engstruct.2023.116759.

[Gao98] Gao, L.; Hsu, C.-T. T.: Fatigue of Concrete under Uniaxial Compression Cyclic Loading. *In*: ACI Materials Journal Vol. 95 (5), 1998. DOI: 10.14359/407.

[Gel18] Gelbrich, S.; Funke, H. L.; Ehrlich, A., et al.: Flexible fiber-reinforced plastic formworks for the production of curved textile-reinforced concrete. *In*: Advances in Structural Engineering Vol. 21 (4), 2018, pp. 580–588. DOI: 10.1177/1369433217732681.

[Gha20] Ghadioui, R. E.: Bemessung carbonbewehrter Betonbauteile unter besonderer Betrachtung des Gebrauchszustandes: Entwicklung eines Modells zur wirklichkeitsnahen Verformungsberechnung. Dissertation. Darmstadt: TU Darmstadt, 2020. DOI: 10.26083/tuprints-00024337.

[Gha22] Ghadioui, R. E.; Wagner, J.; Klein, J., et al.: RC members with a flexural–strengthening layer of CFRP textile–reinforced concrete under monotonic and cyclic long–term loading. *In*: Structural Concrete Vol. 23 (2), 2022, pp. 939–953. DOI: 10.1002/suco.202100452.

[Gie24] Gielis, C.; El Kadi, M.; Snoeck, D., et al.: 3D Textile Reinforced Cement (TRC) composites with integrated synthetic microfibres: Evaluation of mechanical response and crack formation in bending. *In*: Construction and Building Materials Vol. 426, 2024, p. 136120. DOI: 10.1016/j.conbuildmat.2024.136120.

[Gil01] Gilbert, R. I.: Shrinkage, Cracking and Deflection - the Serviceability of Concrete Structures. *In*: Electronic Journal of Structural Engineering Vol. 1 (1), 2001, pp. 15–37.

[Gol13] Goldfeld, Y.; Klar, A.: Damage Identification in Reinforced Concrete Beams Using Spatially Distributed Strain Measurements. *In*: Journal of Structural Engineering Vol. 139 (12), 2013. DOI: 10.1061/(ASCE)ST.1943-541X.0000795.

[Got71] Goto, Y.: Cracks formed in Concrete around deformed tension bars. *In*: ACI Journal Vol. 68 (4), 1971, pp. 244–251. DOI: 10.14359/11325.

[Gri16] Gries, T.; Raina, M.; Quadflieg, T., et al.: Manufacturing of textiles for civil engineering applications. *In*: *Textile Fibre Composites in Civil Engineering*. Ed. by Triantafillou, T. Woodhead Publishing series in civil and structural engineering. Oxford: Woodhead Publishing, 2016, pp. 3–24. ISBN: 1782424466. DOI: 10.1016/B978-1-78242-446-8.00002-1.

[Gri22] Gries, T.; Bettermann, I.; Blaurock, C., et al.: Aachen Technology Overview of 3D Textile Materials and Recent Innovation and Applications. *In*: Applied Composite Materials Vol. 29 (1), 2022, pp. 43–64. DOI: 10.1007/s10443-022-10011-w.

[Hab97] Habel, W. R.; Hofmann, D.; Hillemeier, B.: Deformation measurements of mortars at early ages and of large concrete components on site by means of embedded fiber-optic microstrain sensors. *In*: Cement and Concrete Composites Vol. 19 (1), 1997, pp. 81–102. DOI: 10.1016/s0958-9465(96)00044-3.

[Hai17] Haik, R.; Adiel Sasi, E.; Peled, A.: Influence of three-dimensional (3D) fabric orientation on flexural properties of cement-based composites. *In*: Cement and Concrete Composites Vol. 80, 2017, pp. 1–9. DOI: 10.1016/j.cemconcomp.2017.02.007.

[Har02] Harris, C. E.; Starnes, J. H.; Shuart, M. J.: Design and Manufacturing of Aerospace Composite Structures, State-of-the-Art Assessment. *In*: Journal of Aircraft Vol. 39 (4), 2002, pp. 545–560. DOI: 10.2514/2.2992.

[Hau16] Hausding, J.; Märtin, J.: Warp-Knitted Semi-finished Products and Warp-Knitting Technologies. *In*: *Textile Materials for Lightweight Constructions*. Ed. by Cherif, C. Heidelberg: Springer, 2016, pp. 251–287. ISBN: 978-3-662-46340-6.

[Hav25] Haverkamp, P.; Schmidt, L.; Backes, J. G., et al.: Product Environmental Footprint in the construction sector – Proposal and assessment of a representative product for carbon-reinforced concrete. *In*: Journal of CO2 Utilization Vol. 95, 2025, p. 103078. DOI: 10.1016/j.jcou.2025.103078.

[Heg12] Hegger, J.; Will, N., eds.: Sonderforschungsbereich 532: Textilbewehrter Beton - Grundlagen für die Entwicklung einer neuartigen Technologie. Abschlussbericht. 2012.

[Heg23] Hegger, J.; Will, N.; Bosbach, S.: Biege- und Zugtragverhalten von Biege- und Zugtragverhalten von Bauteilen mit gemischter Bewehrung aus FVK-Stäben und FVK-Gittern. Ed. by Lehrstuhl und Institut für Massivbau. Aachen, 2023.

[Hei23] Heins, K.; Lesker, S.; Pütz, J., et al.: Effect of thermoplastic impregnation on the mechanical behaviour of textile reinforcement for concrete. *In*: SN Applied Sciences Vol. 5 (3), 2023, pp. 1–10. DOI: 10.1007/s42452-023-05305-y. https://link.springer.com/article/10.1007/s42452-023-05305-y.

[Hel90] Helmus, M.: Mindestbewehrung zwangsbeanspruchter dicker Stahlbetonbauteile: DAfStb-Heft 412. Berlin: Beuth Verlag GmbH, 1990.

[Her23] Herbers, M.; Richter, B.; Gebauer, D., et al.: Crack monitoring on concrete structures: Comparison of various distributed fiber optic sensors with digital image correlation method. *In*: Structural Concrete Vol. 2023. DOI: 10.1002/suco.202300062.

[Hol04] Holt, E.; Leivo, M.: Cracking risks associated with early age shrinkage. *In*: Cement and Concrete Composites Vol. 26 (5), 2004, pp. 521–530. DOI: 10.1016/S0958-9465(03)00068-4.

[Hol23] Holz, K.; Curbach, M.: Carbon reinforced concrete exposed to high temperatures. *In*: Structural Concrete Vol. 24 (3), 2023, pp. 3178–3190. DOI: 10.1002/suco.202200343.

[Imj17] Imjai, T.; Guadagnini, M.; Pilakoutas, K.: Bend Strength of FRP Bars: Experimental Investigation and Bond Modeling. *In*: Journal of Materials in Civil Engineering Vol. 29 (7), 2017. DOI: 10.1061/(ASCE)MT.1943-5533.0001855.

[ISO4356] International Organization for Standardization: ISO 4356-1977: Bases for the design of structures - Deformations of buitdings at the serviceability Iimit states. 1977.

[Ive18] Ivey, M. A.; Carey, J. P.; Ayranci, C.: Manufacturing and characterization of braidtruded fiber reinforced polymer rebar. *In*: Polymer Composites Vol. 39 (2), 2018, pp. 337–350. DOI: 10.1002/pc.23940.

[Jan23] Janiak, T.; Becks, H.; Camps, B., et al.: Evaluation of distributed fibre optic sensors in structural concrete. *In*: Materials and Structures Vol. 56 (9), 2023. DOI: 10.1617/s11527-023-02222-9.

[Jes10] Jesse, F.; Curbach, M.: Verstärken mit Textilbeton. *In*: *Beton-Kalender 2010*. Ed. by Bergmeister, K.; Fingerloos, F.; Wörner, J.-D. Beton-Kalender. Berlin: Ernst & Sohn, 2010, pp. 457–565. ISBN: 978-3-433-02931-2.

[Jin20] Jin, C.; Schmidt, C.; Chudoba, R., et al.: Experimentelle Untersuchungen zur Rissbildung in Stahlbetonbauteilen infolge Zwangbeanspruchung. *In*: Beton- und Stahlbetonbau Vol. 115 (11), 2020, pp. 906–916. DOI: 10.1002/best.202000014.

[Jon94] Jonasson, J.-E.; Groth, P.; Hedlund H.: Modelling of temperature and moisture field in concrete to study early age movements as a basis for stress analysis. *In*: *Thermal Cracking in Concrete at Early Ages*. Ed. by Springenschmid, R. CRC Press, 1994, pp. 45–52. ISBN: 9780429078217.

[JSCE97] Japan Society of Civil Engineers: Recommendation for design and construction of concrete structures using continuous fiber reinforcing materials. 1997.

[Kad19] Kadi, M. E.; Tysmans, T.; Verbruggen, S., et al.: Experimental study and benchmarking of 3D textile reinforced cement composites. *In*: Cement and Concrete Composites Vol. 104, 2019, p. 103352. DOI: 10.1016/j.cemconcomp.2019.103352.

[Kam13] Kamaya, M.: Monitoring of inside surface crack growth by strain measurements of the outside surface: Application of multiple strain measurements technique to fatigue crack growth. *In*: Nuclear Engineering and Design Vol. 256, 2013, pp. 202–213. DOI: 10.1016/j.nucengdes.2012.12.019.

[Kat99] Katz, A.; Berman, N.; Bank, L. C.: Effect of High Temperature on Bond Strength of FRP Rebars. *In*: Journal of Composites for Construction Vol. 3 (2), 1999, pp. 73–81. DOI: 10.1061/(ASCE)1090-0268(1999)3:2(73).

[Koe20] Koenig, A.; Mahmoud, H.; Baehre, O., et al.: Alkalinity and Its Consequences for the Performance of Steel-Reinforced Geopolymer Materials. *In*: Molecules (Basel, Switzerland) Vol. 25 (10), 2020. DOI: 10.3390/molecules25102359.

[Kön96] König, G.; Tue, N. V.: Grundlagen und Bemessungshilfen für die Rißbreitenbeschränkung im Stahlbeton und Spannbeton sowie Kommentare, Hintergrundinformationen und Anwendungsbeispiele zu den Regelungen nach DIN 1045, EC2 und Model Code 90: DAfStb-Heft 466. Berlin: Beuth Verlag GmbH, 1996. ISBN: 978-3-410-65666-1.

[Kos24] Koschemann, M.; Curbach, M.: Verbundkriechen und dessen Einfluss auf die Rissbreitenentwicklung. *In*: Bauingenieur Vol. 99 (11), 2024, pp. 374–383. DOI: 10.37544/0005-6650-2024-11-60.

[Kos25] Koschemann, M.; Curbach, M.; Marx, S.: Bond behavior of reinforced high-strength concrete under high-cycle fatigue pull-out loading. *In*: International Journal of Fatigue Vol. 198, 2025, p. 108944. DOI: 10.1016/j.ijfatigue.2025.108944.

[Kro23] Kromoser, B.; Butler, M.; Hunger, M., et al.: Article of RILEM TC 292-MCC: life cycle assessment (LCA) of non-metallic reinforcement for reinforcing concrete: manufacturing, durability, dismantling, recycling and reuse: a review. *In*: Materials and Structures Vol. 56 (7), 2023. DOI: 10.1617/s11527-023-02211-y.

[Kue19] Kueres, S.; Will, N.; Hegger, J.: Flexural design of a modular footbridge system with pretensioned carbon fiber reinforced polymer reinforcement. *In*: Structural Concrete Vol. 20 (6), 2019, pp. 1858–1870. DOI: 10.1002/suco.201900047.

[Kul13] Kulas, C.: Zum Tragverhalten getränkter textiler Bewehrungselemente für Betonbauteile. Dissertation. Aachen: RWTH Aachen University, 2013.

[Kup73] Kupfer, H.: Das Verhalten des Betons unter mehrachsiger Kurzzeitbelastung unter besonderer Berueckksichtigung der zweiachsigen Beanspruchung. *In*: *DAfStb-Heft 229*. Ed. by Deutscher Ausschuss für Stahlbeton. Beuth, 1973, pp. 1–95.

[Kwa06] Kwak, H.-G.; Kim, D.-Y.: Cracking behavior of RC panels subject to biaxial tensile stresses. *In*: Computers & Structures Vol. 84 (5-6), 2006, pp. 305–317. DOI: 10.1016/j.compstruc.2005.09.020.

[Lai19] Laiblová, L.; Pešta, J.; Kumar, A., et al.: Environmental Impact of Textile Reinforced Concrete Facades Compared to Conventional Solutions-LCA Case Study. *In*: Materials (Basel, Switzerland) Vol. 12 (19), 2019. DOI: 10.3390/ma12193194.

[Lan14] Landro, L. D.; Janszen, G.: Composites with hemp reinforcement and bio-based epoxy matrix. *In*: Composites Part B: Engineering Vol. 67, 2014, pp. 220–226. DOI: 10.1016/j.compositesb.2014.07.021.

[Lee04] Lee, S.-K.; Song, Y.-C.; Han, S.-H.: Biaxial behavior of plain concrete of nuclear containment building. *In*: Nuclear Engineering and Design Vol. 227 (2), 2004, pp. 143–153. DOI: 10.1016/j.nucengdes.2003.09.001.

[Lee21] Lee, M.; Mata-Falcón, J.; Kaufmann, W.: Load-deformation behaviour of weft-knitted textile reinforced concrete in uniaxial tension. *In*: Materials and Structures Vol. 54 (6), 2021, p. 210. DOI: 10.1617/s11527-021-01797-5.

[Lem23] Lemcherreq, Y.; Zanuy, C.; Vogel, T., et al.: Strain-based analysis of reinforced concrete pull-out tests under monotonic and repeated loading. *In*: Engineering Structures Vol. 289, 2023, p. 115712. DOI: 10.1016/j.engstruct.2023.115712.

[Li17] Li, Y.; Chudoba, R.; Bielak, J., et al.: A modelling Framework for the Tensile Behavior of Multiple Cracking Composite. *In*: Strain-Hardening Cement-Based Composites. Ed. by Mechtcherine, V.; Slowik, V.; Kabele, P. Springer Verlag, 2017, pp. 418–426. ISBN: 978-94-024-1193-5.

[Li18a] Li, Y.: A modeling framework for the uniaxial behavior of brittle matrix composites. Dissertation. Aachen, 2018.

[Li18b] Li, Y.; Bielak, J.; Hegger, J., et al.: An incremental inverse analysis procedure for identification of bond-slip laws in composites applied to textile reinforced concrete. *In*: Composites Part B: Engineering Vol. 137, 2018, pp. 111–122. DOI: 10.1016/j.compositesb.2017.11.014.

[Li22] Li, Y.; Zhang, J.; He, Y., et al.: A review on durability of basalt fiber reinforced concrete. *In*: Composites Science and Technology Vol. 225, 2022, p. 109519. DOI: 10.1016/j.compscitech.2022.109519.

[Lit95] Litzner, H.-U.: Grundlagen der Bemessung nach Eurocode 2–Vergleich mit DIN 1045 und DIN 4227. *In*: Beton-Kalender Vol. 1995, pp. 519–727.

[Lor07] Lorenzis, L. de; Teng, J. G.: Near-surface mounted FRP reinforcement: An emerging technique for strengthening structures. *In*: Composites Part B: Engineering Vol. 38 (2), 2007, pp. 119–143. DOI: 10.1016/j.compositesb.2006.08.003.

[Lor11] Lorenz, E.; Ortlepp, R.; Hausding, J., et al.: Effizienzsteigerung von Textilbeton durch Einsatz textiler Bewehrungen nach dem erweiterten Nähwirkverfahren. *In*: Beton- und Stahlbetonbau Vol. 106 (1), 2011, pp. 21–30. DOI: 10.1002/best.201000072.

[Lor12] Lorenz, E.; Ortlepp, R.: Bond Behavior of Textile Reinforcements - Development of a Pull-Out Test and Modeling of the Respective Bond versus Slip Reaction. *In*: High Performance Fiber Reinforced Cement Composites 6. Ed. by Parra-Montesinos, G. J.; Reinhardt, H. W.; Naaman, A. E. Dordrecht: Springer Netherlands, 2012, pp. 479–486. ISBN: 978-94-007-2435-8.

[Lor22] Lorenz, P.: Zum Verbund von Stahlbeton und Stahlfaserbeton bei Beachtung des Arbeitsprinzips. Dissertation. Kassel: Universität Kassel, 2022. DOI: 10.17170/kobra-202204266094.

[Lut23] Luthin, A.; Crawford, R. H.; Traverso, M.: Demonstrating circular life cycle sustainability assessment – a case study of recycled carbon concrete. *In*: Journal of Cleaner Production Vol. 433, 2023, p. 139853. DOI: 10.1016/j.jclepro.2023.139853.

[Mar23] Marinković, S.; Josa, I.; Braymand, S., et al.: Sustainability assessment of recycled aggregate concrete structures: A critical view on the current state–of–knowledge and practice. *In*: Structural Concrete Vol. 24 (2), 2023, pp. 1956–1979. DOI: 10.1002/suco.202201245.

[Mas11] Masmoudi, R.; Masmoudi, A.; Ouezdou, M. B., et al.: Long-term bond performance of GFRP bars in concrete under temperature ranging from 20°C to 80°C. *In*: Construction and Building Materials Vol. 25 (2), 2011, pp. 486–493. DOI: 10.1016/j.conbuildmat.2009.12.040.

[MC10] Model Code 2010: fib Model Code for Concrete Structures 2010. 1st ed. Berlin: Ernst Sohn, 2013. ISBN: 978-3-433-03061-5. DOI: 10.1002/9783433604090.

[MC20] Model Code 2020: fib Model Code for Concrete Structures (2020). Lausanne: International Federation of Structural Concrete, 2023. ISBN: 978-2-88394-175-5.

[MC78] Comité euro-international du béton; Féderation internationale de la précontrainte: International System of Unified Standard Codes of Practice for Structures - Volume 2: CEB-FIP Model Code for Concrete Structures. 1978.

[MC90] Fédération internationale de la précontrainte: CEB-FIP model code 1990: Design code. Vol. 213/214. Bulletin d'information / Comité Euro-International du Béton. London: Telford, 1993. ISBN: 978-0-7277-1696-5.

[Mei12] Meier, A.: Der späte Zwang als unterschätzter - aber maßgebender - Lastfall für die Bemessung. *In*: Beton- und Stahlbetonbau Vol. 107 (231), 2012, pp. 216–224. DOI: 10.1002/best.201100085.

[Mei15] Meier, A.: Der späte Zwang als unterschätzter - aber maßgebender - Lastfall für die Bemessung: Teil 2: Hinweise für Tragwerksplaner. *In*: Beton- und Stahlbetonbau Vol. 110 (3), 2015, pp. 179–190. DOI: 10.1002/best.201400097.

[Moo08] Moon, D. Y.; Sim, J.; Oh, H. S., et al.: An exploratory study of GFRP rebar with ribs containing milled glass fibers. *In*: Composites Part B: Engineering Vol. 39 (5), 2008, pp. 882–890. DOI: 10.1016/j.compositesb.2007.09.004.

[Mot11] Motavalli, M.; Czaderski, C.; Pfyl-Lang, K.: Prestressed CFRP for Strengthening of Reinforced Concrete Structures: Recent Developments at Empa, Switzerland. *In*: Journal of Composites for Construction Vol. 15 (2), 2011, pp. 194–205. DOI: 10.1061/(ASCE)CC.1943-5614.0000125.

[Mua19] Muanenda, Y.; Oton, C. J.; Di Pasquale, F.: Application of Raman and Brillouin Scattering Phenomena in Distributed Optical Fiber Sensing. *In*: Frontiers in Physics Vol. 7, 2019, pp. 1–14. DOI: 10.3389/fphy.2019.00155.

[Nad17] Nadiv, R.; Peled, A.; Mechtcherine, V., et al.: Micro- and nanoparticle mineral coating for enhanced properties of carbon multifilament yarn cement-based composites. *In*: Composites Part B: Engineering Vol. 111, 2017, pp. 179–189. DOI: 10.1016/j.compositesb.2016.12.005.

[Naw71] Nawy, E. G.; Neuwerth, G. E.; Phillips, C. J.: Behavior of Fiber Glass Reinforced Concrete Beams. *In*: Journal of the Structural Division Vol. 97 (9), 1971, pp. 2203–2215.

[Neu16] Neupane, K.: Fly ash and GGBFS based powder-activated geopolymer binders: A viable sustainable alternative of portland cement in concrete industry. *In*: Mechanics of Materials Vol. 103, 2016, pp. 110–122. DOI: 10.1016/j.mechmat.2016.09.012.

[Nod24] Nodehi, M.; Aguayo, F.; Madey, N., et al.: A Comparative Review of Polymer, Bacterial-based, and Alkali-Activated (also Geopolymer) Binders: Production, Mechanical, Durability, and Environmental impacts (life cycle assessment (LCA)). *In*: Construction and Building Materials Vol. 422, 2024, p. 135816. DOI: 10.1016/j.conbuildmat.2024.135816.

[Nor93] Noritake, K.; Kakihara, R.; Kumagai, S., et al.: Technora, an Aramid FRP Rod. *In*: *Fiber-Reinforced-Plastic (FRP) Reinforcement for Concrete Structures // Fiber-reinforced-plastic (FRP) reinforcement for concrete structures*. Ed. by Nanni, A. Developments in civil engineering. Amsterdam: Elsevier, 1993, pp. 267–290. ISBN: 9780444896896. DOI: 10.1016/B978-0-444-89689-6.50016-1.

[Ove24] Overmann, S.; Vollpracht, A.; Matschei, T.: Reactivity of Calcined Clays as SCM-A Review. *In*: Materials (Basel, Switzerland) Vol. 17 (2), 2024. DOI: 10.3390/ma17020312.

[Pal22] Palmieri, L.; Schenato, L.; Santagiustina, M., et al.: Rayleigh-Based Distributed Optical Fiber Sensing. *In*: Sensors Vol. 22 (18), 2022. DOI: 10.3390/s22186811.

[Pér13] Pérez Caldentey, A.; Corres Peiretti, H.; Peset Iribarren, J., et al.: Cracking of RC members revisited: influence of cover, $\phi\rho_{s,ef}$ and stirrup spacing - an experimental and theoretical study. *In*: Structural Concrete Vol. 14 (1), 2013, pp. 69–78. DOI: 10.1002/suco.201200016.

[Pér20] Pérez Caldentey, A.; García, R.; Gribniak, V., et al.: Tension versus flexure: Reasons to modify the formulation of MC 2010 for cracking. *In*: Structural Concrete Vol. 21 (5), 2020, pp. 2101–2123. DOI: 10.1002/suco.202000279.

[Pfa02] Pfanner, D.: Zur Degradation von Stahlbetonbauteilen unter Ermüdungsbeanspruchung. Dissertation. Frankfurt am Main, Germany: Ruhr-Universität Bochum, 2002.

[Pre19a] Preinstorfer, P.: Zur Spaltrissbildung von textilbewehrtem Beton. Dissertation. Wien: TU Wien, 2019.

[Pre19b] Preinstorfer, P.; Kromoser, B.; Kollegger, J.: Kategorisierung des Verbundverhaltens von Textilbeton. *In*: Bauingenieur Vol. 94 (11), 2019, pp. 416–424. DOI: 10.37544/0005-6650-2019-11-30.

[Pre20a] Preinstorfer, P.; Kollegger, J.: New insights into the splitting failure of textile-reinforced concrete. *In*: Composite Structures Vol. 243, 2020. DOI: 10.1016/j.compstruct.2020.112203.

[Pre20b] Preinstorfer, P.; Kromoser, B.: Influence of geometrical parameters on the splitting forces in textile-reinforced concrete. *In*: Materials and Structures Vol. 53 (6), 2020, p. 152. DOI: 10.1617/s11527-020-01590-w.

[Pre20c] Preinstorfer, P.; Pinzek, A.; Kollegger, J.: Modellierung des Verankerungsverhaltens getränkter textiler Bewehrungen. *In*: Beton- und Stahlbetonbau Vol. 115, 2020. DOI: 10.1002/best.202000011.

[Pre23] Preinstorfer, P.; Yanik, S.; Kirnbauer, J., et al.: Cracking behaviour of textile-reinforced concrete with varying concrete cover and textile surface finish. *In*: Composite Structures Vol. 312, 2023, p. 116859. DOI: 10.1016/j.compstruct.2023.116859.

[Rao66] Rao, P. S.: Die Grundlagen zur Berechnung der bei statisch unbestimmten Stahlbetonkonstruktionen im plastischen Bereich auftretenden Umlagerungen der Schnittkräfte: DAfStb-Heft 177. Berlin: Wilhelm Ernst & Sohn, 1966.

[Reh68] Rehm, G.; Martin, H.: Zur Frage der Rißbegrenzung im Stahlbetonbau. *In*: Beton- und Stahlbetonbau Vol. 63 (8), 1968, pp. 175–182.

[Reh79] Rehm, G.; Eligehausen, R.: Bond of ribbed bars under high cycle repeated loads. *In*: Journal of the American Concrete Institute Vol. 76 (2), 1979, pp. 297–309. DOI: 10.18419/opus-376.

[Ric05] Richter, M.: Entwicklung mechanischer Modelle zur analytischen Beschreibung der Materialeigenschaften von textilbewehrtem Feinbeton. Dissertation. Dresden: Technische Universität Dresden, 2005.

[Ric24] Ricker, M.; Kuhn, S.; Feiri, T., et al.: Tensile Load-Bearing Behaviour of Concrete Components Reinforced with Flax Fibre Textiles. *In*: Materials (Basel, Switzerland) Vol. 17 (6), 2024. DOI: 10.3390/ma17061313.

[Riz03] Rizkalla, S.; Hassan, T.; Hassan, N.: Design recommendations for the use of FRP for reinforcement and strengthening of concrete structures. *In*: Progress in Structural Engineering and materials Vol. 5 (1), 2003, pp. 16–28. DOI: 10.1002/pse.139.

[Rob01] Robins, P.; Austin, S.; Chandler, J., et al.: Flexural strain and crack width measurement of steel-fibre-reinforced concrete by optical grid and electrical gauge methods. *In*: Cement and Concrete Research Vol. 31 (5), 2001, pp. 719–729. DOI: 10.1016/S0008-8846(01)00465-3.

[Rob18] Robayo-Salazar, R. A.; Mejía de Gutiérrez, R.: Natural volcanic pozzolans as an available raw material for alkali-activated materials in the foreseeable future: A review. *In*: Construction and Building Materials Vol. 189, 2018, pp. 109–118. DOI: 10.1016/j.conbuildmat.2018.08.174.

[Rol18] Rolland, A.; Quiertant, M.; Khadour, A., et al.: Experimental investigations on the bond behavior between concrete and FRP reinforcing bars. *In*: Construction and Building Materials Vol. 173, 2018, pp. 136–148. DOI: 10.1016/j.conbuildmat.2018.03.169.

[Ros76] Rostásy, F. S.; Koch, R.; Leonhardt, F.: Zur Mindestbewehrung für Zwang von Außenwänden aus Stahlleichtbeton: DAfStb-Heft 267. Berlin: Wilhelm Ernst & Sohn, 1976.

[Roy07] Roye, A.; Gries, T.: 3-D Textiles for Advanced Cement Based Matrix Reinforcement. *In*: Journal of Industrial Textiles Vol. 37 (2), 2007, pp. 163–173. DOI: 10.1177/1528083707078136.

[Rud97] Rudlof, M.: Zur Spannungsumlagerung zwischen Spannstahl und Betonstahl bei Spannbeton mit nachträglichem Verbund. Dissertation. Aachen: RWTH Aachen University, 1997.

[Sch02] Schutter, G. D.: Fundamental study of early age concrete behaviour as a basis for durable concrete structures. *In*: Materials and Structures Vol. 35 (1), 2002, pp. 15–21. DOI: 10.1007/BF02482085.

[Sch09] Scheffler, C.; Gao, S. L.; Plonka, R., et al.: Interphase modification of alkali-resistant glass fibres and carbon fibres for textile reinforced concrete I: Fibre properties and durability. *In*: Composites Science and Technology Vol. 69 (3-4), 2009, pp. 531–538. DOI: 10.1016/j.compscitech.2008.11.027.

[Sch13] Schlicke, D.; Tue, N. V.: Consideration of Viscoelasticity in Time Step FEM-Based Restraint Analyses of Hardening Concrete. *In*: Journal of Modern Physics Vol. 04 (10), 2013, pp. 9–14. DOI: 10.4236/jmp.2013.410A2002.

[Sch14] Schlicke, D.: Mindestbewehrung für zwangbeanspruchten Beton: Festlegung unter Berücksichtigung der erhärtungsbedingten Spannungsgeschichte und der Bauteilgeometrie. Doctoral Thesis. Graz: Technische Universität Graz, 2014.

[Sch15] Scholzen, A.; Chudoba, R.; Hegger, J.: Thin-walled shell structures made of textile-reinforced concrete: Part I: Structural design and construction. *In*: Structural Concrete Vol. 16 (1), 2015, pp. 106–114. DOI: 10.1002/suco.201300071.

[Sch18] Schneider, K.; Michel, A.; Liebscher, M.; Mechtcherine, V.: Verbundverhalten mineralisch gebundener und polymergebundener Bewehrungsstrukturen aus Carbonfasern bei Temperaturen bis 500 °C. *In*: Beton- und Stahlbetonbau Vol. 113 (12), 2018, pp. 886–894. DOI: 10.1002/best.201800072.

[Sch19a] Schneider, K.; Michel, A.; Liebscher, M.; Terreri, L., et al.: Mineral-impregnated carbon fibre reinforcement for high temperature resistance of thin-walled concrete structures. *In*: Cement and Concrete Composites Vol. 97, 2019, pp. 68–77. DOI: 10.1016/j.cemconcomp.2018.12.006.

[Sch19b] Schöck Bauteile GmbH: Allgemeine bauaufsichtliche Zulassung Z-1.6-238: Bewehrungsstab Schöck ComBAR aus glasfaserverstärktem Kunststoff Nenndurchmesser: 8, 12, 16, 20, 25 und 32 mm. Ed. by DIBt - Deutsches Institut für Bautechnik. Berlin, July 8, 2019.

[Sch20a] Schlaich, M.; Apitz, A.; Jesse, F.: Brücken aus vorgespanntem Carbonbeton. *In*: Beton- und Stahlbetonbau Vol. 115 (9), 2020, pp. 684–696. DOI: 10.1002/best.202000018.

[Sch20b] Schumann, A.; May, M.; Schladitz, F., et al.: Carbonstäbe im Bauwesen: Teil 2: Verbundverhalten - Verbundversuche an unterschiedlichen Carbonstäben. *In*: Beton- und Stahlbetonbau Vol. 115 (12), 2020, pp. 962–971. DOI: 10.1002/best.202000047.

[Sch21a] Schlicke, D.; Dorfmann, E. M.; Fehling, E., et al.: Calculation of maximum crack width for practical design of reinforced concrete. *In*: Civil Engineering Design Vol. 3 (3), 2021, pp. 45–61. DOI: 10.1002/cend.202100004.

[Sch21b] Schmidt, C.; Bollin, M.; Cramer, J., et al.: Untersuchungen zur Rissbildung in durchgehend bewehrten Betonfahrbahnen. *In*: Bauingenieur Vol. 96 (10), 2021, pp. 358–375. DOI: 10.37544/0005-6650-2021-10-56.

[Sch22] Schlicke, D.; Krenn, C.; Mayer, M., et al.: FE–basierte Verifikation der Rissbreitenberechnung nach DAfStb–Heft 466. *In*: Beton- und Stahlbetonbau Vol. 117 (9), 2022, pp. 666–679. DOI: 10.1002/best.202200055.

[Sch23a] Schmidt, C.; Chudoba, R.; Jin, C., et al.: Experimental investigations on early crack development in fully restrained reinforced concrete members with active zero-displacement control. *In*: Materials and Structures Vol. 56 (6), 2023. DOI: 10.1617/s11527-023-02200-1.

[Sch23b] Schmidt, C.; Hegger, J.: Ableitung einer Verbundbeziehung zur Berechnung der Rissbreiten in Carbonbetonbauteilen. *In*: Beiträge zur 10. DAfStb-Jahrestagung mit 62. Forschungskolloquium. Ed. by Claßen, M.; Hegger, J.; Matschei, T., et al. 2023, pp. 95–106. DOI: 10.18154/RWTH-2023-06679.

[Sch23c] Schumann, A.; May, S.; May, M., et al.: Experimental Investigations of the Bond Behavior between Carbon Rebars and Concrete in Germany. *In*: Buildings Vol. 13 (12), 2023. DOI: 10.3390/buildings13122932.

[Sch24a] Schmidt, C.; Bosbach, S.; Camps, B., et al.: Derivation of a Bond Strength for Prediction of Crack Width in Non-metallic Textile Reinforced Concrete Members. *In*: *Ultra-High Performance Concrete and High Performance Building Materials for Sustainability Construction*. Ed. by Fehling, E.; Middendorf, B.; Thiemicke, J. Structural materials and engineering series. Kassel, 2024, pp. 165–168. ISBN: 978-3-7376-1159-6.

[Sch24b] Schmidt, C.; Classen, M.; Hegger, J.: Bond Behaviour and Crack Width Prediction in Non-metallic Textile-Reinforced Concrete Members. *In*: *Transforming Construction: Advances in Fiber Reinforced Concrete*. Ed. by Mechtcherine, V.; Signorini, C.; Junger, D. Vol. 54. Cham: Springer Nature Switzerland, 2024, pp. 642–651. ISBN: 978-3-031-70144-3. DOI: 10.1007/978-3-031-70145-0_77.

[Sch25a] Schmidt, C.; Chudoba, R.; Jin, C., et al.: Experimental investigations on the crack development in reinforced concrete members subject to uniaxial tensile strain. *In*: Structural Concrete Vol. 2025. DOI: 10.1002/suco.70118.

[Sch25b] Schmidt, C.; Hegger, J.: Experimental investigations on bond behaviour and crack development in concrete members reinforced with carbon textile grids subjected to cyclic loading. *In*: Construction and Building Materials Vol. 466, 2025, p. 140168. DOI: 10.1016/j.conbuildmat.2025.140168.

[Sch89] Schießl, P.: Grundlagen der Neuregelung zur Beschränkung der Rißbreite. *In*: *DAfStb-Heft 400*. Ed. by Deutscher Ausschuss für Stahlbeton. Beuth, 1989. ISBN: 9783410658009.

[Sch96] Schutter, G. D.; Taerwe, L.: Degree of hydration-based description of mechanical properties of early age concrete. *In*: Materials and Structures Vol. 29, 1996, pp. 335–344.

[Sin25] Sinning, A.; Adam, V.; Classen, M., et al.: Design of RAC Structures - Do Conservative Design Approaches Outweigh Ecological Benefits? *In*: 4th fib International Conference on Concrete Sustainability (ICCS2024). Ed. by Barros, J. A. O.; Cunha, Vítor M. C. F.; Sousa, H. S., et al. Cham: Springer Nature Switzerland, 2025, pp. 3–10. ISBN: 978-3-031-80671-1. DOI: 10.1007/978-3-031-80672-8_1.

[sol.24] solidian GmbH: Allgemeine bauaufsichtliche Zulassung Z-1.6-308: Carbon-Bewehrungsgitter solidian GRID zur Bewehrung von Betonbauteilen mit nichtmetallischer Bewehrung. Ed. by DIBt - Deutsches Institut für Bautechnik. Berlin, Aug. 1, 2024.

[Sol20] Solyom, S.; Balázs, G. L.: Bond of FRP bars with different surface characteristics. *In*: Construction and Building Materials Vol. 264, 2020, p. 119839. DOI: 10.1016/j.conbuildmat.2020.119839.

[Spa23] Spartali, H.; Hegger, J.; Chudoba, R.: Phenomenological comparison between the flexural performance of steel- and CFRP-reinforced concrete elements. *In*: Engineering Structures Vol. 294, 2023, p. 116755. DOI: 10.1016/j.engstruct.2023.116755.

[Spe19] Spelter, A.; Bergmann, S.; Bielak, J., et al.: Long-Term Durability of Carbon-Reinforced Concrete: An Overview and Experimental Investigations. *In*: Applied Sciences Vol. 9 (8), 2019. DOI: 10.3390/app9081651.

[Spe23] Spelter, A.: Long-Term Durability of Carbon Reinforced Concrete. Dissertation. Aachen: RWTH Aachen University, 2023. DOI: 10.18154/RWTH-2023-06350. https://publications.rwth-aachen.de/record/960708.

[Spr94] Springenschmid, R., ed.: Thermal Cracking in Concrete at Early Ages. CRC Press, 1994. ISBN: 9780429078217. DOI: 10.1201/9781482271294.

[Sta19] Stark, A.; Classen, M.; Hegger, J.: Bond behaviour of CFRP tendons in UHPFRC. *In*: Engineering Structures Vol. 178, 2019, pp. 148–161. DOI: 10.1016/j.engstruct.2018.10.002.

[Ste21] Steinbock, O.: Verstärkung von Stahl- und Spannbetonbrücken mit Carbonbeton. Dissertation. Dresden: Technische Universität Dresden, 2021.

[Tan15] Tang, S. W.; Yao, Y.; Andrade, C., et al.: Recent durability studies on concrete structure. *In*: Cement and Concrete Research Vol. 78, 2015, pp. 143–154. DOI: 10.1016/j.cemconres.2015.05.021.

[Tas13] Tastani, S. P.; Pantazopoulou, S. J.: Reinforcement and Concrete Bond: State Determination along the Development Length. *In*: Journal of Structural Engineering Vol. 139 (9), 2013, pp. 1567–1581. DOI: 10.1061/(ASCE)ST.1943-541X.0000725.

[Tow65] Townsend, C. L.: Control of Temperature Cracking in Mass Concrete. Ed. by US Department of the Interior, Bureau of Reclamation. Washington D.C., 1965.

[Tro67] Trost, H.: Auswirkungen des Superpositionsprinzipes auf Kriech- und Relaxationsprobleme bei Beton und Spannbeton. *In*: Beton- und Stahlbetonbau Vol. 7 (10), 1967, pp. 230–238.

[Tue20] Tue, N. V.; Schlicke, D.: Zwangbeanspruchung und Rissbreitenbeschränkung in Stahlbetonbauteilen auf Grundlage der Verformungskompatibilität. *In*: *2020 Beton Kalender*. Ed. by Bergmeister, K.; Fingerloos, F.; Wörner, J. D. Berlin, Germany: Ernst & Sohn, a Wiley brand, 2020, pp. 831–887. ISBN: 978-3-433-03268-8.

[Tur16] Turner, K.; Schlicke, D.; Tue, N. V.: Zwangbeanspruchung von Stahlbetonbauteilen. *In*: Beton- und Stahlbetonbau Vol. 111 (5), 2016, pp. 301–309. DOI: 10.1002/best.201600003.

[Tur17] Turner, K.; Ehmann, R.: Zwangbeanspruchung bei dicken, gerissenen Stahlbetonquerschnitten. Ed. by Bundesanstalt für Wasserbau. Karlsruhe, 2017.

[Uij96] Uijl, J. A. d.; Bigaj, A.: A bond model for ribbed bars based on concrete confinement. *In*: HERON Vol. 41 (3), 1996, pp. 201–226.

[Val20] Valeri, P.; Fernàndez Ruiz, M.; Muttoni, A.: Tensile response of textile reinforced concrete. *In*: Construction and Building Materials Vol. 258, 2020, First Published Online. DOI: 10.1016/j.conbuildmat.2020.119517.

[Vil13] Villalba, S.; Casas, J. R.: Application of optical fiber distributed sensing to health monitoring of concrete structures. *In*: Mechanical Systems and Signal Processing Vol. 39 (1-2), 2013, pp. 441–451. DOI: 10.1016/j.ymssp.2012.01.027.

[Vil15] Vilanova, I.; Baena, M.; Torres, L., et al.: Experimental study of bond-slip of GFRP bars in concrete under sustained loads. *In*: Composites Part B: Engineering Vol. 74, 2015, pp. 42–52. DOI: 10.1016/j.compositesb.2015.01.006.

[Vis21] Viswanath, S.; LaFave, J. M.; Kuchma, D. A.: Concrete compressive strain behavior and magnitudes under uniaxial fatigue loading. *In*: Construction and Building Materials Vol. 296, 2021, p. 123718. DOI: 10.1016/j.conbuildmat.2021.123718.

[Vol16] Vollpracht, A.; Lothenbach, B.; Snellings, R., et al.: The pore solution of blended cements: a review. *In*: Materials and Structures Vol. 49 (8), 2016, pp. 3341–3367. DOI: 10.1617/s11527-015-0724-1.

[Vol24] Vollpracht, A.; Gluth, G. J. G.; Rogiers, B., et al.: Report of RILEM TC 281-CCC: insights into factors affecting the carbonation rate of concrete with SCMs revealed from data mining and machine learning approaches. *In*: Materials and Structures Vol. 57 (9), 2024. DOI: 10.1617/s11527-024-02465-0.

[Vor21] Vorwagner, A.; Kwapisz, M.; Lienhart, W., et al.: Verteilte Rissbreitenmessung im Betonbau mittels faseroptischer Sensorik – Neue Anwendung von verteilten faseroptischen Messsystemen. *In*: Beton- und Stahlbetonbau Vol. 116 (10), 2021, pp. 727–740. DOI: 10.1002/best.202100060.

[Wag19] Wagner, J.; Curbach, M.: Bond Fatigue of TRC with Epoxy Impregnated Carbon Textiles. *In*: Applied Sciences Vol. 9 (10), 2019, p. 1980. DOI: 10.3390/app9101980.

[Wan21] Wang, Q.; Ding, Y.; Randl, N.: Investigation on the alkali resistance of basalt fiber and its textile in different alkaline environments. *In*: Construction and Building Materials Vol. 272, 2021, p. 121670. DOI: 10.1016/j.conbuildmat.2020.121670.

[Web82] Weber, V.: Untersuchung des Riss- und Verformungsverhaltens segmentärer Spannbetonbauteile. Dissertation. Braunschweig: Technische Universität Braunschweig, 1982.

[Wei09] Weiland, S.: Interaktion von Betonstahl und textiler Bewehrung bei Biegeverstärkung mit textilbewehrtem Beton. Dissertation. Dresden: Technische Universität Dresden, 2009.

[Wei98] Weiss, W. J.; Yang, W.; Shah, S. P.: Shrinkage Cracking of Restrained Concrete Slabs. *In*: Journal of Engineering Mechanics Vol. 124 (7), 1998, pp. 765–774. DOI: 10.1061/(ASCE)0733-9399(1998)124:7(765).

[Wid66] Widom, B.: Random Sequential Addition of Hard Spheres to a Volume. *In*: The Journal of Chemical Physics Vol. 44 (10), 1966, pp. 3888–3894. DOI: 10.1063/1.1726548.

[Yoo11] Yoon, Y.-S.; Yang, J.-M.; Min, K.-H., et al.: Flexural Strength and Deflection Characteristics of High-Strength Concrete Beams with Hybrid FRP and Steel Bar Reinforcement. *In*: SP-275: Fiber-Reinforced Polymer Reinforcement for Concrete Structures 10th International Symposium. Ed. by Sen, R.; Seracino, R.; Shield, C., et al. American Concrete Institute, 2011, pp. 1–22. ISBN: 9780870314124. DOI: 10.14359/51682414.

[Zas03] Zastrau, B.; Richter, M.; Lepenies, I.: On the Analytical Solution of Pullout Phenomena in Textile Reinforced Concrete. *In*: Journal of Engineering Materials and Technology Vol. 125 (1), 2003, pp. 38–43. DOI: 10.1115/1.1526125.

[Zhe95] Zheng, Z.; Feldmann, D.: Synthetic fibre-reinforced concrete. *In*: Progress in Polymer Science Vol. 20 (2), 1995, pp. 185–210. DOI: 10.1016/0079-6700(94)00030-6.

[Zhu20] Zhu, H.; Hu, Y.; Li, Q., et al.: Restrained cracking failure behavior of concrete due to temperature and shrinkage. *In*: Construction and Building Materials Vol. 244, 2020, p. 118318. DOI: 10.1016/j.conbuildmat.2020.118318.

[Zil14] Zilch, K.; Niedermeier, R.; Finckh, W., eds.: Strengthening of concrete structures with adhesively bonded reinforcement: Design and dimensioning of CFRP laminates and steel plates. 1. ed. BetonKalender. Berlin: Ernst, 2014. ISBN: 978-3-433-60403-8.

Appendices

Appendix A Excursions on the applicability of fibre optic sensors

A.1 Influences of fibre type, coating and gauge length

Using fibre optic sensors requires choosing a feasible fibre type, particularly the fibre coating, as well as defining the gauge length and gage pitch. As outlined in Section 3.5.1, numerous types and coatings are available, depending on the field of application. In this thesis, two types of coating were used: a polyimide coating and an acrylate coating. Prior to conducting the various experimental campaigns presented in this thesis, a small feasibility study was performed to determine the most effective configuration. Two aspects were essential: First, the robustness of the optical fibre to enable strain measurement throughout most of the tests. This was particularly important for high reinforcement utilisation up to strain values of 10 mm/m and for cyclic loading phases. Secondly, the accuracy of the optical fibre was considered, referring to how precisely the actual reinforcement strain is represented by the FOS strain values. These two aspects contradict each other, as a more robust optical fibre requires more elastic behaviour, including that of the coating. This, however, results in less accuracy. While this thesis focused on applying optical fibres to reinforced concrete, Becks et al. [Bec25b] conducted an extensive study on application methods and fibre types regarding the feasibility of measuring crack opening on concrete surfaces.

The feasibility study considered three configurations. The first configuration involved a polyimide-coated fibre with a gage pitch of 0.65 mm, which is the highest resolution provided by the FOS system. The second configuration involved a gage pitch of 2.60 mm, which resulted in the strain values being smoothed prior to any post-processing. The third configuration was an acrylate-coated fibre with a gage pitch of 0.65 mm, which is more elastic and therefore more robust than the polyimide-coated fibre.
Two criteria were considered for the study. The first criterion focuses on robustness by analysing the number of dropouts, which are the NaN values. For a quantitative-based evaluation, the number of dropouts per metre fibre length was analysed, as well as the relative dropout rate, referring to the number of dropouts in relation to all strain values measured by the fibre optic sensor. The second criterion refers to the accuracy of the measurement. Therefore, the bond stress evolution and the mean bond stress-slip relation obtained after applying the post-processing steps described in Section 3.5.2 were considered. The results of the uniaxial tensile tests CG1-static-1 (acrylate coating, gage pitch 0.65 mm), CG1-cyclic-1 (polyimide, gage pitch 0.65 mm) and CG1-cyclic-2 (polyimide, gage pitch 2.60 mm) were used for the study. The results are provided in Figure A.1.

At first, referring to the dropouts obtained in the three tests, which are visualised in Figure A.1a, the use of the acrylate-coated fibre resulted in a significantly lower number of dropouts at an identical strain utilisation compared to polyimide-coated fibre. In absolute terms, only four dropouts per metre were determined on average for a strain below 4 mm/m with the acrylate coating, while 39.5 and 46.2 dropouts were registered for the fibres with the polyimide coating. As the larger gage pitch provided fewer values per metre, the relative number of dropouts was approximately 10%. For the gage pitch of 0.65 mm, only 4.2% of all values were NaN.
While both polyimide fibres failed during the cyclic loading phase, which was not analysed in this study, failure of the entire sensor with an acrylate-coated fibre occurred at a strain of approximately 10 mm/m. The diagram also shows that, prior to sensor failure, only around 25% of values were dropouts, which still allowed for an accurate evaluation of strain when post-processing steps

were applied. Using a larger gage pitch does not increase robustness against exterior damage, for example, crack opening or cyclic loading. The absolute number of dropouts per metre was comparable for the two gage pitch values used for the polyimide-coated fibres. Notably, a larger gage pitch enables a higher measuring frequency to be applied by the system. This can be used in post-processing to eliminate dropout values without compromising the accuracy of the provided values. Consequently, in terms of the robustness of the optical fibre, the acrylate coating proved favourable due to the significantly lower dropout rate and robustness against cyclic loading. This was demonstrated later in the experimental campaigns by applying this fibre to numerous specimens undergoing cyclic testing and enabling high-strain measurements. This is also why the acrylate-coated fibre was used in all following tests after the uniaxial test series CG1-cyclic and CG2-cyclic.

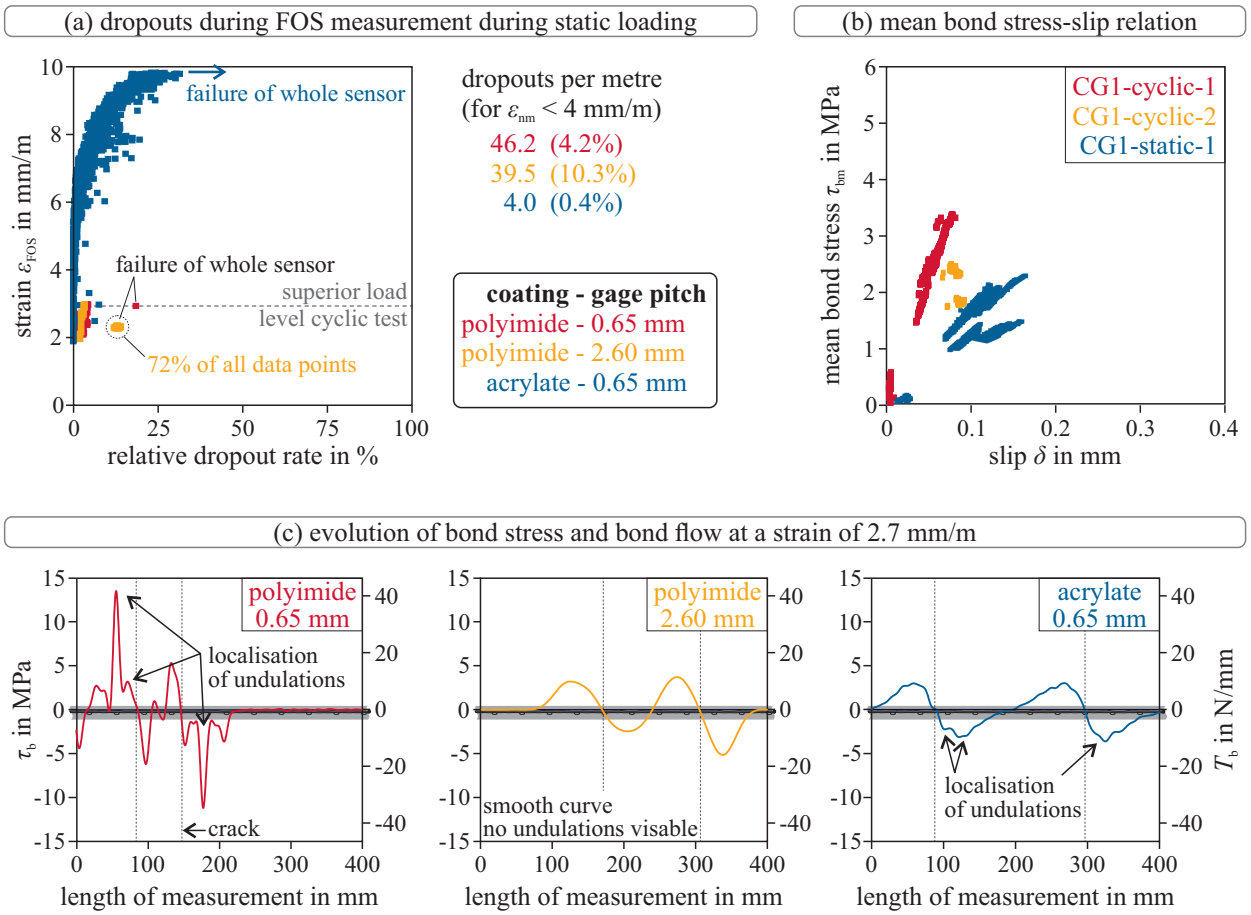


Figure A.1: Influence of different coating and gage pitch on the number of dropouts and the provided values of bond stress when using fibre optic sensors

The inefficiency of using a gage pitch of 2.60 mm with regard to the scope of this thesis is demonstrated by evaluating the bond stress evolution, as shown in Figure A.1c. While the other two configurations allowed for identifying the influence of local undulation on the force transfer, the smoothing provided by the larger gage pitch prevented this. In contrast, using a gage pitch of 0.65 mm for the polyimide-coated fibre resulted in significant bond stress fluctuations, mostly attributed to the location of local undulations. The high bond stress values are explained by the potential for greater force transfer given the small bond surface area, which often results in concrete splitting as a typical failure mode in concrete members reinforced with textile grids. The bond stress evolution obtained using the acrylate-coated fibre shows a smoother curve than that obtained using the polyimide-coated fibre with an identical gage pitch. The maximum bond stress obtained was significantly lower at about 4 MPa, compared to a maximum of 13 MPa for the polyimide-

coated fibre.
This results in a different mean bond stress-slip relation. The polyimide-coated fibre allows for the interpretation of a stiffer bond behaviour than the acrylate-coated fibre. As apparent, the large individual bond stress values obtained using the polyimide-coated fibre led to higher mean bond stress values. Despite this, the significantly greater robustness of the acrylate-coated fibre, in addition to its ability to localise undulations, made it the more feasible fibre type for the experimental campaigns.

A.2 Determination of the crack width on the concrete surface

In selected test series, fibre optic sensors were additionally applied to the concrete surface. The aim was to investigate the feasibility of an alternative method to determine the crack width on the concrete surface by using the approach expressed in Equation 3-7, which is restated to

$$w_{\mathrm{FOS,surf}} = \int_{x_\mathrm{a}}^{x_\mathrm{b}} \varepsilon_{\mathrm{FOS}}(x)\mathrm{d}x \tag{A-1}$$

by integrating the individual strain values measured by FOS $\varepsilon_{\mathrm{FOS}}$ along the length between x_a and x_b. The integration length is determined identically as done for the optical fibres applied on the reinforcement (cf. Section 3.5.3). It is noteworthy that the considered strain values are not corrected by any factor considering the actual reinforcement strain, as the resulting fibre strains directly account for the crack opening. The FOS measurement was therefore only smoothed using a Bessel filter in the same way as done for the measurements where FOS was directly applied on the fibre strand (cf. Section 3.5.2). In contrast to the use of a cyanoacrylate adhesive, an epoxy resin was applied to fixate the optical fibre on the concrete surface. This particular consideration was selected to ensure enhanced reliability of the measurement in the event of an initial large opening of a crack, which could result in the failure of the optical fibre. The FOS was applied to the surface that was in contact with the formwork, as this provided a smooth surface. As also illustrated on the right-hand side of Figure 4.1, this is the same concrete surface on which the speckle field was sprayed for the DIC measurements.

An evaluation of the determined crack width at the concrete surface of specimen CG1-cyclic-1 utilising both the DIC and FOS method is provided for a selection of load steps in Figure A.2. As apparent, the obtained strain values of the fibre optic measurements are not in resemblance with the actual strain of the reinforcement. For example, addressing the last plotted load step in Figure A.2b, the reinforcement strain was about $\sigma_{\mathrm{nm}}/E_{\mathrm{nm}} = 6.7$ mm/m, while the fibre optic measurement on the concrete surface at crack (6f) read 11 mm/m. This is due to the fact that the crack opening on the concrete surface was larger compared to the elongation of the textile fibre strand. Consequently, the optical fibre on the surface experienced significant deformation, which needs to be bridged by the additional elongation. In addition, this elongation led to a loss of fixation of the FOS on the concrete in the crack itself. Despite these influencing factors on the determined crack width, the approach of using the integral relation expressed in Equation A-1 proved to be robust, as the provided values were very well met by the DIC evaluation and the evaluation in Figure A.2c confirms. The only considerable differences between both measurement techniques were found for crack (3s) at the last plotted step and for crack (5c). Addressing the difference in crack widths of about 0.05 mm for crack (3s) at a reinforcement stress of 789 MPa, the consideration of the strain evolution indicates that an exact determination of the transfer length on the left side of the crack was not possible due to the interference with the termination of the optical fibre. While for the other evaluated load steps the influence of the termination on determining the end of the transfer length is not significant, the

further opening of the crack next to crack (3s) led to the situation that the local minimum in the strain evolution was outside the measured length. In the case of the overestimation of the crack width of crack (5c) by the FOS measurement compared to the DIC results, for all three evaluated load steps linear increases close to the crack are visible in the strain evolution. This *capping* of the strain evolution is similar to the observations discussed in Section 3.5.2. A possible explanation is that during the load cycles, some delamination of the optical fibre to the concrete occurred. The optical fibre is then deformed with a constantly increasing value towards the crack, providing for a measurement of strain values which did not resemble a fully intact bond between optical fibre and concrete. The effect of capping on the accuracy of the FOS measurement is not always as pronounced as in the case of (5c). For example, the FOS strain evolution on the right-hand side of (4s) in Figure A.2b revealed capping at the last three evaluated steps, but the differences in the determined values of crack width between FOS and DIC were only marginal. Similar observations on the influence of capping were found in the extensive study on applying FOS on the concrete surface in [Bec25b].

This brief study shows the feasibility of FOS when apllied on the concrete surface to determine the crack opening. Conversely, a derivation of the reinforcement strain and bond stress is not possible when using this concept, as the determined length between x_a and x_b does not represent the actual transfer length.

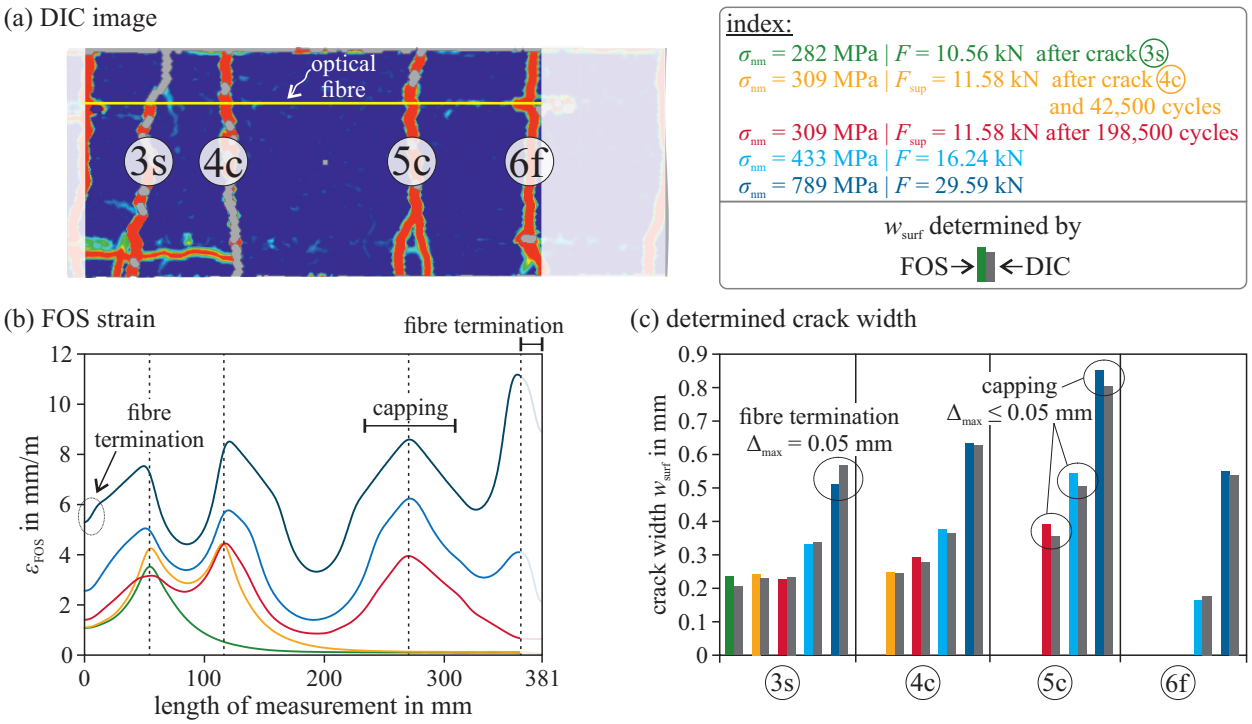


Figure A.2: Evaluation of the crack widths on the concrete surface using DIC and FOS measurements (specimen CG1-cyclic-1)

Appendix B Material characteristics

B.1 Concretes

Three distinct mixtures, characterised by their maximum aggregate size, were utilised to produce a normal-strength concrete (NSC) with a nominal strength class of C30/37 (acc. to [EC2]). Furthermore, the a mixture for high-strength concrete (HSC), categorised as C80/95, was considered. All mixtures are provided in Table B.1. With the exception of mixture NSC-8mm, which was produced in the prefabrication plant, the others were mixed directly at the laboratory.

Table B.1: Concrete mixtures

composition	NSC-5.6mm	NSC-8mm	NSC-16mm	HSC-5.6mm
CEM I 52.5 R Sulfo [kg/m^3]	300.0	-	290.0	450.0
CEM I 52.5 R Wotan [kg/m^3]	-	300.0	-	-
microsilica [kg/m^3]	40.0	62.5	153.4	70.0
superplasticizer [kg/m^3]	1.23	0.60	-	8.10
sand 0/1 [kg/m^3]	567.1	-	498.6	560.7
sand 0/2 [kg/m^3]	-	708.3	-	-
aggregates 1/2 [kg/m^3]	402.4	-	191.8	397.9
aggregates 2/4 [kg/m^3]	-	-	191.8	-
aggregates 2/5.6 [kg/m^3]	859.8	-	-	850.1
aggregates 2/8 [kg/m^3]	-	1116.0	-	-
aggregates 5/8 [kg/m^3]	-	-	383.6	-
aggregates 8/16 [kg/m^3]	-	-	498.6	-
water [kg/m^3]	180.0	165.0	180.0	105.0
water-cement ratio	0.57	0.55	0.62	0.30

In order to determine the compressive strength, Young's modulus and tensile strength of the concrete, a series of material tests were conducted. The methodology involved the assessment of three individual tests for each characteristic, followed by the calculation of the average value. The tests were carried out using cylinders (diameter 150 mm, height 300 mm) and cubes (length 150 mm) to determine the compressive strength [DIN19b] and the Young's modulus [DIN21]. The tensile strength was determined by conducting splitting tests on cylinders with a diameter of 150 mm and a height of 300 mm [DIN10b]. The resulting tensile strength $f_{ct,sp}$ was utilised to calculate the uniaxial tensile strength

$$f_{ct} = 0.9 \cdot f_{ct,sp} \tag{B-1}$$

in accordance with Eurocode 2 [EC2].

The material tests were situated in the same environment and subjected to identical treatment as the specimens considered for the experimental campaigns. The formwork was removed 24 hours

after concreting. The tests were stored in a dry-air environment at approximately 20°C and 60% air-humidity until the day of testing, following the procedure given in [DIN19a].
The obtained average values of strength and Young's modulus for each set of material tests are presented in Figure B.1, with the data plotted against the concrete age. For reference, the mean values and the 5% and 95% fractiles according to [EC2] for the corresponding strength class are given. As the storage environment was characterised by a dry-air condition, in contrast to the water-saturated environment specified in [EC2], the code provision values of the compressive strength were adapted in accordance with the proposed method outlined in [DIN10a]:

$$f_{\mathrm{c}} = \begin{cases} f_{\mathrm{c,EC2}}/0.92 & \text{for strength class } \leq \text{ C50/60} \\ f_{\mathrm{c,EC2}}/0.95 & \text{for strength class } \geq \text{ C55/67} \end{cases} \tag{B-2}$$

As demonstrated in Figure B.1, the average strength values obtained for the three different normal-strength concretes were found to be within the code provision's range of the 5% and 95% fractiles. It was observed that only two data points were below the prescribed range for cubic compressive strength, while one data point was above this range. The Young's modulus of the concrete was found to be lower than the average curve proposed in [EC2]. This phenomenon is attributed to the fact that a proportion of all aggregates exhibited some degree of roundness.
In the case of the high-strength concrete, a total of four test dates were required for the experimental campaigns that were conducted. As demonstrated in Figure B.1, the evaluation reveals no substantial anomalies. It is observed that the average values of the material tests exceed the code provision's curve. However, this is primarily attributed to the substantial reduction in the influence of the aggregate form in the context of high-strength concrete.

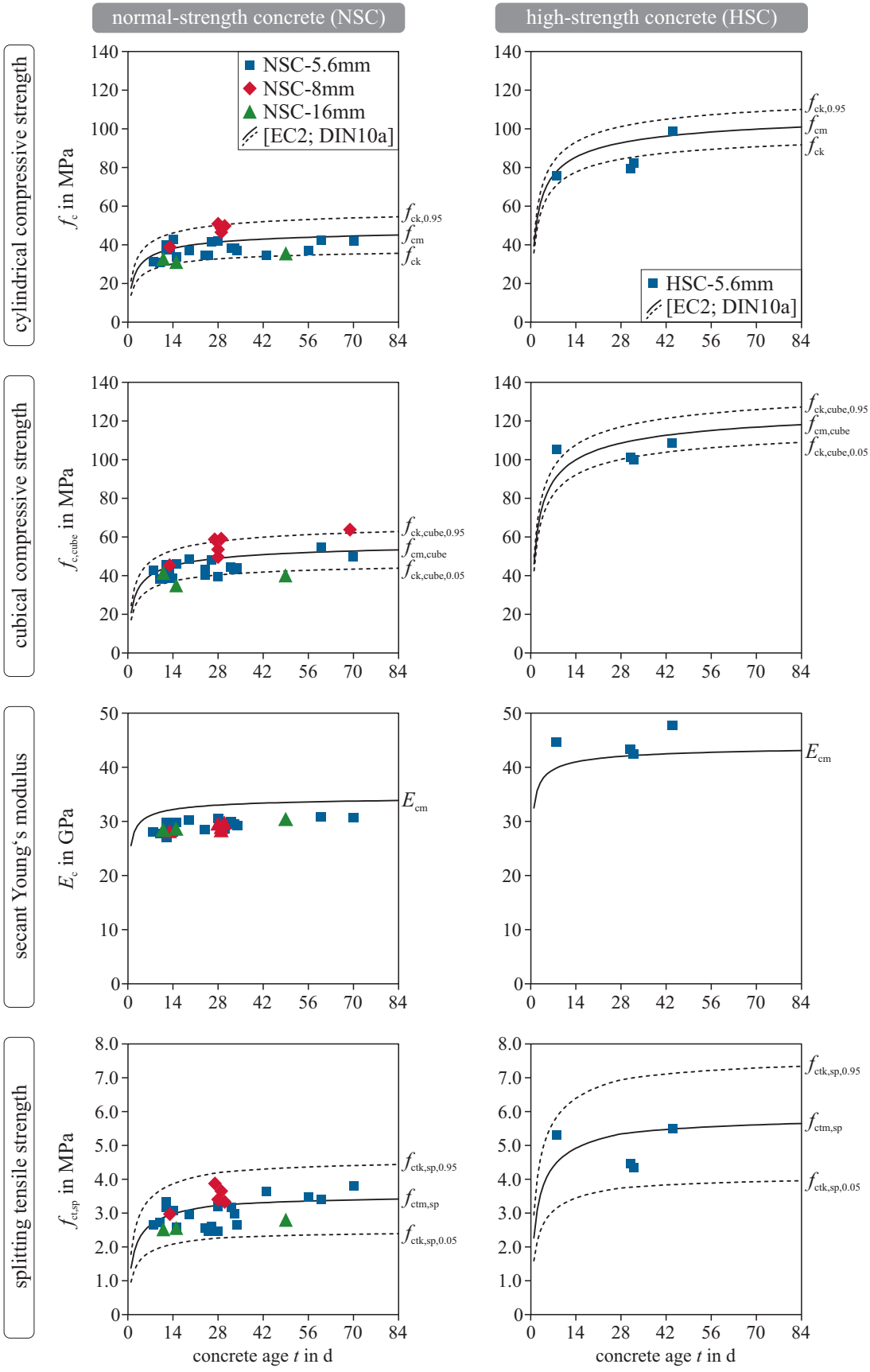


Figure B.1: Average values of concrete strength and Young's modulus determined in material tests with code provision curves acc. to [EC2, DIN10a]

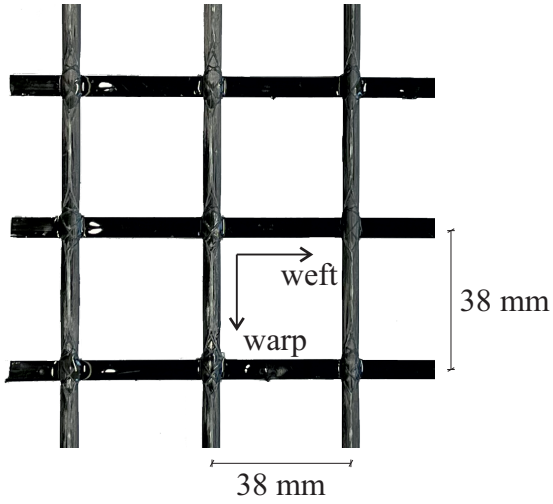
B.2 Reinforcements

textile reinforcement CG1

fibre material:	carbon
impregnation:	epoxy resin
manufacturer:	solidian GmbH
name:	solidian GRID Q95-CCE-38-E5

geometric specifications	warp (0°)	weft (90°)
nominal cross-sectional area A_{nm} [mm²]:	7.5	8.7
fibre strand cross-sectional area $A_{f,nm}$ [mm²]:	3.62	3.62
textile cross-sectional area a_{nm} (nominal) [mm²/m]:	197	229
textile cross-sectional area $a_{f,nm}$ (fibre strand) [mm²/m]:	95	95
yarn spacing y_{nm} [mm]:	38	38
yarn width (mean) [mm]:	4.8	5.5
yarn height (mean)[mm]:	2.6	2.5
equivalent diameter d_{nm} [mm][1)]:	3.09	3.33
Young's modulus		
average value E_{nm} (nominal) [MPa]:	118,205	106,403
average value $E_{f,nm}$ (fibre strand) [MPa]:	244,899	220,449
coefficient of variation:	0.050	0.037
tensile strength		
rupture strength f_{nm} (nominal) [MPa]:	1597	1568
rupture strength $f_{f,nm}$ (fibre strand) [MPa]:	3309	3248
coefficient of variation:	0.107	0.027
rupture strain $\varepsilon_{nm,u}$ [mm/m]:	13.58	14.75

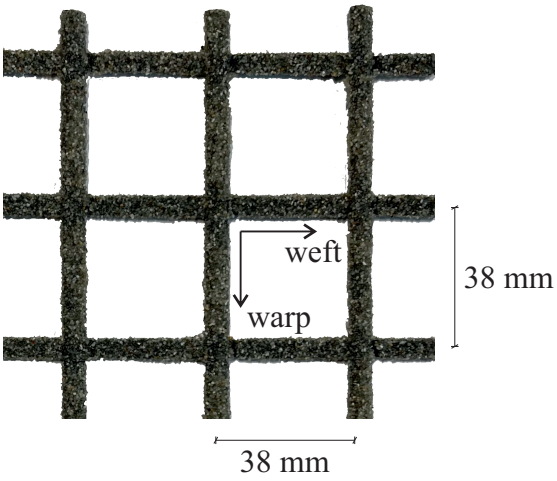
[1)] determined assuming a circular cross section



textile reinforcement CG1sc

fibre material:	carbon
impregnation:	epoxy resin + sand coating
manufacturer:	solidian GmbH
name:	solidian ANTICRACK Q95-CCE-38

geometric specifications	warp (0°)	weft (90°)
nominal cross-sectional area A_{nm} [mm²]:	15.4	16.3
fibre strand cross-sectional area $A_{f,nm}$ [mm²]:	3.62	3.62
textile cross-sectional area a_{nm} (nominal) [mm²/m]:	406	429
textile cross-sectional area $a_{f,nm}$ (fibre strand) [mm²/m]:	95	95
yarn spacing y_{nm} [mm]:	38	38
yarn width (mean) [mm]:	5.7	6.2
yarn height (mean)[mm]:	4.5	4.5
equivalent diameter d_{nm} [mm][1)]:	4.43	4.56
Young's modulus[2)]		
average value E_{nm} (nominal) [MPa]:	57,455	56,757
average value $E_{f,nm}$ (fibre strand) [MPa]:	244,899	220,449
coefficient of variation:	0.050	0.037
tensile strength[2)]		
rupture strength f_{nm} (nominal) [MPa]:	776	836
rupture strength $f_{f,nm}$ (fibre strand) [MPa]:	3309	3248
coefficient of variation:	0.107	0.027
rupture strain $\varepsilon_{nm,u}$ [mm/m]:	13.58	14.75



[1)] determined assuming a circular cross-section

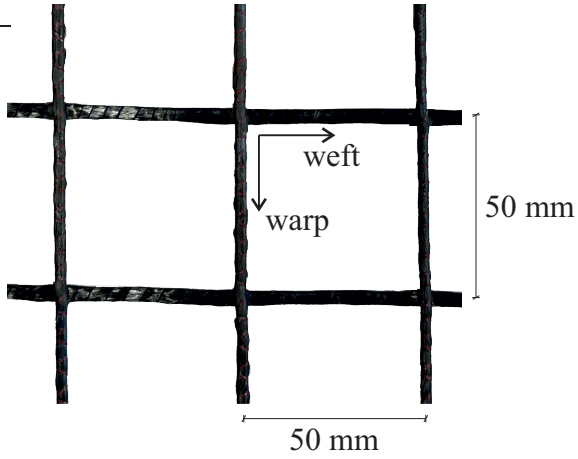
[2)] taken from tensile tests on CG1 assuming identical tensile force at rupture

textile reinforcement CG2

fibre material:	carbon
impregnation:	polystyrene resin
manufacturer:	WILHELM KNEITZ Solutions in Textile GmbH
name:	SIT grid 050/050

geometric specifications	warp (0°)	weft (90°)
nominal cross-sectional area A_{nm} [mm²]:	6.3	5.4
fibre strand cross-sectional area $A_{f,nm}$ [mm²]:	3.62	3.62
textile cross-sectional area a_{nm} (nominal) [mm²/m]:	126	108
textile cross-sectional area $a_{f,nm}$ (fibre strand) [mm²/m]:	72	72
yarn spacing y_{nm} [mm]:	50	50
yarn width (mean) [mm]:	3.5	3.0
yarn height (mean)[mm]:	2.3	2.3
equivalent diameter d_{nm} [mm][1)]:	2.83	2.62
Young's modulus		
average value E_{nm} (nominal) [MPa]:	132,594	136,035
average value $E_{f,nm}$ (fibre strand) [MPa]:	230,758	202,925
coefficient of variation:	0.089	0.041
tensile strength		
rupture strength f_{nm} (nominal) [MPa]:	1795	1650
rupture strength $f_{f,nm}$ (fibre strand) [MPa]:	3124	2461
coefficient of variation:	0.133	0.177
rupture strain $\varepsilon_{nm,u}$ [mm/m]:	13.57	12.09

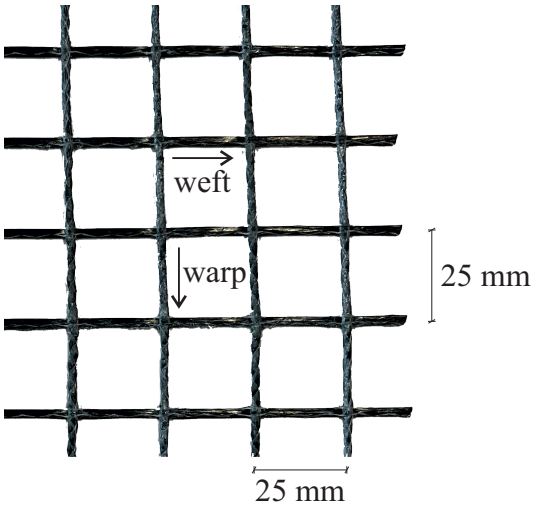
[1)] determined assuming a circular cross-section



textile reinforcement CG3

fibre material:	carbon
impregnation:	polystyrene resin
manufacturer:	Hitexbau GmbH
name:	HTC 25/25-80-UWX

geometric specifications	warp (0°)	weft (90°)
nominal cross-sectional area A_{nm} [mm²]:	3.3	3.2
fibre strand cross-sectional area $A_{f,nm}$ [mm²]:	1.82	1.82
textile cross-sectional area a_{nm} (nominal) [mm²/m]:	132	128
textile cross-sectional area $a_{f,nm}$ (fibre strand) [mm²/m]:	73	73
yarn spacing y_{nm} [mm]:	25	25
yarn width (mean) [mm]:	2.5	2.5
yarn height (mean)[mm]:	1.7	1.6
equivalent diameter d_{nm} [mm][1)]:	2.05	2.02
Young's modulus		
average value E_{nm} (nominal) [MPa]:	116,850	101,847
average value $E_{f,nm}$ (fibre strand) [MPa]:	211,871	179,072
coefficient of variation:	0.384[2)]	0.192[2)]
tensile strength		
rupture strength f_{nm} (nominal) [MPa]:	1509	1614
rupture strength $f_{f,nm}$ (fibre strand) [MPa]:	2736	2838
coefficient of variation:	0.074	0.132
rupture strain $\varepsilon_{nm,u}$ [mm/m]:	14.52	16.35



[1)] determined assuming a circular cross-section

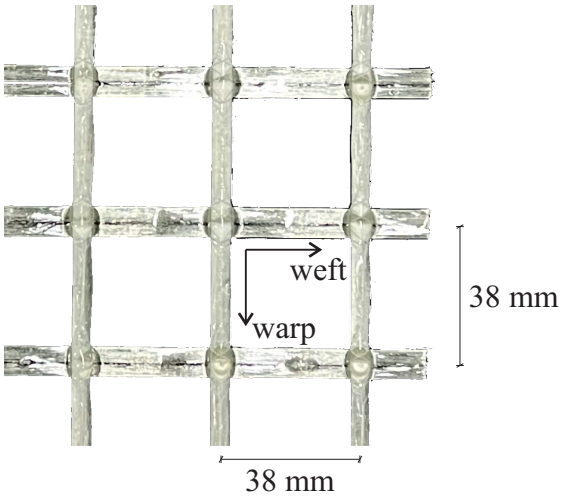
[2)] large deviations due to sensitivity of fibre strand and low number of valid tests

textile reinforcement GG

fibre material:	alkali resistant glass
impregnation:	epoxid resin
manufacturer:	solidian GmbH
name:	solidian GRID Q121-RRE-38

geometric specifications	warp (0°)	weft (90°)
nominal cross-sectional area A_{nm} [mm²]:	10.25	10.00
fibre strand cross-sectional area $A_{f,nm}$ [mm²]:	4.62	4.62
textile cross-sectional area a_{nm} (nominal) [mm²/m]:	270	263
textile cross-sectional area $a_{f,nm}$ (fibre strand) [mm²/m]:	122	122
yarn spacing y_{nm} [mm]:	38	38
yarn width (mean) [mm]:	5.7	7.7
yarn height (mean)[mm]:	3.2	2.4
equivalent diameter d_{nm} [mm][1)]:	3.61	3.57
Young's modulus		
average value E_{nm} (nominal) [MPa]:	35635	37970
average value $E_{f,nm}$ (fibre strand) [MPa]:	79060	82187
coefficient of variation:	0.019	0.020
tensile strength		
rupture strength f_{nm} (nominal) [MPa]:	617	840
rupture strength $f_{f,nm}$ (fibre strand) [MPa]:	1368	1819
coefficient of variation:	0.048	0.056
rupture strain $\varepsilon_{nm,u}$ [mm/m]:	17.30	22.14

[1)] determined assuming a circular cross-section



Appendix C Additions to approaches and methodologies

C.1 Explicit analytical formulations for the 1D representation of SPOc and COT tests

The analytical representation of the single-sided pull-out test (SPOc) and the crack opening tensile test (COT) follows the principle consideration of a one dimensional representation. This allows the consideration of an infinitesimal element, as shown in the middle column of Figure C.1, and the derivation of a physically based formulation to describe the load-slip behaviour of the composite material. The following equations and assumptions follow the description in [Li18a, Li18b] for the so-called *direct pull-out problem*, while no finite element analysis was utilised.

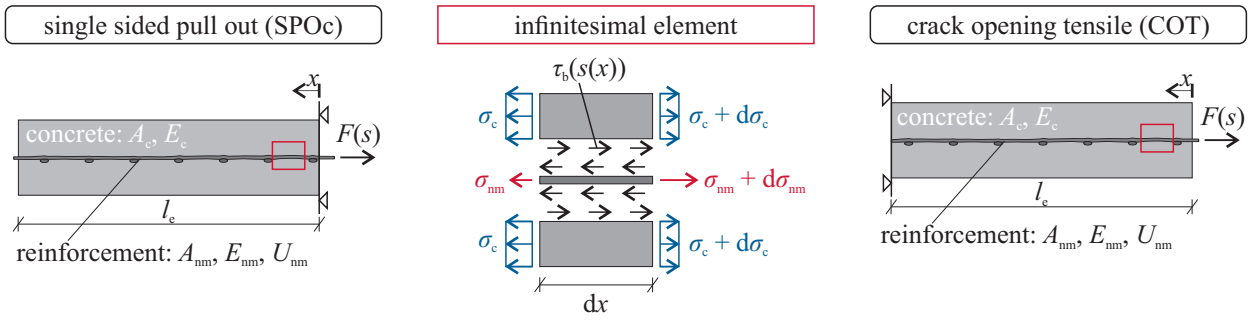


Figure C.1: Representation of the SPOc and COT and the stress state at an infinitesimal element

The slip is described as the difference in displacement between reinforcement and matrix, which is the concrete,

$$s(x) = u_{\mathrm{nm}}(x) - u_{\mathrm{c}}(x)\,. \tag{C-1}$$

The displacement is obtained integrating the material's deformation, in the case of reinforcement

$$\frac{\mathrm{d}u_{\mathrm{nm}}(x)}{\mathrm{d}x} = \varepsilon_{\mathrm{nm}}(x) \tag{C-2}$$

and the concrete

$$\frac{\mathrm{d}u_{\mathrm{c}}(x)}{\mathrm{d}x} = \varepsilon_{\mathrm{c}}(x)\,. \tag{C-3}$$

The constitutive laws are derived assuming Hooke's law for the reinforcement strain

$$\varepsilon_{\mathrm{nm}} = \frac{\sigma_{\mathrm{nm}}}{E_{\mathrm{nm}}} \tag{C-4}$$

and the concrete strain

$$\varepsilon_{\mathrm{c}} = \frac{\sigma_{\mathrm{c}}}{E_{\mathrm{c}}}\,. \tag{C-5}$$

At an infinitesimal element, change in force, which is the force transfer between reinforcement and concrete, is expressed assuming a bond stress. The change in reinforcement stress

$$\frac{\mathrm{d}\sigma_{\mathrm{nm}}(x)}{\mathrm{d}x} = \frac{U_{\mathrm{nm}}}{A_{\mathrm{nm}}} \cdot \tau_{\mathrm{b}}(s(x)) \tag{C-6}$$

and the change in concrete stress

$$\frac{\mathrm{d}\sigma_\mathrm{c}(x)}{\mathrm{d}x} = \frac{U_\mathrm{nm}}{A_\mathrm{c}} \cdot \tau_\mathrm{b}(s(x)) \tag{C-7}$$

provide for the other two constitutive laws. To obtain the displacements, the derivations must be integrated, which requires the utilisation of equilibrium conditions and boundary conditions to solve this problem.

For both test setups, the equilibrium conditions are obtained by assuming that at the end of the bond length l_b, the displacements between both materials are equivalent:

$$u_\mathrm{nm}(x = l_\mathrm{b}) = u_\mathrm{c}(x = l_\mathrm{b}) \tag{C-8}$$

Consequently, the deformation at an infinitesimal element are equal, and therefore strain equivalence is assumed:

$$\varepsilon_\mathrm{nm}(x = l_\mathrm{b}) = \varepsilon_\mathrm{c}(x = l_\mathrm{b}) \tag{C-9}$$

The formulations of the equilibrium conditions require the determination of the bond length. The three remaining boundary conditions are dependent on the represented test setup and enable the mathematical solution of the constitutive laws.
The mathematical solution requires the assumption of the bond stress in relation to the slip. The most simple solution is the representation of a constant bond stress evolution along the bond length. Otherwise, the bond stress is determined using the slip occurring at the considered infinitesimal element, which necessitates a numerical solution as the slip must be determined iteratively.

Boundary conditions of the SPOc setup
In the case of a SPOc test, the displacement of the concrete at the loaded side is fixated:

$$u_\mathrm{c}(x = 0) = 0 \tag{C-10}$$

In addition, force equilibrium at the loaded side provides for the other two conditions. In the case of the reinforcement

$$F - \sigma_\mathrm{nm}(x = 0) \cdot A_\mathrm{nm} = 0 \tag{C-11}$$

and for the concrete

$$F + \sigma_\mathrm{c}(x = 0) \cdot A_\mathrm{c} = 0\,. \tag{C-12}$$

Consequently, the three remaining boundary conditions are defined.

Finally, a differentiation is required whether the displacements are determined inside the bond length or outside the bond length, where strain equilibrium is present. The displacement of the reinforcement is

$$u_\mathrm{nm}(x) = \begin{cases} \frac{F^2 \cdot \rho\,\alpha_\mathrm{e}}{2 \cdot A_\mathrm{nm} \cdot E_\mathrm{nm} \cdot U_\mathrm{nm} \cdot \tau_\mathrm{b}(s(x))} & \text{for } x \geq l_\mathrm{b} \\ \frac{1}{A_\mathrm{nm} \cdot E_\mathrm{nm}} \cdot \left[\frac{\tau_\mathrm{b}(s(x)) \cdot U_\mathrm{nm} \cdot x^2}{2} + F \cdot x + \frac{F^2 \cdot (1 + \rho\,\alpha_\mathrm{e})}{2 \cdot \tau_\mathrm{b}(s(x)) \cdot U_\mathrm{nm}} \right] & \text{for } 0 \leq x \leq l_\mathrm{b} \end{cases} \tag{C-13}$$

and the displacement of the concrete

$$u_\mathrm{c}(x) = \begin{cases} \frac{F^2}{2 \cdot A_\mathrm{c} \cdot E_\mathrm{c} \cdot U_\mathrm{nm} \cdot \tau_\mathrm{b}(s(x))} & \text{for } x \geq l_\mathrm{b} \\ -\frac{1}{A_\mathrm{c} \cdot E_\mathrm{c}} \cdot \left[\frac{\tau_\mathrm{b}(s(x)) \cdot U_\mathrm{nm} \cdot x^2}{2} + F \cdot x \right] & \text{for } 0 \leq x \leq l_\mathrm{b} \end{cases} \tag{C-14}$$

These two equations are sufficient for the determination of the slip and the derivation of parameters describing the bond behaviour as done in Section 5.4.2.

An advancement to the determination of the two parameters C and α is provided in the following, considering the case of having test data representing the slip at the unloaded side. In this case, again the explicit formulation in Equation 5-5 is used, while now considering the state of slip when the bond length exceeds the embedded length. Having determined an analytical description of the F-s_{unl} relation, which is in the following also the simple power-law approach with two parameters $A_{\mathrm{SPO,unl}}$ and α_{SPO} obtained by a curve fitting method, the parameter C_{unl} is derived as

$$C_{\mathrm{unl}} = \frac{A_{\mathrm{SPO,unl}}^2 \cdot \rho\,\alpha_{\mathrm{e}}}{2 \cdot U_{\mathrm{nm}} \cdot A_{\mathrm{nm}} \cdot E_{\mathrm{nm}}}\,. \tag{C-15}$$

As apparent, these two parameters must be linked to the corresponding parameters for the derivation performed on the loaded side when referring to Equations 5-7 and 5-8, as the bond stress evolution is required to be consistent. Therefore, the exponential parameters are required to be equal and the pre-factors are related as follows:

$$C_{\mathrm{unl}} = C \cdot \sqrt{1 + \frac{1}{\rho\,\alpha_{\mathrm{e}}}} \tag{C-16}$$

The utilisation of the explicit formulation and the derivation of a bond stress-slip relation for the case of obtaining solely the slip at the unloaded side from experimental tests is enabled by these two last equations. Consequently, slip at the unloaded side is imperative to occur almost immediately with force application. In the case of the SPOc tests, this was solely the case for small embedded lengths equivalent to the yarn spacing. Furthermore, the observed force-slip behaviour of these series was found to be significantly different when compared to the other test series, which had larger embedded lengths. Consequently, when considering SPOc tests, it is necessary to determine the slip at the loaded side in order to derive a feasible analytical solution to describe the bond behaviour.

In addition, similar to the proposed method to determine a β-value using the COT tests as described in Section 5.4.4, an expression for β in the case of the SPOc is provided:

$$\beta_{\mathrm{SPO}} = 1 - \frac{(\rho\,\alpha_{\mathrm{e}})^2}{8 \cdot \alpha_{\mathrm{SPO}}} \tag{C-17}$$

Boundary conditions of the COT setup

In the case of a COT test, the displacement of the concrete at the unloaded side is fixated:

$$u_{\mathrm{c}}(x = l_{\mathrm{e}}) = 0 \tag{C-18}$$

In addition, force equilibrium at the loaded side provides for the other two conditions. In the case of the reinforcement

$$F - \sigma_{\mathrm{nm}}(x = 0) \cdot A_{\mathrm{nm}} = 0 \tag{C-19}$$

and for the concrete

$$\sigma_{\mathrm{c}}(x = 0) \cdot A_{\mathrm{c}} = 0\,. \tag{C-20}$$

A differentiation is required whether the displacements are determined inside the bond length or when strain equilibrium is present. The displacement of the reinforcement is

$$u_{\mathrm{nm}}(x) = \begin{cases} \frac{F\cdot(l_{\mathrm{b}}+x)}{A_{\mathrm{c}}\cdot E_{\mathrm{c}}\cdot(1+\rho\alpha_{\mathrm{e}})} & \text{for } x \geq l_{\mathrm{b}} \\ \frac{1}{2\cdot A_{\mathrm{nm}}\cdot E_{\mathrm{nm}}}\left[\frac{F^2}{\tau_{\mathrm{b}}(s(x))\cdot U_{\mathrm{nm}}\cdot(1+\rho\alpha_{\mathrm{e}})}+x\cdot(2F+\tau_{\mathrm{b}}(s(x))\cdot U_{\mathrm{nm}}\cdot x)\right] & \\ \quad -\frac{1}{2\cdot A_{\mathrm{c}}\cdot E_{\mathrm{c}}}\cdot\left[\frac{F^2}{\tau_{\mathrm{b}}(s(x))\cdot U_{\mathrm{nm}}\cdot(1+\rho\alpha_{\mathrm{e}})^2}-\frac{F\cdot l_{\mathrm{b}}}{1+\rho\alpha_{\mathrm{e}}}\right] & \text{for } 0 \leq x \leq l_{\mathrm{b}} \end{cases} \tag{C-21}$$

and the displacement of the concrete

$$u_{\mathrm{c}}(x) = \begin{cases} \frac{F\cdot(l_{\mathrm{b}}+x)}{A_{\mathrm{c}}\cdot E_{\mathrm{c}}\cdot(1+\rho\alpha_{\mathrm{e}})} & \text{for } x \geq l_{\mathrm{b}} \\ -\frac{1}{2\cdot A_{\mathrm{c}}\cdot E_{\mathrm{c}}}\left[\frac{F^2}{\tau_{\mathrm{b}}(s(x))\cdot U_{\mathrm{nm}}\cdot(1+\rho\alpha_{\mathrm{e}})^2}-\frac{F\cdot l_{\mathrm{b}}}{1+\rho\alpha_{\mathrm{e}}}+\tau_{\mathrm{b}}(s(x))\cdot U_{\mathrm{nm}}\cdot x^2\right] & \text{for } 0 \leq x \leq l_{\mathrm{b}} \end{cases} \tag{C-22}$$

C.2 Iterative determination of strain distribution and deflections

The determination of the strain distribution, which is required to derive the cross-sectional curvature and deformation, follows the strategy depicted in Figure 6.7. Therefore, an equilibrium of the internal forces of the cross-section

$$\sum_{\mathrm{i}=1}^{k} F_{\mathrm{nm,i}} + F_{\mathrm{c}} = 0 \tag{C-23}$$

is iteratively obtained, considering the reinforcement layers and the concrete. The linear elastic material behaviour of the non-metallic textile reinforcement

$$F_{\mathrm{nm,i}} = \varepsilon_{\mathrm{nm,i}} \cdot E_{\mathrm{nm}} \cdot A_{\mathrm{nm}} \tag{C-24}$$

and of the concrete

$$F_{\mathrm{c}} = \int_0^{x_{\mathrm{c}}} \sigma_{\mathrm{c}}(\varepsilon(x)) \cdot b_{\mathrm{c}}(x)\,\mathrm{d}x = F_{\mathrm{ct}} + \sum_{i=0}^{50} \frac{\sigma_{\mathrm{c}}(\varepsilon(x_{\mathrm{i}})) + \sigma_{\mathrm{c}}(\varepsilon(x_{\mathrm{i+1}}))}{2} \cdot \frac{x_{\mathrm{c}}}{50} \cdot b \tag{C-25}$$

requires the approximation of the strain distribution. In the model derived in this thesis, the force attributed to the concrete's tensile behaviour is neglected. The material behaviour of concrete subject to uniaxial compression is described using the non-linear formulation provided in [EC2]

$$\sigma_{\mathrm{c}}(\varepsilon(x)) = f_{\mathrm{cm}} \cdot \frac{k\cdot\eta(x) - \eta(x)^2}{1+(k-2)\cdot\eta(x)}\,. \tag{C-26}$$

The factors

$$k = \frac{1.05 E_{\mathrm{cm}} \cdot \varepsilon_{\mathrm{c1}}}{f_{\mathrm{cm}}} \tag{C-27}$$

and

$$\eta(x) = \frac{\varepsilon(x)}{\varepsilon_{\mathrm{c1}}} \tag{C-28}$$

are determined using the material parameters of the concrete, which were determined in corresponding material tests.

As evident, to obtain a force equilibrium, the strain distribution has to be iteratively solved. The solving strategy uses a non-linear optimisation approach to find the local minimum, which is in this

case the force equilibrium. The initial strain values considered at the start of the iteration are the maximum absolute strain values of the materials, which are the rupture strain of the reinforcement $\varepsilon_{\mathrm{nm,u}}$ and the ultimate compressive strain of the concrete $\varepsilon_{\mathrm{c1,u}}$. To reduce iterations required and avoid problems raised due to searching for a local minimum, which might not be the global minimum and the therefore the actual solution for force equilibrium, a differentiation is introduced: in the case of the initial force difference $\Delta F = \sum F_{\mathrm{nm,i}} + F_{\mathrm{c}}$ being below zero, rupture of the reinforcement is assumed, consequently reducing the concrete compressive strain. Otherwise, in the case of ΔF exceeding zero, concrete compression failure is assumed and the reinforcement strain is reduced to fulfil force equilibrium.
Having established equilibrium and finding the strain distribution of the concrete cross-section, the curvature of a cracked section is obtained

$$\kappa_{\mathrm{II}} = \frac{\varepsilon_{\mathrm{nm,1}} - \varepsilon_{\mathrm{c,min}}}{h - d_1} \tag{C-29}$$

focusing on the most-tensioned and most-compressed fibres of the cross-section. In the case of an uncracked section, defined as region where the bending-moment is below the crack moment M_{cr},

$$\kappa_{\mathrm{I}} = \frac{2 \cdot \mid \varepsilon_{\mathrm{c,min}} \mid}{h}. \tag{C-30}$$

Consequently, the bending moment distribution along the member has to be considered when introducing a differentiation between cracked and uncracked concrete sections.

The deflection is analytically described as double integral of the curvature in longitudinal direction (z-direction) of the member, referred to as span:

$$u(z) = \int_0^z \int_0^z \kappa(z)\, \mathrm{d}z\, \mathrm{d}z \tag{C-31}$$

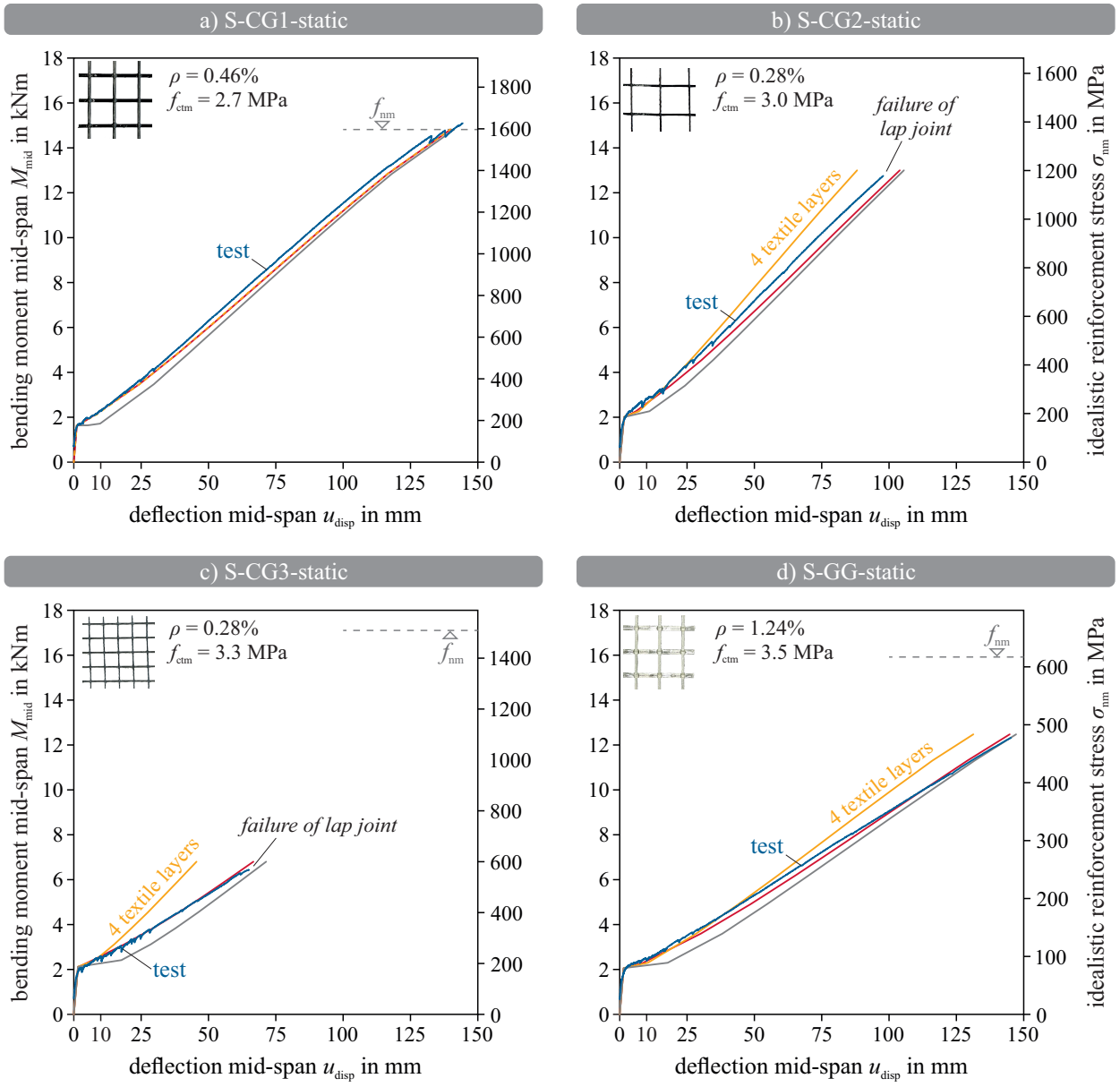
Using the trapezoidal rule and dividing the span L_{Span} into 2000 segments of equal distance, the deflection is obtained considering the following boundary conditions for a four-point bending test: deflection at the supports are zero ($u(z=0) = 0$ and $u(z = L_{\mathrm{Span}}) = 0$) and the rotation of the cross-section in mid-span is zero ($\phi(z = L_{\mathrm{Span}}/2) = 0$). The rotation is obtained as integral of the curvature.

As introduced in Equation 6-9, a consideration of tension stiffening is simple to realise in the described solving algorithm and provides for very accurate predictions.

Furthermore, addressing the influence of cyclic loading as visualised in Figure 6.13, is also possible within this algorithm. This was achieved by solely updating the minimal concrete strain $\varepsilon_{\mathrm{c,min}}$ in the determination of the strain distribution by considering the cyclic strain increase, expressed as $\phi \cdot \varepsilon_{\mathrm{c,cyc}}$ (cf. Equation 6-10). It is crucial that the concrete strain used to calculate the concrete force remains at its original value without consideration of the cyclic strain increase. This strategy enables the determination of the changed strain distribution resulting from cyclic loading, which attributes for the reduced inner lever and the increase reinforcement utilisation, while the concrete force remains identical. As mentioned in Section 6.5.4, this strategy is only valid when assuring that the superior load did not require a concrete strain utilisation being beyond $\varepsilon_{\mathrm{c1}}$ (the strain at compressive strength).

C.3 Results on deflection predictions

In Chapter 6 the predicted deflections are only provided in extracts. In the following, the graphical evaluations for all twelve conducted four-point bending tests are provided. Figure C.2 shows the moment-deflection prediction of the purely statically loaded slabs.



Approach 1:	Approach 2:	Approach 3:
no tension stiffening	direct consideration of tension stiffening with distribution factor ζ:	indirect consideration of tension stiffening using average curvature:
$\kappa = \frac{\varepsilon_{nm,1} - \varepsilon_{c,min}}{h - d_1}$ acc. to Eq. 6-1	$\kappa_{m,II} = \frac{\zeta \cdot \varepsilon_{nm,1} - \varepsilon_{c,min}}{h - d_1}$ acc. to Eq. 6-9	$\kappa_m = \zeta \cdot \kappa_{II} + (1 - \zeta) \cdot \kappa_I$ acc. to [MC20]
$u(z) = \int_0^l \int_0^l \kappa(z)\, dz\, dz$ acc. to Eq. 6-3	$u(z) = \int_0^l \int_0^l \kappa(z)\, dz\, dz$	$u_{disp} = 0.1034 \cdot l^2 \cdot \kappa_m$ acc. to Eq. 6-8

Figure C.2: Moment-deflection prediction of analytical-based approaches in the case of purely statical loading

The moment-deflection prediction for the slabs with an additional cyclic phase, denoted as "cyclic-2", are shown in Figure C.3. The approach and considerations to determine the influence of cyclic loading on the compression zone is provided in Section 6.5.4.

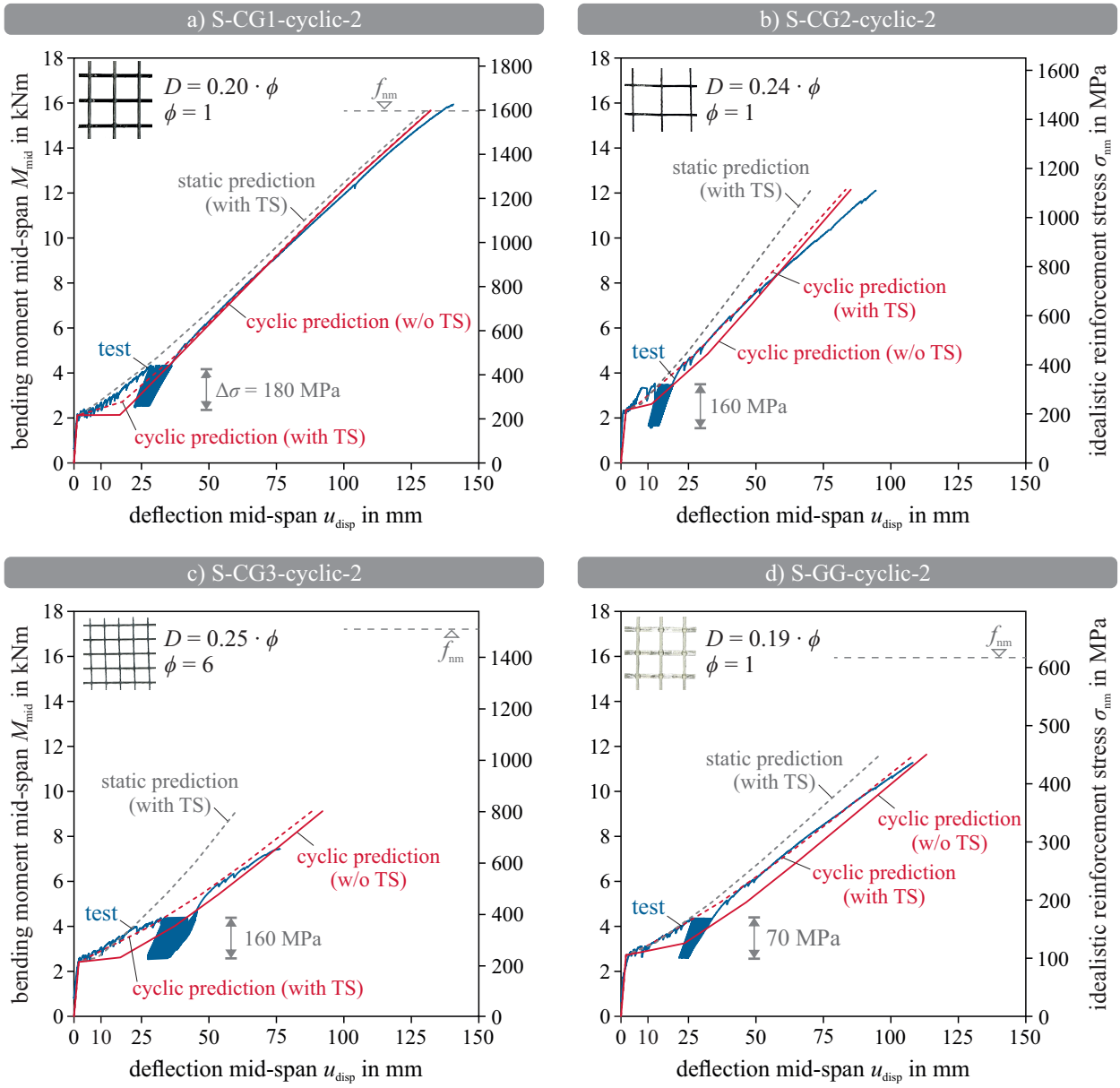


Figure C.3: Moment-deflection prediction of analytical-based approaches for the second cyclically loaded slab of each series

C.4 Methodology for a simplified derivation of the bond stress approximation

This section provides for some thoughts regarding a simplified determination of the bond stress values required to utilise a feasible crack width prediction in instances where a continuous force-crack opening relation is not available, and taking into account the observations made during the evaluation of the COT experimental campaign (cf. Sections 3.4 and 3.5). Moreover, a strategy is introduced on how to consider the contribution of tension stiffening in the cases where the tension stiffening factor β cannot be quantified due to the lack of a continuous reinforcement strain measurement. The methodology presented has recently been discussed as a concept for evaluating the characteristic value of bond stress required to apply a design concept for limiting crack width. This is expected to be part of the second generation DAfStb Guideline "Concrete members with non-metallic reinforcement". The Guideline is intended to supersede Annex R in the National Annex of Germany of the next generation of Eurocode 2 [FprEC2].

The utilisation of COT tests to obtain an mean value of the bond stress in dependency on the crack opening, as demonstrated in Section 5.4.3, is a profound method to apply the previously evaluated crack width prediction approaches. Nevertheless, any methodology which provides for a feasible force-slip relation or force-crack opening relation may be used. In instances where the determination of the transfer length and the contribution of tension stiffening cannot be achieved by the selected methodology, a simplified derivation of the average value of bond stress is required.
This derivation was introduced in Section 5.2 and is revisited. The basis of this methodology is to focus on the single cracking stage, with its physically based description expressed in Equation 5-4. The utilisation of a description of the force-crack opening relation serves as a basis for the subsequent analysis. To illustrate this point, a power-law approach is considered as expressed in Equation 5-2. This method enables the determination of an average value of bond stress. Only the contribution of tension stiffening must be assumed, denoted by the factor β.

In the interest of simplicity, it is possible to set $\beta = 0$ in the case of single cracking and thus obtain a solution for the bond stress relation (according to Equations 2-18 and 5-4). While this is feasible from a purely calculative perspective, it is not mechanically sound. Furthermore, it is critical to acknowledge that the application of this bond stress relation to the approaches for the adjacent/stabilised stage results in a significant underestimation of the actual width. The fundamental problem is the assumption of an unrepresentative high bond capacity, which consequently determines unrealistic small crack spacing.
However, remaining at the single cracking stage, the resulting theoretical reinforcement strain evolution is illustrated as grey lines in Figure C.4. From a calculation-based perspective, any value of the parameter β below 1.0 is deemed justifiable. In the case of a constant force transfer along the transfer length, corresponding to a linear strain evolution, the tension stiffening factor β is 0.5, as shown by the black coloured line in Figure C.4. It is reasonable to assume that, in general, the non-linear strain evolution is below the linear case, as depicted by the blue-coloured non-linear strain evolution.
When following a conservative approach, β is assumed to be 0.5. However, the experimental results obtained in this thesis justify a higher value. The motivation behind setting β to a fixed value besides zero is twofold: to address the viable force transfer and bond acting in textile reinforced concrete members in the case of single cracking; and to provide an average value of mean bond stress τ_{bm} that is obtained on a physically based derivation method rather than providing a non-realistic value that is significantly higher than the actual material characteristic when assuming $\beta = 0$. For example, the conducted COT tests allowed for determined β-values at single cracking

ranging from 0.58 (for CG1) to 0.68 (for CG3).
A β-value below 0.5 indicates a strain evolution referring to a low magnitude of force transfer close to the crack, followed by significant force transfer, as shown by the blue curve in Figure C.4. While this form of evolution, referring to bond softening close to the crack at large slip, was observed for adjacent cracks, this was not evident at single cracking. In instances where characterisation tests for the bond behaviour demonstrate no bond softening at values of slip representing the service-ability stage, or when adjacent cracking occurs, as for example in the COT tests, it is reasonable to neglect this scenario. Consequently, the assumption of a β-value below 0.5 is not required for a single crack.

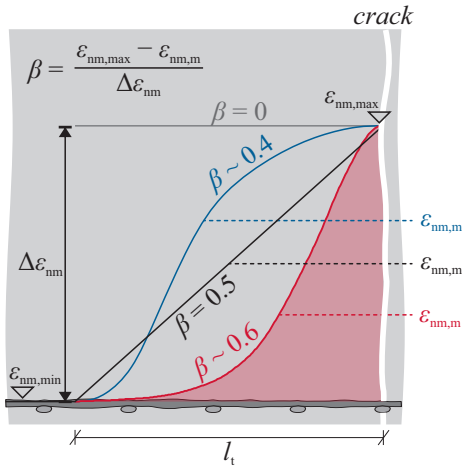


Figure C.4: Schematic representation of reinforcement strain evolution and corresponding value of the tension stiffening factor β

Considering a power-law approximation of the force-crack opening relation, the exponent α allows for two simplifications, which differentiate between the value of α being at least 0.5 or below 0.5. As illustrated in Figure C.5, a graphical representation has been provided in order to evaluate the influence of different α-values on the transferred force. In the approximation $F = C \cdot s^{\alpha}$, the parameter C was set to 5 for the sake of simplicity. In Figure C.5c, the case of choosing β to 0.5 is plotted, showing that the bond stress evolutions only change in value in comparison to the case of no contribution of tension stiffening assumed (Figure C.5b).
In instances where the value of α is equivalent to 0.5, the average value of bond stress is shown to be constant. For values of α greater than 0.5 and tending towards the case of pure friction ($\alpha = 1.0$), the average value of bond stress, determined according to Equation 5-4, increases at larger crack opening. This refers to a state of bond hardening where the application of larger slip and the utilisation of additional transfer length provides for an increased force transfer. In the context of pure friction, the increase in bond stress is linear. In contrast, when the value of α is less than 0.5, immediate bond softening occurs. This is because the average value of bond stress decreases with increasing crack opening, as demonstrated in Figure C.5b+c. It is worth to note that values of α exceeding 1.0 are conceivable, and would pertain to a state in which a substantial degree of force is transferred after the occurrence of some slip. This is the case when the transfer lengths must propagate at first to a region where friction or mechanical interlocking is able to act. The case of $\alpha = 0$ refers to a theoretical consideration in which a constant force is transferred independently of the crack opening.

In instances where a single value of bond stress is required for a range of crack widths, the value of α facilitates the following differentiation: In cases where $\alpha < 0.5$, the value of bond stress at the

largest crack width of the specified range is to be used. In the cases where $\alpha \geq 0.5$, it is necessary to employ the value of bond stress at the smallest crack width within the specified range.

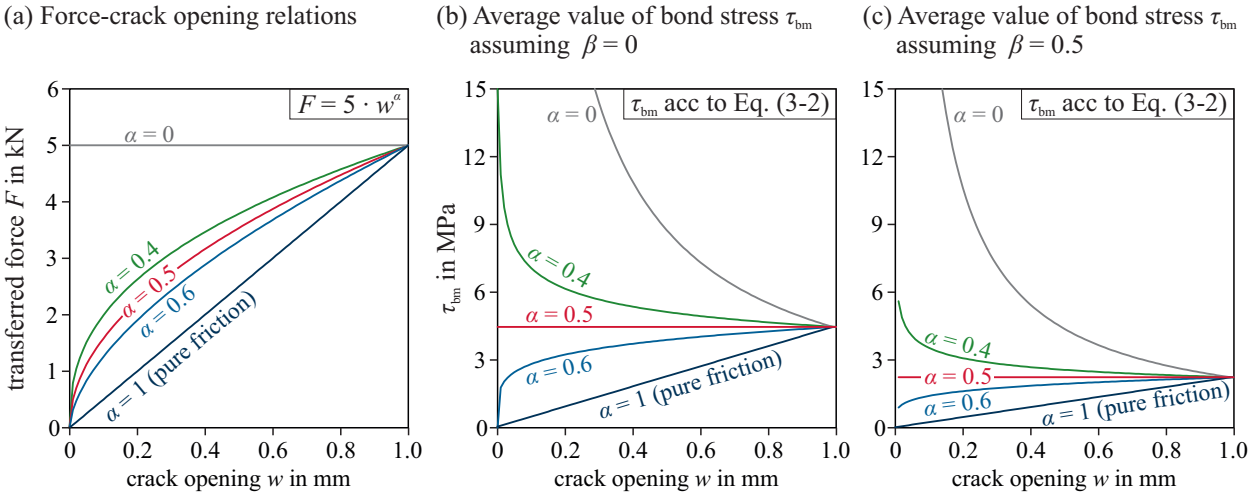


Figure C.5: Influence of the exponent α of a power-law approximation on the evolution of the mean value of bond stress

Appendix D Experimental results

D.1 Single-sided pull-out tests (SPOc)

The results of the 200 SPOc tests in 40 series are provided in the following appendix. The results of the tests, which were neglected in the evaluation, are given in brackets. An overview of the test configuration and the observed failure is given in Table D.1, differentiating between three failure types: SP = concrete splitting; PO = pull-out of fibre strand; TR = tensile rupture of fibre strand.

The derived average pull-out force-to-slip relations allow for an analytical description using the power-law approximation in Equation 5-1. To derive the parameters A_{SPO} and α_{SPO} for each test series, a curve fitting method using a non-linear least squares method to fit the power-law approach in Equation 5-1 was utilised on the mean pull-out force-slip curves. The accuracy of the fitted curve is expressed using the coefficient of variation V_δ determined according to Annex D, Section 8.2.2.4 of Eurocode 0 [EC0], considering a log-normal distribution of the error variable as the parameters are derived based on tests highly dependent on the material characteristics [Fis01]. Both parameters and the coefficient of variation are presented in Table D.2.

For each textile grid, one series was conducted in which the transverse fibre strands (weft direction) were mechanically removed. Photographs of the reinforcements with removed fibre strands are provided in Figure D.1. In the case of CG1, CG2 and GG, a flat surface was found after the removing of the transverse fibre strand. No alteration in the cross-sectional area was found. Conversely, a reduced cross-section was found for CG3 at the location of the transverse fibre strand (Figure D.1c).

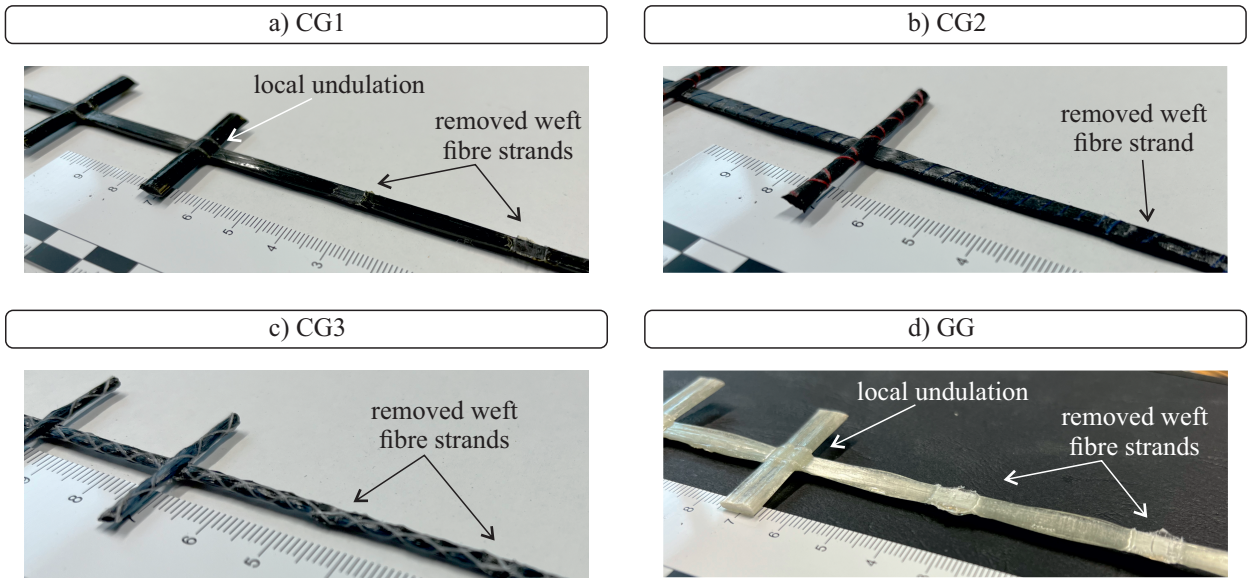


Figure D.1: Textile grids with removed fibre strands

Table D.1: Parameters of the bond tests conducted for the textile FRP grids

grid and orientation	concrete strength	$d_{g,max}$ [mm]	t [mm]	l_e [mm]	f_{ctm} [1)] [MPa]	number of valid tests	observed failure
CG1-0°	NSC	5.6	30	38	2.6	5	2×SP / 3×PO
				114		4	4×SP
				250	3.0	5	3×SP / 2×TR
				500		4	4×SP / 1×TR
				114 w/o[2)]	2.6	5	5×SP
	HSC			114	4.8	4	2×SP / 2×TR
				250		4	2×SP / 2×TR
CG1-90°	NSC			114	3.0	4	4×SP
	HSC				4.8	4	3×SP / 1×TR
CG1-0°	NSC	16	50	114	2.5	4	4×SP
CG1sc-0°	NSC	5.6	30	38	2.6	5	5×SP
				114		5	3×SP / 2×TR
				114 w/o[2)]		4	4×SP
CG2-0°	NSC	5.6	30	38	2.6	5	5×PO
				150		4	3×SP / 1×PO
				250	3.0	5	5×TR
				500		5	5×TR
				150 w/o[2)]	2.6	5	3×SP / 1×PO / 1×TR
	HSC			150	4.8	4	4×TR
				250		4	4×TR
CG2-90°	NSC			150	2.7	4	4×PO
	HSC				4.8	5	5×PO
CG2-0°	NSC	16	50	150	2.5	5	1×TR / 4×PO
CG3-0°	NSC	5.6	30	75	2.7	5	5×PO
				250		4	5×TR
				500		4	2×SP / 2×TR
				75 w/o[2)]	2.6	4	4×PO
	HSC			75	4.8	4	4×TR
				250		4	4×TR
CG3-90°	NSC			75	2.7	3	3×PO
	HSC				4.8	2	2×TR
GG-0°	NSC	5.6	30	38	2.6	5	5×SP
				114		4	4×SP / 1×TR
				250	3.0	5	5×TR
				500		5	5×TR
				114 w/o[2)]	2.6	4	3×SP / 1×TR
	HSC			114	4.8	2	2×TR
				250		4	4×TR
GG-90°	NSC			114	3.0	5	5×SP
	HSC				4.8	2	2×SP
GG-0°	NSC	16	50	114	2.5	5	3×SP / 1×TR

[1)] obtained from splitting test: $f_{ctm} = 0.9 \cdot f_{ct,sp}$ acc. to [EC2]

[2)] transverse fibre strand removed prior to concreting

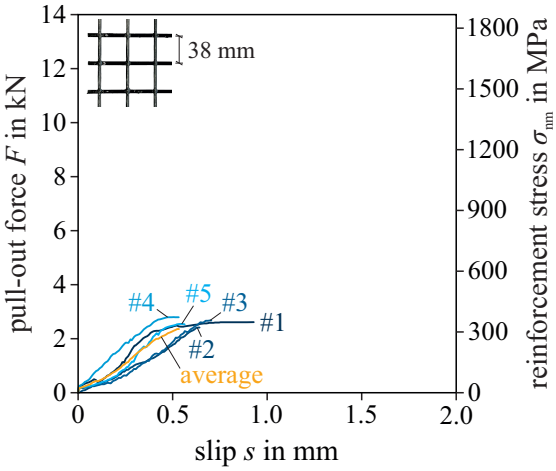
Table D.2: Derived parameters A_{SPO} and α_{SPO} and maximum value of slip for the validity of the analytical description of the pull-out force-slip relation according to Equation 5-1

textile grid	orientation	concrete strength	$d_{g,max}$ [mm]	l_e [mm]	A_{SPO} [-] (V_x [%])	α_{SPO} [-] (V_x [%])	$s \leq$ [mm]
CG1	0°	NSC	5.6	38	4600	1	0.5
	0°+ 90°	NSC + HSC	5.6	≥ 114	8200 (7.6)	0.5 (11.0)	0.8
	0°	NSC	5.6	114 w/o	8100	0.85	0.8
			16	114	8800	0.66	0.5
CG1sc	0°	NSC	5.6	38	8000	0.74	0.3
				114	10000	0.88	1.0
				114 w/o	8000	0.79	
CG2	0°	NSC	5.6	50	2500	0.87	1.0
	0°	NSC	5.6 + 16	≥ 150	8000 (13.1)	0.72 (6.5)	1.0
		HSC	5.6	≥ 150		0.59	0.4
		NSC		150 w/o	1500	0.87	1.5
	90°	NSC		150	5400	0.71	1.2
		HSC		150	5100	0.34	0.3
CG3	0°	NSC	5.6	75	3400	0.55	1.0
				250	6100	0.73	0.4
				500	5500	1.00	0.7
				75 w/o	1700	1.00	1.5
		HSC		75	2900	0.65	0.3
				250	5400	1.00	0.2
	90°	NSC		75	3300	0.20	1.0
		HSC		75	4900	0.88	0.7
GG	0°	NSC	5.6	38	3800	1.00	0.5
				114	6600 (12.8)	0.31	1.0
				250		0.41	0.7
				500		0.51	0.7
			16	114		0.51	1.3
		HSC	5.6	≥ 114		0.53 (4.3)	0.5
		NSC		114 w/o	4700	1.00	1.0
	90°	NSC		114	5500	0.47	0.8
		HSC			8000	0.39	0.4

SPOc-CG1-NSC-0°-38

reinforcement: CG1 (solidian GRID Q95-CCE-38)
direction of investigation: 0° (warp direction)
embedded length l_e: 38 mm | 1 × y_{nm}

normal strength concrete	
composition:	NSC-5.6mm
concrete age at material test:	34 d
compressive strength	
$f_{c,cycl}$ [MPa]: 37.0	$f_{c,cube}$ [MPa]: 43.9
Young's modulus	
E_{cm} [MPa]: 29,148	
tensile strength	
$f_{ct,sp}$ [MPa]: 2.9	$f_{ctm,calc}$ [MPa]: 2.6



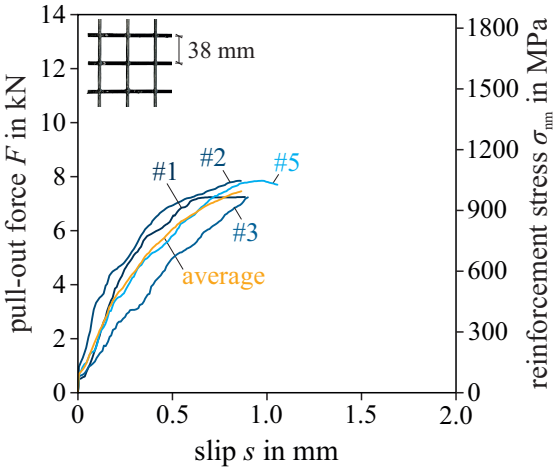
geometry of specimen	
width b [mm]:	38
thickness t [mm]:	30
concrete coverage c [mm]:	13.5

test results					
test number	-1	-2	-3	-4	-5
concrete age at test [d]			31		
maximum load F_{max} [kN]	2.61	2.42	2.67	2.80	2.55
at slip s [mm]	0.93	0.65	0.70	0.51	0.52
type of failure	PO	PO	PO	SP	SP
load at slip of 0.2 mm $F_{0.2}$ [kN]	0.87	0.51	0.47	1.46	0.62
load at occurrence of slip at unloaded side F_{unl} [kN]	1.94	2.40	1.78	1.71	2.40

SPOc-CG1-NSC-0°-114

reinforcement: CG1 (solidian GRID Q95-CCE-38)
direction of investigation: 0° (warp direction)
embedded length l_e: 114 mm | 3 × y_{nm}

normal strength concrete			
composition:	NSC-5.6mm		
concrete age at material test:	12 d		
compressive strength			
$f_{c,cycl}$ [MPa]:	37.4	$f_{c,cube}$ [MPa]:	45.6
Young's modulus			
E_{cm} [MPa]:	29,755		
tensile strength			
$f_{ct,sp}$ [MPa]:	3.3	$f_{ctm,calc}$ [MPa]:	3.0



geometry of specimen	
width b [mm]:	38
thickness t [mm]:	30
concrete coverage c [mm]:	13.5

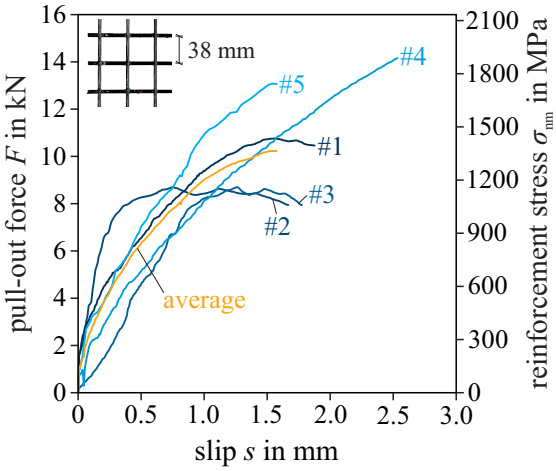
test results					
test number	-1	-2	-3	(-4)	-5
concrete age at test [d]			10		
maximum load F_{max} [kN]	7.25	7.85	7.32	(7.37)	7.85
at slip s [mm]	0.89	0.85	0.90	(-0.94)	0.97
type of failure	SP	SP	SP	(PO)	SP
load at slip of 0.2 mm $F_{0.2}$ [kN]	3.73	4.56	2.56	(0.22)	3.43
load at occurrence of slip at unloaded side F_{unl} [kN]	5.63	5.86	7.32	(-)	6.51

SPOc-CG1-NSC-0°-250

reinforcement: CG1 (solidian GRID Q95-CCE-38)
direction of investigation: 0° (warp direction)
embedded length l_e: 250 mm | 6.6 × y_{nm}

normal strength concrete	
composition:	NSC-5.6mm
concrete age at material test:	12 d
compressive strength	
$f_{c,cycl}$ [MPa]: 37.4	$f_{c,cube}$ [MPa]: 45.6
Young's modulus	
E_{cm} [MPa]: 29,755	
tensile strength	
$f_{ct,sp}$ [MPa]: 3.3	$f_{ctm,calc}$ [MPa]: 3.0

geometry of specimen	
width b [mm]:	38
thickness t [mm]:	30
concrete coverage c [mm]:	13.5

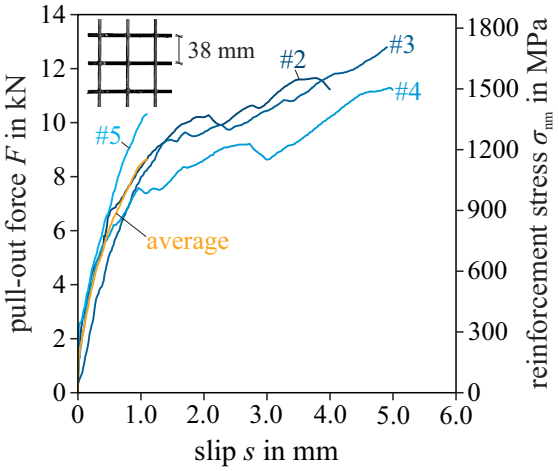


test results					
test number	-1	-2	-3	-4	-5
concrete age at test [d]			10		
maximum load F_{max} [kN]	10.76	8.70	8.70	14.19	13.08
at slip s [mm]	1.54	0.76	1.27	2.55	1.55
type of failure	SP	SP	TR	TR	SP
load at slip of 0.2 mm $F_{0.2}$ [kN]	4.52	6.50	1.45	2.97	3.81
load at occurrence of slip at unloaded side F_{unl} [kN]	9.06	7.26	7.56	9.31	10.77

SPOc-CG1-NSC-0°-500

reinforcement: CG1 (solidian GRID Q95-CCE-38)
direction of investigation: 0° (warp direction)
embedded length l_e: 500 mm | 13.2 × y_{nm}

normal strength concrete			
composition:	NSC-5.6mm		
concrete age at material test:	12 d		
compressive strength			
$f_{c,cycl}$ [MPa]:	37.4	$f_{c,cube}$ [MPa]:	45.6
Young's modulus			
E_{cm} [MPa]:	29,755		
tensile strength			
$f_{ct,sp}$ [MPa]:	3.3	$f_{ctm,calc}$ [MPa]:	3.0



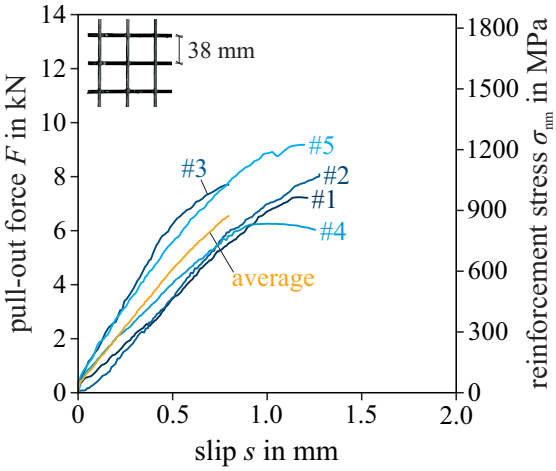
geometry of specimen	
width b [mm]:	38
thickness t [mm]:	30
concrete coverage c [mm]:	13.5

test results					
test number	(-1)	-2	-3	-4	-5
concrete age at test [d]			11		
maximum load F_{max} [kN]	(6.43)	11.65	12.80	11.29	10.32
at slip s [mm]	(0.61)	3.73	4.92	4.95	1.10
type of failure	(SP)	SP	TR	SP	SP
load at slip of 0.2 mm $F_{0.2}$ [kN]	(3.28)	4.09	2.21	3.87	4.29
load at occurrence of slip at unloaded side F_{unl} [kN]	(-)	(-)	(-)	(-)	(-)

SPOc-CG1-NSC-0°-114-w/o

reinforcement: CG1 (solidian GRID Q95-CCE-38) with removed transverse fibre strands
direction of investigation: 0° (warp direction)
embedded length l_e: 114 mm | 3 × y_{nm}

normal strength concrete	
composition:	NSC-5.6mm
concrete age at material test:	24 d
compressive strength	
$f_{c,cycl}$ [MPa]: 34.5	$f_{c,cube}$ [MPa]: 43.2
Young's modulus	
E_{cm} [MPa]: 28,428	
tensile strength	
$f_{ct,sp}$ [MPa]: 2.9	$f_{ctm,calc}$ [MPa]: 2.6



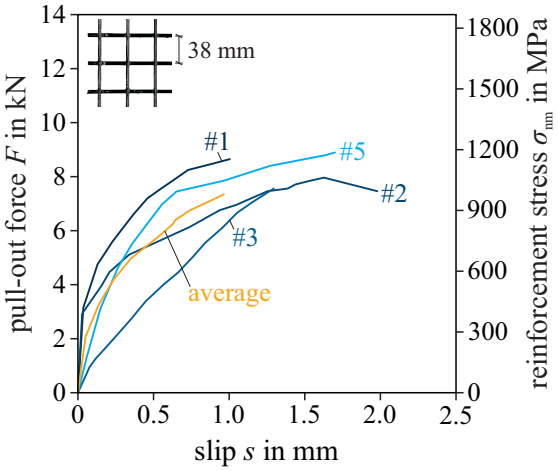
geometry of specimen	
width b [mm]:	38
thickness t [mm]:	30
concrete coverage c [mm]:	13.5

test results					
test number	-1	-2	-3	-4	-5
concrete age at test [d]			24		
maximum load F_{max} [kN]	7.23	7.70	8.09	6.26	9.19
at slip s [mm]	1.15	0.79	1.34	0.97	1.21
type of failure	SP	SP	SP	SP	SP
load at slip of 0.2 mm $F_{0.2}$ [kN]	1.43	2.64	1.15	2.04	2.74
load at occurrence of slip at unloaded side F_{unl} [kN]	4.65	5.24	4.62	3.63	4.83

SPOc-CG1-HSC-0°-114

reinforcement: CG1 (solidian GRID Q95-CCE-38)
direction of investigation: 0° (warp direction)
embedded length l_e: 114 mm | 3 × y_{nm}

high strength concrete			
composition:	HSC-5.6mm		
concrete age at material test:	8 d		
compressive strength			
$f_{c,cycl}$ [MPa]:	75.7	$f_{c,cube}$ [MPa]:	105.2
Young's modulus			
E_{cm} [MPa]:	44,587		
tensile strength			
$f_{ct,sp}$ [MPa]:	5.3	$f_{ctm,calc}$ [MPa]:	4.8



geometry of specimen	
width b [mm]:	38
thickness t [mm]:	30
concrete coverage c [mm]:	13.5

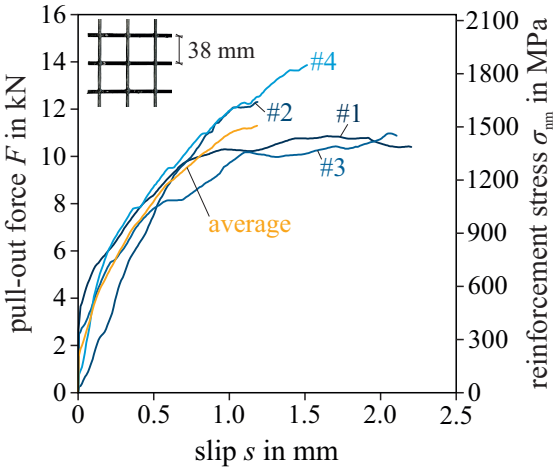
test results					
test number	-1	-2	-3	(-4)	-5
concrete age at test [d]			8		
maximum load F_{max} [kN]	8.65	7.96	8.06	(1.94)	9.20
at slip s [mm]	1.00	1.63	1.56	(0.77)	2.56
type of failure	SP	TR	SP	(-)	TR
load at slip of 0.2 mm $F_{0.2}$ [kN]	4.85	4.16	1.36	(1.59)	3.90
load at occurrence of slip at unloaded side F_{unl} [kN]	4.77	6.30	5.38	(-)	6.68

SPOc-CG1-HSC-0°-250

reinforcement: CG1 (solidian GRID Q95-CCE-38)
direction of investigation: 0° (warp direction)
embedded length l_e: 250 mm | 6.6 × y_{nm}

high strength concrete	
composition:	HSC-5.6mm
concrete age at material test:	8 d
compressive strength	
$f_{c,cycl}$ [MPa]: 75.7	$f_{c,cube}$ [MPa]: 105.2
Young's modulus	
E_{cm} [MPa]: 44,587	
tensile strength	
$f_{ct,sp}$ [MPa]: 5.3	$f_{ctm,calc}$ [MPa]: 4.8

geometry of specimen	
width b [mm]:	38
thickness t [mm]:	30
concrete coverage c [mm]:	13.5

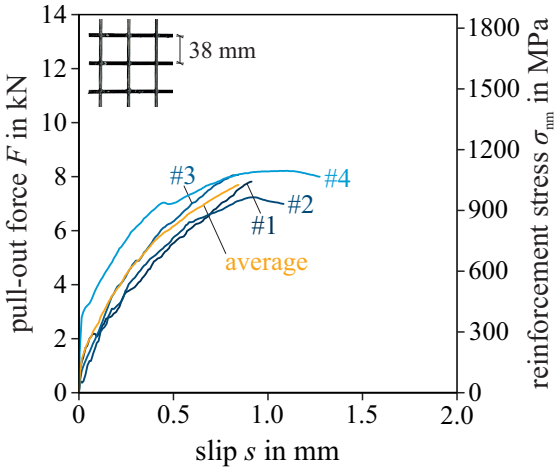


test results					
test number	-1	-2	-3	-4	(-5)
concrete age at test [d]			8		
maximum load F_{max} [kN]	10.86	12.55	10.97	13.88	(11.07)
at slip s [mm]	1.65	1.26	2.05	1.51	(0.22)
type of failure	SP	TR	SP	TR	(-)
load at slip of 0.2 mm $F_{0.2}$ [kN]	5.95	2.89	5.43	6.02	(8.43)
load at occurrence of slip at unloaded side F_{unl} [kN]	10.83	11.88	10.59	13.83	(-)

SPOc-CG1-NSC-90°-114

reinforcement: CG1 (solidian GRID Q95-CCE-38)
direction of investigation: 90° (weft direction)
embedded length l_e: 114 mm | 3 × y_{nm}

normal strength concrete			
composition:	NSC-5.6mm		
concrete age at material test:	12 d		
compressive strength			
$f_{c,cycl}$ [MPa]:	37.4	$f_{c,cube}$ [MPa]:	45.6
Young's modulus			
E_{cm} [MPa]:	29,755		
tensile strength			
$f_{ct,sp}$ [MPa]:	3.3	$f_{ctm,calc}$ [MPa]:	3.0



geometry of specimen	
width b [mm]:	38
thickness t [mm]:	30
concrete coverage c [mm]:	13.5

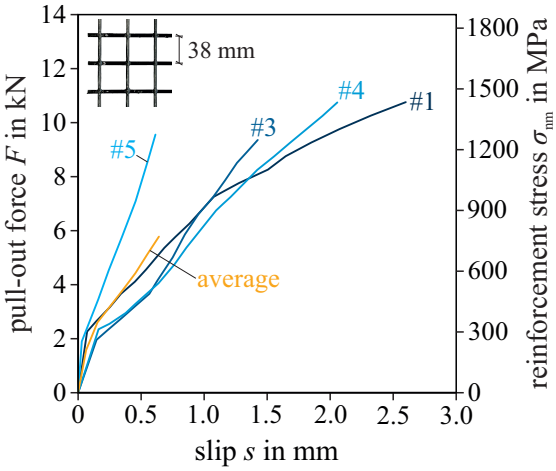
test results					
test number	-1	-2	-3	-4	(-5)
concrete age at test [d]			11		
maximum load F_{max} [kN]	7.84	7.24	8.07	8.21	(8.08)
at slip s [mm]	0.92	0.92	0.85	1.05	(0.42)
type of failure	SP	SP	SP	SP	(SP)
load at slip of 0.2 mm $F_{0.2}$ [kN]	3.03	3.18	3.85	5.12	(6.91)
load at occurrence of slip at unloaded side F_{unl} [kN]	7.11	6.19	6.15	6.98	(-)

SPOc-CG1-HSC-90°-114

reinforcement: CG1 (solidian GRID Q95-CCE-38)
direction of investigation: 90° (weft direction)
embedded length l_e: 114 mm | 3 × y_{nm}

high strength concrete			
composition:	HSC-5.6mm		
concrete age at material test:	8 d		
compressive strength			
$f_{c,cycl}$ [MPa]:	75.7	$f_{c,cube}$ [MPa]:	105.2
Young's modulus			
E_{cm} [MPa]:	44,587		
tensile strength			
$f_{ct,sp}$ [MPa]:	5.3	$f_{ctm,calc}$ [MPa]:	4.8

geometry of specimen	
width b [mm]:	38
thickness t [mm]:	30
concrete coverage c [mm]:	13.5

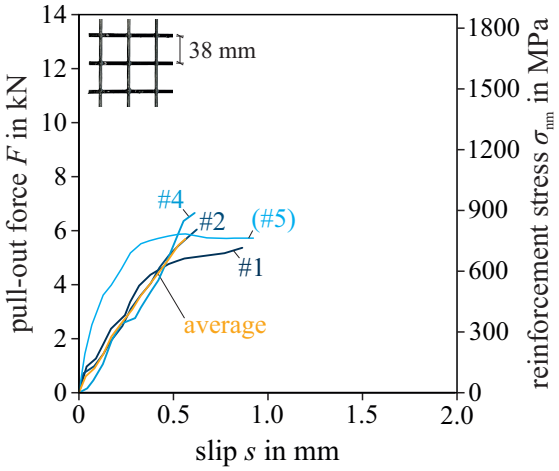


test results					
test number	-1	(-2)	-3	-4	-5
concrete age at test [d]			14		
maximum load F_{max} [kN]	10.76	(8,48)	9.36	10.75	9.69
at slip s [mm]	2.60	(-0.03)	1.43	2.06	0.59
type of failure	SP	(SP)	SP	SP	SP
load at slip of 0.2 mm $F_{0.2}$ [kN]	2.76	(0.30)	1.96	2.35	3.86
load at occurrence of slip at unloaded side F_{unl} [kN]	5.50	(-)	8.74	6.76	9.65

SPOc-CG1-NSC-0°-114-16mm

reinforcement: CG1 (solidian GRID Q95-CCE-38)
direction of investigation: 0° (warp direction)
embedded length l_e: 114 mm | 3 × y_{nm}

normal strength concrete			
composition:	NSC-16mm		
concrete age at material test:	11 d		
compressive strength			
$f_{c,cycl}$ [MPa]:	32.8	$f_{c,cube}$ [MPa]:	41.5
Young's modulus			
E_{cm} [MPa]:	28,412		
tensile strength			
$f_{ct,sp}$ [MPa]:	2.8	$f_{ctm,calc}$ [MPa]:	2.5



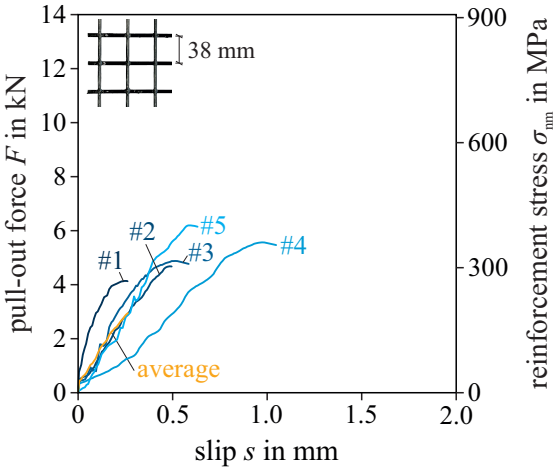
geometry of specimen	
width b [mm]:	38
thickness t [mm]:	50
concrete coverage c [mm]:	23.5

test results					
test number	-1	-2	(-3)	-4	-5
concrete age at test [d]			11		
maximum load F_{max} [kN]	5.57	6.39	(9.47)	7.16	5.89
at slip s [mm]	1.01	0.70	(-17.61)	0.66	0.56
type of failure	SP	SP	(SP)	SP	SP
load at slip of 0.2 mm $F_{0.2}$ [kN]	2.57	2.22	(5.99)	2.16	4.26
load at occurrence of slip at unloaded side F_{unl} [kN]	4.37	4.26	(-)	4,08	4.77

SPOc-CG1sc-NSC-0°-38

reinforcement: CG1sc (solidian ANTICRACK Q95-CCE-38)
direction of investigation: 0° (warp direction)
embedded length l_e: 38 mm | 1 × y_{nm}

normal strength concrete	
composition:	NSC-5.6mm
concrete age at material test:	24 d
compressive strength	
$f_{c,cycl}$ [MPa]: 34.5	$f_{c,cube}$ [MPa]: 43.2
Young's modulus	
E_{cm} [MPa]: 28,428	
tensile strength	
$f_{ct,sp}$ [MPa]: 2.9	$f_{ctm,calc}$ [MPa]: 2.6



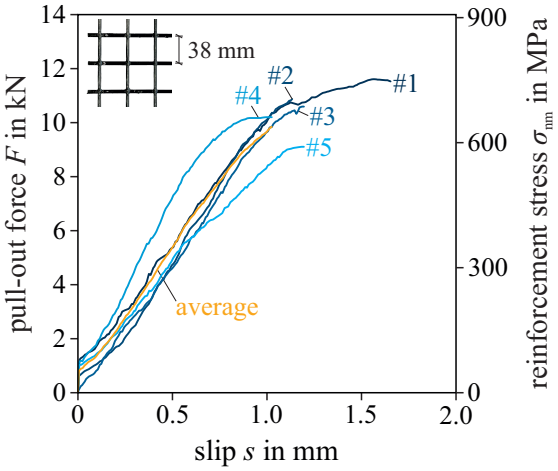
geometry of specimen	
width b [mm]:	38
thickness t [mm]:	30
concrete coverage c [mm]:	13.5

test results					
test number	-1	-2	-3	-4	-5
concrete age at test [d]			23		
maximum load F_{max} [kN]	4.14	4.69	4.88	5.57	6.20
at slip s [mm]	0.26	0.49	0.50	0.98	0.58
type of failure	SP	SP	SP	SP	SP
load at slip of 0.2 mm $F_{0.2}$ [kN]	4.02	2.31	2.84	0.95	1.92
load at occurrence of slip at unloaded side F_{unl} [kN]	3.31	3.62	4.33	3.18	4.84

SPOc-CG1sc-NSC-0°-114

reinforcement: CG1sc (solidian ANTICRACK Q95-CCE-38)
direction of investigation: 0° (warp direction)
embedded length l_e: 114 mm | 3 × y_{nm}

normal strength concrete			
composition:	NSC-5.6mm		
concrete age at material test:	24 d		
compressive strength			
$f_{c,cycl}$ [MPa]:	34.5	$f_{c,cube}$ [MPa]:	43.2
Young's modulus			
E_{cm} [MPa]:	28,428		
tensile strength			
$f_{ct,sp}$ [MPa]:	2.9	$f_{ctm,calc}$ [MPa]:	2.6



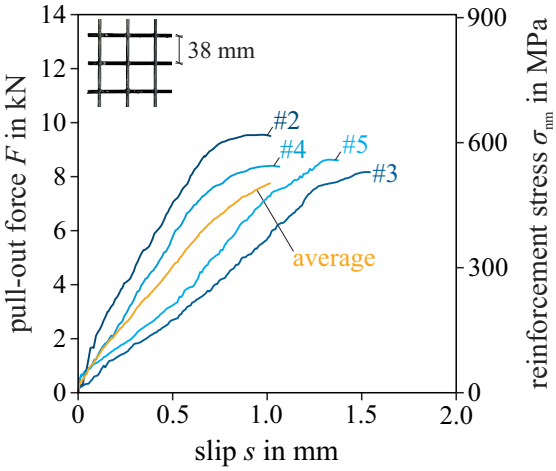
geometry of specimen	
width b [mm]:	38
thickness t [mm]:	30
concrete coverage c [mm]:	13.5

test results					
test number	-1	-2	-3	-4	-5
concrete age at test [d]			23		
maximum load F_{max} [kN]	11.61	10.87	10.59	10.20	9.11
at slip s [mm]	1.55	1.12	1.18	0.98	1.18
type of failure	TR	TR	SP	SP	SP
load at slip of 0.2 mm $F_{0.2}$ [kN]	2.46	1.68	1.99	2.94	2.15
load at occurrence of slip at unloaded side F_{unl} [kN]	11.50	10.98	10.68	10.31	9.20

SPOc-CG1sc-NSC-0°-114-w/o

reinforcement: CG1sc (solidian ANTICRACK Q95-CCE-38) with removed transverse fibre strands
direction of investigation: 0° (warp direction)
embedded length l_e: 114 mm | 3 × y_{nm}

normal strength concrete	
composition:	NSC-5.6mm
concrete age at material test:	24 d
compressive strength	
$f_{c,cycl}$ [MPa]: 34.5	$f_{c,cube}$ [MPa]: 43.2
Young's modulus	
E_{cm} [MPa]: 28,428	
tensile strength	
$f_{ct,sp}$ [MPa]: 2.9	$f_{ctm,calc}$ [MPa]: 2.6



geometry of specimen	
width b [mm]:	38
thickness t [mm]:	30
concrete coverage c [mm]:	13.5

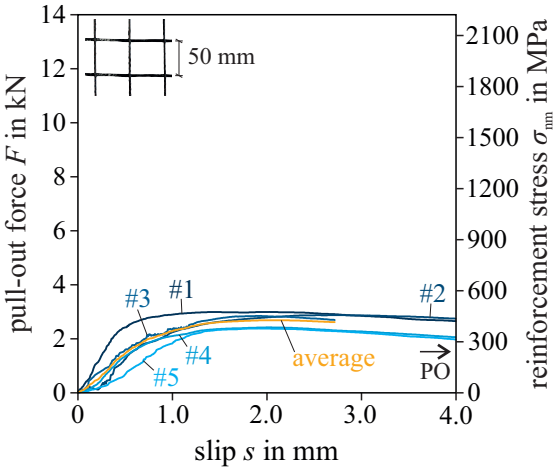
test results					
test number	(-1)	-2	-3	-4	-5
concrete age at test [d]			23		
maximum load F_{max} [kN]	(0.44)	9.55	8.17	8.40	8.63
at slip s [mm]	(0.25)	0.97	1.52	1.03	1.32
type of failure	(TR)	SP	SP	SP	SP
load at slip of 0.2 mm $F_{0.2}$ [kN]	(0.41)	3.52	1.26	2.33	1.63
load at occurrence of slip at unloaded side F_{unl} [kN]	(-)	8.86	7.75	7.23	8.50

SPOc-CG2-NSC-0°-50

reinforcement: CG2 (SIT grid 050)
direction of investigation: 0° (warp direction)
embedded length l_e: 50 mm | 1 × y_{nm}

normal strength concrete			
composition:	NSC-5.6mm		
concrete age at material test:	24 d		
compressive strength			
$f_{c,cycl}$ [MPa]:	34.5	$f_{c,cube}$ [MPa]:	43.2
Young's modulus			
E_{cm} [MPa]:	28,428		
tensile strength			
$f_{ct,sp}$ [MPa]:	2.9	$f_{ctm,calc}$ [MPa]:	2.6

geometry of specimen	
width b [mm]:	50
thickness t [mm]:	30
concrete coverage c [mm]:	14

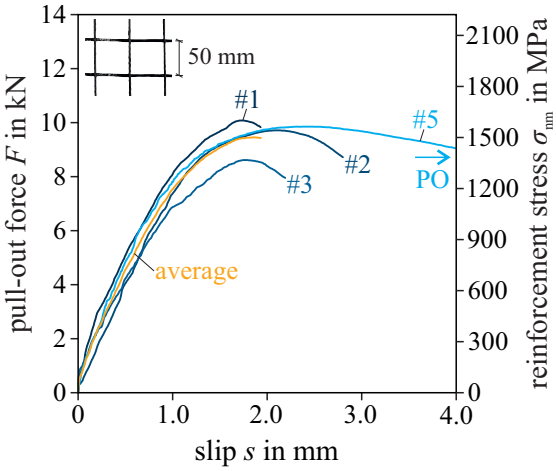


test results					
test number	-1	-2	-3	-4	-5
concrete age at test [d]			24		
maximum load F_{max} [kN]	2.99	2.88	2.85	2.42	2.38
at slip s [mm]	2.00	2.74	1.89	2.00	1.91
type of failure	PO	PO	PO	PO	PO
load at slip of 0.2 mm $F_{0.2}$ [kN]	1.08	0.14	0.69	0.29	0.16
load at occurrence of slip at unloaded side F_{unl} [kN]	1.21	1.05	0.78	0.92	0.76

SPOc-CG2-NSC-0°-150

reinforcement: CG2 (SIT grid 050)
direction of investigation: 0° (warp direction)
embedded length l_e: 150 mm | 3 × y_{nm}

normal strength concrete	
composition:	NSC-5.6mm
concrete age at material test:	12 d
compressive strength	
$f_{c,cycl}$ [MPa]: 37.4	$f_{c,cube}$ [MPa]: 45.6
Young's modulus	
E_{cm} [MPa]: 29,755	
tensile strength	
$f_{ct,sp}$ [MPa]: 3.3	$f_{ctm,calc}$ [MPa]: 3.0



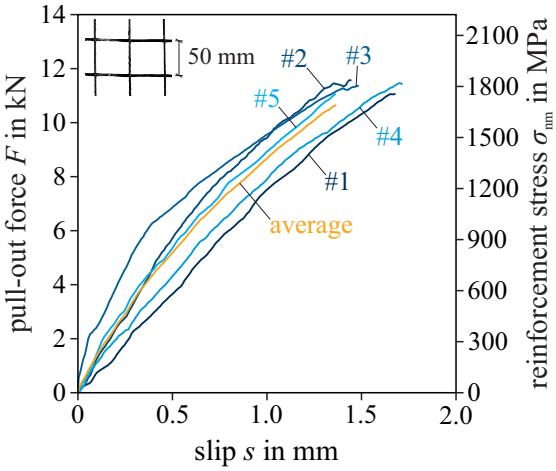
geometry of specimen	
width b [mm]:	50
thickness t [mm]:	30
concrete coverage c [mm]:	14

test results					
test number	-1	-2	-3	(-4)	-5
concrete age at test [d]			13		
maximum load F_{max} [kN]	10.08	9.72	8.61	(10.24)	9.85
at slip s [mm]	1.70	2.09	1.75	(0.56)	2.29
type of failure	SP	SP	SP	(SP)	PO
load at slip of 0.2 mm $F_{0.2}$ [kN]	2.99	1.65	2.25	(7.69)	2.30
load at occurrence of slip at unloaded side F_{unl} [kN]	8.48	8.40	7.00	(-)	8.01

SPOc-CG2-NSC-0°-250

reinforcement: CG2 (SIT grid 050)
direction of investigation: 0° (warp direction)
embedded length l_e: 250 mm | 5 × y_{nm}

normal strength concrete			
composition:	NSC-5.6mm		
concrete age at material test:	12 d		
compressive strength			
$f_{c,cycl}$ [MPa]:	37.4	$f_{c,cube}$ [MPa]:	45.6
Young's modulus			
E_{cm} [MPa]:	29,755		
tensile strength			
$f_{ct,sp}$ [MPa]:	3.3	$f_{ctm,calc}$ [MPa]:	3.0



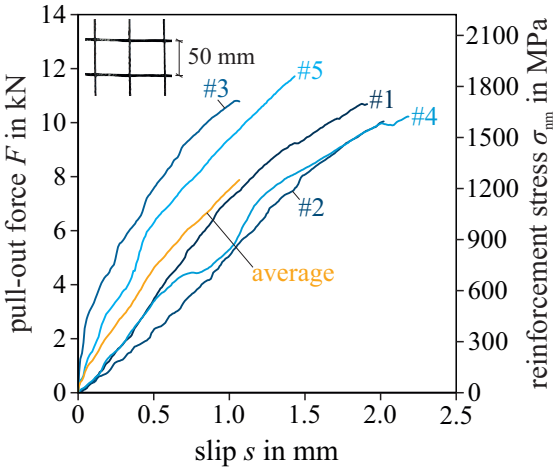
geometry of specimen	
width b [mm]:	50
thickness t [mm]:	30
concrete coverage c [mm]:	14

test results					
test number	-1	-2	-3	-4	-5
concrete age at test [d]			12		
maximum load F_{max} [kN]	11.08	11.60	11.37	11.48	11.05
at slip s [mm]	1.68	1.44	1.48	1.70	1.36
type of failure	TR	TR	TR	TR	TR
load at slip of 0.2 mm $F_{0.2}$ [kN]	1.35	2.33	3.82	1.98	2.71
load at occurrence of slip at unloaded side F_{unl} [kN]	7.44	7.44	6.44	9.11	8.00

SPOc-CG2-NSC-0°-500

reinforcement: CG2 (SIT grid 050)
direction of investigation: 0° (warp direction)
embedded length l_e: 500 mm | 10 × y_{nm}

normal strength concrete			
composition:	NSC-5.6mm		
concrete age at material test:	12 d		
compressive strength			
$f_{c,cycl}$ [MPa]:	37.4	$f_{c,cube}$ [MPa]:	45.6
Young's modulus			
E_{cm} [MPa]:	29,755		
tensile strength			
$f_{ct,sp}$ [MPa]:	3.3	$f_{ctm,calc}$ [MPa]:	3.0



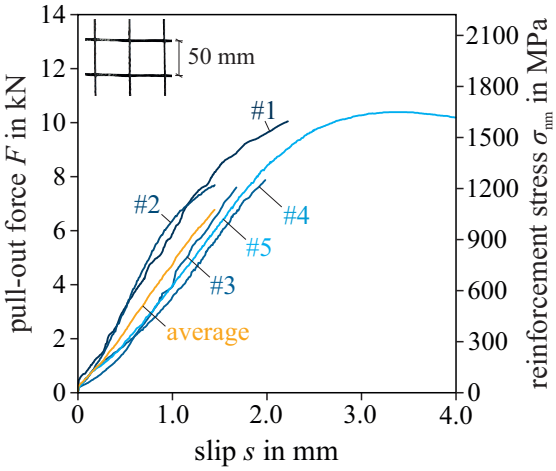
geometry of specimen	
width b [mm]:	50
thickness t [mm]:	30
concrete coverage c [mm]:	14

test results					
test number	-1	-2	-3	-4	-5
concrete age at test [d]			12		
maximum load F_{max} [kN]	10.70	10.05	10.81	10.23	11.73
at slip s [mm]	1.88	2.02	1.04	2.18	1.43
type of failure	TR	TR	TR	TR	TR
load at slip of 0.2 mm $F_{0.2}$ [kN]	1.12	0.81	4.38	1.30	3.01
load at occurrence of slip at unloaded side F_{unl} [kN]	6.88	8.12	9.06	7.64	10.61

SPOc-CG2-NSC-0°-150-w/o

reinforcement: CG2 (SIT grid 050) with removed transverse fibre strands
direction of investigation: 0° (warp direction)
embedded length l_e: 150 mm | 3 × y_{nm}

normal strength concrete			
composition:	NSC-5.6mm		
concrete age at material test:	24 d		
compressive strength			
$f_{c,cycl}$ [MPa]:	34.5	$f_{c,cube}$ [MPa]:	43.2
Young's modulus			
E_{cm} [MPa]:	28,428		
tensile strength			
$f_{ct,sp}$ [MPa]:	2.9	$f_{ctm,calc}$ [MPa]:	2.6



geometry of specimen	
width b [mm]:	50
thickness t [mm]:	30
concrete coverage c [mm]:	14

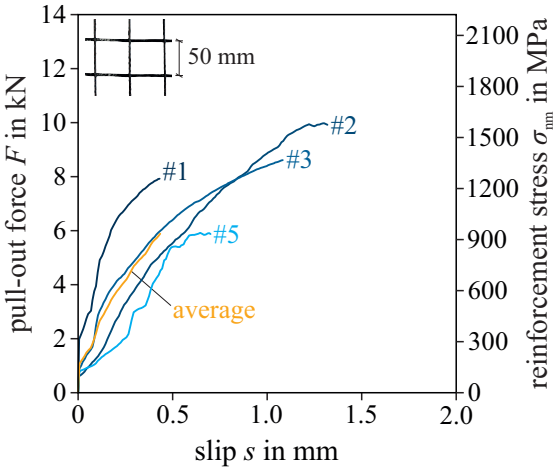
test results					
test number	-1	-2	-3	-4	-5
concrete age at test [d]			24		
maximum load F_{max} [kN]	10.06	7.70	7.62	7.91	10.39
at slip s [mm]	2.22	1.45	1.68	1.99	3.29
type of failure	SP	TR	SP	TR	PO
load at slip of 0.2 mm $F_{0.2}$ [kN]	1.27	1.10	0.58	0.93	0.91
load at occurrence of slip at unloaded side F_{unl} [kN]	7.05	5.24	6.78	5.04	8.03

SPOc-CG2-HSC-0°-150

reinforcement: CG2 (SIT grid 050)
direction of investigation: 0° (warp direction)
embedded length l_e: 150 mm | 3 × y_{nm}

high strength concrete			
composition:	HSC-5.6mm		
concrete age at material test:	8 d		
compressive strength			
$f_{c,cycl}$ [MPa]:	75.7	$f_{c,cube}$ [MPa]:	105.2
Young's modulus			
E_{cm} [MPa]:	44,587		
tensile strength			
$f_{ct,sp}$ [MPa]:	5.3	$f_{ctm,calc}$ [MPa]:	4.8

geometry of specimen	
width b [mm]:	50
thickness t [mm]:	30
concrete coverage c [mm]:	14



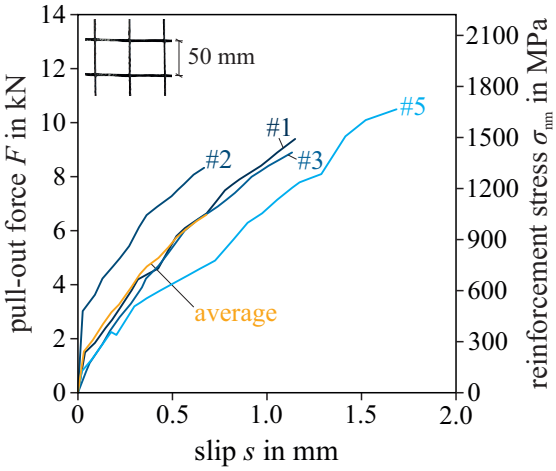
test results					
test number	-1	-2	-3	(-4)	-5
concrete age at test [d]			10		
maximum load F_{max} [kN]	7.93	9.98	8.63	(10.31)	5.94
at slip s [mm]	0.43	1.30	1.08	(0.47)	0.69
type of failure	TR	TR	TR	(TR)	TR
load at slip of 0.2 mm $F_{0.2}$ [kN]	6.28	2.73	4.11	(9.93)	1.69
load at occurrence of slip at unloaded side F_{unl} [kN]	6.30	7.41	5.63	(-)	5.38

SPOc-CG2-HSC-0°-250

reinforcement: CG2 (SIT grid 050)
direction of investigation: 0° (warp direction)
embedded length l_e: 250 mm | 5 × y_{nm}

high strength concrete			
composition:	HSC-5.6mm		
concrete age at material test:	8 d		
compressive strength			
$f_{c,cycl}$ [MPa]:	75.7	$f_{c,cube}$ [MPa]:	105.2
Young's modulus			
E_{cm} [MPa]:	44,587		
tensile strength			
$f_{ct,sp}$ [MPa]:	5.3	$f_{ctm,calc}$ [MPa]:	4.8

geometry of specimen	
width b [mm]:	50
thickness t [mm]:	30
concrete coverage c [mm]:	14

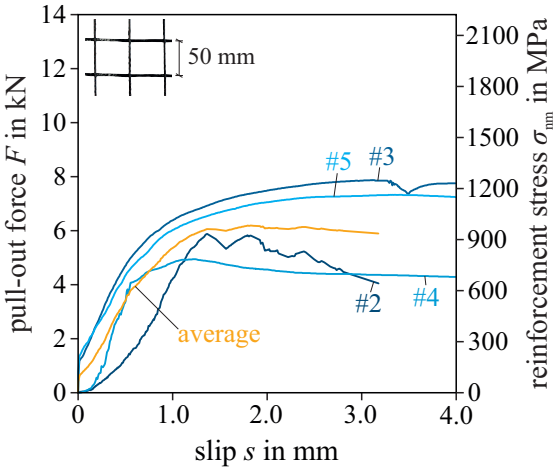


test results					
test number	-1	-2	-3	(-4)	-5
concrete age at test [d]			10		
maximum load F_{max} [kN]	9.40	8.48	8.90	(1.94)	10.49
at slip s [mm]	1.15	0.69	1.13	(0.41)	1.69
type of failure	TR	TR	TR	(TR)	TR
load at slip of 0.2 mm $F_{0.2}$ [kN]	2.70	4.68	2.30	(0.38)	2.79
load at occurrence of slip at unloaded side F_{unl} [kN]	4.76	8.80	9.00	(-)	8.30

SPOc-CG2-NSC-90°-150

reinforcement: CG2 (SIT grid 050)
direction of investigation: 90° (weft direction)
embedded length l_e: 150 mm | 3 × y_{nm}

normal strength concrete			
composition:	NSC-5.6mm		
concrete age at material test:	19 d		
compressive strength			
$f_{c,cycl}$ [MPa]:	36.9	$f_{c,cube}$ [MPa]:	48.4
Young's modulus			
E_{cm} [MPa]:	30,234		
tensile strength			
$f_{ct,sp}$ [MPa]:	3.0	$f_{ctm,calc}$ [MPa]:	2.7



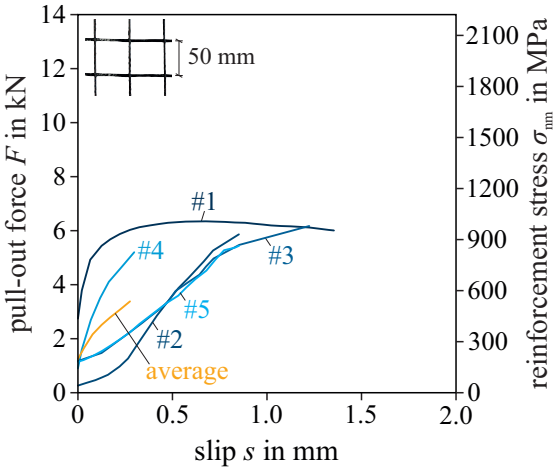
geometry of specimen	
width b [mm]:	50
thickness t [mm]:	30
concrete coverage c [mm]:	14

test results					
test number	(-1)	-2	-3	-4	-5
concrete age at test [d]			19		
maximum load F_{max} [kN]	(3.57)	5.89	7.87	4.95	7.33
at slip s [mm]	(10.05)	1.36	3.13	1.23	3.29
type of failure	(PO)	PO	PO	PO	PO
load at slip of 0.2 mm $F_{0.2}$ [kN]	(0.07)	0.29	2.59	0.52	2.51
load at occurrence of slip at unloaded side F_{unl} [kN]	(-)	5.80	4.94	3.90	4.94

SPOc-CG2-HSC-90°-150

reinforcement: CG2 (SIT grid 050)
direction of investigation: 90° (weft direction)
embedded length l_e: 150 mm | 3 × y_{nm}

high strength concrete			
composition:	HSC-5.6mm		
concrete age at material test:	8 d		
compressive strength			
$f_{c,cycl}$ [MPa]:	75.7	$f_{c,cube}$ [MPa]:	105.2
Young's modulus			
E_{cm} [MPa]:	44,587		
tensile strength			
$f_{ct,sp}$ [MPa]:	5.3	$f_{ctm,calc}$ [MPa]:	4.8



geometry of specimen	
width b [mm]:	50
thickness t [mm]:	30
concrete coverage c [mm]:	14

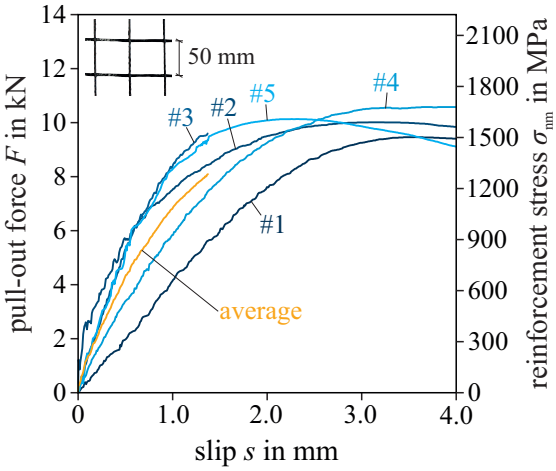
test results

test number	-1	-2	-3	-4	-5
concrete age at test [d]			10		
maximum load F_{max} [kN]	6.34	5.86	6.17	5.20	5.45
at slip s [mm]	0.57	0.85	1.22	0.30	0.85
type of failure	PO	PO	PO	PO	PO
load at slip of 0.2 mm $F_{0.2}$ [kN]	5.79	0.66	1.47	4.10	1.89
load at occurrence of slip at unloaded side F_{unl} [kN]	5.00	6.00	5.50	5.50	4.46

SPOc-CG2-NSC-0°-150-16mm

reinforcement: CG2 (SIT grid 050)
direction of investigation: 0° (warp direction)
embedded length l_e: 150 mm | 3 × y_{nm}

normal strength concrete	
composition:	NSC-16mm
concrete age at material test:	11 d
compressive strength	
$f_{c,cycl}$ [MPa]: 32.8	$f_{c,cube}$ [MPa]: 41.5
Young's modulus	
E_{cm} [MPa]: 28,412	
tensile strength	
$f_{ct,sp}$ [MPa]: 2.8	$f_{ctm,calc}$ [MPa]: 2.5



geometry of specimen	
width b [mm]:	50
thickness t [mm]:	30
concrete coverage c [mm]:	14

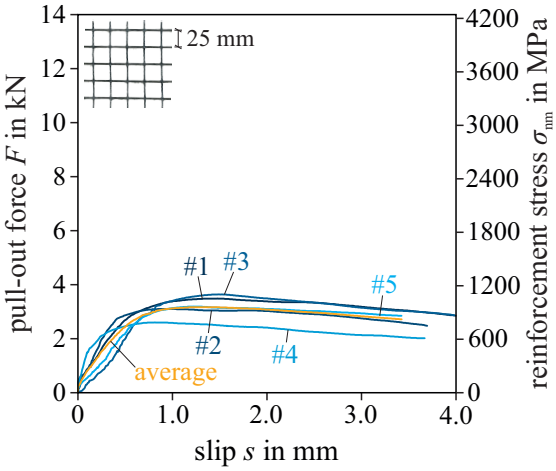
test results

test number	-1	-2	-3	-4	-5
concrete age at test [d]			12		
maximum load F_{max} [kN]	9.46	10.01	9.60	10.58	10.13
at slip s [mm]	3.53	3.04	1.37	3.63	2.24
type of failure	PO	PO	TR	PO	PO
load at slip of 0.2 mm $F_{0.2}$ [kN]	0.76	3.34	2.18	1.62	2.20
load at occurrence of slip at unloaded side F_{unl} [kN]	5.14	3.80	5.68	6.82	6.55

SPOc-CG3-NSC-0°-75

reinforcement: CG3 (Hitexbau HTC 25/25-80-UWX)
direction of investigation: 0° (warp direction)
embedded length l_e: 75 mm | 3 × y_{nm}

normal strength concrete			
composition:	NSC-5.6mm		
concrete age at material test:	24 d		
compressive strength			
$f_{c,cycl}$ [MPa]:	34.5	$f_{c,cube}$ [MPa]:	43.2
Young's modulus			
E_{cm} [MPa]:	28,428		
tensile strength			
$f_{ct,sp}$ [MPa]:	3.0	$f_{ctm,calc}$ [MPa]:	2.7



geometry of specimen	
width b [mm]:	25
thickness t [mm]:	30
concrete coverage c [mm]:	14

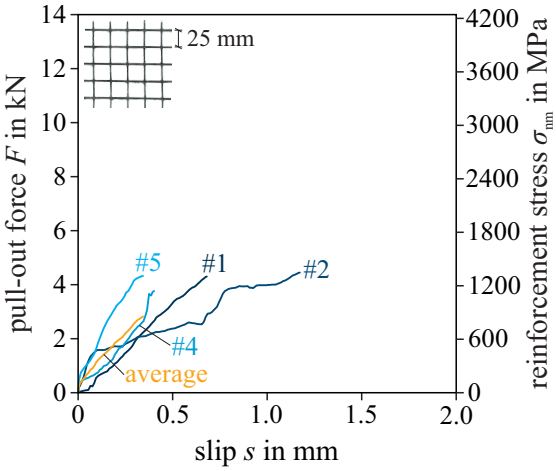
test results					
test number	-1	-2	-3	-4	-5
concrete age at test [d]			20		
maximum load F_{max} [kN]	3.49	3.11	3.64	2.61	3.19
at slip s [mm]	1.43	0.94	1.46	0.79	1.21
type of failure	PO	PO	PO	PO	PO
load at slip of 0.2 mm $F_{0.2}$ [kN]	1.30	1.56	0.70	1.91	0.90
load at occurrence of slip at unloaded side F_{unl} [kN]	2.90	2.90	2.94	2.29	2.86

SPOc-CG3-NSC-0°-250

reinforcement: CG3 (Hitexbau HTC 25/25-80-UWX)
direction of investigation: 0° (warp direction)
embedded length l_e: 250 mm | 10 × y_{nm}

normal strength concrete			
composition:	NSC-5.6mm		
concrete age at material test:	19 d		
compressive strength			
$f_{c,cycl}$ [MPa]:	36.9	$f_{c,cube}$ [MPa]:	48.4
Young's modulus			
E_{cm} [MPa]:	30,234		
tensile strength			
$f_{ct,sp}$ [MPa]:	3.0	$f_{ctm,calc}$ [MPa]:	2.7

geometry of specimen	
width b [mm]:	25
thickness t [mm]:	30
concrete coverage c [mm]:	14

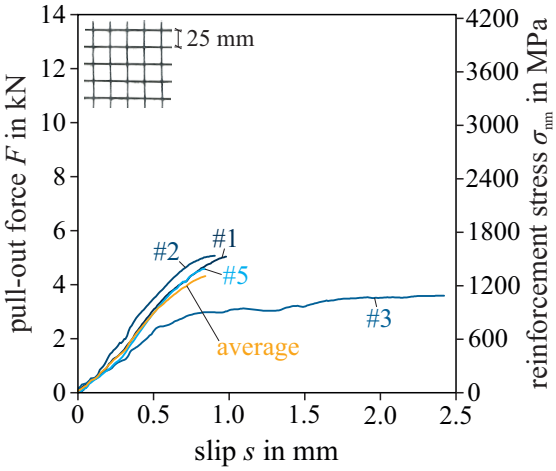


test results					
test number	-1	-2	(-3)	-4	-5
concrete age at test [d]			19		
maximum load F_{max} [kN]	4.32	4.47	(4.19)	4.10	4.33
at slip s [mm]	0.68	1.17	(-1.00)	0.39	0.35
type of failure	TR	TR	(TR)	TR	TR
load at slip of 0.2 mm $F_{0.2}$ [kN]	1.09	1.72	(-)	1.37	3.13
load at occurrence of slip at unloaded side F_{unl} [kN]	4.47	4.68	(-)	2.75	4.18

SPOc-CG3-NSC-0°-500

reinforcement: CG3 (Hitexbau HTC 25/25-80-UWX)
direction of investigation: 0° (warp direction)
embedded length l_e: 500 mm | 20 × y_{nm}

normal strength concrete			
composition:	NSC-5.6mm		
concrete age at material test:	19 d		
compressive strength			
$f_{c,cycl}$ [MPa]:	36.9	$f_{c,cube}$ [MPa]:	48.4
Young's modulus			
E_{cm} [MPa]:	30,234		
tensile strength			
$f_{ct,sp}$ [MPa]:	3.0	$f_{ctm,calc}$ [MPa]:	2.7



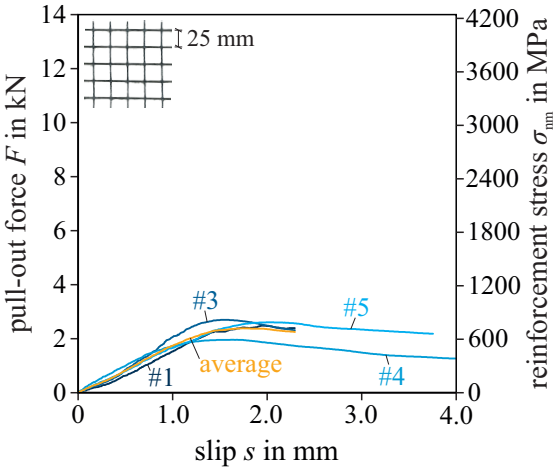
geometry of specimen	
width b [mm]:	25
thickness t [mm]:	30
concrete coverage c [mm]:	14

test results					
test number	-1	-2	-3	(-4)	-5
concrete age at test [d]			19		
maximum load F_{max} [kN]	5.04	5.07	3.59	(3.52)	4.58
at slip s [mm]	0.98	0.91	2.39	(0.56)	0.83
type of failure	TR	SP	TR	(TR)	SP
load at slip of 0.2 mm $F_{0.2}$ [kN]	0.96	1.36	0.83	(0.81)	0.83
load at occurrence of slip at unloaded side F_{unl} [kN]	4.17	5.14	2.92	(-)	4.30

SPOc-CG3-NSC-0°-75-w/o

reinforcement: CG3 (Hitexbau HTC 25/25-80-UWX) with removed transverse fibre strands
direction of investigation: 0° (warp direction)
embedded length l_e: 75 mm | 3 × y_{nm}

normal strength concrete	
composition:	NSC-5.6mm
concrete age at material test:	24 d
compressive strength	
$f_{c,cycl}$ [MPa]: 34.5	$f_{c,cube}$ [MPa]: 43.2
Young's modulus	
E_{cm} [MPa]: 28,428	
tensile strength	
$f_{ct,sp}$ [MPa]: 2.9	$f_{ctm,calc}$ [MPa]: 2.6



geometry of specimen	
width b [mm]:	25
thickness t [mm]:	30
concrete coverage c [mm]:	14

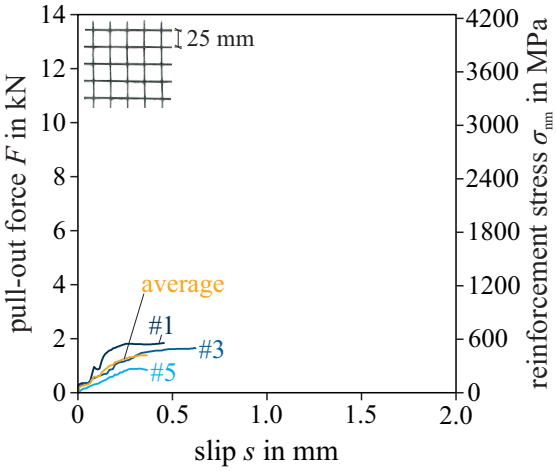
test results

test number	-1	(-2)	-3	-4	-5
concrete age at test [d]			24		
maximum load F_{max} [kN]	2.48	(-)	2.70	1.96	2.61
at slip s [mm]	1.95	(-)	1.54	1.60	1.99
type of failure	PO	(-)	PO	PO	PO
load at slip of 0.2 mm $F_{0.2}$ [kN]	0.20	(-)	0.26	0.43	0.32
load at occurrence of slip at unloaded side F_{unl} [kN]	0.96	(-)	1.23	0.79	0.82

SPOc-CG3-HSC-0°-75

reinforcement: CG3 (Hitexbau HTC 25/25-80-UWX)
direction of investigation: 0° (warp direction)
embedded length l_e: 75 mm | 3 × y_{nm}

high strength concrete			
composition:	HSC-5.6mm		
concrete age at material test:	8 d		
compressive strength			
$f_{c,cycl}$ [MPa]:	75.7	$f_{c,cube}$ [MPa]:	105.2
Young's modulus			
E_{cm} [MPa]:	44,587		
tensile strength			
$f_{ct,sp}$ [MPa]:	5.3	$f_{ctm,calc}$ [MPa]:	4.8



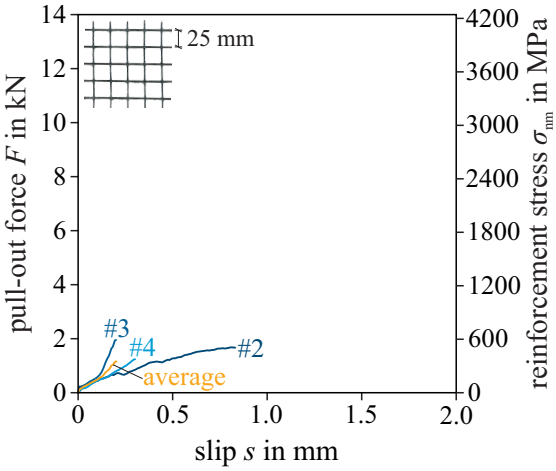
geometry of specimen	
width b [mm]:	25
thickness t [mm]:	30
concrete coverage c [mm]:	14

test results					
test number	-1	(-2)	-3	(-4)	-5
concrete age at test [d]			14		
maximum load F_{max} [kN]	1.85	(0.91)	1.67	(0.46)	0.89
at slip s [mm]	0.45	(0.05)	0.61	(0.32)	0.32
type of failure	TR	(-)	TR	(-)	TR
load at slip of 0.2 mm $F_{0.2}$ [kN]	1.69	(0.90)	1.05	(0.27)	0.66
load at occurrence of slip at unloaded side F_{unl} [kN]	1.95	(-)	1.11	(-)	1.09

SPOc-CG3-HSC-0°-250

reinforcement: CG3 (Hitexbau HTC 25/25-80-UWX)
direction of investigation: 0° (warp direction)
embedded length l_e: 250 mm | 10 × y_{nm}

high strength concrete			
composition:	HSC-5.6mm		
concrete age at material test:	8 d		
compressive strength			
$f_{c,cycl}$ [MPa]:	75.7	$f_{c,cube}$ [MPa]:	105.2
Young's modulus			
E_{cm} [MPa]:	44,587		
tensile strength			
$f_{ct,sp}$ [MPa]:	5.3	$f_{ctm,calc}$ [MPa]:	4.8



geometry of specimen	
width b [mm]:	25
thickness t [mm]:	30
concrete coverage c [mm]:	14

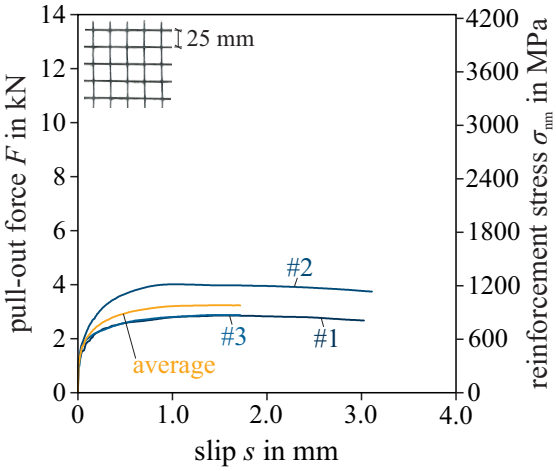
test results

test number	(-1)	-2	-3	-4	(-5)
concrete age at test [d]			14		
maximum load F_{max} [kN]	(0.66)	1.68	1.96	1.27	(-)
at slip s [mm]	(0.29)	0.81	0.20	0.30	(-)
type of failure	(-)	TR	TR	TR	(-)
load at slip of 0.2 mm $F_{0.2}$ [kN]	(0.54)	0.71	1.96	0.79	(-)
load at occurrence of slip at unloaded side F_{unl} [kN]	(-)	1.78	2.23	1.55	(-)

SPOc-CG3-NSC-90°-75

reinforcement: CG3 (Hitexbau HTC 25/25-80-UWX)
direction of investigation: 90° (weft direction)
embedded length l_e: 75 mm | 3 × y_{nm}

normal strength concrete			
composition:	NSC-5.6mm		
concrete age at material test:	19 d		
compressive strength			
$f_{c,cycl}$ [MPa]:	36.9	$f_{c,cube}$ [MPa]:	48.4
Young's modulus			
E_{cm} [MPa]:	30,234		
tensile strength			
$f_{ct,sp}$ [MPa]:	3.0	$f_{ctm,calc}$ [MPa]:	2.7



geometry of specimen	
width b [mm]:	25
thickness t [mm]:	30
concrete coverage c [mm]:	14

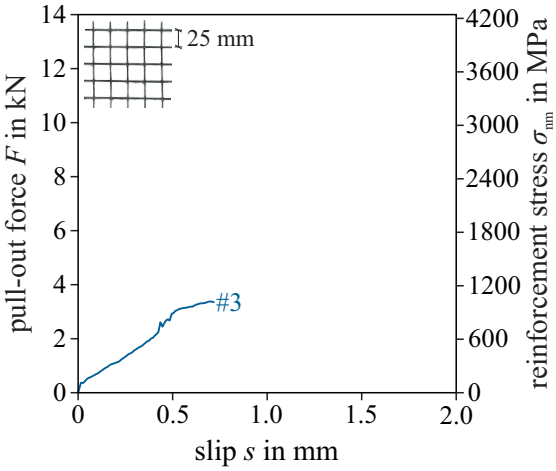
test results

test number	-1	-2	-3	(-4)	(-5)
concrete age at test [d]			20		
maximum load F_{max} [kN]	2.86	4.02	2.88	(1.05)	(1.92)
at slip s [mm]	1.54	1.04	1.42	(0.27)	(0.22)
type of failure	PO	PO	PO	(-)	(-)
load at slip of 0.2 mm $F_{0.2}$ [kN]	2.23	2.88	2.22	(0.99)	(1.86)
load at occurrence of slip at unloaded side F_{unl} [kN]	2.00	2.50	2.51	(-)	(-)

SPOc-CG3-HSC-90°-75

reinforcement: CG3 (Hitexbau HTC 25/25-80-UWX)
direction of investigation: 90° (weft direction)
embedded length l_e: 75 mm | 3 × y_{nm}

high strength concrete			
composition:	HSC-5.6mm		
concrete age at material test:	8 d		
compressive strength			
$f_{c,cycl}$ [MPa]:	75.7	$f_{c,cube}$ [MPa]:	105.2
Young's modulus			
E_{cm} [MPa]:	44,587		
tensile strength			
$f_{ct,sp}$ [MPa]:	5.3	$f_{ctm,calc}$ [MPa]:	4.8



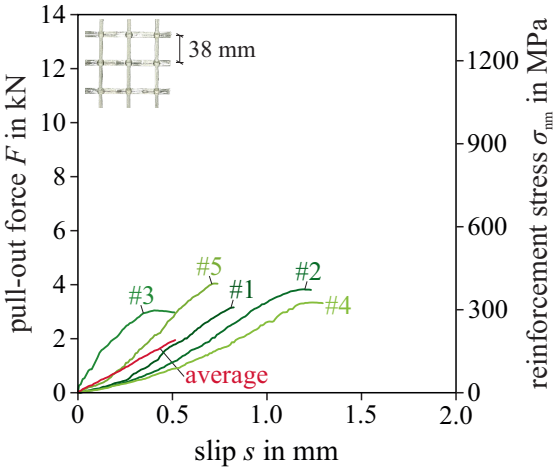
geometry of specimen	
width b [mm]:	25
thickness t [mm]:	30
concrete coverage c [mm]:	14

test results					
test number	(-1)	(-2)	-3	(-4)	(-5)
concrete age at test [d]			14		
maximum load F_{max} [kN]	(0.35)	(-)	3.41	(0.36)	(0.69)
at slip s [mm]	(4.51)	(-)	0.69	(0.35)	(0.09)
type of failure	(-)	(-)	TR	(-)	(-)
load at slip of 0.2 mm $F_{0.2}$ [kN]	(0.03)	(-)	1.11	(0.34)	(0.67)
load at occurrence of slip at unloaded side F_{unl} [kN]	(-)	(-)	3.33	(-)	(-)

SPOc-GG-NSC-0°-38

reinforcement: GG (solidian GRID Q121-RRE-38)
direction of investigation: 0° (warp direction)
embedded length l_e: 38 mm | 1 × y_{nm}

normal strength concrete			
composition:	NSC-5.6mm		
concrete age at material test:	24 d		
compressive strength			
$f_{c,cycl}$ [MPa]:	34.5	$f_{c,cube}$ [MPa]:	43.2
Young's modulus			
E_{cm} [MPa]:	28,428		
tensile strength			
$f_{ct,sp}$ [MPa]:	2.9	$f_{ctm,calc}$ [MPa]:	2.6



geometry of specimen	
width b [mm]:	38
thickness t [mm]:	30
concrete coverage c [mm]:	13.5

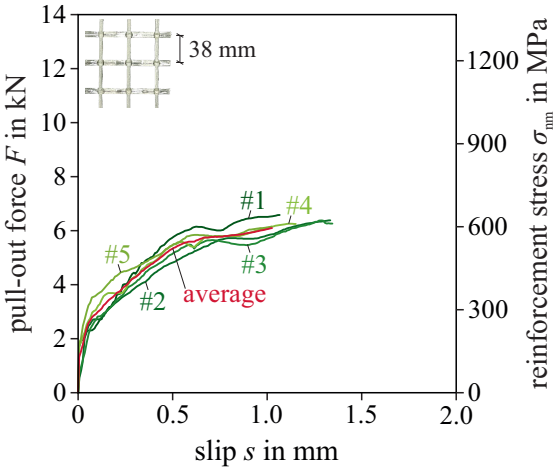
test results					
test number	-1	-2	-3	-4	-5
concrete age at test [d]			24		
maximum load F_{max} [kN]	3.16	3.83	3.06	3.35	4.05
at slip s [mm]	0.82	1.18	0.40	1.23	0.71
type of failure	SP	SP	SP	SP	SP
load at slip of 0.2 mm $F_{0.2}$ [kN]	0.37	0.29	2.02	0.27	0.77
load at occurrence of slip at unloaded side F_{unl} [kN]	1.20	0.81	0.39	1.29	2.11

SPOc-GG-NSC-0°-114

reinforcement: GG (solidian GRID Q121-RRE-38)
direction of investigation: 0° (warp direction)
embedded length l_e: 114 mm | 3 × y_{nm}

normal strength concrete	
composition:	NSC-5.6mm
concrete age at material test:	12 d
compressive strength	
$f_{c,cycl}$ [MPa]: 37.4	$f_{c,cube}$ [MPa]: 45.6
Young's modulus	
E_{cm} [MPa]: 29,755	
tensile strength	
$f_{ct,sp}$ [MPa]: 3.3	$f_{ctm,calc}$ [MPa]: 3.0

geometry of specimen	
width b [mm]:	38
thickness t [mm]:	30
concrete coverage c [mm]:	13.5

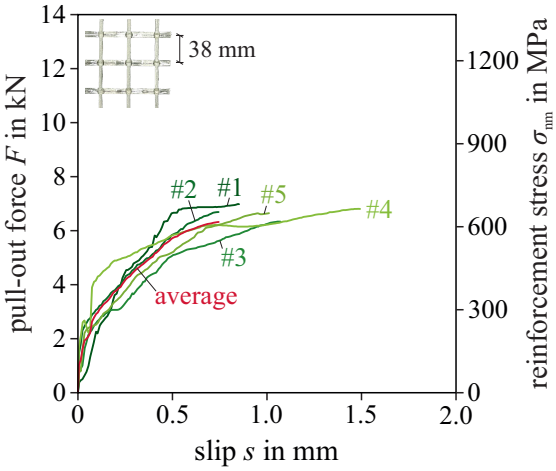


test results					
test number	-1	-2	-3	-4	-5
concrete age at test [d]			12		
maximum load F_{max} [kN]	6.58	6.39	6.43	6.26	6.15
at slip s [mm]	1.07	1.32	1.30	1.11	1.02
type of failure	SP	SP	TR	SP	SP
load at slip of 0.2 mm $F_{0.2}$ [kN]	3.39	3.33	3.43	3.69	4.26
load at occurrence of slip at unloaded side F_{unl} [kN]	(-)	(-)	(-)	(-)	(-)

SPOc-GG-NSC-0°-250

reinforcement: GG (solidian GRID Q121-RRE-38)
direction of investigation: 0° (warp direction)
embedded length l_e: 250 mm | 6.6 × y_{nm}

normal strength concrete	
composition:	NSC-5.6mm
concrete age at material test:	12 d
compressive strength	
$f_{c,cycl}$ [MPa]: 37.4	$f_{c,cube}$ [MPa]: 45.6
Young's modulus	
E_{cm} [MPa]: 29,755	
tensile strength	
$f_{ct,sp}$ [MPa]: 3.3	$f_{ctm,calc}$ [MPa]: 3.0



geometry of specimen	
width b [mm]:	38
thickness t [mm]:	30
concrete coverage c [mm]:	13.5

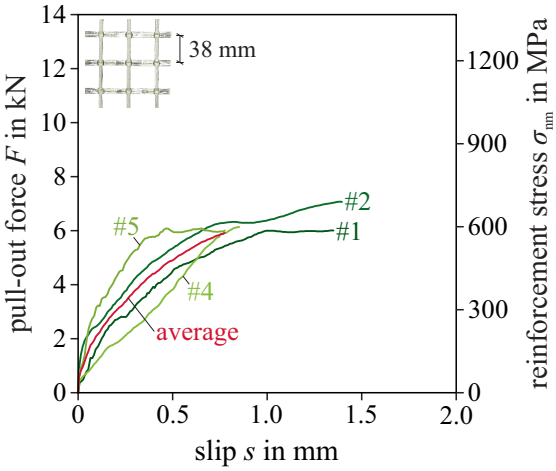
test results

test number	-1	-2	-3	-4	-5
concrete age at test [d]			12		
maximum load F_{max} [kN]	6.99	6.69	6.36	6.81	6.65
at slip s [mm]	0.85	0.74	1.07	1.47	1.01
type of failure	TR	TR	TR	TR	TR
load at slip of 0.2 mm $F_{0.2}$ [kN]	3.45	3.69	3.07	4.88	3.42
load at occurrence of slip at unloaded side F_{unl} [kN]	6.74	5.96	4.75	4.84	4.67

SPOc-GG-NSC-0°-500

reinforcement: GG (solidian GRID Q121-RRE-38)
direction of investigation: 0° (warp direction)
embedded length l_e: 500 mm | 13.2 × y_{nm}

normal strength concrete	
composition:	NSC-5.6mm
concrete age at material test:	12 d
compressive strength	
$f_{c,cycl}$ [MPa]: 37.4	$f_{c,cube}$ [MPa]: 45.6
Young's modulus	
E_{cm} [MPa]: 29,755	
tensile strength	
$f_{ct,sp}$ [MPa]: 3.3	$f_{ctm,calc}$ [MPa]: 3.0



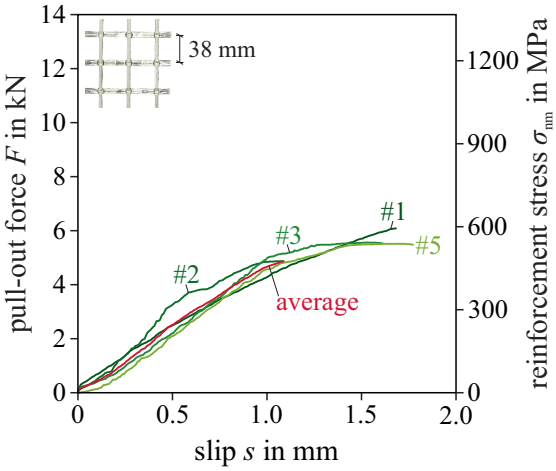
geometry of specimen	
width b [mm]:	38
thickness t [mm]:	30
concrete coverage c [mm]:	13.5

test results					
test number	-1	-2	(-3)	-4	-5
concrete age at test [d]			12		
maximum load F_{max} [kN]	6.01	7.08	(6.22)	6.14	6.14
at slip s [mm]	1.35	1.38	(0.33)	0.85	0.46
type of failure	TR	TR	(TR)	TR	TR
load at slip of 0.2 mm $F_{0.2}$ [kN]	2.67	3.24	(5.01)	1.84	4.23
load at occurrence of slip at unloaded side F_{unl} [kN]	4.69	4.80	(-)	5.70	6.05

SPOc-GG-NSC-0°-114-w/o

reinforcement: GG (solidian GRID Q121-RRE-38) with removed transverse fibre strands
direction of investigation: 0° (warp direction)
embedded length l_e: 114 mm | 3 × y_{nm}

normal strength concrete			
composition:	NSC-5.6mm		
concrete age at material test:	24 d		
compressive strength			
$f_{c,cycl}$ [MPa]:	34.5	$f_{c,cube}$ [MPa]:	43.2
Young's modulus			
E_{cm} [MPa]:	28,428		
tensile strength			
$f_{ct,sp}$ [MPa]:	2.9	$f_{ctm,calc}$ [MPa]:	2.6



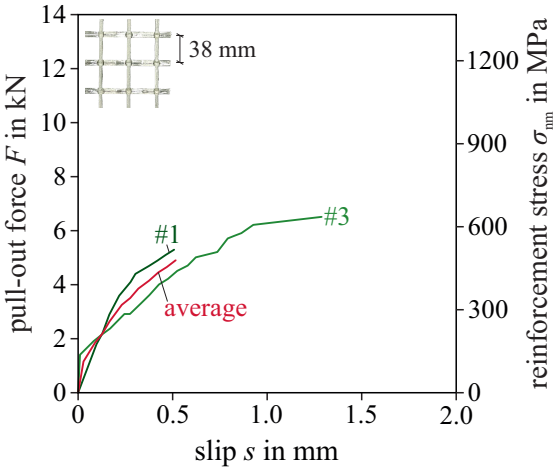
geometry of specimen	
width b [mm]:	38
thickness t [mm]:	30
concrete coverage c [mm]:	13.5

test results					
test number	-1	-2	-3	(-4)	-5
concrete age at test [d]			24		
maximum load F_{max} [kN]	6.09	4.87	5.56	(5.89)	5.52
at slip s [mm]	1.68	1.08	1.51	(2.53)	1.69
type of failure	TR	SP	SP	(SP)	SP
load at slip of 0.2 mm $F_{0.2}$ [kN]	1.15	1.06	0.73	(0.81)	0.47
load at occurrence of slip at unloaded side F_{unl} [kN]	3.23	4.72	5.30	(-)	5.25

SPOc-GG-HSC-0°-114

reinforcement: GG (solidian GRID Q121-RRE-38)
direction of investigation: 0° (warp direction)
embedded length l_e: 114 mm | 3 × y_{nm}

high strength concrete			
composition:	HSC-5.6mm		
concrete age at material test:	8 d		
compressive strength			
$f_{c,cycl}$ [MPa]:	75.7	$f_{c,cube}$ [MPa]:	105.2
Young's modulus			
E_{cm} [MPa]:	45,587		
tensile strength			
$f_{ct,sp}$ [MPa]:	5.3	$f_{ctm,calc}$ [MPa]:	4.8



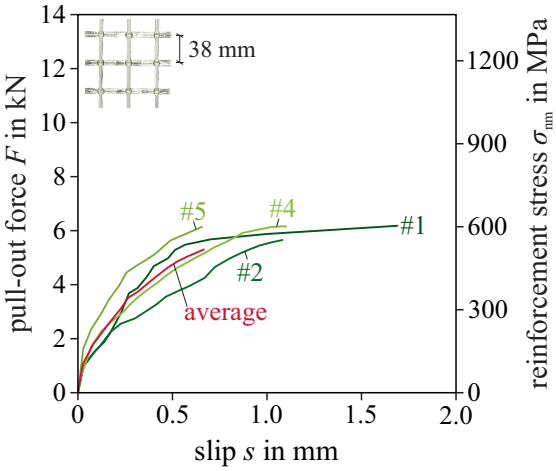
geometry of specimen	
width b [mm]:	38
thickness t [mm]:	30
concrete coverage c [mm]:	13.5

test results					
test number	-1	(-2)	-3	(-4)	(-5)
concrete age at test [d]			7		
maximum load F_{max} [kN]	5.30	(4.51)	6.51	(5.38)	(4.21)
at slip s [mm]	0.51	(-0.37)	1.29	(0.05)	(0.35)
type of failure	TR	(SP)	TR	(SP)	(TR)
load at slip of 0.2 mm $F_{0.2}$ [kN]	3.00	(4.51)	2.61	(5.38)	(3.61)
load at occurrence of slip at unloaded side F_{unl} [kN]	5.50	(-)	6.50	(-)	(-)

SPOc-GG-HSC-0°-250

reinforcement: GG (solidian GRID Q121-RRE-38)
direction of investigation: 0° (warp direction)
embedded length l_e: 250 mm | 6.6 × y_{nm}

high strength concrete			
composition:	HSC-5.6mm		
concrete age at material test:	8 d		
compressive strength			
$f_{c,cycl}$ [MPa]:	75.7	$f_{c,cube}$ [MPa]:	105.2
Young's modulus			
E_{cm} [MPa]:	45,587		
tensile strength			
$f_{ct,sp}$ [MPa]:	5.3	$f_{ctm,calc}$ [MPa]:	4.8



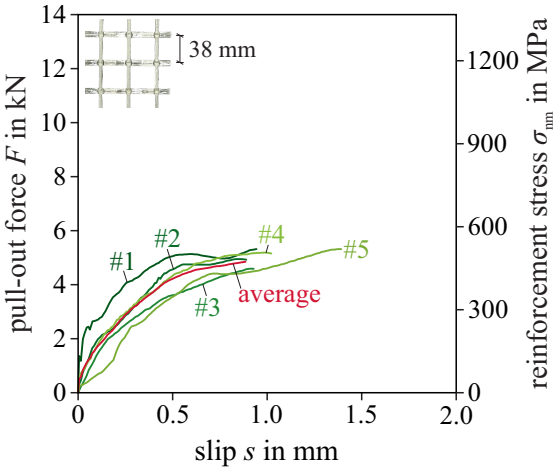
geometry of specimen	
width b [mm]:	38
thickness t [mm]:	30
concrete coverage c [mm]:	13.5

test results					
test number	-1	-2	(-3)	-4	-5
concrete age at test [d]			7		
maximum load F_{max} [kN]	6.18	5.66	(5.82)	6.17	6.14
at slip s [mm]	1.69	1.08	(0.36)	1.08	0.66
type of failure	TR	TR	(TR)	TR	TR
load at slip of 0.2 mm $F_{0.2}$ [kN]	2.28	2.36	(5.02)	2.76	3.44
load at occurrence of slip at unloaded side F_{unl} [kN]	5.80	5.70	(-)	6.14	6.00

SPOc-GG-NSC-90°-114

reinforcement: GG (solidian GRID Q121-RRE-38)
direction of investigation: 90° (weft direction)
embedded length l_e: 114 mm | 3 × y_{nm}

normal strength concrete	
composition:	NSC-5.6mm
concrete age at material test:	12 d
compressive strength	
$f_{c,cycl}$ [MPa]: 37.4	$f_{c,cube}$ [MPa]: 45.6
Young's modulus	
E_{cm} [MPa]: 29,755	
tensile strength	
$f_{ct,sp}$ [MPa]: 3.3	$f_{ctm,calc}$ [MPa]: 3.0



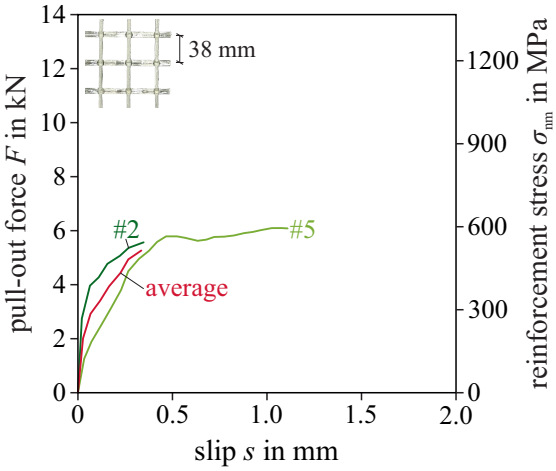
geometry of specimen	
width b [mm]:	38
thickness t [mm]:	30
concrete coverage c [mm]:	13.5

test results					
test number	-1	-2	-3	-4	-5
concrete age at test [d]			11		
maximum load F_{max} [kN]	5.32	4.95	4.60	5.19	5.32
at slip s [mm]	0.94	0.85	0.92	0.98	1.38
type of failure	SP	SP	SP	SP	SP
load at slip of 0.2 mm $F_{0.2}$ [kN]	3.60	2.44	2.23	2.75	1.39
load at occurrence of slip at unloaded side F_{unl} [kN]	3.87	3.90	2.68	3.67	4.47

SPOc-GG-HSC-90°-114

reinforcement: GG (solidian GRID Q121-RRE-38)
direction of investigation: 90° (weft direction)
embedded length l_e: 114 mm | 3 × y_{nm}

high strength concrete			
composition:	HSC-5.6mm		
concrete age at material test:	8 d		
compressive strength			
$f_{c,cycl}$ [MPa]:	75.7	$f_{c,cube}$ [MPa]:	105.2
Young's modulus			
E_{cm} [MPa]:	45,587		
tensile strength			
$f_{ct,sp}$ [MPa]:	5.3	$f_{ctm,calc}$ [MPa]:	4.8



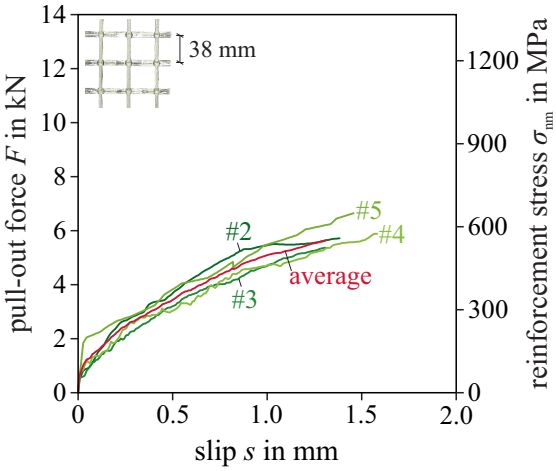
geometry of specimen	
width b [mm]:	38
thickness t [mm]:	30
concrete coverage c [mm]:	13.5

test results					
test number	(-1)	-2	(-3)	(-4)	-5
concrete age at test [d]			7		
maximum load F_{max} [kN]	(4.41)	5.57	(5.67)	(5.10)	6.10
at slip s [mm]	(0.68)	0.35	(0.67)	(0.76)	1.07
type of failure	(SP)	SP	(SP)	(SP)	SP
load at slip of 0.2 mm $F_{0.2}$ [kN]	(4.11)	4.87	(0.27)	(2.20)	3.38
load at occurrence of slip at unloaded side F_{unl} [kN]	(-)	5.70	(-)	(-)	5.89

SPOc-GG-NSC-0°-114-16mm

reinforcement: GG (solidian GRID Q121-RRE-38)
direction of investigation: 0° (warp direction)
embedded length l_e: 114 mm | 3 × y_{nm}

normal strength concrete	
composition:	NSC-16mm
concrete age at material test:	11 d
compressive strength	
$f_{c,cycl}$ [MPa]: 32.8	$f_{c,cube}$ [MPa]: 41.5
Young's modulus	
E_{cm} [MPa]: 28,412	
tensile strength	
$f_{ct,sp}$ [MPa]: 2.8	$f_{ctm,calc}$ [MPa]: 2.5



geometry of specimen	
width b [mm]:	38
thickness t [mm]:	30
concrete coverage c [mm]:	13.5

test results

test number	(-1)	-2	-3	-4	-5
concrete age at test [d]			11		
maximum load F_{max} [kN]	(5.61)	5.72	5.37	5.88	6.65
at slip s [mm]	(1.59)	1.38	1.31	1.58	1.46
type of failure	(TR)	SP	SP	SP	TR
load at slip of 0.2 mm $F_{0.2}$ [kN]	(0.53)	2.40	1.88	1.96	2.45
load at occurrence of slip at unloaded side F_{unl} [kN]	(-)	5.93	5.56	5.57	5.20

D.2 Crack opening tensile tests (COT)

The following appendices provide the results of the 70 COT tests divided into 14 series. The test setup is depicted in Figure 3.7. The results of tests not considered in the evaluation are given in brackets.

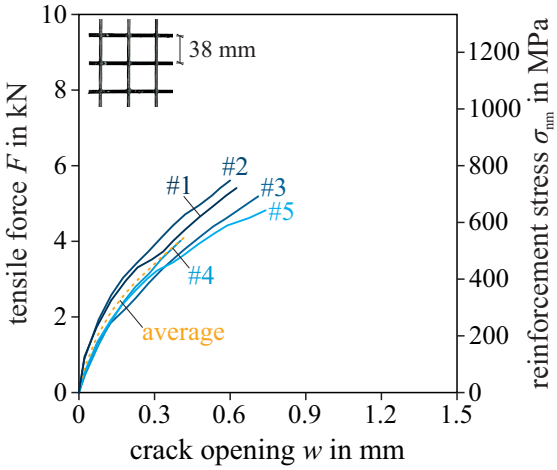
COT-CG1-NSC-0°

reinforcement:	CG1 (solidian GRID Q95-CCE-38)
direction of investigation:	0° (warp direction)
investigation length l_f:	2 × 114 mm = 228 mm
clamping length:	200 mm

normal strength concrete			
composition:	NSC-5.6mm		
concrete age at material test:	26 d		
compressive strength			
$f_{c,cycl}$ [MPa]:	41.5	$f_{c,cube}$ [MPa]:	48.2
Young's modulus			
E_{cm} [MPa]:	30,465[1)]		
tensile strength			
$f_{ct,sp}$ [MPa]:	3.3	$f_{ctm,calc}$ [MPa]:	3.0

[1)] after 28 days

geometry of specimen	
width b [mm]:	60
thickness t [mm]:	30
concrete coverage c [mm]:	13.5



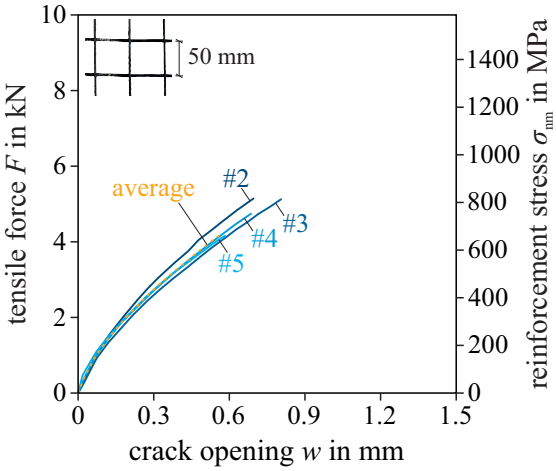
test results					
test number	-1	-2	-3	-4	-5
concrete age at test [d]			27		
load until occurrence of second crack F [kN]	5.41	5.61	5.19	4.02	4.82
at crack opening w [mm]	0.63	0.60	0.71	0.40	0.74

COT-CG2-NSC-0°

reinforcement: CG2 (SIT grid 050)
direction of investigation: 0° (warp direction)
investigation length l_f: 2 × 152 mm = 304 mm
clamping length: 200 mm

normal strength concrete	
composition:	NSC-5.6mm
concrete age at material test:	28 d
compressive strength	
$f_{c,cycl}$ [MPa]: 34.5[1)]	$f_{c,cube}$ [MPa]: 39.6
Young's modulus	
E_{cm} [MPa]: 28,667[2)]	
tensile strength	
$f_{ct,sp}$ [MPa]: 2.7	$f_{ctm,calc}$ [MPa]: 2.5

[1)] after 25 days [2)] after 30 days



geometry of specimen	
width b [mm]:	60
thickness t [mm]:	30
concrete coverage c [mm]:	14

test results

test number	(-1)	-2	-3	-4	-5
concrete age at test [d]			24		
load until occurrence of second crack F [kN]	(4.22)	5.34	5.53	4.95	4.35
at crack opening w [mm]	(0.37)	0.78	0.90	0.72	0.62

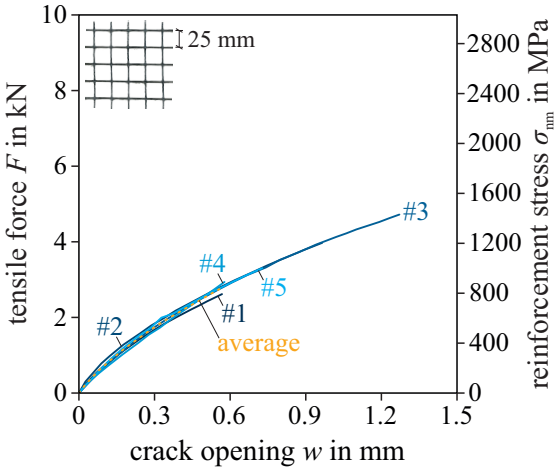
COT-CG3-NSC-0°

reinforcement: CG3 (Hitexbau HTC 25/25-80-UWX)
direction of investigation: 0° (warp direction)
investigation length l_f: 2 × 152 mm = 304 mm
clamping length: 200 mm

normal strength concrete	
composition:	NSC-5.6mm
concrete age at material test:	28 d
compressive strength	
$f_{c,cycl}$ [MPa]: 34.5[1)]	$f_{c,cube}$ [MPa]: 39.6
Young's modulus	
E_{cm} [MPa]: 28,667[2)]	
tensile strength	
$f_{ct,sp}$ [MPa]: 2.7	$f_{ctm,calc}$ [MPa]: 2.5

[1)] after 25 days [2)] after 30 days

geometry of specimen	
width b [mm]:	60
thickness t [mm]:	30
concrete coverage c [mm]:	14



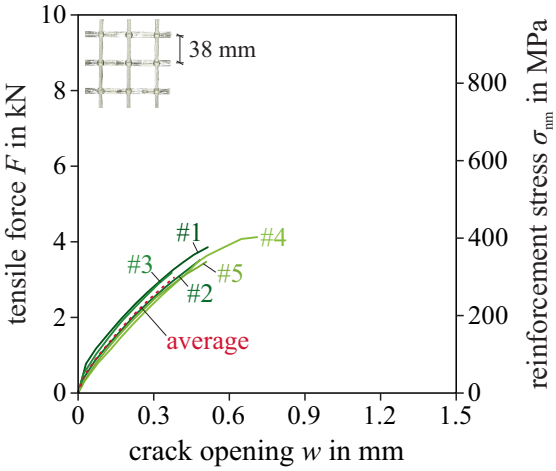
test results					
test number	-1	-2	-3	-4	-5
concrete age at test [d]			24		
load until occurrence of second crack F [kN]	2.83	4.18	4.92	3.13	3.51
at crack opening w [mm]	0.64	1.05	1.37	0.62	0.80

COT-GG-NSC-0°

reinforcement: GG (solidian GRID Q121-RRE-38)
direction of investigation: 0° (warp direction)
investigation length l_f: 2 × 114 mm = 228 mm
clamping length: 200 mm

normal strength concrete	
composition:	NSC-5.6mm
concrete age at material test:	26 d
compressive strength	
$f_{c,cycl}$ [MPa]: 41.5	$f_{c,cube}$ [MPa]: 48.2
Young's modulus	
E_{cm} [MPa]: 30,465[1)]	
tensile strength	
$f_{ct,sp}$ [MPa]: 2.9	$f_{ctm,calc}$ [MPa]: 2.6

[1)] after 28 days



geometry of specimen	
width b [mm]:	60
thickness t [mm]:	30
concrete coverage c [mm]:	13.5

test results					
test number	-1	-2	-3	-4	-5
concrete age at test [d]			26		
load until occurrence of second crack F [kN]	4.08	3.72	3.39	4.29	3.87
at crack opening w [mm]	0.57	0.53	0.41	0.78	0.58

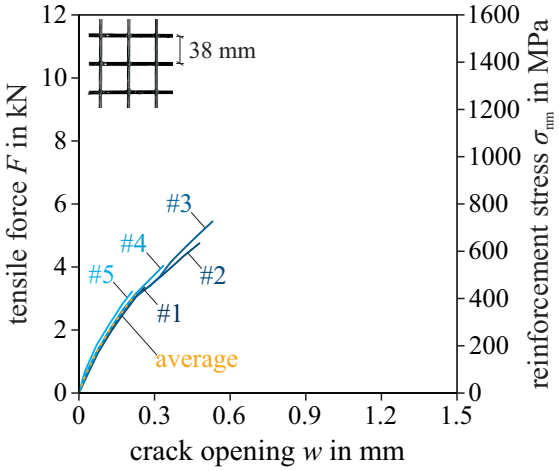
COT-CG1-NSC-0° with FOS

reinforcement: CG1 (solidian GRID Q95-CCE-38)
direction of investigation: 0° (warp direction)
investigation length l_f: 2 × 114 mm = 228 mm
clamping length: 200 mm

normal strength concrete			
composition:	NSC-5.6mm		
concrete age at material test:	26 d		
compressive strength			
$f_{c,cycl}$ [MPa]:	41.5	$f_{c,cube}$ [MPa]:	48.2
Young's modulus			
E_{cm} [MPa]:	30,465[1)]		
tensile strength			
$f_{ct,sp}$ [MPa]:	2.9	$f_{ctm,calc}$ [MPa]:	2.6

[1)] after 28 days

geometry of specimen	
width b [mm]:	60
thickness t [mm]:	30
concrete coverage c [mm]:	13.5



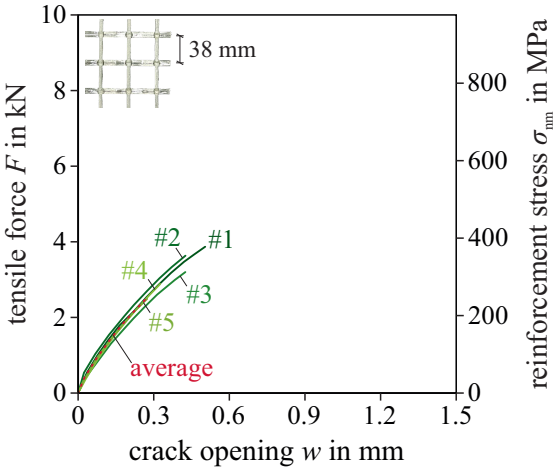
test results					
test number	-1	-2	-3	-4	-5
concrete age at test [d]	24	24	24	25	25
load until occurrence of second crack F [kN]	3.35	4.85	5.50	4.14	3.22
at crack opening w [mm]	0.26	0.49	0.54	0.35	0.21

COT-GG-NSC-0° with FOS

reinforcement: GG (solidian GRID Q121-RRE-38)
direction of investigation: 0° (warp direction)
investigation length l_f: 2 × 114 mm = 228 mm
clamping length: 200 mm

normal strength concrete	
composition:	NSC-5.6mm
concrete age at material test:	26 d
compressive strength	
$f_{c,cycl}$ [MPa]: 41.5	$f_{c,cube}$ [MPa]: 48.2
Young's modulus	
E_{cm} [MPa]: 30,465[1)]	
tensile strength	
$f_{ct,sp}$ [MPa]: 2.9	$f_{ctm,calc}$ [MPa]: 2.6

[1)] after 28 days



geometry of specimen	
width b [mm]:	60
thickness t [mm]:	30
concrete coverage c [mm]:	13.5

test results

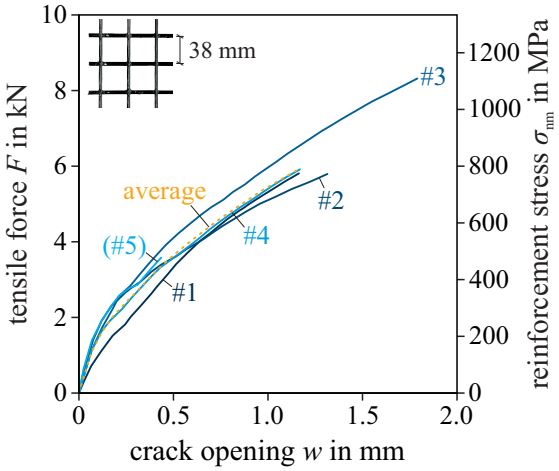
test number	-1	-2	-3	-4	-5
concrete age at test [d]	25	25	25	25	26
load until occurrence of second crack F [kN]	4.07	3.92	3.40	3.29	2.69
at crack opening w [mm]	0.55	0.48	0.47	0.39	0.30

COT-CG1-HSC-0°

reinforcement: CG1 (solidian GRID Q95-CCE-38)
direction of investigation: 0° (warp direction)
investigation length l_f: 2 × 152 mm = 304 mm
clamping length: 200 mm

high strength concrete			
composition:	HSC-5.6mm		
concrete age at material test:	32 d		
compressive strength			
$f_{c,cycl}$ [MPa]:	79.5[1)]	$f_{c,cube}$ [MPa]:	100.0
Young's modulus			
E_{cm} [MPa]:	42,455		
tensile strength			
$f_{ct,sp}$ [MPa]:	4.8	$f_{ctm,calc}$ [MPa]:	4.3

[1)] after 31 days



geometry of specimen	
width b [mm]:	60
thickness t [mm]:	30
concrete coverage c [mm]:	13.5

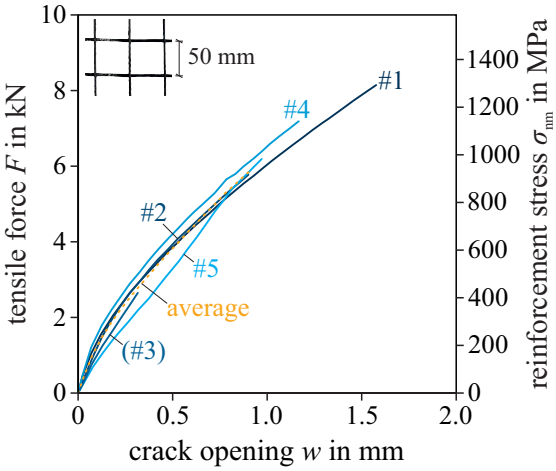
test results					
test number	-1	-2	-3	-4	(-5)
concrete age at test [d]			32		
load until occurrence of second crack F [kN]	6.01	5.99	8.51	6.11	(3.78)
at crack opening w [mm]	1.23	1.40	1.87	1.24	(0.48)

COT-CG2-HSC-0°

reinforcement: CG2 (SIT grid 050)
direction of investigation: 0° (warp direction)
investigation length l_f: 2 × 152 mm = 304 mm
clamping length: 200 mm

high strength concrete	
composition:	HSC-5.6mm
concrete age at material test:	32 d
compressive strength	
$f_{c,cycl}$ [MPa]: 79.5[1)]	$f_{c,cube}$ [MPa]: 100.0
Young's modulus	
E_{cm} [MPa]: 42,455	
tensile strength	
$f_{ct,sp}$ [MPa]: 5.0	$f_{ctm,calc}$ [MPa]: 4.5

[1)] after 31 days



geometry of specimen	
width b [mm]:	60
thickness t [mm]:	30
concrete coverage c [mm]:	14

test results					
test number	-1	-2	(-3)	-4	-5
concrete age at test [d]			31		
load until occurrence of second crack F [kN]	8.34	5.98	(3.15)	7.39	6.44
at crack opening w [mm]	1.64	0.95	(0.38)	1.22	1.02

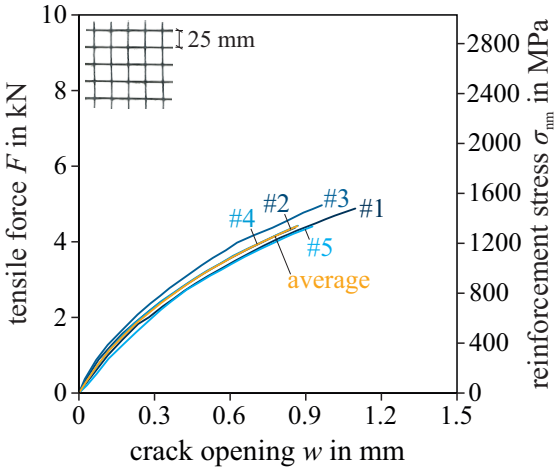
COT-CG3-HSC-0°

reinforcement: CG3 (Hitexbau HTC 25/25-80-UWX)
direction of investigation: 0° (warp direction)
investigation length l_f: 2 × 152 mm = 304 mm
clamping length: 200 mm

high strength concrete			
composition:	HSC-5.6mm		
concrete age at material test:	32 d		
compressive strength			
$f_{c,cycl}$ [MPa]:	79.5[1)]	$f_{c,cube}$ [MPa]:	100.0
Young's modulus			
E_{cm} [MPa]:	42,455		
tensile strength			
$f_{ct,sp}$ [MPa]:	5.0	$f_{ctm,calc}$ [MPa]:	4.5

[1)] after 31 days

geometry of specimen	
width b [mm]:	60
thickness t [mm]:	30
concrete coverage c [mm]:	14



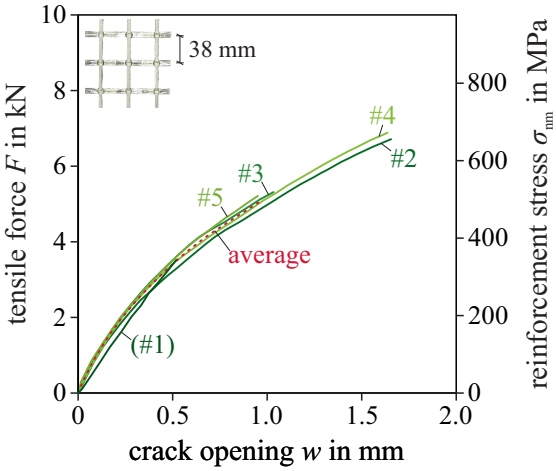
test results					
test number	-1	-2	-3	-4	-5
concrete age at test [d]			31		
load until occurrence of second crack F [kN]	5.09	4.56	5.20	4.62	4.60
at crack opening w [mm]	1.20	0.93	1.04	0.94	1.01

COT-GG-HSC-0°

reinforcement: GG (solidian GRID Q121-RRE-38)
direction of investigation: 0° (warp direction)
investigation length l_f: 2 × 152 mm = 304 mm
clamping length: 200 mm

high strength concrete	
composition:	HSC-5.6mm
concrete age at material test:	32 d
compressive strength	
$f_{c,cycl}$ [MPa]: 79.5[1)]	$f_{c,cube}$ [MPa]: 100.0
Young's modulus	
E_{cm} [MPa]: 42,455	
tensile strength	
$f_{ct,sp}$ [MPa]: 4.8	$f_{ctm,calc}$ [MPa]: 4.3

[1)] after 31 days



geometry of specimen	
width b [mm]:	60
thickness t [mm]:	30
concrete coverage c [mm]:	13.5

test results					
test number	(-1)	-2	-3	-4	-5
concrete age at test [d]			32		
load until occurrence of second crack F [kN]	(3.72)	6.91	5.51	7.09	5.41
at crack opening w [mm]	(0.56)	1.75	1.10	1.74	1.02

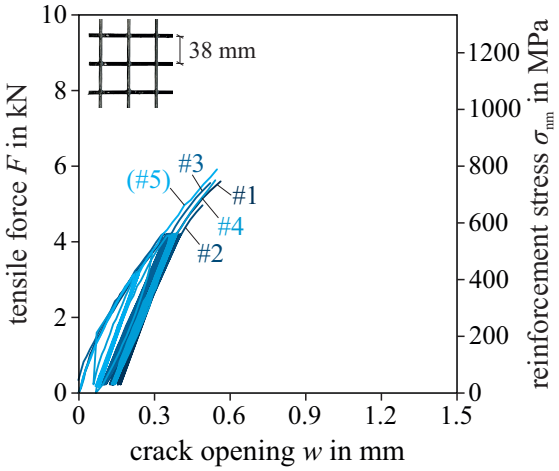
COT-CG1-NSC-0°-cyclic

reinforcement: CG1 (solidian GRID Q95-CCE-38)
direction of investigation: 0° (warp direction)
investigation length l_f: 2 × 152 mm = 304 mm
clamping length: 200 mm

normal strength concrete			
composition:	NSC-5.6mm		
concrete age at material test:	33 d		
compressive strength			
$f_{c,cycl}$ [MPa]:	38.2[1)]	$f_{c,cube}$ [MPa]:	43.3
Young's modulus			
E_{cm} [MPa]:	29,562		
tensile strength			
$f_{ct,sp}$ [MPa]:	3.4	$f_{ctm,calc}$ [MPa]:	3.1

[1)] after 32 days

geometry of specimen	
width b [mm]:	60
thickness t [mm]:	30
concrete coverage c [mm]:	13.5



test results					
test number	-1	-2	-3	-4	(-5)
concrete age at test [d]	32	32	32	32	(31)
superior load level F_{sup} [kN]	4.50	4.50	4.50	4.50	(3.50)
inferior load level F_{inf} [kN]	0.50	0.50	0.50	0.50	(0.50)
crack opening w_0 at F_{sup} prior to cyclic loading [mm]	0.338	0.356	0.334	0.361	(0.212)
crack opening w_1 at F_{sup} after first load cycle [mm]	0.360	0.383	0.346	0.370	(0.233)
increase crack opening $\Delta w = w_{10} - w_0$ [mm] during cyclic loading	0.046	0.049	0.035	0.027	(0.041)
load until occurrence of second crack F [kN]	5.60	4.97	5.56	5.63	(5.92)
at crack opening w [mm]	0 56	0 49	0 52	0.54	(0 55)

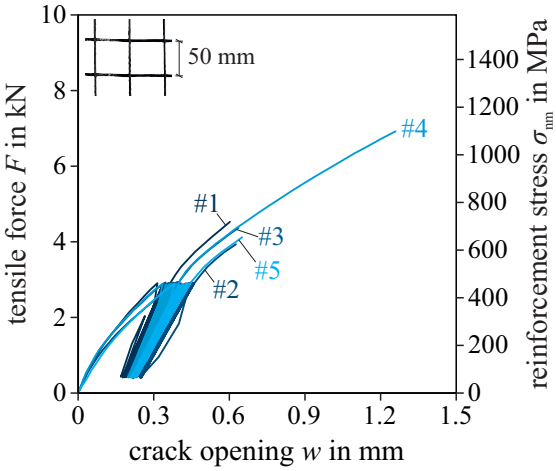
COT-CG2-NSC-0°-cyclic

reinforcement: CG2 (SIT grid 050)
direction of investigation: 0° (warp direction)
investigation length l_f: 2 × 152 mm = 304 mm
clamping length: 200 mm

normal strength concrete	
composition:	NSC-5.6mm
concrete age at material test:	28 d
compressive strength	
$f_{c,cycl}$ [MPa]: 34.5[1)]	$f_{c,cube}$ [MPa]: 39.6
Young's modulus	
E_{cm} [MPa]: 28,667[2)]	
tensile strength	
$f_{ct,sp}$ [MPa]: 2.7	$f_{ctm,calc}$ [MPa]: 2.5

[1)] after 25 days [2)] after 30 days

geometry of specimen	
width b [mm]:	60
thickness t [mm]:	30
concrete coverage c [mm]:	14



test results					
test number	-1	-2	-3	-4	-5
concrete age at test [d]			25		
superior load level F_{sup} [kN]	3.00	3.00	3.00	3.00	3.00
inferior load level F_{inf} [kN]	0.50	0.50	0.50	0.50	0.50
crack opening w_0 at F_{sup} prior to cyclic loading [mm]	0.314	0.410	0.347	0.335	0.381
crack opening w_1 at F_{sup} after first load cycle [mm]	0.338[1)]	0.431	0.363	0.352	0.400
increase crack opening $\Delta w = w_{10} - w_0$ [mm] during cyclic loading	0.056	0.055	0.058	0.064	0.067
load until occurrence of second crack F [kN]	4.53	3.93	4.37	6.92	4.12
at crack opening w [mm]	0.60	0.63	0.64	1.26	0.65

[1)] after the second load cycle

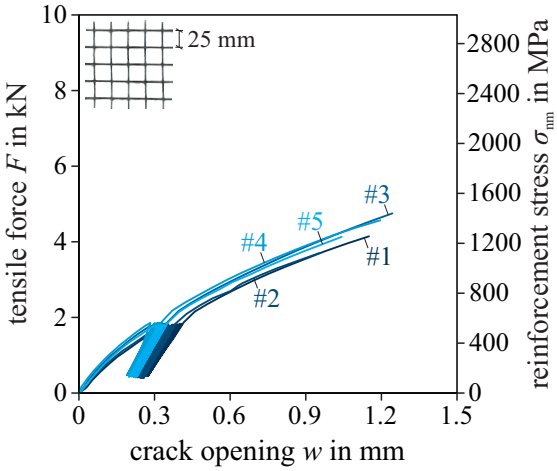
COT-CG3-NSC-0°-cyclic

reinforcement: CG3 (Hitexbau HTC 25/25-80-UWX)
direction of investigation: 0° (warp direction)
investigation length l_f: 2 × 152 mm = 304 mm
clamping length: 200 mm

normal strength concrete	
composition:	NSC-5.6mm
concrete age at material test:	28 d
compressive strength	
$f_{c,cycl}$ [MPa]: 34.5[1)]	$f_{c,cube}$ [MPa]: 39.6
Young's modulus	
E_{cm} [MPa]: 28,667[2)]	
tensile strength	
$f_{ct,sp}$ [MPa]: 2.7	$f_{ctm,calc}$ [MPa]: 2.5

[1)] after 25 days [2)] after 30 days

geometry of specimen	
width b [mm]:	60
thickness t [mm]:	30
concrete coverage c [mm]:	14



test results					
test number	-1	-2	-3	-4	-5
concrete age at test [d]			25		
superior load level F_{sup} [kN]	1.90	1.90	1.90	1.90	1.90
inferior load level F_{inf} [kN]	0.50	0.50	0.50	0.50	0.50
crack opening w_0 at F_{sup} prior to cyclic loading [mm]	0.355	0.331	0.302	0.284	0.308
crack opening w_1 at F_{sup} after first load cycle [mm]	0.369	0.342	0.312	0.299	0.316
increase crack opening $\Delta w = w_{10} - w_0$ [mm] during cyclic loading	0.061	0.050	0.050	0.047	0.042
load until occurrence of second crack F [kN]	4.15	3.70	4.75	4.57	4.13
at crack opening w [mm]	1.15	0.95	1.24	1.20	1.04

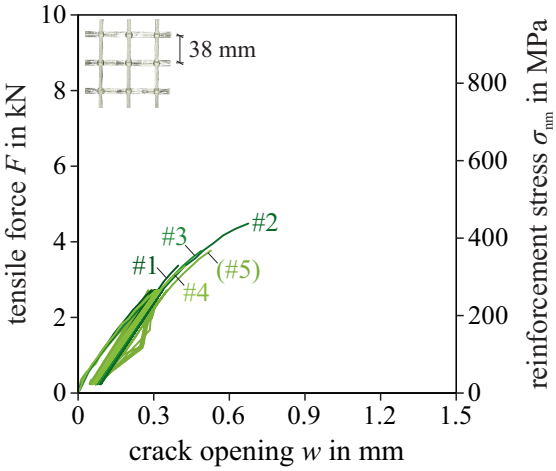
COT-GG-NSC-0°-cyclic

reinforcement: GG (solidian GRID Q121-RRE-38)
direction of investigation: 0° (warp direction)
investigation length l_f: 2 × 152 mm = 304 mm
clamping length: 200 mm

normal strength concrete	
composition:	NSC-5.6mm
concrete age at material test:	33 d
compressive strength	
$f_{c,cycl}$ [MPa]: 38.2[1)]	$f_{c,cube}$ [MPa]: 43.3
Young's modulus	
E_{cm} [MPa]: 29,562	
tensile strength	
$f_{ct,sp}$ [MPa]: 3.4	$f_{ctm,calc}$ [MPa]: 3.1

[1)] after 32 days

geometry of specimen	
width b [mm]:	60
thickness t [mm]:	30
concrete coverage c [mm]:	13.5



test results					
test number	-1	-2	-3	-4	(-5)
concrete age at test [d]			31		
superior load level F_{sup} [kN]	3.00	3.00	3.00	3.00	(3.00)
inferior load level F_{inf} [kN]	0.50	0.50	0.50	0.50	(0.50)
crack opening w_0 at F_{sup} prior to cyclic loading [mm]	0.290	0.318	0.309	0.308	(0.318)
crack opening w_1 at F_{sup} after first load cycle [mm]	0.301[1)]	0.323	0.313	0.312	(0.289)[2)]
increase crack opening $\Delta w = w_{10} - w_0$ [mm] during cyclic loading	0.033	0.026	0.023	0.026	(0.022)
load until occurrence of second crack F [kN]	3.37	4.48	3.76	3.35	(3.77)
at crack opening w [mm]	0 40	0 68	0 49	0 42	(0 53)

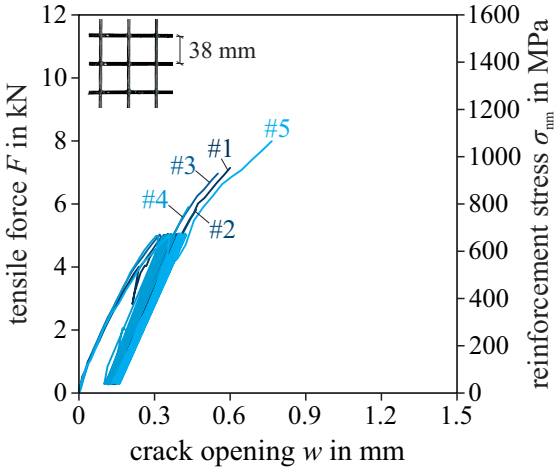
[1)] after the second load cycle
[2)] irregular measurement: until the 6th load cycle the crack opening decreased

COT-CG1-NSC-0°-cyclic with FOS

reinforcement: CG1 (solidian GRID Q95-CCE-38)
direction of investigation: 0° (warp direction)
investigation length l_f: 2 × 152 mm = 304 mm
clamping length: 200 mm

normal strength concrete	
composition:	NSC-5.6mm
concrete age at material test:	33 d
compressive strength	
$f_{c,cycl}$ [MPa]: 38.2[1)]	$f_{c,cube}$ [MPa]: 43.3
Young's modulus	
E_{cm} [MPa]: 29,562	
tensile strength	
$f_{ct,sp}$ [MPa]: 3.4	$f_{ctm,calc}$ [MPa]: 3.1

[1)] after 32 days



geometry of specimen	
width b [mm]:	60
thickness t [mm]:	30
concrete coverage c [mm]:	13.5

test results

test number	-1	-2	-3	-4	-5
concrete age at test [d]			33		
superior load level F_{sup} [kN]	4.50	4.50	4.50	4.50	4.50
inferior load level F_{inf} [kN]	0.50	0.50	0.50	0.50	0.50
crack opening w_0 at F_{sup} prior to cyclic loading [mm]	0.356	0.337	0.320	0.314	0.359
crack opening w_1 at F_{sup} after first load cycle [mm]	0.377	0.369	0.345	0.333	0.396[1)]
increase crack opening $\Delta w = w_{10} - w_0$ [mm] during cyclic loading	0.055	0.073	0.059	0.059	0.081
load until occurrence of second crack F [kN]	5.96	4.85	5.81	4.92	6.66
at crack opening w [mm]	0 60	0 47	0 55	0.43	0 76

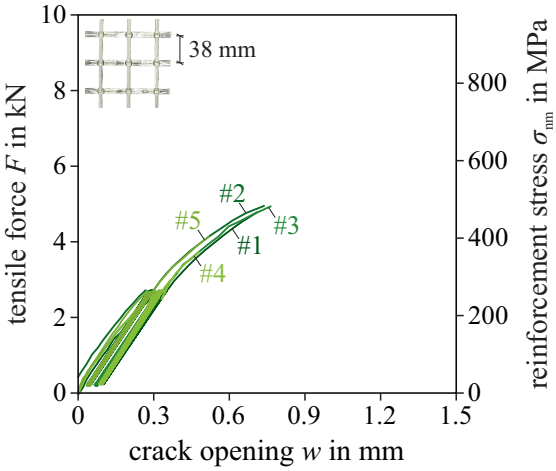
[1)] after the second load cycle

COT-GG-NSC-0°-cyclic with FOS

reinforcement: GG (solidian GRID Q121-RRE-38)
direction of investigation: 0° (warp direction)
investigation length l_f: 2 × 152 mm = 304 mm
clamping length: 200 mm

normal strength concrete	
composition:	NSC-5.6mm
concrete age at material test:	33 d
compressive strength	
$f_{c,cycl}$ [MPa]: 38.2[1)]	$f_{c,cube}$ [MPa]: 43.3
Young's modulus	
E_{cm} [MPa]: 29,562	
tensile strength	
$f_{ct,sp}$ [MPa]: 3.4	$f_{ctm,calc}$ [MPa]: 3.1

[1)] after 32 days



geometry of specimen	
width b [mm]:	60
thickness t [mm]:	30
concrete coverage c [mm]:	13.5

test results

test number	-1	-2	-3	-4	-5
concrete age at test [d]	33	33	32	32	32
superior load level F_{sup} [kN]	3.00	3.00	3.00	3.00	3.00
inferior load level F_{inf} [kN]	0.50	0.50	0.50	0.50	0.50
crack opening w_0 at F_{sup} prior to cyclic loading [mm]	0.321	0.268	0.305	0.303	0.270
crack opening w_1 at F_{sup} after first load cycle [mm]	0.331	0.278	0.315	0.315	0.279
increase crack opening $\Delta w = w_{10} - w_0$ [mm] during cyclic loading	0.039	0.037	0.036	0.039	0.031
load until occurrence of second crack F [kN]	4.80	4.96	4.95	3.75	4.15
at crack opening w [mm]	0.71	0.74	0.76	0.48	0.52

D.3 Uniaxial tensile tests (UT)

The following appendices provide the results of the 34 UT tests divided into 12 series. The test setup is depicted inFigure 4.1.

UT-CG1-NSC-0°

reinforcement:	CG1 (solidian GRID Q95-CCE-38)
direction of investigation:	0° (warp direction)
number of reinforcement layers:	1
number of longitudinal fibre strands:	5
reinforcement area:	37.5 mm²

normal strength concrete				
composition:	NSC-5.6mm			
batch number:	1		2	
concrete age at material test [d]:	12	14	60	70
$f_{c,cycl}$ [MPa]:	40.1	42.1	42.2	42.1
$f_{c,cube}$ [MPa]	43.1	47.8	54.5	49.8
E_{cm} [MPa]:	30,892	30,538	30,797	30,628
$f_{ct,sp}$ [MPa]:	3.5	3.7	3.4	3.8
$f_{ctm,calc}$ [MPa]:	3.3	3.1	3.1	3.4

geometry of specimen	
width b [mm]:	190
thickness t [mm]:	30
concrete coverage c [mm]:	13.5
reinforcement ratio ρ_l [%]:	0.66

test results					
test number	static-1	static-2	cyclic-1	cyclic-2	cyclic-3
concrete age at test [d]	12	13	66	60	62
load at initial crack F_{int} [kN]	13.24	11.30	12.25	12.13	11.89
initial crack opening w_{int} [mm]	0.17	0.10	0.14	0.14	0.11
stabilised cracking					
reinforcement stress σ_{nm} [MPa]:	408	896	961	520	753
number of cracks n_{cr} [-]:	7	7	7	6	9
average crack width w_m[mm]:	0.30	0.60	0.68	0.42	0.40
maximum crack width w_{max}[mm]:	0.38	0.76	0.87	0.61	0.70
average crack spacing s_{rm}[mm]:	79	81	92	88	60
maximum crack spacing $s_{r,max}$[mm]:	125	109	157	98	83
maximum load F_{max} [kN]	59.17	56.34	59.87	66.44	61.54
maximum reinforcement stress $\sigma_{nm,max}$ [MPa]:	1578	1502	1597	1772	1641
type of failure:	rupture of fibre strands				

UT-CG2-NSC-0°

reinforcement:	CG2 (SIT grid 050)
direction of investigation:	0° (warp direction)
number of reinforcement layers:	1
number of longitudinal fibre strands:	4
reinforcement area:	25.2 mm²

normal strength concrete

composition:	NSC-5.6mm			
batch number:	1		2	
concrete age at material test [d]:	12	14	60	70
$f_{c,cycl}$ [MPa]:	40.1	42.1	42.2	42.1
$f_{c,cube}$ [MPa]	43.1	47.8	54.5	49.8
E_{cm} [MPa]:	30,892	30,538	30,797	30,628
$f_{ct,sp}$ [MPa]:	3.5	3.7	3.4	3.8
$f_{ctm,calc}$ [MPa]:	3.3	3.1	3.1	3.4

geometry of specimen

width b [mm]:	190
thickness t [mm]:	30
concrete coverage c [mm]:	13.5
reinforcement ratio ρ_l [%]:	0.44

test results

test number	static-1	static-2	cyclic-1	cyclic-2	cyclic-3
concrete age at test [d]	13	14	69	73	68
load at initial crack F_{int} [kN]	17.49	18.76	11.51	9.74	12.27
initial crack opening w_{int} [mm]	0.49	0.47	0.25	0.16	0.17
stabilised cracking					
reinforcement stress σ_{nm} [MPa]:	869	1075	1346	1142	794
number of cracks n_{cr} [-]:	4	4	5	6	4
average crack width w_m[mm]:	0.90	1.05	1.02	0.90	0.71
maximum crack width w_{max}[mm]:	1.33	1.54	1.86	1.41	1.25
average crack spacing s_{rm}[mm]:	149	150	110	109	134
maximum crack spacing $s_{r,max}$[mm]:	177	177	125	164	135
maximum load F_{max} [kN]	29.97	38.45	41.26	46.84	44.59
maximum reinforcement stress $\sigma_{nm,max}$ [MPa]:	1189	1526	1637	1859	1769
type of failure:	rupture of fibre strands				

UT-CG3-NSC-0°

reinforcement:	CG3 (HTC 25/25-80 UWX)
direction of investigation:	0° (warp direction)
number of reinforcement layers:	1
number of longitudinal fibre strands:	7 / 8
reinforcement area:	23.1 / 26.4 mm²

normal strength concrete		
composition:	NSC-5.6mm	
concrete age at material test [d]:	10	15
$f_{c,cycl}$ [MPa]:	30.7	33.5
$f_{c,cube}$ [MPa]	38.5	38.7
E_{cm} [MPa]:	26,915	27,988
$f_{ct,sp}$ [MPa]:	3.1	n/a
$f_{ctm,calc}$ [MPa]:	2.8	n/a

geometry of specimen	
width b [mm]:	190
thickness t [mm]:	30
concrete coverage c [mm]:	14
reinforcement ratio ρ_l [%]:	0.41 / 0.46

test results			
test number	static ρ_l = 0.41%	cyclic-1 ρ_l = 0.46%	cyclic-2 ρ_l = 0.41%
concrete age at test [d]	14	14	13
load at initial crack F_{int} [kN]	12.71	12.04	11.28
initial crack opening w_{int} [mm]	0.19	0.18	0.15
stabilised cracking			
reinforcement stress σ_{nm} [MPa]:	1260	749	1158
number of cracks n_{cr} [-]:	8	8	7
average crack width w_m[mm]:	0.66	0.47	0.71
maximum crack width w_{max}[mm]:	0.86	0.78	1.03
average crack spacing s_{rm}[mm]:	74	72	91
maximum crack spacing $s_{r,max}$[mm]:	103	111	112
maximum load F_{max} [kN]	33.85	31.93	33.94
maximum reinforcement stress $\sigma_{nm,max}$ [MPa]:	1466	1210	1469
type of failure:	rupture of fibre strands		

UT-GG-NSC-0°

reinforcement:	GG (solidian GRID Q121-RRE-38)
direction of investigation:	0° (warp direction)
number of reinforcement layers:	1
number of longitudinal fibre strands:	5
reinforcement area:	51.2 mm²

normal strength concrete		
composition:	NSC-5.6mm	
concrete age at material test [d]:	10	15
$f_{c,cycl}$ [MPa]:	30.7	33.5
$f_{c,cube}$ [MPa]	38.5	38.7
E_{cm} [MPa]:	26,915	27,988
$f_{ct,sp}$ [MPa]:	3.1	n/a
$f_{ctm,calc}$ [MPa]:	2.8	n/a

geometry of specimen	
width b [mm]:	190
thickness t [mm]:	30
concrete coverage c [mm]:	13.5
reinforcement ratio ρ_l [%]:	0.90

test results			
test number	static	cyclic-1	cyclic-2
concrete age at test [d]	10	9	10
load at initial crack F_{int} [kN]	10.42	9.75	10.06
initial crack opening w_{int} [mm]	0.10	0.13	0.10
stabilised cracking			
reinforcement stress σ_{nm} [MPa]:	340	505	403
number of cracks n_{cr} [-]:	11	11	11
average crack width w_m[mm]:	0.43	0.68	0.61
maximum crack width w_{max}[mm]:	0.71	1.02	1.01
average crack spacing s_{rm}[mm]:	57	61	58
maximum crack spacing $s_{r,max}$[mm]:	81	80	88
maximum load F_{max} [kN]	33.71	29.20	26.61
maximum reinforcement stress $\sigma_{nm,max}$ [MPa]:	658	570	519
type of failure:	rupture of fibre strands		

UT-CG1-HSC-0°

reinforcement:	CG1 (solidian GRID Q95-CCE-38)
direction of investigation:	0° (warp direction)
number of reinforcement layers:	1
number of longitudinal fibre strands:	5
reinforcement area:	37.5 mm²

high strength concrete		
composition:	HSC-5.6mm	
concrete age at material test [d]:	8	44
$f_{c,cycl}$ [MPa]:	75.7	98.9
$f_{c,cube}$ [MPa]	105.2	108.5
E_{cm} [MPa]:	44,587	47,713
$f_{ct,sp}$ [MPa]:	5.3	5.5
$f_{ctm,calc}$ [MPa]:	4.8	5.0

geometry of specimen	
width b [mm]:	190
thickness t [mm]:	30
concrete coverage c [mm]:	13.5
reinforcement ratio ρ_l [%]:	0.66

test results			
test number	cyclic-1	cyclic-2	cyclic-3
concrete age at test [d]	49	50	46
load at initial crack F_{int} [kN]	27.21	28.54	23.99
initial crack opening w_{int} [mm]	0.46	0.40	0.19
stabilised cracking			
reinforcement stress σ_{nm} [MPa]:	663	915	920
number of cracks n_{cr} [-]:	4	5	7
average crack width w_m[mm]:	0.65	0.92	0.59
maximum crack width w_{max}[mm]:	0.80	1.28	0.89
average crack spacing s_{rm}[mm]:	106	123	88
maximum crack spacing $s_{r,max}$[mm]:	113	167	133
maximum load F_{max} [kN]	58.20	60.72	57.52
maximum reinforcement stress $\sigma_{nm,max}$ [MPa]:	1552	1619	1534
type of failure:	rupture of fibre strands		

UT-CG2-HSC-0°

reinforcement:	CG2 (SIT grid 050)
direction of investigation:	0° (warp direction)
number of reinforcement layers:	1
number of longitudinal fibre strands:	4
reinforcement area:	25.2 mm²

high strength concrete		
composition:	HSC-5.6mm	
concrete age at material test [d]:	8	44
$f_{c,cycl}$ [MPa]:	75.7	98.9
$f_{c,cube}$ [MPa]	105.2	108.5
E_{cm} [MPa]:	44,587	47,713
$f_{ct,sp}$ [MPa]:	5.3	5.5
$f_{ctm,calc}$ [MPa]:	4.8	5.0

geometry of specimen	
width b [mm]:	190
thickness t [mm]:	30
concrete coverage c [mm]:	13.5
reinforcement ratio ρ_l [%]:	0.44

test results			
test number	cyclic-1	cyclic-2	cyclic-3
concrete age at test [d]	53	52	44
load at initial crack F_{int} [kN]	27.46	25,40	25,68
initial crack opening w_{int} [mm]	0.60	0,64	0,56
stabilised cracking			
reinforcement stress σ_{nm} [MPa]:	799	752	936
number of cracks n_{cr} [-]:	3	3	3
average crack width w_m[mm]:	0.96	1,14	1,11
maximum crack width w_{max}[mm]:	1.27	1,40	1,49
average crack spacing s_{rm}[mm]:	146	190	151
maximum crack spacing $s_{r,max}$[mm]:	164	191	151
maximum load F_{max} [kN]	39.03	38,35	38,73
maximum reinforcement stress $\sigma_{nm,max}$ [MPa]:	1549	1522	1537
type of failure:	rupture of fibre strands		

UT-CG1-NSC-0°-2L

reinforcement:	CG1 (solidian GRID Q95-CCE-38)
direction of investigation:	0° (warp direction)
number of reinforcement layers:	2
number of longitudinal fibre strands:	5 per layer
reinforcement area:	75 mm²

normal strength concrete		
composition:	NSC-5.6mm	
concrete age at material test [d]:	8	13
$f_{c,cycl}$ [MPa]:	31.2	37.5
$f_{c,cube}$ [MPa]	38.4	46.0
E_{cm} [MPa]:	27,805	29,790
$f_{ct,sp}$ [MPa]:	2.6	2.7
$f_{ctm,calc}$ [MPa]:	2.3	2.4

geometry of specimen	
width b [mm]:	190
thickness t [mm]:	34
concrete coverage c [mm]:	13.5
reinforcement ratio ρ_l [%]:	1.16

test results			
test number	static	cyclic-1	cyclic-2
concrete age at test [d]	8	9	8
load at initial crack F_{int} [kN]	12.29	15,13	12,30
initial crack opening w_{int} [mm]	0.05	0,08	0,09
stabilised cracking			
reinforcement stress σ_{nm} [MPa]:	1116	1106	1189
number of cracks n_{cr} [-]:	15	11	14
average crack width w_m[mm]:	0.38	0,47	0,38
maximum crack width w_{max}[mm]:	0.74	0,66	0,69
average crack spacing s_{rm}[mm]:	45	58	41
maximum crack spacing $s_{r,max}$[mm]:	65	80	60
maximum load F_{max} [kN]	0.50	0,65	0,46
maximum reinforcement stress $\sigma_{nm,max}$ [MPa]:	0.85	0,90	0,69
type of failure:	rupture of fibre strands		

UT-CG1-NSC-0°-2L+

reinforcement:	CG1 (solidian GRID Q95-CCE-38)
direction of investigation:	0° (warp direction)
number of reinforcement layers:	2
number of longitudinal fibre strands:	5 per layer
reinforcement area:	75 mm²

normal strength concrete		
composition:	NSC-5.6mm	
concrete age at material test [d]:	8	13
$f_{c,cycl}$ [MPa]:	31.2	37.5
$f_{c,cube}$ [MPa]	38.4	46.0
E_{cm} [MPa]:	27,805	29,790
$f_{ct,sp}$ [MPa]:	2.6	2.7
$f_{ctm,calc}$ [MPa]:	2.3	2.4

geometry of specimen	
width b [mm]:	190
thickness t [mm]:	46
concrete coverage c [mm]:	13.5
reinforcement ratio ρ_l [%]:	0.86

test results			
test number	static	cyclic-1	cyclic-2
concrete age at test [d]	14	13	10
load at initial crack F_{int} [kN]	18.13	20.08	16.93
initial crack opening w_{int} [mm]	0.10	0.10	0.07
stabilised cracking			
reinforcement stress σ_{nm} [MPa]:	644	324	495
number of cracks n_{cr} [-]:	10	9	10
average crack width w_m[mm]:	0.32	0.15	0.22
maximum crack width w_{max}[mm]:	0.47	0.24	0.34
average crack spacing s_{rm}[mm]:	59	68	67
maximum crack spacing $s_{r,max}$[mm]:	86	84	84
maximum load F_{max} [kN]	120.20	125.29	121.55
maximum reinforcement stress $\sigma_{nm,max}$ [MPa]:	1603	1670	1621
type of failure:	rupture of fibre strands		

UT-CG1-NSC-0°-4L

reinforcement:	CG1 (solidian GRID Q95-CCE-38)
direction of investigation:	0° (warp direction)
number of reinforcement layers:	4
number of longitudinal fibre strands:	5 per layer
reinforcement area:	150 mm²

normal strength concrete		
composition:	NSC-5.6mm	
concrete age at material test [d]:	43	56
$f_{c,cycl}$ [MPa]:	34.7	37.0
$f_{c,cube}$ [MPa]	42.6	41.3
E_{cm} [MPa]:	27,992	28,717
$f_{ct,sp}$ [MPa]:	3.1	3.6
$f_{ctm,calc}$ [MPa]:	2.8	3.3

geometry of specimen	
width b [mm]:	190
thickness t [mm]:	46
concrete coverage c [mm]:	13.5
reinforcement ratio ρ_l [%]:	1.72

test results			
test number	static	cyclic-1	cyclic-2
concrete age at test [d]	43	57	55
load at initial crack F_{int} [kN]	18.36	25.07	22.10
initial crack opening w_{int} [mm]	0.03	0.04	0.07
stabilised cracking			
reinforcement stress σ_{nm} [MPa]:	721	1022	934
number of cracks n_{cr} [-]:	14	20	19
average crack width w_m[mm]:	0.23	0.25	0.25
maximum crack width w_{max}[mm]:	0.33	0.51	0.46
average crack spacing s_{rm}[mm]:	42	32	33
maximum crack spacing $s_{r,max}$[mm]:	56	57	56
maximum load F_{max} [kN]	241.03	213.69	204.49
maximum reinforcement stress $\sigma_{nm,max}$ [MPa]:	1607	1425	1363
type of failure:	anchorage failure in clamping		

UT-CG1-NSC-0°-16mm

reinforcement:	CG1 (solidian GRID Q95-CCE-38)
direction of investigation:	0° (warp direction)
number of reinforcement layers:	1
number of longitudinal fibre strands:	5
reinforcement area:	37.5 mm²

normal strength concrete		
composition:	NSC-16mm	
concrete age at material test [d]:	15	49
$f_{c,cycl}$ [MPa]:	31.1	35.6
$f_{c,cube}$ [MPa]	35.0	40.2
E_{cm} [MPa]:	28,633	30,399
$f_{ct,sp}$ [MPa]:	2.6	2.8
$f_{ctm,calc}$ [MPa]:	2.3	2.5

geometry of specimen	
width b [mm]:	190
thickness t [mm]:	50
concrete coverage c [mm]:	23.5
reinforcement ratio ρ_l [%]:	0.39

test results	
test number	static
concrete age at test [d]	50
load at initial crack F_{int} [kN]	19.36
initial crack opening w_{int} [mm]	0.21
stabilised cracking	
reinforcement stress σ_{nm} [MPa]:	1138
number of cracks n_{cr} [-]:	5
average crack width w_m[mm]:	1.04
maximum crack width w_{max}[mm]:	1.57
average crack spacing s_{rm}[mm]:	117
maximum crack spacing $s_{r,max}$[mm]:	169
maximum load F_{max} [kN]	60.20
maximum reinforcement stress $\sigma_{nm,max}$ [MPa]:	1605
type of failure:	rupture of fibre strands

UT-CG2-NSC-0°-16mm

reinforcement:	CG2 (SIT grid 050)
direction of investigation:	0° (warp direction)
number of reinforcement layers:	1
number of longitudinal fibre strands:	4
reinforcement area:	25.2 mm²

normal strength concrete		
composition:	NSC-16mm	
concrete age at material test [d]:	15	49
$f_{c,cycl}$ [MPa]:	31.1	35.6
$f_{c,cube}$ [MPa]	35.0	40.2
E_{cm} [MPa]:	28,633	30,399
$f_{ct,sp}$ [MPa]:	2.6	2.8
$f_{ctm,calc}$ [MPa]:	2.3	2.5

geometry of specimen	
width b [mm]:	190
thickness t [mm]:	50
concrete coverage c [mm]:	23.5
reinforcement ratio ρ_l [%]:	0.27

test results	
test number	static
concrete age at test [d]	46
load at initial crack F_{int} [kN]	21.94
initial crack opening w_{int} [mm]	0.59
stabilised cracking	
reinforcement stress σ_{nm} [MPa]:	1237
number of cracks n_{cr} [-]:	3
average crack width w_m[mm]:	1.35
maximum crack width w_{max}[mm]:	1.85
average crack spacing s_{rm}[mm]:	147
maximum crack spacing $s_{r,max}$[mm]:	200
maximum load F_{max} [kN]	39.41
maximum reinforcement stress $\sigma_{nm,max}$ [MPa]:	1564
type of failure:	rupture of fibre strands

UT-GG-NSC-0°-16mm

reinforcement:	GG (solidian GRID Q121-RRE-38)
direction of investigation:	0° (warp direction)
number of reinforcement layers:	1
number of longitudinal fibre strands:	5
reinforcement area:	51.2 mm²

normal strength concrete		
composition:	NSC-16mm	
concrete age at material test [d]:	15	49
$f_{c,cycl}$ [MPa]:	31.1	35.6
$f_{c,cube}$ [MPa]	35.0	40.2
E_{cm} [MPa]:	28,633	30,399
$f_{ct,sp}$ [MPa]:	2.6	2.8
$f_{ctm,calc}$ [MPa]:	2.3	2.5

geometry of specimen	
width b [mm]:	190
thickness t [mm]:	50
concrete coverage c [mm]:	23.5
reinforcement ratio ρ_l [%]:	0.54

test results	
test number	static
concrete age at test [d]	43
load at initial crack F_{int} [kN]	22.36
initial crack opening w_{int} [mm]	0.47
stabilised cracking	
reinforcement stress σ_{nm} [MPa]:	500
number of cracks n_{cr} [-]:	8
average crack width w_m[mm]:	1.05
maximum crack width w_{max}[mm]:	2.09
average crack spacing s_{rm}[mm]:	65
maximum crack spacing $s_{r,max}$[mm]:	104
maximum load F_{max} [kN]	29.96
maximum reinforcement stress $\sigma_{nm,max}$ [MPa]:	585
type of failure:	rupture of fibre strands

D.4 Slabs with textile reinforcement (S)

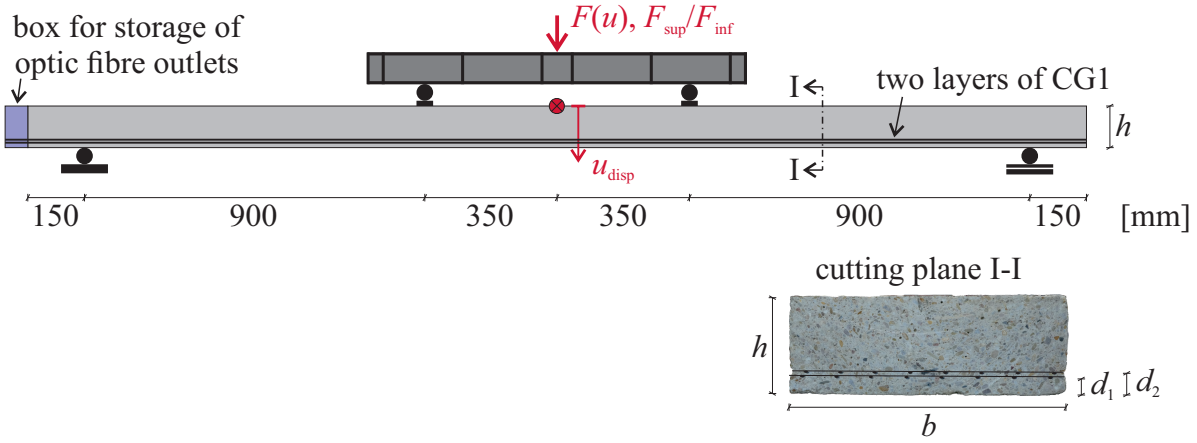
The following appendices refer to the slabs evaluated in Chapter 6, which were investigated in a four-point bending test setup. In addition to the geometrical properties and the reinforcement layout, the major values obtained in the conducted iterative determination of the cross-sectional curvature are also given, followed by the crack pattern obtained after the test. In the case of series S-CG2 and S-CG3, lap joints were placed in mid-span. In the case of series S-GG, an additional reinforcement layer was placed in mid-span, thus accounting for the higher bending moments present in this section.

S-CG1-NSC-0°

reinforcement:	CG1 (solidian GRID Q95-CCE-38)
direction of investigation:	0° (warp direction)
number of reinforcement layers:	2
reinforcement area:	120 mm²

normal strength concrete				
composition:	NSC-8mm			
concrete age at material test [d]:	13	28	29	114
$f_{c,cycl}$ [MPa]:	38.8	n/a	46.5	n/a
$f_{c,cube}$ [MPa]	45.4	49.6	n/a	55.4
E_{cm} [MPa]:	28,198	n/a	28,370	n/a
$f_{ct,sp}$ [MPa]:	3.0	3.4	n/a	n/a
$f_{ctm,calc}$ [MPa]:	2.7	3.1	n/a	n/a

geometry			
specimen	static	cyclic-1	cyclic-2
height h [mm]:	106	107	110
width b [mm]:	300	300	300
depth d [mm]:	87	87	91
concrete coverage c [mm]:	15.5	15.5	15.0
slenderness a/d [-]:	10.3	10.3	9.9
reinforcement ratio ρ_l [%] (referred to cross-section $b \cdot d$):	0.46	0.46	0.44
distance d_1 [mm]:	17	17	16
distance reinforcement layer (d_2 - d_1) [mm]:	5	6	5



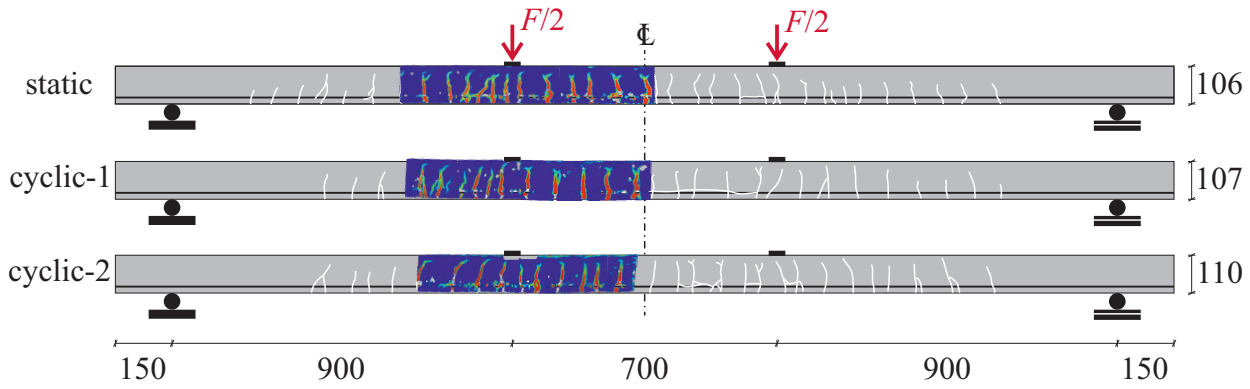
test results			
test number	static	cyclic-1	cyclic-2
concrete age at start of test [d]	13	14	114
bending moment[1)] at initial crack M_{cr} [kNm]:	1.73	1.68	2.18
bending moment[1)] at SLS criterion $l/250$ M_{SLS} [kNm]:	2.31	2.23	2.67
maximum bending moment[1)] M_{max} [kNm]:	15.09	14.76	15.94
deflection at maximum bending moment u_{max} [mm].	144.3	143.4	140.6
average crack spacing s_{rm} [mm]:	52	53	63
maximum crack spacing $s_{r,max}$[mm]:	78	80	85
cyclic loading			
bending moment[1)] at superior load level M_{sup} [kNm]:	-	4.0	4.4
bending moment[1)] at inferior load level M_{inf} [kNm]:	-	1.7	2.6
deflection at M_{sup} prior to cyclic loading $u_{sup,0}$ [mm].	-	28.7	28.2
increase in deflection after cyclic loading Δu_{sup} [mm].	-	12.5	7.5
type of failure:	rupture of fibre strands		

[1)] bending moment at mid-field including self-load and traverse

iterative determination of the cross-sectional curvature			
test number	static	cyclic-1	cyclic-2
at maximum bending moment			
reinforcement stress σ_{nm} [MPa] [2)]:	1597	1597	1597
force in compression zone F_c [kN]:	185.1	183.9	184.3
height of compression zone x [mm]:	16.0	15.8	15.9
calculated bending moment $M_{max,calc}$ [kNm]:	14.8	14.8	15.6
reinforcement stress at superior load level $\sigma_{nm,sup}$ [MPa] [2)]:	-	429	448
reinforcement stress at inferior load level $\sigma_{nm,inf}$ [MPa] [2)]:	-	181	264

[2)] at most-tensioned layer in mid-field

crack pattern

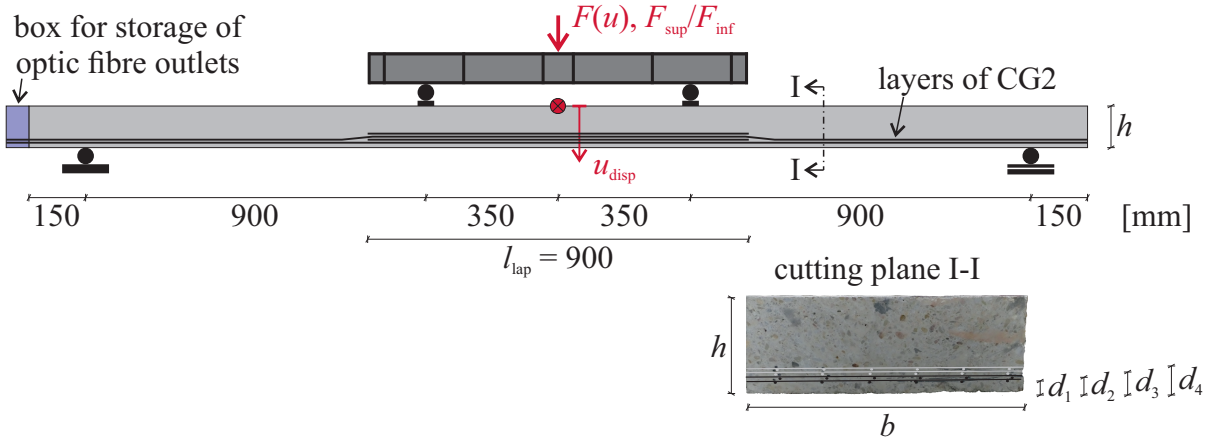


S-CG2-NSC-0°

reinforcement:	CG2 (SIT grid 050)
direction of investigation:	0° (warp direction)
number of reinforcement layers:	2 plus lap joints
reinforcement area:	75.6 mm² (151.2 mm² in lap)

normal strength concrete			
composition:	NSC-8mm		
concrete age at material test [d]:	29	30	117
$f_{c,cycl}$ [MPa]:	n/a	49.7	51.3
$f_{c,cube}$ [MPa]	45.4	49.6	n/a
E_{cm} [MPa]:	n/a	29,737	30,586
$f_{ct,sp}$ [MPa]:	n/a	3.3	3.9
$f_{ctm,calc}$ [MPa]:	n/a	3.0	3.5

geometry			
specimen	static	cyclic-1	cyclic-2
height h [mm]:	106	107	103
width b [mm]:	300	300	300
depth d [mm]:	90	90	90
concrete coverage c [mm]:	13.0	14.0	12.0
slenderness a/d [-]:	10.0	10.0	10.0
reinforcement ratio ρ_l [%] (referred to cross-section $b \cdot d$ and mid-span):	0.28	0.28	0.29
distance d_1 [mm]:	14	15	13
distance reinforcement layer (d_2 - d_1) [mm]:	5	5	5
distance reinforcement layer (d_3 – d_2) [mm]:	5	5	5
distance reinforcement layer (d_4 – d_3) [mm]:	5	5	5



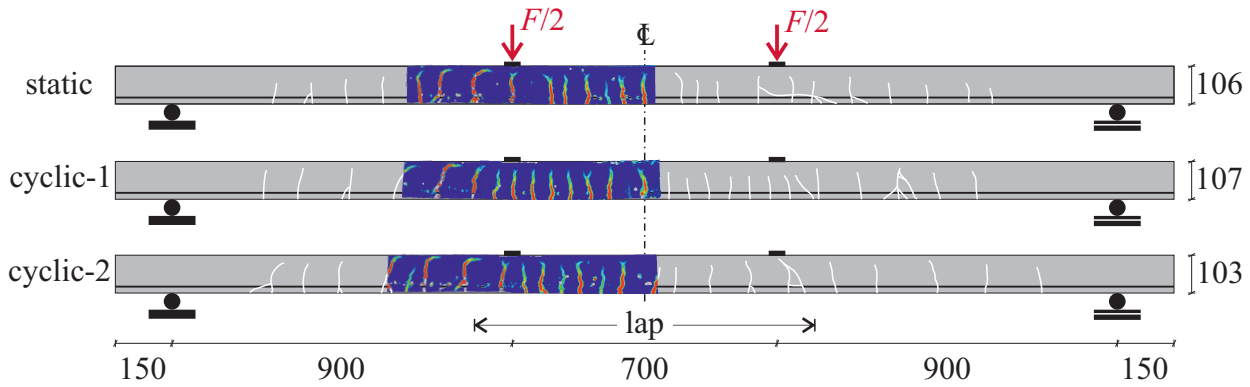
test results			
test number	static	cyclic-1	cyclic-2
concrete age at start of test [d]	29	30	117
bending moment[1)] at initial crack M_{cr} [kNm]:	2.02	1.84	2.29
bending moment[1)] at SLS criterion $l/250$ M_{SLS} [kNm]:	2.81	2.63	2.94
maximum bending moment[1)] M_{max} [kNm]:	12.76	13.15	12.11
deflection at maximum bending moment u_{max} [mm].	97.8	112.4	94.4
average crack spacing s_{rm} [mm]:	67	51	60
maximum crack spacing $s_{r,max}$[mm]:	113	91	107
cyclic loading			
bending moment[1)] at superior load level M_{sup} [kNm]:	-	4.3	3.5
bending moment[1)] at inferior load level M_{inf} [kNm]:	-	1.5	1.7
deflection at M_{sup} prior to cyclic loading $u_{sup,0}$ [mm].	-	27.5	14.3
increase in deflection after cyclic loading Δu_{sup} [mm].	-	14.4	4.7
type of failure:		splicing of laps	

[1)] bending moment at mid-span including self-load and traverse

iterative determination of the cross-sectional curvature			
test number	static	cyclic-1	cyclic-2
at maximum bending moment			
reinforcement stress σ_{nm} [MPa] [2)]:	1200	1291	1109
force in compression zone F_c [kN]:	162.7	173.2	150.9
height of compression zone x [mm]:	17	25	19
calculated bending moment $M_{max,calc}$ [kNm]:	13.0	13.2	12.1
reinforcement stress at superior load level $\sigma_{nm,sup}$ [MPa] [2)]:	-	433	317
reinforcement stress at inferior load level $\sigma_{nm,inf}$ [MPa] [2)]:	-	151	156

[2)] at most-tensioned layer in mid-span

crack pattern

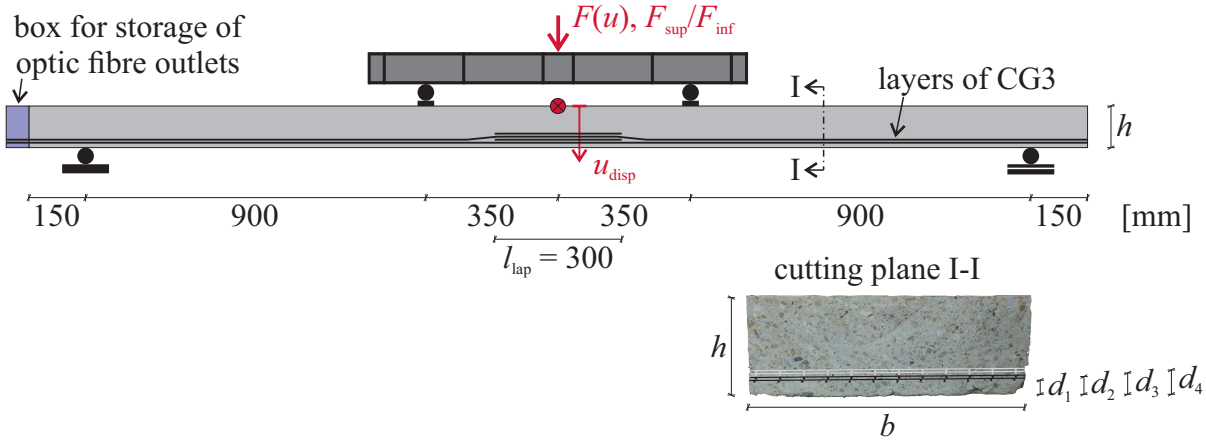


S-CG3-NSC-0°

reinforcement:	CG3 (HTC 25/25-80 UWX)
direction of investigation:	0° (warp direction)
number of reinforcement layers:	2 plus lap joints
reinforcement area:	79.2 mm² (158.4 mm² in lap)

normal strength concrete			
composition:	NSC-8mm		
concrete age at material test [d]:	28	29	117
$f_{c,cycl}$ [MPa]:	n/a	49.7	51.3
$f_{c,cube}$ [MPa]	59.0	n/a	61.1
E_{cm} [MPa]:	n/a	28,950	28,779
$f_{ct,sp}$ [MPa]:	n/a	3.7	3.8
$f_{ctm,calc}$ [MPa]:	n/a	3.3	3.4

geometry			
specimen	static	cyclic-1	cyclic-2
height h [mm]:	300	300	300
width b [mm]:	110	110	110
depth d [mm]:	93	93	93
concrete coverage c [mm]:	14.0	14.0	14.0
slenderness a/d [-]:	9.7	9.7	9.7
reinforcement ratio ρ_l [%] (referred to cross-section $b \cdot d$ and mid-span):	0.28	0.28	0.28
distance d_1 [mm]:	15	15	15
distance reinforcement layer (d_2 - d_1) [mm]:	5	5	5
distance reinforcement layer (d_3 – d_2) [mm]:	5	5	5
distance reinforcement layer (d_4 – d_3) [mm]:	5	5	5



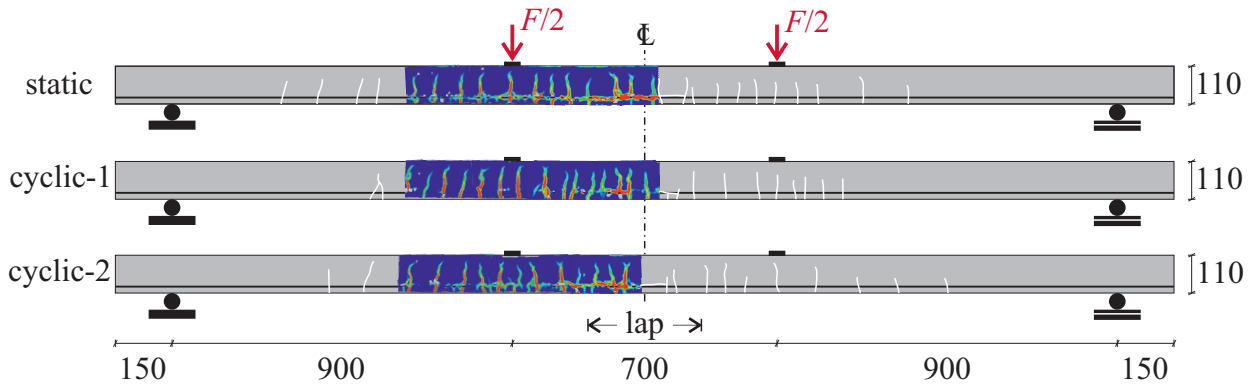
test results			
test number	static	cyclic-1	cyclic-2
concrete age at start of test [d]	28	46	116
bending moment[1)] at initial crack M_{cr} [kNm]:	2.04	1.96	2.60
bending moment[1)] at SLS criterion $l/250$ M_{SLS} [kNm]:	2.57	2.47	3.03
maximum bending moment[1)] M_{max} [kNm]:	6.45	8.28	7.45
deflection at maximum bending moment u_{max} [mm].	65.3	88.4	76.6
average crack spacing s_{rm} [mm]:	45	43	50
maximum crack spacing $s_{r,max}$[mm]:	81	57	76
cyclic loading			
bending moment[1)] at superior load level M_{sup} [kNm]:	-	4.4	4.4
bending moment[1)] at inferior load level M_{inf} [kNm]:	-	2.6	2.6
deflection at M_{sup} prior to cyclic loading $u_{sup,0}$ [mm].	-	35.5	33.7
increase in deflection after cyclic loading Δu_{sup} [mm].	-	12.0	10.4
type of failure:		splicing of laps	

[1)] bending moment at mid-span including self-load and traverse

iterative determination of the cross-sectional curvature			
test number	static	cyclic-1	cyclic-2
at maximum bending moment			
reinforcement stress σ_{nm} [MPa] [2)]:	600	750	658
force in compression zone F_c [kN]:	82.4	101.9	94.0
height of compression zone x [mm]:	13	24	24
calculated bending moment $M_{max,calc}$ [kNm]:	6.8	8.1	7.7
reinforcement stress at superior load level $\sigma_{nm,sup}$ [MPa] [2)]:	-	409	391
reinforcement stress at inferior load level $\sigma_{nm,inf}$ [MPa] [2)]:	-	241	231

[2)] at most-tensioned layer in mid-span

crack pattern

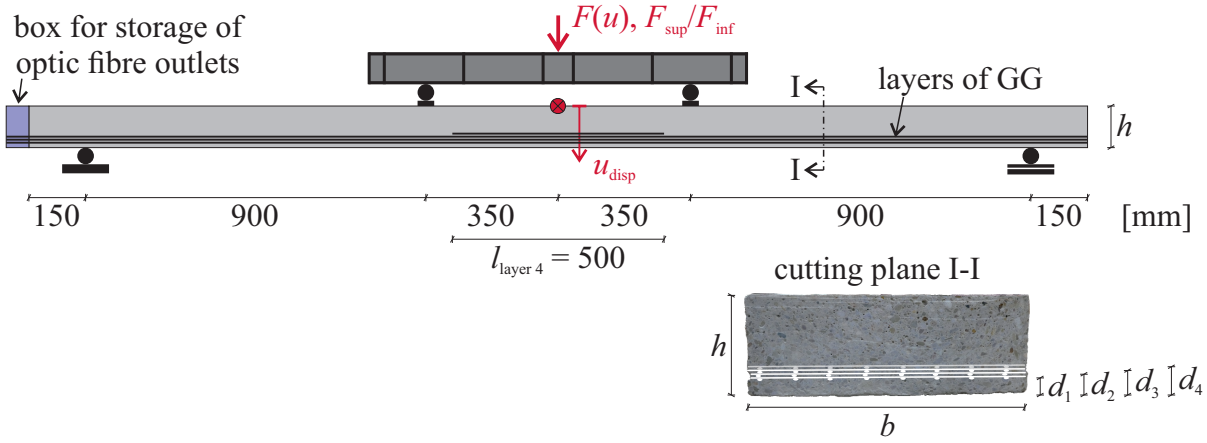


S-GG-NSC-0°

reinforcement:	GG (solidian GRID Q121-RRE-38)
direction of investigation:	0° (warp direction)
number of reinforcement layers:	3 plus addition layer in mid-span
reinforcement area:	246.0 mm² (and 328.0 mm² in mid-span)

normal strength concrete				
composition:	NSC-8mm			
concrete age at material test [d]:	27	28	69	112
$f_{c,cycl}$ [MPa]:	n/a	50.8	n/a	55.6
$f_{c,cube}$ [MPa]	58.7	n/a	63.8	69.3
E_{cm} [MPa]:	n/a	29,586	n/a	30,379
$f_{ct,sp}$ [MPa]:	3.9	n/a	n/a	4.1
$f_{ctm,calc}$ [MPa]:	3.5	n/a	n/a	3.7

geometry			
specimen	static	cyclic-1	cyclic-2
height h [mm]:	300	300	300
width b [mm]:	110	110	110
depth d [mm]:	88	90	90
concrete coverage c [mm]:	13.5	12.5	12.5
slenderness a/d [-]:	10.2	10.0	10.0
reinforcement ratio ρ_l [%] (referred to cross-section $b \cdot d$ and mid-span):	1.24	1.21	1.21
distance d_1 [mm]:	5	4	4
distance reinforcement layer (d_2 - d_1) [mm]:	5	4	4
distance reinforcement layer (d_3 – d_2) [mm]:	5	4	4
distance reinforcement layer (d_4 – d_3) [mm]:	4	4	4



test results			
test number	static	cyclic-1	cyclic-2
concrete age at start of test [d]	27	54	117
bending moment[1)] at initial crack M_{cr} [kNm]:	2.00	2.52	2.74
bending moment[1)] at SLS criterion $l/250$ M_{SLS} [kNm]:	2.39	3.21	3.11
maximum bending moment[1)] M_{max} [kNm]:	12.33	11.60	11.28
deflection at maximum bending moment u_{max} [mm].	145.5	115.2	108.3
average crack spacing s_{rm} [mm]:	53	48	52
maximum crack spacing $s_{r,max}$[mm]:	106	86	79
cyclic loading			
bending moment[1)] at superior load level M_{sup} [kNm]:	-	4.4	4.4
bending moment[1)] at inferior load level M_{inf} [kNm]:	-	2.6	2.6
deflection at M_{sup} prior to cyclic loading $u_{sup,0}$ [mm].	-	24.6	26.4
increase in deflection after cyclic loading Δu_{sup} [mm].	-	17.1	8.0
type of failure:	rupture of fibre strands		

[1)] bending moment at mid-span including self-load and traverse

iterative determination of the cross-sectional curvature			
test number	static	cyclic-1	cyclic-2
at maximum bending moment			
reinforcement stress σ_{nm} [MPa] [2)]:	530	450	437
force in compression zone F_c [kN]:	154.4	136.5	132.7
height of compression zone x [mm]:	15	16	15
calculated bending moment $M_{max,calc}$ [kNm]:	12.5	11.6	14.8
reinforcement stress at superior load level $\sigma_{nm,sup}$ [MPa] [2)]:	-	172	170
reinforcement stress at inferior load level $\sigma_{nm,inf}$ [MPa] [2)]:	-	101	100

[2)] at most-tensioned layer in mid-span

crack pattern

